Spin Labeling with Nitroxide, Trityl, and Copper Labels for Protein Structure Elucidation by EPR Spectroscopy

Dissertation

zur

Erlangung des Doktorgrades (Dr. rer. nat.)

der

Mathematisch-Naturwissenschaftlichen Fakultät

der

Rheinischen Friedrich-Wilhelms-Universität Bonn

vorgelegt von

Caspar Anton Heubach

aus

Adenau

Bonn 2024

Angefertigt mit Genehmigung der Mathematisch-Naturwissenschaftlichen Fakultät
der Rheinischen Friedrich-Wilhelms-Universität Bonn

Gutachter/Betreuer: Prof. Dr. Olav Schiemann
Gutachter: Prof. Dr. Ulrich Kubitscheck

Tag der Promotion: 10.10.2024
Erscheinungsjahr: 2024

Die vorliegende Arbeit wurde am *Clausius-Institut für Physikalische und Theoretische Chemie* der *Rheinischen Friedrich-Wilhelms-Universität Bonn* in dem Zeitraum von November 2018 bis März 2024 unter der Leitung von *Prof. Dr. Olav Schiemann* angefertigt.

Eigenständigkeitserklärung gemäß Promotionsordnung der Mathematisch-Naturwissenschaftlichen Fakultät der Rheinischen Friedrich-Wilhelms-Universität Bonn (§9, Absatz 1-3)

Hiermit versichere ich, dass ich die vorliegende Arbeit unter Einhaltung der Regeln guter wissenschaftlicher Praxis selbstständig verfasst habe, keine anderen als die hier angegebenen Quellen und Hilfsmittel verwandet und alle Zitate kenntlich gemacht habe. Während der Promotion und dem erstellen dieser Arbeit wurden keinerlei entgeltliche oder unentgeltliche Beratungs- oder Hilfsdienstleistungen in Anspruch genommen.

Parts of this thesis have been published in:

Peer-reviewed journals

K. Ackermann, **C. A. Heubach**, O. Schiemann, B. Bode*, "Pulse Dipolar Electron Paramagnetic Resonance Spectroscopy Distance Measurements at Low Nanomolar Concentrations: The Cu^{II}-Trityl Case", *J. Phys. Chem. Lett.* **2024**, 15, 1455–1461.

C. A. Heubach†, Z. Hasanbasri†, D. Abdullin, A. Reuter, B. Korzekwa, S. Saxena, O. Schiemann*, "Differentiating between Label and Protein Conformers in Pulsed Dipolar EPR Spectroscopy with the dHis-Cu^{2+}(NTA) Motif", *Chem. Eur. J.* **2023**, 29, e202302541.

O. Schiemann*, **C. A. Heubach**, D. Abdullin, K. Ackermann, M. Azarkh, E. G. Bagryanskaya, M. Drescher, B. Endeward, J. H. Freed, L. Galazzo, D. Goldfarb, T. Hett, L. E. Hofer, L. F. Ibáñez, E. J. Hustedt, S. Kucher, I. Kuprov, J. E. Lovett, A. Meyer, S. Ruthstein, S. Saxena, S. Stoll, C. R. Timmel, M. Di Valentin, H. S. Mchaourab*, T. F. Prisner*, B. E. Bode*, E. Bordignon*, M. Bennati*, G. Jeschke*, "Benchmark Test and Guidelines for DEER/PELDOR Experiments on Nitroxide-Labeled Biomolecules", *J. Am. Chem. Soc.* **2021**, 143, 43, 17875–17890.

N. Fleck, **C. A. Heubach**, T. Hett, S. Spicher, S. Grimme, O. Schiemann*, "Ox-SLIM: Synthesis and Site-Specific Labelling with a Highly Hydrophilic Trityl Spin Label", *Chem. Eur. J.* **2021**, 27, 5292–5297.

N. Fleck, **C. A. Heubach**, T. Hett, F. R. Haege, P. P. Bawol, H. Baltruschat, O. Schiemann*, "SLIM: A short-linked, highly redox-stable trityl label for high sensitivity in cell EPR distance measurements", *Angew. Chem. Int. Ed.* **2020**, 59, 9767–9772.

J. J. Jassoy†, **C. A. Heubach**†, T. Hett, F. Bernhard, F. Haege, G. Hagelueken, O. Schiemann*, "Site Selective and Efficient Spin Labeling of Proteins with a Maleimide-Funktionalized Trityl Radical for Pulsed Dipolar EPR Spectroscopy", *Molecules* **2019**, 24, 2735.

Theses

F. Haege, "A Stability Study of Trityl and Nitroxide Spin Labels for in-cell EPR Spectroscopy", *Master Thesis*, Rheinische Friedrich-Wilhelms-Universität Bonn, **2019**.

B. Korzekwa, "Application of Metal Ion Spin Labels for EPR Distance Measurements based on the Double-Histidine Motif", *Master Thesis*, Rheinische Friedrich-Wilhelms-Universität Bonn, **2019**.

Further Publications:

D. Nguyen, D. Abdullin, **C. A. Heubach**, T. Pfaffeneder, A. Nguyen,A. Heine, K. Reuter, F. Diederich, O. Schiemann, G. Klebe*, "Unraveling a Ligand-Induced Twist of a Homodimeric Enzyme by Pulsed Electron–Electron Double Resonance", *Angew. Chem. Int. Ed.* **2021**, 60, 23419–23426.

M.F. Peter, A.T. Tuukkanen, **C. A. Heubach**, A. Selsam, F.G. Duthie, D.I. Svergun, O. Schiemann, G. Hagelueken*, "Studying Conformational Changes of the Yersinia Type-III-Secretion Effector YopO in Solution by Integrative Structural Biology", *Structure* **2019**, 27, 1416–1426.

† These authors contributed equally.

* Corresponding author.

Acknowledgments

First and foremost, I would like to express my deep gratitude to my PhD supervisor, Prof. Olav Schiemann, for giving me the opportunity to pursue my PhD in his group. Over the past five years, he has been incredibly supportive of my work, always encouraging and promoting me and my research endeavors, and providing valuable advice whenever I needed it. I appreciate the opportunity he gave me to contribute to several scientific publications and his support for several grants and travel funds. I greatly enjoyed our discussions, which were rarely limited to scientific matters alone.

Moreover, I want to express my sincere gratitude to Prof. Ulrich Kubitscheck for serving as the second reviewer of my thesis, Jun. Prof. Ala Bunescu for chairing my doctoral committee, and Prof. U. Benjamin Kaupp for acting as an additional member of the examination committee.

Although the cover of this thesis features my name alone, scientific progress and success are rarely achieved by a single individual. Teamwork is the key, and the achievements presented in this thesis would not have been possible without the valuable contributions and discussions with my colleagues and collaboration partners, and I am deeply grateful to all of them. Here, I would like to express my sincere gratitude, especially to Dr. Tobias Hett for his invaluable contributions to the EPR measurements, insightful discussions, and for teaching me how to set up EPR measurements on my own. I also want to thank Dr. Nico Fleck for providing most of the spin labels used in this work and his enthusiasm for driving the success of our projects. Furthermore, I would like to thank Dr. Dinar Abdullin for his support in setting up the RIDME measurements and for the data evaluation using PDSFit. Lastly, I would like to give special thanks to my collaborators: Dr. Zikri Hasanbasri and Prof. Sunil Saxena from the University of Pittsburgh and Dr. Katrin Ackermann and Dr. Bela Bode from the University of St Andrews for their valuable contributions to the collaborative projects.
Furthermore, I would like to thank all the members of the Schiemann group - especially the biochemistry lab crew consisting of Maria Vicino, Alina Geis, Olivia Kendall, Yannik Limbach, and Catrin Allar - for making my PhD journey enjoyable and memorable, both in the lab and during our group activities. In addition, I would like to thank Anja Burbiel for her helping hand in all organizational matters and to Hamed Alaei for his efforts in spectrometer maintenance and his role as the group's photographer. A special thanks goes to the former group members PD Dr. Gregor Hagelüken, Nicole Florin, Dr. Peer Depping, Gabriele Alonso Rodriguez, and Jean Jacques Jassoy, who provided invaluable support in the early stages of my academic career.

I would like to thank my family for their continuous support throughout my entire academic journey – it would not have been possible without them. Last but not least, I would like to thank the two most important people in my life – my wife Lara and my daughter Carla – for supporting (and enduring) me throughout the time I spent working on this thesis, for lifting me up in tiring times, and for grounding me when needed. My gratitude to them is beyond words.

Abstract

Enzymatic activity of proteins and other biomolecules is closely linked to their three-dimensional structure and dynamics. From the vast toolbox of biophysical techniques to unravel biomolecular structures, pulsed dipolar electron paramagnetic resonance spectroscopy (PDS-EPR) is a widely applied method to investigate these structures and structural rearrangements. Commonly utilized nitroxide spin labels such as the methanethiosulfonate spin label MTSL are suitable for *in vitro* experiments and have been used to investigate protein complex formation, track conformational changes, and localize metal ions. However, there are currently three main issues regarding the application of nitroxide spin labels for the structural investigation of biomacromolecules. Despite their widespread use, there are no standardized guidelines for spin labeling, quantification of the labeling efficiencies, sample preparation, and data evaluation, which impedes the reproducibility of results and the drawing of biological conclusions. Together with the ever-increasing complexity of biological systems, it becomes more and more important to investigate these systems not as singular entities but within the context of their native environment, specifically at ambient temperatures and within cells. While nitroxide spin labels quickly degrade under the reductive conditions present in the cellular environment, redox-stable tetrathiatriarylmethyl (trityl, TAM) spin labels represent a promising alternative. While their characteristic EPR properties such as a narrow line width and long relaxation times at non-cryogenic temperatures make their application highly desirable, their inherent hydrophobicity imposes great challenges for efficient protein spin labeling, work-up, and data acquisition. In addition, the rotational flexibility of the bioconjugation group and the linker to the spin-bearing motif can add to the conformational distribution of the biomolecule and obstruct the detection of conformational changes of the biomolecule itself.

In the context of these challenges, this PhD thesis addresses the following points: (1) Giving community-approved, generalized guidelines for site-directed spin labeling (SDSL), quantification of labeling efficiencies, and acquisition of PDS data using the commonly utilized MTSL spin label. (2) Establishing a reliable spin labeling protocol for trityl-based spin labels. (3) Devising an approach to differentiate between label and protein conformers in EPR-derived distance restraints.

Addressing the first key point, using the *Yersinia* outer protein O (YopO) as a model system, a strategy to successfully label proteins with MTSL was implemented and high labeling efficiencies were confirmed. Designed as a multi-laboratory benchmark test, samples were shipped to collaborating research groups and each group performed Pulsed Electron-Electron Double Resonance (PELDOR) experiments. The resulting distance distributions were highly consistent across the individual laboratories and confirmed the robustness of sample preparation and data analysis. To address the second key challenge of unreliable protein spin labeling using trityl labels, an assessment of the labeling performance of a methanethiosulfonate- and a maleimide-conjugated trityl spin label highlighted the importance of the bioconjugation group. Fine-tuning of the chosen labeling conditions enabled the establishment of a reliable labeling protocol for maleimide-conjugated trityl spin labels. Using the next-generation trityl spin labels SLIM and Ox-SLIM, a first *in-cell* trityl-trityl double quantum coherence (DQC) time trace of a protein sample in *Xenopus laevis* oocytes could be recorded. Exploiting the sensitivity of these new trityl spin labels, EPR-based distance measurements at a protein concentration down to 10 nM were shown to be feasible. Encouraged by these results, preliminary steps were undertaken to demonstrate the applicability of the SLIM label in transfection experiments using more native eukaryotic systems such as HeLa cells. Many of the EPR-derived distance distributions of the herein performed studies on YopO showed bi- or even multimodal distance distributions, which could not be unequivocally assigned to either distinct protein or spin label conformations, induced by the flexible

bioconjugation groups connecting the label to the cysteine residue. To unravel these ambiguous results and address the third main objective, the conformationally restricted bipedal double histidine motif loaded with paramagnetic copper(II) nitrilotriacetic acid (dHis-Cu^{2+}(NTA)) was employed to distinguish between label and protein conformations. Exploiting the reduced conformational flexibility of the dHis-Cu^{2+}(NTA) spin label, it was revealed that the α-helical backbone of YopO adopts a single conformation in solution and that the bipedal label is a well-suited alternative to conventional spin labels for solving small-scale conformational differences, even in proteins with high native histidine abundance where unspecific labeling can be avoided by stoichiometric Cu^{2+}(NTA) addition.

The herein presented results provide valuable guidelines to the EPR community as well as non-experts for the application of nitroxide spin labels and PDS-EPR in structural biology, outline a reliable protocol for the routine application of maleimide-functionalized trityl spin labels in PDS-EPR, and showcases an approach to differentiate between spin label and protein conformations using the dHis-Cu^{2+}(NTA) spin label.

Table of Contents

1. Introduction

When the architect *Luis H. Sullivan* coined his famous dogma "(…) of all things organic and inorganic, of all things human and superhuman (…) *form ever follows function*" in 1896,[1] he was unaware that in the context of structural biology, the reverse – function follows form – holds true.[2] The shape of a biomolecule dictates its chemical properties, reactivity, molecular interactions, and enzymatic function, which ultimately determines its role in the cellular ensemble.[3] Knowing the form of a biological macromolecule enables the prediction of the molecular function, and a loss of form often comes along with a loss of function or, in the worst case, is the source of severe diseases such as Alzheimer's and Parkinson's disease.[4] The research field of structural biology is devoted to correlating the biomacromolecular function to its structure and dynamics.

1.1 Biomolecular Structure Elucidation

Over the period 2009 to 2018, the average development cost of a new drug approved by the United States Food and Drug Administration (FDA) ranged from $ 765.9 million to $ 2,771.6 million.[5] According to a study by *Kiriiri* et al. in 2020, the likeliest cause for failure of a potential drug candidate in clinical trials is poor efficacy to the drug target (Figure 1).[6]

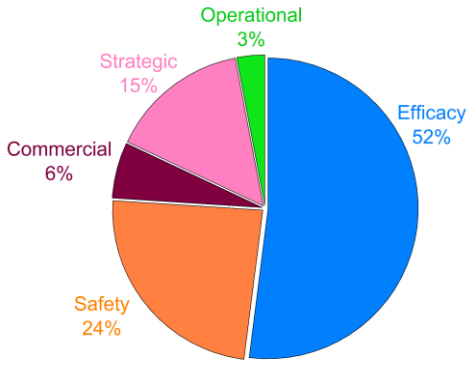

Figure 1: Pie chart displaying the causes of attrition in the discovery and development process of a novel drug. Adapted from reference [6].

Pharmaceutical companies are therefore urged to find ways for high-throughput and low-cost screenings in drug development to identify more easily suitable drug candidates that will pass clinical trials.[7] Since the initial success of the first rationally designed drugs based on structural information in the early 1990s against the proteinase of the human immunodeficiency virus type-1 (HIV-1),[8–10] structure-based drug design has played a key role in the development of new drugs.[11] Here, the three-dimensional structure of a target is used to identify potential leads, e.g. inhibitory compounds that bind to the target of interest. With structural information at hand, further refinement of these leads can enhance their affinity to the drug target, reduce their toxicity, and increase their stability.[12] Especially in the development of antibacterial drugs, structure-based drug design plays an important role in facilitating the discovery of new drugs and new drug targets alike to keep up with the rapidly increasing number of antibiotic-resistant bacterial strains.[13,14] Pioneered by *Alexander Fleming*, who discovered the antimicrobial effects of a green *Penicillium* mold fungus that led to the development of the first modern-era antibiotic penicillin,[15,16] early antibacterial drug research focused on screening thousands of bacterial and fungal species for signs of antibiotic activity, which is a time-consuming and costly process.[17]

According to a study by the Pew Research Institute from February 2015, 34 out of 37 antibacterial programs in clinical trials in the United States used structure-based methods to guide the development of inhibitory high-affinity small molecules.[18]
The demand for three-dimensional models and structural information on potential drug targets is reflected in the ever-growing number of macromolecular structures deposited in the Protein Data Bank (PDB). Initially developed as an archive for protein crystal structures at the Brookhaven National Laboratories in 1971,[19] the platform contained approximately 10,500 macromolecular structures in the year 2000 and by January 2023, the number of structures available on the platform exceeded 200,000 – an increase of almost 2,000%. This tremendous increase over the past decades was achieved by several factors. On the one hand, improved techniques in both, molecular biology and purification techniques, enhanced the scope of potentially available targets. On the other hand, rapid innovation of established biophysical methods such as X-ray crystallography,[20,21] nuclear magnetic resonance (NMR) spectroscopy,[22] and cryo-electron microscopy (cryo-EM) as well as the development of completely new ways to gather structural information of biomolecules such as molecular dynamics (MD) or artificial intelligence (AI) guided neural networks enabled researchers worldwide to pursue increasingly hard-to-obtain structural information.[12]

1.1.1 X-ray Crystallography

Until today, X-ray crystallography is the main method for structure elucidation of biological macromolecules at atomic resolution. Since the first discovery of X-rays by *Wilhelm Conrad Röntgen* in 1895,[23,24] it took more than half a century for the first atomistic model of a biomacromolecule solved by X-ray crystallography to be published. Benefiting from the discoveries of X-ray diffraction on crystalline matter by *Max von Laue*,[25,26] the underlying scattering fundamentals known as Bragg's law derived by *William Lawrence Bragg*,[27] and the possibility to crystalize enzymes demonstrated by *James Sumner*,[28] *John Kendrew* succeeded to solve the crystal structure of sperm whale myoglobin in 1957 at a resolution of 6 Å.[29] Three years earlier, *James Watson* and *Francis Crick* predicted the double-helix nature of desoxyribonucleic acid (DNA) based on images of the distinct diffraction pattern of DNA fibers generated by *Rosalind Franklin*.[30,31] However, it took almost 30 years to visualize the double-helix structure of DNA on an atomic level.[32] Following these initial success stories, the fast-paced development of increasingly more powerful light sources such as synchrotron radiation, new methods to overcome the phase problem, and better screening techniques for crystal growth led to a rapidly increasing number of biomacromolecular structures solved by X-ray crystallography. The dominance of X-ray crystallography in structural biology is reflected by the fraction of published structures on the PDB, where more than 85% were solved by X-ray crystallography (April 2023).
X-ray crystallography provides atomic resolution of crystalline samples without size restriction to the biomolecule and is especially useful for the investigation of highly ordered, rigid structures.[33] However, this limits the target scope of the method since well-diffracting crystals are mandatory for good diffraction images. Especially for disordered and flexible proteins or integral membrane proteins that are embedded in detergents or membrane mimetics, small crystal contact areas and poor crystal uniformity hamper crystal formation and may lead to low-resolution diffraction images.[34] In addition, crystal packing effects can perturb the native structure or select a subset of the total conformational ensemble the molecule adopts in solution.[35]

1.1.2 Nuclear Magnetic Resonance Spectroscopy

In contrast to X-ray crystallography, NMR spectroscopy allows for structure determination in the liquid state without the necessity of crystals. Since the pioneering work of *Felix Bloch* and *Edward*

M. Purcell who demonstrated the magnetic resonance of hydrogen nuclei in a static external magnetic field in 1946,[36,37] NMR became a routine method for the characterization and identification of small molecules in chemistry and biology. Initially considered unsuitable for application to larger molecules, the first NMR spectrum of a protein, the enzyme Ribonuclease 1, was published by *Martin Saunders* in 1957.[38] With the advent of superconducting magnets, Fourier transform (FT) spectroscopy, 2-D spectroscopy, and the possibility of isotope enrichment of ^{13}C and ^{15}N, NMR spectroscopy allowed researchers to build atomistic models of biomolecules that were not amenable by X-ray crystallography. In 1984, the group of Nobel laureate *Kurt Wüthrich* was able to solve the first *de novo* structure of a protein, the proteinase inhibitor IIA.[39] In general, to avoid overlapping signals due to the high abundance of ^{1}H nuclei in a protein, two-dimensional NMR experiments such as nuclear Overhauser enhancement spectroscopy (NOESY) and correlation spectroscopy (COSY) are used and the individual signals are assigned to specific atoms, thereby generating a set of restraints from which an atomic model can be built.[40] Notably, this technique has been used to solve the three-dimensional structure of an isotope-labeled protein within living cells.[41] While common solution NMR is suited for proteins with molecular weights up to 100 kDa,[42] the increasing number of signals, spectral overlap, and indistinguishability of the signals in larger systems make data analysis and assignment to the individual residues increasingly difficult.[43,44] In addition, for membrane proteins that are especially difficult to crystalize or large insoluble complexes such as amyloid fibrils, magic-angle spinning solid-state NMR (MAS SSNMR) enables structure determinations in native environments such as lipid bilayers.[45]

1.1.3 Cryo-Electron Microscopy

In recent years, single-particle cryo-electron microscopy (cryo-EM) has emerged as the third powerful method for biomolecular structure elucidation at a near-atomic resolution. Awarded the Nobel prize in 2017, *Richard Henderson*, *Joachim Frank*, and *Jacques Dubochet* helped to overcome limiting factors of cryo-EM such as sample preparation and data evaluation.[46–48] Initially providing only low-resolution envelope structures, the introduction of cameras directly detecting electrons leaped the achievable resolution limit into new spheres and enabled atomic resolution.[49,50]

For high-resolution cryo-EM imaging, no crystallization is required and the investigated biomolecule is diluted and dispersed as a thin liquid film on a support grid, usually a holey carbon film, and then frozen in liquid ethane before the measurement.[51] To avoid radiation damage caused to the sample by the electrons, only a low electron dose (about 20-40 electrons per $Å^2$) is applied in the imaging process and the resulting low contrast is compensated by averaging many particles. The image of a single particle reflects a two-dimensional projection of the object with higher contrast in structurally denser areas. If the particles are randomly oriented on the grid, computational alignment of the two-dimensional Fourier transforms permits the generation of a three-dimensional model.[52] In contrast to X-ray crystallography, the frozen-solution conditions of cryo-EM make difficult targets amenable. Thus, structural information can be gained for systems of high molecular weight, e.g. multi-domain complexes like fungal fatty acid synthases (FAS) and detergent-solubilized or membrane-mimetic embedded integral membrane proteins that generate low crystal contacts.[53,54] Outstanding examples of structures solved by single-particle cryo-EM are the structures of the Zika virus and the 100S ribosome dimer of gram-positive *S. aureus*.[55,56] As proven by these examples, the method has virtually no limitation towards higher molecular weight particles. However, its feasibility is limited for smaller molecules (below 50 kDa), where the small size of the particles results in low contrast to the surrounding buffer, and averaging over more particles is necessary to achieve a high resolution.[57] While the heterogeneity

of the sample composition in single-particle cryo-EM imposes difficulties in the correct alignment of the individual images,[58] it also offers the opportunity to visualize distinct relevant conformational states of a biomolecule free from crystal-packing effects or knock-out mutations and thereby decipher the structural basis for the underlying enzymatic mechanism.[59]

1.1.4 Förster Resonance Energy Transfer

Structural information of biomolecules does not necessarily need to be obtained at atomic resolution. An optical technique for the visualization of nanometer-scale proximity detection is Förster resonance energy transfer (FRET). Based on the initial experiments of *Günther Cario* and *James Franck*, *Theodore Förster* finalized the theory of the non-radiative energy transfer from a donor to an acceptor chromophore in 1946.[60,61] The specific requirements for FRET are an overlap of the emission spectrum of the donor fluorophore and the excitation spectrum of the acceptor fluorophore as well as the proximity of the two fluorophores in the range of usually 1-10 nm.[62] By exiting the donor chromophore with a wavelength that is not absorbed by the acceptor fluorophore, the donor can excite a nearby acceptor which then emits a lower energy wavelength (Figure 2a). The efficiency of this transfer is inversely proportional to the sixth power of the distance between both chromophores as well as their relative orientation, hence enabling extraction of the inter-chromophore distance from the emitted light intensity (Figure 2b).[63]

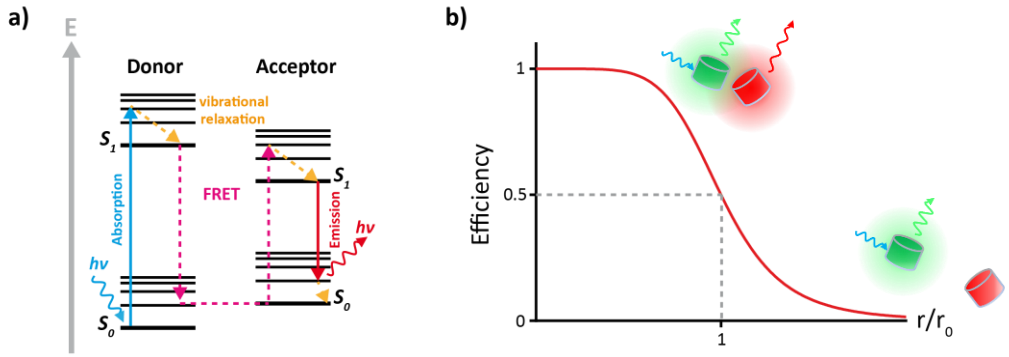

Figure 2: FRET effect between a donor and an acceptor fluorophore and the distance dependence. **a)** Exemplifying Jablonski diagram of FRET with a donor and an acceptor fluorophore. **b)** Scheme showcasing the distance dependence of the FRET efficiency based on the inter-fluorophore distance, with r being the distance between the donor-acceptor pair and r_0 the Förster distance where the transfer efficiency is exactly 50%. Adapted from reference [63].

Since the distance range at which FRET occurs is on the length scale of many biological systems, FRET can provide distance information between two chromophores and is thereby often termed a molecular ruler.[64] FRET measurements can detect intramolecular conformational changes of a biomolecule, e.g. upon substrate binding to an enzyme, monitor intermolecular oligomerization events, or study kinetics. Similar to NMR, FRET is an ensemble technique that can be measured in solution at ambient temperature and that can be performed in living cells.[62] In the special case of single-molecule FRET (smFRET), conformational states of a single biomolecule can be traced directly, thereby circumventing asynchronicity and averaging of conformational dynamics of the bulk molecules as in the conventional ensemble approach.[65] Except for homoFRET,[66] the donor and acceptor chromophores in a FRET experiment need to be different, rendering conventional labeling strategies inefficient due to statistic chromophore matching and ensuing lower FRET efficiencies.[67] However, statistic chromophore matching can be avoided by using orthogonal labeling approaches or fluorescent fusion proteins such as the green fluorescence protein (GFP) from the jellyfish *Aequoria victoria*.[68] Additionally, most chromophores consist of extended

conjugated π-systems with flexible linkers, a requirement for the correct alignment of the donor and acceptor dipoles to enable FRET, and their size relative to the biomolecule can be significant. This can potentially cause interference with the protein backbone or the reporter fluorophore and make the detection of small-scale conformational changes challenging.[69]

1.1.5 Computational Structural Biology

Driven by the rapid advancement in computer performance and user accessibility of software applications in the 20th and 21st centuries, computational methods have gained increased attention in structural biology. Complementary to the aforementioned experimental methods, computational methods such as MD simulations,[70] sequence alignments for structure predictions based on known homologs,[71] and machine learning algorithms offer new ways to shed light on previously unknown or experimentally undeterminable biomolecular structures, their dynamics, or ligand affinities.

Following the first 9.2 ps-long MD simulation of bovine pancreatic trypsin inhibitor (BPTI), a 58 amino acid peptide, by the group of *Martin Karplus*,[72] hardware and software innovations as well as steadily decreasing cost for computational time led to a rapid development in the field of computational structural biology, nowadays allowing for MD simulation of much larger molecules and complexes for an extended simulation time (up to 1 ms).[73,74] Based on empirical physical models, so-called force fields,[75] MD simulations are especially powerful for studying the spatiotemporal dynamics of biomolecules at atomic resolution, e.g. structural fluctuations, ion migration through channel proteins, substrate binding trajectories, or the sequential changes in a biomolecular structure upon ligand binding.[76] The accuracy of classical MD simulations heavily depends on the chosen force field and constitutes a balance between accuracy and time efficiency,[77] but the results of the molecular mechanics (MM) simulations can be improved at the cost of computational time by including more sophisticated computational methods such as density functional theorems (DFT) in quantum mechanics (QM) simulations using a hybrid MM/QM scheme.[78] In addition, most MD applications rely on accurate structural input models, often provided as experimental data, since preliminary *ab initio* folding of enzymes remains a challenging and computationally costly task.[79]

According to Anfinsen's dogma postulated by Nobel laureate *Christian Anfinsen*, each globular protein possesses a unique structure of minimal free energy that is determined solely by its amino acid sequence.[80] However, protein folding is an immensely complex process and according to *Cyrus Levinthal*, this process has to proceed via directed and predefined low-energy intermediate states of protein sub-regions before the global tertiary structure is adopted.[81] The prediction of said protein structure based on its amino acid sequence is known as the "protein folding problem" and solving it has become one of the largest goals in structural biology.[82] A widely recognized breakthrough in protein structure prediction was achieved in 2020 at the 14th biannual **C**ritical **A**ssessment of **P**rotein **S**tructure **P**rediction (CASP) contest, a benchmark competition in *de novo* protein structure prediction, by the neural network AlphaFold2 developed by DeepMind.[83] For the given CASP14 dataset, AlphaFold2 achieved a median backbone accuracy of 0.96 Å root-mean-square deviation at 95% residue coverage ($rmsd_{95}$), which is considered competitive with experimental methods.[83] Simultaneously, the RoseTTaFold neural network was developed and published, which enables structure prediction of proteins on a similar confidence level as AlphaFold2 and can predict protein-protein complexes.[84] In brief, AlphaFold2 and RoseTTaFold are machine-learning algorithms that combine empirical knowledge about protein structures such as torsion angles, bond lengths, and steric interactions with existing experimental structures deposited in the PDB and sequence alignments. While the prediction accuracy of the neural networks is remarkable for most sequences, they struggle when coping with novel or unexpected

sequences and structural features that are not included or iterations of the initial training sets, hence making experimental cross-validation of the predicted models mandatory.[85] Since the only input information is the amino acid sequence, the algorithms cannot include bound metal ions, cofactors, or other ligands, which are often key to enzymatic function.[86] Nevertheless, the quality of the models provided by AlphaFold2 and similar networks enable new opportunities to verify hypotheses of protein structures, refine existing models, or provide starting points for experimental design setups.[87]

1.1.6 Integrative Structural Biology

As outlined in sections 1.1.1 to 1.1.5, all methods for biomacromolecular structure elucidation have their unique strengths and weaknesses, making it impossible to address any given problem using only one methodology. Understanding biological function often involves the characterization and interplay of multiple molecular entities in higher-order molecular assemblies and complexes, which can evade structural characterization by a single method.[88] While some methods such as X-ray crystallography provide atomic resolution, they cannot visualize heterogeneity or molecular motion and dynamics that other methods, e.g. FRET, can provide, thereby leading to potentially ambiguous conclusions. To map the molecular architecture of complex systems with a higher level of confidence, an approach called integrative structural biology has gained widespread attention in modern-era structural biology. While the information obtained by a single experimental setup may be insufficient to build a comprehensive model or theory, all available structural information gathered by two or more complementary techniques is combined in integrative structural biology to overcome the limitations of the individual methods with the ultimate goal of generating a holistic model.[89] Experimental as well as theoretical data gathered by the individual methods are combined and each data set contributes by giving a unique set of restraints, e.g. distance restraints for amino acid pairs obtained by FRET, low-resolution density envelopes by small-angle X-ray scattering (SAXS), proximity restraints by cross-linking mass spectrometry (XL-MS), or stoichiometry coefficients obtained by mass spectrometry. From these restraints, an integrative structural model is built that complies with the individual input information in their estimated error ranges (Figure 3).[90] Remarkable examples of the potential of integrative methods to structurally characterize complex systems are the sub-nanometer-resolution structure of the ~52 MDa nuclear pore complex (NPC) of yeast consisting of 552 proteins or the atomic model of the insoluble type-III secretion system (T3SS) needle of *Salmonella typhimurium*.[91,92]

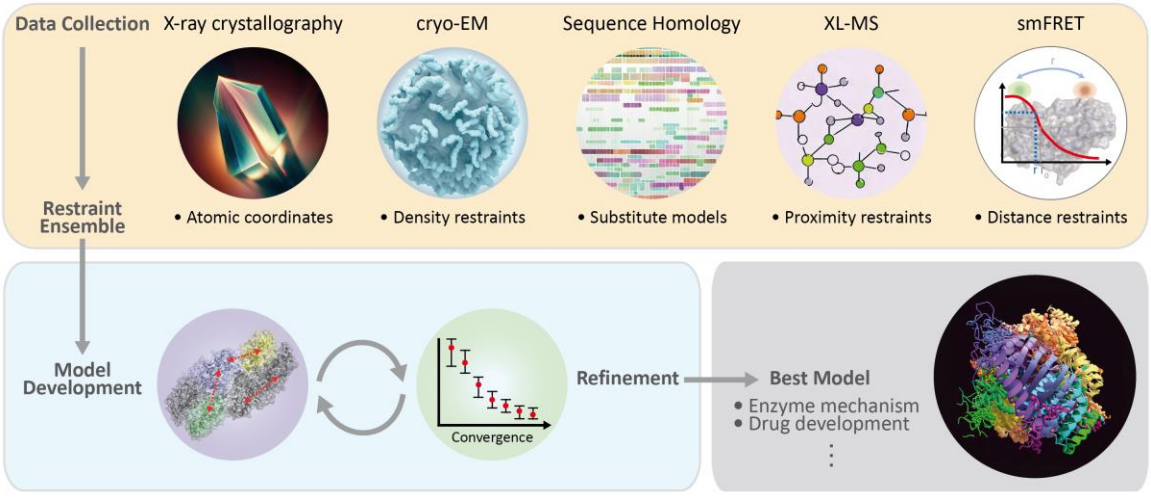

Figure 3: Schematic representation of an arbitrary integrative structural biology workflow. After data collection with various complementary techniques, an ensemble of individual restraints is generated (orange box) and used to develop an initial model, which is refined in an iterative process (blue box). The resulting best model after convergence may then be used to hypothesize about the enzymatic mechanism or to identify leads for structure-based drug design (grey box). Individual images were generated using Microsoft Bing Image Generator.

1.2 EPR Spectroscopy

An increasingly popular technique in structural biology is electron paramagnetic resonance (EPR) spectroscopy, also referred to as electron spin resonance (ESR). Initially discovered in 1944 by *Yevgeny Zavoisky*, who observed the microwave radiation resonance absorption of $CuCl_2 \cdot H_2O$ in an externally applied magnetic field,[93] EPR spectroscopy is closely related to NMR spectroscopy and based on the microwave-induced electron-spin transition of unpaired electrons in an external magnetic field.[94] Contrary to NMR, where nuclear-spin transitions are achieved using radio frequencies, EPR requires electromagnetic radiation of higher frequency (microwaves) and, consequently, lower magnetic fields to achieve resonance. Compared to NMR, EPR is approximately three orders of magnitude more sensitive.[95]

EPR has widespread applications in chemistry, physics, or material science to detect and characterize systems containing one or more unpaired electrons. In the context of structural biology, EPR spectroscopy can be applied to biological systems containing one or more paramagnetic centers to probe the local binding environment of the spin center, investigate residual conformational flexibilities, or obtain distance distributions of two or more paramagnetic centers in a biomolecule.[95]

1.2.1 Theoretical Background

The theoretical background of EPR spectroscopy is given in the following section and resembles a summary from a set of textbooks, educational scrips, and publications.[96–106] The fundamental concepts of EPR spectroscopy presented on the pages 8 to 10 are largely adapted from reference [96].

The experimental observation by *Stern* and *Gerlach* in 1922 of a discontinuous deflection pattern of a silver atom beam in an external magnetic field gave proof of the quantization of the electron's angular momentum, which is referred to as the so-called electron spin $\vec{s}$.[107] As a charged particle with an angular momentum, the electron possesses a magnetic moment

$$\overrightarrow{\mu_e} = -g_e \frac{e}{2m_e} \vec{s} \qquad \text{(eq. 1)}$$

where $g_e = 2.0023$ denotes the Landé factor (g-factor), e the elementary charge, m_e the electron mass, and $\vec{s}$ the electron-spin vector. The length of the electron-spin vector is defined as

$$|\vec{s}| = \sqrt{s(s+1)}\hbar \qquad \text{(eq. 2)}$$

where $s = \frac{1}{2}$ denotes the spin quantum number, and $\hbar$ is the reduced Planck constant. In an external magnetic field $\overrightarrow{B_0}$, the electron-spin $\vec{s}$ will align parallel or antiparallel to the magnetic field. The spin contribution along the magnetic field axis B_0, commonly the z-direction in a laboratory coordinate system, is defined as

$$s_z = m_s \hbar \qquad \text{(eq. 3)}$$

where m_s is the magnetic quantum number with discrete values of $\pm\frac{1}{2}$ for a $s = \frac{1}{2}$ system. Due to the Heisenberg uncertainty principle, the s_x- and s_y-components cannot be determined alongside s_z and the magnitude $|\vec{s}|$. Following the z-orientation of the electron spin along the magnetic field, the contribution of the magnetic moment $\overrightarrow{\mu_e}$ in z-direction is given by

$$\mu_{e,z} = -g_e \frac{e\hbar}{2m_e} m_s = -g_e \mu_B m_s \qquad \text{(eq. 4)}$$

where μ_B denotes the Bohr magneton. A simplified energy scheme of the electron magnetic moment in an external magnetic field B_0 as a function of the angle Θ between the magnetic field and the dipole axis is given in Figure 4.

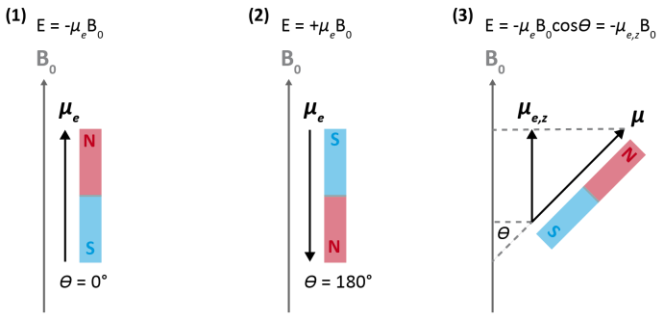

Figure 4: Energy scheme of an electron magnetic moment in an external magnetic field as a function of the angle Θ between the magnetic field B_0 and the electron dipole axis. For $\Theta = 0°$ **(1)** the energy is minimal, while for $\Theta = 180°$ **(2)** the energy is maximal. For all intermediate angles Θ, the energy lies between these two extremes **(3)**. Adapted from reference [106].

While both spin orientations $m_s = \pm\frac{1}{2}$ are energetically degenerate in the absence of an external magnetic field, the energy levels split upon applying a magnetic field.

$$E = -\mu_{e,z} B_0 = g_e \mu_B m_s B_0 \begin{cases} \nearrow E_{(m_s=+\frac{1}{2})} = +\frac{1}{2} g_e \mu_B B_0 \\ \searrow E_{(m_s=-\frac{1}{2})} = -\frac{1}{2} g_e \mu_B B_0 \end{cases} \quad \text{(eq. 5)}$$

The splitting of the energy levels is known as the electron-Zeeman effect. Both energy levels are separated by

$$\Delta E = E_{(m_s=+\frac{1}{2})} - E_{(m_s=-\frac{1}{2})} = g_e \mu_B B_0 \quad \text{(eq. 6)}$$

and the population of each energy level is governed by the Boltzmann distribution. Therefore, the ratio between both $m_s = \pm\frac{1}{2}$ spin states is given by

$$\frac{N_{(m_S=+\frac{1}{2})}}{N_{(m_S=-\frac{1}{2})}} = e^{-\frac{\Delta E}{k_B T}} = e^{-\frac{g_e \mu_B B_0}{k_B T}} \quad \text{(eq. 7)}$$

where $N_{(m_s=\pm\frac{1}{2})}$ is the population number of the given spin state, k_B is the Boltzmann constant, and T the temperature. At a magnetic field of $B_0 = 340$ mT and a temperature of $T = 300$ K, the ratio between both spin states is 0.999,[96] meaning that the excited $m_s = +\frac{1}{2}$ state is only slightly less populated than the $m_s = -\frac{1}{2}$ ground state. According to eq. 7, the population of the ground state can be increased by higher magnetic field strength and by reducing the temperature. Electron-spin transitions from the ground state to the excited state can be induced by microwave radiation that fulfills the resonance condition with the radiation energy

$$\mathrm{h}\nu = \Delta E = g_e \mu_B B_0 \quad \text{(eq. 8)}$$

where h is the Planck constant and ν is the frequency of the microwave radiation. If the resonance condition is met, a transition from the ground state to the excited state occurs and the absorption of microwave radiation is observed (Figure 4a+b). Since the population difference between both spin states and therefore the microwave absorbance is low, common EPR spectrometers are equipped with a resonator and a lock-in detector that creates a second external magnetic field modulated at a frequency of ~100 kHz to enhance sensitivity. This comes at the price of a limited bandwidth and commercial resonators are available only for certain microwave frequency ranges (Table 1). While keeping the microwave frequency constant at the resonator frequency, the magnetic field is swept until the resonance condition is met. This experimental setup is called continuous-wave (cw) field-swept EPR and the obtained spectrum is the first derivative of the absorption spectrum (Figure 5).

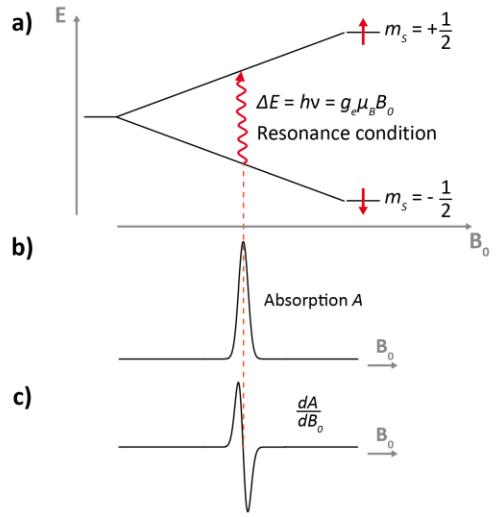

Figure 5: Schematics of the Zeeman effect. **a)** Zeeman splitting of an electron spin in an external magnetic field B_0. **b)** Observed microwave absorption when the resonance condition is met. **c)** First derivative of the absorption in **(b)** obtained by the field modulation as commonly applied in cw-EPR.

Table 1: Most common EPR frequency bands and their respective microwave frequency and magnetic field ranges for a *g*-factor = 2.

Frequency band	for *g*-factor = 2	
	Frequency (GHz)	**Magnetic Field (T)**
S-band	2 – 4	0.07 – 0.42
X-band	9 – 10	0.32 – 0.36
Q-band	33 – 35	1.2 – 1.3
W-band	> 94	3.4

The energy gap at which the resonance condition is met depends on both, the magnetic field strength and microwave frequency. Similar to the chemical shift in NMR, the position of the absorption line in EPR is given by the *g*-factor, an intrinsic and characteristic property of the spin system. The *g*-factor is defined as

$$g = \frac{h\nu}{\mu_B B_0} = \left(7.144775 \cdot 10^{-2} \frac{mT}{MHz}\right) \frac{\nu}{B_0} \qquad \text{(eq. 9)}$$

and is a dimensionless unit. For a free electron, the *g*-factor is $g = g_e = 2.0023$. When located in a molecular or atomic orbital, the *g*-factor of an unpaired electron differs from g_e due to electronic interactions and spin-orbit coupling. While organic radicals have *g*-values close to g_e, the *g*-value of unpaired electrons in metal centers can differ significantly from g_e. Thus, the *g*-factor can be used to distinguish multiple paramagnetic species in a mixture or to characterize the local binding and coordination sphere of a spin center.

In addition to spin-orbit coupling, the magnetic moment of the electron spin can couple to nuclei with a nuclear spin-quantum number $I > 0$, causing the splitting of the absorption line into $M = 2I + 1$ lines. This splitting is referred to as hyperfine splitting and the hyperfine coupling constant A_{iso}, which determines the width of splitting, has a linear dependency on the nuclear magnetic moment μ_I of the coupled nucleus as well as the spin density $|\psi(r)|^2$ of the unpaired electron at the position of the nucleus ($r = 0$) (Fermi contact interaction). In most cases, the unpaired electron is located in energetically higher *p*-, *d*-, or π-orbitals, which have no electron density at the nucleus' position ($r = 0$). However, they induce polarization of the spin density of the *s*-orbitals, therefore causing a shift in the spin density at the nucleus' position, which in turn leads to hyperfine coupling.

For a nitroxide radical, where the unpaired electron is located in a π-orbital of the N–O$^\bullet$ group, the electron spin $s = \frac{1}{2}$ is coupled to the nuclear spin $I = 1$ of the ^{14}N nucleus. In an externally applied magnetic field B_0, the Zeeman splitting and hyperfine coupling to the ^{14}N nucleus leads to six distinct energy levels with three allowed transitions according to the selection rules $\Delta m_s = \pm 1$ and $\Delta m_I = 0$, giving rise to the characteristic three-line EPR spectrum of a nitroxide (Figure 6).

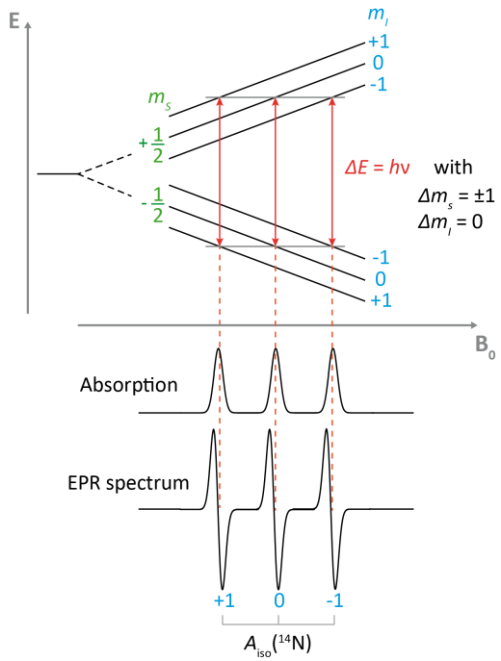

Figure 6: Zeeman scheme of an arbitrary nitroxide spin system with an electron spin $m_s = \pm\frac{1}{2}$ coupled to a ^{14}N nucleus with a nuclear spin quantum number $I = 1$ in an externally applied magnetic field B_0 (top). The three allowed transitions according to the selection rules matching the resonance condition are indicated as red arrows. The microwave absorption and the resulting EPR spectrum as the first derivative of the absorption (bottom). The hyperfine coupling constant $A_{iso}(^{14}N)$ can be obtained from the spectrum as the distance between the signal centers.

Often, the spin density of the paramagnetic center is partially delocalized, and coupling to multiple nuclei is observed. In such cases, the spectrum resembles a multiplet of multiplets. For all of the above-mentioned cases, the rotational correlation time τ_C of the paramagnetic center by far exceeds the EPR time scale, meaning that there is no preferential orientation of the spin system relative to the external magnetic field B_0, and the spectrum is isotropic. Here, the individual *g*-values g_x, g_y, and g_z and hyperfine coupling constants A_x, A_y, and A_z are indistinguishable and are averaged to g_{iso} and A_{iso}. This is mostly the case for small molecules in solution.

With increasing immobilization of the spin center and/or viscosity of the solvent, the rotational correlation time τ_C increases and the molecular motion no longer averages out anisotropic effects. At the point where $\tau_C \gg$ ~300 ns and in the solid state, each molecule has a distinct orientation to the magnetic field B_0 and the resulting spectrum is anisotropic (Figure 7a). In the case of a non-spherical spin system, g_{iso} splits into a 3x3 *g*-tensor. For a system with axial symmetry, $g_x = g_y \neq g_z$ and two distinct *g*-values are obtained, mostly referred to as $g_\parallel$ for g_z and $g_\perp$ for g_x and g_y are obtained, whereas, for rhombic symmetry, all *g*-values $g_x \neq g_y \neq g_z$ are unique (Figure 7b).

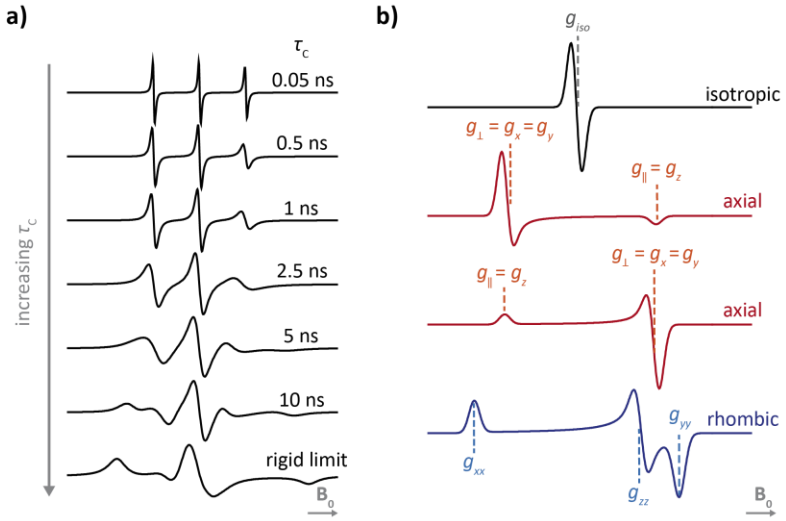

Figure 7: Nitroxide immobilization and types of *g*-anisotropy. **a)** X-band cw-EPR spectra of a nitroxide spin center at different rotational correlation times τ_C simulated by EasySpin[108] (simulation parameters *g* = 2.003, 2.006, 2.008 and *A* = 20 MHz, 20 MHz, 90 MHz). **b)** Simulated X-band cw-EPR spectra of a $s = \frac{1}{2}$ system showcasing different symmetries of the *g*-tensor: isotropic (top, black, simulation parameters g_{iso} = 2.14); axial (red, middle, simulation parameters $g_\parallel$ = 2.03 and $g_\perp$ = 2.25 (upper spectrum) or $g_\parallel$ = 2.25 and $g_\perp$ = 2.03 (lower spectrum)), and rhombic (blue, bottom, simulation parameters g_{xx} = 2.30, g_{yy} = 2.00, g_{zz} = 2.05). The dashed lines indicate the positions of the respective *g*-values. Spectra were simulated using EasySpin. Adapted from reference [97].

While the *g*-anisotropy of metal centers is often observed even at X-band, it is rarely resolved for organic radicals. Since the *g*-value separation linearly scales with the magnetic field strength and the microwave frequency, *g*-anisotropy of organic radicals can be resolved using higher frequency instrumentation such as Q- and W-Band. Similarly, the individual hyperfine coupling constants $A_{x/y/z}$ of an anisotropic spin system, which are independent of the magnetic field, are the sum of the isotropic part A_{iso} and an anisotropic, purely dipolar part $A_{x/y/z,dip}$, which depends on the distance $|\vec{r}|$ between the electron and the nucleus as well as on the angle Θ between the distance vector $\vec{r}$ and the external magnetic field B_0. From the dependency of the cw-EPR shape on the species' rotational correlation time τ_C, for spheric particles, the hydrodynamic radius *r* of the paramagnetic system

$$r = \sqrt[3]{\frac{3\tau_C k_B T}{4\pi\eta}} \qquad \text{(eq. 10)}$$

can be obtained by simulation of the EPR spectrum, where k_B is the Boltzmann constant, *T* the temperature, and η the viscosity.

1.2.1.1 Electron-Electron Interactions

If two spin centers are located on the same molecule and/or in close proximity, the magnetic moments μ_e of the unpaired electrons A and B can interact. The electron-electron coupling ν_{AB} is the sum of an isotropic part *J* and an anisotropic part *D* and is given by

$$\nu_{AB} = J + D \qquad \text{(eq. 11)}$$

The isotropic contribution *J* is referred to as exchange coupling and strongly depends on the inter-spin distance r_{AB}. Exchange coupling originates from the orbital overlap of spin A and spin B, which

is typically possible at interspin distances below 10 Å or in conjugated systems. For an exchange-coupled system, the individual spin quantum numbers s of spin A and B cannot be treated separately anymore and are insufficient to describe the system. While the exchange coupling *J* can have enormous effects on the shape of an EPR spectrum as well as on the physical properties of the molecule itself, due to its short-distance dependence and the typical absence of conjugated two- or multi-spin systems in most cases, it's contribution to ν_{AB} is often minor compared to the anisotropic dipolar contribution.

The dipolar coupling occurs through space and is based on the interaction between the magnetic moments of the two spin centers A and B. Assuming that the exchange coupling of the given two-spin system equals zero, e.g. if both spins are separated by at least ~15 Å, are not conjugated, and that the difference in the Larmor frequencies ω of both spin A and B is much larger than the dipolar coupling frequency ω_{Dip} (high field approximation), the dipolar coupling *D* (in angular frequency units) is given by

$$D = \omega_{Dip}(1 - 3\cos^2\Theta) = 2\pi\nu_{Dip}(1 - 3\cos^2\Theta) \qquad \text{(eq. 12)}$$

with ω_{Dip} being the dipolar coupling frequency and Θ the angle between the inter-spin distance vector $\vec{r}_{AB}$ and the external magnetic field B_0 (Figure 8a). Since the dipolar coupling constant *D* depends on the angle Θ, it can be resolved only if the spin-bearing molecules have a defined orientation with respect to the external magnetic field B_0, e.g. in frozen-solution or in a powder. The dipolar coupling frequency ν_{Dip} is defined as

$$\nu_{Dip} = \frac{\mu_B^2 g_A g_B \mu_0}{4\pi h} \cdot \frac{1}{r_{AB}^3} \qquad \text{(eq. 13)}$$

where μ_B is the Bohr magneton, g_A and g_B are the *g*-values of spin A and B, μ_0 is the vacuum magnetic permeability, h is the Planck constant, and r_{AB} the inter-spin distance. In cw-EPR spectroscopy, the dipolar coupling between two electrons is observed as an additional line splitting if the splitting is larger than the inhomogenous linewidth of the EPR spectrum. This is usually the case for interspin distances lower than 20 Å as with larger distances, the dipolar splitting is hidden within the intrinsic linewidth of the EPR spectrum. Assuming equal *g*-values of $g_A = g_B = 2$ and combining of eq. 12 and eq. 13, the expression of ω_{Dip} simplifies to

$$\omega_{Dip} = \frac{4\mu_B^2\mu_0}{4\pi h} \cdot 2\pi \cdot \frac{1}{r_{AB}^3}(1 - 3\cos^2\Theta) = D_{Dip} \cdot \frac{1}{r_{AB}^3}(1 - 3\cos^2\Theta) \qquad \text{(eq. 14)}$$

with $D_{Dip} = 2\pi \cdot 52$ MHz nm^3 being the dipolar coupling constant (Figure 8b). At $\theta \approx 54.74°$, the so-called magic angle, the dipolar coupling vanishes as the latter term $(1 - 3\cos^2\Theta)$ equals zero. The magic angle is the working principle for MAS SSNMR, as spinning the sample at 54.74° relative to the magnetic field B_0 averages out all anisotropic contributions such as the dipolar coupling between all spins, and the spectral resolution and sensitivity is significantly enhanced. For a uniformly distributed spin pair in the solid state with no preferred orientation relative to the magnetic field, the distribution of the interspin vector $\vec{r}_{AB}$ and therefore the angle Θ is proportional to $\sin\Theta$. This correlation between the dipolar coupling frequency ω_{Dip} and the angle Θ gives rise to the characteristic dipolar spectrum, the so-called Pake doublet (also referred to as Pake pattern) named after its discoverer *George Pake* (Figure 8c).

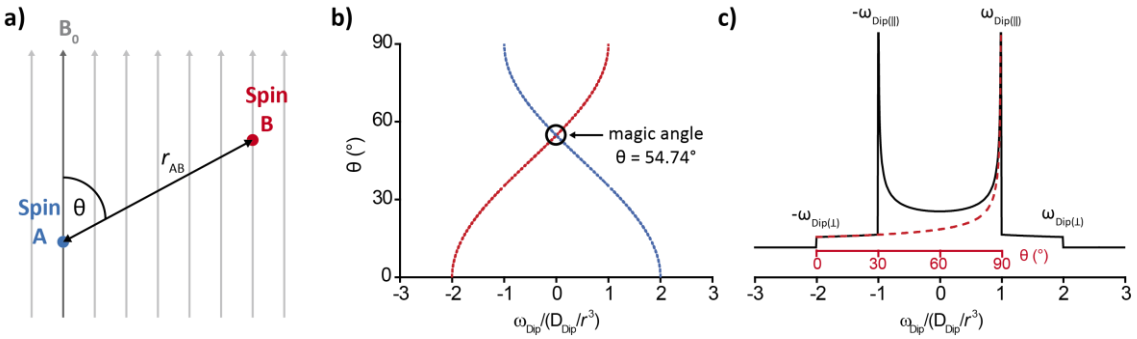

Figure 8: Spin pair orientation in a magnetic field, the angular dependence of the dipolar coupling, and the Pake pattern. **a)** Dipolar coupling of two spins A and B in a magnetic field B_0 described by their interspin distance vector $\vec{r}_{AB}$ and the angle Θ between the distance vector and the magnetic field. **b)** Dependence of the dipolar coupling frequency and the angle Θ according to eq. 14 (red) and the mirror image (blue) obtained for the second spin by altering the sign of ω_{Dip}. **c)** Pake pattern for a uniformly distributed spin pair ensemble in the solid state. Adapted from reference [104].

At the singularity of the Pake pattern (Θ = 90), eq. 14 simplifies to

$$\omega_{Dip}(\Theta = 90°) = \frac{D_{Dip}}{r_{AB}^3} \qquad \text{(eq. 15)}$$

and reading of the dipolar frequency ω_{Dip} allows determining the inter-spin distance r_{AB} through the inverse cubic proportion $\omega_{Dip} \sim \frac{1}{r_{AB}^3}$.

1.2.1.2 The Spin Hamiltonian Concept

All the aforementioned concepts of electron interactions can be unified within the spin Hamiltonian formalism to give the total energy of the spin system. Here, the spin Hamiltonian $\hat{\mathcal{H}}_S$ is defined as

$$\hat{\mathcal{H}}_S = \hat{\mathcal{H}}_{EZI} + \hat{\mathcal{H}}_{NZI} + \hat{\mathcal{H}}_{HFI} + \hat{\mathcal{H}}_{EI} + \hat{\mathcal{H}}_{DI} \qquad \text{(eq. 16)}$$

with

$$\hat{\mathcal{H}}_{EZI} = \sum_i \frac{\boldsymbol{g}_i \mu_B B_0}{\hbar} \hat{S}_i \qquad \text{(Electronic Zeeman Interaction)}$$

$$\hat{\mathcal{H}}_{NZI} = -\sum_k \frac{\boldsymbol{g}_k \mu_N B_0}{\hbar} \hat{I}_k \qquad \text{(Nuclear Zeeman Interaction)}$$

$$\hat{\mathcal{H}}_{HFI} = \sum_i \sum_k \hat{S}_i \boldsymbol{A_{ik}} \hat{I}_k \qquad \text{(Hyperfine Interaction)}$$

$$\hat{\mathcal{H}}_{EI} = \sum_i \sum_{j \neq i} -2\boldsymbol{J} \hat{S}_i \hat{S}_j \qquad \text{(Exchange Interaction)}$$

$$\hat{\mathcal{H}}_{DI} = \sum_i \sum_{j \neq i} \hat{S}_i \boldsymbol{D} \hat{S}_j \qquad \text{(Dipolar Interaction)}$$

Note that the spin Hamiltonian $\hat{\mathcal{H}}_S$ given in eq. 16 neglects the contribution of the zero-field splitting (ZFS) and the nuclear quadrupole interaction (NQI) as this would exceed the scope of this thesis. The parameters of the individual contributors to the spin Hamiltonian can be determined

using DFT calculations or by fitting experimental data and they are the basis for spectral simulations within the EPR community.

1.2.2 Pulsed EPR Spectroscopy

While cw-EPR is suitable to characterize strong couplings to electrons and nuclei in the close vicinity of a spin center and thus give information about its local environment, weaker couplings are often not resolved using this setup. Here, pulsed EPR methods provide an alternative to resolve weaker couplings to more distant nuclei or electrons, or to selectively address a distinct coupling by choosing an appropriate pulse sequence to disentangle otherwise overlapping signals. While in cw-EPR the sample is constantly irradiated with low-energy microwaves, in pulsed EPR the paramagnetic spin system is excited by short (typically nanosecond), high-power microwave pulses, and the transient emissive response of the spins is detected.

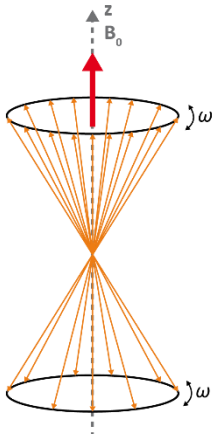

Figure 9: Precession of spins with their Larmor frequency ω relative to the B_0 main axis z. Orange arrows indicate the magnetic moments μ_e of the individual spins and the red arrow indicates the net magnetization *M* of the system.

As described in section 1.2.1, spins will align parallel or antiparallel to the external magnetic field B_0. However, the spins will not align perfectly with the magnetic field main axis, but they will precess around the B_0 main axis at their Larmor frequency ω. Given by the Boltzmann distribution, at thermal equilibrium more spins will occupy the ground state and the spin ensemble will give rise to a net magnetization *M* along the magnetic field axis z (Figure 9). In pulsed EPR, the perpendicular component (xy-plane) of the magnetization *M* is the measured quantity.

For a single electron spin with $s = \frac{1}{2}$, an isotropic *g*-value, and upon neglection of relaxation, the dynamics of the magnetization *M* caused by the spin is given by the torque equation

$$\frac{d}{dt}M = \frac{g_e \mu_B}{\hbar}[B_0 + B_{1lin}(t)] \cdot M \qquad \text{(eq. 17)}$$

with the linearly oscillating magnetic field component of the microwave radiation $B_{1lin} = 2B_1 \cos(\omega_{MW} t)$ along the x-axis (perpendicular to B_0) and the microwave frequency ω_{MW}. A magnetic field perpendicular to the magnetization *M* induced by a microwave pulse will tilt the magnetization away from the z-axis into the xy-plane (90°). In pulsed EPR, microwave pulses are either applied as 90° ($\pi/2$) or 180° (π) pulses and are defined by their length and amplitude. Thus, a 180° pulse has twice the length and the same power as a 90° pulse or the same length with double the power, respectively. Immediately after a 90° pulse, in a multi-spin system, the spins will form so-called spin packets with the same orientation and frequency (phase coherence) and the system has a maximal magnetization M_{xy}. The spin packets will then precess in the xy-plane with their respective Larmor frequency and the net magnetization M_{xy} will decay over time in a process called free induction decay (FID).

1.2.2.1 Hahn Echo Pulse Sequence

Due to technical limitations such as spectrometer dead times, direct recording of the FID is challenging. Therefore, it is rarely the initial magnetization decay after the $\pi/2$-pulse that is measured, but rather an echo created by refocusing of the precessing spin packets using a two-pulse sequence $\pi/2 - \tau - \pi - \tau - HE$ (Figure 10a). This refocused echo is called Hahn echo (HE) and is named after its discoverer *Erwin Hahn*.[109] The $\pi/2$-pulse rotates the net magnetization M_z

into the +y-direction and the spins have phase coherence. Now, the spin packets start to dephase and precess in the xy-plane with their respective Larmor frequencies. The second pulse, a π-pulse, is applied after a distinct time interval τ and flips all spins by 180° from the +y- to the -y-axis. Here, the spins keep their precession frequencies and directions and start to rephase again in the -y-direction. The magnetization built up in the -y-direction, which is maximal after the time interval 2τ, is called Hahn echo (Figure 10b-f).

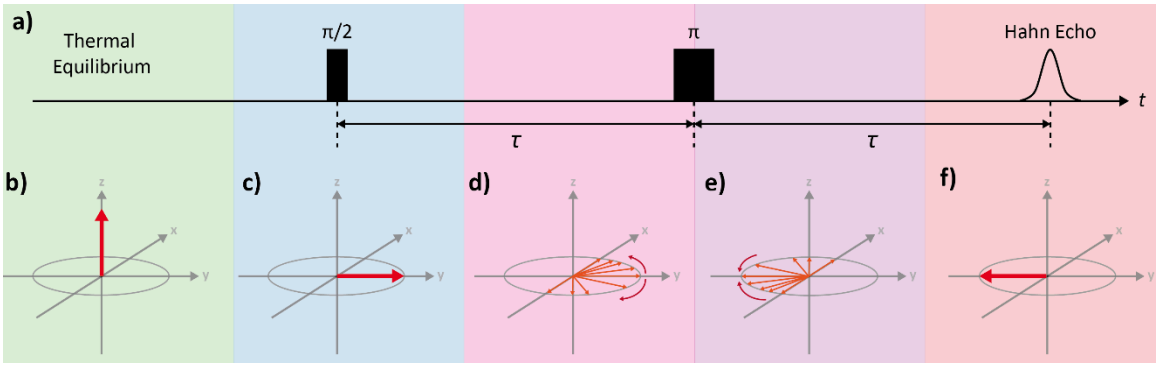

Figure 10: The Hahn echo experiment. **a)** Hahn echo sequence following the $\pi/2 - \tau - \pi - \tau - HE$ pulse scheme. **b-d)** Illustration of the net magnetization (red arrows, **b**, **c**, and **f**) and spin precession (orange arrows, **d** and **e**) following the individual steps of the pulse sequence in (**a**) highlighted by the background color. Figure adapted from reference [96].

1.2.2.2 Spin Relaxation

The pulse-induced transverse magnetization and initial phase coherence shifts the spin system out of the thermal equilibrium. Due to interactions of the spin with the environment and with other spins in the system, the thermal equilibrium is reinstalled in a process called spin relaxation.[105] Owing to the Boltzmann distribution, the small population difference between the ground and the excited Zeeman state is easily leveled by microwave absorption and if the system does not relax back into the thermal equilibrium, the microwave absorbance equals the emission of the system and there is no net EPR signal. This phenomenon is called saturation, which can be described by a saturation factor *s* with

$$s = \frac{1}{1+\gamma^2 B_1^2 T_1 T_2} \qquad \text{(eq. 18)}$$

where γ is the electron gyromagnetic ratio, B_1 the microwave-induced magnetic field, T_1 the electron spin-lattice relaxation time, and T_2 the electron spin-spin relaxation time. If the saturation factor $s < 1$, e.g. due to high-power microwave radiation (i.e., large B_1), the system is in saturation and the amplitude of the EPR signal decreases.

As governed by eq. 18, spin relaxation proceeds via two pathways, each with their distinct relaxation times. The first relaxation pathway is spin-lattice relaxation, also referred to as longitudinal relaxation. Here, the return of the magnetization along the magnetic field B_0 main axis and into thermal equilibrium occurs via energy transfer of the spin system to the surrounding environment (the lattice). This relaxation process is temperature-dependent and the spin-lattice relaxation time T_1 dictates the necessary timeframe before a pulse sequence can be repeated, namely the shot repetition time (SRT) of a pulsed EPR experiment. In general, the spin-lattice relaxation time is shorter for metal-centered spin systems and longer for organic radicals and typically ranges between micro- to milliseconds. The T_1 relaxation time can be measured by an inversion recovery experiment (Figure 11a), where the initial magnetization in +z-direction is

inverted into the -z-direction by a π-pulse and the magnetization return to thermal equilibrium is followed using the Hahn echo sequence after a variable timeframe T. The amplitude $y(T)$ of the spin echo follows an exponential function[110]

$$y(T) = A_0 \cdot \exp\left(-\frac{T}{T_1}\right) + C \qquad \text{(eq. 19)}$$

where A_0 is the initial echo amplitude at the time $T = 0$ (Figure 11b). At $T = T_1$, the initial amplitude A_0 has decayed by a factor of $1/e$.

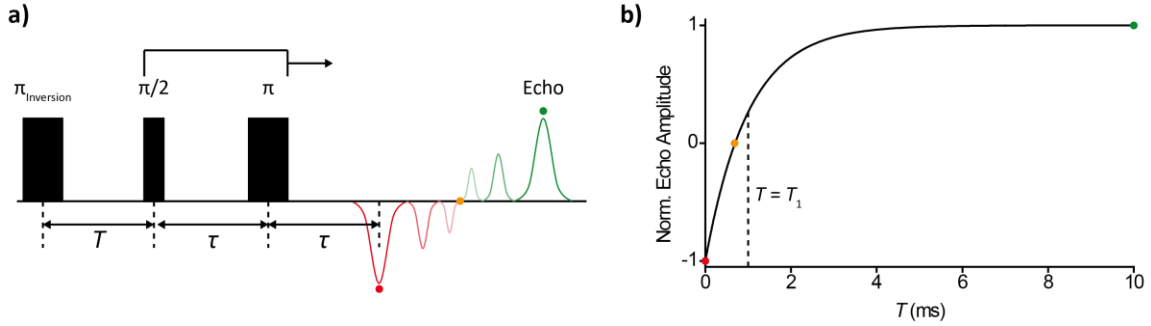

Figure 11: The inversion recovery experiment. **a)** Inversion recovery pulse sequence. By incrementing the time T between the inversion pulse and the Hahn echo sequence, the transition of the magnetization in -z-direction ($T = 0$) back to the thermal equilibrium in +z-direction ($T \gg T_1$) is monitored. **b)** Simulated inversion recovery curve with $T_1 = 1$ ms. The colored dots correspond to the maximum magnetization in the -z-direction (red), the zero crossing (orange), and the thermal equilibrium (green) with the maximum magnetization in +z-direction as shown schematically in (**a**). The spin-lattice relaxation time T_1 is marked as a dashed line.

The second relaxation pathway proceeds via spin-spin relaxation, also called transverse relaxation. Transverse relaxation describes the loss of phase coherence within a spin packet in the xy-plane over time due to spin-spin interactions and is an entropy-driven process. As the phase coherence decays, the resulting echo intensity of a refocused spin echo declines until the point where phase coherence is lost and the spins cannot be refocused anymore. The spin-spin relaxation can be characterized by the spin-spin relaxation time constant T_2, which is accessible by fitting an exponential function to the FID. As mentioned before, direct access to the FID is not trivial and hence, in an experimental setup, the decay of the Hahn echo amplitude is monitored in a pulse sequence called two-pulse electron spin echo envelope modulation (2pESEEM) as a function of the interpulse delay τ (Figure 12a). Here, the dead time of the experimental setup is twice the initial interpulse delay τ and the amplitude of the echo is given as a function of 2τ, as spin-spin relaxation occurs in a 2τ time interval. In most experimental cases, the decay of the Hahn echo can be described by a stretched exponential function[111]

$$y(2\tau) = A_0 \cdot \exp\left(-\frac{2\tau}{T_M}\right)^x \qquad \text{(eq. 20)}$$

where A_0 is the initial Hahn echo amplitude at $\tau = 0$, x a stretch exponent, and T_M the phase memory time, a constant that comprises the spin-spin relaxation time T_2 as well as other decoherence contributions such as nuclear spin diffusion. If nuclei with a nuclear spin quantum number $I \neq 0$ are in close proximity to the electron, the resulting 2pESEEM trace is modulated by the Larmor frequency of the coupled nuclear spins, which is referred to as electron spin echo envelope modulation (ESEEM) (Figure 12b).

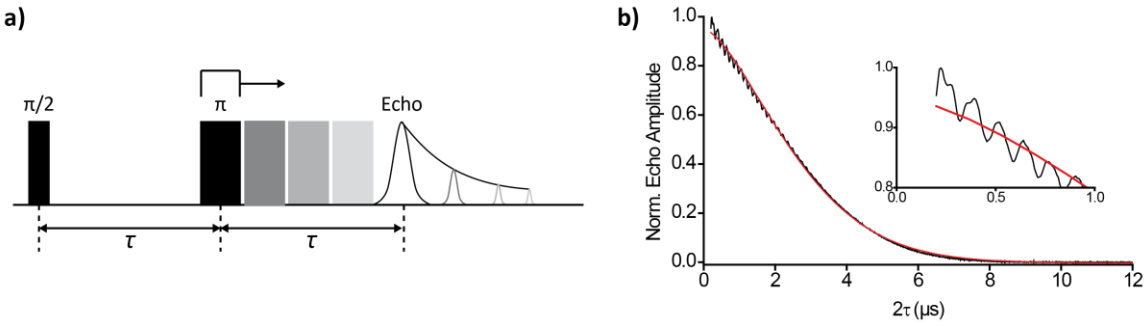

Figure 12: The two-pulse electron spin echo envelope modulation experiment. **a)** Pulse scheme of the 2pESEEM experiment. While the time interval τ in the Hahn echo sequence is incremented, a decline of the echo amplitude is observed as a consequence of the phase coherence loss. **b)** Experimental 2pESEEM Hahn echo decay curve in deuterated solvent (black) with the corresponding fit according to eq. 20 (red). The inset highlights the oscillation of the trace by deuterium ESEEM as a consequence of the electron spin coupling to the ^{2}H nucleus with a nuclear spin-quantum number $I = 1$.

The phase memory time T_M is commonly in the range of microseconds for organic paramagnetic centers and decreases with elevated temperatures. In pulsed dipolar EPR spectroscopy (section 1.2.2.3), the phase memory time is an important parameter as it is the limiting factor for the dipolar evolution time of an experiment and thus the maximum resolvable interspin distance r_{AB}, hence making longer phase memory times desirable. The extent of nuclear spin diffusion and dephasing of the electron spins is proportional to the gyromagnetic ratio of the coupled nucleus, hence a reduction of the nuclear magnetic moment in the proximity of the spin center enhances the phase memory time. As most biological samples are dissolved in aqueous buffer, a hydrogen-deuterium exchange in the buffer,[112] the spin bearing group,[113] or the biomolecule itself[114–116] prolongs the phase memory time due to the significantly smaller magnetic moment of ^{2}H (μ_D/μ_N = 0.857) compared to ^{1}H (μ_H/μ_N = 2.973). Furthermore, other measures such as a reduced spin concentration (diamagnetic dilution)[117] and adding glass-forming additives such as glycerol or ethylene glycol[118] can prolong the phase memory time T_M and are frequently employed in sample preparation processes.

1.2.2.3 Pulsed Dipolar EPR Spectroscopy

Pulsed dipolar EPR spectroscopy (PDS-EPR) is a generic term for EPR experiments designed to measure the dipolar coupling frequency ω_{Dip} of two electrons. As described in section 1.2.1.1 and by eq. 14, the dipolar coupling frequency between two spins A and B is proportional to the inverse cube of the interspin distance ($\omega_{AB} \sim r_{AB}^{-3}$). While the dipolar coupling frequency of interspin distances below ~2 nm can be accessed via cw-EPR spectroscopy, the dipolar coupling of longer interspin distances is hidden within the inhomogeneous linewidth of the EPR spectrum.[119] By employing suitable PDS pulse schemes for a given spin system, the spectral resolution is enhanced and a spin echo that is modulated by the dipolar coupling frequency ω_{AB} is obtained. Monitoring the echo amplitude as a function of the dipolar evolution time yields the so-called time trace, which encodes the dipolar coupling in the form of oscillations. As the cube of the interspin distance r_{AB} is inversely proportional to the dipolar coupling frequency, longer distances have longer oscillation periods and the maximum resolvable distance is limited by the phase memory time, which determines the length of the time trace. Commonly, the interspin distance retrievable by PDS ranges between 1.5 and 10 nm,[120] but in special setups even longer distances up to 16 nm can be reliably resolved.[116] Since the nanometer length scale lies within the spatial dimensions of most biomolecules, PDS is a valuable tool in structural biology and, similar to FRET, serves as a "molecular ruler" to provide distance information.

As the dipolar coupling ranges through space, it occurs between spins located within the same molecule (intramolecular coupling) and between spins located on different molecules in close proximity (intermolecular coupling). The resulting dipolar signal $V(t)$ is the product of both contributions

$$V(t) = V_{intra}(t) \cdot V_{inter}(t) \qquad \text{(eq. 21)}$$

where $V_{intra}(t)$ is the intramolecular and $V_{inter}(t)$ the intermolecular contribution. $V_{intra}(t)$ contains the dipolar coupling frequency in the form of oscillations whereas $V_{inter}(t)$ is the non-modulated background of the time trace in the case that the spins are homogenously distributed within the sample with no preferred orientation relative to the magnetic field. In order to obtain the intramolecular distance information, which is encoded in the oscillations of $V_{intra}(t)$, $V(t)$ has to be disentangled into its two contributing parts. The intramolecular background contribution is approximated by an exponential or polynomial function $B(t)$ and subsequently, $V(t)$ is divided by $B(t)$ to yield the background-free, intramolecular contribution of $V_{intra}(t)$ (Figure 13a).
The resulting, background-corrected time trace is characterized by the oscillation period, the modulation depth Δ, and the noise level σ (Figure 13b). Since PDS is an ensemble measurement technique, slight variations of the individual interspin distance r_{AB} of a single molecule within the ensemble lead to different oscillation periods and, due to destructive interference, the oscillations are dampened. Fast-Fourier transformation (FFT) of the time trace yields the aforementioned, characteristic Pake pattern (Figure 13c). The modulation depth Δ is a measure of the fraction of excited, dipolar coupled spins and depends on the strength, length, and shape of the excitation pulses as well as the spectral width of the respective spin center. In the absence of dipolar coupling between the spins, the modulation depth would equal zero and the dipolar signal $V(t)$ would be solely comprised of the intermolecular background function $B(t)$.
As PDS is an ensemble technique, the interspin distance r_{AB} is not obtained as a single value but rather as a probability distribution $P(r)$ of each interspin distance observed in the ensemble. Technically, the intramolecular contribution $V_{intra}(t)$ is fitted following

$$V_{intra}(t) = K(t,r) \cdot P(r) \qquad \text{(eq. 22)}$$

with $K(t,r)$ being the so-called Kernel matrix. Since small variations in $V_{intra}(t)$ such as noise, variations in the background function, or systematic errors can translate into large deviations in $P(r)$, one speaks of an ill-posed problem.[121] A plethora of computer programs such as DeerAnalysis,[122] DEERNet,[123] DeerLab,[124] or PeldorFit,[125] each with their specific assumptions on the spin system, have been developed to convert $V_{intra}(t)$ into $P(r)$ using different approaches to solve this mathematical problem and to stabilize the solution. DeerAnalysis, the program most commonly used by the EPR community to analyze dipolar EPR data, uses a two-step approach of background division followed by a penalized least-square fitting called Tikhonov regularization.[121,122] To avoid noise-fitting which would lead to “spiky” (many unique) distance distributions $P(r)$, Tikhonov regularization penalizes the roughness of the distribution and the goodness of the simulated fit to the time domain by mean-square deviation (MSD) and smoothing is achieved by a so-called regularization parameter α (Figure 13d). In addition, DeerAnalysis enables the user to validate the obtained distance distribution $P(r)$ with an integrated validation tool. Here, the influence of, e.g., added white noise or varying background functions $B(t)$ on $P(r)$ are checked, resulting in a so-called confidence interval which encloses all possible solutions within the chosen validation boundaries (Figure 13e).[126]

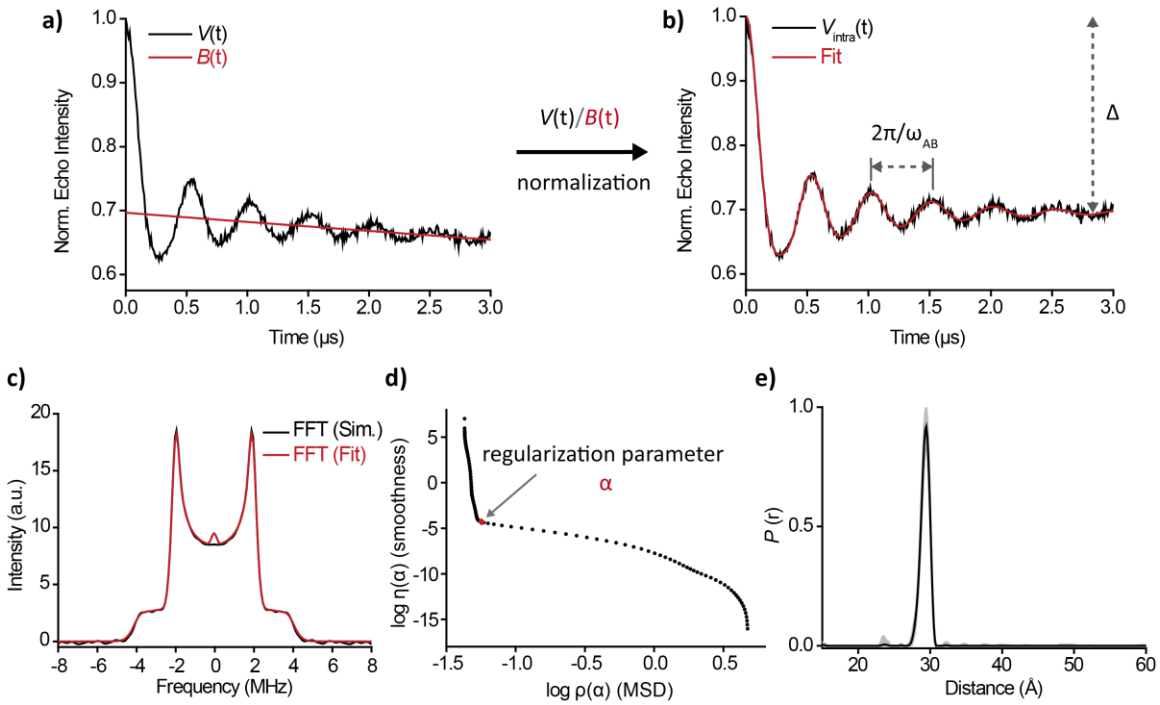

Figure 13: Data processing steps by DeerAnalysis of a primary time trace to yield a distance distribution. **a)** Simulated time trace for a Gaussian distribution using EasySpin[108] with a mean distance ⟨*r*⟩of 30 Å and a full width at half maximum (FWHM) Δ*r* of 2.6 Å. White noise was added and the simulated time trace was multiplied with *B*(t) (red) to yield *V*(t) (black). **b)** Intramolecular dipolar contribution V_{intra}(t) (black) after dividing *V*(t) by *B*(t) in (**a**). V_{intra}(t) is characterized by the dipolar oscillation frequency ω_{AB} and the modulation depth Δ. The fit of the time trace provided by DeerAnalysis is shown in red. **c)** Dipolar spectrum (Pake pattern) obtained by FFT of the simulated trace and fit in (**b**), respectively. **d)** L-curve of the Tikhonov regularization with the chosen regularization parameter α shown in red. **e)** Normalized distance distribution provided by DeerAnalysis (black) with the confidence interval shown as grey shaded area.

DEERNet, a relatively new software package introduced in 2018, uses a deep-learning neural network trained with a large dataset of simulated traces to directly convert $V(t)$ into $P(r)$ in an automated single-step approach.[123] As all computer programs rely on different approaches, there is no "right" program to use and each approach has its unique advantages or disadvantages, e.g. DeerAnalysis allows the user to manually vary the fitting parameters which can help to process out-of-norm data but gives room for user bias. DEERNet is basically user-bias-free, but there is a chance that the input data is not in agreement with the given training set, and data analysis is refused.

1.2.2.4 Pulse Sequences for PDS

There is a plethora of pulse sequences available to detect the dipolar coupling between two spins and the appropriate pulse sequence for a given spin system mainly depends on two factors: First, the width of the EPR spectrum, and second, the relaxation properties of the dipolar-coupled spin system. The width of the EPR spectrum determines how many spins can be inverted by a microwave pulse. A large spectral width exceeds the excitation bandwidth of common rectangular pulses and only a fraction of spins is addressed by a microwave pulse. This gives rise to a phenomenon called orientation selection where not all angles Θ are evenly excited by the microwave pulse and only an incomplete Pake pattern is obtained, which eventually can cause distortions in the obtained distance distribution.[127–129] The spin-lattice relaxation time T_1 determines whether the inversion of a spin in the spin pair is preferably achieved using microwave

pulses or by spontaneous flipping due to longitudinal relaxation.[96] In the following, four PDS techniques are briefly described and compared.

The probably most common PDS sequence employed is the **P**ulsed **El**ectron-Electron **Do**uble **R**esonance (PELDOR) technique, also referred to as **D**ouble **E**lectron-**E**lectron **R**esonance (DEER).[120] Initially developed by *Milov* et al. as a three-pulse technique,[130,131] today an improved dead-time-free four-pulse sequence introduced by *Martin* et al. is the commonly utilized method (Figure 14).[132,133]

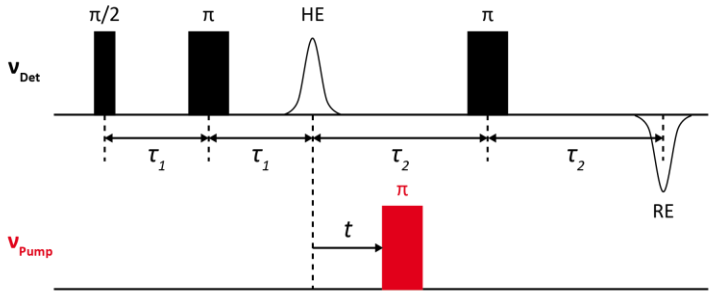

Figure 14: The four-pulse PELDOR sequence. The abbreviations HE and RE correspond to Hahn Echo and Refocused Echo, respectively. The pulse sequence applied at the detection frequency ν_{Det} is shown in the top row while the inversion π-pulse is applied at the pump frequency ν_{Pump}. Adapted from *Pannier* et al.[132]

As shown in Figure 14, the PELDOR pulse sequence operates at two distinct microwave frequencies, the detection frequency ν_{Det} which is in resonance with spin A, and the pump frequency ν_{Pump} which is in resonance with spin B. The PELDOR sequence is therefore often termed a "pump-probe" experiment. At the observer frequency ν_{Det}, the $\pi/2-\tau-\pi-\tau$ sequence generates a Hahn echo of spin A. A π-pulse at the pump frequency ν_{Pump} after the HE-sequence at ν_{Det} inverts spin B and if both spins A and B are dipolar-coupled, the inversion of spin B changes the local magnetic field at spin A and shifts its Larmor frequency by ω_{Dip}. The second π-pulse applied at the detection frequency ν_{Det} refocuses the Hahn echo and generates an inverted, refocused echo whose intensity is changed due to the resulting phase shift of $\pm\omega_{Dip}t$. Incrementing the dipolar evolution time t after which the pump pulse is applied in the first time interval of τ_2 leads to an oscillating signal $V(t)$, which corresponds to the PELDOR time trace.
The PELDOR sequence performs best for spin pairs with similar longitudinal relaxation times T_1 and moderately broad EPR spectra as both, the detection and pump pulses, need to be separated by a sufficient frequency offset to selectively address the individual spins A and B and to avoid pulse overlap that causes artifacts in the time trace. However, the spectrum still needs to be narrow enough to pump a sufficient amount of spins B. A prominent example of spin centers suitable for PELDOR experiments are nitroxides as their spectral width (~9 mT at Q-band)[134] is sufficiently broad to apply both, pump and detection pulses (~1.5-2.5 mT width) at a frequency offset of ~80-100 MHz with minimal pulse overlap, while still addressing a sufficient fraction of spins to provide good sensitivity.

Another PDS technique to measure the dipolar coupling between two spin centers is the **R**elaxation **I**nduced **D**ipolar **M**odulation **E**nhancement (RIDME) experiment first described by *Kulik* et al.[135] Initially developed as a three-pulse method, further extensions of the sequence to a five- and six-pulse sequence removed the dead time and dealt with artifacts in the resulting time trace.[136,137] In contrast to PELDOR, RIDME is a single-frequency technique where the dipolar modulation is generated by the spontaneous relaxation of one of the two spins (Figure 15).

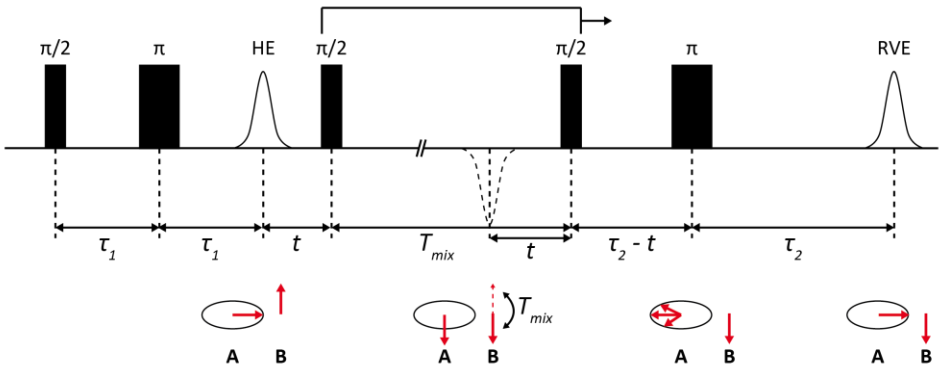

Figure 15: The five-pulse RIDME sequence. The abbreviations HE and RVE correspond to Hahn Echo and Refocused Virtual Echo, respectively. Spin A is in resonance with the microwave radiation while spin B is not addressed by the microwave pulses. The small schematics below the pulse sequence represent the current orientations of spin A and B at the given step in the pulse sequence. Adapted from *Kulik* et al.[135]

In the five-pulse RIDME sequence, first, a classical Hahn Echo sequence is applied that generates a Hahn Echo after the time interval $2\tau_1$ and, in the time interval t after the echo, the spin packets start to defocus again. In the time interval t, the spin packets of A start to precess in the xy-plane and after another $\pi/2$-pulse, their magnetization is shifted in the z-direction. In the following time interval T_{mix}, the B spins flip statistically due to longitudinal relaxation and change the local dipolar field at spin A, thereby changing the Larmor frequency of the spin packets. As the spin-lattice relaxation usually is in the range of microseconds, the condition $T_{mix} \gg T_{1,B}$ must hold for efficient inversion of spin B. Application of another $\pi/2 - \pi$ sequence generates a refocused virtual echo (RVE) at a constant position in time. The resulting echo intensity is hence modulated by the Larmor frequency shift caused by the spontaneous spin flip of spin B. It is a prerequisite for spin B to flip an odd number of times during the time interval T_{mix} to generate a frequency shift on spin A. For a spin system with $s = \frac{1}{2}$, the fraction of spins B to flip an odd number of times is given by

$$f_{odd}(T_{mix}) = \frac{1}{2}\left[1 - \exp\left(-\frac{T_{mix}}{T_1}\right)\right] \qquad \text{(eq. 23)}$$

and therefore depends on both, the spin-lattice relaxation time T_1 as well as the mixing time T_{mix}. If $T_{mix} \gg T_{1,B}$, the fraction of spins B flipping an odd number of times is ~0.5, hence giving a theoretical modulation depth of 50%.[136]

The RIDME sequence is suited best for pairs of unequal spins A and B with significantly different longitudinal relaxation times $T_{1,A} \gg T_{1,B}$. This situation is often encountered for a spin pair consisting of an organic radical and a metal center, where the pulse sequence is applied to the spectrally narrow and slowly-relaxing organic radical while the fast-relaxing and spectrally broad metal spin flips statistically during T_{mix}. Due to their *g*-anisotropy, the EPR spectrum of metal centers is often very broad compared to organic radicals, and the lack of a selective inversion pulse and the utilization of spontaneous relaxation can help to minimize orientational selection if longitudinal relaxation times are equal across the whole spectrum.[138] Although the broad EPR spectrum exceeds the resonator bandwidth, the effect of spontaneous flips of spin B across the whole spectrum during T_{mix} can be probed on the resonant spin A, hence T_{mix} can be regarded as an infinitely broad inversion pulse.

Besides RIDME, there are two other prominent single-frequency techniques to measure the dipolar coupling between two spin centers, namely the **D**ouble **Q**uantum **C**oherence (DQC)[139–141] and the **Si**ngle **F**requency **Te**chnique for **R**efocusing Dipolar Couplings (SIFTER)[142,143] pulse sequences (Figure 16).[144]

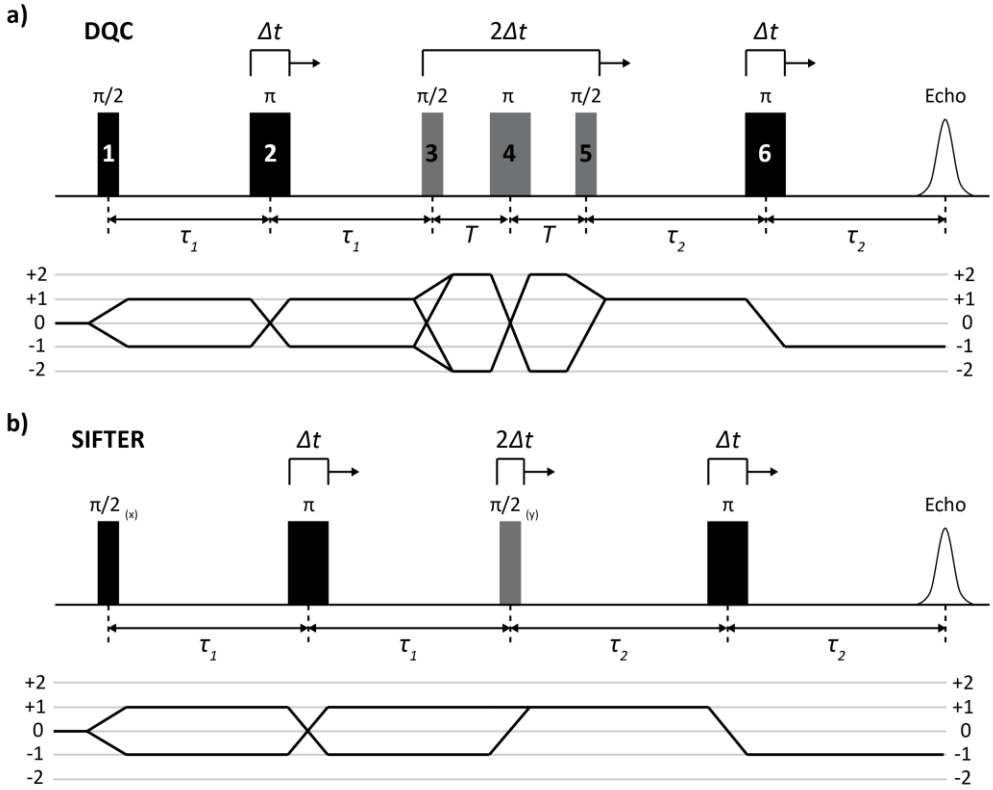

Figure 16: The six-pulse DQC and four-pulse SIFTER sequences with their respective coherence order maps. **a)** Six-pulse DQC sequence (top) with the double-quantum filter sequence (grey) sandwiched by two refocusing π-pulses and the respective coherence order map (bottom). **b)** Four-pulse SIFTER sequence (top) with the $\pi/2$ propagation pulse (grey) sandwiched by two refocusing π-pulses and the respective coherence order map (bottom). Adapted from Reference [144].

In contrast to PELDOR and RIDME, where the spin pairs are divided into two groups A and B, and their dipolar coupling is revealed by manipulating the other spin group with either microwave pulses (PELDOR) or spontaneous spin flips (RIDME), DQC and SIFTER work under the principle of spin coherence orders. In brief, there are three relevant coherence orders *p*, namely zero-quantum coherence ($p = 0$) describing the longitudinal magnetization in *z*-direction, single-quantum coherence ($p = \pm1$) corresponding to transverse magnetization with the in-phase ($p = -1$) and anti-phase ($p = +1$) coherence, and double-quantum coherence ($p = \pm2$) where the net-magnetization of the system equals zero. Importantly, in EPR spectroscopy only in-phase coherence ($p = -1$) is observable. The coherence generation and transitions between the coherence levels are induced by microwave pulses. A $\pi/2$-pulse either generates or changes coherence from zero-quantum coherence with $\Delta p = 1$ ($p = 0 \rightarrow p = \pm1$) or by an uneven number, e.g. $\Delta p = 3$, whereas a π-pulse inverts the coherence order ($-p \rightarrow +p$; $+p \rightarrow -p$). If the spin packets precess an equal time interval τ in both single-quantum coherence orders $p = +1$ and -1, and dipolar coupling between two spins is present, a spin echo occurs that is modulated by the dipolar-coupling frequency.

In the six-pulse DQC sequence, the first $\pi/2$-pulse generates single-quantum coherence and after a time interval τ_1, the coherence order is inverted and the spin packets are refocused by a π-pulse,

thus generating a Hahn echo after a second time interval τ_1. Next, pulses 3 to 5 (the so-called double-quantum filter) separated by a fixed interpulse delay T generate double-quantum coherence (pulse 3) that is refocused by the inversion π-pulse (pulse 4) and converted into anti-phase single-quantum coherence (pulse 5). After a time interval τ_2, the final π-pulse refocuses the spin packets and inverts the coherence order into detectable in-phase coherence (p = -1), which results in a modulated echo at τ_2 after the last pulse. By incrementing τ_1 and decrementing τ_2 with the same time step Δt while maintaining the interpulse delays T of the double-quantum filter and shifting the double-quantum filer sequence with $2\Delta t$, the DQC experiment generates an echo at a constant temporal position. Integration of the echo as a function of $\tau_1 - \tau_2$ yields a symmetric time trace with the maximum amplitude at the position where $\tau_1 = \tau_2$. Therefore, DQC is termed a constant-time experiment, where the duration of the complete pulse sequence is given by $t_{DQC} = 2\tau_1 + 2\tau_2 + 2T$. The double-quantum filter sequence selectively marks the pathways involving double-quantum coherence, which are extracted using a 64-step phase cycle that eliminates all other unwanted contributions to the signal.

The four-pulse SIFTER sequence consists of the $(\pi/2)_x - \tau - (\pi/2)_y - \tau - Echo$ solid-echo sequence known from NMR spectroscopy with additional π-pulses after each $\pi/2$-pulse. While the solid-echo sequence is unable to completely refocus the spins due to distributions of g-values and hyperfine couplings, the π-pulses allow the refocusing of these inhomogeneities and yield an echo that is solely modulated by the dipolar coupling. Similar to the DQC experiment, the first $\pi/2$-pulse generates single-quantum coherence, which is refocused and inverted by the following π-pulse after the time interval τ_1. Unlike DQC, where the double-quantum filter sequence is used to generate anti-phase coherence, SIFTER uses a 90° phase-shifted $\pi/2$-pulse for coherence transfer that exchanges the anti-phase coherence of both spins. After the time interval τ_2, a final refocusing π-pulse generates detectable in-phase coherence, and an echo modulated by the dipolar frequency is observed after a second time interval τ_2. As the interpulse delays τ_1 and τ_2 are incremented and decremented, respectively, in a similar way as in DQC, SIFTER is also a constant time experiment that generates a symmetric echo with its maximum amplitude at the condition $\tau_1 = \tau_2$.

As stated above, in DQC and SIFTER the spins of a system are not subdivided into two groups, A and B, and as a consequence, both techniques perform best on spin centers with a narrow EPR line width that ideally can be fully excited by the microwave pulses. If this condition is fulfilled, both techniques offer a high signal-to-noise ratio (SNR) and due to the full spectral excitation, orientation selection is excluded. DQC and SIFTER mainly differ in their respective intermolecular background decays. While the double-quantum filter sequence in conjunction with the 64-step phase cycle in DQC efficiently suppresses non-modulated contributions from single spins and only the contribution of dipolar-coupled spin pairs prevails, SIFTER lacks this double-quantum filter and hence the SIFTER background is more susceptible to the contributions of unpaired spins.[145]

1.3 EPR in Structural Biology

The vast majority of biomolecules contain only six key elements: carbon, nitrogen, oxygen, hydrogen, phosphorus, and sulfur.[146] Except for oxygen and sulfur, each of these elements or their naturally abundant isotopes possess a nuclear magnetic moment, thereby making almost all biomolecules amenable for structure elucidation via NMR spectroscopy. In strong contrast, there is a relatively low abundance of naturally occurring paramagnetic centers in bio(macro)molecules rendering most of them EPR-silent.[147] If paramagnetic sites are present, they mainly consist of endogenously bound paramagnetic metal ions with a catalytic function,[148,149] metal clusters such as the iron-sulfur clusters that mediate electron transfers,[150] or short-lived organic radical

intermediate species such as tyrosyl radicals.[151,152] While the low abundance of paramagnetic centers limits the contribution of unwanted signals to the EPR spectrum and enhances the specificity and distinguishability of the signals, it also implies that most biomacromolecules first have to be labeled with a paramagnetic center, also referred to as spin label, to be targeted by EPR spectroscopy. If a biomolecule has been successfully labeled, EPR measurements can contribute to structural biology in two ways:[153] On the one hand, accessibility studies can reveal surface exposure of protein residues[154] and the conformational flexibility of secondary structural elements through the EPR line shape.[155–157] If EPR data are recorded as a function of time, structural changes and fluctuations can be followed in a time-resolved manner.[154,158] On the other hand, distance distributions derived by pulsed dipolar EPR provide unique information about the structure of a biomolecule on the nanometer length scale, which may be unavailable from other complementary biophysical methods (see section 1.1) due to their specific limitations.[119,153] PDS-EPR has been applied to proteins[159] and nucleic acids[160] in buffered solutions,[161,162] in membranes,[163] and within cells[164] to trace conformational changes[165] and the time scale of these structural rearrangements,[166,167] to localize metal ions via trilateration,[129] and to gain insights into biomacromolecular complex formation.[168] The following sections provide an overview of labeling strategies and spin labels used in biomolecular structure elucidation of proteins via EPR spectroscopy.

1.3.1 Labeling Strategies

Early-stage EPR characterization of biomolecules via cw-EPR relied on the aforementioned intrinsic spin centers[169] before *McConnell* and coworkers reported on the labeling of cysteines in diamagnetic biomolecules with paramagnetic spin labels in 1965.[170,171] Subsequently, research focused on the design of new spin-labeling reagents that target different amino acids such as lysine,[172,173] tyrosine,[174] or arginine.[175] However, these initial labeling attempts were selective rather than specific, meaning that proteins were labeled at one or more prescribed positions of the targeted amino acid dictated by the amino acid sequence of the biomolecule.[176] This in turn limited the applicability of these early labeling strategies, especially for PDS experiments, as the labeling positions remained arbitrary and the degree of labeling was highly dependent on the abundance and accessibility of the target amino acid.[119]

The general strategy for labeling biomolecules was dramatically changed by the pioneering work of the *Hubbell* group, which introduced the concept of site-directed spin labeling (SDSL).[177,178] SDSL is a general term for the site-selective attachment of a spin label at designated positions and the technique can be applied to both, proteins and oligonucleotides.[179] Here, the spin label serves as a reporter group and as only the specifically selected and labeled residues contribute to the EPR signal, the size of the biomacromolecular system is basically arbitrary.[180] In the case of proteins, site-directed mutagenesis is used to generate unique labeling sites for the selective bioconjugation of spin labels, hence significantly enhancing the label specificity and making data interpretation less involved. In principle, any amino acid X can be replaced by a unique residue Y, which is compatible with the bioconjugation of a spin label selective to residue Y.[178] SDSL of nucleic acids can be achieved either by the direct incorporation of a spin-labeled nucleotide during solid-phase synthesis of an oligonucleotide or post-synthetically at pre-functionalized positions.[179,181–183] In strong contrast to fluorophore labeling for FRET applications, PDS experiments allow for unequal label pairs but do not necessarily require two distinguishable label types, thereby simplifying the SDSL strategy for most cases.[184]

The most common SDSL approach for proteins is the labeling of a cysteine residue with a spin label. The cysteine residue is introduced by the genetic alteration of a residue of interest to a cysteine and subsequent post-translational modification of the free sulfhydryl (R-SH) group with

a spin label.[180] To avoid unspecific labeling of solvent-exposed native cysteines, these residues can conversely be altered to a non-reactive amino acid by site-directed mutagenesis. The advantage of cysteine as the labeling site is its commonly low natural abundance and high reactivity compared to any other proteinogenic amino acid.[185] High reactivity is needed as the labeling reaction commonly has to be conducted at mild reaction conditions, meaning at ambient temperatures and pH values in the physiological range to preserve the protein folding. Cysteine nucleophilicity is highest under slightly alkaline conditions (pH > 7)[186] where the thiol has a high propensity to form the thiolate anion (pK_a ~ 8.2)[187] whose nucleophilicity can be exploited for coupling with a suitable electrophilic bioconjugation group such as halo-alkanes and arenes, maleimides and their derivatives, thiosulfonates, or Michael acceptors (Figure 17).[188]

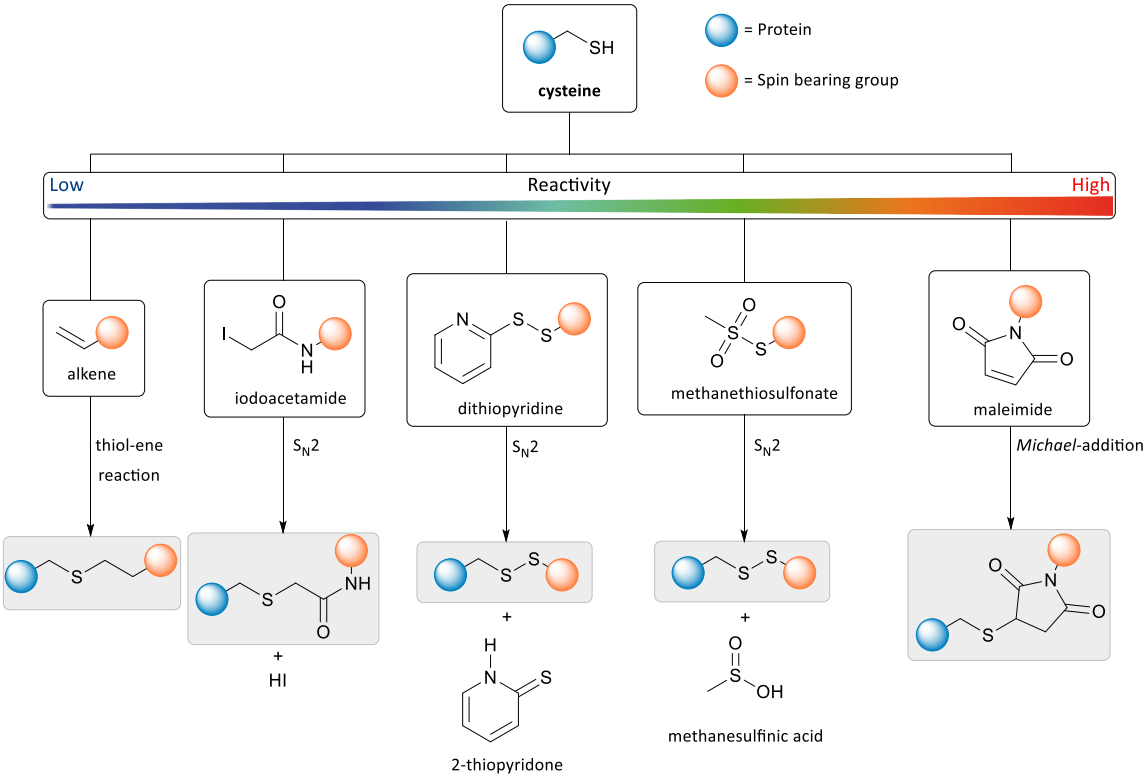

Figure 17: Schematics for cysteine bioconjugation. The scheme displays a selection of commonly used cysteine-reactive bioconjugation groups (black frames) and their coupling products upon cysteine conjugation (grey boxes) with the respective reaction type noted next to the corresponding arrows. The bioconjugation groups are qualitatively sorted by their relative reactivity towards cysteines from low reactivity (left) to high reactivity (right). Blue dots represent the protein while red dots mark the spin-bearing group.

To achieve high labeling efficiencies, cysteine modifications are commonly conducted *in vitro* on purified protein samples as selective intracellular labeling of a target cysteine is challenging due to the abundance of free thiols such as glutathione (GSH) present in life cells (0.5-10 mM GSH, 30-200 µM free cysteine from other proteins).[188,189] The choice of the bioconjugation group not only affects the rate of the reaction but also the site specificity, and the resulting linker function of the adduct has consequences for later applications. The fast S_N2 reaction of thiolates with thiosulfonates or dithiopyridines yields disulfide-bridged coupling products. Although the reaction of the soft thiosulfonate and the soft thiolate anion is highly preferred according to HSAB theory, side reactions with harder nucleophiles such as alcohols and amines, which are functional groups in the pool of proteinogenic amino acids, have been reported (Figure 18a).[190] In addition, the

slightly alkaline labeling conditions favoring the thiolate anion promote the disproportionation of the thiosulfonate resulting in disulfide-bridged by-products (Figure 18b).[191] Disulfide bonds are stable in aqueous, buffered solutions and suitable for *in vitro* experiments but under reductive cellular conditions, the S-S bond is readily broken by reductive cleavage within the cytosol.[192] Alkene, iodoacetamide, or maleimide conjugation to cysteine yields a more stable thioether function with a higher persistence under reductive cellular conditions.[188] Owing to their high reactivity towards nucleophiles arising from ring strain and electron deficiency of the carbon-carbon double bond due to the electron-withdrawing imide motif, maleimides are more susceptible to side reactions with other nucleophiles such as free amines (e.g. of lysine) than thiosulfonates. Therefore, the pH of the solution must be carefully adjusted to achieve a tradeoff between high thiol(ate) reactivity on the one hand, while avoiding side reactions with free amines and deactivating hydrolysis of the maleimide group.[193] Usually, maleimide conjugation to cysteines is carried out at pH 6.5 to pH 7.5, as the reactivity of maleimides towards thiolates at pH 7 is 1,000-fold higher than towards free amines.[194] In addition, maleimide-conjugates can undergo a possible thiol-exchange reaction (e.g. with GSH) as a consequence of retro-*Michael* addition. Furthermore, the thiosuccinimide is prone to a ring opening upon hydrolysis (Figure 18c).[195,196]

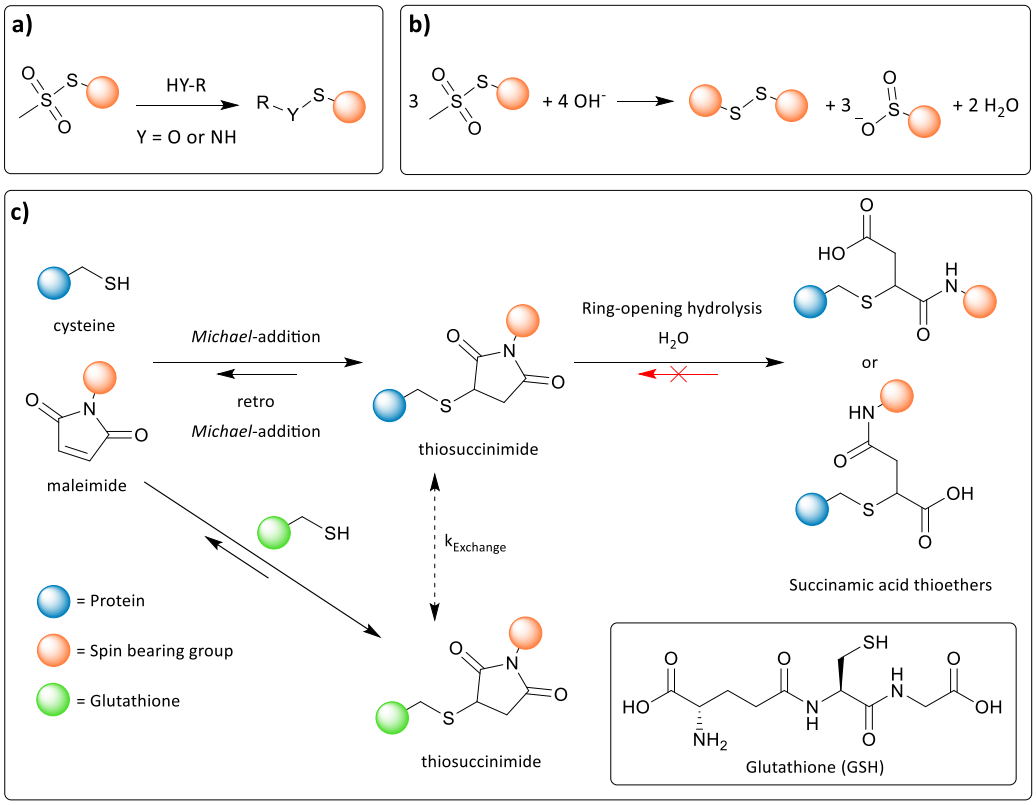

Figure 18: Schematics for thiosulfonate side reactions and maleimide conjugation. **a)** Thiosulfonate side reaction with alcohols and amides, and the resulting coupling products. **b)** Disproportionation of thiosulfonates highlighting the disulfide-bridged by-product. **c)** The *Michael*-addition to cysteines is a reversible reaction with the equilibrium shifted towards the thiosuccinimide. *In cellulo*, a thiol exchange with GSH via the free maleimide is possible to form the GSH-coupled side product. The overall exchange rate can be described by the exchange constant $k_{Exchange}$. Irreversible ring-opening hydrolysis of the thiosuccinimide yields one of two possible succinamic acid thioethers that can no longer undergo a thiolexchange reaction. Blue dots represent the protein, red dots the spin-bearing group, and green dots the GSH.

If the protein of interest (POI) contains many native cysteines and/or cysteine(s) relevant for enzymatic function, the SDSL approach via cysteine modification is unfeasible. In these cases, labeling of other proteinogenic amino acids such as tyrosine with the so-called Nox label in a *Mannich*-type reaction provides a suitable alternative,[197] albeit this reaction shows a relatively low labeling efficiency of only 10% to 14%, even in the excess of 80 equivalents of spin label reagent, and native tyrosines have to be altered to generate tyrosine-free mutants for site specificity.[198]

Alternatively, bioorthogonal spin-labeling reactions with non-canonical functional groups enable site-selective labeling of the POI while retaining enzymatic function.[199] Bioorthogonal functional groups are introduced using amber codon suppression,[200] a technique where an unnatural amino acid (UAA) is incorporated at the desired position of the POI by a modified transfer-RNA (tRNA) that recognizes one of the natural stop codons.[201] Coupling of spin labels functionalized with azides[202–204] or alkynes[164,205] to UAAs via copper(I)-catalyzed azide-alkyne cycloaddition (CuAAC) click chemistry,[206] hydroxylamine coupling to *p*-acetyl phenylalanine,[207] and tetrazine-functionalized labeling by strain-promoted inverse electron demand Diels-Alder (IEDDA) reactions have been reported (Figure 19a-c).[208] Besides these post-translational modification methods, direct incorporation of the spin label in the form of modified amino acids provides a suitable alternative.[209–212] This routine is mainly applied in Boc- or Fmoc-based step-by-step peptide synthesis, which limits the application for larger POIs where the correct folding of the synthetic protein cannot be guaranteed (Figure 19d).[179] Direct incorporation of a spin-bearing unnatural amino acid in overexpressed proteins comes along with severe challenges, as the stability of most spin labels is limited in the cellular environment and suitable tRNAs for recognizing spin-bearing UAAs have to be identified and isolated in an evolving process. To date, there is only one report of a lysine-derived nitroxide-bearing UAA, which has been successfully incorporated into an overexpressed protein, but the low label stability hampered further applications beyond this proof of concept.[213,214]

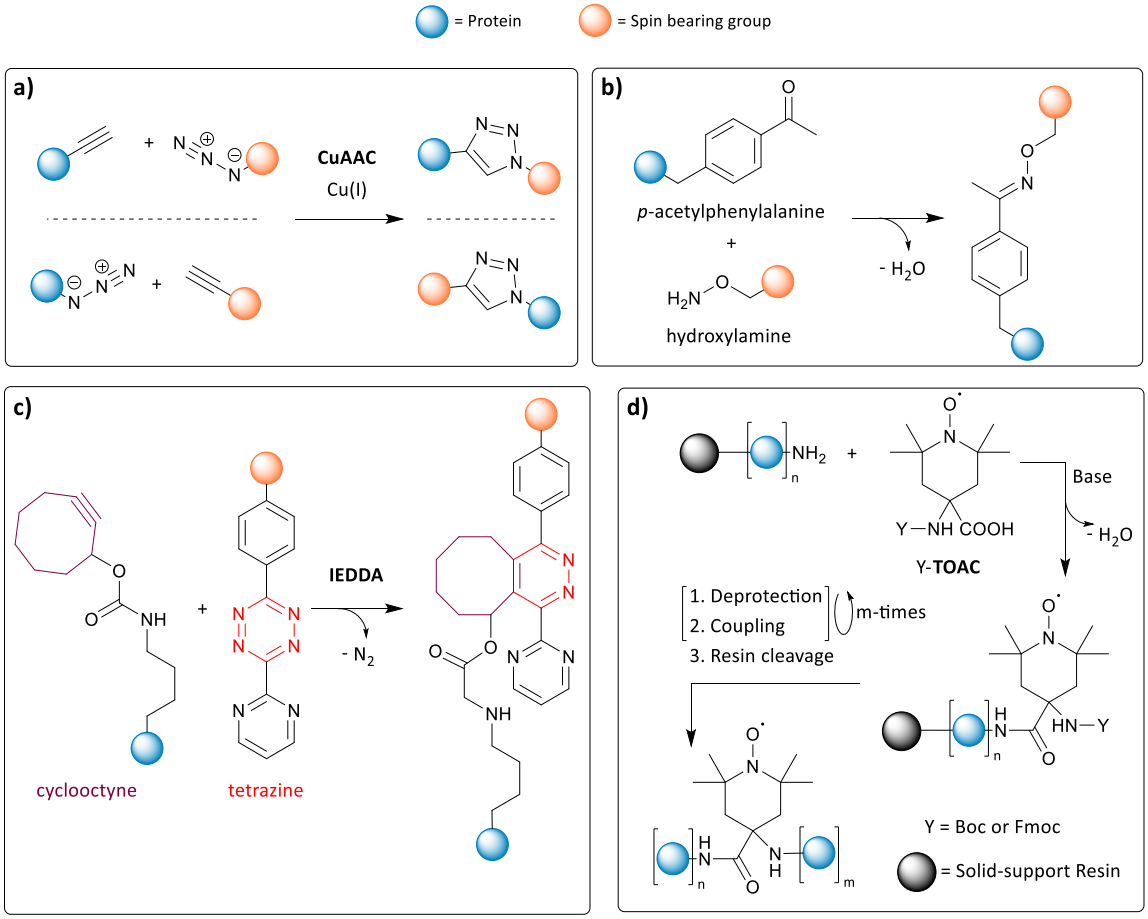

Figure 19: Selection of bioorthogonal labeling strategies for SDSL. **a)** Copper(I)-catalyzed CuAAC labeling scheme. The azide and alkyne moieties can be interchanged between protein and spin label. **b)** Condensation reaction of *p*-acetylphenylalanine and a hydroxylamine-functionalized spin label to yield the ketoxime coupling product. **c)** Strain-promoted IEDDA of a cyclooctyne-functionalized UAA and a tetrazine-conjugated spin label. **d)** Solid-support peptide synthesis scheme for the incorporation of the Boc- or Fmoc-protected spin label 2,2,6,6-tetramethyl-N-oxyl-4-amino-carboxylic acid (Y-TOAC) into a synthetic peptide.

The main advantage of these bioorthogonal labeling strategies is their applicability within cells due to their high chemoselectivity.[199] Drawbacks of UAA incorporation are generally lower protein expression levels, especially within eukaryotic cells, due to the competition of endogenous release factors (RFs) and other competitors responsible for the translational termination and the UAA-loaded tRNAs, resulting in abortion products and lower yields of full-length UAA-modified proteins.[215]

Besides the SDSL approaches described above where the POI is directly spin-labeled, paramagnetic centers can also be introduced indirectly via labeling of bioactive molecules and substrates,[163,216,217] or by labeling highly selective nanobodies, which have been used to report on conformational changes of proteins within cellular membranes.[218]

1.3.2 Spin Labels

A large variety of spin labels is available for SDSL, each with unique advantages, disadvantages, and fields of application. Apart from the spectroscopic properties of the labels, they differ in their chemical and reductive stability, solubility, and bioconjugation motifs. In general, spin labels are categorized according to their spin-bearing group, and until today, most labels belong to one of the following spin label classes: nitroxide spin labels, tetrathiatriarylmethyl (TAM, trityl) spin

labels, and metal chelates.[219] The next sections give an overview of these three label classes and their respective field of application.

1.3.2.1 Nitroxide Spin Labels

Today, the by far most utilized class of spin labels is nitroxide-based, as evident by the plethora of commercially available labels.[220] The nitroxyl (N-O•) radical is embedded in a heterocyclic five- or six-membered ring, mainly piperidine, pyrroline, pyrrolidine, or isoindoline derivatives (Figure 20, top). While unsubstituted nitroxide radicals disproportionate rapidly in a bi-molecular reaction to form a nitrone and hydroxylamine due to α-hydrogen abstraction,[221] their stability can be significantly enhanced by alkyl substitution on the α-carbon atoms.[222] A key structural feature of nitroxide spin labels are the two quaternary α-carbon atoms of the heterocycle whose alkyl side chains sterically shield the radical from the environment and eliminate the option of α-hydrogen abstraction towards the respective nitrone. Nonetheless, nitroxide radicals are susceptible to redox processes to form the hydroxylamine upon reduction or the oxoammonium cation upon oxidation (Figure 20, bottom).[220]

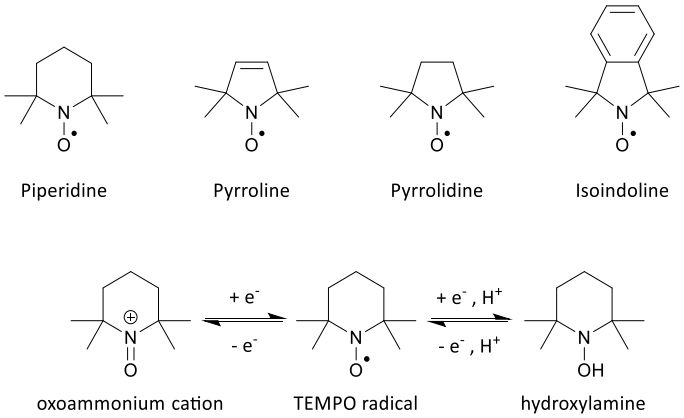

Figure 20: Common parental nitroxides and nitroxide redox scheme. Top row: Structures of frequently used gem-dimethyl nitroxides. Bottom row: Redox scheme of (2,2,6,6-tetramethylpiperidin-1-yl)oxyl (TEMPO) with the nitroxide radical in the middle, the oxidized oxoammonium cation (left) and the reduced hydroxylamine (right).

To form the final spin label, opposite to the radical center, a bioconjugation group is installed that is connected to the heterocycle via a linker group. Figure 21 displays a selection of literature-reported and commercially available nitroxide spin labels with their bioconjugation groups and linker regions highlighted.

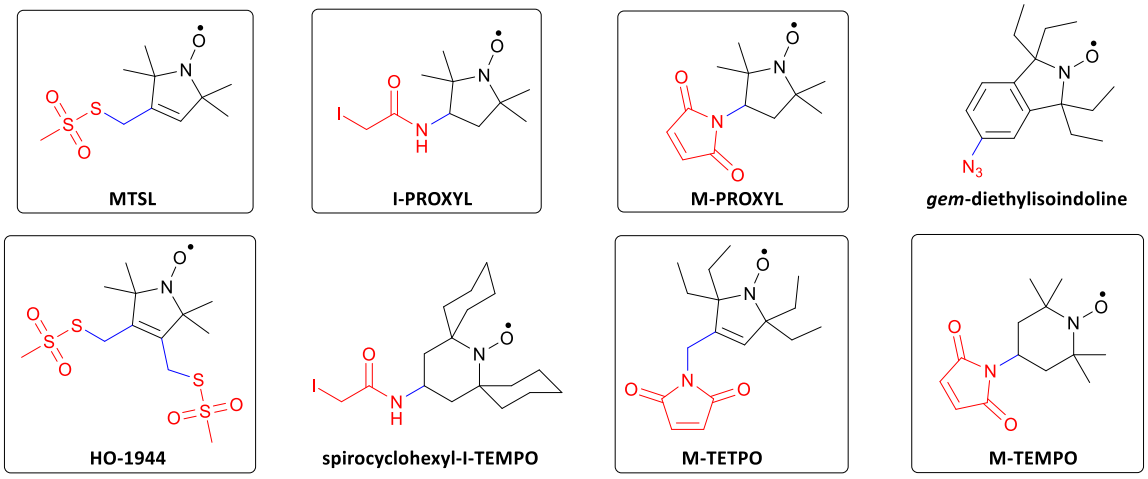

Figure 21: Selection of nitroxide spin labels. Top row (from left to right): **M**ethane**t**hiosulfonate **s**pin **l**abel (MTSL),[223] 3-(2-**i**odacetamido)-**p**yrrolidinyl**oxyl** (I-Proxyl), 3-**m**aleimido-**p**yrrolidinyl**oxyl** (M-PROXYL), and *gem*-diethylisoindoline spin label.[224] Notably, the *gem*-diethylisoindoline label was only used for CuAAC "click reaction" with RNA but bioorthogonal labeling of alkyne-functionalized UAA-containing proteins should be feasible. Bottom row (from left to right): Bipedal methane thiosulfonate spin label (HO-1944),[225] spirocyclohexyl-*p*-**i**odoacteamido-**te**tra**m**ethyl-**p**iperidinyl**o**xyl (spirocyclohexyl-I-TEMPO),[226] 3-**m**aleimido-**t**etra**et**hyl-**p**yrrolidinyl**o**xyl (M-TETPO)[227], and *p*-**m**aleimido-**te**tra**m**ethyl-**p**iperidinyl**o**xyl (M-TEMPO). The bioconjugation groups are highlighted in red and the linker bonds are shown in blue. The framed spin labels are commercially available.

The methanethiosulfonate spin label (MTSL) first introduced by *Berliner* et al. is the most widely used nitroxide-based spin label and is regarded as the "gold standard" for PDS-EPR on biomolecules.[223] The label is highly reactive towards cysteines and after bioconjugation, the label is connected to the protein backbone by a disulfide bridge with five rotatable bonds in total. This modified side chain is commonly referred to as the R1 side chain (Figure 22a).[228] The R1 side chain has a size comparable to large amino acid side chains such as arginine and tryptophane and is generally assumed to not perturb the protein structure.[229] As the differences in the free energies of different label conformations are generally lower than the thermal energy, the conformational degree of freedom induced by the flexible linker translates into broader distance distributions.[230] However, studies on the protein azurin from *Pseudomonas aeruginosa* have demonstrated that the R1 side chain can interact with the protein backbone and select a subset of preferred label conformations.[231] Conformational degrees of freedom can be constrained by stiffer (e.g. *gem*-diethylisoindoline spin label) or shorter (e.g. M-PROXYL and M-TEMPO) linker groups as well as by a bipedal attachment of the spin label like the HO-1944 nitroxide that forms the Rx residue upon bioconjugation (Figure 22b).[232] The drawback of a bipedal label attachment is the necessity for two rather than just one exchanged native amino acids which might have implications on protein structure and dynamics.

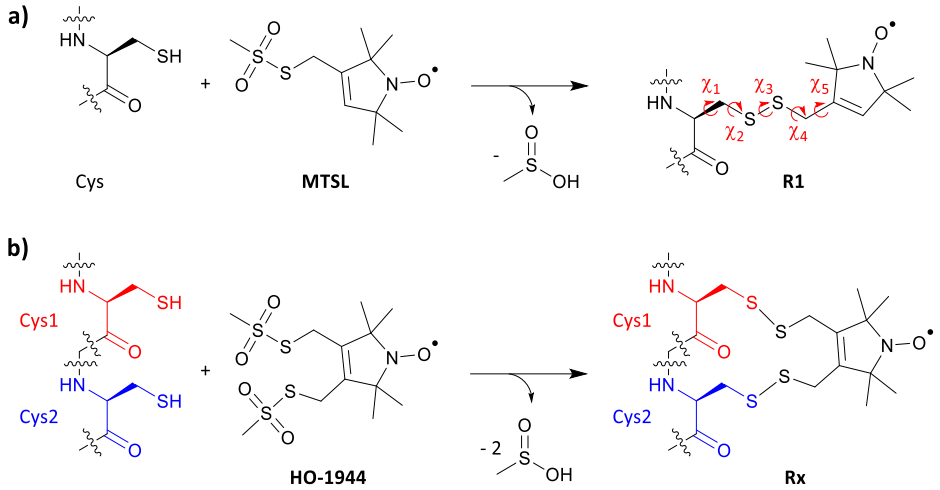

Figure 22: Labeling schemes of MTSL and HO-1944. **a)** Cysteine-conjugation of MTSL yielding the **R1** side chain. The five freely rotatable bonds $\chi_1 - \chi_5$ are indicated by red arrows. **b)** Labeling of two cysteines Cys1 (red) and Cys2 (blue) in spatial vicinity with the HO-1944 spin label yielding the bipedal **Rx** side chain.

Nitroxide spin labels have been widely applied to study proteins *in vitro* but their usefulness for intracellular studies is limited by their susceptibility to reduction.[233,234] There are two handles to tune the chemical stability of the nitroxides:[219] First, the ring size influences the stability of the nitroxide group with six-membered rings generally being less stable than five-membered rings, and unsaturated pyrroline-based nitroxides are more prone to reduction than saturated pyrrolidine derivatives.[235,236] Secondly, the substitution pattern on the α-carbon atoms can significantly enhance the stability of the radical in reductive processes. Methyl substitution provides the least steric protection of the nitroxyl radical followed by bulkier spiro-cyclohexyl residues, and ethyl substitution provides the best steric shielding of the spin-bearing group due to the unrestricted rotational motion of the ethyl chains compared to the more restricted spiro-cyclohexyl rings.[235,237]

Despite their rapid reduction to hydroxylamines in the cellular environment, nitroxide spin labels have been used for *in vivo* studies or measurements in cell extracts.[233] After the first reported *in-cell* EPR study by *Igarashi* et al. in 2010 on M-PROXYL labeled human ubiquitin injected into *Xenopus laevis* oocytes,[238] only a few *in-cell* studies followed using the shielded nitroxide M-TETPO[227] or additional oxidizing agent potassium ferricyanide ($K_3[Fe(CN)_6]$) to regenerate the nitroxide,[239,240] each with limited incubation periods to prevent degradation of the label.

Nitroxides are $s = \frac{1}{2}$ systems with the unpaired electron localized in the π-orbital of the N-O bond with approximately 60% of the spin density residing on the oxygen and 40% spin density on the nitrogen atom.[241] Nitroxides have anisotropic *g*-values with $g_{xx} > g_{yy} > g_{zz}$ with g_{xx} and g_{yy} close to the free electron *g*-value g_e.[220] The spectral width of nitroxides (~9 mT at Q-band)[134] induced by the nitrogen hyperfine splitting of A_{zz} makes PELDOR the most sensitive PDS technique for nitroxides as both, pump and observer pulses, can be sufficiently separated to avoid frequency overlap while still exciting a large fraction of spins.[242] As the phase memory time T_M for *gem*-dimethyl nitroxides is generally low at elevated temperatures, PDS measurements are commonly conducted in a glassy frozen solution with the optimal balance between the T_M and T_1 relaxation times at typically ~50 K.[243] However, T_M is significantly influenced by the direct surrounding of the spin center and by restricting the mobility of the α-carbon substituents, e.g. by substitution of methyl groups with cyclohexyl rings, T_M is significantly enhanced and labeling of T4 lysozyme with

the spirocyclohexyl-I-TEMPO spin label allowed for inter-spin distance measurements at 295 K in a glassy trehalose matrix.[226]

1.3.2.2 Triarylmethyl Spin Labels

The second important class of organic spin labels is based on the carbon-centered triarylmethyl (trityl) radical. Initially discovered by *Moses Gomberg* in 1900 by chance in the search of hexaphenylethane, the simplest trityl, namely the triphenylmethyl radical, rapidly dimerizes to form the so-called Gomberg's dimer (Figure 23a).[244] The asymmetric dimerization between the central carbon atom and a carbon atom in *para*-position can be rationalized by the steric demand of the phenyl substituents that prevent the formation of hexaphenylethane, as well as the delocalization of the unpaired electron across the three phenyl rings that gives rise to free-radical reactivity of the secondary carbon atoms in the peripheral phenyl substituents. Accordingly, dimerization and therefore paramagnetic quenching can be prevented by reducing the overlap of the p_z-orbital of the central carbon atom bearing the free electron and the π-orbitals of the adjacent phenyl substituents, which in turn enhances the kinetic stability. This can be achieved by extensive substitution of the phenyl rings with sterically demanding residues in *ortho*- and *meta*-position such as halides[245,246] or methyl ethers[247] leading the phenyl rings to tilt out of the main symmetry plane (Figure 23b+c).

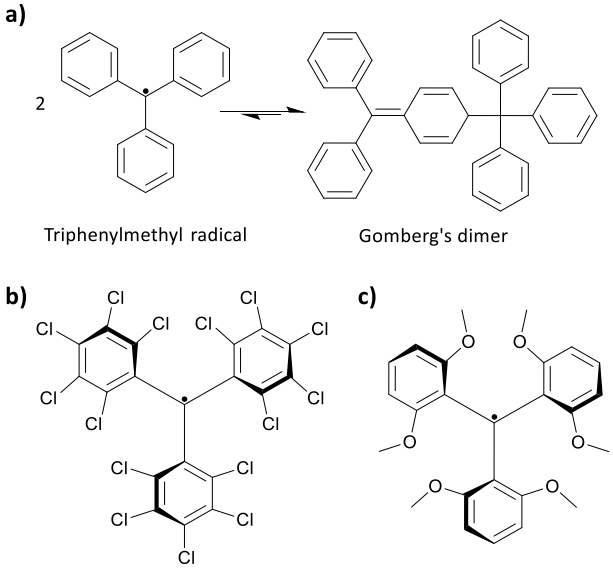

Figure 23: Gomberg's dimer formation and stable triphenylmethyl radicals **a)** Dimerization of two triphenylmethyl radicals to form Gomberg's dimer. At elevated temperatures, the equilibrium shifts in favor of the homolytic dissociation to the triphenylmethyl radical. **b)** Perchlorated triphenylmethyl radical.[246,247] **c)** 2,6-methoxy substituted triphenylmethyl radical.[247] The steric demand of the substitution pattern in **(b)** and **(c)** tilt the phenyl rings out of the central plane, giving these radicals a propeller-like shape and higher stability.

While the perchlorated trityl radical is chemically stable under oxidative conditions and at elevated temperatures, reducing conditions such as ascorbic acid or cellular environments as well as exposure to UV light lead to a fast decay of the EPR signal, therefore hampering a widespread application of this class of trityl radicals.[248] In analogy to the aforementioned halide and methoxy substitution options to "twist" the phenyl rings, the radical stability can be greatly increased upon (thio)ketal substitution to the phenyl rings with thioketal moieties being more stable than ketals.[249] First introduced and patented by *Nycomed* in the 1990s as a contrast agent for magnetic resonance imaging (MRI), a water-soluble tetrathiatriarylmethyl (TAM) radical, the so-called Finland trityl, showed remarkable redox stability suitable for *in vivo* MRI applications as well as

oximetry studies (Figure 24a).[250–252] Here, ~70% of the spin density resides on the central carbon while the remaining ~30% is delocalized in the surrounding aryl rings.[253,254] While also the Finland trityl is not inert to reductive processes within biological systems and enzymatic aerobic and anaerobic metabolism pathways were identified,[255,256] its enhanced intra-cellular lifetime compared to the previously mentioned trityls and most nitroxides makes it a suitable platform for EPR studies in biological environments.[257] Owing to its modular synthesis,[249,258] the basal Finland trityl body offers a multitude of diversification anchors. For example, the carboxylates in *para*-position can be esterified for dendritic PEGylation,[259,260] attached to oligopeptides via amidation reaction,[261] or coupled to dextran-fibers,[262] with all of these options enhancing the solubility of the TAM radical and preventing hydrophobic interactions with proteins and local clustering.[260,263] Beyond carboxylate modification, *Fleck* et al. recently demonstrated the potential of C-C cross-coupling reactions on iodinated Finland trityl precursors in *para*-positions, paving the way for new diversification options with non-statistical, asymmetric TAM functionalization.[264] However, the solubility increase achieved by modification of the carboxylates comes along with the drawback of a significant extension of the molecular framework that hampered further applications beyond the proof of concept.[265] A way to circumvent this issue is the replacement of the methyl groups on the six thioketal moieties with hydroxyethyl sidechains which enhance the water solubility and additionally prevent reductive degradation due to increased steric shielding. This modified version of the Finland trityl is the so-called Ox063 trityl (Figure 24a).[265,266] An overview of the trityl scaffold functionalization options is given in Figure 24b.

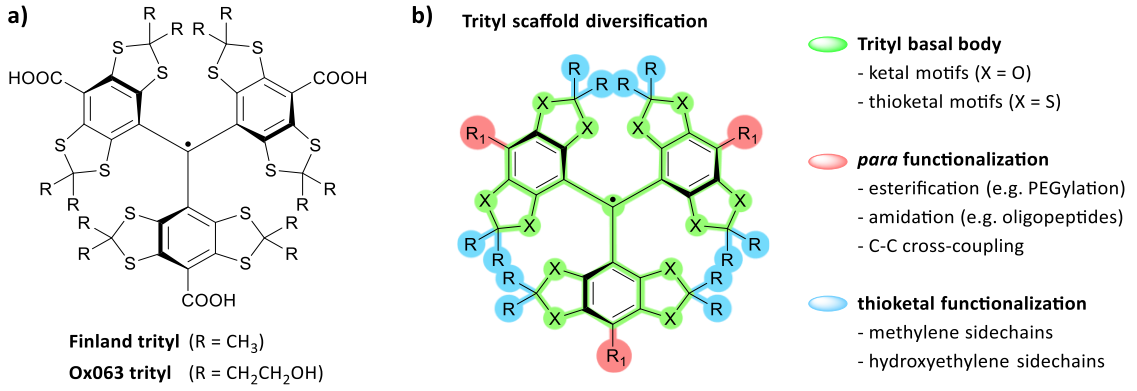

Figure 24: TAM radicals and trityl diversification. **a)** Structures of the Finland trityl (R = CH_3) and the Ox063 trityl (R = (CH_2CH_2OH). **b)** Diversification options of the trityl scaffold with the trityl basal body highlighted in green, the *para*-positions (R_1) in red, and the substituents (R) on the (thio)ketals in blue.

Beyond their application as MRI contrast agents and oxygen sensing probes, TAM radicals have gained increased attention as potential spin labels due to their previously stated redox stability and diversification options, as well as their unique spectroscopic properties. The absence of atoms with a non-zero nuclear spin directly bound to the aryl rings prevents the broadening of the EPR spectrum due to hyperfine interactions and gives TAM radicals their typical narrow (~0.1 mT at Q-band),[267] single-line EPR spectrum (with weak satellite signals stemming from the 1% ^{13}C natural isotope abundance) with small *g*-anisotropy.[257,268,269] Upon deuteration of the thioketal methyl moieties, weak coupling to these peripheral protons can be excluded and the linewidth can be reduced further.[270] Besides the sharp EPR signal, some TAM radicals exhibit transverse relaxation times T_M in the range of microseconds in liquid solution at physiological temperatures, making them promising candidates for PDS-EPR experiments under near-physiological conditions.[271,272] The applicability of TAM radicals as spin probes for distance determination in PDS-EPR has been

demonstrated on a series of model compounds where the single frequencies techniques SIFTER and DQC profited from the narrow linewidth of the EPR signal and outperformed the PELDOR experiment in terms of sensitivity.[145,253] Peripheral modifications of the Finland trityl with a bioconjugation group yielded a variety of trityl spin labels (TSL) for SDSL of proteins (Figure 25).

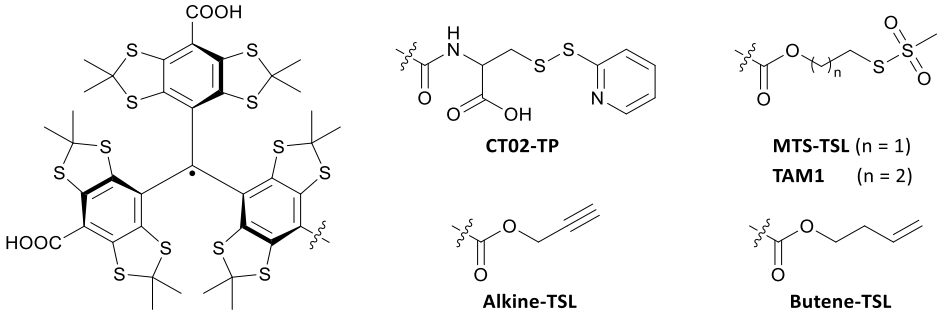

Figure 25: TAM spin labels for protein labeling. Top left: Cysteine-selective dithiopyridine-functionalized CT02-TP label.[273] Top right: Cysteine-selective methanethiosulfonate-functionalized MTS-TSL (n = 1)[164] and TAM1 (n = 2)[274] label. Bottom left: Azido-phenylalanine-selective Alkine-TSL.[164] Bottom right: Cysteine-selective butene-functionalized Butene-TSL.[164]

Using the CT02-TP spin label, *Yang* et al. demonstrated the applicability of TAM radicals as spin labels for biological systems by immobilizing T4 lysozyme on a Sepharose matrix, subsequently labeling the protein, and performing DQC experiments at near-physiological temperatures (4 °C).[273] Following this work, *Shevelev* et al. adapted and expanded the concept to obtain distance information on a TAM-labeled DNA-duplex model system immobilized on NucleosilDMA particles at an increased temperature of 37 °C.[275] The versatility of the basal Finland core for diverse biocompatible functionalization was demonstrated by *Jassoy* et al. synthesizing the MTS-TSL, Alkine-TSL, and Butene-TSL by esterification of one carboxylic acid residue in the Finland trityl. Using Butene-TSL in combination with the intrinsic Fe^{3+}-containing heme cofactor of Cytochrome P450 CYP101, the superior stability of trityls in cellular environments was demonstrated by injecting the labeled protein into *Xenopus laevis* oocytes and recording the first intracellular trityl PDS time trace (TAM-Fe^{3+} RIDME).[164]

However, despite their favorable spectroscopic and redox-chemical properties, the application of TAM spin labels for protein structure elucidation beyond the aforementioned studies has been sparse. The limited application of TAM radicals as spin labels can mainly be rationalized by the high hydrophobicity of the Finland scaffold, which imposes challenges for site-selective labeling as well as protein stability.[273] In addition to the reports of unspecific binding to proteins such as albumin,[263] studies revealed a self-assembly tendency of the Finland trityl at concentrations above 60 µM to form dimers and even nanometer-sized supramolecular entities at millimolar concentrations.[276] In accordance, labeling of the *E. coli* membrane protein BtuB with TAM1 in isolated outer membranes revealed a high tendency of the label to aggregate in the membrane and non-specifically bind to the protein.[277] These aggregation tendencies can potentially be prevented using spin label derivatives where the Finland core is exchanged with the more hydrophilic Ox063 core, but numerous studies revealed synthetic inaccessibility of the Ox063 scaffold following the patented synthetic route and no Ox063-type spin label was reported until the beginning of this work in 2018.[278,279] Another potential drawback of TAM-type spin labels is their relatively large size compared to e.g. nitroxide labels resulting from the bulky spin-bearing trityl core connected via an ester group to a more or less flexible tether and bioconjugation group. Owing to these intrinsic properties, the resulting distance restraints are often broader compared

to respective nitroxide analogs, hence complicating conclusive statements on the biomolecular structure under investigation.[164,274]

1.3.2.3 Metal Chelates as Spin Label

Next to the organic nitroxide and trityl spin labels, the third major class of labels consists of paramagnetic metal cations. In principle, every stable open-shell metal center can serve as a potential spin label and applicability for PDS experiments has been demonstrated for low-spin cobalt(II), low- and high-spin iron(III), manganese(II), copper(II), and gadolinium(III).[280] However, as gadolinium and copper are the most frequently applied cations for SDSL, this section will only focus on spin labels containing one of these two metal centers.

In brief, the Gd^{3+} ion is a high-spin system with half-filled 4f valence orbitals resulting in a $s = \frac{7}{2}$ system with an isotropic *g*-value of ~2. The characteristic EPR spectrum of Gd^{3+} is dominated by the central $|-1/2\rangle \leftrightarrow |1/2\rangle$ transition with the underlying broader, less intense higher electron spin transitions.[281] In strong contrast to organic radicals such as nitroxides, where the spectral width increases with higher magnetic fields as the *g*-anisotropy is resolved, the width of the Gd^{3+} EPR spectrum narrows with increased magnetic field strength, hence making high-field measurements favorable.[282] Typically, PELDOR is the PDS method applied in combination with gadolinium tags.[281] Using high-affinity chelating ligands for the Gd^{3+} ions such as dipicolinic acid (DPA) or tetraxetan (DOTA) derivatives, a set of gadolinium spin labels for both, proteins and oligonucleotides, have been developed (Figure 26).[283]

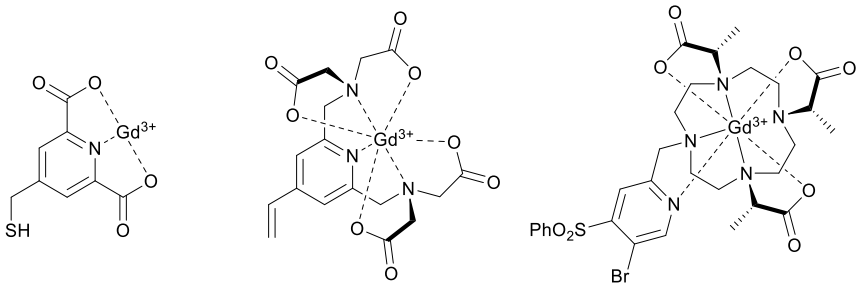

Gd-4MMDPA **Gd-4-vinylPyMTA** **Gd-DO3MA-3BrPy**

Figure 26: Selection of cysteine-selective gadolinium-based spin labels. From left to right: Gd-4MMDPA tag,[284] Gd-4-vinylPyMTA tag,[285] and Gd-DO3MA-3BrPy tag.[286]

One of the main advantages of Gd^{3+}-tags compared to nitroxides is their high redox stability, making them ideal nitroxide substitutes for PDS experiments in cellular environments. Following the initial proof of concept for PDS on Gd^{3+}-labeled proteins by *Goldfarb* et al.,[284] numerous studies followed demonstrating the potential of gadolinium for the investigation of transmembrane helices,[287] their enhanced sensitivity at high magnetic fields,[288] and application as spin labels for *in-cell* distance measurements.[218,285,286,289] However, the application of Gd^{3+} spin labels comes along with a set of challenges. Firstly, owing to the short transverse relaxation time T_M at elevated temperatures, measurements have to be conducted at cryogenic temperatures between 3 K (Q-band) and 10 K (W-Band).[281] Combined with the necessity of high-field instrumentation to exploit the sensitivity enhancement, the applicability of Gd^{3+} spin centers for PDS is limited to a selected number of laboratories with appropriate equipment. Secondly, the multidentate chelator tags necessary for Gd^{3+} complexation possess an intrinsically larger size than common nitroxide labels and, combined with the flexible tethers bearing the bioconjugation motif, lead to a broader distribution that may complicate the translation to the biomolecular structure. However, similar to trityl labels, the chemo-diversity of the chelators allows for linker

adjustments and restricted rotational flexibility[290] as in the case of the Gd-DO3MA-3BrPy label, where the nitrogen atom of the pyridine carrying the bioconjugation group serves as an additional coordination site.[286] In PELDOR, the modulation depth of Gd^{3+} labels is typically low (< 10%) when using common rectangular pulses.[281] Here, however, Gd^{3+} can be treated as a $s = \frac{1}{2}$ system and the dipolar coupling frequency can be readily extracted from the time trace, therefore simplifying data analysis. Notably, this is not the case when applying the RIDME sequence, as here the higher harmonics of the dipolar coupling frequency ($2\nu_{Dip}$ and $3\nu_{Dip}$) additionally modulate the time trace and hence complicate data analysis.[280]

The second frequently applied metal ion in PDS-EPR is copper(II). The Cu^{2+} ion has a $s = \frac{1}{2}$ ground state, an anisotropic *g*-tensor, and an anisotropic hyperfine coupling tensor to the copper nuclear spin ($I = \frac{3}{2}$) resulting in a broad EPR spectrum exceeding common resonator bandwidths.[291,292] Initial PDS studies on biomolecules relied on intrinsic Cu^{2+}-coordination sites that were, for example, used to localize inhibitory copper binding sites of the EcoRI endonuclease,[293] obtain information about the relative orientation of the two Cu^{2+} centers in the homodimeric Copper Amine Oxidase,[294] or triangulate the Cu^{2+} position in the soluble blue copper protein Azurin by PELDOR using the Cu^{2+}-nitroxide spin pair.[129] All of the aforementioned studies revealed orientational selection for the PELDOR experiment at both, X- and Q-band frequencies, owing to the width and *g*-anisotropy of the Cu^{2+} center and multiple time traces recorded across the Cu^{2+} spectrum were necessary to obtain reliable distance information. While this in principle makes data analysis more involved, fitting the time traces using geometric models that take the *g*-anisotropy and orientational effects explicitly into account can yield further information beyond the distance restraints such as angular information about the Cu^{2+} *g*-frame orientation.[129,295] Recently, copper(II) gained widespread interest as a potential spin label for SDSL after *Saxena* et al. introduced the copper(II)-iminodiacetic acid [Cu^{2+}(IDA)][296,297] and copper(II)-nitrilotriacetic acid [Cu^{2+}(NTA)][298] complexes that coordinate to two adjacent histidines (dHis)[299] in a protein. Coordination of the Cu^{2+}(IDA) or Cu^{2+}(NTA) complex by two histidines separated by three amino acids (HXXXH) in the case of α-helices or one amino acid (HXH) in β-sheets yields the dHis-Cu^{2+}(IDA) or (NTA) motif, respectively. As the tetra-dentate NTA ligand occupies the remaining four coordination sites of the octahedral Cu^{2+} coordination sphere upon dHis conjugation, it shows a four-fold higher site-selectivity towards α-helical dHis motifs compared to the tri-dentate IDA ligand and is nowadays the preferred ligand (Figure 27).[298]

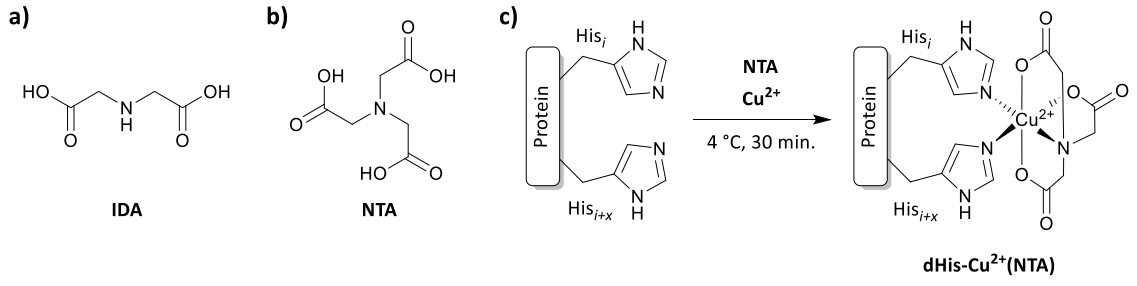

Figure 27: Copper(II) chelators and dHis-Cu^{2+}(NTA) labeling scheme. **a)** Iminodiacetic acid (IDA) **b)** Nitrilotriacetic acid (NTA). **c)** Labeling of a dHis-site with Cu^{2+}(NTA) to form the dHis-Cu^{2+}(NTA) motif.

In analogy to the HO-1944 nitroxide spin label, the bipedal coordination of Cu^{2+}(NTA) to the protein backbone restricts the conformational flexibility of the dHis-Cu^{2+}(NTA) label and was shown to yield distance distributions up to five times narrower than the ones obtained with MTSL.[296,297] Exploiting this narrow distribution width, the dHis-Cu^{2+}(NTA) label has been used to

resolve small-scale conformational changes in proteins[300,301] and for the trilateration of native metal binding sites.[302] In addition to the high-resolution PDS distance information obtained with the dHis-Cu^{2+}(NTA) label, the exothermic labeling process is straightforward,[303] does not require post-translational covalent modification,[304] and labeling is achieved in ~30 min.[305] Determination of the Cu^{2+}(NTA) binding constant using RIDME modulation depth analysis in a pseudo-titration series at nanomolar concentrations revealed high binding affinities and equilibrium constants at a higher precision than achievable with isothermal calorimetry (ITC).[306] However, currently the dHis-Cu^{2+}(NTA) labeling methodology has only been applied to systems with either no native histidines,[296,298,301,303] one buried histidine,[307,308] or five native histidines,[301] and a thorough assessment of the site-specific coordination of Cu^{2+}(NTA) to the dHis motif in histidine-rich proteins is still lacking.

1.4 Protein Model Systems

The following sub-sections will introduce the protein systems investigated and utilized throughout this work.

1.4.1 *Yersinia* outer protein O

The Gram-negative bacterium *Yersinia pestis* is the causative agent of the plague, a highly infectious disease responsible for a set of devastating epidemics in the Middle Ages up until the modern era with millions of casualties throughout Europe and Asia.[309] From the vast variety of different *Yersiniae s*trains, three, namely *Y. pestis* and its close relatives *Y. enterocolitica* and *Y. pseudotuberculosis*, show pathogenicity against mammals and harbor a unique ~70 kb *Yersinia* virulence plasmid (pYV) encoding for ~30 proteins that enable the bacteria to evade its host's innate immune response consisting of macrophages and dendritic cells.[310] Similar to other pathogenic bacteria such as *Salmonella sp.* or *Pseudomonas aeruginosa*, pathogenic *Yersiniae* utilize a specialized protein delivery system known as type-III secretion system (T3SS) to deliver its main virulence factors, extracellular effector proteins known as ***Y****ersinia* **o**uter **p**roteins (Yops), into the immune cells and evade digestion.[311] The T3SS is a syringe-like structure consisting of multiple proteins whose gene expression is calcium- and thermoregulated. While gene expression is suppressed at 26 °C, temperatures of 37 °C and millimolar calcium concentration significantly up-regulate gene transcription of the secretion system and Yops. Upon immune cell contact, the T3SS penetrates the cell membrane of the immune cell and translocation of the effector proteins proceeds.[312,313]

There are six known *Yersinia* effector proteins (YopE, YopH, YopJ, YopM, YopO, and YopT), each with a uniquely tailored function that modulates distinct host cell signaling pathways, thereby preventing bacterial digestion. Interestingly, all effector proteins are in a dormant state before translocation and get activated only upon host substrate contact, presumably as a self-preservation measure of the bacterium.[314] The effector-protein function can be subdivided into two main courses of action: On the one hand, YopJ and YopM prevent inflammatory immune response while triggering simultaneous apoptosis, while the four other Yops disrupt the actin-based cytoskeleton to prevent phagocytosis by phagocytic cup formation.[315] YopJ is a ubiquitin-like cysteine protease with additional acetyl-transferase activity.[316] Using acetyl-coenzyme A (CoA), YopJ inhibits phosphorylation of MAPKK6 and thereby shuts down the mitogen-activated protein kinase (MAPK) and nuclear factor *κ*B (NF-*κ*B) signaling pathways critical for immune response.[317] YopM sequesters and inhibits caspase-1 activity and thereby acts as a potent antagonist against pyroptosis, an inflammatory cell death mechanism of the innate immune response as a protective measure against pathogens.[318] In addition, YopM acts as an E3 ubiquitin ligase and was shown to induce necrotic cell death upon ubiquitination of the crucial NLRP3

receptor.[319] The actin cytoskeleton is mis-regulated by the concerted action of YopE, YopH, YopT, and YopO. While YopH is a powerful phosphotyrosine phosphatase that disrupts focal adhesion of the bacterium to the immune cell by dephosphorylation of the p130CAS focal adhesion kinase (FAK),[320] both, YopE and YopT, interact with monomeric GTPases of the Rho-family by acting as a GTPase-activating protein and switching the targeted GTPases to their 'off'-form (YopE)[321] or cleaving Rho-family proteins from the membrane, thereby causing a depolymerizing effect on actin (YopT).[322]

YopO from *Y. enterocolitica* (and its structure homolog *Yersinia* protein kinase A (YpkA) from *Y. pestis* and *Y. pseudotuberculosis*) is a 729 amino-acid (732 residues in YpkA) membrane-associated protein.[323] In the Yop family, YopO is the only protein consisting of two distinct enzymatic domains, an N-terminal serine/threonine kinase domain and a C-terminal Rac/Rho GTPase binding domain (Figure 28a).[324–326] YopO was shown to be an essential virulence factor of *Yersinia* and is heavily involved in the disruption of the actin cytoskeleton (Figure 28b).[324,326–328] The structure of the isolated C-terminal sequence (residues 430-729) in complex with Rac1 was solved in 2006 by *Prehna* et al. and revealed high structural similarities with eukaryotic guanidine nucleotide dissociation inhibitors (GDIs),[326] thereby enabling inhibition of GTPase nucleotide exchange crucial for the regulation of actin polymerization (Figure 28c).[329] The N-terminal kinase domain (residues 90-429) shares a high sequence homology with eukaryotic Ser/Thr kinases and, in analogy to the other Yops, is catalytically autoinhibited before translocation to the host cell.[324,325] YopO was shown to form a tight 1:1 complex with monomeric actin (G-actin) and thereby inhibits the ability of the bound actin to incorporate and form filamentous actin (F-actin).[328,330] *Trasak* et al. revealed that the last 19 amino-acid residues on the C-terminal end of YopO show sequence homology to the actin-binding protein coronin and are essential to form the YopO/actin complex.[330] In addition, binding of G-actin triggers autophosphorylation of the YopO residues S90 and S95,[330] thereby releasing the kinase inhibition and enabling YopO to use actin as a bait to phosphorylate and mis-regulate proteins involved in the regulation of actin polymerization such as VASP, WASP, EVL, and gelsolin.[328,331] While there is no atomistic model of the full-length apo-YopO, the crystal structure of truncated $YopO_{89\text{-}729}$ in complex with actin was solved in 2015 by Lee *et al.* (Figure 28c).[328]

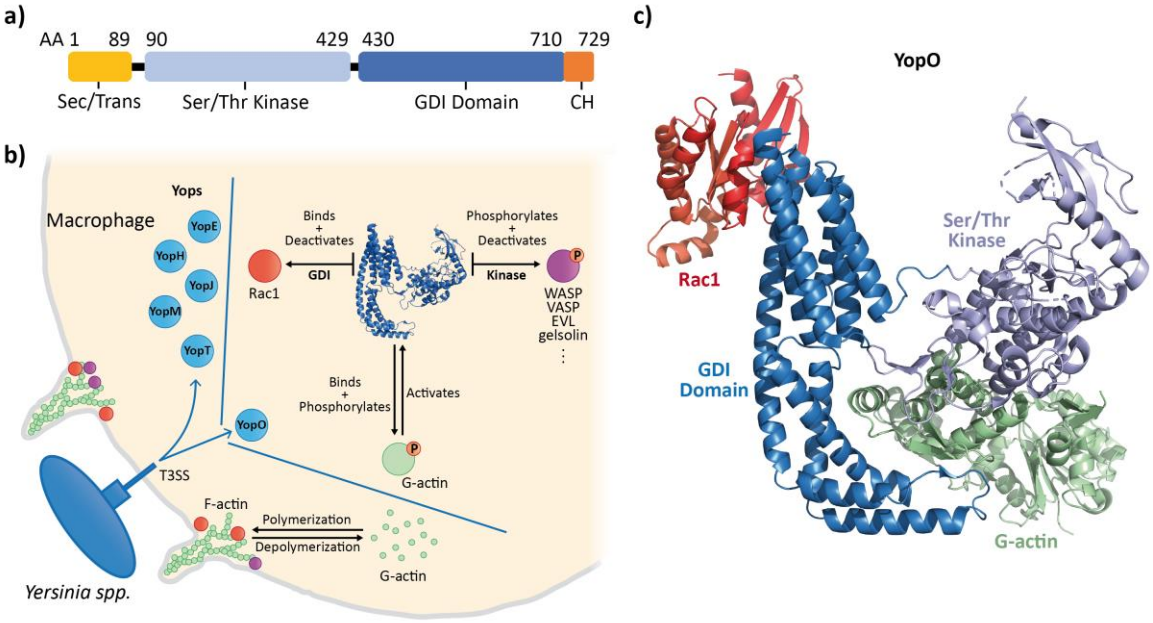

Figure 28: Protein organization, virulence pathways, and crystal structure of YopO. **a)** Simplified domain organization of YopO with the secretion and translocation domain (1-89) shown in orange, the Ser/Thr kinase domain (90-429) shown in light blue, the GDI-like domain (430-710) shown in dark blue, and the coronin homology region (710-729) necessary for actin binding shown in orange. **b)** Schematic representation of the *Yersinia* defense mechanism against macrophages and the involvement of YopO in the disruption of the actin cytoskeleton. **c)** Combined crystal structures of the PDB-IDs 4ci6 ($YopO_{89-729}$/actin complex)[328] and 2h7v ($YpkA_{434-732}$/Rac1 complex)[326] with YopO shown in blue color tones, G-actin in green, and Rac1 in red.

In the $YopO_{89-729}$/actin complex structure, G-actin forms a large contact interface with the kinase domain and the C-terminal part (residues 710-729) of the GDI domain and is wedged in between those two subdomains of YopO. In the crystal structure, the active site of the kinase domain is highly accessible, thereby explaining YopO's capability to phosphorylate actin-regulatory proteins sequestered by the G-actin bound below. Structural comparison of the isolated GDI domain (PDB-ID 2h7o) and the $YopO_{89-729}$/actin complex reveals a straight conformation of the α-helical backbone in the isolated GDI domain while the helical backbone is bent in the $YopO_{89-729}$/actin complex.[328] Based on these findings, *Lee* et al. hypothesized that in the absence of G-actin, YopO adopts a different conformation with an inaccessible kinase domain flipped 'over' the GDI domain, thereby causing autoinhibition of the apo-state and a straight backbone helix of the GDI domain. Actin binding then triggers a multistage activation process and a conformational change resulting in a bent helical backbone of the GDI domain, the actin being sandwiched between the two YopO domains, and an accessible active site. However, this hypothesis was recently disproven by studies from *Peter* et al. who used EPR spectroscopy in combination with SAXS to reveal that in solution, the kinase and GDI domain of YopO are highly flexible towards each other in the absence of actin and inhibition of the kinase by steric hindrance is unlikely.[332] Notably, an integrative structural model of the $YopO_{89-729}$/actin complex using PELDOR and SAXS restraints in conjunction with rigid body docking of the crystal structure subdomains revealed striking differences in the solution structure compared to the crystal structure. In the resulting low-resolution model, the kinase domain seems to be tilted 'backward' compared to the crystal structure and the GDI domain has a straight backbone helix similar to the crystal structure of the isolated GDI and the authors concluded a more flexible YopO/actin complex in solution than the crystal structure might suggest.[332] A potential blockage of the kinase active site in the apo state by the N-terminal lobe

(residues 89-109) that is not resolved in the crystal structure was ruled out, as PELDOR experiments on MTSL-labeled N-terminal lobe and kinase domain revealed a high conformational flexibility of the lobe, hence making a steric inhibition of the kinase active site implausible.[332] As of today, there is no structural model for the full-length protein and the underlying mechanism of kinase activation is yet unresolved.

1.4.2 Myoglobin

Myoglobin (Mb) is a muscle tissue protein that, similar to hemoglobin,[333] reversibly binds oxygen.[334] Compared to hemoglobin, myoglobin does not form multimeric species and has a higher affinity towards oxygen, thereby serving as an oxygen depot within the tissue.[335] The 17 kDa Mb-protein belongs to the class of globins, an evolutionary highly conserved enzyme superfamily characterized by their distinct tertiary structure consisting of eight alpha helices as well as their common heme-cofactors.[336] In myoglobin, the heme-cofactor is an iron-containing protoporphyrin IX (heme B), where oxygen occupies the remaining free, axial coordination site to form the bright-red oxymyoglobin (MbO_2) (Figure 29a).[337] However, the ferrous iron Fe^{2+} center of MbO_2 is relatively unstable and readily oxidized to Fe^{3+}, thereby yielding the more stable, brownish metmyoglobin (MetMb).[338] As pointed out in section 1.1.1, due to its high stability and relatively high abundance, myoglobin from the sperm whale was the first protein whose three-dimensional structure was solved by X-ray crystallography (Figure 29b).[29]

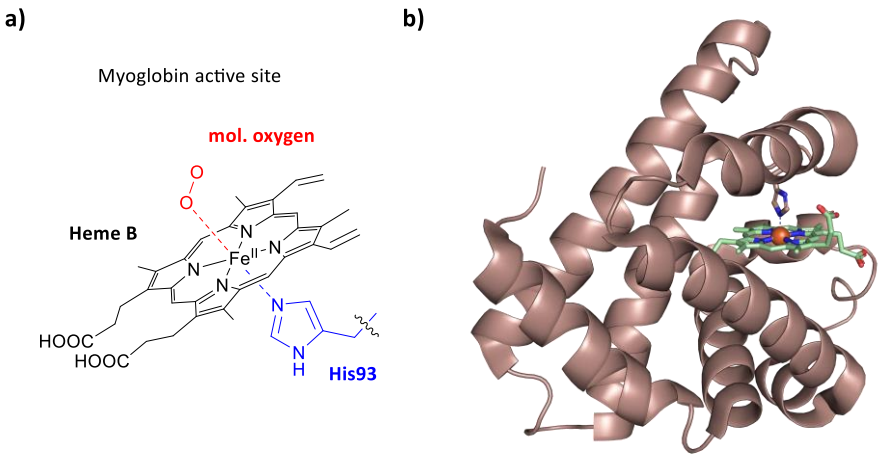

Figure 29: Myoglobin active site and crystal structure. **a)** Schematic representation of the MbO_2 active site with the heme B cofactor displayed in black, the coordinating His93 of the myoglobin backbone in blue, and the bound oxygen in red. **b)** Crystal structure of recombinant horse heart myoglobin (PDB-ID 1wla,[339] bronze) with the coordinating His93 residue highlighted as a stick model and the heme B cofactor shown in green.

As one of the best-studied proteins in biological sciences, myoglobin has gained interest in the EPR community as a model system owing to the intrinsic paramagnetic Fe^{3+}-center of MetMb. For example, the transition from a high-spin (hs) to low-spin (ls) electron configuration upon azide binding to the Fe^{3+}-cofactor[340] in MetMb was used for kinetic studies and calibration of rapid freeze-quenching (RFQ)[341] as well as microsecond freeze-hyperquenching (MHQ) devices.[166] In addition, as the EPR high-field approximation breaks down in the hs-MetMb case due to the large zero-field splitting, MetMb was used as a model system to expand PDS methodologies to spin systems that do not obey the high-field approximation.[342]

1.4.3 *Streptococcal* Protein G B1 domain

The protein G from *Streptococcus sp.* is a ~60 kDa protein located at the cell surface and belongs to the class of immunoglobulin-binding proteins (IBPs).[343,344] Protein G is capable of non-immune binding to the Fc region of immunoglobulin G (IgG) antibodies,[345] thereby counteracting the formation of the C1 complex and inhibiting opsonization in the complement cascade of the immune response of infected host cells.[346] Exploiting the high affinity of protein G towards IgG antibodies, albumin-binding deficient recombinant protein G immobilized on a solid-support resin is frequently used for the purification of monoclonal antibodies.[347]

The 57 amino-acid residue subdomain B1 of protein G (GB1) is an extensively studied protein model system (Figure 30a). Owing to its small size, high expression rates, and good solubility, GB1 has been used to investigate the mechanisms and principles of protein folding,[348] to establish new methodologies for protein structure elucidation such as *in-cell* NMR,[349] and was established as a protein tag to enhance the solubility of poorly soluble proteins.[350] The GB1 structure consists of two β-hairpin motifs on one side of the protein that are connected via an α-helix on the opposing side of the protein (Figure 30b+c).[348,351]

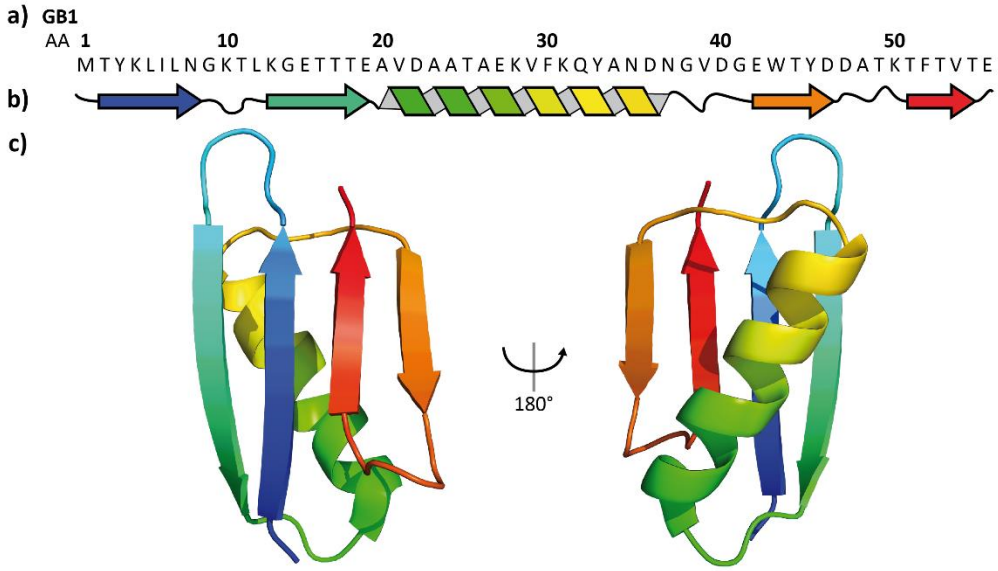

Figure 30: GB1 amino acid sequence and structure. **a)** Amino acid sequence of GB1 from *Streptococcus sp. G148*. **b)** Simplified scheme correlating the sequence with the β-hairpin (arrows) and α-helix motifs. **c)** NMR solution structure of GB1 (PDB-ID 3gb1)[351] with the β-hairpin side (left) and the α-helix side (right) facing the viewer. For better comparability, **(b)** and **(c)** share the same color code.

In the field of PDS-EPR, GB1 is often utilized as a model system and was the protein of choice for the development of the dHis-Cu^{2+}(IDA)[297] and dHis-Cu^{2+}(NTA)[298] labeling strategies as well as expansions and evaluations of the concept.[296,302,303,305,306] In addition, a Gd^{3+}-labeled GB1 mutant was used for PELDOR measurements in HeLa cells to demonstrate the feasibility of a new gadolinium(III) spin label.[352]

2. Aims of this Study

EPR has become an increasingly important method in structural biology. With the evolution and emergence of complementary methodologies providing biomacromolecular structures at (near)-atomic resolution such as AlphaFold2 or cryo-EM, EPR-derived distance information provide restraints to verify those models and offers insights into structure and dynamics in aqueous solutions. While the commonly employed MTSL nitroxide spin label in combination with PELDOR spectroscopy has been used in numerous studies, there are to date no community-defined standards on sample preparation, data acquisition, interpretation, and reporting of the results. To comply with the requirements, set by a workshop of the integrative structural biology community,[353] a multi-laboratory ring test driven by the EPR community was set out to define community-approved guidelines and establish best-practice standards for quality assurance in sample preparation and data analysis. In the first section of the work presented herein, the intention was to develop a generalized protocol for labeling proteins with the MTSL spin label followed by standardized quantification and structural integrity assessment routines. By comparing the PELDOR measurements and distance information obtained by all participants of the ring test, the accuracy, reliability, and reproducibility of PELDOR measurements were to be elaborated and guidelines set for future work within the EPR community.

As outlined in section 1.3.2.2, despite their beneficial chemical and spectroscopic properties, a widespread application of TAM spin labels is hampered by challenges arising in the labeling procedure, quantification of the labeling efficiencies, and stability of biomolecules upon trityl bioconjugation. Owing to their inherent hydrophobicity, TAM labels tend to non-covalently bind to protein surfaces or membranes and cause proteins to precipitate. Using an established methanethiosulfonate-functionalized TAM label as well as newly designed maleimide-functionalized trityl spin labels of the *Schiemann* group, these challenges are addressed in the second part of this thesis. Firstly, a reliable and reproducible labeling strategy for TAM labels and a quantification routine focused on selective labeling of the protein and quantitative removal of any excess label was to be developed on the example of the well-controlled protein YopO as a model system. Following up, the scope of the established labeling strategy was to be expanded to other protein systems and the performance of the TAM-labeled proteins with regards to their SNR, distance distribution width, redox properties, and suitability for *in-cell* PDS applications was to be assessed.

In PDS-EPR, the width of the obtained distance distribution is influenced by the length and conformational flexibility of the linker motif connecting the spin-bearing group to the protein backbone. This in turn can complicate data interpretation, as a decisive assignment of the individual contributions of the flexibility of the protein backbone and the spin label to broad or multimodal distance distributions is difficult. In the first two parts of this work, multimodal distance distributions were obtained for the MTSL- and TAM-labeled α-helical backbone of YopO, and the origin of these multimodalities was ambiguous as two structural models of the helix backbone are available (see section 1.4.1). To verify whether indeed two distinct protein conformations are present in solution or the observed multimodalities originate from preferred conformations of the previously utilized spin labels, in the third section of this thesis, the more rigid dHis-Cu^{2+}(NTA) spin label was used to minimize the effects of conformational label flexibility. Since the dHis-Cu^{2+}(NTA) spin label was hitherto utilized only with smaller model systems or proteins with a low native histidine abundance, in the context of this work, the general applicability of the postulated labeling scheme is evaluated on the example of YopO, a protein with a high native histidine abundance. As the spectroscopic properties of Cu^{2+} enable PELDOR

and RIDME, both pulse sequences are compared regarding their SNR and susceptibility to orientational selectivity. From the resulting distance distributions, the helix backbone conformation of YopO in solution ought to be unequivocally determined.

3. Results and Discussion

3.1 Guidelines for Side-directed Spin Labeling with Nitroxides

Parts of this chapter have been published in:

[354] O. Schiemann, C. A. Heubach, D. Abdullin, K. Ackermann, M. Azarkh, E. G. Bagryanskaya, M. Drescher, B. Endeward, J. H. Freed, L. Galazzo, D. Goldfarb, T. Hett, L. Esteban Hofer, L. Fábregas Ibáñez, E. J. Hustedt, S. Kucher, I. Kuprov, J. E. Lovett, A. Meyer, S. Ruthstein, S. Saxena, S. Stoll, C. R. Timmel, M. Di Valentin, H. S. Mchaourab, T. F. Prisner, B. E. Bode, E. Bordignon, M. Bennati, G. Jeschke, "*Benchmark Test and Guidelines for DEER/PELDOR Experiments on Nitroxide-Labeled Biomolecules*", *J. Am. Chem. Soc.* **2021**, 143, 17875–17890.

The following sections summarize the results and discussion of the best-practice guideline development for nitroxide-based SDSL of proteins. Since MTSL (Figure 20) is by far the most utilized spin and is regarded as the "gold standard", it was chosen to serve as the reference spin label. A truncated version of YopO ($YopO_{89\text{-}729}$) lacking the first 88 N-terminal amino acid residues (translocation/secretion domain) served as the protein model system since YopO is known as well-behaving, meaning it is soluble, stable, can be expressed in sufficient yields, and contains only one native cysteine (C219) which can be replaced by alanine without loss of function.[332] This $YopO_{89\text{-}729}$ C219A construct is henceforth referred to as YopO-wt. For the following ring test, four double-cysteine YopO constructs originating from the YopO-wt, all with varying expected interspin distances, were designed. For the first three mutants, namely YopO S585C/Q603C, YopO V599C/N624C, and YopO Y588C/N624C, the labeling positions spanned the long α-helical backbone of YopO's GDI domain with a total of 18, 25, or 36 amino acid residues in between the labeling sites (Figure 31a). Hence, the PELDOR experiments are expected to yield rather narrow distance distributions and show a shift towards longer distances upon increasing the number of residues between the labeling sites. On the other hand, the fourth construct, YopO S353C/Q635C, with one labeling site on the lower GDI domain (Q635) and the second site located in a loop region (S353), is expected to yield a rather broad distance distribution in conjunction with the previous findings of high flexibility between both, the kinase and GDI domain, of YopO in the apo-state.[332] All labeling sites and *in silico* distance distributions obtained by mtsslWizard[355] are displayed below (Figure 31b).

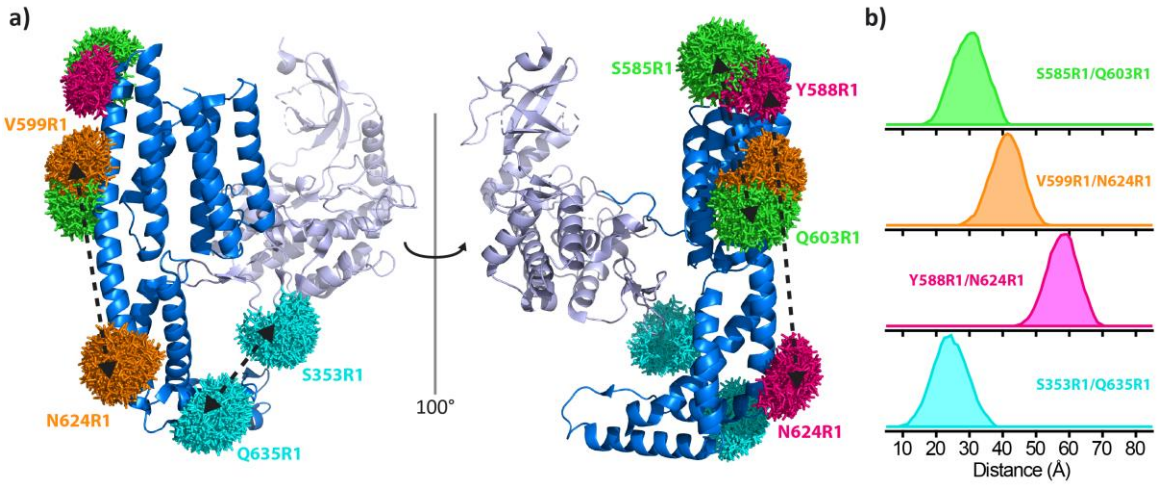

Figure 31: YopO labeling sites and *in silico* distance distributions. **a)** Depiction of the $YopO_{89-729}$ crystal structure (PDB-ID 4ci6, actin removed) from two angles and the rotamer clouds of the R1 side chain generated with mtsslWizard (clash setting: loose) using the PDB-ID 4ci6 as input structure. For simplicity, each of the R1 spin pairs is highlighted in the same color code (YopO S585R1/Q603R1 green, YopO V599R1/N624R1 orange, YopO Y588R1/N624R1 pink, YopO S353R1/Q635R1 cyan). **b)** *In silico* distance distributions derived by mtsslWizard of the R1 spin pairs shown in **(a)** using the same color code. Note that in the *in silico* prediction, YopO S353R1/Q635R1 shows a short and narrow distribution, which was disproven by *Peter* et al.[332]

3.1.1 Design, Expression, and Purification of YopO Mutants

As the site-directed mutagenesis of any of the chosen native amino acid residues to cysteine did not impact the expression, purification, and total yield of YopO, the site-directed mutagenesis and protein purification is described and discussed on the example of the YopO S585C/Q603C construct. Notably, a plasmid encoding for YopO S353C/Q635C already existed from previous studies, hence making site-directed mutagenesis for this construct redundant.

After *QuickChange* mutagenesis and vector amplification by polymerase chain reaction (PCR), the crude PCR product was analyzed via agarose gel electrophoresis (Figure 32a). Here, both the sample lane 2 as well as the control lane 3 without added polymerase showed a primer cloud in the low molecular weight regions (below 200 bp) of the gel but, in contrast to the control, the sample lane 2 exhibited an intense, high molecular weight band at ~6900 bp, indicative of successful mutagenesis and PCR amplification of the pGEX-6P-1 target vector (4984 bp) containing the glutathione *S*-transferase (GST)-fused YopO gene (1923 bp). After *DpnI* digestion and amplification in *E. coli* DH5α cells, the purified vector was sequenced and successful mutation and construct identity was confirmed (Figure 32b).

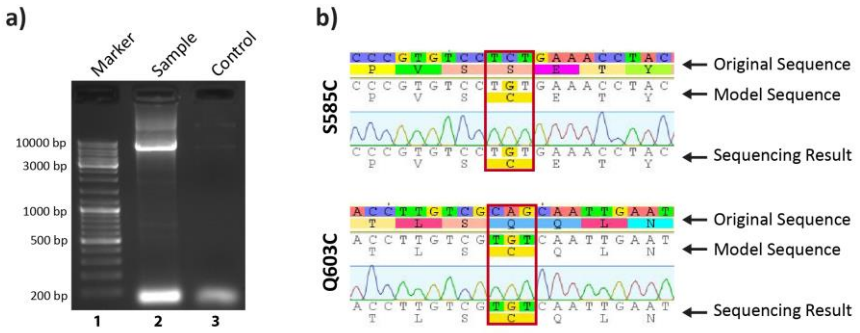

Figure 32: Agarose gel and Sanger sequencing results for YopO S585C/Q603C. **a)** 1% agarose gel with the marker (lane 1), the sample lane loaded with the crude PCR product (lane 2), and the control lane containing a PCR sample without added polymerase (lane 3). **b)** Sequencing results confirming the identity of YopO S585C/Q603C. The exchanged bases coding for the respective amino acid residue are highlighted by the red boxes for S585C (top) and Q603C (bottom), respectively.

The expression and purification progress of YopO S585C/Q603C can be visualized by sodium dodecyl sulfate-polyacrylamide gel electrophoresis (SDS-PAGE) (Figure 33a). GST-YopO S585C/Q603C was expressed in *E. coli* Rosetta DE3 cells. Successful protein expression is evident by the strong band appearing at ~100 kDa (GST-YopO Mw = 99.5 kDa) after induction with isopropyl β-D-1-thiogalactopyranoside (IPTG) (lane 2+3). While a fraction of the target protein remained in the insoluble cell debris after sonication and lysis (lane 4), a sufficient amount of the soluble GST-YopO S585C/Q603C remained in the supernatant fraction after centrifugation and removal of insoluble cell debris (lane 5). In an initial chromatographic step, passing the supernatant over Sepharose-immobilized glutathione beads and subsequent buffer wash removed a large portion of unwanted *E. coli* protein impurities while causing minimal loss of the target protein (lane 6+7). On-bead cleavage with PreScission protease quantitatively removed the GST-tag from the target protein, as a mass shift of the then-cleaved and eluted YopO S585C/Q603C (71.2 kDa) in the PreScission cleavage flow-through is observed (lane 8). Sepharose bead recovery by elution of the GST-tag (28.3 kDa) revealed a minor loss of PreScission-cleaved target protein, which was still bound to the column resin (lane 9). For further protein purification, the fraction containing YopO S585C/Q603C was loaded onto an anion exchange column (Figure 33b). Here, non-proteinogenic contaminations where successfully removed, as the flow-through fractions showed absorbance at 280 nm (purple bar) but no protein was found during gel electrophoresis (lane 10). After sample application and wash, an increasing sodium chloride gradient eluted the target protein at a conductivity above 13 mS/cm (lane 11-15, green bar). Notably, in the fractions containing YopO, some proteins of lower molecular weight (25 kDa to 40 kDa) appeared as visualized by the SDS gel and eluted alongside the target protein. These bands were previously analyzed by *Gregor Hagelueken* and assigned to protease-cleaved YopO fragments held together via noncovalent interactions, thereby retaining their physicochemical properties and eluting together with the uncleaved, intact YopO S585C/Q603C. Notably, the addition of various protease inhibitors did not improve the ratio of uncleaved to cleaved protein (unpublished results).

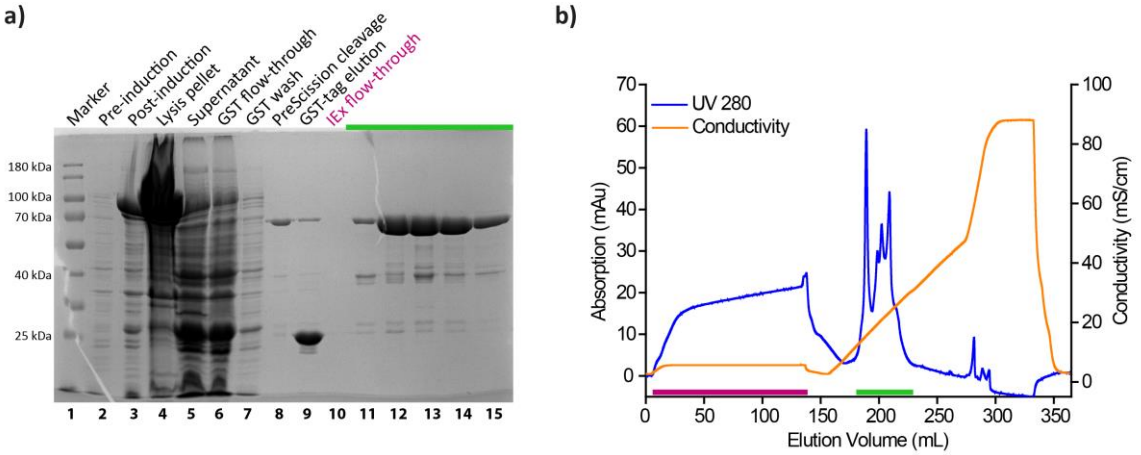

Figure 33: SDS-PAGE and anion exchange chromatogram of YopO S585C/Q603C. **a)** Coomassie-stained 10% polyacrylamide gel after SDS-PAGE showing the initial steps of expression and purification of YopO S585C/Q603C. **b)** Chromatogram of the ENrich™ Q 10/100 anion exchange run of YopO S585C/Q603C showing the absorption at 280 nm (blue) and conductivity (orange). Horizontal bars indicate the fractions taken and loaded onto the gel in **(a)**.

The pooled and concentrated fractions containing YopO were loaded onto a gel filtration column for a final purification step (Figure 34a). Notably, the gel filtration elution profile of YopO showed two distinct absorbance peaks after the void volume of the column, indicative of two distinct molecular weight components in the sample. SDS-PAGE revealed pure YopO protein in both of the elution peaks (Figure 32b, lane 2-10), thereby suggesting a homo-dimerization of YopO either via disulfide bridges between the introduced cysteine residues or via non-covalent interactions. The non-covalent dimerization of YopO was investigated in earlier studies but the amount and stability of this homo-dimer is considered negligible in comparison to the monomeric protein for any of the upcoming applications.[356,357] In addition, SEC-SAXS scattering curves of apo-YopO$_{89-729}$ showed no indication of a dimeric species, which is another indication for the low relative homo-dimer proportion compared to the total protein.[332]

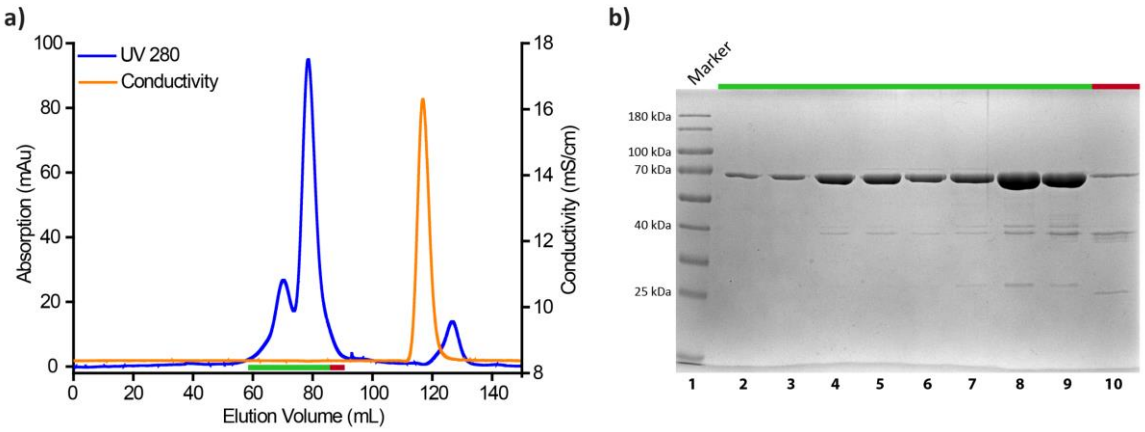

Figure 34: Gel filtration chromatogram and SDS-PAGE of YopO S585C/Q603C. **a)** Chromatogram of the HiLoad® 16/600 Superdex® 200 pg gel filtration run of YopO S585C/Q603C showing the absorbance at 280 nm (blue) and conductivity (orange). The green and red horizontal bars indicate the fractions taken for SDS-PAGE analysis. **b)** Coomassie-stained 10% polyacrylamide gel of the fractions shown in **(a)** after SDS-PAGE. Only the fractions indicated by the green bar were pooled and concentrated further while the fraction indicated by the red bar was discarded.

The protein-containing fractions (lane 2-9) were pooled and 5 mg purified protein was obtained in total. In summary, the herein-presented purification protocol for YopO including three chromatographic steps (GSH affinity chromatography, anion exchange chromatography, and gel filtration chromatography) is reproducible and yields a sufficient amount of protein for spin-labeling experiments with a high degree of purity.
The sequencing results and final gel filtration runs and SDS-PAGE gels of YopO-wt, YopO V599C/N624C, YopO Y588C/N624C, and YopO S353C/Q635C are shown in the appendix (Figure A1+A2). For all YopO constructs, the protein yield varied between 5 mg to 17 mg of total protein.

3.1.2 MTSL labeling of $YopO_{89-729}$

The spin-labeling reaction with MTSL can be performed at different stages of the protein work-up. While *in situ* labeling on an endogenous membrane transporter[163] and protein labeling on solid-supports during the purification process have been reported,[342] the approach chosen here was to attach the spin label in solution after the protein purification, as the spin labeling of purified proteins in solution offers two advantages: Firstly, due to the removal of impurities and contaminants beforehand, the protein concentration can often be determined more reliably and hence the ratios between the added spin label and protein are less error-prone. This in turn makes the labeling reactions more reproducible and, in the case of over-labeling or low labeling efficiencies, protein-to-spin label ratios can be adjusted easily. Secondly, in contrast to solid-support labeling where the spin label is added in the mobile phase and larger volumes and therefore higher amounts of the spin label are required to achieve high labeling efficiencies, labeling volumes and concentrations can be adjusted easily when performing the labeling in solution and in general, less spin label amounts is required. This is beneficial, especially in cases where the spin label availability is limited due to cost restraints or the synthetic accessibility of the label.
The labeling reactions were carried out in the YopO gel filtration buffer as the basic pH of 8.0 promotes thiolate anion formation and thereby the S_N2 reaction with the electrophilic methanethiosulfonate bioconjugation group of MTSL.[188] Since all cysteine residues of the four $YopO_{89-729}$ mutants are highly solvent-exposed, the protein was incubated with a 100-fold molar excess of the reducing agent dithiothreitol (DTT) before labeling to remove potential disulfide bridges and break covalent protein homo-dimers. These dimers can decrease the labeling efficiency in later stages and, more importantly, cause artificial distance peaks during the PELDOR experiment due to the presence of doubly-labeled homo-dimers or multimers. However, as DTT can readily reduce the spin label MTSL to the corresponding diamagnetic hydroxylamine and, owing to its two sulfhydryl moieties, can compete in the following labeling reaction with the cysteines or cleave the protein-label disulfide bridges, quantitative removal of the reducing agent before adding the spin label is mandatory.
After removal of the reducing agent via size-exclusion chromatography (SEC), MTSL was immediately added to the reduced YopO in a 20-fold molar excess per cysteine to start the labeling reaction and prevent the formation of new protein dimers. The excess ratio of 20:1 (label : cysteine) was chosen to obtain a good trade-off between a high labeling efficiency of the cysteines while on the other hand allowing for quantitative removal of the excess spin label after completion of the coupling reaction.[358] While there are reports on quantitative MTSL labeling within minutes,[342] an extended incubation period of 18 h at reduced temperatures (2 h at room temperature, then 16 h at 4 °C) was chosen here to reduce protein dimer formation and prevent thermal degradation of YopO during the labeling process. To stop the labeling reaction, the excess

spin label was removed via SEC using a HiPrep™ 26/10 Desalting column on an Äkta chromatography system as exemplarily shown for YopO V599C/N624C (Figure 35).

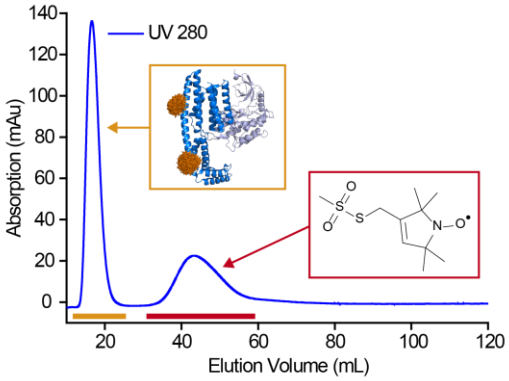

Figure 35: HiPrep™ 26/10 desalting chromatogram of YopO V599C/N624C after labeling with MTSL with the absorbance at 280 nm shown in blue. The first elution peak indicated by an orange bar corresponds to the elution fraction of the labeled protein (orange box) at the void volume of the SEC column while the second elution peak indicated by a red bar corresponds to the elution fraction of the free, unreacted excess MTSL (red box).

While in principle any benchtop desalting column (e.g., a PD-10 desalting column) is suited to remove the excess MTSL, the UV-detector of the Äkta system attached downstream of the column can visualize the separation of YopO (orange bar and box) by the absorbance at 280 nm. YopO elutes at an earlier stage of the SEC due to its higher hydrodynamic radius whereas the smaller MTSL (red bar and box) elutes at a larger retention volume, thereby leading to two distinct peaks in the elution chromatogram.[359] Whether the protein is indeed labeled cannot be assessed at this stage, as the strong protein absorbance at 280 nm masks the absorbance of the label in the first elution peak. The protein-containing fractions were pooled, concentrated, and rebuffered in deuterated buffer for subsequent PELDOR measurements. In the last purification step, the protein solution was spun at 18,000 rcf for 1 min in a micro centrifugal tube to remove any precipitates, and the supernatant was carefully collected for further analysis. For all constructs, the protein recovery yield over all labeling-, purification-, and rebuffering steps varied between 50% (YopO S585C/Q603C) and 76% (YopO Y588C/N624C).
The labeling efficiencies of the individual labeling reactions were determined using a combination of UV-vis spectroscopy, quantitative cw-EPR spin-counting (Figure 36 + Table 2), and mass spectrometry (MS) (Figure 37 + Table 3).

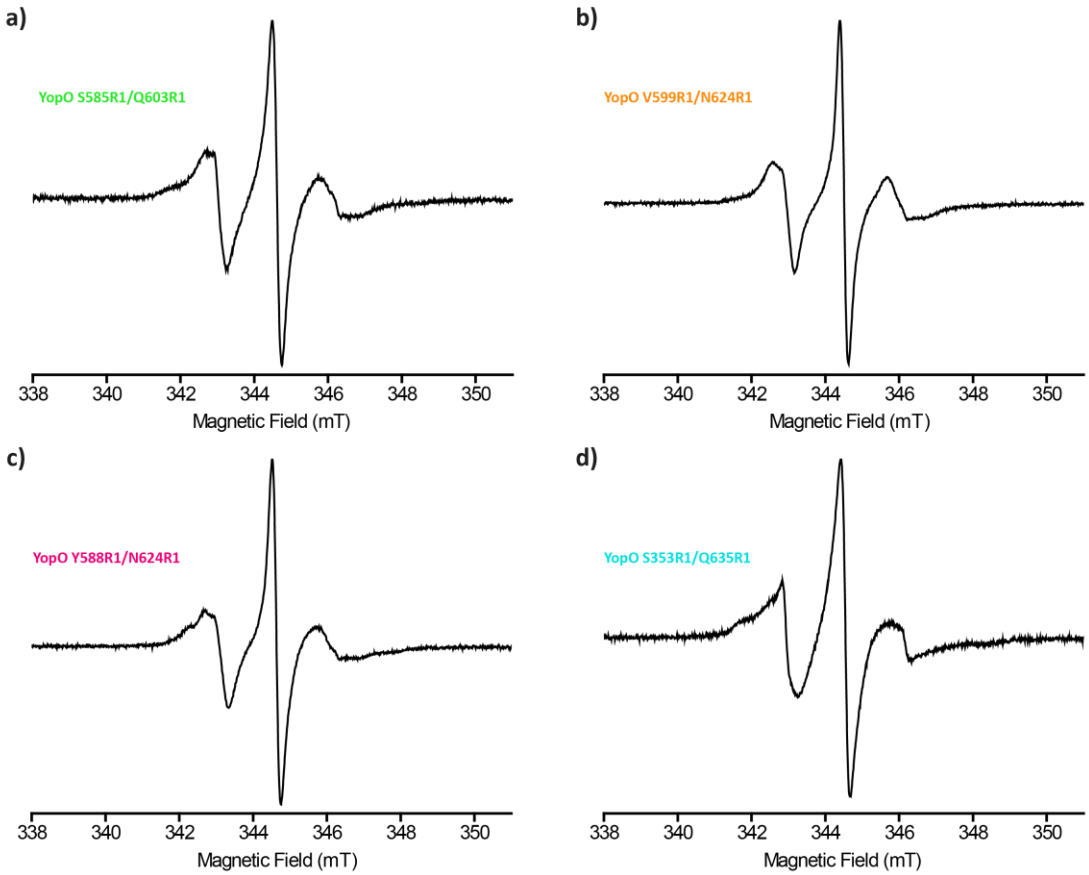

Figure 36: Room temperature cw-EPR spectra of the four MTSL-labeled YopO constructs YopO S585R1/Q603R1 **(a)**, YopO V599R1/N624R1 **(b)**, YopO Y588R1/N624R1 **(c)**, and YopO S353R1/Q635R1 **(d)**. Spectra were recorded on a Bruker EMXnano spectrometer. Measurement settings: 9.6 GHz microwave frequency, 10.00 mW microwave power, 100 kHz modulation frequency, 1.0 G modulation amplitude, 20.48 ms time constant, 100 pts/mT.

Table 2: Labeling efficiencies of the four MTSL-labeled YopO constructs. Protein concentrations were obtained by UV-vis spectroscopy (NanoDrop™ 2000) and spin concentrations were determined using the internal spin-count routine of the EMXnano spectrometer.

Construct	Protein concentration (µM)	Spin concentration (µM)	Labeling efficiency (%)
YopO S585R1/Q603R1	100	175	87
YopO V599R1/N624R1	107	187	87
YopO Y588R1/N624R1	91	173	95
YopO S353R1/Q635R1	105	190	90

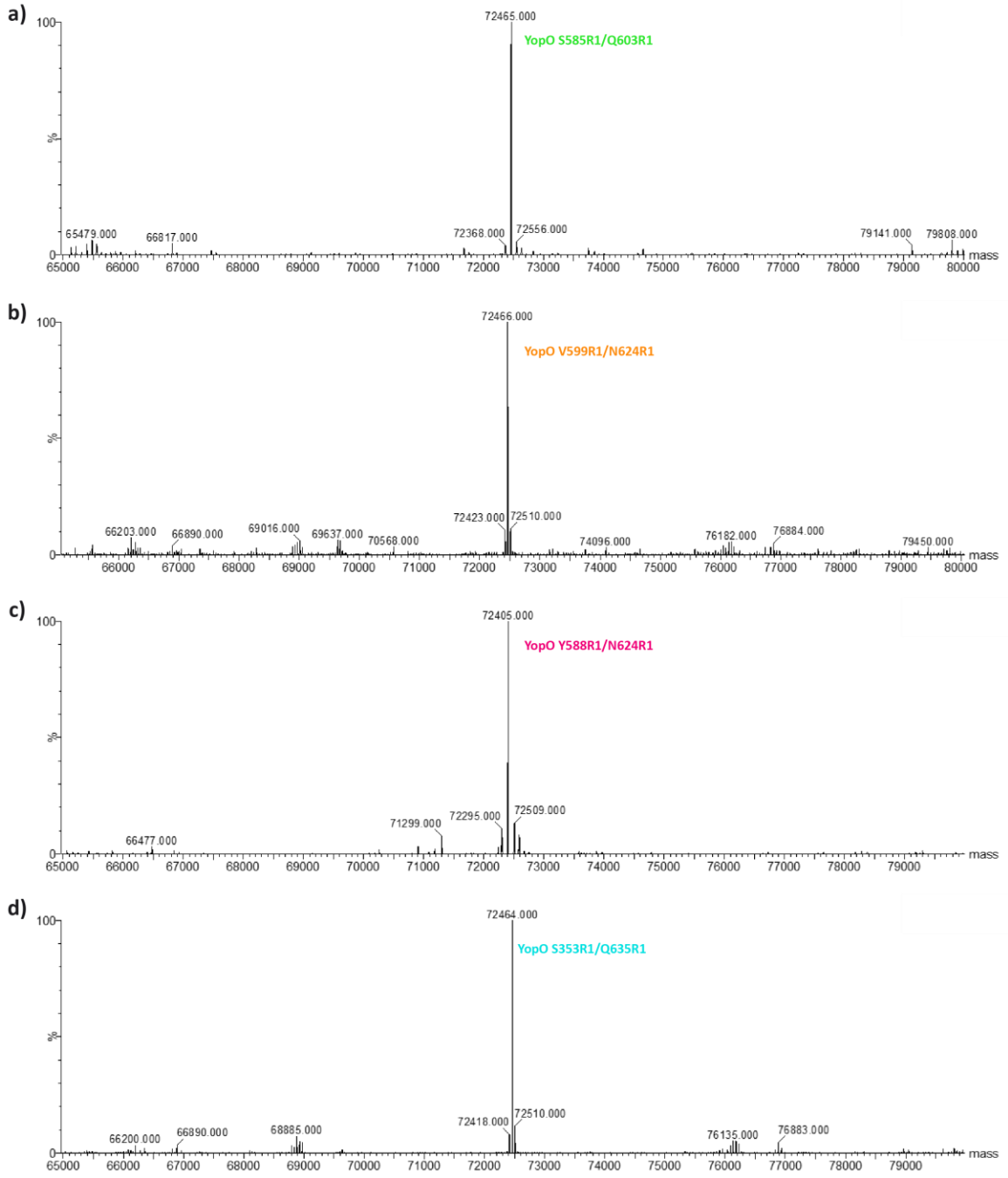

Figure 37: Deconvoluted positive-mode high-resolution electronspray ionization mass spectrometry (ESI(+)-MS) spectra of the four MTSL-labeled YopO constructs YopO S585R1/Q603R1 **(a)**, YopO V599R1/N624R1 **(b)**, YopO Y588R1/N624R1 **(c)**, and YopO S353R1/Q635R1 **(d)**. ESI(+)-MS spectra were recorded and deconvoluted by the mass spectrometry facility in Marburg on a Synapt G2-Si spectrometer. Note: Mass spectrometry samples were taken before the buffer exchange into deuterated buffer. The raw spectra are shown in the appendix (Figure A3).

Table 3: Calculated and experimentally found masses of the unlabeled and MTSL-labeled YopO constructs.

Construct	Calc. unlabeled (Da)	Calc. labeled (Da)	Experimental (Da)
YopO S585R1/Q603R1	72,100	72,468	72,465
YopO V599R1/N624R1	72,102	72,470	72,466
YopO Y588R1/N624R1	72,038	72,406	72,405
YopO S353R1/Q635R1	72,100	72,468	72,464

For each labeled mutant, the solution cw-EPR spectra showed a broadened nitroxide signal compared to free MTSL, which is caused by an increased rotational correlation time indicative of successful bioconjugation (Figure 34).[97] In addition, except for YopO S353R1/Q635R1, none of the spectra showed signs of free-label remnants as no sharp secondary signals were observed. For YopO S353R1/Q635R1, the sharp feature at 342.8 mT can be rationalized by the labeling site S353R1, which is located in a loop region on the kinase domain and hence likely to result in a higher flexibility of the spin label. Comparing the spin concentrations with the protein concentrations determined by UV-vis revealed labeling efficiencies ranging from 87% to 95% (Table 2). ESI(+)-MS spectra showed a high sample purity and quantitative labeling of all four double-cysteine mutants as only a single, high-intensity mass peak with a mass increase of approximately +368 Da (+184 Da per R1 residue) compared to the respective unlabeled protein was observed (Figure 35 + Table 3).
Hence, the protocol for labeling soluble proteins with MTSL presented herein on the example of YopO, provides high labeling efficiencies of ~90%, complete removal of any excess label, and good to high protein recovery yields throughout the labeling and purification steps.

3.1.3 Activity Assay of MTSL-labeled YopO$_{89\text{-}729}$

To exclude large-scale structural perturbation of YopO upon spin-label attachment, the autophosphorylation capability of MTSL-labeled YopO in the presence of G-actin was investigated.[330] For this purpose, MTSL-labeled YopO was incubated with G-actin in the presence of ATP and the phosphorylation of YopO was visualized using the phospho-residue sensitive Pro-Q™ Diamond stain (Figure 38).

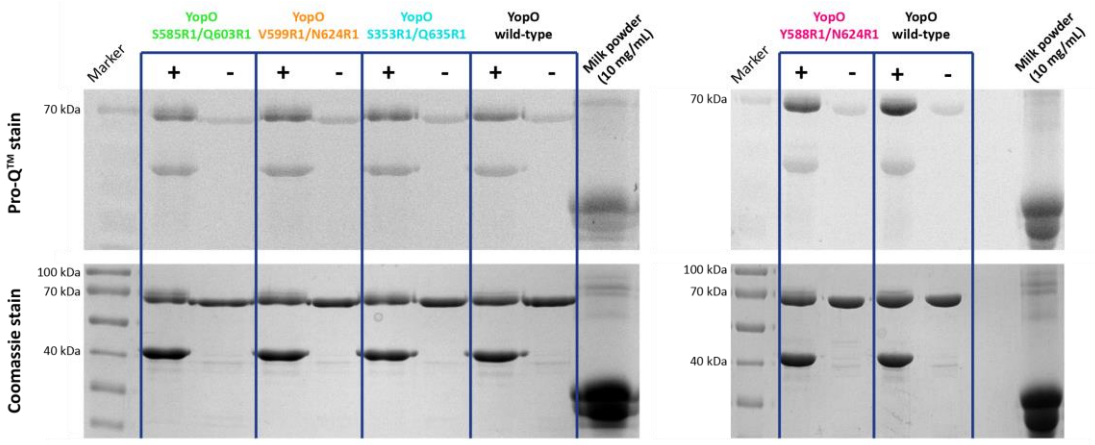

Figure 38: Activity assay of MTSL-labeled YopO constructs. Samples were loaded onto 10% polyacrylamide gels and stained with Pro-Q™ (top row, negative image) to visualize phosphorylated proteins and subsequently with Coomassie stain (bottom row) for visualization of total protein content. The lanes indicated with a (+)-sign contain G-actin while the lanes indicated with a (–)-sign are negative controls in the absence of G-actin. The lanes containing milk powder serve as positive controls.

In the absence of actin (lanes indicated by (–)-sign), only a weak band at 70 kDa is observed in the Pro-Q™ stain, presumably caused by low emission activity of unphosphorylated YopO at the detection wavelength. Samples containing G-actin (lanes indicated by (+)-sign) show a significantly stronger band at 70 kDa in the Pro-Q™ stain, hence indicating autophosphorylation capability of all tested YopO constructs. Notably, besides the autophosphorylation of YopO, the additional phosphorylation of G-actin was observed in all cases, hence prompting the assumption that G-actin is another substrate of the YopO kinase. In both gels, milk powder served as a positive control as it contains the highly phosphorylated proteins α- and β-casein (~24-28 kDa). As subsequent Coomassie-staining of the same gels revealed an equal amount of YopO in all lanes, the stronger bands in the Pro-Q™ stain must indeed have been caused by phosphorylation of YopO. Based on the above observations, MTSL-labeling at the chosen sites does not change the autophosphorylation behavior of the various YopO mutants compared with YopO-wt and large-scale structural perturbations can be excluded.

3.1.4 PELDOR Measurements and Data Analysis

In prospect of the following ring test, 50% v/v deuterated ethylene glycol as a cryoprotectant was added to the mother batches of the four MTSL-labeled YopO constructs before aliquoting and flash-freezing in liquid nitrogen for transport on dry ice to the participating laboratories. All laboratories were asked to perform four-pulse PELDOR experiments at Q-band frequencies using rectangular pulses and to analyze the data by Tikhonov regularization as implemented in DeerAnalysis.

The in-house PELDOR experiments and validations were conducted together with *Tobias Hett* and *Dinar Abdullin*. The pump pulse was applied at ν_B = 33.7 GHz at the maximum of the notroxide spectrum while the detection pulses were applied at the frequency ν_A set 80 MHz below ν_B (Figure 39a). For each sample, the optimal pump pulse length was determined by a transient nutation experiment ($\pi_{nut} - T - \pi/2 - \tau - \pi - \tau - echo$) to achieve maximum inversion of the Hahn echo (Figure 39b). In the PELDOR experiment, the initial time value of the interpulse delay τ_1 was set to the first maximum of the two-pulse ESEEM trace (Figure 39c) and deuterium ESEEM was suppressed by nuclear modulation averaging.[243]

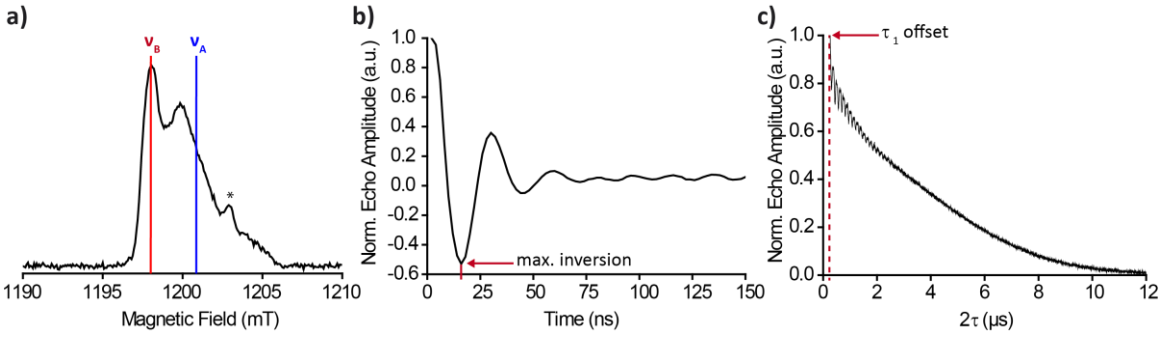

Figure 39: Exemplary field-swept EPR spectrum, transient nutation, and two-pulse ESEEM trace of YopO V599R1/N624R1. **a)** Field-swept EPR spectrum with field indications for the pump (red) and observer (blue) pulses. The signal marked by an asterisk is an endogenous signal of the EPR quartz glass tube. **b)** Three-pulse nutation experiment with the time point of the maximal echo inversion (16 ns) highlighted by a red arrow. **c)** Two-pulse ESEEM trace with visible deuterium oscillation and the initial τ_1 offset marked by a red arrow.

As showcased on the example of YopO V599R1/N624R1 (Figure 39a-c), the typical field-swept nitroxide EPR spectrum was obtained. Fitting of the two-pulse ESEEM trace (Figure 39c) of this construct using eq. 20 gave a phase memory time T_M of 4.7 µs, which confirms the efficient

deuteration of the sample and allows for long dipolar evolution times in the subsequent PELDOR experiment. Four-pulse PELDOR traces with the standard pulse sequence $\pi/2\,(\nu_A) - \tau_1 - \pi(\nu_A) - (\tau_1 + t) - \pi(\nu_B) - (\tau_2 - t) - \pi(\nu_A) - echo$ were recorded at 50 K. The dipolar evolution time was chosen such that at least 1.5 oscillations of a given distance-dependent modulation frequency were resolved (Figure 40a-d). A detailed summary of the individual setup parameters for all YopO constructs is given below (Table 4).

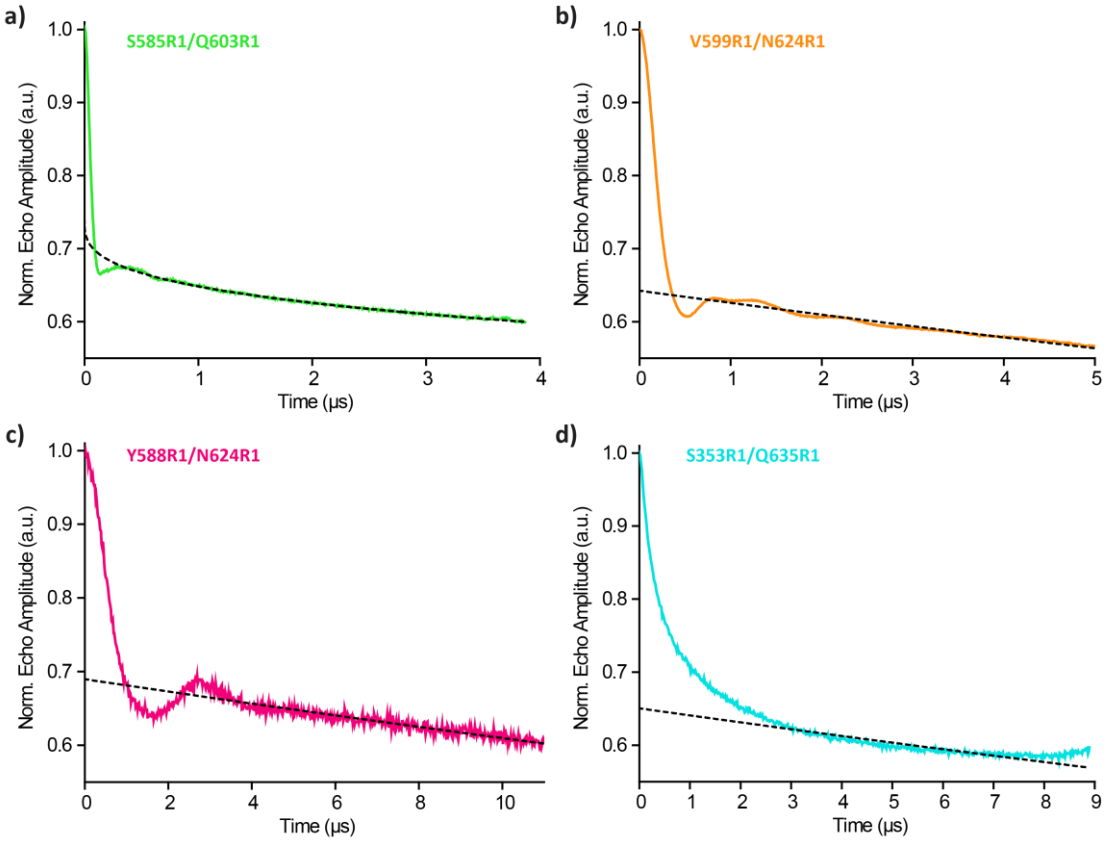

Figure 40: Four-pulse PELDOR time traces of YopO S585R1/Q603R1 (**a,** green), YopO V599R1/N624R1 (**b**, orange), YopO Y588R1/N624R1 (**c**, magenta), and YopO S353R1/Q635R1 (**d**, cyan). The black dashed line in each panel corresponds to the homogenous 1.04 **(a)** or three-dimensional **(b-d)** background functions obtained by DeerAnalysis2019.

Table 4: Four-pulse PELDOR setup parameters for the four MTSL-labeled YopO constructs.

Parameter	YopO S585R1/Q603R1	YopO V599R1/N624R1	YopO Y588R1/N624R1	YopO S353R1/Q635R1
$(\pi/2)_A$	16	16	12	16
π_A (ns)	32	32	24	32
π_B (ns)	14	14	16	16
τ_1 (ns)	232	232	260	232
τ_2 (ns)	4,000	5,500	12,000	9,000
Δt (ns)	4	8	16	16
SRT (ms)	4	4	4	4
SPP[a]	10	10	10	10
No. of averages	33	124	517	59

[a]: Shots per point.

For all samples, time traces with a modulation depth Δ between 26% (YopO S585R1/Q603R1) and 36% (YopO V599R1/N624R1) were obtained (Table 5). This is in good agreement with the expected modulation depth Δ of 0.3-0.5 for homogenously distributed biomolecules with a labeling efficiency λ close to 100% at Q-band frequencies when pumping at the maximum of the nitroxide spectrum.[360] Only for the YopO S585R1/Q603R1 construct, where a lower-dimensional (1.04) background function was required to yield a reasonable background decay function, the modulation depth was slightly lower than the expected value. This is presumably caused by the short interspin distance of the two nitroxide centers leading to a steeper decay of the background function at the start of the time trace, which is insufficiently described by the commonly applied homogenous three-dimensional background function. The SNR of the traces was calculated as the ratio between the modulation depth Δ as a measure of the signal intensity and the standard deviation of the imaginary channel after phase correction as the noise level σ_N. Only for YopO S353R1/Q635R1, where the noise levels between the real and imaginary parts of the quadrature signal differed strongly, the SNR was calculated as the standard deviation of the time trace and the Tikhonov fit. For all time traces, an SNR well above 100 (Table 5) was obtained with the lowest SNR of 144 corresponding to YopO S353R1/Q635R1 as a result of an imperfect fit at the end of the time trace.

Table 5: Modulation depth Δ and SNR of the various time traces in Figure 40.

Parameter	YopO S585R1/Q603R1	YopO V599R1/N624R1	YopO Y588R1/N624R1	YopO S353R1/Q635R1
Δ	26	36	31	35
SNR	474	721	355	144

Except for YopO S353R1/Q635R1, the time traces show visible oscillations after the initial decay and a varying extent of oscillation damping. For YopO S585R1/Q603R1, the initial oscillation is rapidly damped as the short interspin distance is close to the accessible lower limit of PELDOR,[361,362] whereas the spin pairs V599R1/N624R1 and Y588R1/N624R1 exhibit multiple prominent oscillation periods. Distance distributions were obtained by analyzing the time trace with DeerAnalysis using Tikhonov regularization with the respective background functions shown in Figure 40. In each case, a regularization parameter α close to the intersection of the L-curve (L-curve corner criterion) was chosen. The uncertainty of the resulting distance distribution was assessed using the implemented validation tool of DeerAnalysis (Figure 41). The complete analysis by DeerAnalysis (Backgrounds, fits, L-curves, and distance distributions) is given in the appendix (Section 6.1, Figure A4).

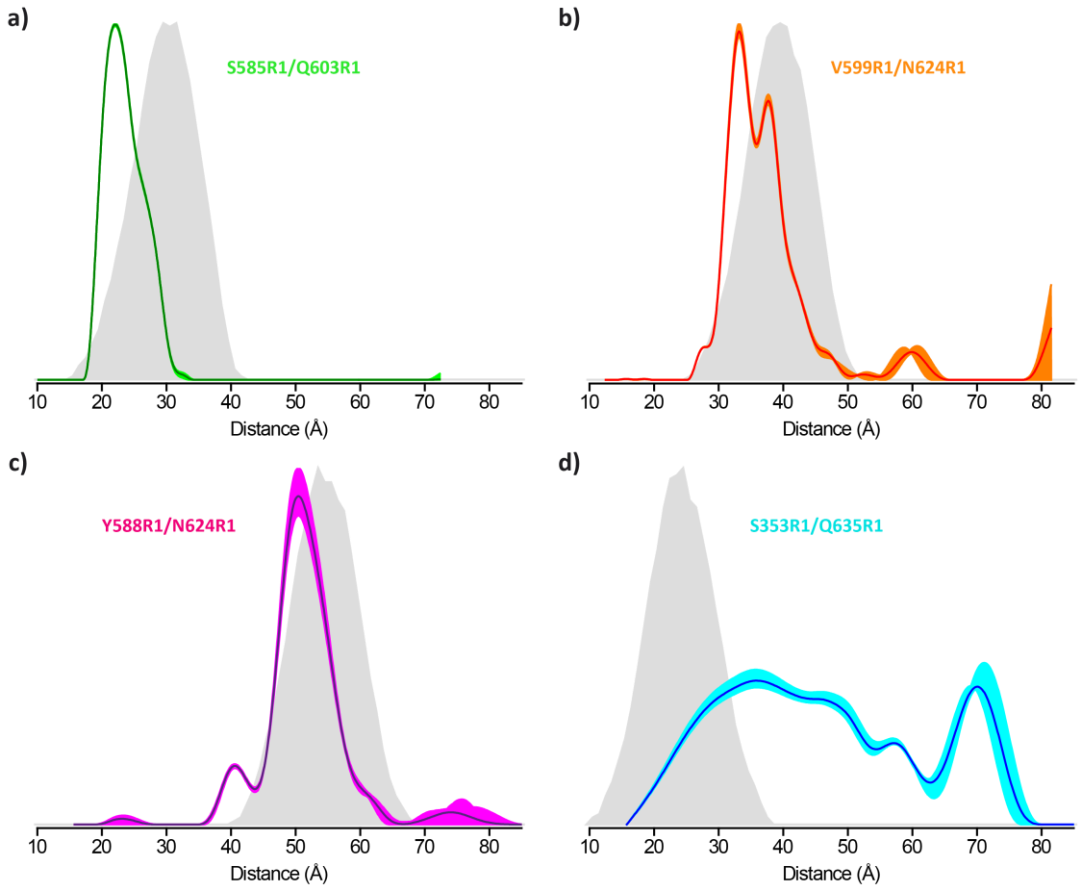

Figure 41: Distance distributions of **(a)** YopO S585R1/Q603R1 (green), **(b)** YopO V599R1/N624R1 (red), **(c)** YopO Y588R1/N624R1 (purple), and **(d)** YopO S353R1/Q635R1 (blue) obtained by Tikhonov regularization in DeerAnalysis. The colored areas in each panel correspond to the DeerAnalysis validation while the grey-shaded areas correspond to the distance distributions derived *in silico* by mtsslWizard using the PDB-ID 2h7o **(a-c)** or 4ci6 (**d**) as a template (rotamer clash treatment: loose).

For all spin pairs residing on the α-helical GDI-backbone of YopO (Figure 41a-c), rather narrow distance distributions with a full width at half maximum (FWHM) ranging from 7.3 (YopO S585R1/Q603R1) to 9.5 Å (YopO V599R1/N624R1) are obtained by Gaussian fitting. These results suggest a rather rigid α-helical backbone structure. In these three cases, the distance distributions derived experimentally match well with the *in silico* predictions of mtsslWizard using the apo crystal structure of the YopO GDI domain (PDB-ID 2h7o) as a template structure, albeit the most probable distances are shifted slightly to shorter distances. Notably, the distance distribution obtained from YopO 599R1/N624R1 does not have the shape of a single Gaussian as the *in silico* prediction for this construct, but two separate peaks. Whether this bimodality originates from two distinct conformations of the α-helical backbone of YopO present in solution, namely a straight α-helix similar to the crystal structure of the apo protein (PDB-ID 2h7o) and a bent α-helix as observed for the YopO-actin complex (PDB-ID 4ci6), or two subsets of preferred label orientations is not clear at this point. To a lesser extent, the same phenomenon can be observed for YopO S585R1/Q603R1 but here, the two peaks are not distinctly separated but merge due to their width and create a longer-distance shoulder in the main peak of the distribution.

In strong contrast to the first three YopO mutants with well-defined interspin distances, YopO S353R1/Q635R1 shows a significantly broader distribution spanning from 16 Å to 78 Å (Figure 41d). Here, the multitude of dipolar oscillations from different interspin distances in the

ensemble result in destructive interference causing the previously described featureless time trace (Figure 40d). The obtained results are similar to previous PELDOR measurements on the same mutant that, in conjunction with SAXS experiments, revealed a high flexibility between the kinase domain harboring the labeling site S353R1 and the GDI domain with the labeling position Q635R1 located at the lower end of the GDI domain.[332]

The PELDOR time traces provided by the participants of the ring test (Figure 42) showed only minor differences within the respective subset of a constructs and to the in-house measurements (Figure 40), as is expected for samples from the same mother batch. While the background decays within a subset are almost identical as evident from their nearly parallel shape, variations between the individual laboratories and experiments arise in terms of modulation depth which ranges from 19% obtained for YopO S353R1/Q635R1 from Lab D (blue, Figure 42d) up to 48% for YopO Y588R1/N624R1 by Lab B (magenta, Figure 42c). These differences stem from slight deviations in the different experimental setups such as the pump pulse length and resonator type as well as individually different estimates of the background functions.[120] A detailed description of the individual setup parameters by the individual laboratories can be found in the primary publication.[354]

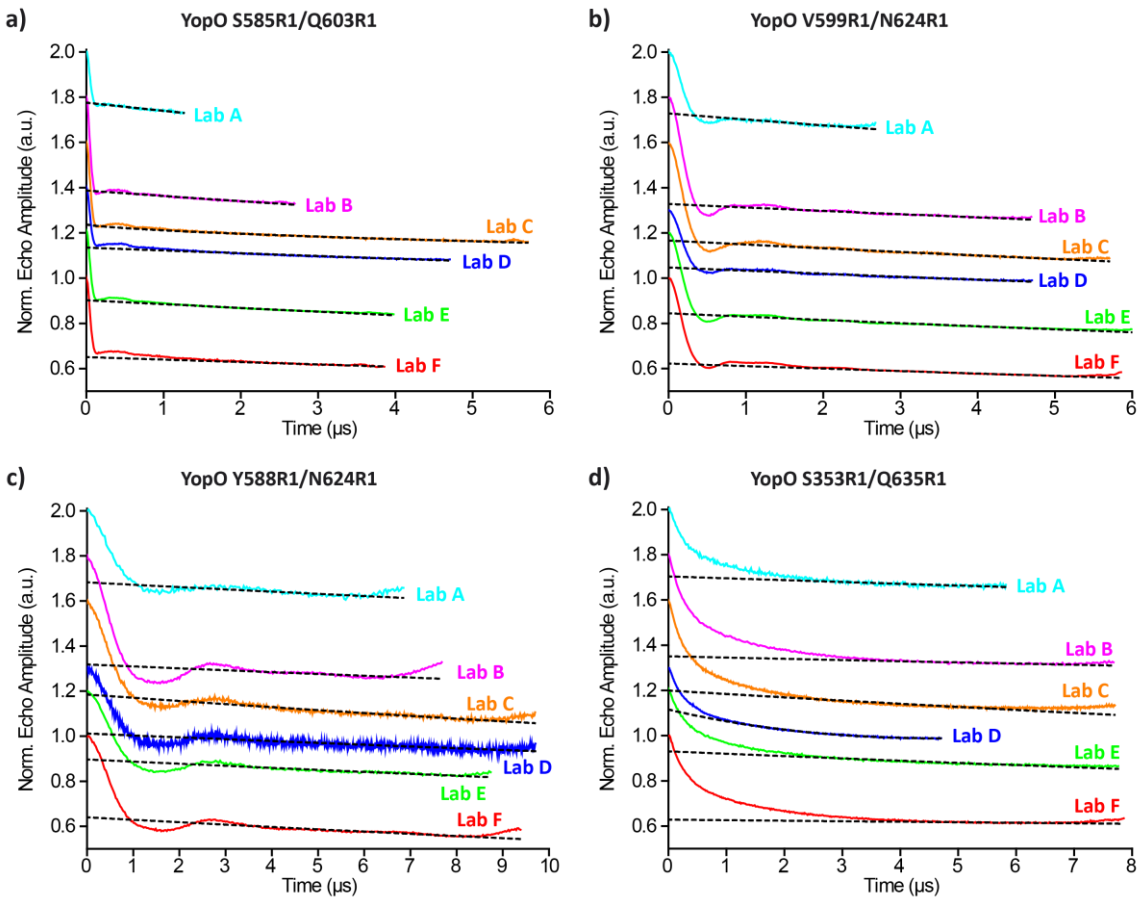

Figure 42: Four-pulse PELDOR time traces of **(a)** YopO S585R1/Q603R1, **(b)** YopO V599R1/N624R1, **(c)** YopO Y588R1/N624R1, and **(d)** YopO S353R1/Q635R1 provided by the ring test participants Lab A to F. For clarity, the time traces are shifted on the ordinate axis. The black dashed lines in each panel correspond to the homogenous three-dimensional background functions to the respective time traces provided by the ring test participants.

As expected for near-identical PELDOR time traces, the resulting distance distributions for a given mutant agree well with each other (Figure 43).

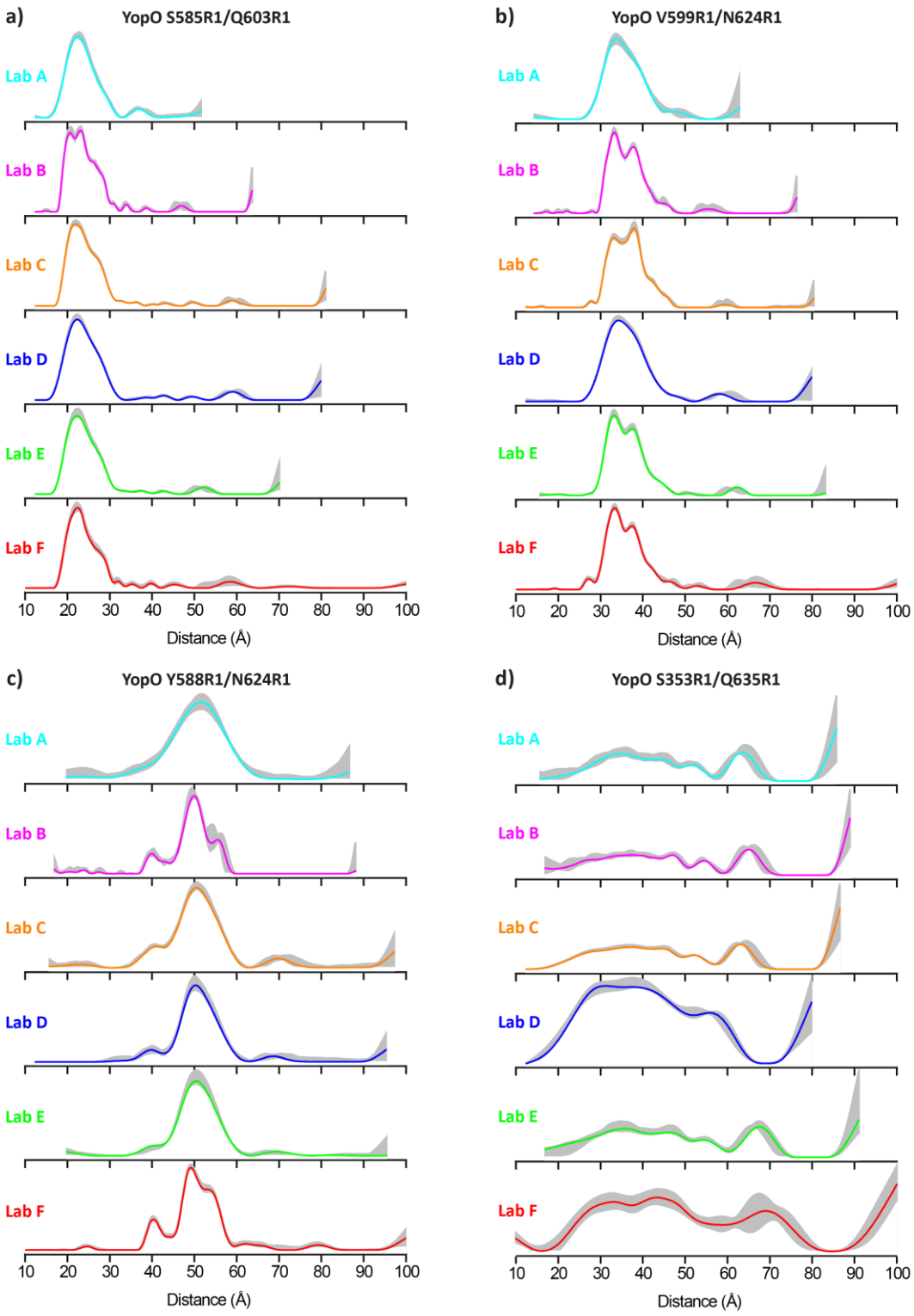

Figure 43: Distance distributions of **(a)** YopO S585R1/Q603R1, **(b)** YopO V599R1/N624R1, **(c)** YopO Y588R1/N624R1, and **(d)** YopO S353R1/Q635R1 obtained by Tikhonov regularization in DeerAnalysis provided by the ring test participants Lab A to F. The grey-shaded areas correspond to the DeerAnalysis validations.

For the mutants with the spin pairs residing on the α-helical backbone and defined inter spin distances (Figure 43a-c), the 2σ-confidence interval of the averaged mean distances ⟨*r*⟩ (Gaussian distribution obtained from DeerAnalysis) is below 1 Å, which is lower than the estimated uncertainty of 3 Å for rotamer modeling approaches.[355] While the overall distribution width for each of these mutant-subsets is comparable, differences arise in the shape of the distance distributions with some showing the previously observed distinct bimodality for YopO V599R1/N624R1 (Lab B, C, E, and F) while in the distributions provided by Lab A and D, a single distance peak with a more or less pronounced shoulder is observed. The same holds true for the short-distance construct YopO S585R1/Q603R1 and even YopO Y588R1/N624R1 where in contrast to the in-house distance distribution (Figure 38c), some distance distributions show a splitting of the main distance peak (~50 Å) into two distinct peaks (Lab B and F) while the distributions of the other laboratories show a single main peak. These differences in the distribution shapes can be attributed to the considerable differences in the respective L-curves caused by the SNR and trace length of the individual PELDOR experiments. Depending on the chosen regularization parameter α at the intersection of the L-curve, the distributions get either smoothened (larger regularization parameter α) or "spikier" (smaller regularization parameter α). In all cases and owing to uncertainties in the background separation, long-distance artifacts in the distributions appear beyond 65 Å (depending on the trace length) which in most cases are sufficiently suppressed by the subsequent validation, except for YopO S353R1/Q635R1 where the background estimation of the featureless time traces causes difficulties.

Besides the two-step analysis (background elimination followed by distance extraction) via Tikhonov regularization discussed above, all data sets were additionally subjected to analysis by the neural network DEERNet 2.0,[363] by one-step Tikhonov regularization with DeerLab utilizing an automated regularization parameter selection,[124] by multi-Gaussian fitting with DD,[364] and the ComparativeDeerAnalyzer implemented in DeerAnalysis2021, which compares neural network and regularization results. Here, all tested approaches yielded similar results regarding the obtained distance distributions while, on the other hand, varied substantially in the resulting uncertainty estimates. While for DEERNet, the full variation of all distance distributions was not governed by the individual uncertainty estimates, the opposite is true for the multi-gaussian DD-analysis where the uncertainty estimates by far exceeded the distance variations. The deviations in the individual distance distributions and uncertainty estimates are again related to differences in the length of the time traces resulting in uncertainties of the background separation. A detailed summary of the different analysis approaches and the corresponding distance distributions is given in the supplementary information of the primary publication (SI section S2).[354]

3.1.5 Guidelines for Labeling, Sample Preparation, PELDOR Setup and Data Analysis

Ensuing the ring test and discussions among the participants, general guidelines on sample preparation, PELDOR measurements, data analysis, and data deposition were proposed by the authors. While a complete coverage of these guidelines is beyond the scope of this work, the following section summarizes the guidelines on spin labeling, structural integrity assessment, PELDOR measurements, and data analysis and interpretation, which are directly related to the results presented above. The detailed guidelines can be found in the primary publication:

[354] O. Schiemann, C. A. Heubach, D. Abdullin, K. Ackermann, M. Azarkh, E. G. Bagryanskaya, M. Drescher, B. Endeward, J. H. Freed, L. Galazzo, D. Goldfarb, T. Hett, L. Esteban Hofer, L. Fábregas Ibáñez, E. J. Hustedt, S. Kucher, I. Kuprov, J. E. Lovett, A. Meyer, S. Ruthstein, S. Saxena, S. Stoll, C. R. Timmel, M. Di Valentin, H. S. Mchaourab, T. F. Prisner, B. E. Bode, E. Bordignon, M. Bennati, G. Jeschke, "*Benchmark Test and Guidelines for DEER/PELDOR Experiments on Nitroxide-Labeled Biomolecules*", *J. Am. Chem. Soc.* **2021**, 143, 17875–17890.

Spin labeling: In general, labeling of functional cysteine residues and buried cysteines should be avoided to maintain enzyme activity, prevent structural perturbation of the protein, and ensure high labeling efficiencies. Incubation of the protein with a reducing agent such as DTT can help to cleave disulfide-bridged protein dimers and enhance the yield of the labeling reaction. To avoid interference of the reducing agent with the labeling reaction, e.g., in the form of spin label reduction, the reducing agent has to be completely removed before adding the spin label. To achieve high labeling efficiencies, a spin label excess (10 to 20-fold per cysteine) should be applied. However, as MTSL is usually dissolved in DMSO, the volume of spin label added to the protein should not exceed 10% of the total incubation volume as DMSO can destabilize the protein structure.[365,366] After the labeling reaction, the excess spin label needs to be removed either by column chromatography (e.g., desalting column) or by dialysis and the remaining free label should not exceed 10% of the total spin concentration. The protein concentration should be determined using UV-vis spectroscopy while spin label attachment to the protein and spin concentration should be assessed by cw-EPR spectroscopy and spin-counting against an internal or external reference. Correlation of the protein and spin concentration then yields the labeling efficiency, which can additionally be confirmed using mass spectrometry. It is best practice to exclude unspecific labeling of the wild-type POI and/or a cysteine-free construct of the POI at the chosen labeling conditions.

Structural integrity: As the amino acid mutagenesis and label attachment can affect the structure or interfere with the function of the protein, the structural and functional integrity of the labeled protein should be controlled. If possible, functional assays of the enzymatic activity are preferable. Additionally, alterations in the secondary and tertiary structure upon labeling can be assessed, for example using circular dichroism (CD) spectroscopy, UV-vis melting curves, or SAXS curves against the wild-type POI reference.

Sample preparation: To prevent the formation of ice crystals and avoid protein aggregation leading to local clusters of high spin concentration, a suitable cryoprotectant that is known not to interfere with the protein structure such as glycerol or ethylene glycol should be added to the sample before freezing. Usually, 10-50% cryoprotectant (v/v) is sufficient for glass formation.[155] To prolong the phase memory time T_M and thereby enhance the resolution and accessible distance range in the PDS measurement, both the solvent and the cryoprotectant should be deuterated.[112,113] For investigation of distant spin pairs (above 100 Å), the additional deuteration of the protein can significantly enhance T_M and expand the accessible-distance limit.[115,116] For a high-power (150 W) Q-band setup, a good SNR can be achieved at a spin concentration of 20-50 µM within a reasonable time frame (<12 h). In the case of heterogeneously dispersed samples such as aggregates, fibrils, and proteins embedded in membranes or membrane mimetics, diamagnetic dilution with unlabeled proteins can enhance T_M due to a reduction of instantaneous diffusion mechanisms by electron-electron interactions.[105,117] In addition, diamagnetic dilution can be used to disentangle intra- from inter-molecular

contributions to a distance distribution.[367] For soluble samples, a final centrifugation step to remove any precipitates that might cause artifacts in the PELDOR experiment is recommended before transferring the sample into the EPR tube and flash-freezing.

PELDOR measurement: The given PELDOR parameter guidelines aim for a high-power (150 W) Q-band spectrometer setup and nitroxide labels. Measurements should be set up at 50 K, as higher temperatures significantly reduce the phase memory time and thus the obtainable distances. An offset of 80-100 MHz between the pump (length: 12-16 ns) and the observer (length: 12-32 ns) pulses is ideal to minimize pulse overlap. The SRT should allow ≥80% of the echo amplitude to recover (~5 ms at 50 K). The interpulse delay τ_1 must exceed the dead time of the spectrometer (typically ~150-200 ns) and should be in the regime of 260-400 ns, which provides a good compromise between the T_M-related echo decay and a negative time t before the maximum of the PELDOR trace to reliably determine the zero-time t_0. To counter ESEEM effects, nuclear modulation averaging (8 or 10 steps) should be performed with the incrementation interval $\Delta\tau$, which is given by the inverse of the observed ESEEM frequency divided by the number of modulation-averaging steps. In addition, a phase cycle to eliminate receiver baseline offsets and unwanted echoes should be applied. The time interval τ_2 is limited by T_M and should ideally be maximized so that as many oscillation periods as possible can be recorded. For reliable quantification of the mean distance, at least one period of the slowest dipolar oscillation must be resolved while for a meaningful interpretation of individual features in a distance distribution, two or more oscillations of the lowest dipolar frequency need to be resolved. To exclude potential aliasing effects of high-frequency oscillations in the time trace, a time increment Δt of 8 or 12 ns between the individual data points is suggested and it should not exceed 32 ns as this complicates the reliable determination of t_0. The window for echo integration should be centered at the echo maximum with a length comparable to the observer π-pulse.

Data analysis: Owing to its mathematically ill-posed nature, the PELDOR data processing workflow gives room for subjective decision-making and user bias. Although the two-step approach of background elimination followed by distance determination is the most popular and widely applied method for PELDOR data analysis to date, in consideration of the availability of novel, automated single-step analysis workflows such as DEERNet or DeerLab, the two-step approach is discouraged due to its susceptibility for subjective decision-making. Independent of the analysis software used, users must check that the input data complies with the Kernel matrix used by the software. Assumptions of the standard Kernel are a dilute spin pair A-B, the absence of orientational effects and exchange coupling, as well as only weak overlap of the excitation profiles of observer and pump pulses. The signal-to-noise ratio of a PELDOR trace should be estimated using either the standard deviation of multiple individual PELDOR scans recorded on the same sample, the deviation from a good fit to the time domain, or, in the case of low phase drift and noise, as the root-mean-square amplitude of the imaginary part after phase correction. Distance distributions should be validated and the uncertainty of the distribution stated in the form of a 95% confidence interval. As the validation does not necessarily include model bias of the utilized software, comparison of the results of two or more different analysis approaches is encouraged.

Distance interpretation: The shape and width of a distance distribution depends on multiple factors such as the conformational flexibility of the spin label itself, the interaction of the spin label with neighboring side chains and the protein backbone, and the intrinsic protein heterogeneity and backbone dynamics. Disentangling these individual contributions to the

observed distance distribution is vital for data interpretation and conclusions on the underlying biomolecular structure and/or mechanistic insights. Hypothetic models and structures can be validated either by *in silico* labeling using rotamer libraries such as MMM[368] or mtsslWizard[355], or molecular dynamics approaches such as CREST/MD[369] and comparison of the distance restraints derived *in silico* with the distance distributions obtained experimentally.
Most experimentally encountered distance distributions can be classified as one (or a combination) of five individual cases (Table 6). For each of these cases, in addition to the characteristic features of the distance distribution, a rudimental interpretation guideline is provided.[354]

Table 6: Most common experimental distance distributions and their interpretation.

Case 1	Case 2	Case 3	Case 4	Case 5
		Shape characteristics		
Unimodal (Very narrow) FWHM < 5 Å	**Unimodal** FWHM ≈ 10 Å	**Unimodal (Very broad)** FWHM >> 20 Å	**Bimodal** Distinguishable peaks with Δr > 10 Å	**Bimodal** Main peak and shoulder with Δr > 10 Å
		Interpretation		
• Rare case • Orientational effects? • Motion of spin label is hindered • Changes difficult to correlate to protein motion • Change of label is advised	**PDB model available?** **<u>Yes</u>** • If the rmsd of r_{exp} vs r_{sim} is approx. 2-3 Å → Good correlation • If the rmsd of r_{exp} vs r_{sim} is >> 10 Å → Poor correlation Check: rotamer library limitations, second spin pair, MD simulations, change label **<u>NO</u>** • Use as distance restraint for model development	• Biological repeat to rule out aggregation • Protein dynamics are encoded in the width • Qualitative analysis feasible • Verify with other biophysical methods • Change label	• Check rotamer approach with two models if available • Biophysical interpretation of equilibria with high confidence • Change the relative ratio of the peaks by, e.g., ligand addition or dilution	• Can be difficult to interpret • Two backbone conformations? • Anisotropy of the frozen label rotamers? • Biological and/or technical repeats preferred, confirm with second spin pair, change label • Combine with other biochemical information

According to the scheme presented in Table 6, the ring test constructs can be classified as follows: YopO S585R1/Q603R1 with a near-Gaussian shape and a FWHM of ~7 Å is an example of case 2. YopO V599R1/N624R1 showed a bimodal distance distribution for almost all analysis variations with a peak-to-peak distance difference Δr below 10 Å, therefore matching the criteria of case 5. As YopO Y588R1/N624R1 showed a bimodal distribution only in certain cases (see Figure 43, Lab B, C, and F), sometimes as two separate peaks and sometimes as a shoulder-like feature, while in other cases yielded a unimodal distribution with a FWHM of ~11 Å, this construct is borderline of the cases 2 and 5. As there are two structural models for the α-helical backbone conformation of YopO (Figure A5), additional experiments and repeats are mandatory for YopO V599R1/N624R1 and YopO Y588R1/N624R1 to disentangle individual contributions of, e.g., different protein conformations and label conformers, to the distance distribution. On the other hand, YopO S353R1/Q635R1 is a prime example of a case 3 distance distribution with a width by far

exceeding 20 Å. As biological repeats and complementary SAXS scattering experiments have demonstrated, the broad distribution is the result of high flexibility between the kinase and the GDI domain in the absence of G-actin.[332]

3.2 Site-directed Spin Labeling of Proteins with Maleimide-Functionalized Trityl Spin Labels and their Application in PDS-EPR

Parts of this chapter have been published in:

[370] J. J. Jassoy, C. A. Heubach, T. Hett, F. Bernhard, F. R. Haege, G. Hagelueken, O. Schiemann, "*Site Selective and Efficient Spin Labeling of Proteins with a Maleimide-Functionalized Trityl Radical for Pulsed Dipolar EPR Spectroscopy*", *Molecules* **2019**, 24, 2735.

[371] N. Fleck, C. A. Heubach, T. Hett, F. R. Haege, P. P. Bawol, H. Baltruschat, O. Schiemann, "*SLIM: A Short-Linked, Highly Redox-Stable Trityl Label for High-Sensitivity In-Cell EPR Distance Measurements*", *Angew. Chem. Int. Ed.* **2020**, 59, 9767–9772.

[372] N. Fleck, C. Heubach, T. Hett, S. Spicher, S. Grimme, O. Schiemann, "*Ox-SLIM: Synthesis of and Site-Specific Labelling with a Highly Hydrophilic Trityl Spin Label*", *Chem. Eur. J.* **2021**, 27, 5292–5297.

[373] K. Ackermann, C. A. Heubach, O. Schiemann, B. E. Bode, "*Pulse Dipolar Electron Paramagnetic Resonance Spectroscopy Distance Measurements at Low Nanomolar Concentrations: The Cu^{II}-Trityl Case*", *J. Phys. Chem. Lett.* **2024**, 15, 1455–1461.

As highlighted in section 1.3.2.2, the spectroscopic and chemical characteristics of trityl-type spin labels make them highly desirable for challenging EPR studies such as *in-cell* experiments where other spin label classes fail to fulfill the demand for high redox stability and high signal intensity. Initial attempts to reproduce and transfer the spin-labeling protocol designed by *Jassoy* et al. for Cytochrome P450 CYP101[164] to $YopO_{89\text{-}729}$ double-cysteine mutants using the methanethiosulfonate linked MTS-TSL **1•** (Figure 44) failed due to the aforementioned difficulties in free-label separation and, additionally, strong over-labeling of YopO was observed.[357] In foresight of potential *in-cell* applications, *Jassoy* and co-workers synthesized the novel, maleimide-functionalized trityl spin-label Mal-TSL **2•** (Figure 44), whose maleimide bioconjugation group is suitable for applications within a reductive environment (see section 1.3.1).

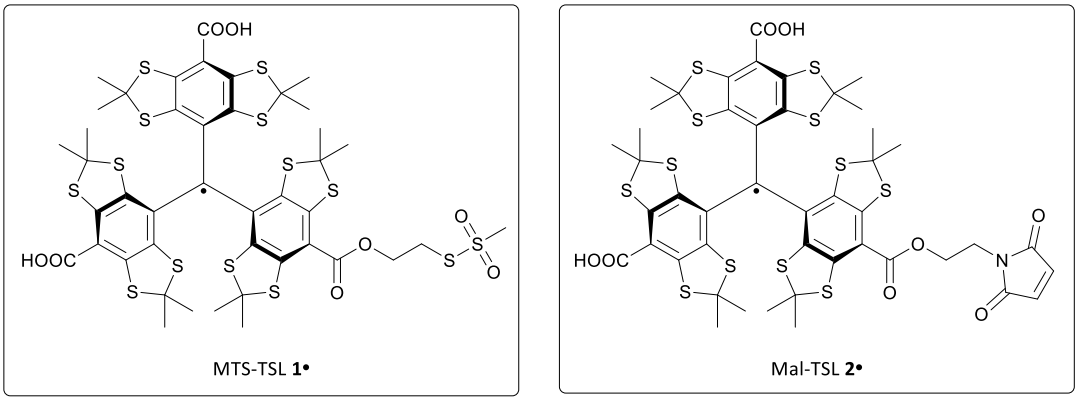

Figure 44: Chemical structures of MTS-TSL **1•** (left) and Mal-TSL **2•** (right)

The main goal of this project was to develop an efficient and reproducible spin-labeling protocol for trityl spin labels that complies with the community-approved guidelines on SDSL presented in

section 3.1.5. The following sections summarize the results and discussion on the development of the spin-labeling protocol and the subsequent applications of the labeled proteins for EPR studies.

3.2.1 Comparison of Methanethiosulfonate- and Maleimide-functionalized Trityl Spin Labels

Despite the evidence that the Finland trityl shows high aggregation tendencies at concentrations above 60 µM,[276] all literature-reported protein spin-labeling procedures using trityl spin labels worked with higher concentrations (100-1500 µM)[164,273,277,374] exceeding the critical self-aggregation concentration of the Finland trityl. To verify whether the reported over-labeling and inseparability of excess label originates from hydrophobic interactions of the trityl with non-polar regions in the protein or whether it is caused by self-aggregation of the spin label due to high concentrations during the labeling process, it was tested if labeling reactions conducted at concentrations below the 60 µM self-aggregation threshold of the Finland trityl can facilitate the separation of excess label.

As an initial setup, the cysteine-free YopO-wt was incubated with the two trityl spin labels MTS-TSL **1•** and Mal-TSL **2•** and, as an additional reference, with Finland trityl to exclude any effects on excess-label separation related to the bioconjugation groups of **1•** and **2•**. Since the YopO-wt does not possess any bioconjugation site for the two spin labels, none of the three incubations should show remaining trityl remnants after label removal via SEC. To disfavor competing lysine-labeling reactions and deactivation of the maleimide moiety by hydrolysis in **2•**,[193,194] the incubations were carried out in phosphate buffer at pH = 6.8. While a 20-fold molar excess per cysteine was employed to achieve high labeling efficiencies in the previously described MTSL-labeling scheme (see section 3.1.2), this approach is unfeasible for trityl labeling owing the self-aggregation tendencies; thus, only a 10-fold molar excess of trityl per YopO-wt was employed. The trityl stock solutions (in DMSO) were pre-diluted in 2.5 mL phosphate buffer to a concentration of 84 µM before addition to the protein solutions (20 nmol in 3.5 mL), resulting in final incubation concentrations of 35 µM trityl and 3.5 µM YopO-wt. After an incubation period of 16 h at 4 °C in the dark, the excess label was removed via SEC using a benchtop PD-10 column. To not exceed the column capacity, the labeling incubations were split into three fractions (2 mL each) and run successively over the SEC column to avoid insufficient trityl removal. After SEC separation, the protein-containing fractions were collected, concentrated to approximately 5 µM, and analyzed by UV-vis and cw-EPR spectroscopy (Figure 45).

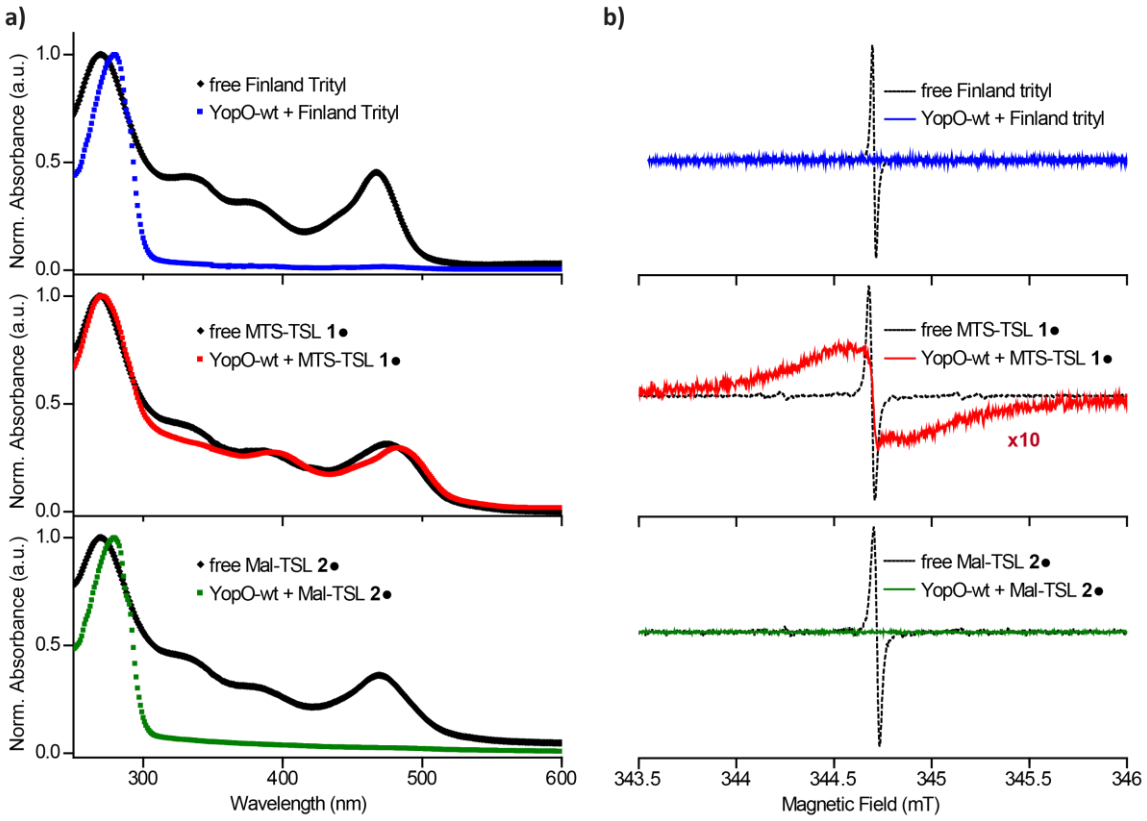

Figure 45: UV-vis and cw-EPR spectra of the YopO-wt incubations recorded after separation of excess trityl. **a)** Normalized UV-vis spectra of the YopO-wt incubations with Finland trityl (blue, top), MTS-TSL **1•** (red, middle), and Mal-TSL **2•** (green, bottom) after excess label separation via SEC and the respective pure trityl species at a concentration of 20 µM in phosphate buffer (black) as a reference. UV-vis spectra were recorded on a Cary100 UV-vis spectrometer. **b)** Corresponding X-band cw-EPR spectra with the color-code adapted from (**a**) and the pure trityl spin label in phosphate buffer (20 µM) underlying as a reference (black dashed lines). Spectra were recorded on a Bruker EMXnano spectrometer. Measurement settings: 9.6 GHz microwave frequency, 6.310 mW microwave power, 100 kHz modulation frequency, 0.1 G modulation amplitude, 20.48 ms time constant, 428 pts/mT.

According to the UV-vis and cw-EPR spectra, the low concentrations utilized in the labeling incubations allowed successful separation of Finland trityl and Mal-TSL **2•** from the protein via SEC as indicated by the absence of the characteristic trityl UV-vis absorbance band at ~467 nm and the absence of an EPR signal (Figure 45a+b, blue and green curves). In strong contrast, even the low-concentration setup did not result in a successful and quantitative separation of MTS-TSL **1•** from the protein fraction. Here, the UV-vis spectrum after SEC showed a strong absorbance in the ~467 nm fingerprint region of **1•** alongside a significantly broadened EPR spectrum compared to free **1•** in phosphate buffer (Figure 45a+b, red and black curves). In addition to the UV-vis and cw-EPR characterization, the incubation sample of YopO-wt with **2•** was analyzed via ESI(+)-MS to check for potential unspecific, covalent attachment of **2•** to any of the 35 lysine residues present in the YopO-wt (Figure 46).

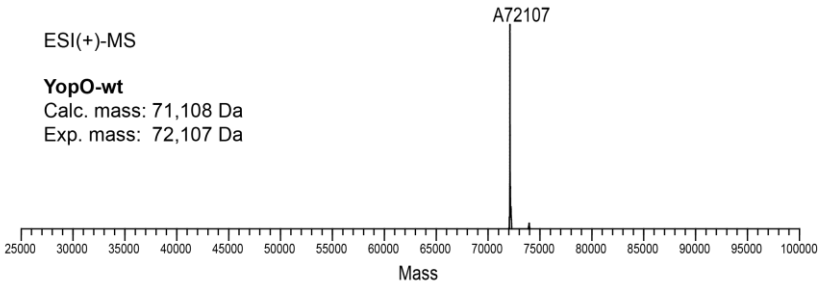

Figure 46: Deconvoluted high-resolution ESI(+)-MS of YopO-wt incubated with Mal-TSL **2•**. Calculated mass of unlabeled YopO-wt: 71,108 Da, found: 71,207 Da. The ESI(+)-MS spectrum was recorded and deconvoluted by the CECAD mass spectrometry facility in Cologne using a Q-Exactive Plus Orbitrap spectrometer. The raw spectrum is shown in the Appendix (Figure A6).

Here, no signs of unspecific lysine labeling were found and only one intense mass peak corresponding to the unlabeled YopO-wt was observed, which highlights the compatibility of the chosen labeling conditions with a slightly acidic pH of 6.8 towards a high lysine abundance.
To rationalize the contrary behavior of **1•** and **2•** concerning the excess label removal, both labels were subjected to additional chemical stability and aggregation studies (Figure 47). For the stability studies executed by *Florian Haege* in the context of his Master thesis,[375] both labels were diluted in PBS buffer with and without a 25-fold molar excess of the reducing agent sodium ascorbate, sealed in gas-tight in glass capillaries, and their cw-EPR spectra were monitored for 21 h. Here, Mal-TSL **2•** showed the expected behavior: In the PBS buffer, no signal decay was observed as indicated by the constant double-integral, whereas the label constantly degraded in the presence of 5 mM ascorbate to ~60% of the initial double-integral of the EPR spectrum after 21 h (Figure 47a). In strong contrast, even in PBS buffer without ascorbate, the double-integral of MTS-TSL **1•** decayed rapidly to ~60% of its initial value within the first 6 h before reaching a plateau and remaining constant for the rest of the experiment (Figure 47b). Over the same period, the linewidth of the EPR signal decreased from 0.03 mT to 0.024 mT (data not shown).[370] These findings hint towards the oxygen-depleting generation of diamagnetic trityl anions involving the methanethiosulfonate motif, which stops after all oxygen in the sealed capillary has been consumed.[376] In the presence of 5 mM ascorbate, the signal decay does not show the same linear trend as for **2•** but rather an exponential depletion of the signal with the double-integral value of **1•** already halved after 5 h. These experiments demonstrate the enhanced redox stability of **2•** compared to **1•**, which is especially beneficial for potential *in-cell* applications.
To test whether MTS-TSL **1•** shows the previously observed aggregation tendency (see Figure 45) even in the absence of proteins, both labels **1•** and **2•** were incubated at a final concentration of 25 µM in phosphate buffer for 16 h at 4 °C under the exclusion of light. Subsequently, samples were concentrated, transferred into glass capillaries, and cw-EPR spectra were recorded (Figure 47c+d). While Mal-TSL **2•** again showed no unexpected behavior and a narrow-line EPR spectrum indicative of free trityl was obtained (Figure 47c), the cw-EPR spectrum of MTS-TSL **1•** was significantly broadened (Figure 47d, red line), similar to the incubation with protein (Figure 45). As MTSL can form disulfide-bridged bis-nitroxides in solution over time,[191] conclusively MTS-TSL **1•** can potentially show the same behavior. Hence, the signal-broadening may be related to disulfide-bridged bis-trityls formed during the incubation. This was tested by irradiation of the same sample with UV light (λ = 254 nm) to cleave the disulfide bridges of the bis-trityls and notably, after UV irradiation, the narrow single-line EPR spectrum of free MTS-TSL **1•** in aqueous solution was regained. The total number of spins determined by quantitative EPR spin-count was the same as before the incubation and irradiation (Figure 47, black line). This is a

clear indication of the previous presence of disulfide-bridged bis-trityls and their cleavage upon UV irradiation.

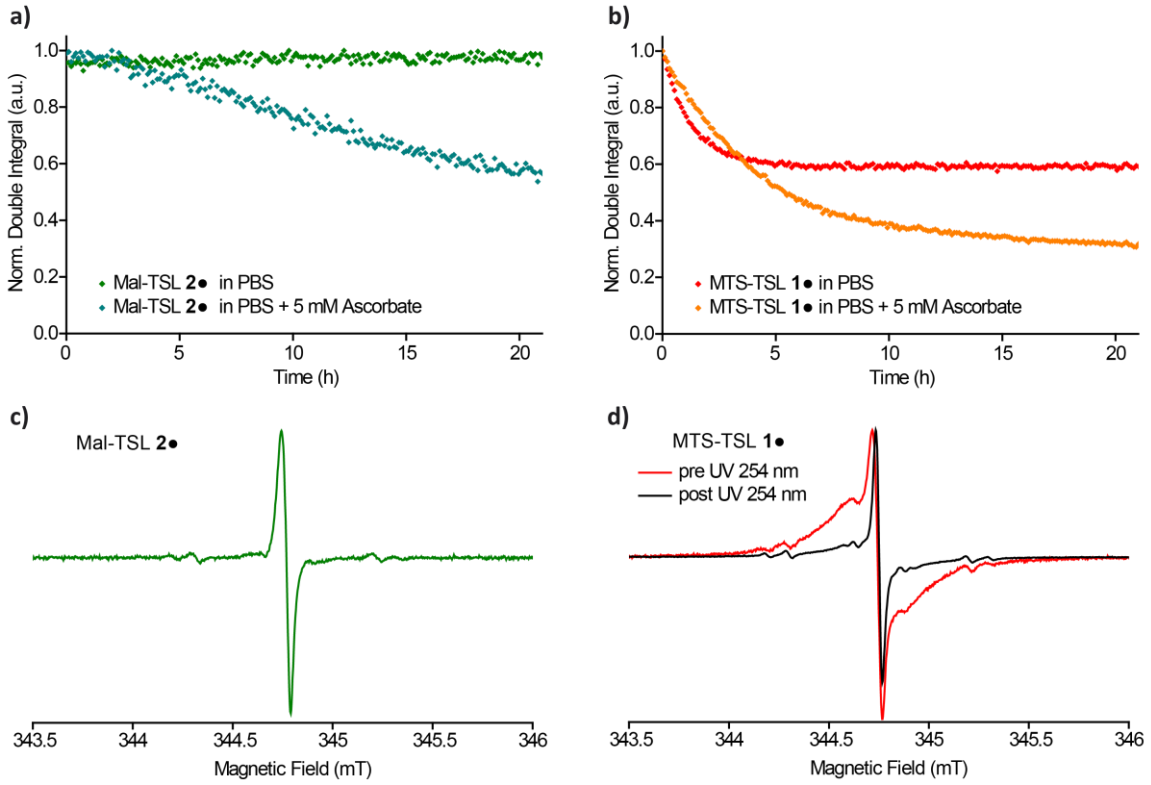

Figure 47: Stability and aggregation studies of Mal-TSL **2•** and MTS-TSL **1•**. **a+b)** Normalized X-band cw-EPR signal double-integral values of 200 µM Mal-TSL **2•** in PBS (**a**, green) and PBS containing 5 mM ascorbate (**a**, teal) or MTS-TSL **1•** in PBS (**b**, red) and PBS containing 5 mM ascorbate (**b**, orange) placed in gas-tight glass capillaries. Spectra were recorded on a Bruker EMXmicro spectrometer. Measurement settings: 9.6 GHz microwave frequency, 0.558 mW microwave power, 100 kHz modulation frequency, 0.1 G modulation amplitude, 20.48 ms time constant, 1000 pts/mT. **c+d)** X-band cw-EPR spectrum of Mal-TSL **2•** (**c**, green) and MTS-TSL **1•** (**d**, red) after incubation in phosphate buffer for 16 h at 4 °C in the dark and MTS-TSL **1•** after irradiation with UV light (λ = 254 nm) for 10 min (**d**, black). Spectra were recorded on a Bruker EMXnano spectrometer. Measurement settings: 9.6 GHz microwave frequency, 6.310 mW microwave power, 100 kHz modulation frequency, 0.1 G modulation amplitude, 20.48 ms time constant, 428 pts/mT.

Considering the results displayed and discussed above, the application of methanethiosulfonate-functionalized trityl spin labels such as MTS-TSL **1•** requires great caution and is generally discouraged due to their apparent shortcomings such as difficult excess label separation, dimer formation, and inferior redox properties. Hence, the following development of a trityl-based spin-labeling protocol specifically focused on maleimide-functionalized trityl labels such as Mal-TSL **2•**, which showed promising traits for site-selective labeling in the initial studies.

3.2.2 Spin-Labeling Protocol for Maleimide-Functionalized Trityl Spin Labels

3.2.2.1 UV-vis Calibration Curve and Extinction Coefficients of Mal-TSL 2•

In the initial studies using the YopO-wt, a qualitative analysis of the UV-vis and cw-EPR spectra was sufficient to prove efficient label separation. However, establishing good-practice guidelines for SDSL of proteins requires a quantitative assessment of both, the protein and the spin label present in the sample. As discussed in section 3.1.5, for MTSL this is usually achieved by UV-vis

concentration determination of the protein and subsequent quantitative EPR spin-count experiments to obtain the spin label concentration, thereby yielding the labeling efficiency. This approach is valid since the absorption of MTSL at 280 nm, the characteristic absorption wavelength of proteins, is usually much smaller than that of the protein itself and hence can be neglected. In contrast, owing their large conjugated π-system, trityls show an intense absorbance peak in the region of 280 nm which cannot be neglected when determining protein concentrations after trityl labeling. Therefore, UV-vis spectra must be deconvoluted to obtain the individual contributions of both, protein and trityl label, to the total absorbance.
To obtain the extinction coefficients of Mal-TSL **2•**, a UV-vis dilution series in phosphate buffer (pH 6.5) was recorded and the absorption values of the two maxima at 280 nm and 467 nm were plotted and linearly fitted (Figure 48 + Table 7).

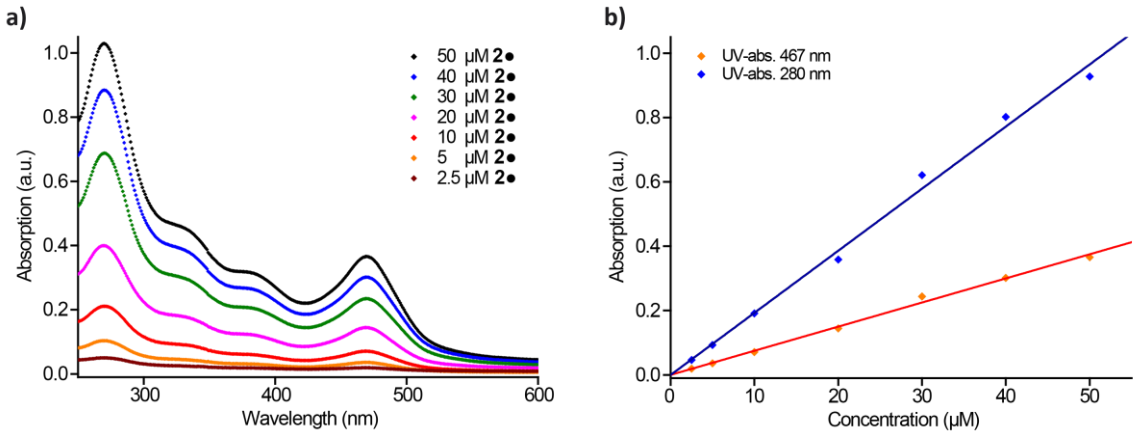

Figure 48: UV-vis dilution series and calibration curves of Mal-TSL **2•**. **a)** UV-vis spectra of Mal-TSL **2•** in phosphate buffer (pH 6.5) at concentrations ranging from 50 µM to 2.5 µM recorded on a Cary100 UV-vis spectrometer (cuvette pathlength 1 cm). **b)** UV-vis absorption values at 280 nm (blue) and 467 nm (orange) from **(a)** plotted against the concentration and the respective linear fits.

Table 7: Linear equations of the fitting curves shown in Figure 48b according to the *Beer-Lambert Law*.

Wavelength		Linear equation
280 nm	(I)	$A_{280} = 0.0193\,\frac{\mathrm{cm}}{\mu\mathrm{M}}\,[2\bullet]\cdot l\,(-1.725\cdot 10^{-4}\mathrm{a.u.})$
467 nm	(II)	$A_{467} = 0.0075\,\frac{\mathrm{cm}}{\mu\mathrm{M}}\,[2\bullet]\cdot l\,(-4.604\cdot 10^{-4}\mathrm{a.u.})$

According to the *Beer-Lambert Law* ($A = \varepsilon_\lambda \cdot c \cdot l$), the extinction coefficients correspond to the slope of the respective lines and were determined after linear fitting of the respective curves to $\varepsilon_{280}(\mathbf{2\bullet}) = 0.0193\,\frac{\mathrm{cm}}{\mu\mathrm{M}}$ and $\varepsilon_{467}(\mathbf{2\bullet}) = 0.0075\,\frac{\mathrm{cm}}{\mu\mathrm{M}}$ for Mal-TSL **2•**. The extinction coefficients can subsequently be used to quantify the protein-to-label ratio of a labeling experiment via UV-vis using the following workflow:

1. From the absorption at 467 nm, the concentration of **2•** can be determined using the *Beer-Lambert Law* and $\varepsilon_{467}(\mathbf{2\bullet}) = 0.0075\,\frac{\mathrm{cm}}{\mu\mathrm{M}}$.
2. Knowing the concentration of **2•**, the contribution of the trityl label to the total absorption at 280 nm can be estimated using $\varepsilon_{280}(\mathbf{2\bullet}) = 0.0193\,\frac{\mathrm{cm}}{\mu\mathrm{M}}$.

3. The remaining absorption at 280 nm can then be attributed to the protein and its concentration calculated using $\varepsilon_{280}(\mathbf{protein})$.

As a slight bathochromic shift of the local absorbance maximum at 467 nm and small spectral deviations of **2•** upon bioconjugation were observed (see section 3.2.2.3), not the exact wavelength absorbance but rather the maxima of the absorbance peaks in the region of ~467 nm and ~280 nm (maximum-peak method) were used for the workflow presented above in combination with the extinction coefficients determined herein.

3.2.2.2 Spin-Labeling Protocol for Mal-TSL 2•

To develop a general labeling procedure for maleimide-functionalized trityl spin labels, various reaction conditions and work-up procedures were screened using YopO double-cysteine mutants with highly accessible surface cysteines (YopO S88C/L113C and YopO L113C/L252C, previously prepared by *Fraser Duthie*). For each condition, the criterion for successful labeling was the trityl-to-protein ratio after SEC determined by UV-vis spectroscopy using the previously described quantification routine (data not shown). The following aspects turned out to be crucial for successful SDSL using Mal-TSL **2•**:

(a) Before SEC-separation of the excess label from the labeled protein, the trityl concentration during the labeling process has to be kept at 35 µM or below. Otherwise, aggregates of **2•** are formed that exceeded the molecular weight cut-off (MWCO) of the PD-10 benchtop SEC columns employed here and eluted alongside the high molecular weight fraction containing the protein.

(b) At the expense of prolonged incubation times (16 h), labeling reactions performed best at slightly acidic buffer conditions (pH 6.5 – 6.8) and low temperatures (4 °C). At pH values above this threshold or alkaline conditions, increased trityl-to-protein ratios indicating undesired lysine labeling were observed.[194] Surprisingly, attempts to increase the reaction rate and labeling efficiencies using elevated temperatures had the contrary effect of lowered trityl-to-protein ratios, presumably caused by hydrolysis and thereby deactivation of the maleimide-moiety of **2•**.[193] While this competing process is usually countered by employing high initial label concentrations, this option is impossible here due to the aspects discussed in (a). In addition, agitation of the reaction tube to enhance the homogeneity of the mixture during incubation led to the precipitation of the protein evidenced by a green precipitate and cloudiness of the reaction solution.

(c) Separation of excess label via PD-10 SEC column worked best when the column was loaded with less than 70 nmol of **2•** (2 mL of a 35 µM solution). Higher trityl loads surpassed the column capacity and led to insufficient separation of the low molecular weight fraction containing **2•** and the high molecular weight fraction of the protein.

The insights obtained from the screening experiments led to the final spin-labeling protocol for Mal-TSL **2•**:

The reduction and spin-labeling reaction is carried out in phosphate buffer (20 mM PO_i, 50 mM NaCl, pH 6.8). Immediately after TCEP-reduction of any disulfide-bridged protein dimers and reducing agent removal via PD-10, a five-fold molar excess of **2•** (dissolved in 2.5 mL phosphate buffer) per cysteine is added to the protein (20 nmol in 3.5 mL, here: YopO) resulting in a total volume of 6 mL containing 3.3 µM protein and 33 µM of **2•**. Subsequently, the solution is gently mixed and incubated for 16 h at 4 °C in the dark without agitation. The free excess label is removed by loading 2 mL of the incubation solution onto a PD-10 desalting column followed by 500 µL of phosphate buffer before elution with 3.5 mL of phosphate buffer. The protein-containing fraction

is eluted and concentrated using a centrifugal concentrator with an MWCO appropriate for the protein.

3.2.2.3 Spin-Labeling and Characterization of YopO labeled with Mal-TSL 2•

To validate the general applicability of the spin-labeling protocol derived in section 3.2.2.2 and the performance of **2•** in pulsed EPR experiments, the two double-cysteine mutants YopO S585C/Q603C and YopO V599C/N624C were labeled with Mal-TSL **2•** (Figure 49a). Since the GDI-backbone structure of YopO was assumed to be rather rigid (see section 3.1.4), the α-helix of YopO was to serve as a "ruler" in assessing the performance of Mal-TSL **2•** with *in silico* derived mean distances of 32.5 Å for YopO S585-**2•**/Q603-**2•** and 40.5 Å for YopO V599-**2•**/N624-**2•** (Figure 49b).

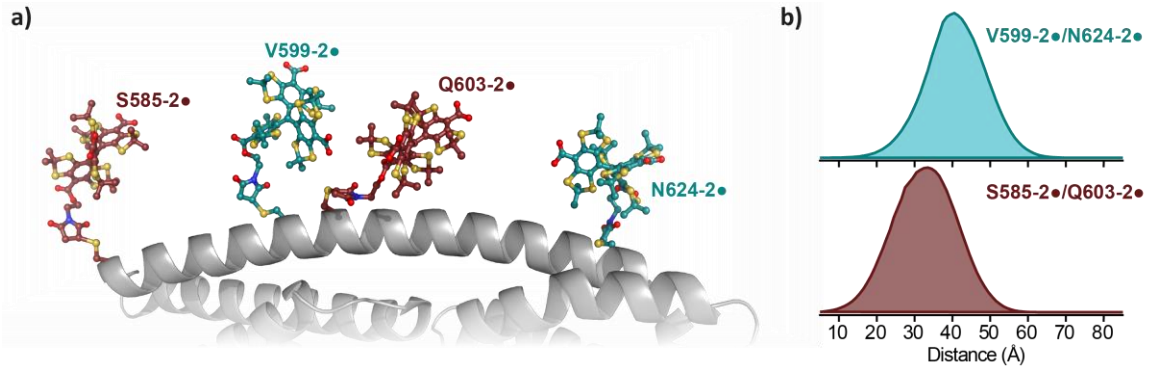

Figure 49: Labeling sites for Mal-TSL **2•** and the corresponding *in silico* derived distance distributions. **a)** Depiction of the $YopO_{89-729}$ GDI α-helix (PDB-ID 4ci6) with a schematic ball-and-stick representation of the color-coded labeling positions S585-**2•**/Q603-**2•** (brown) and V599-**2•**/N624-**2•** (teal). Rotamer clouds were generated with mtsslWizard (clash setting: loose). For clarity, only one conformer state is shown. **b)** *In silico* distance distributions derived by mtsslWizard for the spin pairs shown in **(a)** using the same color code.

Both mutants were labeled following the aforementioned protocol (section 3.2.2.2). After the incubation with Mal-TSL **2•**, excess label separation, and concentrating, both samples were passed over an additional SEC column (HiPrep™ 26/10) on an Äkta Avant system. The characteristic absorption of **2•** at a wavelength of 475 nm was used to check for remaining free label (Figure 50).

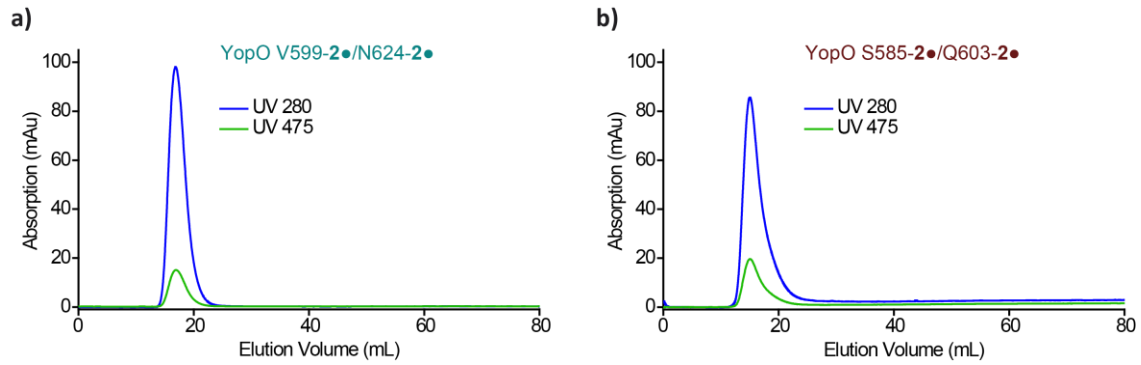

Figure 50: SEC chromatograms for the labeling reactions of YopO V599-**2•**/N624-**2•** and YopO S585-**2•**/Q603-**2•**. **a)** Chromatogram of the HiPrep™ 26/10 run of YopO V599-**2•**/N624-**2•** with the absorption at 280 nm (blue) and 475 nm (green). **b)** Same as **(a)** but for YopO S585-**2•**/Q603-**2•**.

Both SEC elugrams showed only one absorption peak within the bed volume (53 mL) of the column for both wavelengths. As the absorption peak was eluting at the same retention volume for both wavelengths, a complete separation of free trityl **2•** was achieved and the presence of trityl

aggregates was ruled out. After SEC, the fractions showing UV-vis absorption were pooled and concentrated for the determination of the labeling efficiencies via UV-vis (Figure 51). In addition to the aforementioned quantification workflow (maximum-peak method), the UV-vis spectra of the labeled proteins were fitted to the spectra of the unlabeled protein and Mal-TSL **2•** according to

$$[\mathrm{Exp}] = (a \cdot [\mathrm{YopO}] + (1 - a) \cdot [\mathbf{2}\bullet]) \cdot b + c \qquad \text{(eq. 24)}$$

where $[\mathrm{Exp}]$ is the spectrum of the labeled protein, $[\mathrm{YopO}]$ and $[\mathbf{2}\bullet]$ are the reference spectra of YopO-wt and Mal-TSL **2•**, respectively, a is a weighting factor, b is a scaling factor, and c corresponds to an offset-correction factor. The results of both quantification methods are summarized in Table 8.

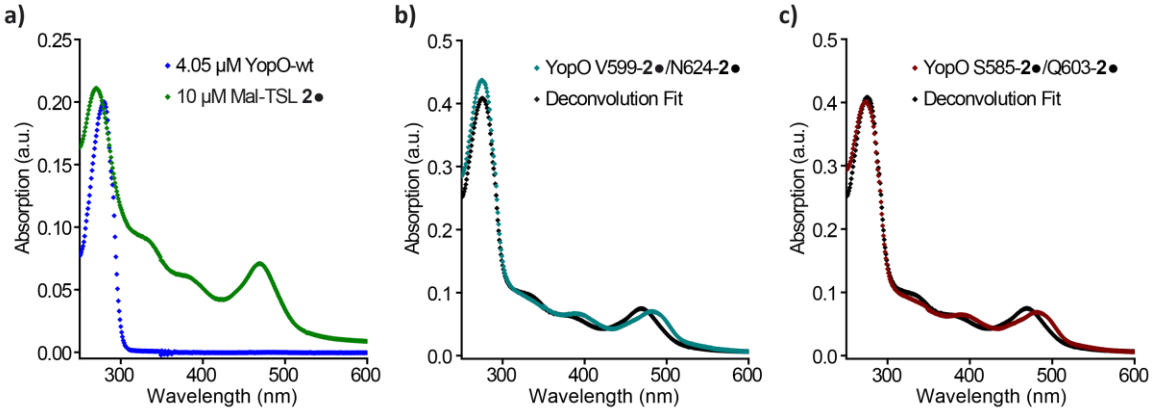

Figure 51: UV-vis spectra of YopO-wt, free Mal-TSL **2•**, and the labeled proteins YopO V599-**2•**/N624-**2•** and YopO S585-**2•**/Q603-**2•**. **a)** UV-vis spectra of the YopO-wt and Mal-TSL **2•** (in phosphate buffer) used as reference spectra for eq. 24. **b)** Experimental spectrum of the labeled protein YopO V599-**2•**/N624-**2•** (teal) and the deconvolution fit (black) using eq. 24 and the spectra in **(a)**. **c)** Same as **(b)**, but for YopO S585-**2•**/Q603-**2•** (brown). Note that the local absorbance maximum of **2•** shifts from 467 nm to 475 nm upon bioconjugation. All spectra were recorded using a Cary100 UV-vis spectrometer.

Table 8: Concentrations of YopO and **2•** in the labeled protein samples YopO V599-**2•**/N624-**2•** and YopO S585-2•/Q603-2• (Figure 51b+c) determined via UV-vis using either the maximum-peak method or deconvolution of the spectra according to eq. 24.

Sample	Maximum-Peak	Deconvolution
YopO V599-**2•**/N624-**2•**	5.2 µM YopO 9.3 µM **2•**	4.7 µM YopO 10.7 µM **2•**
YopO S585-**2•**/Q603-**2•**	4.6 µM YopO 9.1 µM **2•**	3.9 µM YopO 10.9 µM **2•**

Using the maximum-peak method, trityl-to-protein ratios of 1.8 : 1 corresponding to a labeling efficiency of 90% in the case of YopO V599-**2•**/N624-**2•** and of 2 : 1 for YopO S585-**2•**/Q603-**2•** (100% labeling efficiency) were obtained, hence indicating quantitative labeling. Comparison with the ratios obtained by deconvolution of the spectra using eq. 24 shows that the deconvolution method yields slightly lower YopO concentrations and slightly higher Mal-TSL **2•** concentrations for both mutants. This result can be rationalized by the bathochromic shift of **2•** upon

bioconjugation causing the fit function to overestimate the trityl concentration to achieve a better fit in the region above 300 nm. Hence, the maximum-peak method is expected to yield more accurate concentrations and was used for all further labeling quantifications of trityl labelings.
Before rebuffering in deuterated PDS buffer, the labeled proteins were subjected to ESI(+)-MS to check for covalent attachment of the spin label (Figure 52 + Table 9).

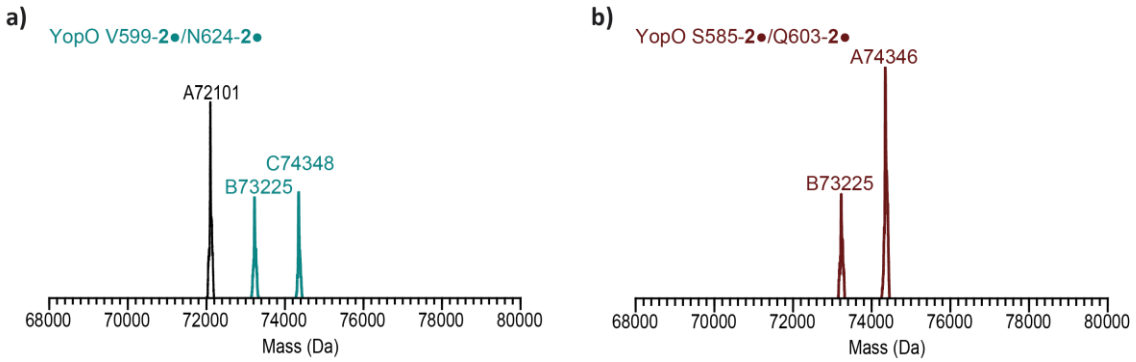

Figure 52: Excerpts of the deconvoluted high-resolution ESI(+)-MS spectra of the labeled proteins YopO V599-**2•**/N624-**2•** and YopO S585-**2•**/Q603-**2•**. **a)** ESI(+)-MS spectrum of YopO V599-**2•**/N624-**2•** with the mass peaks corresponding to the unlabeled protein peak shown in black (A), and the singly- (B) and doubly-labeled (C) proteins in teal. **b)** Same as **(a)** but the peaks corresponding to the labeled protein are shown in brown. The ESI(+)-MS spectra were recorded and deconvoluted by the CECAD mass spectrometry facility in Cologne using a Q-Exactive Plus Orbitrap spectrometer. The raw spectra are shown in the Appendix (Figure A7).

Table 9: Calculated and experimentally found masses of the unlabeled and Mal-TSL **2•**-labeled YopO constructs from the ESI(+)-MS spectra shown in Figure 52.

Sample	Unlabeled (Da)	Singly-labeled (Da)	Doubly-labeled (Da)
YopO V599-**2•**/N624-**2•**	Calc: 74,102 Found: 72,101	Calc: 74,225 Found: 74,225	Calc: 74,348 Found: 74,348
YopO S585-**2•**/Q603-**2•**	Calc: 72,100 Found: -	Calc: 73,223 Found: 74,225	Calc: 74,346 Found: 74,346

For both constructs, mass-peaks corresponding to the doubly-labeled proteins (YopO V599-**2•**/N624-**2•**: 74,348 Da; YopO S585-**2•**/Q603-**2•**: 74,346 Da) were found in ESI(+)-MS spectra. However, in both samples, mass peaks corresponding to singly-labeled YopO and, in the case of YopO V599-**2•**/N624-**2•**, even unlabeled protein, were also observed. As this was contradictory to the SEC and UV-vis results, samples were additionally subjected to MALDI(+)-MS (see appendix, Figure A8), which also revealed non- and singly-labeled protein, but with strongly varying intensities compared to the ESI(+)-MS spectra. Since both MS sample preparations required acidic conditions (trifluoracetic acid), the detachment of the spin label via retro-*Michael* reaction[196] (see Figure 18) and/or label detachment during the measurement process are the most likely reasons for the herein observed under-labeling of both samples as compared to UV-vis quantification. Consequently, the obtained labeling efficiencies are not reflected in the MS spectra. Several attempts to avoid the acidic conditions during sample preparation failed. In addition, for both trityl-labeled proteins, the SNR of the mass spectra is worse than for the unlabeled protein (see Figure 46), therefore suggesting that the trityl-conjugation renders the

protein more labile and prone to precipitation. Hence, careful sample handling is required. Notably, for both samples, the absence of peaks corresponding to three- or higher-fold labeled species indicates the successful suppression of lysine-labeling under the chosen labeling conditions but cannot be fully excluded to the aforementioned difficulties in sample preparation and handling.

Additionally, cw-EPR spectra of both samples were recorded and simulated to check for the immobilization of the spin label upon bioconjugation, to check for remaining free spin label, and to quantify the trityl amount present in the sample by relative EPR spin-count against a reference spectrum of 100 µM free Mal-TSL **2•** (Figure 53 + Table 10). Simulations were performed by *Tobias Hett*.

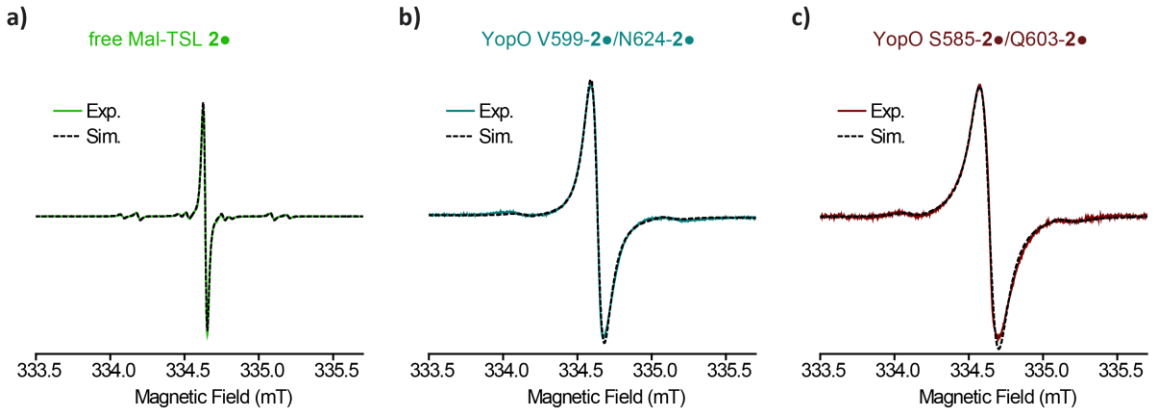

Figure 53: Room Temperature X-band cw-EPR spectra and simulations of free Mal-TSL **2•**, YopO V599-**2•**/N624-**2•**, and YopO S585-**2•**/Q603-**2•**. **a)** X-band cw-EPR spectrum of 100 µM free Mal-TSL **2•** in phosphate buffer (green) and the spectral simulation (black dashed line) obtained with EasySpin. **b)** Same as **(a)** but for YopO V599-**2•**/N624-**2•** (teal) at a protein concentration of 50 µM. **c)** Same as **(a)** but for YopO S585-**2•**/Q603-**2•** (brown) at a protein concentration of 50 µM. Spectra were recorded on a Bruker EMXmicro spectrometer. Measurement settings: 9.6 GHz microwave frequency, 2.783 mW microwave power, 100 kHz modulation frequency, 0.15 G modulation amplitude, 20.48 ms time constant, 670 pts/mT.

Table 10: EasySpin[108] simulation parameters and spin-count for the cw-EPR spectra in Figure 53.

Sample	Simulation parameter	Spin-count
Free Mal-TSL **2•**[a]	g = 2.0034 A_{C1} = 31.3 MHz $A_{C2,C3}$ = 25.3 MHz $A_{C4,C5}$ = 6.8 MHz A_{C6} = 9.4 MHz lwpp = (0.017, 0.018) mT	100 µM (reference)
YopO V599-**2•**/N624-**2•**	g = (2.0041, 2.0043, 2.0015) A = 30.8 MHz lwpp = (0, 0.035) mT τ = 15 ns	109 µM
YopO S585-**2•**/Q603-**2•**	g = (2.0036, 2.0058, 2.0005) A = 31.1 MHz lwpp = (0, 0.031) mT τ = 11 ns	95 µM

[a] Assignment of hyperfine coupling constants A to explicit ^{13}C nuclei of the phenyl ring was done according to *Bowman* et al.[254]

As a consequence of the spin label immobilization upon bioconjugation, the cw-EPR spectra of both trityl-labeled proteins are broadened compared to the free label, but not to an extent indicative of label aggregation (compare Figure 45b). In addition, no sharp features indicative of remaining free label are observed and both spectra could successfully be simulated by a single spin-species with an anisotropic g-tensor and an increased rotational correlation time τ using the "chili"-routine of EasySpin.[108] The obtained simulation parameters agree with literature-reported values for immobilized trityls.[254,267] The relative spin-count of both spectra against the 100 µM reference of free **2•** gave spin labeling efficiencies of 109% (YopO V599-**2•**/N624-**2•**) and 95% (YopO S585-**2•**/Q603-**2•**), which is in good accordance to the previously obtained labeling efficiencies determined by UV-vis spectroscopy (90% for YopO V599-**2•**/N624-**2•**; 100% for YopO S585-**2•**/Q603-**2•**) and well within the error range of both methods.
In compliance with the community-approved guidelines for SDSL of proteins (section 3.1.5), the functional and thus structural integrity of the trityl-labeled proteins was assessed by an auto-phosphorylation assay of YopO in the presence of G-actin (Figure 54).

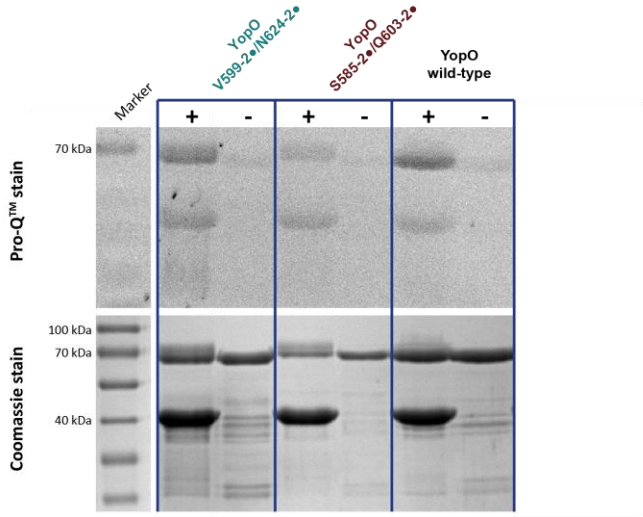

Figure 54: Activity assay of the Mal-TSL **2•**-labeled YopO constructs. Samples were loaded onto 10% polyacrylamide gels and stained with Pro-Q™ (top row, negative image) to visualize phosphorylated proteins and subsequently with Coomassie stain (bottom row) for visualization of total protein content. The lanes indicated with a (+)-sign contain G-actin while the lanes indicated with a (–)-sign are negative controls in the absence of G-actin.

Here, both trityl-labeled YopO constructs showed the reported auto-phosphorylation capability[324,328] and a kinase-activity comparable to YopO-wt. Exact quantification of the activity was not possible since the sample amount loaded onto the SDS gel and therefore the ProQ™ signal was slightly lower for YopO S585-**2•**/Q603-**2•**, as apparent when comparing the corresponding band intensities of the Coomassie stain.

As demonstrated by the two YopO constructs, the spin-labeling protocol for the maleimide-functionalized spin label Mal-TSL **2•** presented herein is reliably, and quantitative removal of the excess spin label is achieved when working at low trityl concentrations. The obtained labeling efficiencies (>85%) are significantly improved as compared to, e.g., butene-TSL (36%, Figure 25).[164] Notably, a similar maleimide-functionalized trityl spin label with the only difference being an amide- rather than an ester-motif connecting the $(CH_2)_2$-maleimide bioconjugation group to the trityl basal body was reported by *Giannoulis* et al. earlier in 2019.[374] Using this amide-derivative of Mal-TSL **2•**, in the following referred to as Mal_{am}-TSL, to label double-cysteine ubiquitin- and GB1-mutants, the authors employed alkaline labeling conditions (pH 8.5), a high trityl concentration (600-1200 µM) in the labeling incubation, elevated temperatures (room temperature) at the expense of a reduced reaction time (6 h) during the labeling reaction, and rudimentary excess label removal via desalting column (a single PD-10 run). In addition to lysine labeling observed in MALDI-TOF as a consequence of the alkaline labeling conditions, both protein samples contained large amounts of free Mal_{am}-TSL (between 22% and 53% of the total trityl amount) that could not be separated and resulted in a lower modulation depth in the reported PDS time traces. These complementary results corroborate the importance of the employed labeling conditions when using maleimide-functionalized trityl spin labels and hence the feasibility of the spin-labeling protocol derived herein to yield high labeling efficiencies while simultaneously removing excess free trityl remnants.

3.2.3 Pulsed EPR Experiments on Mal-TSL 2• labeled YopO

Following the successful labeling of YopO V599-**2•**/N624-**2•** and YopO S585-**2•**/Q603-**2•**, both proteins were rebuffered in YopO PDS buffer and diluted in 50% v/v deuterated ethylene glycol

before PDS-EPR sample preparation. The pulsed EPR experiments of the following sub-sections 3.2.3.1 and 3.2.3.2 were conducted under the guidance and with *Tobias Hett*.

3.2.3.1 Relaxation Time Measurements for Mal-TSL 2•

On the example of YopO V599-**2•**/N624-**2•**, the temperature-dependence of the spin-lattice relaxation time T_1 and phase memory time T_M was determined by inversion recovery and 2pESEEM experiments, respectively, and compared to the MTSL-labeled analog of this mutant (Figure 55 + Table 11).

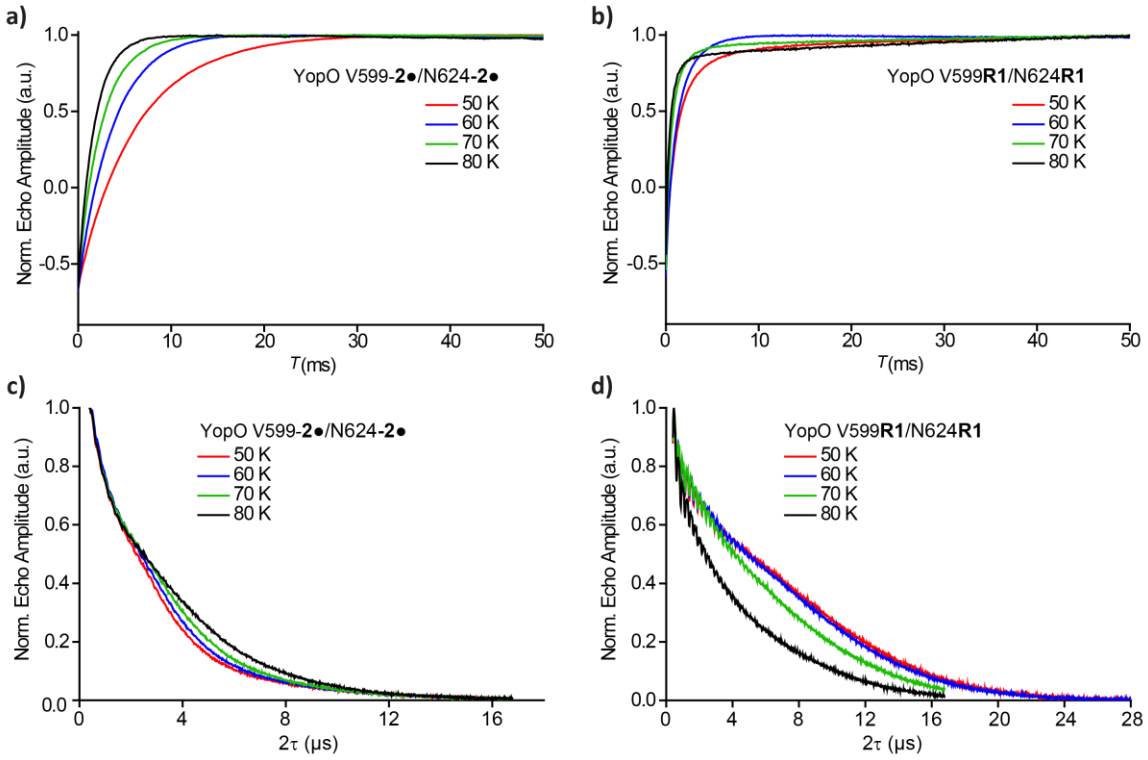

Figure 55: Temperature-dependent relaxation measurements on Mal-TSL **2•**- and MTSL-labeled YopO V599C/N624C. **a**+**b)** Inversion recovery traces for YopO V599-**2•**/N624-**2•** **(a)** and YopO V599R1/N624R1 **(b)** at 50 K (red), 60 K (blue), 70 K (green), and 80 K (black). **c**+**d)** 2pESEEM traces for YopO V599-**2•**/N624-**2•** **(c)** and YopO V599R1/N624R1 **(d)** at 50 K (red), 60 K (blue), 70 K (green), and 80 K (black).

Table 11: Spin lattice relaxation times T_1 and phase memory times T_M of YopO V599-**2•**/N624-**2•** and YopO V599R1/N624R1 obtained by fitting either eq. 19 (Inversion recovery) or eq. 20 (2pESEEM) to the respective traces shown in Figure 55.

Temperature	YopO V599-2•/N624-2•		YopO V599R1/N624R1	
	T_1 (ms)	T_M (µs)	T_1 (ms)	T_M (µs)
50 K	6.3	2.6	1.9	9.2
60 K	3.6	2.8	1.4	9.2
70 K	2.5	3.2	0.9	8.8
80 K	1.7	3.3	0.7	3.0

The spin-lattice relaxation time T_1 shows a similar trend for both, the trityl- and MTSL-labeled protein, with a continuous decrease of T_1 as the temperature increases. However, across the

whole temperature range, the spin-lattice relaxation of the trityl-labeled protein is notably slower as compared to the nitroxide and agrees well with the relaxation times obtained for Mal_{am}-TSL-labeled GB1 and Ubiquitin.[374] On the other hand, for the phase memory time T_M, both spin-species showed opposite trends, with T_M of the trityl-labeled YopO increasing steadily in the range from 50 K to 80 K while the nitroxide-labeled YopO shows the expected trend of a continuous decrease of T_M with increasing temperature.[226] Notably, below 70 K the T_M relaxation time of MTSL-labeled YopO is significantly longer than for Mal-TSL **2•**-labeled YopO and only at 80 K, the phase memory time of the trityl-labeled protein exceeds the one obtained for MTSL-labeled YopO. For Mal-TSL **2•**, the best compromise between T_1 and T_M (fast SRT, long phase memory time, and strong EPR signal) is obtained in the temperature range between 70 K and 80 K.

3.2.3.2 PDS-EPR with Mal-TSL 2•-labeled YopO

The performance of Mal-TSL **2•** in PDS-EPR was tested on both trityl-labeled YopO constructs using the DQC-, SIFTER-, and PELDOR pulse sequences and compared to the MTSL-labeled protein analogs (PELDOR only) regarding SNR and the distance distribution width. Although the optimal measurement temperature for Mal-TSL **2•** is between 70 K and 80 K (see section 3.2.3.1), all PDS data shown in this section was acquired at 50 K to achieve a maximal comparability with the "gold standard" MTSL.

Notably, at the time of data acquisition, the previously presented guidelines on PDS data evaluation (section 3.1.5) were not yet established and published and, in addition, no single-step PDS analysis routines or neural networks trained on trityl datasets were available. Therefore, all acquired PDS data in this chapter was routinely analyzed by background fitting and subsequent division of the experimental time trace by the background fit, followed by Tikhonov regularization and validation in DeerAnalysis. Other than for PELDOR,[377] no analytical treatment of the DQC- and SIFTER-background is known and, in such cases, experimental backgrounds can be obtained by performing PDS experiments on singly-labeled proteins.[267,275] Hence, DQC- and SIFTER-measurements on singly-labeled YopO L113-**2•** (for labeling quantification see appendix Figure A9) were performed and experimental backgrounds were obtained by fitting polynomial functions to the respective time traces (Figure 56).

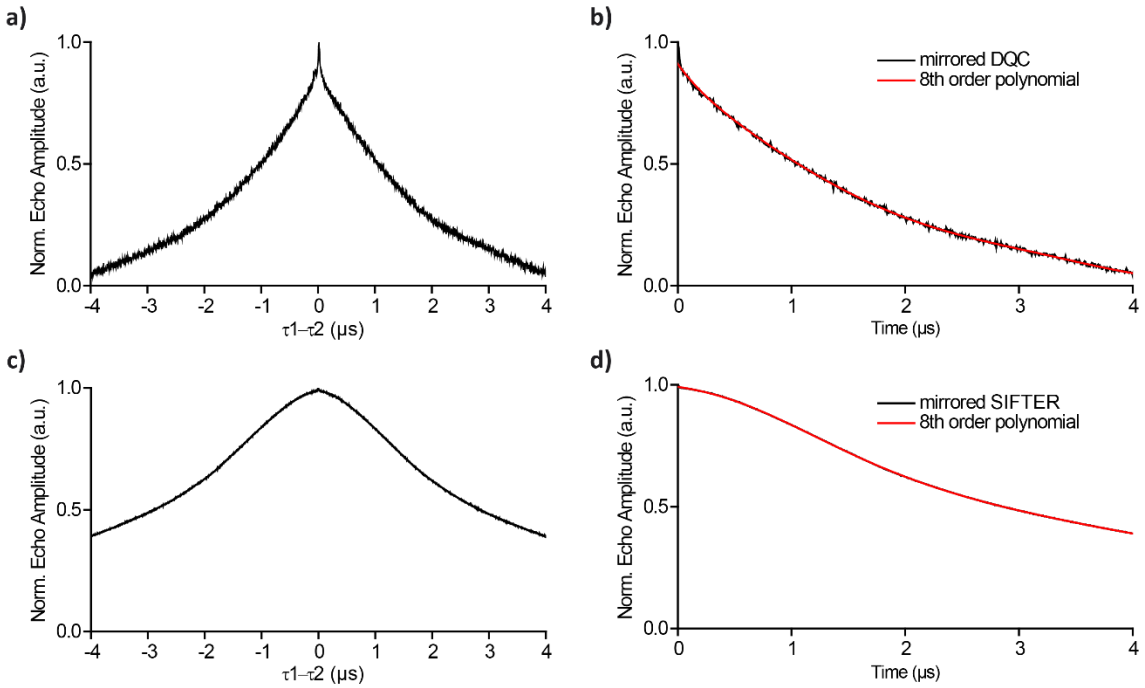

Figure 56: DQC and SIFTER time traces with the experimental background functions obtained from YopO L113-**2•**. **a)** Original DQC time trace for YopO L113-**2•**. **b)** DQC trace from **(a)** mirrored at the maximum (black) with the 8th-order polynomial fit function serving as the experimental background in subsequent PDS experiments. **c**+**d)** Same as **(a**+**b)** but for the SIFTER pulse sequence.

Both pulse sequences showed a decay of the echo amplitude that is not well described by a three-dimensional homogenous background function that is commonly used for PELDOR. Hence, both decays were fitted by an 8th-order polynomial fit to the mirrored time traces which were later used as experimental backgrounds.

Next, DQC-, SIFTER-, and PELDOR experiments were performed on the doubly-labeled constructs YopO V599-**2•**/N624-**2•** and YopO S585-**2•**/Q603-**2•**, as well as PELDOR experiments on the MTSL-labeled analogs (biological repeats of the constructs discussed in section 3.1.4) at a final spin concentration of 50 µM. Time traces were analyzed using DeerAnalysis by applying a three-dimensional homogeneous background (PELDOR) or division of the time traces by the polynomial functions obtained from singly-labeled YopO (DQC, SIFTER), and distance distributions were computed using Tikhonov regularization in DeerAnalysis (Figure 57).

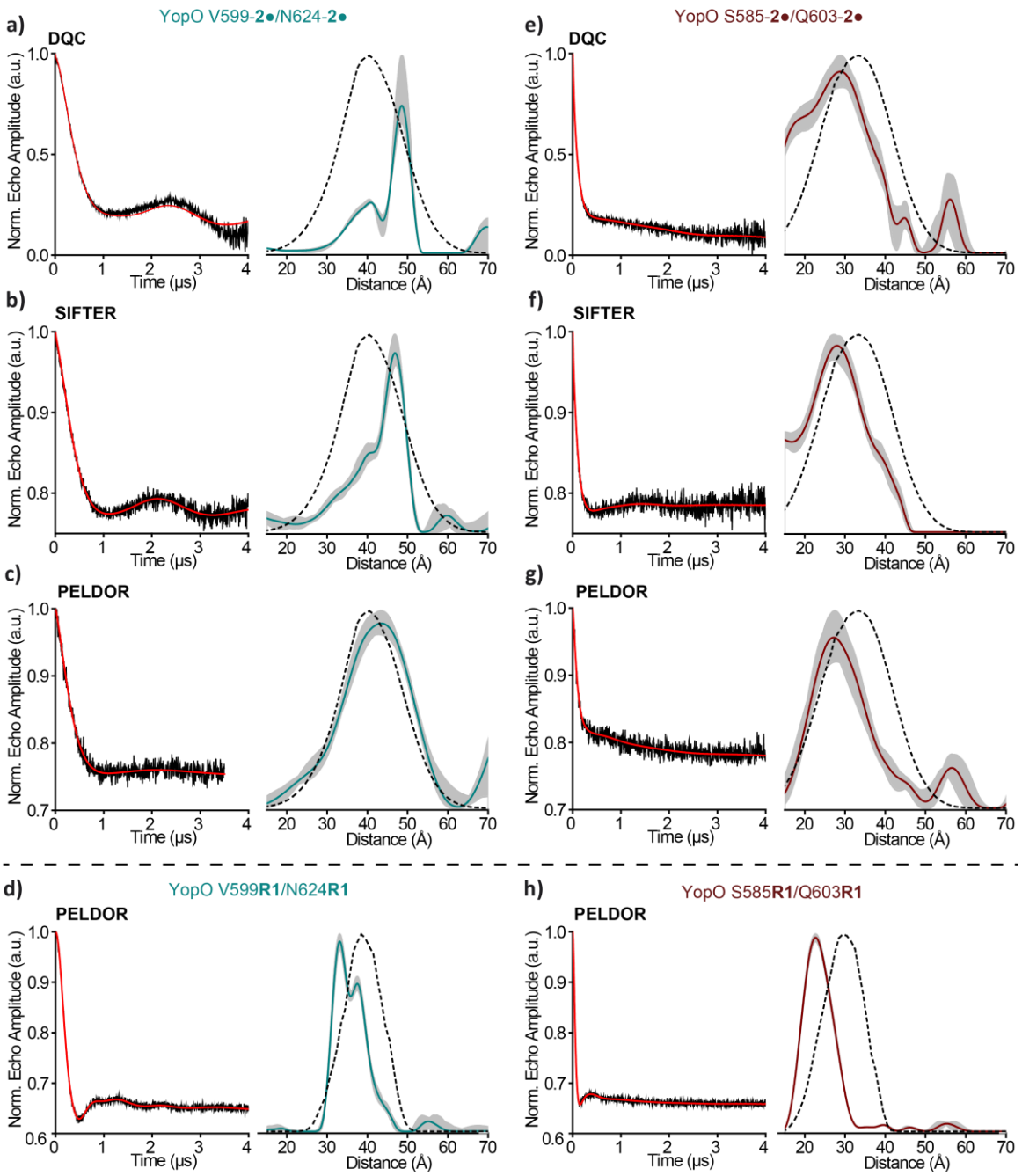

Figure 57: PDS data of YopO V599C/N624C and YopO S585C/Q603C labeled with Mal-TSL **2•** or MTSL. **a-d)** On the left: Background-corrected DQC **(a)**, SIFTER **(b)**, and PELDOR **(c+d)** time traces (black) obtained for YopO V599-**2•**/N624-**2• (a-c)** and YopO V599R1/N624R1 **(d)** with the respective fits obtained by Tikhonov regularization (red). On the right: Resulting distance distributions (teal) with the DeerAnalysis validation shown as grey-shaded areas. *In silico* predictions obtained by mtsslWizard using the PDB-ID 2h7o as a template are shown as dashed black lines (rotamer clash treatment: loose). **e-h)** Same as **(a-d)** but for YopO S585C/Q603C (brown). The complete analysis by DeerAnalysis (Backgrounds, fits, L-curves, and distance distributions) is given in the appendix (Figure A10-A12).

For all label/pulse-sequence combinations, good-quality time traces with varying modulation depth and oscillations were obtained. For the single-frequency techniques DQC and SIFTER, time traces with a modulation depth of ~80% in the case of DQC and ~22% for SIFTER were obtained. The higher modulation depth of DQC compared to SIFTER can be rationalized by the larger number

of phase-cycling steps (64 steps for DQC compared to 16 steps for SIFTER) and the more efficient suppression of intermolecular contributions as a result of the double-quantum filter in the DQC sequence.[144,145] The obtained modulation depth of DQC parallels the ones found for quantitatively labeled oligonucleotides[378] and is only slightly lower than the values obtained for trityl model systems.[145] Notably, it is well above the modulation depths previously reported for trityl-labeled proteins ranging from 20% to 50%,[273,374] which substantiates the high labeling efficiencies and sample purity achieved by the developed trityl-labeling protocol. For trityl-trityl PELDOR at Q-band, modulation depths ranging from 20% (YopO S585-**2•**/Q603-**2•**) to 24% (YopO V599-**2•**/N624-**2•**) were obtained, which are surprisingly three times larger than values reported for PELDOR on Mal_{am}-TSL-labeled proteins at W-Band (~8%).[374] For both MTSL-labeled analogs, the modulation depths were similar as compared to the samples discussed in section 3.1.4 and agreed well with the modulation depth of ~35% expected for nitroxides at Q-band frequencies.

Benefitting from the narrow trityl EPR spectrum of the Mal-TSL **2•**-labeled proteins (0.36 mT for YopO V599-**2•**/N624-**2•**, 0.51 mT for YopO S585-**2•**/Q603-**2•**; Figure A13), which can be fully excited by rectangular pulses, both single-frequency techniques DQC and SIFTER outperformed the PELDOR pulse sequence in terms of SNR by a factor of 6.4 (DQC) and 4.7 (SIFTER) (averaged SNRs for both constructs). While the observation that PELDOR performs the weakest is in line with earlier findings by *Meyer* et al. using trityl-trityl model systems, they found SIFTER to be more sensitive than DQC, which is contrary to the results obtained herein.[145] Notably, both nitroxide-labeled proteins showed an averaged SNR (8.6 $min^{-1/2}$) comparable to the SNR obtained for trityl-trityl DQC (8.0 $min^{-1/2}$); the expected sensitivity advantage of single-frequency techniques on trityl-trityl systems over nitroxide-nitroxide PELDOR measurements[119,141,143] is lost here as a consequence of the increased SRT for the trityl-trityl measurements as compared to nitroxide-nitroxide PELDOR (15 ms vs. 3 ms) as well as the 3.5-times shorter phase memory time of Mal-TSL **2•** compared to MTSL (2.6 µs vs. 9.2 µs, see Table 11). A detailed summary of the modulation depth and SNRs obtained for each experiment is given below (Table 12).

Table 12: Modulation depth Δ and SNR for the time traces shown in Figure 56.

Parameter	DQC (2•)	SIFTER (2•)	PELDOR (2•)	PELDOR (MTSL)
YopO V599C/N624C				
Δ (%)	77	22	24	35
SNR ($min^{-1/2}$)	8.9	5.8	1.4	9.9
YopO S585C/Q603C				
Δ (%)	82	21	19	34
SNR ($min^{-1/2}$)	7.0	5.9	1.1	7.3

All of the experimentally obtained distance distributions resembled a subset of the respective *in silico* distributions. For YopO V599-**2•**/N624-**2•**, both DQC and SIFTER showed similar bimodal distributions with a varying shape and extent of the short-distance peak at ~40 Å and in both cases, the most probable distance peak is much narrower than the in-silico prediction. As a result of the nearly oscillation-free time trace, the PELDOR data analysis gave a broad, unimodal distance distribution matching the *in silico* prediction well in shape, width, and mean distance. The obtained distance distribution of YopO V599R1/N624R1 is bimodal, similar to previous observations (see section 3.1.4), and both, the experimental and *in silico* derived distance distributions are narrower than the ones obtained for the trityl-labeled analog. Although bimodal distributions were observed for both, trityl- and MTSL-labeled proteins, conclusions about the α-helical backbone structure of YopO are difficult to be drawn. This is most likely related to the

flexibility of the Mal-TSL **2•** sidechain caused by the linker group connecting the trityl with the maleimide-bioconjugation motif, which is also reflected by a broad *in silico* prediction. As the probability of the short- and long-distance features in the distance distribution is inverted compared to MTSL, a selection of preferred label rotamers rather than two helix conformations cannot be excluded. All distance distributions obtained for the second construct YopO S585C/Q603C show the same trend, with the distributions obtained by all three pulse sequences on the trityl-labeled protein being broad and, in this case, unimodal whereas the distribution of the MTSL-labeled protein is narrower and in good agreement with previous results (see section 3.1.4).

In summary, good-quality PDS data could be obtained on both trityl-labeled proteins, but the obtained distance distributions were either contradictory (YopO V599-**2•**/N624-**2•**) or significantly broader (YopO S585-**2•**/Q603-**2•**) compared to their respective MTSL-labeled protein analogs. To enhance the application scope of trityl spin labels in structural biology, future endeavors in trityl label synthesis should focus on a shortened or stiffened linker group between the trityl core and the bioconjugation-motif, thereby restricting the conformational flexibility of the label and narrowing the PDS-derived distance distributions.

3.2.4 Short-Linked Maleimide Trityl Spin Label SLIM

Based on the findings in sections 3.2.1 - 3.2.3 where it was shown that a maleimide bioconjugation group is advantageous for site-selective protein labeling with trityls, but long linker groups between the bioconjugation site and the trityl core hamper the gathering of meaningful distance restraints, *Nico Fleck* of the Schiemann group synthesized a new trityl spin label specifically designed to rectify the drawbacks of Mal-TSL **2•**. In this new trityl label termed SLIM (**S**hort-**Li**nked **M**aleimide) **3•**,[371] the long and flexible ethylene linker connected via an ester function to the trityl core in Mal-TSL **2•** is substituted by just one methylene group between the trityl basal body and the maleimide moiety (Figure 58a). Contrary to the first iteration of trityl spin labels derived from the Finland radical, all displaying a narrow single-line cw-EPR spectrum flanked by ^{13}C-satellites (compare Figure 45),[267] the room temperature cw-EPR spectrum of SLIM **3•** displays nine major lines as a result of the hyperfine coupling of the electron spin to the two diastereotopic benzylic hydrogen atoms (H_1 and H_2) caused by the characteristic helical chirality of trityls, and the imido nitrogen atom of the maleimide moiety (Figure 58b). Immobilization of the label by freezing to 100 K resulted in a medium-broad (0.1 mT), two-line EPR spectrum with a line-splitting of 7.44 MHz (Figure 58c). A detailed list of the spectroscopic properties obtained by simulation of the cw-EPR spectra with EasySpin is given in Table 13.

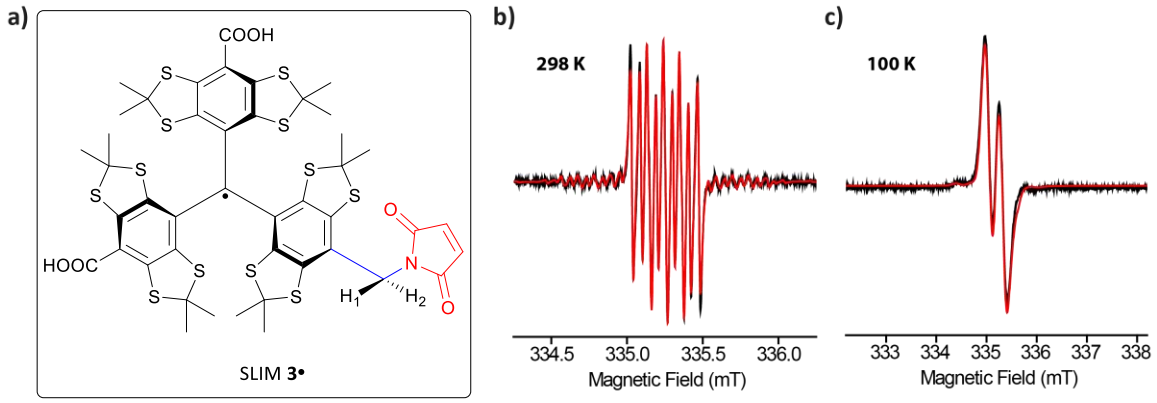

Figure 58: Chemical structure and cw-EPR spectra of the trityl spin label SLIM **3•**. **a)** Chemical structure of SLIM **3•** with the methylene linker group shown in blue and the maleimide motif shown in red. For clarity, the diastereotopic hydrogen atoms of the methylene linker are shown and termed H1 and H2. **b)** Frequency-corrected (9.4 GHz) X-band cw-EPR spectrum of **3•** (50 µM) in PBS buffer at 293 K recorded on an EMXmicro spectrometer (black) and the corresponding EasySpin simulation (red). Measurement settings: 9.394 GHz microwave frequency, 0.5545 mW microwave power, 100 kHz modulation frequency, 0.1 G modulation amplitude, 20.48 ms time constant, 1000 pts/mT. **c)** X-band cw-EPR spectrum of **3•** (50 µM) in PBS buffer at 100 K recorded on an EMXmicro spectrometer (black) and the corresponding EasySpin simulation (red). Measurement settings: 9.459 GHz microwave frequency, 0.0074 mW microwave power, 100 kHz modulation frequency, 0.2 G modulation amplitude, 20.48 ms time constant, 250 pts/mT. Spectra were recorded and simulated by *Tobias Hett*.

Table 13: EasySpin[108] simulation parameters for the cw-EPR spectra of SLIM **3•** at 298 K and 100 K in PBS buffer shown in Figure 58.

Sample	Simulation parameter[a]
SLIM **3•** in PBS (298 K)	g = 2.0034 A_N = 1.71 MHz A_{H1} = 2.96 MHz A_{H2} = 6.00 MHz $A_{C,central}$ = 66.16 MHz A_{C1} = 31.22 MHz $A_{C2,C3}$ = 25.45 MHz $A_{C4,C5}$ = 6.86 MHz A_{C6} = 3.57 MHz lwpp[b] = (0.007, 0.029) mT
SLIM **3•** in PBS (100 K)	g = (2.0028, 2.0036, 2.0040) A_N = (2.69, 0.64, 1.44) MHz A_{H1} = (4.14, 0.75, 2.86) MHz A_{H2} = (7.28, 7.55, 7.49) MHz $A_{C,central}$ = (3.45, 6.24, 185.27) MHz $A_{C,ipso}$ = (37.42, 37.64, 16.24) MHz $A_{C,ipso}$ = (38.11, 35.00, 21.01) MHz $A_{C,ipso}$ = (34.80, 34.87, 23.92) MHz lwpp[b] = (0.089, 0.025) mT

[a] Assignment of hyperfine coupling constants A to explicit ^{13}C nuclei of the phenyl ring was done according to *Bowman* et al.[254]

[b] lwpp: peak-to-peak line width.

3.2.4.1 UV-vis Calibration Curve and Extinction Coefficients of SLIM 3•

Before labeling proteins with the new spin label **3•**, a UV-vis dilution series was recorded - in analogy to Mal-TSL **2•** - to obtain the extinction coefficients of SLIM **3•** at ~460 nm and ~280 nm for quantification of the labeling efficiencies in upcoming SDSL experiments (Figure 59 + Table 14).

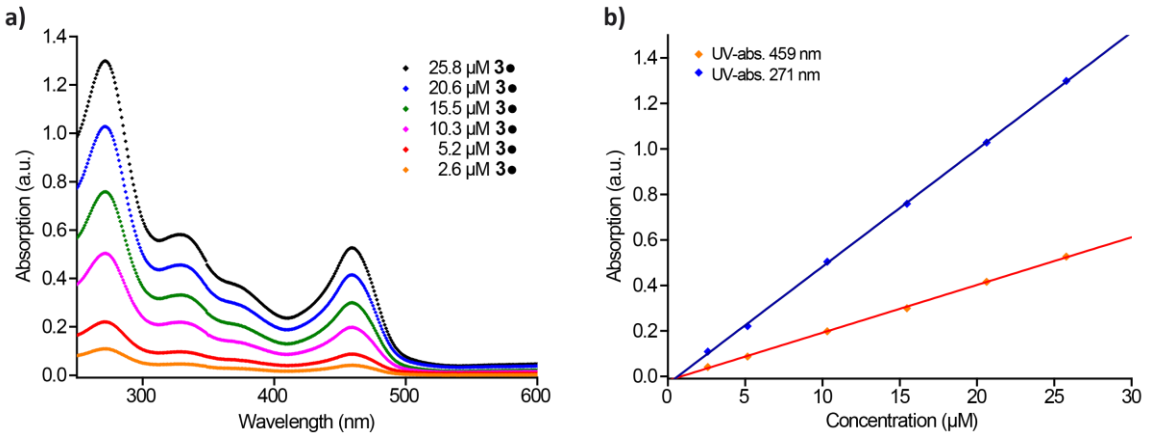

Figure 59: UV-vis dilution series and calibration curves of SLIM **3•**. **a)** UV-vis spectra of SLIM **3•** in phosphate buffer (pH 6.8) at concentrations ranging from 25.8 µM to 2.6 µM recorded on a Cary100 UV-vis spectrometer (cuvette pathlength 1 cm). **b)** UV-vis absorption values at 271 nm (blue) and 459 nm (orange) plotted against the concentrations from **(a)** with the respective linear fits.

Table 14: Linear equations of the fitting curves shown in Figure 48b according to the *Beer-Lambert Law*.

Wavelength		Linear equation
271 nm	(I)	$A_{271} = 0.05152\,\frac{\mathrm{cm}}{\mu\mathrm{M}}\,[3\bullet]\cdot l\,(-3.333\cdot 10^{-2}\mathrm{a.u.})$
459 nm	(II)	$A_{459} = 0.02099\,\frac{\mathrm{cm}}{\mu\mathrm{M}}\,[3\bullet]\cdot l\,(-3.820\cdot 10^{-3}\mathrm{a.u.})$

From the slope of the linear fits to the absorbance maxima at 271 nm and 459 nm, the extinction coefficients of SLIM **3•** were determined as $\varepsilon_{271}(\mathbf{3\bullet}) = 0.05152\,\frac{\mathrm{cm}}{\mu\mathrm{M}}$ and $\varepsilon_{459}(\mathbf{3\bullet}) = 0.02099\,\frac{\mathrm{cm}}{\mu\mathrm{M}}$. Compared to the previously used Mal-TSL **2•**, the new SLIM label **3•** showed slightly shifted absorbance maxima at ~460 nm, which is also visually observed by differences in the coloration of both labels dissolved in phosphate buffer, where Mal-TSL **2•** shows a brownish to yellow coloration while the SLIM **3•** appears brightly green.

3.2.4.2 Site-directed Spin Labeling with SLIM 3•

To probe the site-selectivity of SLIM **3•** and the separability from the protein fraction, the cysteine-free YopO-wt served as a model protein for initial labeling tests. It was incubated with **3•** following the previously established labeling protocol (see section 3.2.2.2) and the sample was then subjected to SEC, UV-vis spectroscopy, and MALDI(+)-MS (Figure 60).

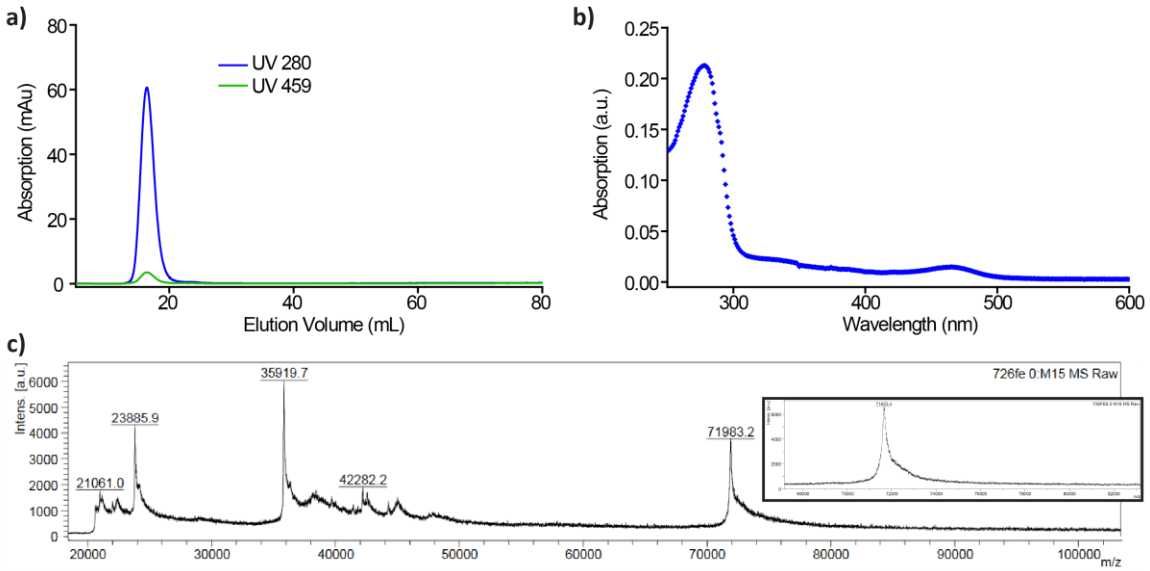

Figure 60: SEC chromatogram, UV-vis spectrum, and MALDI(+)-MS spectrum of YopO-wt incubated with SLIM **3•**. **a)** Chromatogram of the HiPrep™ 26/10 run with the absorption at 280 nm (blue) and 459 nm (green) after YopO-wt incubation with **3•**. **b)** UV-vis spectrum of YopO-wt after excess label removal recorded on a Cary100 UV-vis spectrometer. **c)** Whole-range MALDI(+)-MS spectrum of YopO-wt after incubation with **3•** and excess label removal, recorded on a Bruker Daltonics ultrafleXtreme TOF/TOF spectrometer. The inset shows an excerpt of the mass peaks at ~72,000 m/z (complimentary measurement).

The SEC chromatogram (Figure 60a) shows a weak absorbance at 459 nm in the first elution peak that corresponds to YopO-wt fraction. While this observation indicates that some SLIM **3•** could not be separated from the protein fraction, the weak absorbance at 459 nm compared to the absorbance at 280 nm suggests only minor amounts of unspecifically bound label. This presumption is confirmed by UV-vis spectroscopy (Figure 60b), where quantification of SLIM **3•** and protein via the main-peak method (see section 3.2.2.1) gave 0.07 equivalents of SLIM **3•** per YopO-wt molecule. Subsequent MALDI(+)-MS analysis revealed that this excess label is likely non-covalently bound to the protein as only a single, high-intensity mass peak (71,983.2 Da) corresponding to YopO-wt (calculated: 72,108 Da) was observed (Figure 60c). While these results show that the excess label removal routine previously implemented for Mal-TSL **2•** works slightly less efficiently for SLIM **3•** and the new label has a higher tendency to bind unspecifically to the protein, the overall low remnant of free 3• is likely tolerable in subsequent PDS studies.
Besides assessing the site-selectivity of the new SLIM label **3•** using a cysteine-free YopO construct, the bioconjugation efficiency was tested on a single-cysteine construct, namely YopO N624C (purification results for this construct are shown in appendix Figure A14). Following the bioconjugation via the established labeling scheme, the sample was analyzed via SEC, UV-vis spectroscopy, cw-EPR spectroscopy, and ESI(+)-MS (Figure 61 + Table 15).

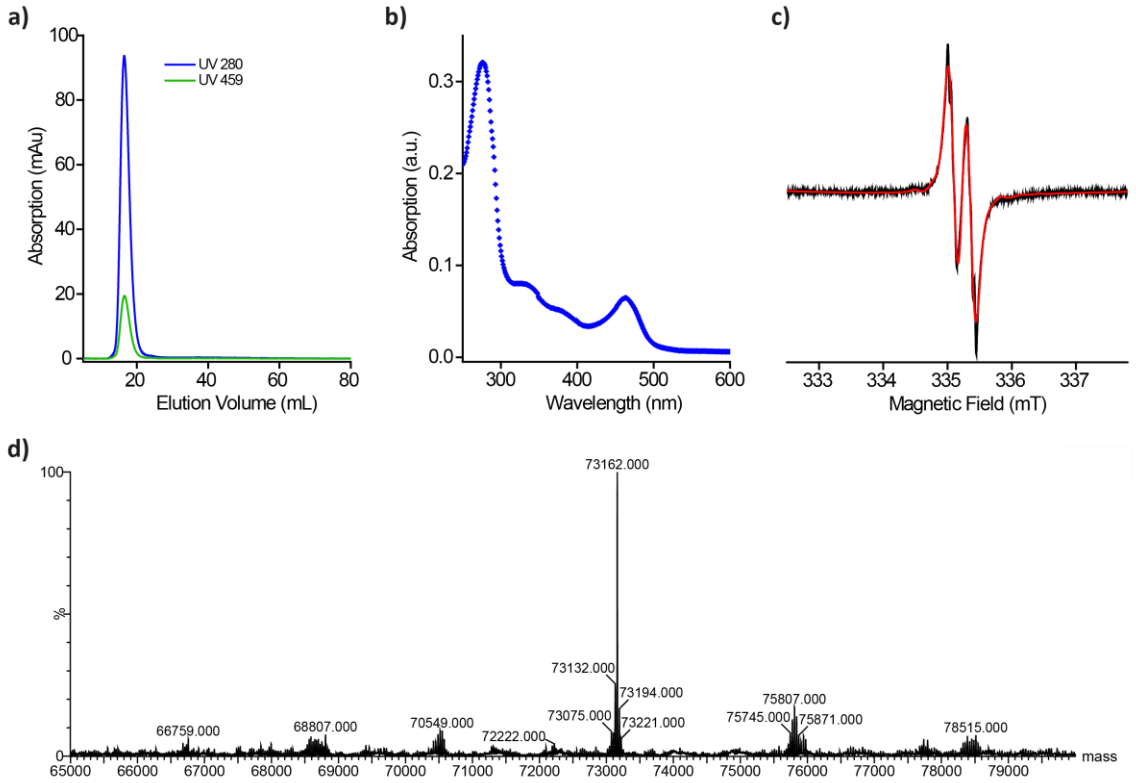

Figure 61: SEC chromatogram, UV-vis spectrum, cw-EPR spectrum, and ESI(+)-MS spectrum of YopO N624C labeled with SLIM **3•**. **a)** Chromatogram of the HiPrep™ 26/10 run with the absorption at 280 nm (blue) and 459 nm (green) after incubation of YopO N624C with **3•**. **b)** UV-vis spectrum of YopO N624C after excess label removal recorded on a Cary100 UV-vis spectrometer. **c)** Frequency-corrected (9.4 GHz) X-band cw-EPR spectrum of YopO N624C (50 µM) labeled with **3•** in phosphate buffer at 293 K recorded on an EMXmicro spectrometer (black) and the corresponding EasySpin simulation (red). Measurement settings: 9.856 GHz microwave frequency, 0.5730 mW microwave power, 100 kHz modulation frequency, 0.3 G modulation amplitude, 20.48 ms time constant, 500 pts/mT. **d)** Deconvoluted high-resolution ESI(+)-MS spectrum of YopO N624C after incubation with **3•** and excess label removal recorded on a Waters Synapt G2-SI spectrometer by the mass spectrometry facility in Marburg. The raw spectrum is shown in appendix Figure A15.

Table 15: EasySpin[108] simulation parameters for the cw-EPR spectrum of YopO N624-**3•** shown in Figure 60c.

Sample	Simulation parameter[a]
YopO N624-**3•** (293 K)	g = (2.0034, 2.0034, 2.0035) A_N = (2.19, 0.14, 0.94) MHz A_{H1} = (3.64, 1.25, 2.36) MHz A_{H2} = (6.96, 5.05, 7.99) MHz $A_{C,central}$ = (3.92, 6.53, 184.78) MHz $A_{C,ipso}$ = (36.92, 37.14, 15.75) MHz $A_{C,ipso}$ = (37.61, 34.50, 21.49) MHz $A_{C,ipso}$ = (34.30, 34.37, 24.42) MHz lwpp = (0.051, 0.079) mT

[a] Assignment of hyperfine coupling constants A to explicit ^{13}C nuclei of the phenyl ring was done according to *Bowman* et al.[254]

As evident from the SEC run (Figure 61a) and the subsequently recorded UV-vis spectrum (Figure 61b), excess label separation and site-selective labeling were successful, as no additional UV-absorbing elution peaks appeared in the chromatogram and the labeling efficiency determined from the UV-vis spectrum is 95% (0.95 equivalents of SLIM per YopO molecule). In addition, the successful bioconjugation is confirmed by cw-EPR (Figure 61c), as the recorded spectrum looks remarkably similar to the spectrum of immobilized free SLIM **3•** at 100 K (compare Figure 58c) with only a few additional spikey features, presumably caused by remaining spin label motion. The spectrum could be simulated well by slight adjustment of the simulation parameters of immobilized free SLIM **3•** at 100 K (Table 13). Thus, the restricted rotation of **3•** upon bioconjugation brings the spin label close to the rigid limit and allows to distinguish between bound and free SLIM. A quantitative spin-count against a 50 µM reference solution of free **3•** confirmed the high labeling efficiency (108%), which is in good agreement with the results obtained by UV-vis spectroscopy and well within the error of both quantification methods. In addition to the results discussed above, the high-resolution ESI(+)-MS spectrum (Figure 61d) showed a single high-intensity mass peak at 73,162 Da, which is in excellent agreement with the calculated mass of 73,162 Da for YopO N624-**3•**. Notably, as no acidic conditions were present during MS sample preparation, previously observed retro-*Michael* reactions (see section 3.2.2.3) are successfully suppressed and the MS-results reflect more accurately the labeling efficiencies achieved herein.

To test the effect of the reduced linker length of SLIM 3• on PDS-derived distance distributions, the previously introduced double-cysteine mutant YopO Y588C/N624C (section 3.1.1) was labeled with SLIM 3• (Figure 62a), Mal-TSL **2•** (labeling results are shown in appendix Figure A16), and MTSL (biological repeat of the sample discussed in section 3.1.2). According to the *in silico* derived distance distributions for all three labels (Figure 62b), the reduced linker length of SLIM 3• leads to a significant reduction of the distribution width (Gaussian fit, FWHM = 16 Å) compared to Mal-TSL **2•** (FWHM = 21 Å), which exhibits a longer and more flexible linker motif, while the simulated distribution width of MTSL (FWHM = 12 Å) is even smaller. The SDSL results for YopO Y588-**3•**/N624-**3•** are depicted in Figure 62c-f.

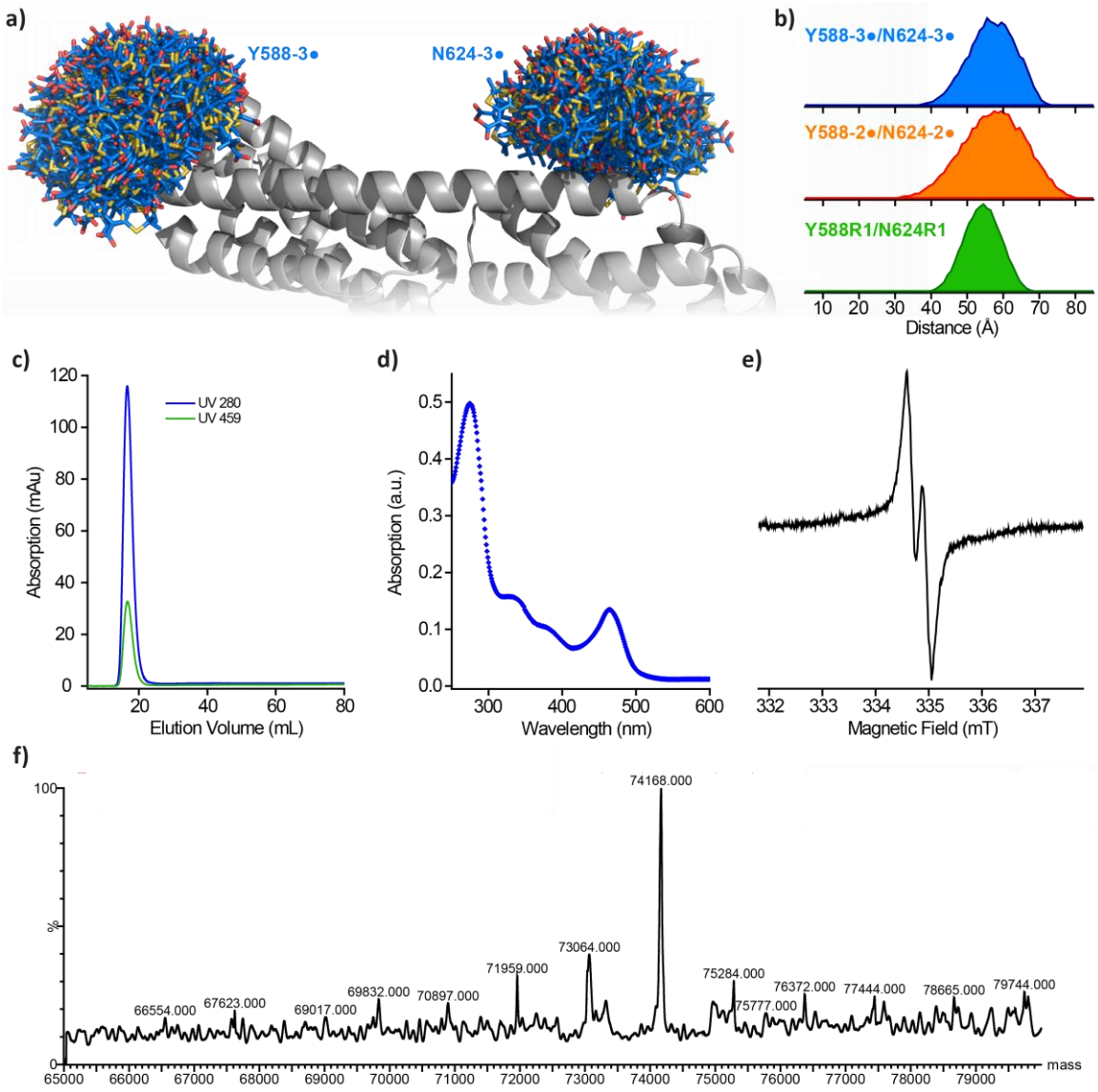

Figure 62: Labeling sites, *in silico* distance distributions, SEC chromatogram, UV-vis spectrum, cw-EPR spectrum, and ESI(+)-MS spectrum of YopO Y588-**3•**/N624-**3•**. **a)** Depiction of the SLIM labeling sites Y588C and N624C on the GDI α-helical backbone (PDB-ID 2h7o) and the rotamer clouds generated with mtsslWizard (clash setting: loose) for YopO Y588-**3•**/N624-**3•**. **b)** *In silico* distance distributions derived by mtsslWizard for the spin label pairs Y588-**3•**/N624-**3•** (blue, top), Y588-**2•**/N624-**2•** (orange, middle), and Y588R1/N624R1 (green, bottom). **c)** Chromatogram of the HiPrep™ 26/10 run with the absorption at 280 nm (blue) and 459 nm (green) of YopO Y588-**3•**/N624-**3•**. **d)** UV-vis spectrum of YopO Y588-**3•**/N624-**3•** after excess label removal recorded on a Cary100 UV-vis spectrometer. **e)** Frequency-corrected (9.4 GHz) room temperature X-band cw-EPR spectrum of YopO Y588-**3•**/N624-**3•** (50 µM) recorded on an EMXmicro spectrometer. Measurement settings: 9.389 GHz microwave frequency, 0.5614 mW microwave power, 100 kHz modulation frequency, 0.2 G modulation amplitude, 20.48 ms time constant, 250 pts/mT. **f)** Deconvoluted high-resolution ESI(+)-MS spectrum of YopO Y588-**3•**/N624-**3•** recorded on a Waters Synapt G2-SI spectrometer by the mass spectrometry facility in Marburg. The raw spectrum is shown in appendix Figure A17.

Compared to the single-cysteine YopO construct, the SEC run for the double-cysteine YopO mutant showed a higher proportion of the UV absorbance at 459 nm and 280 nm, which is expected for doubly trityl-labeled YopO (Figure 62c). Quantification of the protein and SLIM concentrations via UV-vis spectroscopy and quantitative cw-EPR spin-count gave labeling

efficiencies of 96% (UV-vis) and 102% (cw-EPR), respectively, and confirmed almost quantitative labeling (Figure 62d+e). ESI(+)-MS analysis showed a high-intensity mass peak at 74,168 Da corresponding to doubly labeled YopO Y588-**3**•/N624-**3**• and two mass peaks with lower intensity (73,064 Da and 71,959 Da), which likely correspond to singly (73,104 Da) and unlabeled (72,041 Da) YopO, respectively. Notably, the SNR of the ESI(+)-MS spectrum for YopO Y588-**3**•/N624-**3**• was significantly lower than previously observed for the single-cysteine construct YopO N624-**3**• although the same protein amount was subjected to each MS run. As this trend was also observed for the Mal-TSL 2•-labeled YopO construct (Figure A16c), a potential cause might be a decreased protein stability upon bioconjugation of multiple trityl spin labels, which renders the protein to precipitate due to the increased hydrophobic surface area. This in turn makes quantification via the individual mass peak intensities impossible, as the ratio of non- and singly-labeled proteins is artificially higher compared to the partially precipitated doubly-labeled constructs, thereby highlighting the importance of careful sample handling.

3.2.4.3 Relaxation Time Measurements for SLIM 3•

Using the singly-labeled YopO N624-**3**•, the spin-lattice relaxation time T_1 and the phase memory time T_M of the bioconjugated SLIM spin label were determined at 50 K and 70 K by inversion recovery and 2pESEEM experiments (Figure 63 + Table 16).

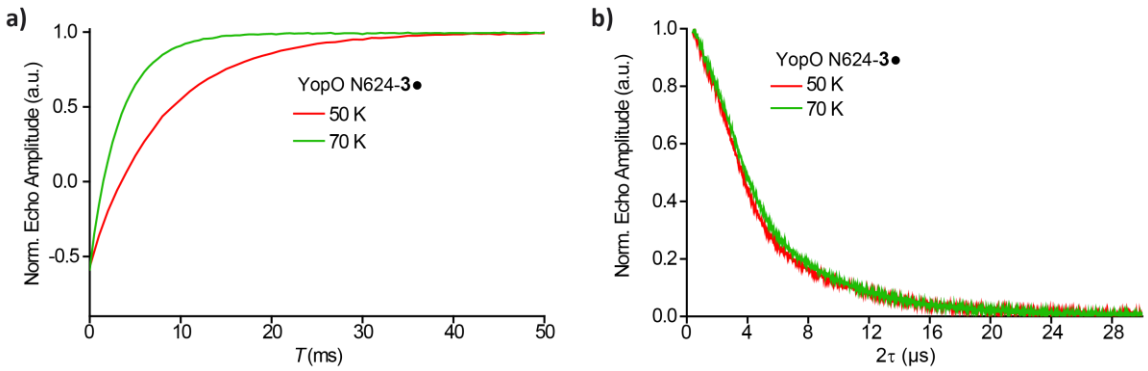

Figure 63: Temperature-dependent relaxation measurements of YopO N624-**3**•. **a)** Inversion recovery traces for YopO N624-**3**• at 50 K (red) and 70 K (green). **b)** 2pESEEM traces for YopO N624-**3**• at 50 K (red) and 70 K (green).

Table 16: Spin lattice relaxation times T_1 and phase memory times T_M of YopO N624-**3**• obtained by fitting either eq. 19 (Inversion recovery) or eq. 20 (2pESEEM) to the respective traces shown in Figure 62.

Temperature	YopO N624-3•	
	T_1 (ms)	T_M (µs)
50 K	8.0	4.2
70 K	3.3	4.7

For both, the spin-lattice relaxation and the phase memory time, a similar trend as for Mal-TSL **2**• (see Table 11) is observed, with decreasing T_1 and increasing T_M when increasing the temperature from 50 K to 70 K. While T_1 is slightly longer for bioconjugated SLIM **3**• than for Mal-TSL **2**•, the phase memory time T_M is significantly longer with 4.2 µs for SLIM **3**• compared to 2.6 µs for Mal-TSL **2**• at 50 K. This is a clear improvement compared to previous trityl spin labels based on an ester[370] or amide[374] motif between the bioconjugation group and the trityl core and hence, using SLIM **3**•, longer dipolar evolution times can be recorded.

3.2.4.4 PDS-EPR with SLIM 3•-labeled YopO

To benchmark and compare SLIM **3•** with MTSL and the previously employed Mal-TSL **2•** concerning SNR, modulation depth, and the width of the distance distribution, DQC (only **3•** and **2•**) and PELDOR experiments were performed at 50 K for maximal comparability on the previously prepared and doubly-labeled YopO Y588C/N624C mutants at a spin concentration of 50 µM (Figure 64 + Table 17). The PDS experiments were conducted under the guidance and with *Tobias Hett*.

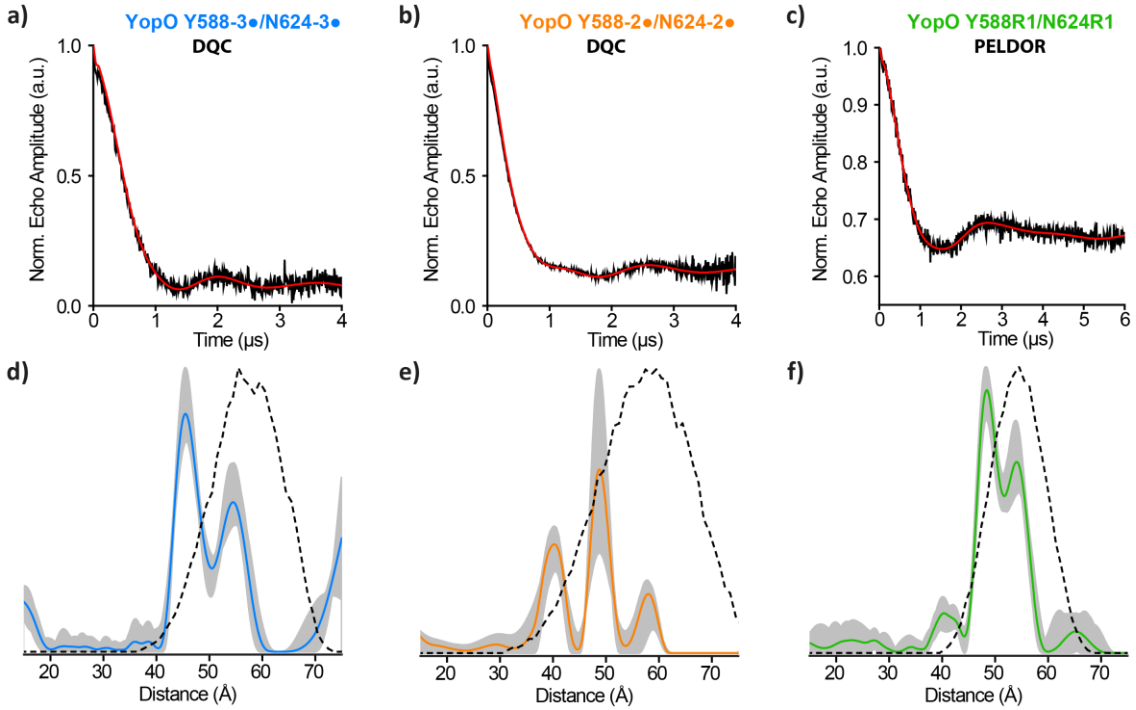

Figure 64: PDS data of YopO Y588C/N624C labeled with SLIM **3•**, Mal-TSL **2•**, and MTSL. **a-c)** Mirrored and background-corrected DQC **(a+b)** and PELDOR **(c)** time traces (black) obtained for YopO Y588-**3•**/N624-**3• (a)**, YopO Y588-**2•**/N624-**2• (b)**, and YopO Y588R1/N624R1 **(c)** with the respective fits obtained by Tikhonov regularization (red) in DeerAnalysis. **d-f)** Resulting distance distributions (colored) of the time traces above **(a-c)** with the DeerAnalysis validation shown as grey-shaded areas. *In silico* predictions obtained by mtsslWizard using the PDB-ID 2h7o as a template are shown as dashed black lines. The complete analysis by DeerAnalysis for all data shown here (backgrounds, fits, L-curves, and distance distributions) and PELDOR results for YopO Y588-**3•**/N624-**3•** and YopO Y588-**2•**/N624-**2•** are given in the appendix (Figure A18-A20).

Table 17: Modulation depth Δ and SNR for the time traces shown in Figure 64 and Figure A18-A20.

Parameter	YopO Y588-3•/N624-3•		YopO Y588-2•/N624-2•		YopO Y588R1/N624R1
	DQC	PELDOR	DQC	PELDOR	PELDOR
Δ (%)	90	21	79	26	32
SNR ($min^{-1/2}$)	11.2	1.9	8.4	2.2	3.6

Contrary to previous data analysis of YopO labeled with Mal-TSL **2•** were an experimental background of singly-labeled YopO was utilized (section 3.2.3.1), here, all time traces were analyzed by manually selecting an appropriate background in DeerAnalysis. For each pulse sequence, high-quality time traces with visible oscillations were obtained. In line with the previous finding on doubly-trityl labeled YopO (section 3.2.3.2) and owing to the narrow spectral width of

trityls (Figure A21), DQC outperformed PELDOR regarding SNR and modulation depth for both SLIM **3•** and Mal-TSL **2•** (Table 17). Notably, for YopO Y588-**3•**/N624-**3•**, a higher SNR and modulation depth was obtained than for the Mal-TSL **2•**-labeled analog, which is likely caused by the enhanced phase memory time T_M of SLIM **3•** compared to Mal-TSL **2•** (Table 16) and potentially a slightly higher labeling efficiency. Contrary to the previous findings, even at 50 K and despite the long shot repetition time (15 ms), both trityl labels showed a higher SNR than the MTSL-labeled analog (Table 17), thereby highlighting the sensitivity gain obtained from the full excitation of the trityl spectrum.

While all of the experimental distance distributions resemble a subset of the *in silico* predictions (Figure 64), there are striking differences between the distributions of both trityl labels and the MTSL analog. While for the Mal-TSL **2•**-labeled YopO Y588C/N624C a trimodal distance distribution with narrow peaks and high uncertainty intervals is obtained, the distributions obtained for SLIM **3•** and MTSL show remarkable similarities with a bimodal distance distribution matching the criteria of a case 5 distribution (compare Table 6). Notably, the bimodality previously observed by multiple laboratories during the ring test (see Figure 43) is clearly resolved here and does not vanish during background validation. These results suggest that the long flexible linker between the maleimide motif and the trityl core in Mal-TSL **2•** enables the spin label to tilt backward to the protein surface and select distinct energetically favored label conformers from the total ensemble of rotamers. This in turn complicates the interpretation of the distance distribution. On the other hand, as the two chemically different spin labels SLIM **3•** and MTSL (maleimide vs. methanethiosulfonate; trityl vs. *gem*-dimethyl nitroxide) and the two pulse sequences (DQC vs. PELDOR) yield remarkably similar distance distributions, both matching the criteria for case 5, these results are highly indicative of two distinct conformations that the α-helical backbone of YopO's GDI domain adopts in (frozen) solution. To emphasize the similarities of both distance distributions, they were fitted using a two-Gaussian model (Figure 65 + Table 18).

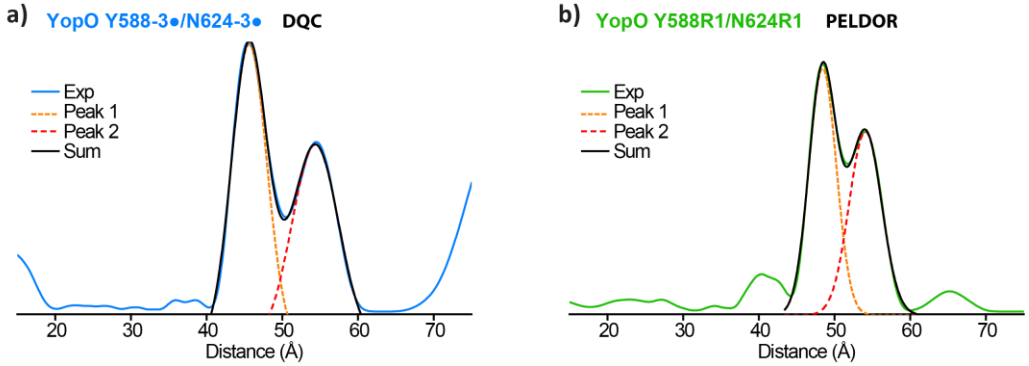

Figure 65: Gaussian fits to the distance distributions obtained for YopO Y588-**3•**/N624-**3•** (DQC) **(a)** and YopO Y588R1/N624R1 (PELDOR) **(b)** with the experimental distance distribution shown as blue (DQC) or green (PELDOR) line, both Gaussian functions as orange (peak 1) and red (peak 2) dotted lines, and the resulting sum of both Gaussian functions as a black line.

Table 18: Gaussian function[a] parameters for the fits shown in Figure 65.

	YopO Y588-3•/N624-3•	YopO Y588R1/N624R1
Peak 1	Center: 45.7 Å Width: 4.3 Å Height: 1.01 Area: 0.55	Center: 48.4 Å Width: 3.5 Å Height: 0.99 Area: 0.44
Peak 2	Center: 54.2 Å Width: 5.4 Å Height: 0.63 Area: 0.43	Center: 54.1 Å Width: 4.3 Å Height: 0.73 Area: 0.39

[a] Gaussian function: $y = A \cdot exp\left(-\frac{(x-c)^2}{2\sigma^2}\right)$; c = center, σ = width.

The center positions of peaks 1 and 2 coincide very well for SLIM **3•** and MTSL with a 3 Å difference for peak 1 and less than 1 Å for peak 2. Both modes in the SLIM distribution are slightly broader compared with MTSL, which is likely related to the differences in the linker length and flexibility for both labels. In addition, the relative height of both peaks is very similar with only 10% difference for peak 2.

As discussed previously, two crystal structures of YopO are known in the PDB, namely PDB-ID 2h7o[326] and PDB-ID 4ci6,[328] where the α-helix of the GDI domain is either straight (PDB-ID 2h7o) or bent (PDB-ID 4ci6). A potential explanation for the observed bimodality is the presence of both helix structures in solution with the shorter distance peak corresponding to the straight and the longer distance peak corresponding to the bent helix. As the bent form is only seen in the crystal structure of YopO in complex with G-actin, this hypothesis was tested by incubation of YopO Y588-**3•**/N624-**3•** with human platelet actin, which has a higher binding affinity to YopO than muscle actin, to drive the conformational equilibrium to the G-actin bound state (Figure 66).

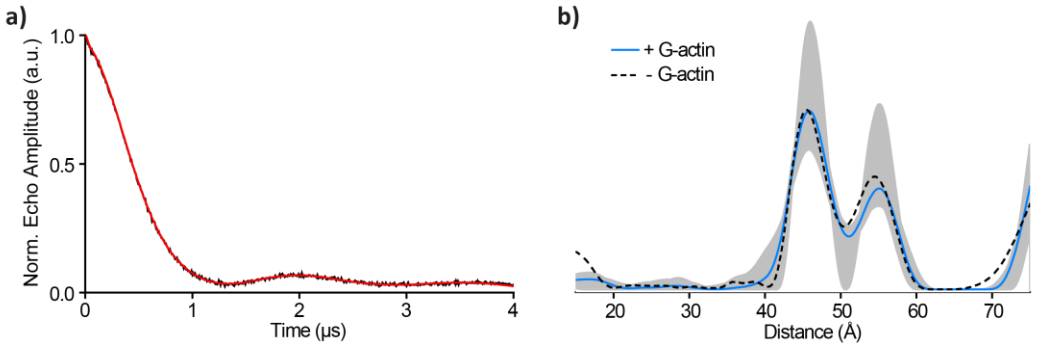

Figure 66: DQC time trace and distance distribution of YopO Y588-**3•**/N624-**3•** incubated with human platelet actin. **a)** Background-corrected DQC time trace (black) of YopO Y588-**3•**/N624-**3•** (25 µM) and 2 eq. of human platelet actin with the fit obtained by Tikhonov regularization (red) in DeerAnalysis. **b)** Distance distribution (blue) obtained from the time trace in **(a)** with the DeerAnalysis validation shown as grey-shaded area and the distance distribution of YopO Y588-**3•**/N624-**3•** in the absence of actin (black dashed line). The complete analysis by DeerAnalysis (raw time trace, background, L-curve, and distance distribution) is given in the appendix (Figure A22).

Surprisingly, the addition of human platelet actin did not show any effect on the resulting distance distribution, hence strongly indicating that the conformation of the GDI backbone α-helix is independent of actin binding.
While the herein presented results highlight key advantages of SLIM **3•** over the previously employed Mal-TSL **2•**, namely a longer phase memory time T_M, a higher SNR, and reduced flexibility of the spin label as a result of the reduced linker length, the nature of the chosen model system with presumably two conformational states of the protein as well as two flexible spin labels is unsuitable to fully demonstrate the effect of the shortened linker on the distance distribution width.

3.2.5 Comparing the Distribution Width of SLIM 3•, Mal-TSL 2• and MTSL

Following the results discussed in section 3.2.4.4 and to further investigate the influence of the reduced linker length and flexibility of SLIM **3•** compared to Mal-TSL **2•**, the idea was to label a rigid, single-cysteine protein containing a rigid intrinsic spin-center such as a metal ion. The resulting distance distribution should then be solely influenced by the conformational freedom of the post-translationally attached spin label, which allows quantifying the improvement in distance resolution gained by using SLIM **3•**. Here, the horse heart myoglobin (Mb) mutant Mb Q8C,[342] a protein containing an intrinsic heme group as the second spin center, was chosen as the model system to compare the distribution widths obtained from **3•** and **2•** (Figure 67).

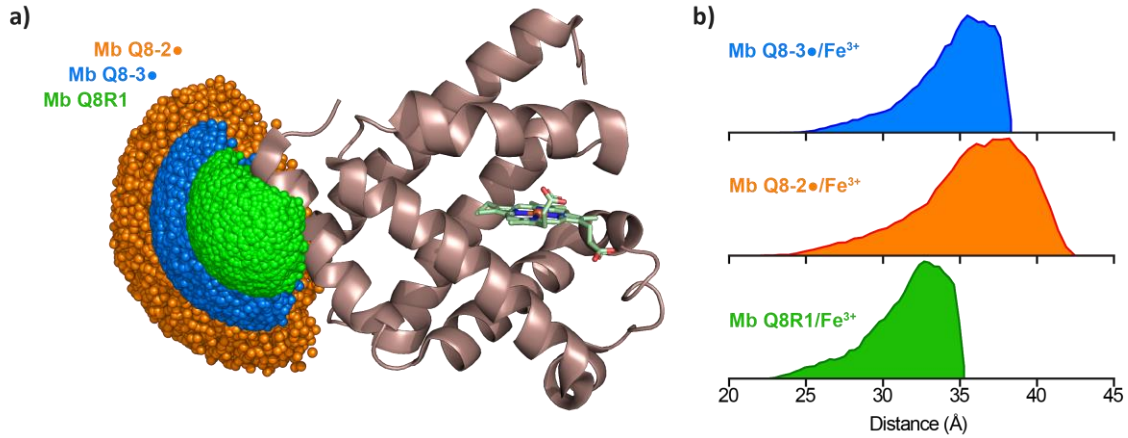

Figure 67: Spin center distribution and *in silico* derived distance distributions of Mb Q8C labeled with **3•**, **2•**, and MTSL. **a)** Structure of Mb Q8C (PDB-ID 1wla, bronze) overlaid with sphere-depictions of the central carbon atoms of the trityls **3•** (blue) and **2•** (orange), and the center of the N-O bond in MTSL (green), each harboring the unpaired electron. Spheres were extracted from the rotamer clouds (20,000 rotamers per label) generated with mtsslWizard (clash setting: loose) using the PDB-ID 1wla as a template structure (bronze, heme B cofactor shown in green). **b)** *In silico* derived distance distributions between the iron center of the heme B cofactor and the spin centers of **3•** (blue, top), **2•** (orange, middle), and MTSL (green, bottom) shown in **(a)**.

3.2.5.1 Expression and Purification of Mb Q8C

The expression and purification scheme for Mb Q8C was adapted from previously established protocols.[342] As multiple labeling experiments for Mb Q8C with different spin labels were planned, in this case the protein was labeled after purification to enable individual labeling experiments on the same protein mother batch for maximal comparability.
The expression and purification of Mb Q8C was followed via SDS-PAGE analysis (Figure 68a). Following cell lysis, a substantial amount of undesired protein was removed alongside the cell debris in the initial centrifugation step (lane 2), while a faint band below 25 kDa (orange box,

His_6-Mb Q8C: 20.1 kDa) together with other protein impurities remained in the deeply red supernatant (lane 3). Batch binding to HisPur™ Ni-NTA resin and subsequent wash of the resin removed a substantial amount of the remaining protein impurities (lane 4+5). After TEV-cleavage of the His_6-tag, Mb Q8C (17.1 kDa) eluted alongside a small amount of high molecular weight protein contaminants (lane 6-8). Notably, the TEV-cleavage and Mb recovery from the beads was incomplete (lane 9), as substantial amounts of cleaved Mb Q8C and uncleaved His_6-Mb Q8C eluted alongside the TEV protease (red box, TEV protease: 27 kDa) in the high-imidazole wash for bead restoration. Purification proceeded with a reverse anion exchange chromatography step (Figure 68b), where Mb Q8C did not bind to the anion exchange resin, as a strong absorbance at the characteristic wavelength of 409 nm was observed.[379] Almost pure Mb Q8C protein (lane 10+11) eluted in the flow-through of the column while the previously observed high-molecular weight contaminants could successfully be separated and eluted in the later salt gradient over a broad conductivity range (lane 12-15).

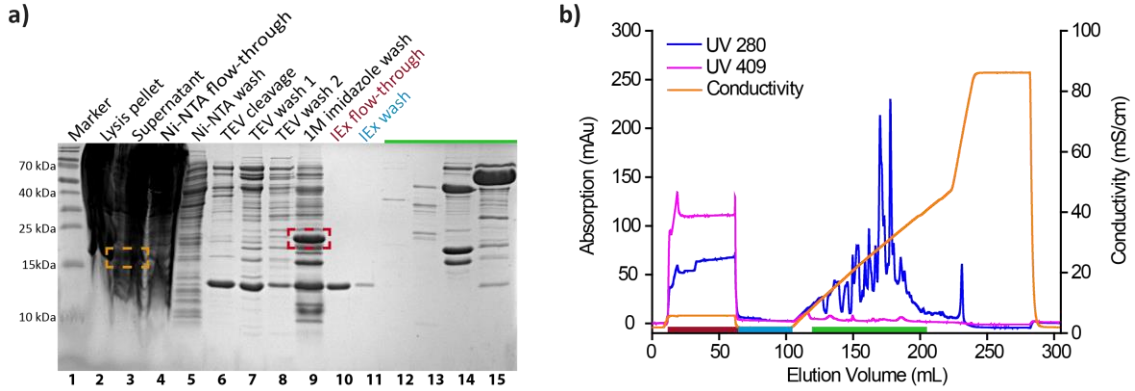

Figure 68: SDS-PAGE and anion exchange chromatogram of Mb Q8C. **a)** Coomassie-stained 15% polyacrylamide gel after SDS-PAGE showing the initial steps of the Mb Q8C purification. The orange box highlights the His_6-Mb Q8C band and the red box the TEV protease. **b)** Chromatogram of the ENrich™ Q 10x100 anion exchange run of Mb Q8C showing the absorption at 280 nm (blue), 409 nm (pink), and conductivity (orange). Horizontal bars indicate the fractions taken and loaded onto the gel in **(a)**.

As the ion exchange flow-through contained the Mb Q8C protein, it was pooled, concentrated, and subjected to a final gel filtration purification step (Figure 69).

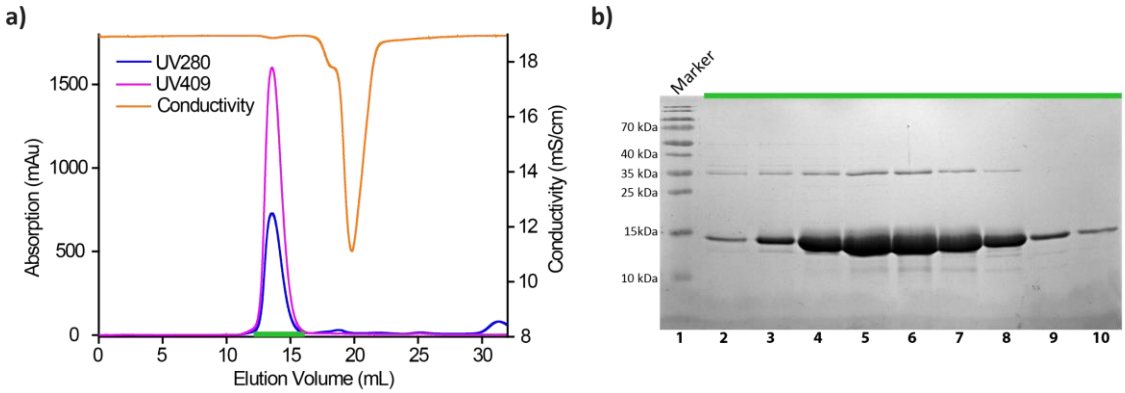

Figure 69: Gel filtration chromatogram and SDS-PAGE of Mb Q8C. **a)** Chromatogram of the Superdex® 75 10/300 GL gel filtration run of Mb Q8C showing the absorbance at 280 nm (blue), 409 nm (pink), and conductivity (orange). The green horizontal bar indicates the fractions taken for SDS-PAGE analysis. **b)** Coomassie-stained 10% polyacrylamide gel of the fractions shown in **(a)** after SDS-PAGE. All fractions indicated by the green bar were pooled and concentrated further.

The elution chromatogram of the gel filtration showed a single peak with absorbance at 280 nm and 409 nm (Figure 69a), while the fractions of this peak taken for SDS-PAGE showed two protein bands, a strong band at ~15 kDa and a very weak band at ~35 kDa (Figure 69b). As both protein entities eluted within the same peak in the gel filtration, the band at 15 kDa can be attributed to monomeric Mb Q8C while the weak band at ~35 kDa can be assigned to disulfide-bridged Mb Q8C dimers formed overnight and insufficiently cleaved by β-mercaptoethanol in the SDS loading buffer. After the final concentration step, a total of 2.2 mg purified Mb Q8C was obtained.
The UV-vis spectrum of purified Mb Q8C showed the Soret band characteristic of oxymyoglobin (MbO_2) at 417 nm and the α- and β-band at 544 nm and 583 nm, respectively (Figure 70).[379]

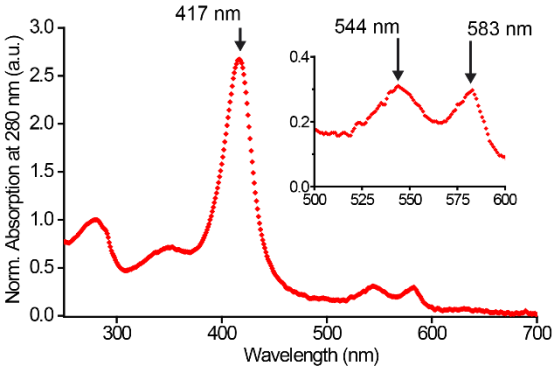

Figure 70: UV-vis spectrum of purified and concentrated Mb Q8C after the gel filtration run, normalized to the absorbance peak at 280 nm. The inset highlights the positions of the α- and β-band. The spectrum was recorded on a NanoDrop™ 2000.

3.2.5.2 Site-Directed Spin Labeling of Mb Q8C

Spin labeling of Mb Q8C was performed according to the previously described labeling schemes for MTSL (see section 3.1.2), Mal-TSL **2•**, and SLIM **3•** (see section 3.2.2.2). To convert Fe^{2+} of MbO_2 into EPR-active Fe^{3+} (MetMb form), the spin-labeled and concentrated Mb solutions were incubated with a 20-fold molar excess of the oxidizing agent potassium ferricyanide ($K_3[Fe(CN)_6]$), before removing excess label on the ÄKTA system (**2•** and **3•**, Figure 71a) or by PD-10 desalting column (MTSL).[380] The conversion of MbO_2 to MetMb was confirmed by UV-vis spectroscopy on the MTSL-labeled Mb Q8C construct (Figure 71b).

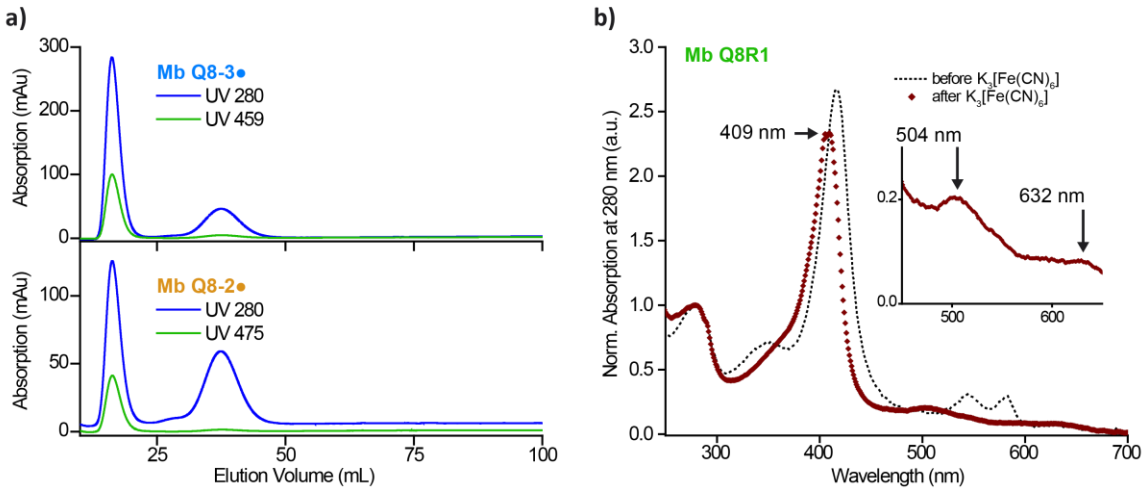

Figure 71: SEC chromatograms of Mb Q8-**3•** and Mb Q8-**2•**, and UV-vis spectrum of Mb Q8R1. **a)** Chromatograms of the HiPrep™ 26/10 runs of Mb Q8-**3•** (top) and Mb Q8-**2•** (bottom) with the absorption at 280 nm (blue) and 459 nm/475 nm (green) after incubation with $K_3[Fe(CN)_6]$. **b)** UV-vis spectrum of Mb Q8R1 before (black) and after incubation and removal of $K_3[Fe(CN)_6]$ normalized to the absorption at 280 nm. The inset highlights the shift of the α- and β-band compared to Figure 70. The spectrum was recorded on a NanoDrop™ 2000.

Both SEC runs for the trityl-labeled Mb Q8C (Figure 71a) showed two elution peaks with the first peak at 16 mL corresponding to spin-labeled Mb Q8C and the second peak corresponding to the successfully separated oxidizing agent $K_3[Fe(CN)_6]$. Notably, for the trityl-labeled samples, the conversion of MbO_2 to MetMb cannot be followed by UV-vis due to the spectral overlap of trityl and the Mb Soret band. Hence, only for Mb Q8R1 a UV-vis spectrum was recorded (Figure 71b), which confirmed quantitative conversion to MetMb upon incubation with a 20-fold molar excess of $K_3[Fe(CN)_6]$, as evident from the characteristic shift of the Soret band of MetMb compared to MbO_2. Notably, despite increasing the amount of 5-aminolevulinic acid (2.4 mM vs. 2 mM in the original protocol) which is necessary to build the heme scaffold during myoglobin expression,[342] incomplete heme-loading of recombinantly expressed myoglobin was observed, as the ratio of the absorbance peaks at 409 nm and 280 nm (2.7 : 1) for MetMb Q8C was below the expected and literature-reported ratio of ~5.1:1 for native horse heart metmyoglobin.[381,382] Further attempts to increase the heme-loading of MetMb using varying concentrations of 5-aminolevulinic acid during the expression of myoglobin did not result in an improved heme-loading of the purified protein (data not shown).

Owing to the strong absorbance of MetMb at 409 nm, adapting the routines established to quantify the labeling efficiency of trityl-labeled YopO using UV-vis spectroscopy is unfeasible as the strong spectral overlap between trityl and the MetMb Soret bands does not allow deconvoluting the spectrum into its three contributors (Mb apo-protein, heme B, and trityl). Therefore, the labeling efficiencies of MetMb Q8-**3•**, MetMb Q8-**2•**, and MetMb Q8R1 were estimated based on MALDI(+)-MS analysis (Figure A23 + Table 19). Q-band EPR samples were prepared according to the spin concentration obtained from room temperature cw-EPR spin-count (Figure 72).

Table 19: Calculated (without heme B) and experimentally found masses by MALDI(+)-MS for unlabeled and labeled MetMb Q8C. The labeling efficiencies were estimated as the ratio of the baseline-corrected peak intensities for singly-labeled and unlabeled MetMb. MALDI(+)-MS spectra are shown in Figure A23.

Construct	Calc. unlabeled (Da)	Calc. labeled (Da)	Experimental (Da)	Est. lab. Efficiency
MetMb Q8C	17,186	-	17,185	-
MetMb Q8-3•	17,186	18,251	18,249	>90%
MetMb Q8-2•	17,186	18,309	18,309	>85%
MetMb Q8R1	17,186	17,370	17,369	Quantitative

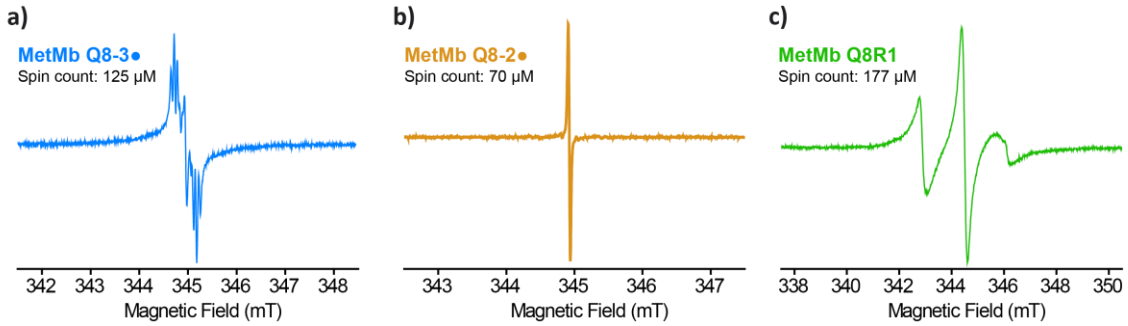

Figure 72: Room temperature X-band cw-EPR spectra and spin-count results for MetMb Q8-**3•** **(a)**, MetMb Q8-**2•** **(b)**, and MetMb Q8R1 **(c)**. Spectra were recorded on an EMXnano spectrometer. Measurement settings: **(a)** 9.635 GHz microwave frequency, 0.3162 mW microwave power, 100 kHz modulation frequency, 0.5 G modulation amplitude, 20.48 ms time constant, 200 pts/mT; **(b)** 9.635 GHz microwave frequency, 0.3162 mW microwave power, 100 kHz modulation frequency, 0.15 G modulation amplitude, 20.48 ms time constant, 660 pts/mT; **(c)** 9.635 GHz microwave frequency, 1.000 mW microwave power, 100 kHz modulation frequency, 1 G modulation amplitude, 20.48 ms time constant, 100 pts/mT.

According to MALDI(+)-MS (Figure A23 + Table 19), high labeling efficiencies were achieved for all spin labels. Compared to the MALDI(+)-MS spectra of doubly trityl-labeled YopO (see Figure A8), the mass spectra of singly trityl-labeled Mb Q8C had a significantly higher SNR, hence indicating an increased protein stability upon the bioconjugation of just one trityl label per protein which is in agreement with earlier findings (see section 3.2.4.2). Notably, the mass spectrum of MetMb Q8-**3•** showed additional peaks at higher molecular weight and of low intensity with a mass increase of +1,017 m/z and +2,106 m/z compared to the singly-labeled MetMb Q8-**3•**. These additional peaks are an indication of unspecific over-labeling and can be attributed to a small fraction of doubly (2x +1,063 m/z) and triply (3x +1,063 m/z) SLIM-labeled MetMb Q8C.

For both trityl-labeled Mb constructs, cw-EPR spectra with narrow line widths and, in the case of **3•**, partially resolved hyperfine splitting were obtained (Figure 72a+b). The cw-EPR spectra differed significantly from the broadened spectra previously obtained for trityl-labeled YopO constructs. These deviations can be rationalized by the significantly reduced rotational correlation time τ_c of 2.44 ns[342] for the smaller Mb (17.1 kDa) compared to approximately 13 ns (average τ_c of the simulation parameters in Table 10) obtained for the larger YopO (71.2 kDa). The cw-EPR spectrum of MetMb Q8R1 (Figure 72c) showed no indication of free MTSL and was comparable with spectra obtained previously for this construct.[342]

To simplify the subsequent acquisition and analysis of the PDS data, a 200-fold excess of sodium azide was added to each sample to convert the Fe^{3+}-center in the heme B group from the $S = \frac{5}{2}$ high-spin (hs) state into the $S = \frac{1}{2}$ low-spin (ls) state with a smaller *g*-anisotropy.[340] The complete

conversion of hs-MetMb to ls-MetMb was confirmed by low-temperature cw-EPR spectroscopy (Figure A24).

3.2.5.3 RIDME Measurements on Mb Q8C labeled with 3•, 2•, and MTSL

Owing to the anisotropy of the ls-MetMb *g*-tensor and thereby resulting broad spectrum as well as a fast relaxation times of the Fe^{3+} spin center, RIDME is the optimal pulse sequence for the unequal spin pairs A (here: trityl, nitroxide) and B (here: Fe^{3+}). Spin B flips spontaneously during the RIDME sequence due to longitudinal relaxation and is not affected by the microwave pulses; therefore, orientation selection that might result from incomplete excitation of the broad spectrum of spin B can be excluded.[136,164,383] Hence, six-pulse RIDME experiments[137] were performed at Q-band frequencies at 12 K on all spin-labeled MetMb Q8C mutants, and PDS data were analyzed using the newest iteration of PDSFit[125,384] and a two-component system consisting of two Gaussian functions by *Tobias Hett* (Figure 73 + Table 20).

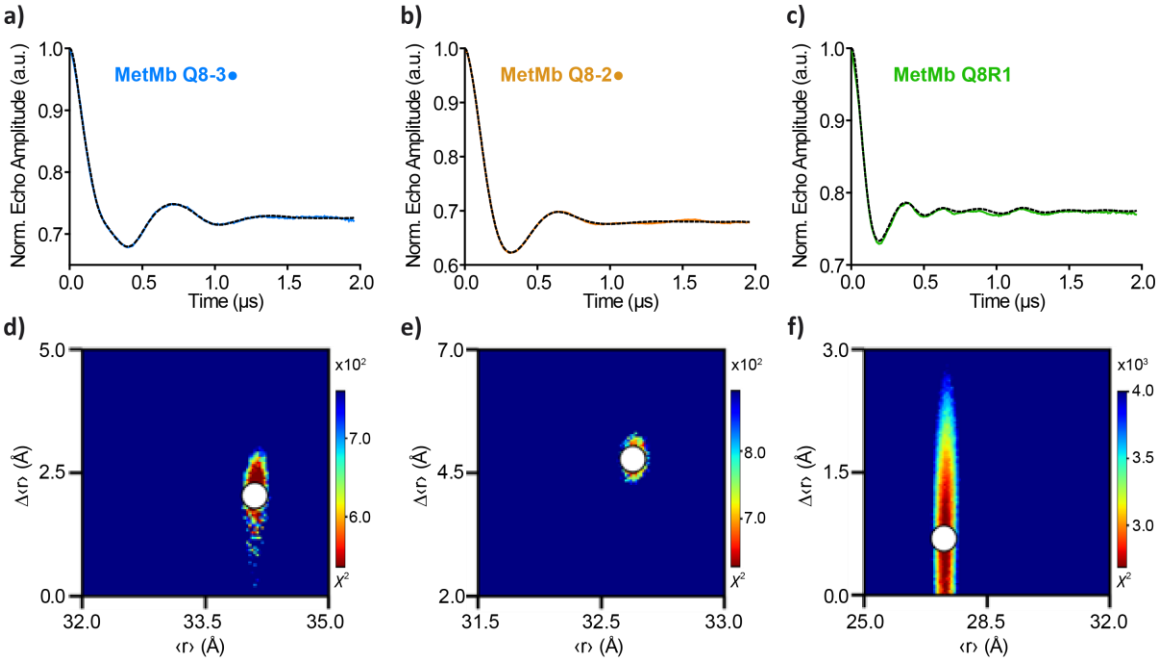

Figure 73: Background-corrected six-pulse RIDME traces and two-dimensional PDSFit error plots for ⟨*r*⟩ and Δ*r* obtained for MetMb Q8-**3•**, MetMb Q8-**2•**, and MetMb Q8R1. **a-c)** Background-corrected six-pulse RIDME time traces (colored) with the fit function obtained by PDSFit (black dashed lines) for Mb Q8-**3• (a)**, Mb Q8-**2• (b)**, and Mb Q8R1 **(c)**. **d-f)** Two-dimensional error surfaces of the mean distance ⟨*r*⟩ against the distribution width Δ*r* (given as FWHM of a Gaussian distribution) of Mb Q8-**3• (d)**, Mb Q8-**2• (e)**, and Mb Q8R1 **(f)** obtained from PDSFit for the more probable distance mode. The complete PDSFit results are given in the appendix (Figure A25-A27).

Table 20: Mean distances ⟨*r*⟩ and distribution widths Δ*r* (given as FWHM of a Gaussian distribution) of the more probable distance mode for MetMb Q8-**3•**, MetMb Q8-**2•**, and MetMb Q8R1 obtained by PeldorFit analysis of the six-pulse RIDME experiments.

Construct	⟨*r*⟩ (Å)	Δ*r* (Å)
MetMb Q8-3•	$34.1^{+0.1}_{-0.1}$	$2.0^{+0.5}_{-0.5}$
MetMb Q8-2•	$32.8^{+0.1}_{-0.1}$	$4.8^{+0.2}_{-0.3}$
MetMb Q8R1	$27.3^{+0.1}_{-0.1}$	$0.7^{+0.3}_{-0.7}$

For all spin-labeled MetMb Q8C samples, six-pulse RIDME time traces with one or more well-pronounced oscillations were obtained (Figure 73a-c). While four oscillation periods were resolved for MetMb Q8R1 before the oscillations were damped, two oscillation periods within the 2 µs time window could be resolved for MetMb Q8-**3•**, and the oscillation of MetMb Q8-**2•** vanished already after one oscillation period. Thereby, visual inspection of the time traces already indicates an increasing distribution width from MTSL via SLIM **3•** to Mal-TSL **2•**, with more dipolar frequencies causing destructive interferences and thereby damping the oscillations in the time trace. For both trityl-labeled constructs, higher modulation depths (MetMb Q8-**3•**: 27%, MetMb Q8-**2•**: 32%) were obtained as compared to Mb Q8R1 (23%), which can be rationalized by the full excitation of the trityl spectrum by the rectangular microwave pulses. Notably, for all cases, the theoretically achievable modulation depth of 50%[136] was not reached as a result of the previously described incomplete heme B loading of MetMb.[383]

PDSFit analysis (Figure 73d-f + Table 20) of the six-pulse RIDME traces confirmed the initial presumption of a reduced distribution width for SLIM **3•** compared to Mal-TSL **2•**. For MetMb Q8-**3•**, PDSFit analysis yielded a distribution width of 2.0 Å, which is 59% narrower than the width obtained for MetMb Q8-**2•** (4.8 Å). These results nicely showcase the significant effect of the reduced linker length of SLIM **3•** on the PDS-derived distance distributions compared to the more flexible Mal-TSL **2•**. For Mb Q8R1, a very narrow distribution of 0.7 Å width was obtained, which deviates from the distribution width previously determined on hs-Mb Q8R1 (1.8 Å).[342]

Notably, for all MetMb constructs, the PDSFit analysis was performed using a two-component system 1 and 2, as analysis with a one-component system resulted in unsatisfactory fits to the time trace (data not shown). In addition, while the angle ⟨ξ⟩ of 80.2° between the g_{zz}-axis and the distance vector for MTSL-labeled MetMb Q8R1 matches well with the expected 90° angle for a spin label oriented perpendicular to the heme B plane, this angle is broadly distributed for MetMb Q8-**3•** (⟨ξ⟩ = 55°) and MetMb Q8-**2•** (⟨ξ⟩ = 77°). Potential reasons for both, the necessity of a two-component system as well as the deviations of the ξ-angle from the expected values, might be the approximations made by PDSFit such as a Gaussian distance and angular distribution, which are in contrast to the *in silico* predictions (Figure 67b) for the Q8C labeling site showing a non-Gaussian shape. On the other hand, structural perturbations upon spin label attachment cannot be excluded either, and further research is needed for complete interpretation of the obtained data.

3.2.6 PDS-EPR with SLIM 3• at Nanomolar Concentrations

In the cellular environment, protein concentrations vary over a broad range from high micromolar concentrations (e.g. 5-50 µM for α-synuclein in neuronal synapses)[385] to low nanomolar concentrations (e.g. 3-170 nM for pro-apoptotic Bax in human cells).[386] To prevent aggregation, a significant shift of the protein fractions within the cell, or even cell death, near-physiological concentrations of spin-labeled proteins are desired to avoid interference with the cellular

signaling and metabolism pathways.[387] Additionally, as a consequence of the low intrinsic concentration of most proteins, important biochemical interactions such as the formation of enzyme-substrate complexes[388] and binding of monoclonal antibodies[389] show high nanomolar binding affinities. While these high binding affinities are commonly investigated by ITC, *Wort* et al. demonstrated the accessibility of nanomolar binding affinities through modulation-depth analysis of RIDME data using the Cu^{2+}/MTSL spin pair.[303] In this section, the feasibility of SLIM **3•** for PDS applications at these low concentrations for future *in-cell* applications and binding studies was assessed.

3.2.6.1 Trityl/Trityl DQC at Nanomolar Concentrations

Prior to the studies presented herein, the lower concentration limit for PDS-EPR using a commercial Q-band spectrometer was reported by *Wort* et al. at a protein concentration of 500 nM using the RIDME pulse sequence on the Cu^{2+}/MTSL spin pair to assess the K_D of Cu^{2+}(NTA) to the dHis motif.[303] Exploiting the enhanced sensitivity and high SNR of SLIM **3•** demonstrated before (see section 3.2.4.4) using the DQC pulse sequence, the feasible concentration limit for the SLIM **3•**/DQC-combination was assessed by dilution of the previously utilized YopO Y588-**3•**/N624-**3•** construct. Samples at a final protein concentration of 180 nM and 90 nM were prepared and DQC experiments were performed and analyzed using DeerAnalysis (Figure 74).

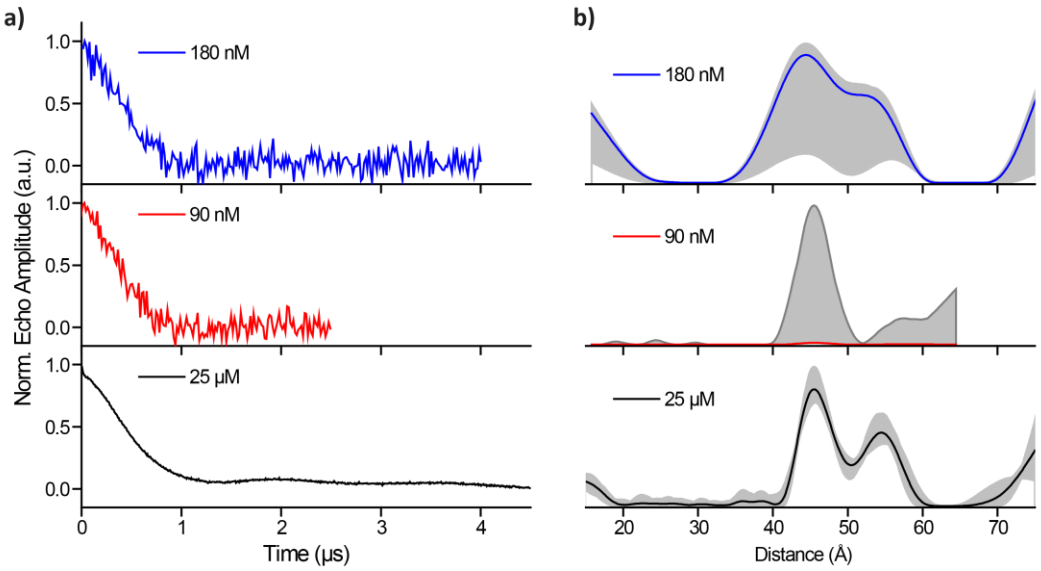

Figure 74: Mirrored DQC time traces of YopO Y588-**3•**/N624-**3•** at various concentrations and the corresponding distance distributions obtained by DeerAnalysis. **a)** Mirrored DQC time traces of YopO Y588-**3•**/N624-**3•** at 180 nM (blue), 90 nM (red), and 25 µM (black). Samples were prepared in deuterated PDS buffer with 30% v/v glycerol-d_8. **b)** Resulting distance distributions of the time traces in **(a)** using the same color code with the DeerAnalysis validation shown as grey shaded areas. The unmirrored raw DQC traces and complete analyses by DeerAnalysis (backgrounds, fits, and L-curves) for the nanomolar samples are given in the appendix (Figure A28).

For both nanomolar concentrations, DQC time traces with an SNR of 2 $h^{-1/2}$ (compare: 674 $h^{-1/2}$ at 25 µM) were obtained with the trace length for the 90 nM sample being shorter than for the 180 nM sample (2.5 µs vs. 4 µs). Despite the significantly lower SNR, both the modulation depth and the oscillation period for the nanomolar dilutions agree well with the 25 µM reference DQC trace discussed before (section 3.2.4.4). For the 180 nM dilution, a distance distribution quite similar to the reference sample at 25 µM was obtained and even the previously observed

bimodality was partially resolved, though with significantly increased uncertainty bounds owing to the reduced trace length and SNR. For the 90 nM dilution, a distance distribution that completely vanished during background validation was obtained, hence prohibiting further interpretation in the context of the biomolecular structure. However, the enhanced uncertainties for both nanomolar concentrations are partially related to the validation by DeerAnalysis: As the software divides the time trace by the applied background function, the high modulation depth of DQC gives rise to an artificially introduced phenomenon called noise explosion,[390] which is especially prominent for the lower SNRs of the nanomolar samples. This in turn leads to a poorer background fitting (usually fitted to the last third of the time trace) and instabilities in the data analysis as small deviations of the background start cause the applied background function (here: homogenous three-dimensional backgrounds) to fluctuate beyond a reasonable limit, resulting even in a negative modulation depth. Therefore, while the shape and width of the distance distributions are not reliable at these low concentrations and should be treated with care, e.g., in model development, the mean distances extracted by DeerAnalysis can be considered reliable even at 90 nM and can be used as restraints in model development and/or refinement.
Conclusively, PDS-EPR at nanomolar concentrations using the SLIM **3•**/DQC-combination on a commercial Q-band spectrometer was shown to reduce the lower concentration limit by a factor of five compared to concentrations reported before and therefore set a new benchmark. Following the work presented herein, studies by the groups of *Bode* and *Bordignon* assessed the PDS sensitivity limits of MTSL/MTSL (100 nM, PELDOR),[391] Cu^{2+}/Cu^{2+} (500 nM, RIDME),[391] Gd^{3+}/Gd^{3+} (200 nM, PELDOR),[387] and Cu^{2+}/MTSL (100 nM, RIDME).[392]

3.2.6.2 Trityl/Cu^{2+} RIDME at Nanomolar Concentrations

Following the demonstration of PDS-EPR at low nanomolar concentrations using SLIM **3•**/DQC, the concept was to be expanded by using SLIM **3•** in combination with the previously described RIDME experiments on Cu^{2+} [391] in collaboration with *Bela Bode* from the University of St Andrews. Here, excitation of the full EPR spectrum of SLIM **3•** is expected to result in a 3 – 4-fold sensitivity increase compared to the previously employed Cu^{2+}/MTSL spin pair with the feasible PDS concentration limit at 100 nM.[392] To enable a direct comparison with the previous study, the same protein, namely GB1 (see section 1.4.3) exhibiting a dHis-site on the α-helix (K28H/Q32H) and a cysteine modification in the β-sheet (I6C), was utilized (Figure 75).

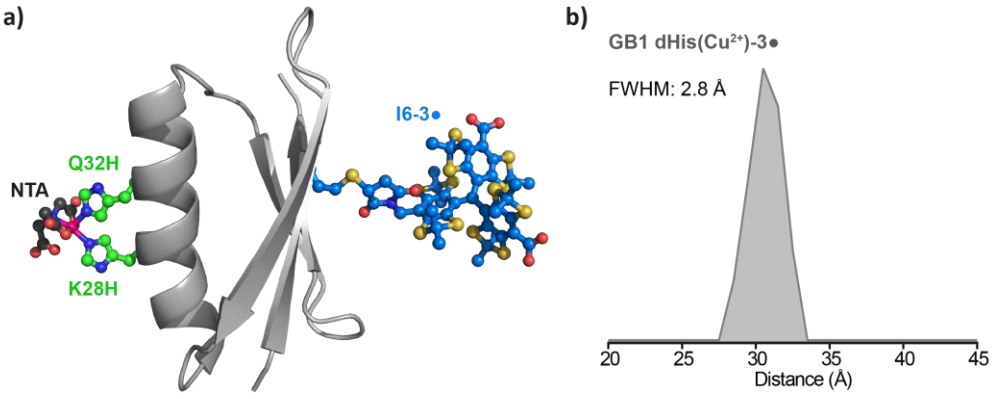

Figure 75: Labeling sites and *in silico* derived distance distribution for GB1 I6C/K28H/Q32H orthogonally labeled with SLIM **3•** and Cu^{2+}(NTA). **a)** Structure of GB1 (PDB-ID 3gb1, grey) labeled with SLIM **3•** (blue) at the position I6C and Cu^{2+}(NTA) (green and black) at the dHis-site K28H/Q32H (green). For clarity, only one rotamer is shown. Rotamers were generated using mtsslWizard for bipedal labels (Colab, clash setting: loose).[393,394] **b)** *In silico* derived distance distribution between dHis-Cu^{2+}(NTA) and SLIM **3•** shown in **(a)**.

All subsequent experiments were performed in the laboratories of *Bela Bode* at the University of St Andrews during a one-month research stay funded by the *Deutscher Akademischer Austauschdienst* (DAAD). The protein construct GB1 I6C/K28H/Q32H (provided by *Katrin Ackermann*), in the following referred to as GB1, was labeled according to the previously established general protocol (see section 3.2.2.2) with SLIM **3•** (Figure 76 + Table 21).

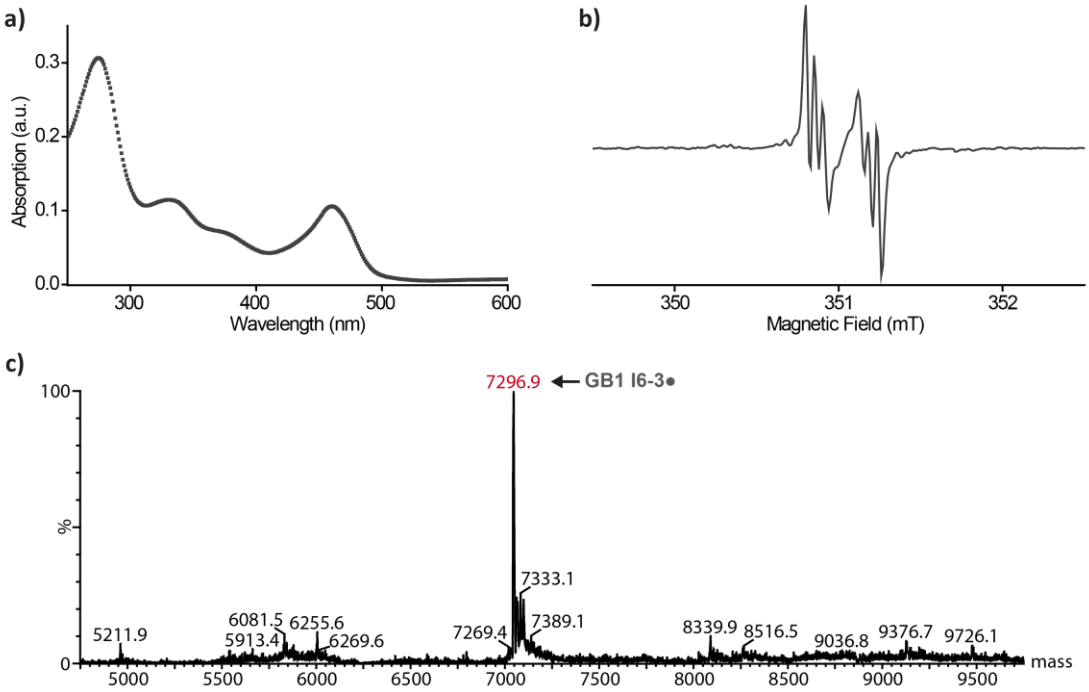

Figure 76: UV-vis spectrum, cw-EPR spectrum, and ESI(+)-MS spectrum of GB1 I6-**3•**. **a)** UV-vis spectrum of GB1 K28H/Q32H/I6-**3•** after excess label removal recorded on a Jenway 6850 double beam spectrophotometer. **b)** Room temperature X-band cw-EPR spectrum of GB1 I6-**3•** (50 µM) recorded on a Bruker EMX 10/12 spectrometer equipped with an ELEXSYS Super Hi-Q resonator. Measurement settings: 9.9 GHz microwave frequency, 2 mW microwave power, 100 kHz modulation frequency, 0.2 G modulation amplitude, 20.48 ms time constant, 100 pts/mT. **c)** Deconvoluted high-resolution ESI(+)-MS spectrum of GB1 I6-**3•** recorded on a Waters Xevo G2 TOF mass spectrometer.

Table 21: Labeling efficiencies of GB1 I6-**3•** determined by UV-vis and cw-EPR spin-count.

Method	GB1 [µM]	SLIM 3• [µM]	Labeling efficiency
UV-vis	66	67	102%
cw-EPR spin-count[a]	-	49[b]	98%

[a] Protein freeze-dried and resuspended in deuterated GB1 PDS buffer to a concentration of 50 µM.
[b] Determined against a 50 µM TEMPO standard (in GB1 PDS buffer).

After labeling GB1 with SLIM **3•** and removing the excess spin label (Äkta start run not shown here, as the UV-detector could monitor only the absorbance at 280 nm), the UV-vis spectrum (Figure 76a) indicated quantitative labeling of GB1 with SLIM **3•** according to the absorbance maxima at 459 nm and 276 nm. Notably, initial labeling experiments of GB1 with SLIM **3•** revealed insufficient separability of the free label from the protein, hence a reduced excess of 3.5 eq. **3•** per GB1 molecule (compared to previously 5 eq. / protein) was applied for the successful labeling of GB1 shown here. These issues with trityl separation are likely caused by the significantly smaller

size of GB1 (6.2 kDa) compared to the previously used proteins (YopO: 71.2 kDa; Myoglobin: 17.1 kDa), resulting in insufficient separation between both species during the SEC steps due to similar hydrodynamic radii. In contrast to the previous buffer exchanges, here, the exchange into deuterated GB1 PDS buffer was achieved by freeze-drying and resuspension of GB1 I6-**3•** with D_2O, as previous studies revealed no structural change and perturbation of the protein using this technique.[303] The cw-EPR spectrum of GB1 I6-**3•** (Figure 76b) showed great similarity with the spectrum obtained for Mb Q8-**3•** (see Figure 72). Again, as a consequence of the shorter rotational correlation time related to the low molecular weight of GB1, the hyperfine splitting of SLIM **3•** was not averaged and is still partially resolved. Quantitative cw-EPR spin-count against a 50 µM TEMPO reference revealed a labeling efficiency of 98%. Finally, successful GB1 labeling was confirmed by ESI(+)-MS, where a single high-intensity mass peak at 7,296.9 Da (calculated: 7,297 Da) with a mass increase of +1,065 Da (MW SLIM **3•**: 1,065.54 Da) compared to unlabeled GB1 (6,231 Da, Figure A29) was detected.

Final PDS samples were prepared by adding Cu^{2+}(NTA) to the SLIM **3•**-labeled GB1. Here, the ratio of Cu^{2+}(NTA) to GB1 was adjusted so that approximate 90% loading of the dHis-site was achieved using the previously determined dissociation constant of K_D = 200 nM for the dHis-site located on the GB1 α-helix.[303] To assess the PDS concentration limit for the Cu^{2+}/SLIM 3• spin pair, RIDME experiments were set up at Q-band frequencies (40 K) and analyzed using Tikhonov regularization by *Bela Bode*. In addition to the standard five-pulse (constant time, ct) RIDME sequence, additional RIDME traces using the recently introduced variable time (vt) RIDME were recorded, which was shown to yield a 2 – 3-fold sensitivity enhancement compared to ctRIDME on the example of the Cu^{2+}/MTSL spin pair.[395] Here, only the background-corrected vtRIDME traces and the corresponding distance distributions are displayed (Figure 77). A detailed summary of the setup parameters and data processing routines can be found in the original publication.[373]

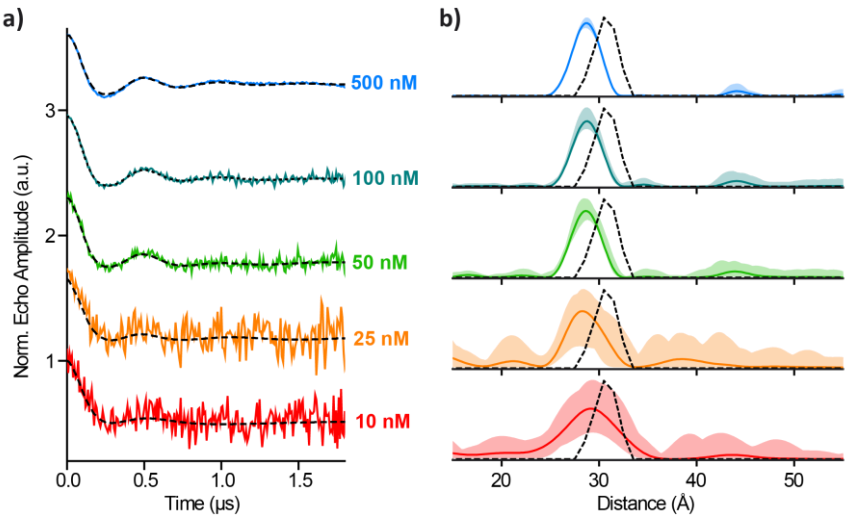

Figure 77: Background-corrected vtRIDME time traces and resulting distance distributions of GB1 I6-**3•**/28H+32H-Cu^{2+}(NTA). **a)** Five-pulse vtRIDME time traces at 500 nM (blue), 100 nM (teal), 50 nM (green), 25 nM (orange), and 50 nM (red) after background correction with their respective fits obtained from the ConsensusDeerAnalyzer2.0. Raw time traces can be found in the primary publication. **b)** Distance distributions corresponding to the time traces shown in **(a)** using the same color code with the validation (95% confidence intervals) shown as shaded areas. The *in silico* prediction is shown as a black dashed line.

Time traces with pronounced oscillations and a modulation depth between 45% (500 nM) and 53% (100 nM) were obtained. The slight deviations in the modulation depths of the individual samples can be attributed to slight deviations in the sample positioning within the resonator and

optimization refinements before the vtRIDME experiments. Tikhonov regularization revealed high-confidence distance distributions down to a concentration of 50 nM, which were similar in width (vtRIDME avg. FWHM = 3.24 Å; mtsslWizard FWHM = 2.83 Å) but slightly shifted to shorter distances compared to the *in silico* prediction from mtsslWizard. Below the 50 nM threshold, an increase of the uncertainty is observed in the distance distribution as a result of the lower SNR, and the distribution width is no longer considered reliable. Notably, even at these low concentrations, the mean distance is still conserved. By increasing the averaging time to approximately 60 h, a vtRIDME trace with well-pronounced oscillations could be obtained, leading to increased stability of the distance distribution in the subsequent analysis (Figure A30). Compared to ctRIDME, the sensitivity of vtRIDME is approximately 2 – 3 times higher, which is in good agreement with the previously found two-fold sensitivity increase of vtRIDME,[395] and an overall sensitivity improvement by a factor of ~8 compared to previous studies using the Cu^{2+}/MTSL spin pair in combination with ctRIDME was achieved.[392] A detailed summary of the sensitivities obtained herein and a comparison to literature-reported sensitivities is given below (Table 22).

Table 22: Sensitivity given as modulation-to-noise ratio for the vtRIDME and ctRIDME Cu^{2+}/SLIM **3•** time traces at various concentrations of GB1 (this study) and literature-reported sensitivities for Cu^{2+}/MTSL (ctRIDME), MTSL/MTSL (PELDOR), and Cu^{2+}/Cu^{2+} (ctRIDME).[373] For better comparability, the sensitivity is given per unit time S_t ($Hz^{1/2}$).

	S_t [$Hz^{1/2}$][a]				
Concentration [nM]	**Cu^{2+}/SLIM 3• (vtRIDME)**	**Cu^{2+}/SLIM 3• (ctRIDME)**	**Cu^{2+}/MTSL (ctRIDME)[392]**	**MTSL/MTSL (PELDOR)[391]**	**Cu^{2+}/Cu^{2+} (ctRIDME)[391]**
500	28.1	10.8	-	4.47	0.45
100	5.15	2.30	0.59	0.30	-
50	2.48	1.04	0.31	-	-
25	0.77	0.27	-	-	-
10	0.43	0.15	-	-	-

[a] The sensitivity per unit time S_t is defined as the normalized ratio of the modulation depth divided by the root-mean-square experimental noise and the square root of the acquisition time.[303]

In summary, the Cu^{2+}/SLIM **3•** spin pair in combination with vtRIDME significantly enhances the sensitivity and conclusively lowers the concentration limit for biomolecular structure elucidation using PDS-EPR. The vtRIDME experiments at a protein concentration of 10 nM presented herein set a new benchmark for low-concentration PDS.

While this study was intentionally designed to assess the concentration limit of the Cu^{2+}/SLIM **3•** spin pair for PDS-EPR, similar to the myoglobin case (section 3.2.5), the dHis-Cu^{2+}(NTA) motif serves here as a rigid spin center and the width of the distance distribution is dominated by the contribution of the more flexible SLIM **3•** label. The high-confidence distance distribution obtained at 500 nM GB1 shows that the distribution (FWHM = 3.24 Å) is only slightly broader than for the GB1 analog labeled with MTSL (FWHM = 1.81 Å)[396] and well below the resolution limit of a 10 Å FWHM needed for model generation from distance restraints (see section 3.1.5, Table 6, case 2).[354] Although there were no complimentary labeling and RIDME experiments for the same GB1 construct using Mal-TSL **2•**, the narrow distribution obtained here for GB1 labeled with SLIM **3•** provides a good estimate of the restrained conformational flexibility of SLIM **3•**. Hence, it can be concluded that the shortened linker indeed leads to narrowed distance distributions.

3.2.7 *In-Cell* PDS-Experiments with SLIM 3•

3.2.7.1 Redox-Stability of SLIM 3•

For PDS in the cellular environment, the redox stability of the spin label is an important property. As outlined in section 1.3.2.2, trityl radicals typically display high redox stability, which was shown to be strongly influenced by the substitution pattern on the *para*-positions of the phenyl rings. The trityl carbanion formed upon reduction is stabilized by electron withdrawing groups such as esters and amides;[376,397,398] this implies that all TAM labels derived from the Finland trityl via esterification or amidation, e.g. MTS-TSL **1**•, Mal-TSL **2**•, and Mal_{am}-TSL, have an increased redox potential compared to the Finland trityl itself and are more prone to reduction. On the other hand, the imidomethylene substituent of SLIM **3**• has an electron-donating effect, thereby destabilizing the carbanion and decreasing the redox potential compared to the Finland trityl and all predecessor spin labels. To test whether this hypothesis holds and whether SLIM **3**• is indeed more redox-stable, solutions of Finland trityl and SLIM **3**• were subjected to cyclic voltammetry (CV) by *Pawel Bawol* of the *Baltruschat* group (Figure 78).

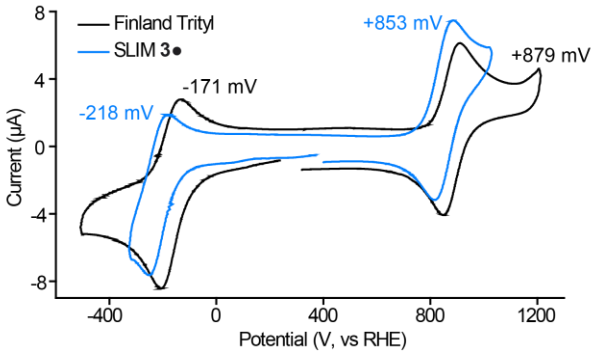

Figure 78: Cyclic voltammograms of Finland trityl (black) and SLIM **3**• (blue), each at 500 µM in PBS buffer and measured against a reversible hydrogen electrode (RHE) at pH 7.4 as a reference. A scan rate of 50 mV/s was applied in clockwise direction.

Indeed, according to CV, the redox potential of SLIM **3**• is lowered by 43 mV compared to the Finland trityl, thereby confirming enhanced stability towards reductive processes, which is related to the electron donating imidomethylene substituent. As a direct consequence, the oxidation of SLIM **3**• is slightly favored by 26 mV compared to the Finland trityl; however, no oxidative degradation of the spin label was observed at ambient conditions.

Following these initial studies, the stability of the free spin label **3**• towards ascorbate in comparison with other spin labels was assessed by *Florian Haege* in his Master thesis (Figure 79a).[375] As not only the free-label stability but rather the stability of the spin label upon bioconjugation is crucial for *in-cell* PDS and, additionally, enzymatic reduction of the radical is an important factor,[399] the stability of SLIM **3**• conjugated to YopO N624C (previously employed construct, see Figure 61) was investigated under various cell-mimetic conditions[202,227,400] to demonstrate its applicability for *in-cell* PDS experiments (Figure 79b).

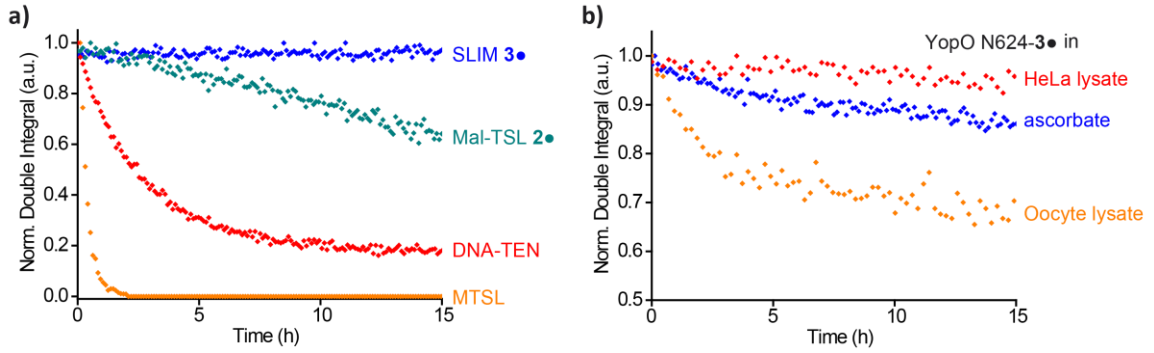

Figure 79: Stability studies of various free spin labels in sodium ascorbate solution and of SLIM **3•** bioconjugated to YopO N624C under cell-mimetic conditions. **a)** Normalized X-band cw-EPR signal double-integral of SLIM **3•** (blue), Mal-TSL **2•** (teal), *gem*-diethylisoindoline nitroxide (TEN, compare Figure 21) bound to DNA (red), and MTSL (orange), each at a concentration of 200 µM in PBS buffer containing 5 mM ascorbate. Spectra were recorded in gas-tight capillaries on a Bruker EMXmicro spectrometer over 15 h with cw-EPR scans every 15 min. To achieve sufficient water solubility of TEN, the spin label was bioconjugated to a modified DNA strand (5'-GGG TGX CTG GTA CCC-3', X = 5-ethynyl-2'dU, obtained from *Metabion*) and subsequently annealed with the complementary, unmodified strand by *Christine Wuebben* in the context of her dissertation[401] following previously established protocols.[224] **b)** Normalized X-band cw-EPR signal double-integral of YopO N624C-**3•** (50 µM) in 5 mM ascorbate (blue), HeLa lysate (red), and *Xenopus laevis* oocyte lysate (orange). Spectra were recorded in gas-tight capillaries on a Bruker EMXmicro spectrometer over 15 h with cw-EPR scans every 15 min.

In the presence of a 25-fold molar excess of ascorbate, SLIM **3•** showed excellent redox stability compared to all other tested labels, and no notable signal decay was observed (Figure 79a, blue). According to the CV measurements, SLIM **3•** is more stable than the Finland trityl-derived Mal-TSL **2•** and indeed, the EPR signal of **2•** decayed to 62% of its initial double-integral over 15 h in the presence of the reducing agent ascorbate (Figure 79a, teal). In addition, SLIM **3•** outperformed both tested nitroxide labels, the *gem*-diethylisoindoline nitroxide bound to DNA (DNA-TEN) which was reduced to 18% in the same time frame (Figure 79a, red), and the *gem*-dimethyl MTSL label which was completely reduced after 1.5 h (Figure 79a, orange). For SLIM **3•** covalently bound to YopO N624C (Figure 79b), only a marginal EPR signal reduction of approximately 10% in the presence of 5 mM ascorbate and even less in HeLa lysate was observed. *Xenopus laevis* oocyte lysate showed the strongest reducing effect on YopO N624-**3•** but even here, the signal decayed only by 29% of its initial double-integral value.
Hence, the introduction of an imidomethylene linker not only reduced the flexibility of the spin label but also shifted the redox potential of SLIM **3•**, thereby rendering the spin label in its free and bioconjugated form more redox-stable than the previously employed trityl[370] and *gem*-dimethyl nitroxide spin labels, and at least on par with *gem*-diethyl nitroxide labels,[202,227] making it an excellent candidate for *in-cell* applications.

3.2.7.2 PDS-EPR Distance Measurements in *Xenopus Laevis* Oocytes

Following the promising results of section 3.2.6.1, the feasibility of SLIM **3•** for *in-cell* PDS structure elucidation of proteins was tested first within *Xenopus laevis* oocytes, an eucaryotic cell model previously employed for *in-cell* PDS studies.[164,227,285,402] As *Xenopus laevis* oocytes showed the highest reducing activity towards SLIM **3•**, this system serves as a benchmark for other *in-cell* applications, e.g. within HeLa cells. In addition, the size of the oocytes allows mimicking the native translocation process of YopO to the host immune cells via the T3SS from *Yersinia* by using a microinjection needle for cell penetration and translocation of the labeled protein into the oocytes.

Using the YopO Y588-**3•**/N624-**3•** mutant (see section 3.2.4.2), bulk spin concentrations of approximately 11 µM were obtained after microinjection into *Xenopus laevis* oocytes. The successful protein delivery was confirmed by echo-detected field-swept EPR and relaxation measurements (Figure 80 + Table 23).

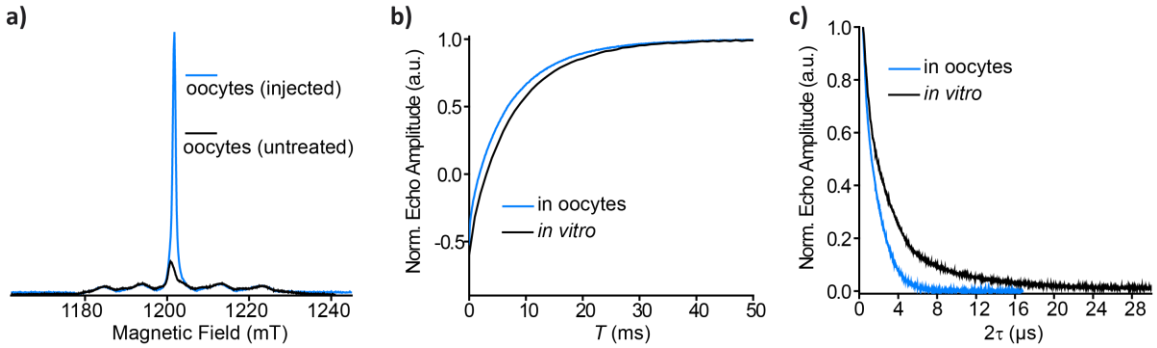

Figure 80: Echo-detected field-swept EPR spectrum and electron spin relaxation measurements of YopO Y588-**3•**/N624-**3•** injected into *Xenopus laevis* oocytes. **a)** Field-swept Q-band EPR spectra of untreated oocytes (black) and oocytes injected with YopO Y588-**3•**/N624-**3•** (blue) at 50 K normalized to the first Mn^{2+} signal at 1184.4 mT. **b)** Inversion recovery traces for YopO Y588-**3•**/N624-**3•** injected into oocytes after 120 min incubation time (blue) and *in vitro* (black) at 50 K. **b)** 2pESEEM traces for YopO Y588-**3•**/N624-**3•** injected into oocytes after 120 min incubation time (blue) and *in vitro* (black) at 50 K.

Table 23: Spin-lattice relaxation times T_1 and phase memory times T_M of SLIM **3•** obtained by fitting either eq. 19 (Inversion recovery) or eq. 20 (2pESEEM) to the respective traces shown in Figure 80.

Sample	T_1 (ms)	T_M (µs)
in oocytes	7.1	1.4
in vitro	7.8	1.5

The field-swept EPR spectrum of untreated oocytes (Figure 80a, black) showed the characteristic manganese(II) signal (1181 mT – 1228 mT)[285,403] reported previously alongside the signal of an endogenous organic radical (1200.9 mT) of unknown origin. After injection of YopO Y588-**3•**/N624-**3•**, the shape of the field-swept EPR spectrum changed considerably and is now dominated by a new signal at 1201.8 mT indicative of the injected trityl. Inversion recovery and 2pESEEM experiments on the maximum of this signal revealed prolonged T_1 and T_M relaxation times compared to the relaxation times at the field positions of manganese(II) and the organic radical (Figure A31b+c), thereby confirming the successful injection and presence of YopO Y588-**3•**/N624-**3•**. In the cellular environment, the transverse and longitudinal relaxation of SLIM **3•** is enhanced compared to the *in vitro* sample, presumably due to relaxation enhancement by the endogenous manganese and/or paramagnetic crowding.[402] Notably, the paramagnetic crowding could be sufficiently reduced upon prolonged incubation times after microinjection, thereby leading to a more uniform distribution of the labeled protein within the oocytes as evidenced by an increased phase memory time after longer incubation periods (Figure A31d).
Next, a DQC time trace of the injected *Xenopus laevis* oocytes was recorded and analyzed using DeerAnalysis (Figure 81). Here, the relatively long phase memory time of SLIM **3•** in the non-deuterated environment of the oocytes enabled a dipolar evolution time window of 3.5 µs, which

is considerably longer than traces recorded with nitroxide-, Gd^{3+}-, and trityl spin labels in previous PDS studies using either *Xenopus laevis* oocytes or *E. coli* cells.[147,227,285,402]

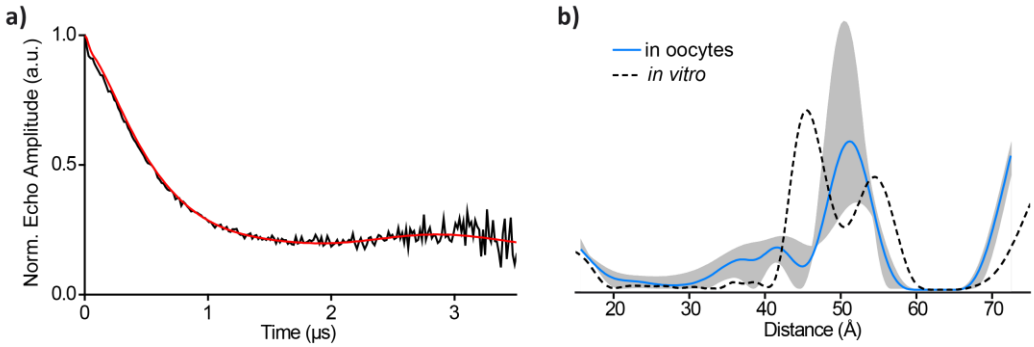

Figure 81: DQC time trace and distance distribution of YopO Y588-**3•**/N624-**3•** injected into *Xenopus laevis* oocytes. **a)** Background-corrected DQC time trace (black) of YopO Y588-**3•**/N624-**3** in oocytes with the fit obtained by Tikhonov regularization (red). **b)** Distance distribution (blue) obtained from the time trace in **(a)** with the DeerAnalysis validation shown as grey-shaded areas and the distance distribution of YopO Y588-**3•**/N624-**3•** obtained *in vitro* as comparison (black dashed line). The complete analysis by DeerAnalysis (raw time trace, background, L-curves, and distance distributions) is given in the appendix (Figure A32).

The DQC time trace showed a modulation depth of 78% and an SNR of 0.4 $min^{-1/2}$. Assuming a linear correlation of the SNR with the spin concentration, an SNR of 2.25 $min^{-1/2}$ is expected for a bulk spin concentration of approximately 11 µM, based on the SNR of 11.2 $min^{-1/2}$ previously obtained *in vitro* for YopO Y588-**3•**/N624-**3•** (see Table 17). The lower SNR and modulation depth can be rationalized by the shorter phase memory time as well as partial reduction of SLIM **3•** within the oocytes during the incubation phase, leading to an increased fraction of singly-labeled proteins not contributing to the DQC signal. Despite this partial reduction of SLIM **3•**, the SNR of the DQC trace was considerably higher than for literature-reported *in-cell* measurements with nitroxide[147,227,402] and trityl[164] labels at Q-band and comparable to the SNRs obtained for PELDOR measurements using trityl and Gd^{3+} labels at W-Band.[289,352,404] As a result of the higher fraction of singly-labeled YopO and the inhomogeneous distribution of the spins within the resonator resulting from the stacked packing of the oocytes within the EPR tube (see Materials and Methods section 5.2.8.1, Figure 112f), a three-dimensional homogenous background as previously utilized for the *in vitro* DQC traces of YopO Y588-**3•**/N624-**3•** was insufficient to describe the DQC background and hence a 3rd-order polynomial function was applied here.
Compared to the DQC trace of YopO Y588-**3•**/N624-**3•** obtained *in vitro*, the oscillation period of the same construct inside oocytes is considerably longer (3 µs in oocytes vs. 2 µs *in vitro*) and, accordingly, the distance distributions obtained *in-cell* and *in vitro* differ from each other. While a pronounced bimodality was observed *in vitro* that was attributed to two conformational states of the α-helical backbone, within the oocytes, the shorter-distance peak at 45 Å is strongly diminished and only a single mode at 51 Å, roughly corresponding to the longer-distance peak, prevailed. This strongly suggests a preferred selection of the bent helix conformation (corresponding to longer inter-spin distances) within the cytosol of the oocytes. Although a correlation of the α-helical backbone conformation and the presence and binding of G-actin to YopO was ruled out (see section 3.2.4.4), the conformational change is likely related to molecular crowding effects[405,406] and/or the binding of other substrates such as Rac1 within the cytosol.[326]

3.2.7.3 Expression, Purification, and Labeling of $YopO_{1\text{-}729}$•$(SycO)_2$

SLIM **3•** showed remarkable redox stability within HeLa cell lysate (see section 3.2.7.1) and thus holds great potential for PDS studies of proteins inside eucaryotic human cells such as HeLa, an immortal human cancer cell line widely applied to study fundamental cellular processes.[407] To expand the application scope of SLIM **3•** to this highly relevant cell-class, the general feasibility of PDS experiments in HeLa cells was to be tested using the full-length construct $YopO_{1\text{-}729}$ labeled with SLIM **3•**. The rationale of using the native, full-length form rather than the previously employed truncated $YopO_{89\text{-}729}$ mutant lacking the secretion and translocation domain was to follow the localization of the protein at the inner surface of the HeLa cell membrane after internalization[323] by fluorescence microcopy, thereby confirming the structural integrity in the native state. In addition, localization and thereby immobilization of full-length YopO at the inner cell membrane potentially reduces molecular tumbling and motional averaging of the dipolar interaction and PDS-EPR can be performed at non-cryogenic or even ambient temperatures without the use of artificial immobilizing additives such as dried trehalose.

The missing first 79 amino acids encoded onto a synthetic gene were cut out using the restriction enzymes *EcoR1* and *Pas1* and cloned in-frame into the pGEX-6p-1 vector that contains $YopO_{89\text{-}729}$-wt. Subsequently, the amino acids E87 and F88 in $YopO_{1\text{-}729}$ encoding for the *Pas1* restriction site were altered to the wild-type amino acids K87 and T88, thereby generating the GST-fused $YopO_{1\text{-}729}$-wt construct, whose identity was confirmed via sequencing (Figure A33). Initial attempts to purify $YopO_{1\text{-}729}$ according to the protocol described by *Juris* et al.[325] failed, as no sufficient amount of protein could be recovered after PreScission protease cleavage of GST-$YopO_{1\text{-}729}$ after affinity binding to GSH beads (Figure 82a). A BugBuster® expression assay monitoring the fraction of soluble GST-$YopO_{1\text{-}729}$ for 16 h at either 16 °C or 25 °C revealed that even at short expression times of 2 h, GST-$YopO_{1\text{-}729}$ is found only in the insoluble fraction of the cell lysate, as a strong band above 100 kDa appears (GST-$YopO_{1\text{-}729}$: 108 kDa). The identity of this band was confirmed by Western blotting (Figure 82b-d).

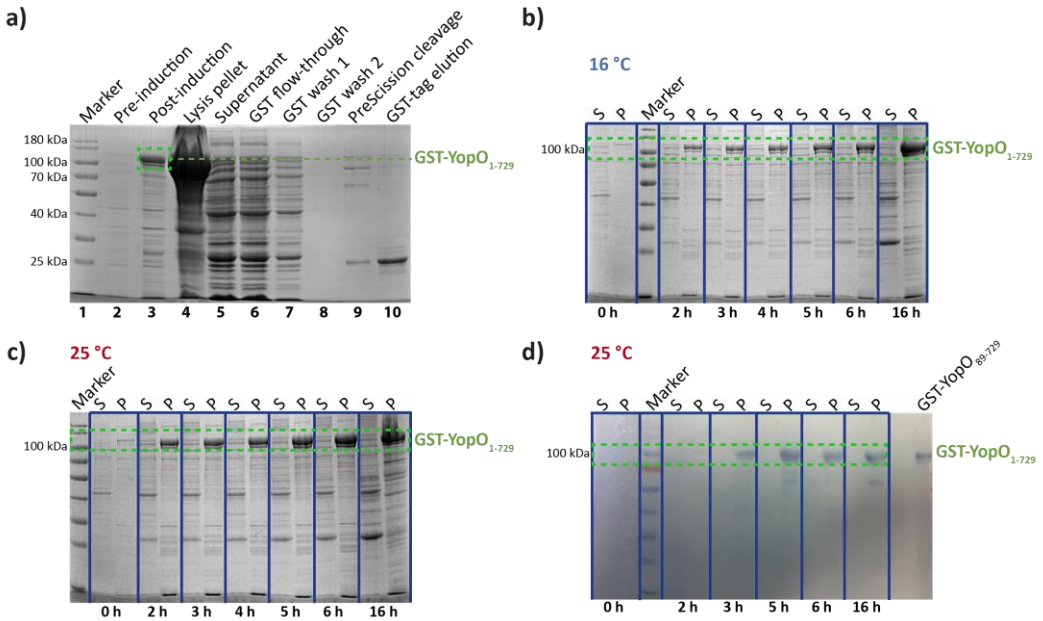

Figure 82: SDS gels and Western blot of the expression and purification of GST-fused $YopO_{1-729}$. **a)** 10% SDS gel of the expression and purification process of $YopO_{1-729}$ following the workflow described by *Juris* et al.[325] The green dashed box indicates the height and successful expression of GST-$YopO_{1-729}$. **b)** 10% SDS gel monitoring the protein amount in the soluble (S) and pellet (P) fraction after IPTG-induction at various time points at 16 °C. Cells were lysed using the BugBuster® 10x Protein Extraction Reagent. **c)** Same as **(b)** but for protein expression at 25 °C. **d)** Western blot with the samples in **(c)** (4 h time stamp missing) and a post-induction sample of GST-$YopO_{89-729}$ (16 h incubation) as a positive control for antibody binding. Primary antibody: Mouse anti-GST; secondary antibody: Goat anti-mouse IgG (HRP conjugated). Picture taken with a smartphone.

These findings of poorly soluble $YopO_{1-729}$ are in line with earlier reports by *Letzelter* et al. who have shown that the aggregation-prone membrane localization domain (MLD) of wild-type $YopO_{1-729}$ is stabilized by the specific *Yersinia* chaperone O (SycO).[408] The chaperone SycO binds to the amino acid residues 20-77 of $YopO_{1-729}$ in a 2:1 stoichiometry, thereby masking the poorly soluble MLD and greatly enhancing the solubility of wild-type $YopO_{1-729}$. To enable expression of $YopO_{1-729}$ at yields sufficient for subsequent labeling and transfection experiments, the $YopO_{1-729}$ and SycO genes were cloned into a pET-Duet-1 vector for co-expression of both proteins (Figure A34).

The expression and purification of $YopO_{1-729}$•$(SycO)_2$ was adapted with small adjustments from the soluble $YopO_{89-729}$ construct described previously. In particular, protein expression was induced using a lower IPTG concentration, the stability of the protein complex was enhanced by the supplement of 5% (v/v) glycerol to all buffers, and the gel filtration step was renounced as sufficiently pure protein was obtained after the anion exchange (Figure 83).

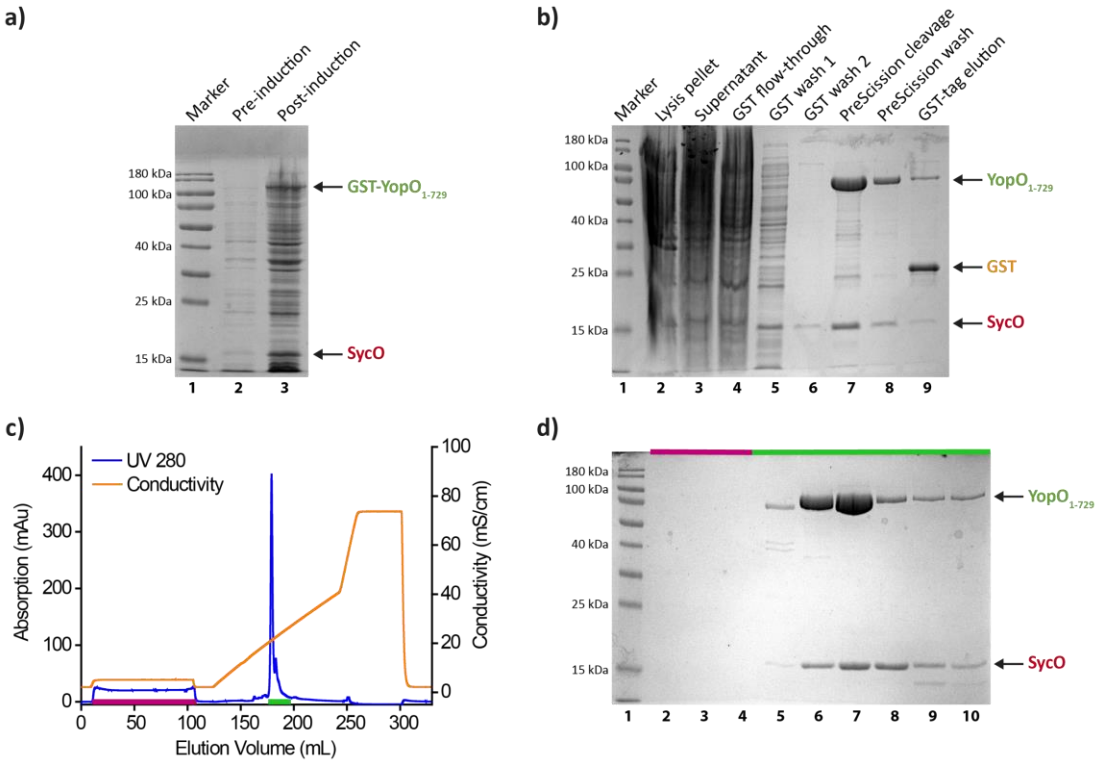

Figure 83: Expression and purification of $YopO_{1-729}$•$(SycO)_2$. **a)** Coomassie-stained 10% SDS gel of the Rosetta DE3 cells pre- and post-induction with IPTG. The band heights of GST-$YopO_{1-729}$ (108 kDa, green) and SycO (17.4 kDa, red) are indicated. **b)** Coomassie-stained 10% SDS gel of the initial purification steps until $YopO_{1-729}$ elution from the GSH beads. Band-heights corresponding to GST-tag cleaved $YopO_{1-729}$ (81.7 kDa, green), free GST (28.3 kDa, orange), and SycO (17.4 kDa, red) are indicated. **c)** Chromatogram of the Capto™ HiRes Q 10/100 anion exchange run of $YopO_{1-729}$•$(SycO)_2$ showing the absorption at 280 nm (blue) and conductivity (orange). The horizontal bars (purple and green) correspond to the fractions taken for SDS-PAGE analysis. **d)** Coomassie-stained 10% SDS gel of the fractions shown in **(c)**. The bands corresponding to $YopO_{1-729}$ and SycO are indicated.

Protein co-expression from the pET-Duet-1 vector revealed successful expression of both, $YopO_{1-729}$ and SycO, as bands at ~100 kDa (GST- $YopO_{1-729}$: 108 kDa) and ~15 kDa (SycO: 17.4 kDa) appeared (Figure 83a). Subsequent cell lysis and purification using GST-affinity chromatography showed that co-expression of $YopO_{1-729}$ in combination with SycO significantly enhances the protein stability, and a large band on the SDS gel corresponding to $YopO_{1-729}$ appeared after cleavage of the GST-tag (Figure 83b, lane 7). In the same elution fraction, a ~15 kDa band was observed on the Coomassie-stained SDS gel, likely corresponding to SycO which is bound to the MLD of $YopO_{1-729}$. Subsequent anion exchange chromatography confirmed this hypothesis, as two proteins with molecular weights of ~80 kDa and ~15 kDa corresponding to the $YopO_{1-729}$ and SycO eluted together at a conductivity of ~22 mS/cm. After concentrating the anion-exchange fractions containing $YopO_{1-729}$•$(SycO)_2$, a total of 5.8 mg protein was obtained, which corresponds to 50 nmol of the protein complex assuming a 2:1 stoichiometry. In summary, the co-expression of $YopO_{1-729}$ with SycO significantly enhanced the stability of full-length YopO and enabled the purification of the protein in sufficient amounts for labeling experiments. Yet, the yields were approximately only a third of the average protein yield usually obtained for the soluble $YopO_{89-729}$ construct, thereby hinting towards a still reduced stability of the $YopO_{1-729}$•$(SycO)_2$ complex compared to truncated YopO.

As there is no structure available for wild-type SycO which contains three native cysteine residues, the accessibility of the present cysteines was assessed by labeling $YopO_{1-729}$•$(SycO)_2$ with MTSL.

Subsequent cw-EPR and PELDOR experiments revealed labeling of at least one of the native cysteines and the presence of dipolar coupling in the PELDOR experiments (Figure A35). In order to enable site-selective labeling with SLIM and a fluorescence dye, the native cysteines C30, C75, and C87 were altered to alanine residues (Figure A36), yielding the $YopO_{1\text{-}729}$•$(SycO_{0\text{-}Cys})_2$ construct, hence forward referred to as $YopO_{fl}$(SycO). The catalytic activity of this construct was confirmed by detecting the autophosphorylation capability in the presence of G-actin (Figure A37). Starting from this construct, the cysteines for spin-labeling with SLIM **3•** were introduced at positions S585C and Q603C in $YopO_{fl}$, and in another construct at residue N624C for fluorophore labeling (Figure A38). The rational for choosing the labeling positions S585C and Q603C for SLIM **3•**-labeling of $YopO_{fl}$(SycO) was the assumed reduced phase memory time in the cellular environment of HeLa cells and the hence reduced achievable dipolar evolution time.
The double-cysteine construct $YopO_{fl}$(SycO) S585C/Q603C was expressed, purified (Figure A39), and subsequently labeled with MTSL and SLIM **3•** (Figure 84 + Table 24). To validate whether the residues 1-88 and the complexation with SycO influence the structure of the labeled α-helical backbone in $YopO_{fl}$, additionally the soluble $YopO_{89\text{-}729}$ S585C/Q603C construct used in previous studies (see section 3.1.1) was also labeled with SLIM **3•** as a reference for *in vitro* PDS experiments (Figure 84 + Table 24).

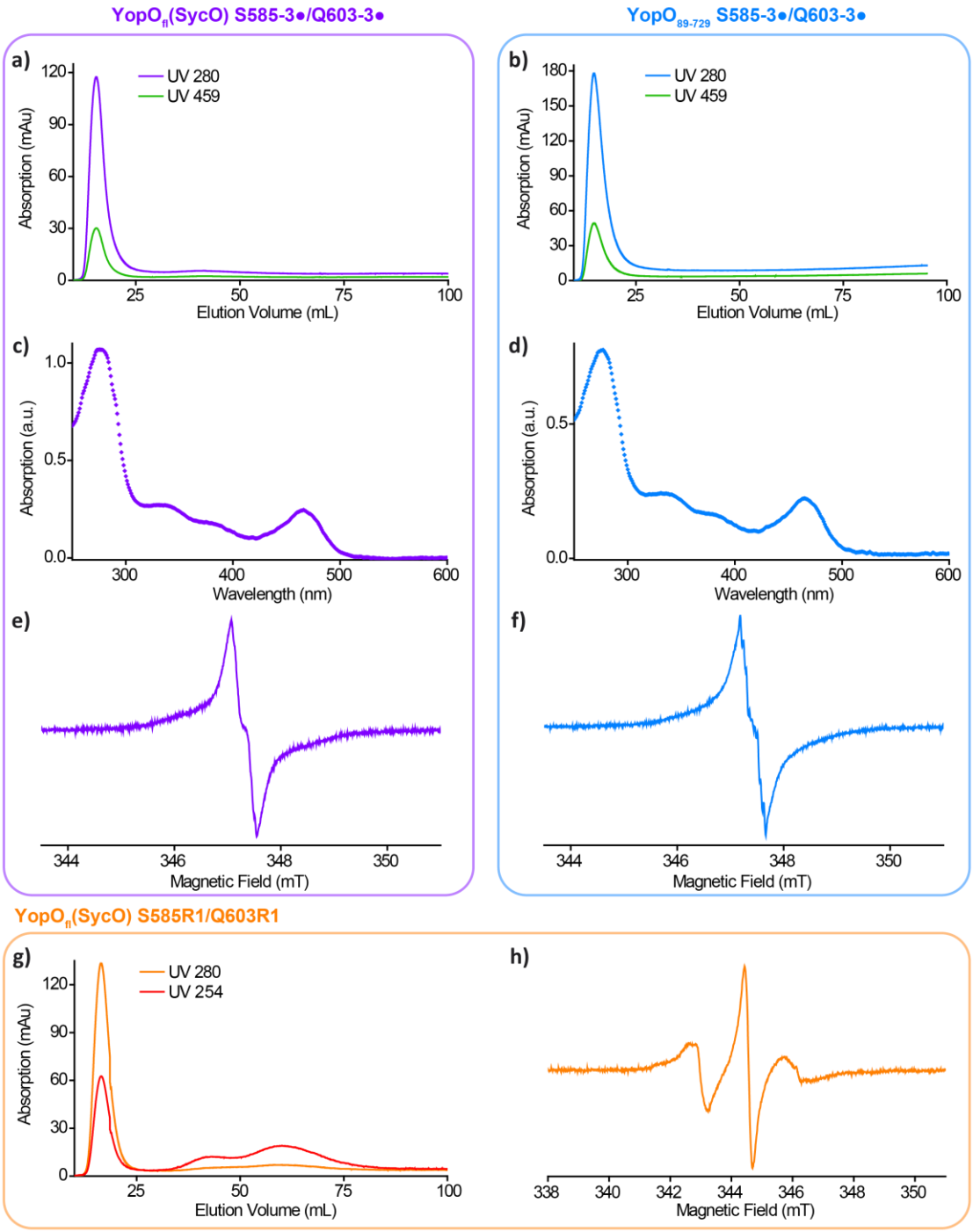

Figure 84: Spin labeling results for YopO$_{fl}$(SycO) S585C/Q603C and the soluble analog YopO$_{89-729}$ S585C/Q603C. **a+b)** Chromatograms of the HiPrep™ 26/10 runs of YopO$_{fl}$(SycO) S585-**3•**/Q603-**3•** **(a)** and YopO$_{89-729}$ S585-**3•**/Q603-**3•** **(b)** after labeling with SLIM **3•**. **c+d)** UV-vis spectra of YopO$_{fl}$(SycO) S585-**3•**/Q603-**3•** (1:3 dilution) **(c)** and YopO$_{89-729}$ S585-**3•**/Q603-**3•** (1:4 dilution) **(d)** after excess label removal recorded on a NanoDrop™ 2000. **e+f)** Room temperature X-band cw-EPR spectra of YopO$_{fl}$(SycO) S585-**3•**/Q603-**3•** (160 µM) **(e)** and YopO$_{89-729}$ S585-**3•**/Q603-**3•** (218 µM) **(f)** recorded on a Bruker EMXnano spectrometer. Measurement settings: 9.635 GHz microwave frequency, 1.0 mW microwave power, 100 kHz modulation frequency, 0.5 G modulation amplitude, 20.48 ms time constant, 200 pts/mT. **g)** Chromatogram of the HiPrep™ 26/10 run of YopO$_{fl}$(SycO) S585R1/Q603R1 after labeling with MTSL. **h)** Room temperature X-band cw-EPR spectra of YopO$_{fl}$(SycO) S585R1/Q603R1 (100 µM) recorded on an EMXnano spectrometer. Measurement settings: 9.635 GHz microwave frequency, 10 mW microwave power, 100 kHz modulation frequency, 1.0 G modulation amplitude, 20.48 ms time constant, 100 pts/mT.

Table 24: Labeling efficiencies of $YopO_{fl}$(SycO) S585-**3•**/Q603-**3•**, $YopO_{89\text{-}729}$ S585-**3•**/Q603-**3•**, and $YopO_{fl}$(SycO) S585R1/Q603R1 derived from UV-vis and cw-EPR spin-count experiments shown in Figure 84.

Sample	$YopO_{fl}$(SycO) S585-3•/Q603-3•	$YopO_{89\text{-}729}$ S585-3•/Q603-3•	$YopO_{fl}$(SycO) S585R1/Q603R1
UV-vis (protein) [µM]	160	218	100
UV-vis (label) [µM]	345	426	-
cw-EPR spin-count [µM]	320	365	100
Labeling efficiency[a]	104%	91%	50%

[a] For SLIM **3•**, the label concentration from UV-vis and cw-EPR spin-count was averaged.

For SLIM **3•**, high labeling efficiencies were obtained for both YopO constructs. Notably, the cw-EPR spectrum is broadened for both constructs in comparison to the spectrum of previously used YopO Y588-**3•**/N624-**3•** and the hyperfine splitting is barely resolved. Here, both spin labels are separated by 17 residues compared to 34 residues in YopO Y588-**3•**/N624-**3•**, and the broadening is attributed to the strong dipolar coupling of the spins resulting from the closer proximity of the labels with interspin distances below the 22 Å threshold.[409] Labeling with MTSL resulted in a labeling efficiency of only 50%, which is well below the previously achieved labeling efficiency of the MTSL-labeled soluble analog of this mutant (see section 3.1.2). A potential reason might be an error in the determination of the protein concentration by UV-vis, as a shift in the ratio of YopO and SycO might have occurred during the labeling and work-up, e.g., by precipitation of YopO while SycO remained in the soluble fraction.

The influence of SycO and the presence of the MLD on the GDI backbone helix structure of YopO was assessed *in vitro* by DQC and PELDOR measurements on the labeled full-length and soluble YopO constructs (Figure 85). DQC experiments were performed at 70 K to exploit the faster T_1 relaxation time of SLIM **3•** and to increase the shot-repetition time.

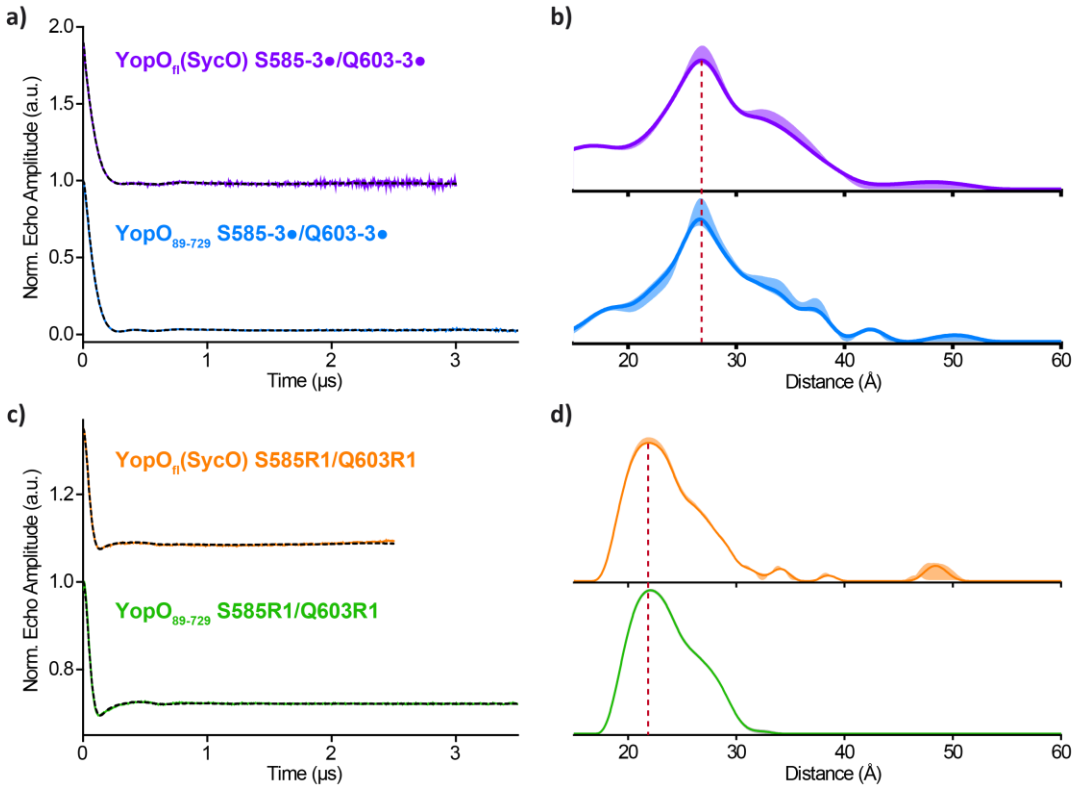

Figure 85: Time traces and distance distributions for the SLIM **3•-** and MTSL-labeled full-length and soluble YopO constucts. **a)** Background-corrected DQC time traces of YopO$_{fl}$(SycO) S585-**3•**/Q603-**3•** (purple) and YopO$_{89-729}$ S585-**3•**/Q603-**3•** (blue) with the fits obtained by Tikhonov regularization (black dashed). For clarity, the trace of YopO$_{fl}$(SycO) S585-**3•**/Q603-**3•** is shifted on the y-axis. **b)** Distance distributions obtained from the time traces in **(a)** using the same color code with the DeerAnalysis validation shown as shaded areas. The red vertical bar corresponds to the most probable distance obtained for the full-length construct. The complete analysis by DeerAnalysis (raw time trace, background, L-curves, and distance distributions) is given in the appendix (Figure A40a+b). **c)** Background corrected PELDOR time traces of YopO$_{fl}$(SycO) S585R1/Q603R1 (orange) and YopO$_{89-729}$ S585R1/Q603R1 (green, taken from section 3.1.4) with the fits obtained by Tikhonov regularization (black dashed). For clarity, the trace of YopO$_{fl}$(SycO) S585R1/Q603R1 is shifted on the y-axis **d)** Distance distributions obtained from the time traces in **(c)** using the same color code with the DeerAnalysis validation shown as shaded areas. The red vertical bar corresponds to the most probable distance obtained for the full-length construct. The complete analysis by DeerAnalysis for YopO$_{fl}$(SycO) S585R1/Q603R1 (background, L-curve, and distance distribution) is given in the appendix (Figure A40c).

For both spin labels, SLIM **3•** and MTSL, the time traces for full-length YopO in complex with SycO obtained for either SLIM **3•**/DQC (Figure 85a) or MTSL/PELDOR (Figure 85c) show the same oscillation period and damped oscillations as the respective truncated YopO$_{89-729}$ analog. Consequently, also the resulting distance distributions for both YopO variants, full-length and soluble, labeled with SLIM **3•** or MTSL, are almost identical (Figure 85b+d) regarding the most probable distance as well as the width and shape of the distributions. Based on these results, the structure of the α-helical GDI backbone of YopO$_{fl}$(SycO) is, at least in the upper region of the GDI backbone helix where the labeling positions S585C and Q603 are located, identical to its soluble YopO$_{89-729}$ analog and not influenced by SycO or the MLD region consisting of the amino acid residues 1-88.

To verify the successful transfection and localization of YopO inside HeLa cells, single-cysteine constructs of full-length and soluble YopO containing the N624C mutation (purification of YopO$_{fl}$(SycO) N624C shown in Figure A41) were labeled with the fluorescence dye Alexa Fluor™

488 C_5 maleimide. Similar to the trityl spin label, the Alexa488 fluorescence dye has a broad absorption range at 280 nm and a maximum absorbance at 493 nm (Figure 86a). To verify the labeling efficiencies, the same quantification routine as for the trityl labels (see section 3.2.2.1) was employed here using the experimental extincition coefficients $\varepsilon_{280}(\mathbf{A_{488}}) = 0.011\,\frac{\mathrm{cm}}{\mu\mathrm{M}}$ and $\varepsilon_{493}(\mathbf{A_{488}}) = 0.0071\,\frac{\mathrm{cm}}{\mu\mathrm{M}}$ for Alexa Fluor™ 488 C_5 maleimide obtained from the UV-vis spectrum of the free dye PBS buffer. Both soluble and full-length YopO were labeled at residue N624C, yielding the fluorescence-labeled constructs $YopO_{fl}$(SycO) N624-A_{488} and $YopO_{89\text{-}729}$ N624-A_{488} (Figure 86b+c + Table 25).

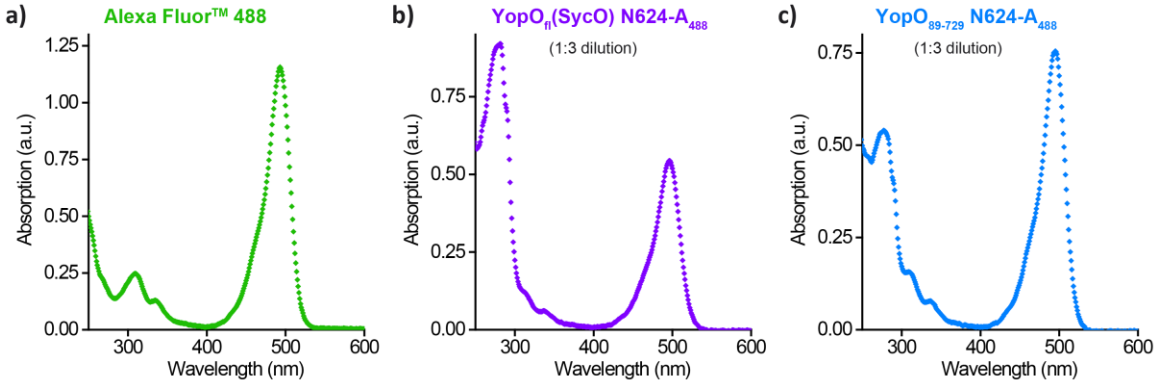

Figure 86: UV-vis spectra of free Alexa Fluor™ 488 and labeled full-length and soluble YopO. **a)** UV-vis spectrum of Alexa Fluor™ 488 (160 µM) in PBS buffer. **b)** UV-vis spectrum of $YopO_{fl}$(SycO) N624-A_{488} (85 µM, 1:3 dilution) in PBS buffer. **c)** UV-vis spectrum of $YopO_{89\text{-}729}$ N624-A_{488} (73 µM, 1:3 dilution) in PBS buffer. All spectra were recorded on a NanoDrop™ 2000.

Table 25: Labeling efficiencies of $YopO_{fl}$(SycO) N624-A_{488} and $YopO_{89\text{-}729}$ N624-A_{488} determined by UV-vis spectroscopy.

Sample	YopO [µM]	Alexa Fluor488™ [µM]	Labeling efficiency
$YopO_{fl}$(SycO) N624-A_{488}	254	230	90%
$YopO_{89\text{-}729}$ N624-A_{488}	220	260	118%

Labeling of the full-length construct was almost quantitative while slight over-labeling (118%) of the soluble YopO construct was observed. However, the small amount of remaining free label was considered negligible for the subsequent transfection experiments.

3.2.7.4 Transfection and PDS-EPR of YopO inside HeLa cells

HeLa cells were shown to have high viability after transfection and recombinant protein delivery via electroporation (EP).[410] As a large number of cells is required to fill the cavity of the EPR resonator, EP was chosen as the delivery method since it is more easily scalable and more cost-efficient than transfection based on chemical permeabilization of the cell membrane. The electroporation protocol was adapted using the workflow described by *Kucher* et al.[387] and HeLa cells were provided by *Philipp Schult* of the *Paeschke* group at the University Clinics Bonn. Initial transfections into HeLa cells were performed using the soluble $YopO_{89\text{-}729}$ construct due to its enhanced stability, availability in high yields, and ease of handling compared to the more aggregation-prone and less stable full-length construct. The idea was to develop a universal EP protocol that can be subsequently applied to other proteins such as full-length YopO.

After the EP and subsequent recovery period (3.5 h), HeLa cells were mostly adherent and appeared healthy upon visual inspection under a light microscope, with some cells already adapting the characteristic epithelial-like shape while others were still rounded as a consequence of an incomplete adherence process during the recovery period (Figure 85a). The successful delivery of YopO S585-**3•**/Q603-**3•** into HeLa cells was confirmed by comparison of the field-swept EPR spectra of HeLa cells electroporated with YopO S585-**3•**/Q603-**3•** and a Mock sample where cells were incubated with YopO S585-**3•**/Q603-**3•** but no EP was performed (Figure 87b+c).

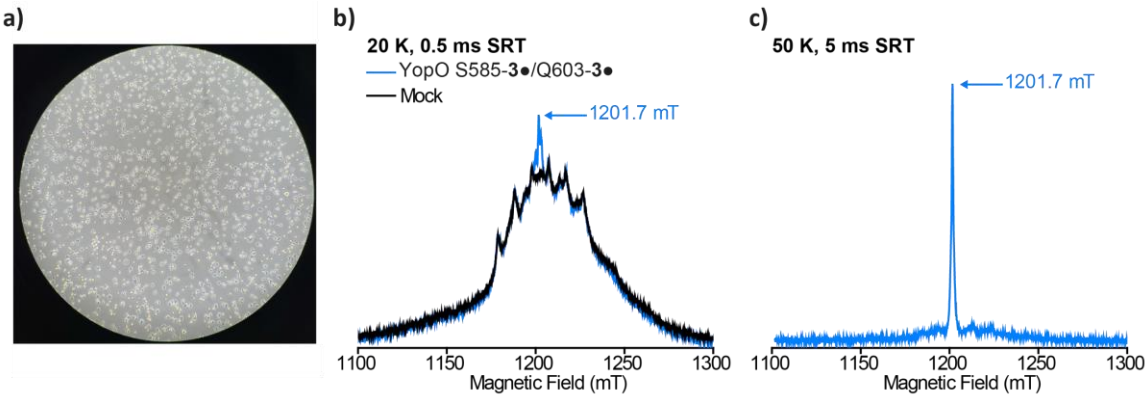

Figure 87: HeLa cell recovery and field-swept EPR spectra of HeLa cells transfected with YopO S585-**3•**/Q603-**3•**. **a)** Light microscope image (24x zoom) of electroporated HeLa cells on the culture dish after 3.5 h recovery. Picture taken through the lens of the microscope with a smartphone. **b)** Q-band field-swept EPR spectra of HeLa cells electroporated with YopO S585-**3•**/Q603-**3•** (blue) and the Mock sample (black, no EP performed) recorded at 20 K with an SRT of 0.5 ms. **c)** Q-band field-swept EPR spectra of the sample with the electroporated cells in **(b)** recorded at 50 K with an SRT of 5 ms.

At 20 K and a short SRT of 0.5 ms, the field-swept EPR spectrum of both, the transfected and the Mock cells, is dominated by the signal of endogenous Mn^{2+} (Figure 87b), similar to the EPR spectrum recorded earlier for *Xenopus laevis* oocytes (see Figure 80a). However, even at these low temperatures, an additional signal at 1201.7 mT is observed in the transfected cells, which is absent in the Mock sample, thereby indicating the successful removal of non-internalized labeled proteins after trypsinization of the cells. At elevated temperatures (50 K) and an increased SRT (5 ms), the field-swept EPR spectrum is dominated by the signal at 1201.7 mt corresponding to YopO S585-**3•**/Q603-**3•** (Figure 87b). Lowering the protein concentrations from 30 µM to 20 µM during the electroporation step of the HeLa cells resulted in a narrowed field-swept EPR spectrum and a longer phase memory time T_M (Figure 88 + Table 26).

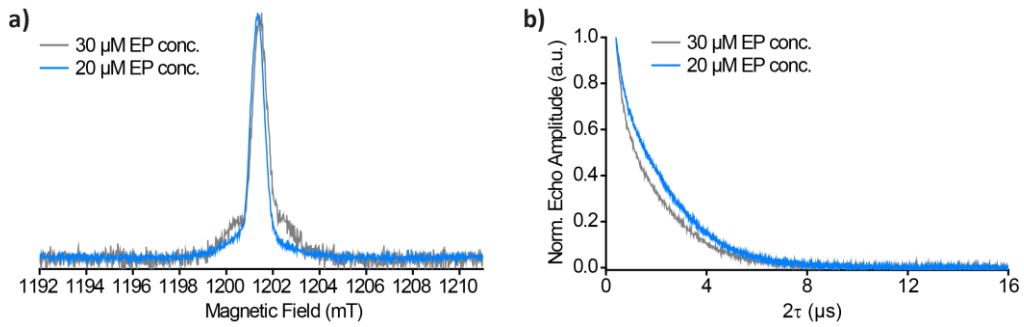

Figure 88: Field-swept EPR spectra and 2pESEEM traces of HeLa cells transfected at varying concentrations of YopO S585-**3**•/Q603-**3**•. **a)** Normalized Q-band field-swept EPR spectra at 70 K of HeLa cells electroporated with 30 µM (grey) and 20 µM (blue) initial YopO S585-**3**•/Q603-**3**• concentration. **b)** Normalized 2pESEEM traces of HeLa cells electroporated at 30 µM (grey) and 20 µM (blue) initial YopO S585-**3**•/Q603-**3**• concentration, recorded at 70 K.

Table 26: Phase memory times T_M of YopO S585-**3**•/Q603-**3**• in HeLa cells at 30 µM and 20 µM initial EP concentration obtained by fitting eq. 20 to the respective traces shown in Figure 88b.

EP concentration	T_M (µs)
30 µM	1.2
20 µM	2.0

The broad shoulders observed in the field-swept EPR spectrum of the 30 µM EP concentration sample are likely caused by spin clustering as a result of protein aggregation, a phenomenon previously observed for the trityl-labeled BtuB membrane protein.[277] This hypothesis is further supported by the shorter phase memory time (T_M = 1.2 µs) obtained for EP concentrations of 30 µM labeled YopO S585-**3**•/Q603-**3**• compared to the lower concentration of 20 µM at the EP step (T_M = 2.0 µs).[402]
Owing to the prolonged phase memory time and the assumed absence of protein aggregation, a DQC time trace on the HeLa cells electroporated with 20 µM YopO S585-**3**•/Q603-**3**• was recorded (Figure 89).

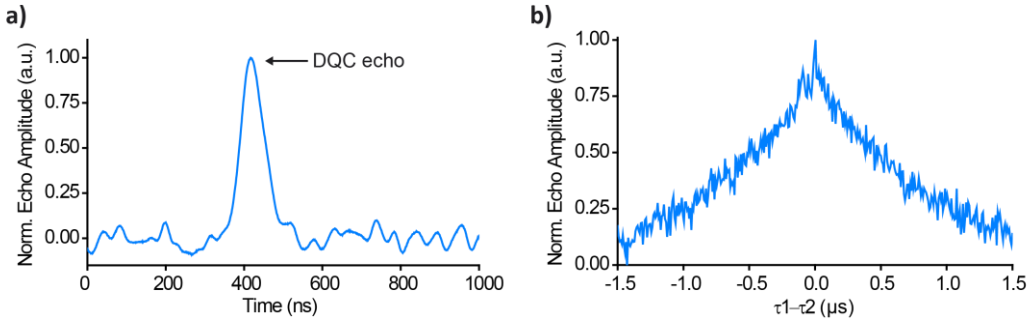

Figure 89: DQC echo and DQC time trace of YopO S585-**3**•/Q603-**3**• transfected into HeLa cells. **a)** Q-band DQC echo of YopO S585-**3**•/Q603-**3**• in HeLa cells at 70 K after the 64-step phase cycle at $\tau_1 = \tau_2$ =950 ns. **b)** Raw DQC time trace of YopO S585-**3**•/Q603-**3**• inside HeLa cells.

Although a clear DQC echo was observed when setting up the DQC experiment (Figure 89a), almost no modulation depth and no oscillations were observed in the final DQC time trace (Figure 89b) and accordingly, no further efforts were undertaken to infer a distance distribution. There are two plausible explanations for the poor quality of the DQC data: First, during the 3.5 h

recovery period of the HeLa cells, partial reduction of the spin centers in YopO S585-**3•**/Q603-**3•** has occurred, leading to singly-labeled YopO and thus a significantly reduced number of dipolar-coupled spins. Secondly, although the field-swept EPR spectrum and the 2pESEEM trace showed no indication of protein aggregation, a substantial amount of YopO S585-**3•**/Q603-**3•** has formed aggregates or clusters within the HeLa cells during the EP process or recovery period, which results in a broad range of interspin distances and therefore no visible oscillations. The first hypothesis is supported by the shape of the DQC time trace of YopO S585-**3•**/Q603-**3•** in HeLa cells, which is similar to the trace obtained for singly-labeled YopO L113-**2•** (see Figure 56), thereby suggesting a stronger reduction of SLIM **3•** in whole cells compared to the previously tested cell lysates. To verify the second hypothesis, fluorescence images of analogously prepared HeLa cells transfected with fluorescence-labeled soluble YopO N624-A_{488} were recorded by *Philipp Schult* (Figure 90).

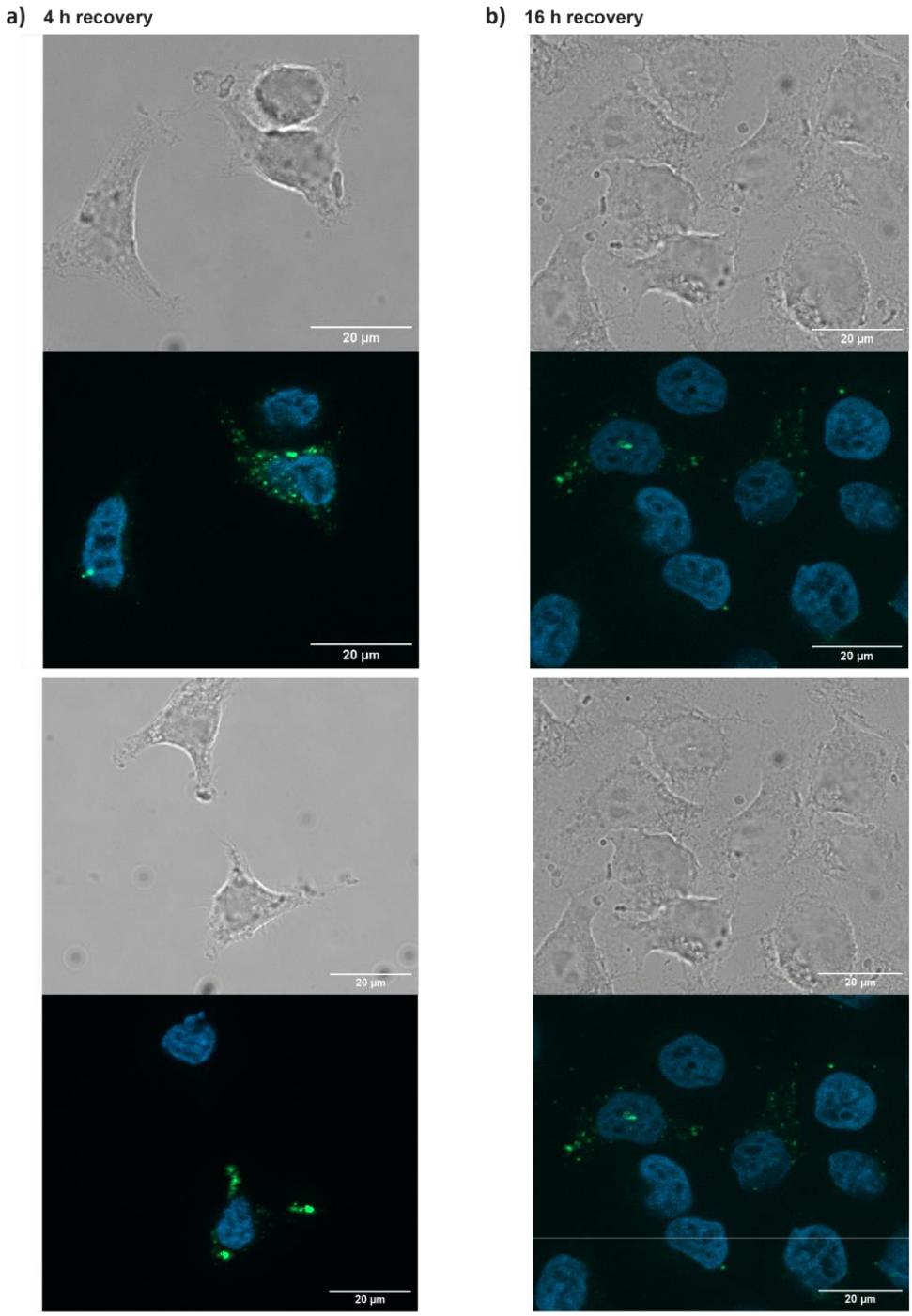

Figure 90: Brightfield and fluorescence images of fixed HeLa cells (4% paraformaldehyde) after 4 h and 16 h recovery electroporated with YopO N624-A_{488} and nuclei stained with 4',6-diamidino-2-phenylindole (DAPI). **a)** Brightfield (top) and corresponding fluorescence image (bottom) of HeLa cells after 4 h recovery. Fluorescence images comprise the merged channels for DAPI excitation at 385 nm (filter cut: 430 nm– 470 nm) and Alexa Fluor™ 488 excitation at 475 nm (filter cut: 500 nm – 550 nm). **b)** Same as **(a)** but here, HeLa cells were fixed after 16 h recovery.

After a recovery period of 4 h, HeLa cells appeared viable (Figure 90a) and mostly adapted the characteristic epithelial-like shape. However, the distribution of YopO N624-A_{488} among the HeLa cells upon electroporation was uneven with some cells containing more fluorescence-labeled protein than others (see Figure 90a, bottom). Additionally, and contrary to the expectation for soluble YopO lacking the membrane localization domain, an inhomogeneous distribution of

fluorescence-labeled protein with large clusters within the HeLa cytosol was observed, evidenced by bright green spots in the cells at an excitation wavelength of 475 nm. After a 16 h recovery period, the same local clustering of YopO within the HeLa cells was observed. These observations indicate that under the chosen EP conditions, YopO forms dense aggregates within the HeLa cytosol and consequently, the DQC time trace shown above (Figure 89b) does not only comprise the intramolecular dipolar coupling but to a large extent also intermolecular contributions.
While these initial experiments could demonstrate that the labeled, truncated $YopO_{89\text{-}729}$ can be transfected into HeLa cells at amounts sufficient to detect an EPR signal and record a DQC time trace as well as to observe a fluorescence signal and localize the protein, the results obtained so far are insufficient for a conclusive biological interpretation. The electroporation procedure is assumed to be the bottleneck of the *in-cell* experiments and needs further optimization to guarantee the structural integrity of YopO while, on the other hand, ensuring the viability of the HeLa cells. Only if these criteria are fulfilled, the method can be applied to more advanced systems such as the full-length YopO construct. The optimization of the EP procedure is subject of ongoing studies within the *Schiemann* group.

3.2.8 Hydroxylated Short-Linked Maleimide Trityl Spin Label Ox-SLIM 4•

The short-linked maleimide motif introduced with SLIM **3•** was shown to reduce the conformational flexibility of the spin label, providing narrow distance distributions, and enhance the redox stability of the label. While the protocol developed herein allows site-selective labeling with maleimide-functionalized trityl spin labels, the labeling and work-up procedure is laborious compared to standard nitroxide labeling with, e.g., MTSL, as it requires larger volumes and two chromatographic steps (benchtop PD-10 column followed by a desalting run on a medium-pressure liquid chromatography (MPLC) system). This more demanding work-up is a consequence of the inherent hydrophobicity of trityl labels and their tendency to self-aggregate[276] and bind unspecifically to protein surfaces.[263] To cope with these hydrophobic interactions and to simplify the spin labeling process, the new trityl spin label Ox-SLIM **4•** (Figure 91) was designed and synthesized by *Nico Fleck*.

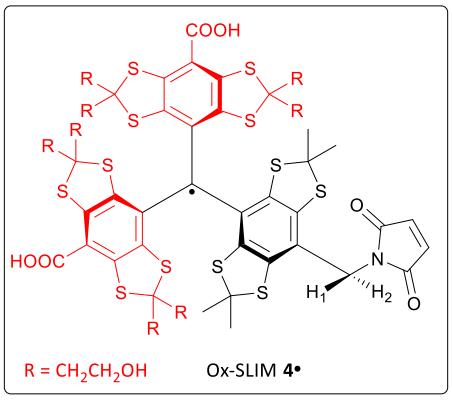

Figure 91: Chemical structure of the Ox-SLIM **4•** trityl spin label. The two bisthioketalaryl moieties displayed in red harbor hydroxyethyl sidechains (R = CH_2CH_2OH) for enhanced water solubility while the aryl substituent shown in black bears the maleimide bioconjugation group. The two chemically inequivalent hydrogen atoms H_1 and H_2 are shown for clarity.

Built of two hydroxylated bisthioketalaryl moieties for enhanced hydrophilicity and one non-hydroxylated bisthioketalaryl unit harboring the benzylic maleimide for bioconjugation, the Ox-SLIM **4•** spin label resembles a chimera of the Ox063 trityl and SLIM **3•**. Cw-EPR

characterization of Ox-SLIM **4•** in PBS buffer by *Nico Fleck* revealed a similar room temperature X-band EPR spectrum as SLIM **3•** with nine resolved lines arising from hyperfine coupling to the benzylic nitrogen atom and the two magnetically inequivalent hydrogen atoms H_1 and H_2 (Figure 92a). However, in contrast to SLIM **3•**, the EPR spectrum in frozen solution gives rise not only to the expected doublet but also exhibits a superimposed Pake pattern with a ratio of 69:31 (Figure 92b). Analysis of the Pake pattern revealed a short interspin distance of 9.9 Å and is attributed to a non-covalent dimer $(\mathbf{4•})_2$ of Ox-SLIM **4•** whose existence is further supported by ESI(-)-MS studies (data not shown) and DFT calculations provided by *Sebastian Spicher*, which revealed a dimer $(\mathbf{4•})_2$ stabilized by hydrogen bonds (Figure 92c).[372]

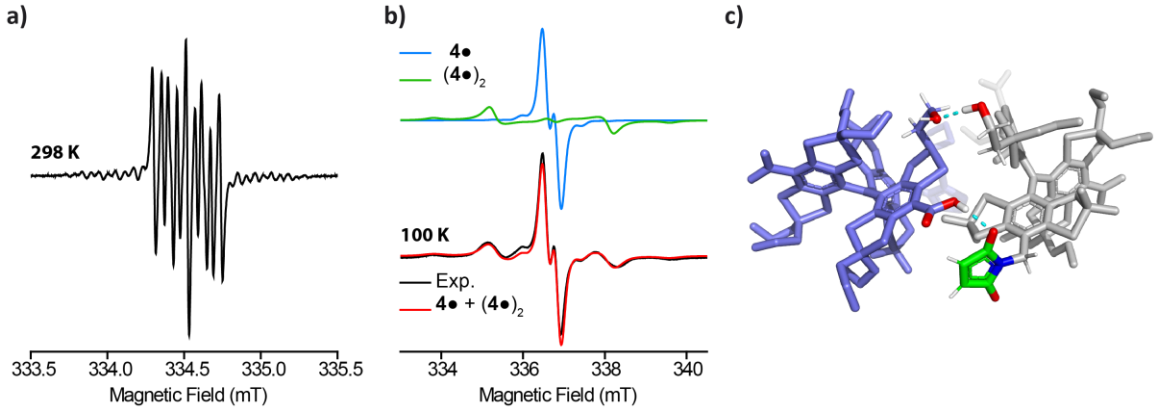

Figure 92: X-band cw-EPR spectra and simulations of Ox-SLIM **4•** and the DFT structure of $(\mathbf{4•})_2$. **a)** X-band cw-EPR spectrum of Ox-SLIM 4• (100 µM) in PBS at 298 K. **b)** X-band cw-EPR spectrum of Ox-SLIM 4• (100 µM) in PBS (+20% glycerol) at 100 K (black, bottom) and the simulation (red, bottom) as the sum of a monomer (blue, top) and dimer (green, top) of Ox-SLIM **4•**. **c)** DFT structure of $(\mathbf{4•})_2$ with the stabilizing hydrogen bonds represented as cyan dashed lines. For measurement parameters and simulation details refer to the primary publication.[372]

3.2.8.1 Site-directed Spin Labeling with Ox-SLIM 4•

To exploit the enhanced water solubility of Ox-SLIM **4•** and assess the separability of the spin label at concentrations above the critical self-assembly concentration of non-hydroxylated trityls (~60 µM), the previously employed cysteine-free YopO-wt and the double-cysteine construct YopO Y588C/N624C were incubated with Ox-SLIM **4•** using a 20-fold molar excess per protein, resulting in a final spin label concentration of 100 µM Ox-SLIM **4•** which is well above the 33 µM used in previous labeling schemes for Mal-TSL **2•** and SLIM **3•**. After work-up via SEC, labeling efficiencies were assessed via UV-vis spectroscopy using the previously introduced main-peak quantification method and extinction coefficients $\varepsilon_{271}(\mathbf{4•}) = 0.0574\,\frac{\mathrm{cm}}{\mu\mathrm{M}}$ and $\varepsilon_{459}(\mathbf{4•}) = 0.0204\,\frac{\mathrm{cm}}{\mu\mathrm{M}}$ for Ox-SLIM **4•** determined from the UV-vis spectrum of the free label (Figure 93 + Table 27).

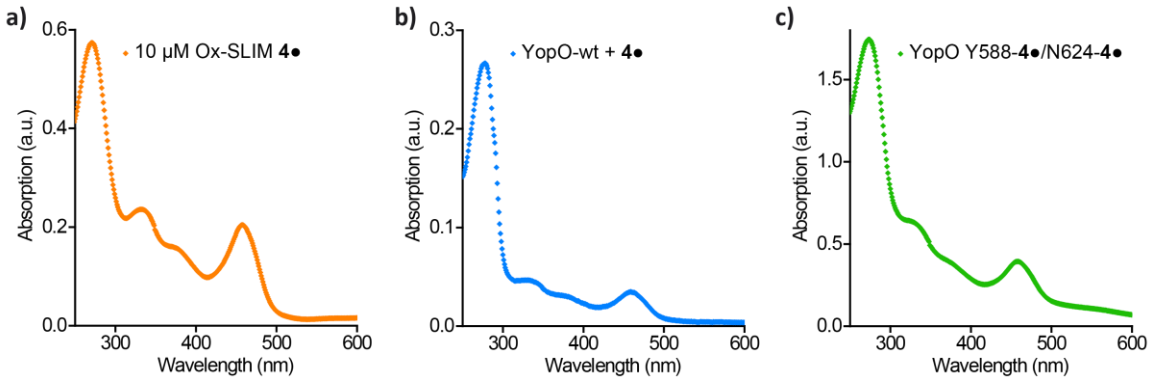

Figure 93: UV-vis spectra of free Ox-SLIM **4•**, and YopO-wt and YopO Y588C/N624C labeled with **4•**. **a)** UV-vis spectrum of free Ox-SLIM **4•** (10 µM) in PBS buffer. **b)** UV-vis spectrum of YopO-wt after incubation with 20 equivalents of **4•** and excess label removal. **c)** UV-vis spectrum of labeled YopO Y588-**4•**/N624-**4•** after excess label removal. All spectra were recorded on a Cary100 UV-vis spectrometer.

Table 27: Labeling efficiencies of YopO-wt and YopO Y588-**4•**/N624-**4•** determined from the UV-vis spectra in Figure 93.

Sample	YopO [µM]	Ox-SLIM 4• [µM]	Labeling efficiency
YopO-wt + 4•	3.39	1.71	50%[a]
YopO Y588-4•/N624-4•	12.8	19.3	75%[b]

[a] Given as equivalents of Ox-SLIM **4•** per YopO-wt molecule.
[b] Given as equivalents of Ox-SLIM **4•** per available cysteine.

Albeit labeling the same YopO construct with SLIM **3•** at a lower label concentration (33 µM) during the labeling reaction resulted in a higher labeling efficiency (~96%), the high-concentration labeling (100 µM) of YopO Y588C/N624C with Ox-SLIM **4•** gave a satisfactory labeling efficiency of 75%. On the other hand, the labeling of the cysteine-free YopO-wt should result in complete separation of Ox-SLIM **4•**; however, after SEC, a substantial amount (0.5 eq. per YopO) of the label remained in the protein-containing fraction and unspecific binding to the protein was suspected. Therefore, the unspecific binding of Ox-SLIM **4•** and the two previously employed trityl spin labels Mal-TSL **2•** and SLIM **3•** to cysteine-free YopO-wt was assessed via cw-EPR spectroscopy (Figure 94a). Binding of the spin label to the protein leads to immobilization, thereby broadening the EPR signal and reducing the peak-to-peak (p2p) signal intensity. This signal depletion has been used previously as a semi-quantitative measure of non-specific label attachment to proteins.[260,263,278] Surprisingly, while Mal-TSL **2•** and SLIM **3•** showed a high tendency to bind to YopO-wt at increased protein concentrations leading to lowered p2p EPR signal intensities, Ox-SLIM **4•** remained inert: Even at a protein concentration of 350 µM, only a marginal decrease of the p2p EPR signal by 3% was observed, thereby indicating no unspecific binding or interaction with the protein surface. Hence, the over-labeling of YopO-wt and the inseparability of Ox-SLIM **4•** after SEC is not related to the binding of the label to the protein, but potentially to the high label excess and the presence of the previously observed label-dimer $(\mathbf{4•})_2$ which is potentially large enough to surpass the SEC exclusion limit and column capacity. The hypothesis of the presence of $(\mathbf{4•})_2$ was verified by DQC experiments on the doubly-labeled YopO Y588-**4•**/N624-**4•** and free label **4•** (Figure 94b).

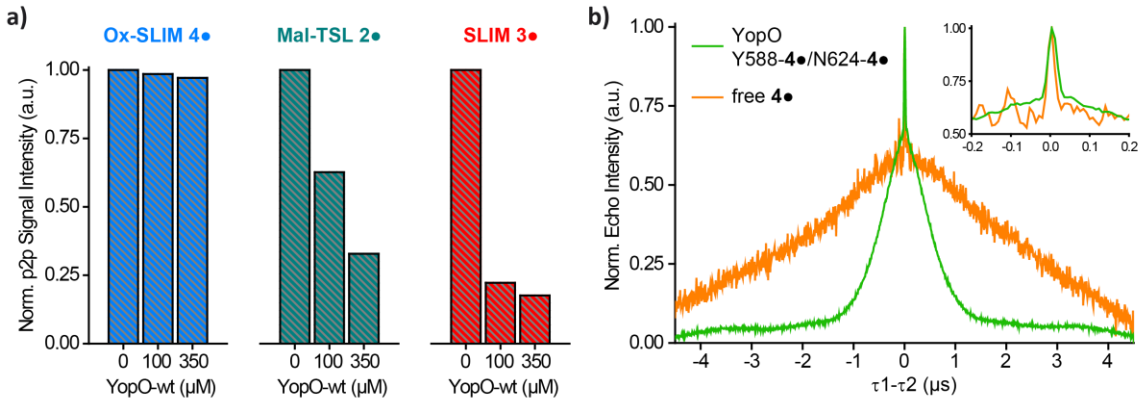

Figure 94: Cw-EPR signal intensities of Ox-SLIM **4•**, Mal-TSL **2•**, and SLIM **3•** incubated with YopO-wt and DQC time traces of YopO Y588-**4•**/N624-**4•** and free Ox-SLIM **4•**. **a)** Bar diagram showing the normalized X-band cw-EPR p2p signal intensities of Ox-SLIM **4•** (blue), Mal-TSL **2•** (cyan), and SLIM **3•** (red) incubated with YopO-wt at various protein concentrations. The cw-EPR spectra (see appendix Figure A42) were recorded on an EMXmicro spectrometer. **b)** Normalized Q-band DQC time traces of YopO Y588-**4•**/N624-**4•** (40 µM spins, green) and free Ox-SLIM **4•** (40 µM, orange) recorded at 50 K. The inset highlights the initial decay from 0.0 µs – 0.2 µs.

Both DQC time traces showed a fast decay (inset Figure 94b) to 67% of the initial echo intensity within 0.05 µs, indicative of short inter-spin distances caused by the presence of (**4•**)$_2$. Interestingly, a similar observation was later found in DQC experiments by *Hasanbasri* et al. for GB1 labeled with a deuterated maleimide-derivative of the Ox063 trityl (mOx063-d$_{24}$).[411] In this study, the authors assigned the sharp initial decay in the DQC time trace to an artifact arising from the first and fourth pulse in the 6-pulse DQC sequence, which is not completely removed by the 64-step phase cycle. As no concentrations for the labeling reaction were stated, no low-temperature cw-EPR spectra were recorded, but complete removal of mOx063-d$_{24}$ from a cysteine-free GB1 control protein was reported, a similar dimerization of the spin label to (mOx063-d$_{24}$)$_2$ can neither be confirmed nor excluded.

To test whether the separation of Ox-SLIM **4•** can be facilitated using the previously established trityl labeling protocol operating at lower trityl concentrations during the labeling and work-up, both YopO-wt and YopO Y588C/N624C were labeled according to that protocol (see section 3.2.2.2) using a 5-fold excess of Ox-SLIM **4•** per cysteine (Figure 95 + Table 28).

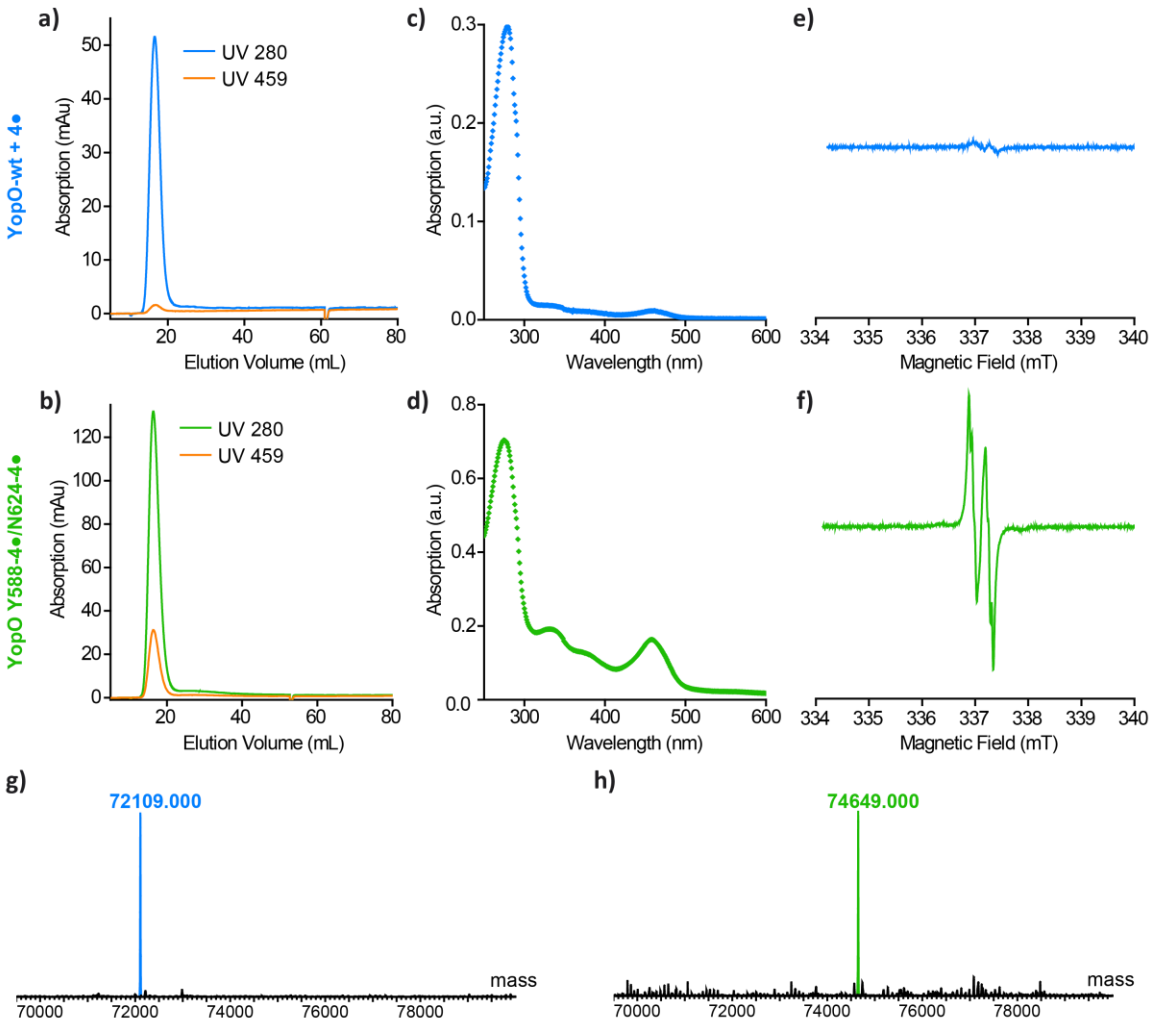

Figure 95: Labeling results for YopO-wt and YopO Y588C/N624C with Ox-SLIM **4•**. **a+b)** Chromatograms of the HiPrep™ 26/10 runs of YopO-wt **(a)** and YopO Y588-**4•**/N624-**4• (b)** after labeling with Ox-SLIM **4•**. **c+d)** UV-vis spectra of YopO-wt **(c)** and YopO Y588-**4•**/N624-**4• (d)** after excess label removal recorded on a Cary100 UV-vis spectrometer. **e+f)** Room temperature X-band cw-EPR spectra of YopO-wt (64 µM) **(e)** and YopO Y588-**4•**/N624-**4•** (43 µM) **(f)** recorded on a Bruker EMXmicro spectrometer. Measurement settings: 9.455 GHz microwave frequency, 0.605 mW microwave power, 100 kHz modulation frequency, 0.2 G modulation amplitude, 20.48 ms time constant, 500 pts/mT. **g+h)** Deconvoluted high-resolution ESI(+)-MS spectra of YopO-wt **(g)** and YopO Y588-**4•**/N624-**4• (h)** recorded on a Waters Synapt G2-SI spectrometer by the mass spectrometry facility in Marburg. The colored peaks correspond to unlabeled YopO-wt (blue) and doubly-labeled YopO Y588-**4•**/N624-**4•** (green), respectively. The raw mass spectra are shown in the appendix (Figure A43).

Table 28: Labeling efficiencies of YopO-wt and YopO Y588-**4•**/N624-**4•** determined from the UV-vis spectra in Figure 95.

Sample	YopO [µM]	Ox-SLIM 4• [µM]	Labeling efficiency
YopO-wt + 4•	5.4	0.4	7%[a]
YopO Y588-4•/N624-4•	4.8	8.1	85%[b]

[a] Given as equivalents of Ox-SLIM **4•** per YopO-wt molecule.
[b] Given as equivalents of Ox-SLIM **4•** per available cysteine.

Contrary to the labeling at high trityl concentrations, lowering the trityl concentration in the labeling process allowed an almost quantitative removal of Ox-SLIM **4•** from the cysteine-free YopO-wt, as only minor UV absorption in the characteristic region at 459 nm was observed in the SEC run. Analysis of the subsequently recorded UV-vis spectrum yielded 0.07 equivalents of **4•** per YopO molecule (Figure 95a+c). Only a weak signal corresponding to the remaining Ox-SLIM **4•** was observed in the X-band cw-EPR spectrum (Figure 95e) and ESI(+)-MS confirmed the absence of covalent labeling with Ox-SLIM 4•, as a single high-intensity mass peak corresponding to unlabeled YopO-wt (calculated mass: 72,108.6 Da) was found (Figure 95g). After labeling of the double-cysteine construct YopO Y588C/N624C with Ox-SLIM **4•** using the same conditions, UV-vis analysis (Figure 95d) revealed a high labeling efficiency (85%) and the corresponding cw-EPR spectrum showed a strong signal with the two-line shape characteristic of highly immobilized SLIM-type trityl labels (Figure 95f). The high labeling efficiency was further confirmed by ESI(+)-MS analysis, where a high-intensity mass peak at 74,649 Da (YopO Y588-**4•**/N624-**4•**: 74,645.7 Da) was observed (Figure 95h) aside from negligible impurities. Notably, the SNR of the ESI(+)-MS spectrum for YopO Y588-**4•**/N624-**4•** was significantly higher than the SNR of the spectra obtained previously for YopO labeled with SLIM **3•** and Mal-TSL **2•**. This is presumably related to the increased water solubility of Ox-SLIM **4•**-labeled YopO conferred by the peripheral hydroxyethyl side chains on two aryl rings of **4•**, thereby enhancing the protein stability compared to the more hydrophobic labels **2•** and **3•**. In compliance with the community-derived guidelines for EPR sample preparation, the autophosphorylation capability of spin-labeled YopO Y588-**4•**/N624-**4•** in the presence of G-actin was confirmed (Figure A44).

3.2.8.2 PDS-EPR with Ox-SLIM 4•-labeled YopO

The spin-lattice relaxation time T_1 and the phase memory time T_M of bioconjugated Ox-SLIM **4•** at 50 K were determined by inversion recovery and 2pESEEM experiments on the doubly-labeled YopO Y588-**4•**/N624-**4•** construct (Figure 96 + Table 29). The EPR experiments were conducted under the guidance and with *Tobias Hett*.

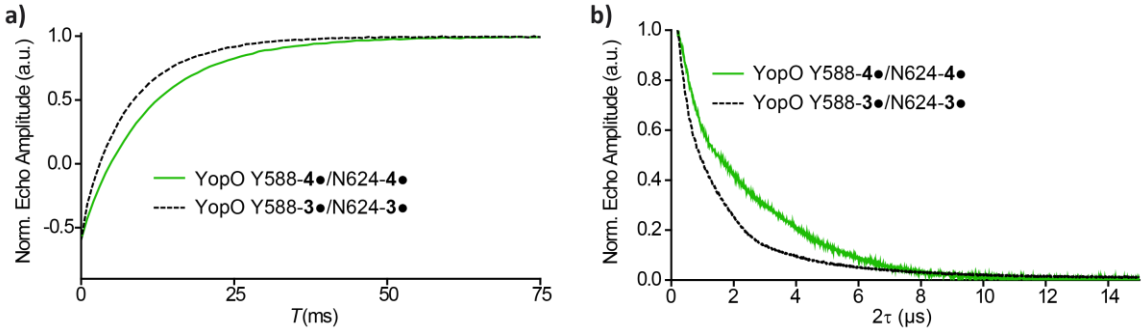

Figure 96: Electron spin relaxation measurements of YopO Y588-**4•**/N624-**4•**. **a)** Inversion recovery trace of YopO Y588-**4•**/N624-**4•** (green) in deuterated PDS buffer at a protein concentration of 18.5 µM at 50 K. For comparison, the inversion recovery trace of YopO Y588-**3•**/N624-**3•** (25 µM) at 50 K is shown as a black dashed line. **b)** 2pESEEM traces for YopO Y588-**4•**/N624-**4•** (green) in deuterated PDS buffer at a protein concentration of 18.5 µM at 50 K. For comparison, the 2pESEEM trace of YopO Y588-**3•**/N624-**3•** (25 µM) at 50 K is shown as a black dashed line.

Table 29: Spin-lattice relaxation times T_1 and phase memory times T_M of YopO Y588-**4•**/N624-**4•** obtained by fitting either eq. 19 (Inversion recovery) or eq. 20 (2pESEEM) to the respective traces shown in Figure 96.

Sample	T_1 (ms)	T_M (µs)
YopO Y588-**4•**/N624-**4•**	11.0	4.0
YopO Y588-**3•**/N624-**3•**	7.8	1.5

The inversion recovery experiments at 50 K revealed a slightly increased spin-lattice relaxation time of Ox-SLIM **4•** compared to SLIM **3•** (Figure 94a), resulting in a longer time before the pulse sequence can be repeated (increased SRT); an undesired effect for PDS experiments.[411] However, the decreased spin-lattice relaxation is compensated by a 2.7-times longer phase memory time for Ox-SLIM **4•** (T_M = 4.0 µs) compared to SLIM **3•** (T_M = 1.5 µs), leading to a significant gain in the sensitivity and the accessible distance range by PDS-EPR. These findings are in good agreement with studies by *Tormyshev* et al. on human serum albumin (HSA) labeled with a methanethiosulfonate-functionalized deuterated Ox063 derivative (T_M = 6.3 µs at 50 K),[412] the aforementioned GB1 labeled with mOx063-d_{24} (T_M = 5.1 µs at 80 K) reported by *Hasanbasri* et al.,[411] and BtuB labeled with a non-deuterated methanethiosulfonate-functionalized Ox063 label (T_M = 5.1 µs at 50 K) reported by *Ketter* et al.[217]

Although the phase memory time of protein-conjugated Ox-SLIM **4•** is shorter compared to Ox063-type trityl labels where all thioketal motifs functionalized by hydroxyethyl groups, a clear improvement compared to SLIM **3•** is evident. To quantify how the enhanced phase memory time affects the performance of Ox-SLIM 4• in DQC experiments, DQC traces were recorded at 50 K on YopO Y588-**4•**/N624-**4•** and the previously shown YopO Y588-**3•**/N624-**3•** analog (see section 3.2.4.4) with a length of 7 µs. In addition, to assess the sensitivity limit, a sample of YopO Y588-**4•**/N624-**4•** at a protein concentration of 45 nM was prepared and a DQC time trace with a length of 4.5 µs was recorded (Figure 97 + Table 30).

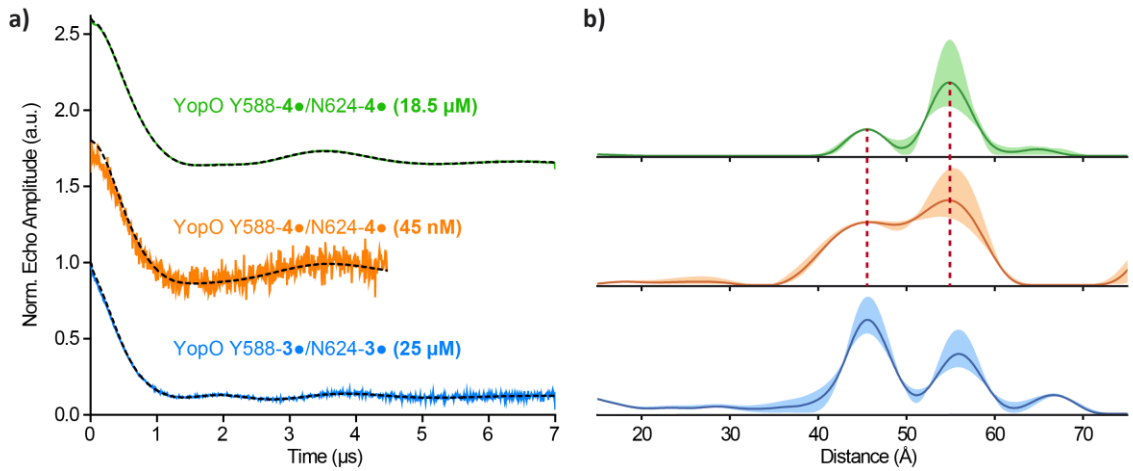

Figure 97: Background-corrected DQC time traces and resulting distance distributions of YopO Y588C/N624C labeled with Ox-SLIM **4•** or SLIM **3•**, respectively. **a)** Background-corrected DQC time traces of YopO Y588-**4•**/N624-**4•** at 18.5 µM (green), 45 nM (orange), and YopO Y588-**3•**/N624-**3•** at 25 µM (blue) protein concentration with the respective fits obtained from DeerAnalysis shown as black dashed lines. **b)** Corresponding distance distributions of the respective time traces in **(a)** using the same color code with the validation by DeerAnalysis shown as colored areas. The red bars indicate the most probable distance of the two main peaks obtained for YopO Y588-**4•**/N624-**4•** at 18.5 µM. The complete analysis by DeerAnalysis (raw time traces, backgrounds, L-curves, and distance distributions) is given in the appendix (Figure A45).

Table 30: SNR of the DQC time traces shown in Figure 97.

SNR related to	YopO Y588-4•/N624-4• (18.5 µM)	YopO Y588-4•/N624-4• (45 nM)	YopO Y588-3•/N624-3• (25 µM)
Acquisition time	2.2 $min^{-1/2}$	0.02 $min^{-1/2}$	0.76 $min^{-1/2}$
Acquisition time / conc.	0.12μM^{-1} $min^{-1/2}$	0.44 μM^{-1} $min^{-1/2}$	0.03 μM^{-1} $min^{-1/2}$

For all samples, high-quality DQC time traces were obtained. Most notably, in the case of Ox-SLIM **4•**-labeled YopO Y588C/N624C, the DQC trace did not show the fast-decay artifact at the beginning of the time trace as observed earlier (compare Figure 92) for protein labeling at high trityl concentrations. These results emphasize the necessity of labeling at low concentrations for complete removal of excess label **4•** and its corresponding dimer $(\mathbf{4•})_2$. The DQC time trace of YopO Y588-**4•**/N624-**4•** exhibited an SNR of 2.2 $min^{-1/2}$ which is almost thrice the SNR obtained for the SLIM **3•**-labeled analog (0.76 $min^{-1/2}$). Even at a concentration of 45 nM YopO Y588-**4•**/N624-**4•**, it was possible to record a DQC time trace with a length of 4.5 µs that showed the same oscillation period as the higher-concentration sample. With a trace length almost twice as long as previously achieved for 90 nM YopO labeled with SLIM **3•** (see section 3.2.6.1), the herein presented trityl/trityl DQC set yet another new benchmark for the sensitivity limit of trityl spin labels.

The distance distribution of YopO Y588-**3•**/N624-**3•** obtained from a DQC trace with a dipolar evolution time of 7 µs is bimodal and thus in good agreement with earlier data with shorter dipolar evolution times (see section 3.2.4.4). The distance distributions obtained at both concentrations - 18.5 µM and 45 nM - of YopO Y588-**4•**/N624-**4•** agreed well, with both distributions displaying bimodality that is more pronounced in the higher-concentrated sample, likely due to the enhanced SNR and trace length. Nonetheless, the most probable distances for both modes coincide extremely well at both concentrations (Figure 95b, red dashed lines), thereby emphasizing the robustness of the data analysis and the quality of the DQC time trace obtained at nanomolar concentrations. Interestingly, for both spin labels **3•** and **4•**, the probability distribution of the two modes is inverted (Figure 97b), thereby indicating that the spin label influences the population of the two postulated α-helix conformations (bent and straight). As these results seemed contradictory, the solution structure and conformation(s) of the YopO GDI domain backbone helix were to be assessed using other spin labeling strategies employing the dHis-Cu^{2+}(NTA) spin label (see chapter 3.3).

3.3 Differentiating between Label and Protein Conformers

Parts of this chapter have been published in:

[413] C. A. Heubach, Z. Hasanbasri, D. Abdullin, A. Reuter, B. Korzekwa, S. Saxena, O. Schiemann, "*Differentiating between Label and Protein Conformers in Pulsed Dipolar EPR Spectroscopy with the dHis-Cu^{2+}(NTA) Motif*", *Chem. Eur. J* **2023**, 29, e202302541.

As shown and discussed in chapters 3.1 and 3.2, PDS derived distance distributions of the α-helical backbone of YopO's GDI domain labeled with MTSL and trityl labels **2•**, **3•**, and **4•** were often bi- or multimodal. In some instances, e.g., for YopO Y588C/N624C, the bimodality was clearly resolved and reproduced to the same extent by two different labels (MTSL and SLIM **3•**, see section 3.2.4.4), which is a strong indication of two distinct conformations of a biomolecule. However, the same double-cysteine construct YopO Y588C/N624C labeled with Ox-SLIM **4•**, a highly hydrophilic label that is assumed to have no hydrophobic interactions with the protein backbone, had a changed distance distribution with the intensities of the two modes inverted compared to the MTSL- and SLIM 3•-labeled YopO construct. Hence, the formation of preferred label conformations cannot be ruled out at this point. A promising approach to disentangle the contributions of protein conformations and the label flexibility to the shape of the distance distribution is using a spin label with restricted conformational flexibility such as the bipedal dHis-Cu^{2+}(NTA) label. While the label was shown to yield narrow distance distributions,[296,297] it was mostly used in combination with the rigid GB1 model protein and, hence, YopO with its two closely related structure models of a straight (PDB-ID 2h7o) and bent (PDB-ID 4ci6) helix is an ideal case study to elucidate the capability of the dHis-Cu^{2+}(NTA) label to differentiate between protein and label conformations.

Two YopO constructs, each bearing two dHis-sites, were designed (Figure 98a) that closely resemble the mutants V599C/N624C and Y588C/N624, which showed the most pronounced bimodality in previous experiments. For the first YopO construct bearing the dHis-sites at A595H/V599H and S620H/N624H, herein referred to as YopO-short, *in silico* prediction by MMM[368,414] yields an interspin distance of 37.5 Å for the straight and 40.5 Å for the bent helix conformation (Figure 98b). For the second YopO construct with the dHis-sites located at Y588H/N592H and S620H/N624H, in the following termed YopO-long, the *in silico* prediction gives longer interspin distances of 48.5 Å (straight) and 50.5 Å (bent). In both cases, the labeling sites span the aforementioned hinge region of the α-helix where the two X-ray structure models deviate (see appendix Figure A5).

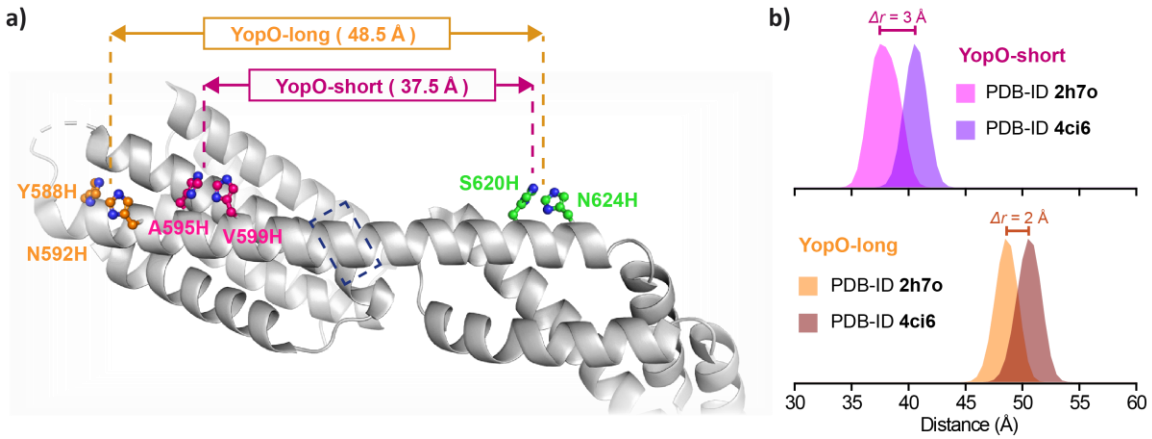

Figure 98: Labeling sites and *in silico* derived distance distributions for YopO-short and YopO-long. **a)** Model of the GDI domain of YopO (PDB-ID 2h7o) with the dHis-sites Y588H/N592H (orange), A595H/V599H (pink), and S620H/N624H (green) depicted as ball-and-stick models. Histidine mutations were introduced via the PyMOL mutagenesis tool. Pink (YopO-short) and orange (YopO-long) arrows indicate the mean distances predicted by MMM (input structure: PDB-ID 2h7o). The dashed blue box indicates the hinge region of the α-helix. **b)** *In silico* derived distance distributions by MMM for YopO-short (top) and YopO-long (bottom) using either PDB-ID 2h7o or PDB-ID 4ci6 as input structures.

3.3.1 Cu^{2+}(NTA) Labeling of YopO-short and YopO-long

Using the YopO-wt vector as a template, the dHis-sites of YopO-short and YopO-long were introduced by site-directed mutagenesis (Figure A46), and YopO-short and YopO-long were expressed and purified according to the protocol for soluble $YopO_{89\text{-}729}$ (Figure A47). Previous studies employing the dHis-Cu^{2+}(NTA) label focused on proteins with a low histidine abundance or without native histidines,[296,298,301] one buried histidine,[307,308] or five native histidines,[301] so a comprehensive study on the site-selectivity of Cu^{2+}(NTA) to the dHis motif in histidine-rich proteins lacks to date. As YopO contains 22 native histidine residues (Figure A48), it is a system suitable to elucidate the selectivity of Cu^{2+}(NTA) to the dHis motif in the vast presence of potentially competing coordination sites.

The labeling procedure with Cu^{2+}(NTA) was adapted from *Gamble Jarvi* et al. where labeling in a phosphate buffer with a 1:1 molar ratio of Cu^{2+}(NTA) to dHis-sites was shown to yield the least unspecific labeling and free Cu^{2+}(NTA).[305] To exclude binding of Cu^{2+}(NTA) to any of the native histidine residues, YopO-wt was labeled with Cu^{2+}(NTA) in addition to YopO-short and YopO-long and subsequently, cw-EPR spectra were recorded at 70 K and compared to a spectrum of free Cu^{2+}(NTA) (Figure 99 + Table 31).

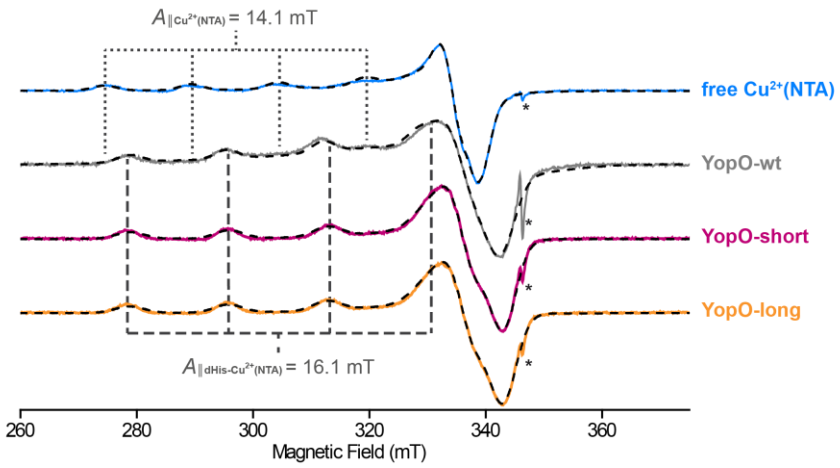

Figure 99: Normalized X-band cw-EPR spectra of free Cu^{2+}(NTA) (blue), YopO-wt incubated with one equivalent of Cu^{2+}(NTA) (grey), and YopO-short (pink) and YopO-long (orange) labeled with a 1:1 molar ratio of Cu^{2+}(NTA) with respect to available dHis-sites. All samples were prepared in dHis buffer (containing 50% v/v ethylene glycol-d_6) and spectra were recorded at 70 K on a Bruker EMXmicro spectrometer. The corresponding simulations by EasySpin are overlaid as black dashed lines. The vertical dotted (free Cu^{2+}(NTA)) and dashed (dHis-Cu^{2+}(NTA)) lines indicate the four peaks of the parallel component ($A_\parallel$) of the hyperfine splitting of Cu^{2+}. The signals marked by an asterisk stem from a resonator background artifact. Measurement settings: 9.400 GHz microwave frequency, 5.460 mW microwave power, 100 kHz modulation frequency, 4.0 G modulation amplitude, 20.48 ms time constant, 12.5 pts/mT.

Table 31: EasySpin[108] simulation parameters for the cw-EPR spectra shown in Figure 99 using the "pepper" function of EasySpin.

Sample		$g_\perp$	$g_\parallel$	$A_\perp$ (mT)	$A_\parallel$ (mT)
Free Cu^{2+}(NTA)		2.070	2.334	0.4	14.1
YopO-wt	Component 1	2.071	2.341	0.7	14.1
	Component 2	2.059	2.281	0.9	15.7
	Component 3	2.062	2.282	0.8	14.5
YopO-short		2.058	2.276	0.9	16.1
YopO-long		2.058	2.277	0.9	16.1

The cw-EPR spectrum of free Cu^{2+}(NTA) (Figure 99, blue) could be simulated using $g_\parallel$ = 2.334 and a hyperfine splitting $A_\parallel$ = 14.1 mT, which is in good agreement with previously reported simulation parameters of free Cu^{2+}(NTA) in phosphate buffer.[305] Interestingly, incubation of YopO-wt with a stoichiometric amount of Cu^{2+}(NTA) did not result in a similar spectrum as free Cu^{2+}(NTA), but in a spectrum with shifted *g*-values and hyperfine coupling constants *A* (Figure 99, grey). This spectrum could be simulated satisfactorily only by using a three-component system with components 1, 2, and 3 in the ratio 0.03 : 0.55 : 0.42. Based on the simulated $A_\parallel$ = 14.1 mT and $g_\parallel$ = 2.341, the minority component 1 is assigned to free Cu^{2+}(NTA) while the two other components 2 and 3 have $A_\parallel$ = 14.5 mT – 15.7 mT and $g_\parallel$ = 2.281 – 2.282, which are close to the shifts reported previously for histidine-bound Cu^{2+}(NTA).[305] Accordingly, in the absence of a dHis-site, unspecific binding of Cu^{2+}(NTA) to native histidines is observed and the resulting inhomogeneous coordination environment of Cu^{2+}(NTA) is emphasized by the necessity of at least three components to simulate the cw-EPR spectrum. As expected, the cw-EPR spectra of the Cu^{2+}(NTA)-labeled constructs YopO-short and YopO-long are shifted compared to free Cu^{2+}(NTA),

and the observed $A_{\parallel}$ = 16.1 mT and $g_{\parallel}$ = 2.276 – 2.277 agree well with the literature-reported values for dHis-Cu^{2+}(NTA) GB1.[415]
However, as $A_{\parallel}$ and $g_{\parallel}$ for YopO-short and YopO-long are very similar to the values obtained for YopO-wt incubated with Cu^{2+}(NTA), it is unclear whether Cu^{2+}(NTA) is bound only to the dHis-sites or also coordinated to other single histidines of YopO. To verify that all Cu^{2+}(NTA) is indeed bound only to the dHis-sites, RIDME experiments were performed on the aforementioned Cu^{2+}(NTA)-labeled YopO-wt and the single-dHis construct YopO S620H/N624H (prepared by *Benedict Korzekwa* during his Master thesis).[416] Both constructs were incubated with one molar equivalent of Cu^{2+}(NTA) (Figure 100).

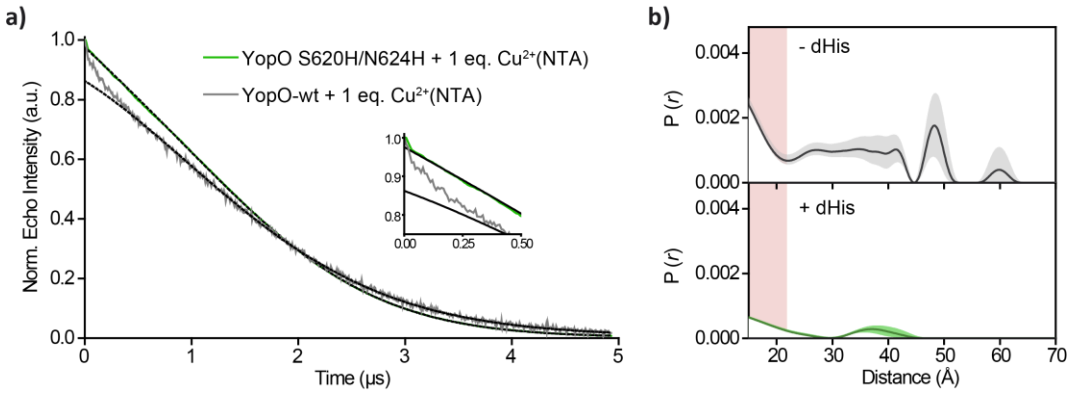

Figure 100: Q-band RIDME time traces and distance distributions of YopO-wt and YopO S620H/N624H labeled with Cu^{2+}(NTA). **a)** RIDME time traces of YopO-wt (100 µM, grey) and YopO S620H/N624H (100 µM, green) labeled with one equivalent of Cu^{2+}(NTA) to YopO. RIDME traces were recorded at 25 K. The corresponding background functions (4^{th}-order polynomial functions) are indicated by black dashed lines. The inset showing the start of the time traces highlights a RIDME artifact and differences in the modulation depths. **b)** Distance distributions of the respective time traces in **(a)** obtained from DeerAnalysis using the same color code. Distances in the region marked in red region stem from the artifact at the start of the RIDME time traces.[134]

The RIDME time trace of YopO-wt incubated with Cu^{2+}(NTA) showed a modulation depth of ~12%, indicative of intramolecular dipolar coupling between Cu^{2+} ions. On the other hand, except for a shallow initial decay attributed to an artifact of the five-pulse RIDME sequence,[134] the RIDME time trace of YopO S620H/N624H labeled with one equivalent of Cu^{2+}(NTA) showed no modulation depth (Figure 100a). The resulting distance distribution for YopO-wt incubated with Cu^{2+}(NTA) is broad and undefined, ranging from 15 Å to 55 Å. For YopO S620H/N624H containing a single dHis-site, the distribution is dominated by a short-distance peak originating from the RIDME artifact and only one additional peak between 30 Å and 45 Å is observed, which vanishes almost completely in the validation (Figure 100b). Conclusively, as soon as one dHis-site is present in YopO, Cu^{2+}(NTA) binds selectively to this motif until complete loading is achieved, and only if a stoichiometric excess of Cu^{2+}(NTA) to dHis-sites is applied, unspecific binding to other histidine residues occurs. These findings are in line with the reported low K_D values of Cu^{2+}(NTA) for dHis-sites located on an α-helix (<500 nM)[303] and highlight the applicability of the equimolar labeling scheme for Cu^{2+}(NTA) to dHis-sites, even in the presence of competing single-histidine residues. In this context, YopO served as a showcase to demonstrate that in contrast to other labeling schemes such as cysteine-SDSL where native cysteines generally have to be altered, a histidine-free construct is not necessary, thereby simplifying the experimental design and enhancing the scope of targetable proteins.

3.3.2 Structural Effects of dHis-Cu^{2+}(NTA) Complexation

To unequivocally resolve the solution structure of the GDI backbone α-helix and distinguish between the two closely related structural models, structure-perturbating effects of the dHis mutations or a stiffening of the helix upon Cu^{2+}(NTA) chelation have to be ruled out. To assess the influence of the dHis-sites and Cu^{2+}(NTA) labeling, CD spectra and melting curves of the labeled and unlabeled YopO mutants were recorded (Figure 101 + Table 32).

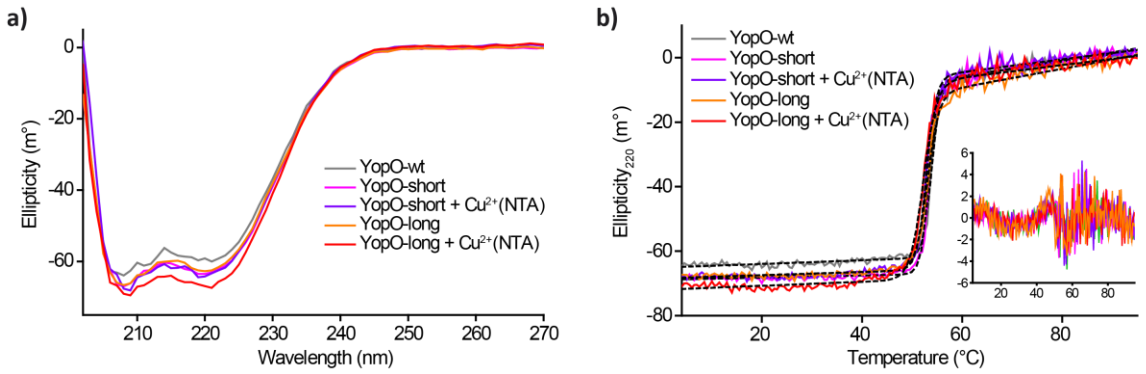

Figure 101: CD spectra and melting curves of Cu^{2+}(NTA)-labeled YopO and unlabeled YopO. **a)** CD spectra of YopO-wt (grey), YopO-short without (pink) and with Cu^{2+}(NTA) (purple), and YopO-long without (orange) and with Cu^{2+}(NTA) (red) at a protein concentration of 0.75 µM. **b)** Thermal melting curves of the samples in **(a)** using the same color code. The black dashed lines indicate fits to the melting curves using a two-state transition model of a monomer.[417] The inset shows the residual of experimental and fit curves.

Table 32: Melting temperatures T_m obtained from the fits to the respective melting curves of the YopO samples shown in Figure 101b.

Sample	T_m (°C)
YopO-wt	53.9
YopO-short	53.4
YopO-short + Cu^{2+}(NTA)	52.9
YopO-long	53.0
YopO-long + Cu^{2+}(NTA)	52.2

According to the CD spectra (Figure 101a), introducing and loading of the dHis-sites with Cu^{2+}(NTA) has a minimal effect on the protein folding as the ellipticity at 220 nm and 208 nm, indicative of a structured and mainly α-helical protein, remained almost unchanged.[418] The small deviations in the ellipticity are likely related to slight differences in the protein concentration during the sample preparation process. Contrary to previous studies on dHis-Cu^{2+}(NTA)-labeled GB1 where a stabilizing effect was observed upon complexation of Cu^{2+}(NTA),[297,298] the melting curves of labeled and unlabeled YopO (Figure 101b) revealed no stabilizing effect upon dHis introduction or Cu^{2+}(NTA) loading: While YopO-wt showed the highest thermal stability, the Cu^{2+}(NTA)-labeled constructs YopO-short and YopO-long had slightly lower melting temperatures than their corresponding unlabeled analogs (ΔT_m < 1 °C). Notably, as the K_D of Cu^{2+}(NTA) binding is temperature-dependent and is increased at higher temperatures,[303] it cannot be ruled out that a large fraction of the dHis-sites are depleted of Cu^{2+}(NTA) close to the thermal denaturing temperature of the protein.

In addition to the CD experiments, the structural integrity and catalytic activity of dHis-Cu^{2+}(NTA)-labeled YopO-short and YopO-long were assessed by monitoring the autophosphorylation capability of the protein in the presence of G-actin (Figure 102).

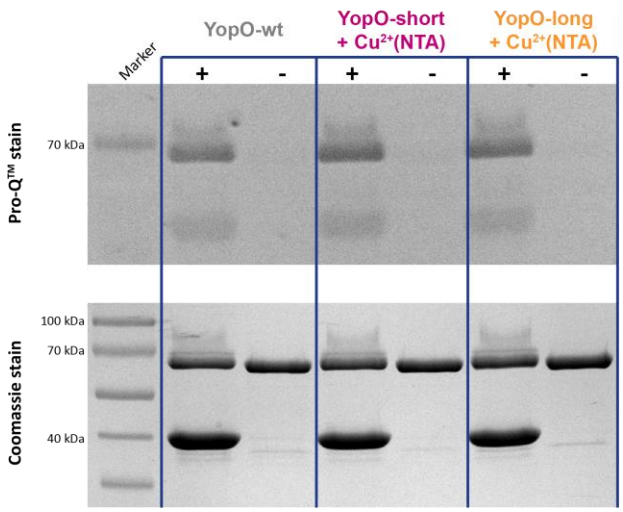

Figure 102: Activity assay of Cu^{2+}(NTA)-labeled YopO-short and YopO-long. Samples were loaded onto 10% polyacrylamide gels and stained with Pro-Q™ (top row, negative image) to visualize phosphorylated proteins and subsequently with Coomassie stain (bottom row) for visualization of the total protein content. The lanes indicated with a (+)-sign contain G-actin while the lanes indicated with a (–)-sign are negative controls in the absence of G-actin.

Labeling of YopO-short and YopO-long with Cu^{2+}(NTA) did not affect the autophosphorylation capability compared with YopO-wt. Therefore, and in agreement with the results of the CD measurements, a structural perturbation or rigidification of YopO upon dHis introduction and loading with Cu^{2+}(NTA) is not expected and the global structure of the YopO GDI domain backbone α-helix remains unaffected.

3.3.3 PDS-EPR with dHis-Cu^{2+}(NTA)-Labeled YopO

3.3.3.1 Relaxation Time Measurements for Cu^{2+}(NTA)

To optimize the following PDS-EPR measurements, the spin-lattice relaxation time T_1 and the phase memory time T_M of YopO-short and YopO-long in deuterated dHis buffer were determined at 20 K and 25 K by inversion recovery and 2pESEEM experiments (Figure 103 + Table 33).

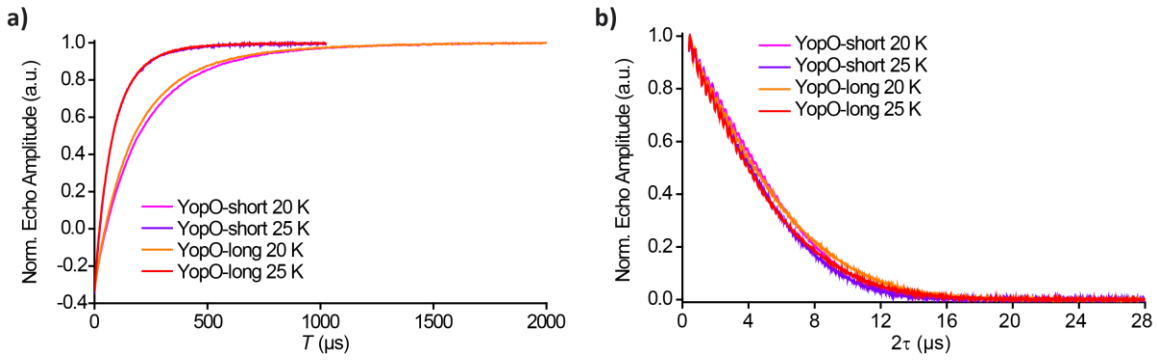

Figure 103: Electron spin relaxation time measurements of YopO-short and YopO-long. **a)** Inversion recovery traces of YopO-short (100 µM) at 20 K (pink) and 25 K (purple), and of YopO-long (100 µM) at 20 K (orange) and 25 K (red). **b)** 2pESEEM traces of YopO-short and YopO-long using the same color code as in **(a)**.

Table 33: Spin-lattice relaxation times T_1 and phase memory times T_M of YopO-short and YopO-long obtained by fitting either eq. 19 (Inversion recovery) or eq. 20 (2pESEEM) to the respective traces shown in Figure 103.

Sample	T_1 (µs)		T_M (µs)	
	20 K	25 K	20 K	25 K
YopO-short	214	86	6.0	5.5
YopO-long	193	87	5.9	5.3

For both constructs, YopO-short and YopO-long, the spin-lattice relaxation times T_1 and phase memory times T_M are almost identical and the differences in the local environment of the labeling sites have only a minor influence on the electron spin relaxation. While the phase memory time T_M remains almost constant between 20 K and 25 K, the spin-lattice relaxation is significantly faster when the temperature increases from 20 K to 25 K. Thus, RIDME experiments are best performed at 25 K to enable a reasonably short mixing interval T_{mix} while still providing a sufficiently long dipolar evolution time. On the other hand, the acquisition temperature of 20 K is best suited for PELDOR experiments due to the sensitivity gain achieved by the longer phase memory time.

3.3.3.2 Performance of RIDME and PELDOR for the dHis-Cu^{2+}(NTA) Label

In principle, for Cu^{2+} spin centers, RIDME and PELDOR are both suited to extract the dipolar coupling for the determination of interspin distances.[280] To exclude bias introduced by pulse-sequence-specific artifacts, YopO-short and YopO-long were subjected to both, RIDME and PELDOR experiments. As the width of the Cu^{2+} spectrum exceeds the narrow bandwidth of rectangular microwave pulses, homogenous sampling of all Cu^{2+} orientations is not possible at one magnetic field position, and orientation selection was previously observed for RIDME[419] and PELDOR[420] on Cu^{2+} spin centers. To minimize these effects, a previously described acquisition scheme for Cu^{2+} PELDOR was used,[307] and RIDME and PELDOR data were acquired at three field positions (Figure 104a+b). Since there is no benchmark study available that compares the performance of both, PELDOR and RIDME, with regards to sensitivity, orientational selectivity, and robustness of data analysis, the experiments were designed as a collaboration study with the *Saxena* lab to provide further insights into the use of both pulse sequences for the dHis-Cu^{2+}(NTA) spin label. RIDME traces were recorded in the *Schiemann* lab while PELDOR traces at the three indicated field positions were obtained by *Zikri Hasanbasri* from the group of *Sunil Saxena*, both at a protein concentration of 100 µM (Figure 104c+d).

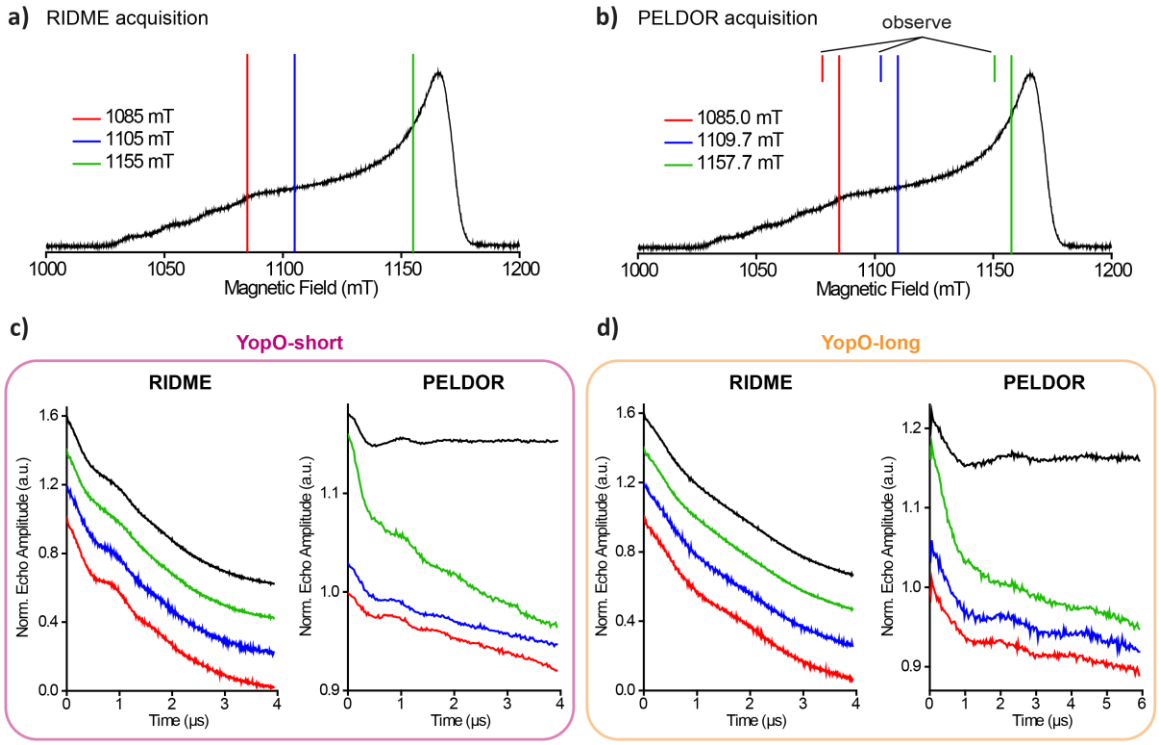

Figure 104: Data acquisition schemes and time traces of YopO-short and YopO-long. **a+b)** Representative Q-band field-swept EPR spectrum of YopO-short with the vertical, colored lines indicating the magnetic field positions for RIDME **(a)** and PELDOR **(b)** data acquisition. For PELDOR, the observer positions (-200 MHz offset) are shown as short lines using the same color code. **c+d)** RIDME (left) and PELDOR (right) time traces of YopO-short **(c)** and YopO-long **(d)** acquired at 25 K (RIDME) and 18 K (PELDOR) at the field positions indicated in **(a)** and **(b)**, respectively. The summed and in the case of PELDOR background-corrected time traces, are shown in black. For detailed acquisition parameters, refer to the primary publication.[413]

RIDME with an averaged SNR of 1.53 $min^{-1/2}$ for both mutants showed a tenfold higher sensitivity compared to PELDOR with an averaged SNR of 0.15 $min^{-1/2}$. While the higher SNR of RIDME is expected since a larger fraction of B spins is flipped in the mixing interval T_{mix} of RIDME as compared to a selective pump pulse in PELDOR, it is still an order of magnitude below the theoretical value.[303] This deviation can be rationalized by the use of CHIRP pulses for PELDOR that enhance the number of flipped spins as a result of the increased bandwidth compared to the rectangular pulses used for RIDME.[421] For RIDME, the modulation depth and the intermolecular background were nearly independent of the field position while for PELDOR, large deviations in the modulation depth and the intermolecular background were observed depending on the field position. In addition, for both pulse sequences, orientation selection is present as seen by differences in the oscillation frequencies in the time traces (Figure 104c+d) and the distorted Pake patterns (Figure 105a+b) at the individual magnetic field positions. This effect is most prominent in the region of the perpendicular component (~1155 mT) of the Cu^{2+} spectrum. To suppress these orientation effects, the individual time traces can be summed up (Figure 104c+d) to obtain the whole Pake pattern and a complete coverage of the dipolar angle Θ (Figure 105).

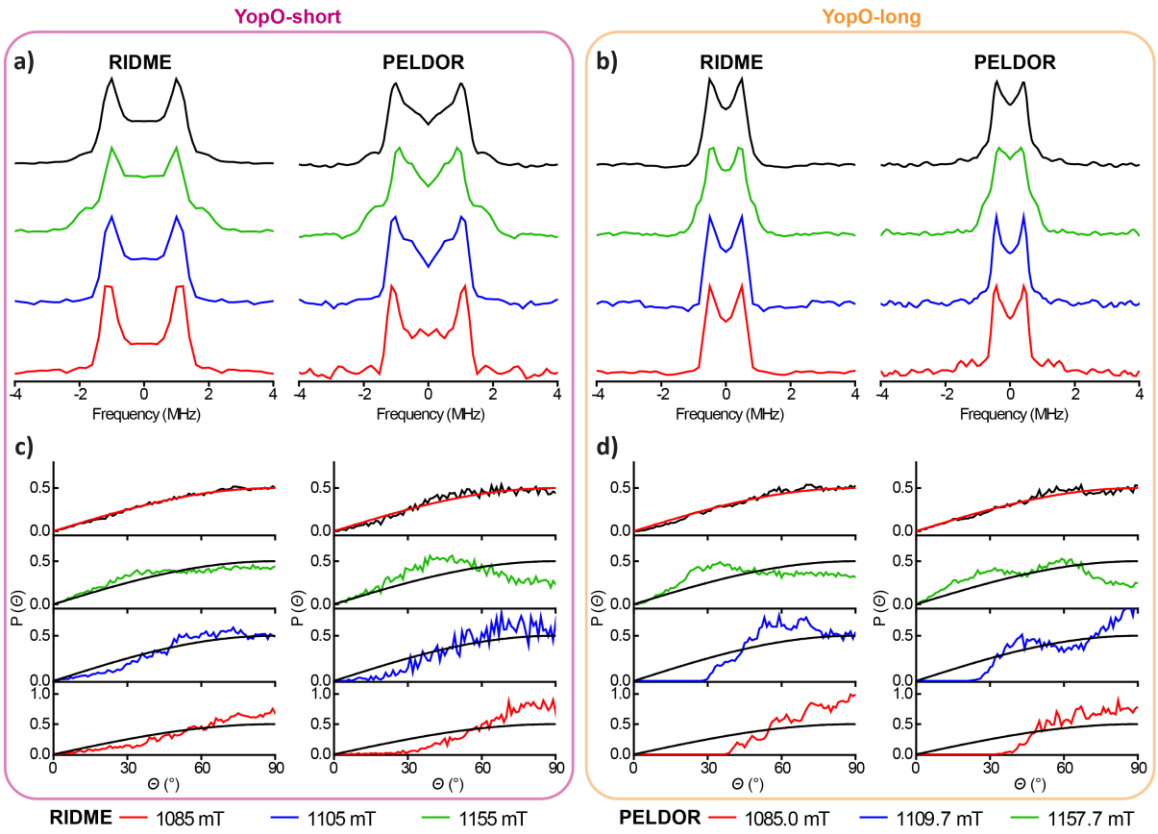

Figure 105: Pake patterns and distributions of the dipolar angle *Θ* of the individual and summed time traces. **a+b)** Pake patterns obtained by PDSFit for the individual and summed RIDME (left) and PELDOR (right) time traces at the indicated magnetic field positions for YopO-short **(a)** and YopO-long **(b)**. **c+d)** Coverage of the dipolar angle *Θ* obtained by PDSFit analysis for the individual and summed RIDME (left) and PELDOR (right) time traces at the indicated magnetic field positions for YopO-short **(c)** and YopO-long **(d)**.

While the individual traces at the chosen magnetic field positions were insufficient to cover all dipolar angles *Θ*, the summation of all traces suppressed the orientation selection and a complete coverage of all orientations *Θ* was achieved (Figure 105c+d).

To verify whether the orientation selection was fully removed using these three magnetic field positions, additional RIDME and PELDOR traces were recorded at fourteen (RIDME) and six (PELDOR) equally spaced field positions (Figure A49). Here, no further improvement was observed upon adding more fields in the case of RIDME and even proved detrimental in the case of PELDOR as a result of oversampling the perpendicular region due to a wider meshed field coverage and less field positions in the region of the parallel component of the Cu^{2+} spectrum owing to the lower sensitivity of PELDOR (Figure A49e+f). Hence, the three-field approach chosen herein provides a good compromise between efficient suppression of orientation selection and short data acquisition times.

3.3.4 Conformation of the YopO GDI Backbone α-Helix

Taking the Cu^{2+} *g*-anisotropy and the presence of orientation selection into account, the RIDME and PELDOR time traces were first analyzed by *Dinar Abdullin* with PDSFit, a program specifically designed to process orientation-selective EPR data of anisotropic spin centers.[384] Interestingly and independent of the chosen pulse sequence (RIDME or PELDOR), for both constructs YopO-short and YopO-long, a unimodal distance distribution was obtained (Figure 106). This finding is in strong contrast to the previously observed bimodal distance distributions found for the more flexible spin labels MTSL, SLIM **3•**, and Ox-SLIM **4•** (see sections 3.1 and 3.2). Notably, allowing

PDSFit to use a model with two independent distance distributions resulted in higher χ^2 values and poorer fits as compared to the unimodal fitting (data not shown).
To exclude bias from the intrinsic assumptions of the geometric PDSFit model, the time traces were also analyzed with DeerAnalysis and DEERNet (Figure 106). To counter the influence of orientation selection on the distance distribution, only the summed time traces (Figure 104, black traces) were processed. As both analysis methods work under the assumption of isotropic spin centers with $g = g_e$, the obtained distance distributions had to be corrected using the cubic proportionality of r and the effective g-value g_{eff} according to

$$r_{corr}^3 = \frac{r^3 g_{eff}^2}{g_e^2} = \frac{r^3 \left(\frac{1}{3}\left(g_{Cu^{2+}}^{zz} + g_{Cu^{2+}}^{xx} + g_{Cu^{2+}}^{yy}\right)\right)^2}{g_e^2} \qquad \text{(eq. 25)}$$

with r_{corr} being distance corrected for g-anisotropy, r the distance obtained by DeerAnalysis or DEERNet, g_{eff} the effective g-value, g_e the g-value of the free electron, and $g^{zz}/g^{xx}/g^{yy}$ the experimental g-values obtained for dHis-bound Cu^{2+} (see Table 31). In addition to the PDS experiments, MD simulations of the dHis-Cu^{2+}(NTA)-labeled constructs YopO-short and YopO-long were performed by *Zikri Hasanbasri* (for details refer to the primary publication)[413] using either the straight (PDB-ID: 2h7o) or bent (PDB-ID: 4ci6, G-actin removed) α-helix as input structure to distinguish between both α-helix conformations (Figure 106).

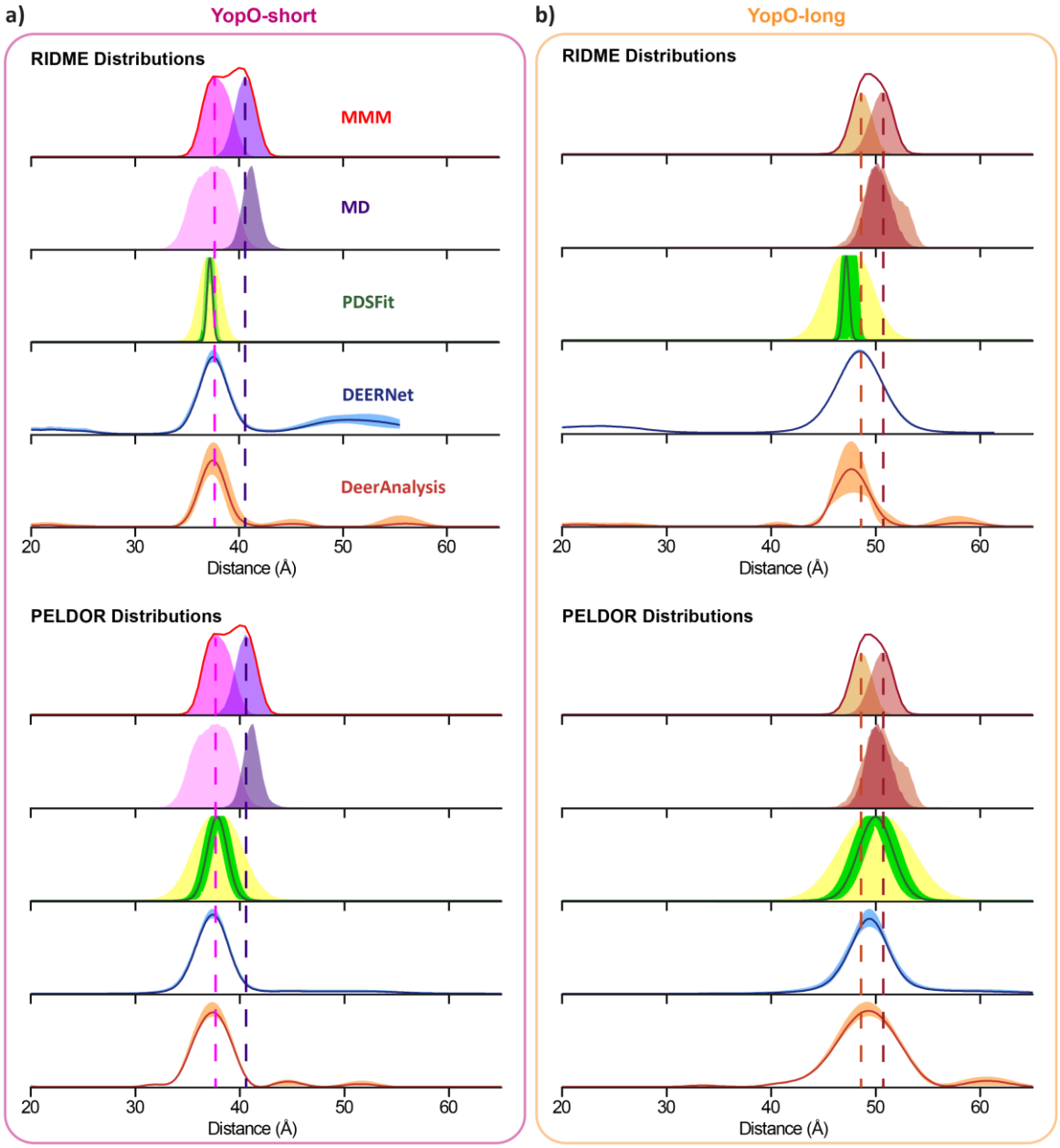

Figure 106: Distance distributions of YopO-short and YopO-long. **a)** Distance distributions of YopO-short obtained by analysis of the RIDME (top panel) or PELDOR (bottom panel) time traces. Panels from top to bottom: *In silico* predictions by MMM for YopO-short (PDB-ID: 2h7o (pink) / 4ci6 (purple)) and their sum (red); MD simulations of YopO-short (input PDB-ID: 2h7o (pink) / 4ci6 (purple)); PDSFit distance distribution (green); DEERNet distance distribution (blue); and DeerAnalysis distance distribution (orange). For PDSFit, the dark line represents the solution with the lowest χ^2, the green-shaded area represents the error introduced by the mean distance $\langle r \rangle$, and the yellow-shaded area is the total 2σ confidence interval. For DEERNet and DeerAnalysis, the shaded areas represent the confidence intervals by the internal validation tools. The dashed vertical bars indicate the most probable distances of the MMM-derived distance distributions using the same color code. **b)** Same as **(a)** but for YopO-long. PDB-ID color code: 2h7o (sand) / 4ci6 (brown). The complete PDSFit, DEERNet, and DeerAnalysis results can be found in the appendix (Figure A50-A52).

Similar to PDSFit, the distance distributions obtained by DeerAnalysis and DEERNet for the RIDME and PELDOR traces were unimodal for YopO-short and YopO-long. For YopO-short, the mean distance $\langle r \rangle$ and the width Δr of the distance distributions were highly consistent between the

three analysis methods (PDSFit, DeerAnalysis, and DEERNet) and the two pulse sequences (RIDME and PELDOR). Only for the DEERNet analysis of the YopO-short RIDME trace, a longer-distance artifact (45 Å - 55Å) was obtained as the time trace had to be shortened to 2.5 µs to enable DEERNet to process the input. In the case of YopO-long, larger deviations between the individual analysis methods and pulse sequences were observed, with PELDOR yielding slightly longer mean distances ⟨*r*⟩ than RIDME. In addition, the distance distributions were slightly broader and more inconsistent as compared to YopO-short. These deviations are likely a result of the limited time trace length and the longer interspin distance, making the distance distribution less shape-reliable. In the MD simulations, the Cu^{2+}-Cu^{2+} interspin distances extracted for YopO-short are well separated and depend on the input structure, but for YopO-long, no differentiation between the two α-helix conformations is possible as both distributions largely overlap. A detailed summary of the obtained mean distances ⟨*r*⟩ and the distribution widths Δ*r* is given below (Table 34).

Table 34: Mean distances ⟨*r*⟩ and widths Δ*r* of the distance distributions shown in Figure 106. DN = DEERNet; DA = DeerAnalysis.

Parameter[a]	RIDME			PELDOR			MMM		MD	
	PDSFit	DN	DA	PDSFit	DN	DA	2h7o	4ci6	2h7o	4ci6
YopO-short										
⟨*r*⟩ (Å)	$37.2^{+0.2}_{-0.2}$	37.5	37.5	$37.8^{+0.5}_{-0.4}$	37.4	37.3	37.9	40.6	37.4	41.1
Δ*r* (Å)	$0.6^{+1.3}_{-0.5}$	3.2	2.9	$2.2^{+2.3}_{-2.2}$	3.6	4.0	3.0	2.3	4.5	1.5
YopO-long										
⟨*r*⟩ (Å)	$47.2^{+0.9}_{-0.3}$	48.5	47.7	$50.0^{+0.7}_{-0.7}$	49.4	49.2	48.6	50.6	50.6	50.2
Δ*r* (Å)	$0.7^{+3.4}_{-0.5}$	5.1	3.6	$3.8^{+2.7}_{-2.8}$	4.6	6.6	2.7	2.5	3.8	2.5

[a] Both parameters ⟨*r*⟩ and Δ*r* are given as the mean value and the FWHM of a Gaussian function fitted to the corresponding distance distribution.

Based on the MMM and MD calculations, the distance distributions for YopO-short obtained for either of the two available crystal structures are sufficiently narrow to distinguish between both α-helix conformations (average Δ⟨*r*⟩ = 3.2 Å). Superposition of both MMM-derived distance distributions resulted in a distribution with discernable features for both helix conformations (Figure 106, top row, red line). Hence, if two backbone conformations are present in solution, these will likely be resolved in the experimental distance distribution. However, all experimentally-derived distance distributions of YopO-short are unimodal and agree well with the *in silico* prediction of the straight GDI α-helix backbone in terms of mean distances ⟨*r*⟩ and widths Δ*r*. On the other hand, for YopO-long the distance difference between both helix conformations is less pronounced in the *in silico* derived distributions of MMM and almost non-existent in the MD simulations, thereby prohibiting a clear differentiation between both α-helix conformations. Additionally, the experimental distance distributions of YopO-long were generally broader and encompassed the *in silico* distributions of both, the straight and the bent α-helix conformations, and it was not possible to distinguish them. Nonetheless, the narrow distribution and high resolution obtained for YopO-short strongly suggests that the YopO GDI α-helix backbone adopts a straight conformation similar to the crystal structure of PDB-ID 2h7o in (frozen) solution. This in turn implies that the bi- or multimodal distance distributions shown in sections 3.1 and 3.2

obtained from the more flexible labels MTSL, Mal-TSL **2•**, SLIM **3•**, and Ox-SLIM **4•** were related to a preferred selection of distinct subsets of label conformers and not two α-helix conformations present in solution.

Prompted by the enhanced distance resolution of dHis-Cu^{2+}(NTA) label, the idea was to induce a conformational transition from the straight to the bent α-helix by adding G-actin and to verify whether this small-scale transition can be resolved by PDS-EPR. However, upon the addition of G-actin to the dHis-Cu^{2+}(NTA)-labeled YopO constructs, the EPR signal of Cu^{2+} vanished completely (data not shown) and no PDS experiments could be performed. While the exact reason of the signal loss remains unclear, a similar behavior of Cu^{2+} has been reported in the presence of amyloid systems.[422] In that context, the loss of signal was interpreted as amyloid-promoted Cu^{2+} aggregation, resulting in significantly decreased spin-lattice relaxation times. The interaction of Cu^{2+} ions and G-actin are currently subject of further investigation within the *Schiemann* group.

3.3.5 Identification and Influence of Label Conformers

To rationalize the influence of conformer selection of flexible spin labels, two dHis-cysteine chimera constructs based on YopO-short were designed. One of the dHis-sites was kept while the other was replaced by a cysteine residue for orthogonal labeling with the more flexible SLIM **3•** spin label, thereby yielding the two constructs YopO V599-**3•**+S620H/N624H and YopO A595H/V599H+N624-**3•** (Figure 107).

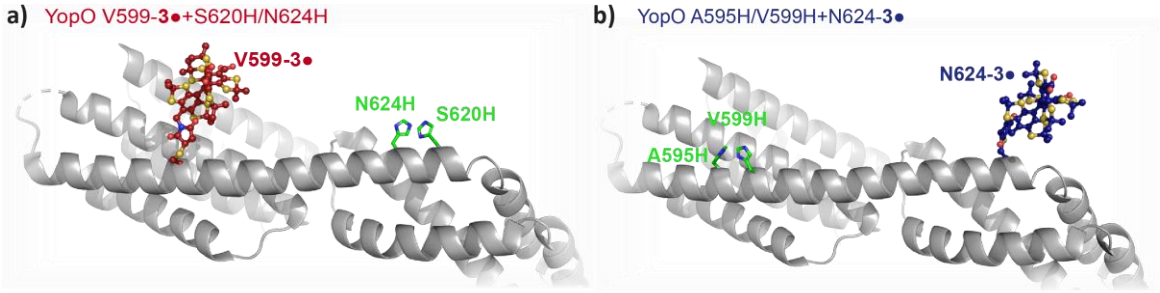

Figure 107: Labeling sites in the dHis-cysteine YopO chimeras. Model of the GDI domain of YopO (PDB-ID 2h7o) showing the labeling sites of YopO V599-**3•**+S620H/N624H **(a)** and YopO A595H/V599H+N624-**3• (b)**. The dHis motifs are indicated by green stick models while the SLIM **3•** labels are depicted as ball-and-stick models. For clarity, only one SLIM conformer is shown for each labeling site.

The rationale for choosing SLIM **3•** over MTSL was the narrow width of the EPR spectrum of SLIM **3•** which can be fully excited by rectangular pulses, thereby minimizing the effects of orientation selection. If label conformers are indeed the reason for the bimodal distance distributions observed previously, the summed distance distributions of both chimera constructs with one rotationally restricted spin label (dHis-Cu^{2+}(NTA)) and the more flexible SLIM **3•** should reflect the bimodal distance distribution obtained for the doubly SLIM **3•**-labeled YopO analog V599C/N624C.

Both dHis-cysteine chimera constructs were generated, purified, and spin-labeled alongside the double-cysteine analog YopO V599C/N624C (Figure A53-A55). Subsequently, RIDME experiments were performed at 40 K at a protein concentration of 100 µM (Figure 108a). RIDME was chosen over PELDOR due to the enhanced SNR and lower susceptibility to orientation selection. The RIDME time traces of both constructs showed pronounced oscillations and exhibited modulation depths of ~42% with an average SNR of 0.72 $min^{-1/2}$, which is in good agreement with the results obtained before for RIDME on the Cu^{2+}/SLIM spin pair (see section 3.2.6.2). As the pulse sequence was applied to the maximum of the isotropic SLIM **3•** EPR spectrum with $g_{SLIM\ 3•} = g_e$, the time

traces were analyzed with DeerAnalysis and no further correction of the obtained distance distributions was necessary (Figure 108b).

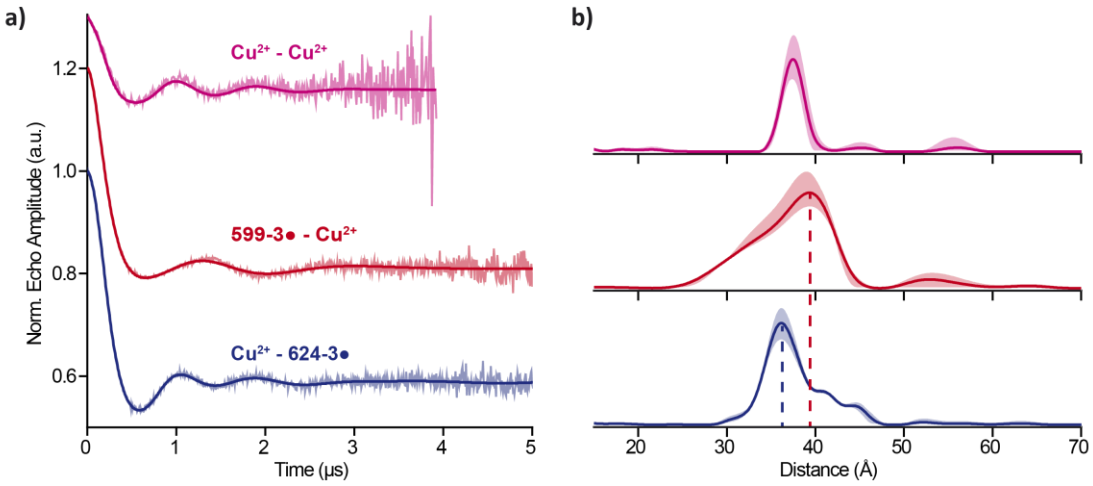

Figure 108: RIDME traces and distance distributions for the dHis-cysteine chimera constructs. **a)** Background-corrected RIDME time traces of YopO-short (pink), YopO V599-**3•**+S620H/N624H (red), and YopO A595H/V599H+N624-**3•** (blue) and the corresponding fits by DeerAnalysis. For clarity, the time traces are shifted on the y-axis. **b)** Distance distributions obtained with DeerAnalysis from the time traces in **(a)** using the same color code. The uncertainty estimates are shown as shaded areas. The colored dashed lines indicate the most probable distance of the respective construct. The complete analysis by DeerAnalysis (backgrounds, L-curves, and distance distributions) is given in the appendix (Figure A56).

As expected for the conformational flexibility of SLIM **3•** conjugated to a cysteine residue, both distance distributions of the orthogonally labeled YopO constructs are broadened compared to the narrow distance distribution of the Cu^{2+}-Cu^{2+} YopO-short analog with two conformationally restricted dHis-Cu^{2+}(NTA) spin labels. Interestingly though, depending on the particular dHis-site that is exchanged and labeled with SLIM **3•**, the most probable distances are shifted (Figure 108, dashed lines). Therefore, for both labeling sites, the complete accessible volume is not sampled uniformly and depending on the labeling site, selected SLIM **3•** conformers are induced and weighted differently. This finding is supported by a contemporaneous study by *Vitali* et al., who showed in a case study of GB1 orthogonally labeled with dHis-Cu^{2+}(NTA) and various nitroxide spin labels that nitroxide conformers are distinctly selected depending on both the labeling site and spin label type.[423]

For direct comparison, a DQC time trace of the doubly SLIM **3•**-labeled YopO V599C/N624C analog was recorded at 70 K at a protein concentration of 50 µM (Figure 109a). The summed distance distribution of the orthogonally Cu^{2+}/SLIM-labeled YopO constructs was then overlaid with the distance distribution obtained for YopO V599-**3•**/N624-**3•** to verify whether the bimodality can be reproduced (Figure 109b).

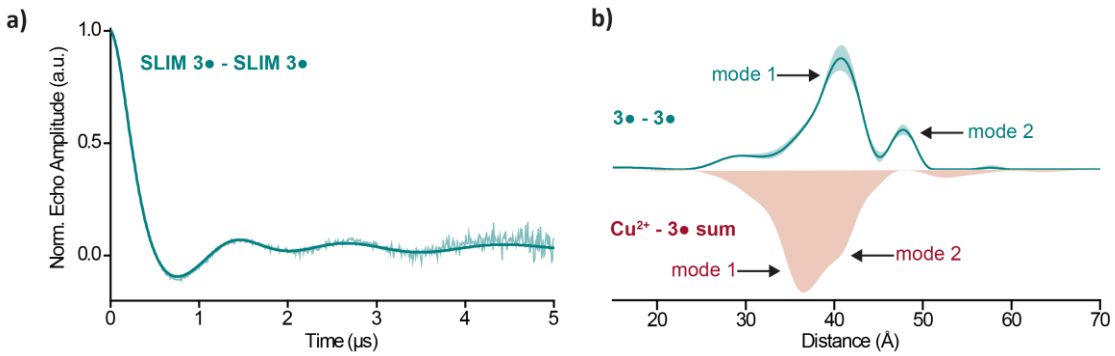

Figure 108: DQC time trace and distance distribution of YopO V599-**3•**/N624-**3•**. **a)** Background-corrected DQC time traces of YopO V599-**3•**/N624-**3•** (teal) and the corresponding fit obtained by Tikhonov regularization. **b)** Distance distribution obtained from the time trace in **(a)** with the DeerAnalysis validation shown as a shaded area (top) and the summed distance distribution (inverted for clarity) obtained for YopO V599-**3•**+S620H/N624H and YopO A595H/V599H+N624-**3•** (see Figure 108) shown in red (bottom). The distinct modes of the individual distributions are highlighted by arrows. The complete analysis of YopO V599-**3•**/N624-**3•** by DeerAnalysis (backgrounds, L-curves, and distance distributions) is given in the appendix (Figure A57).

Similar to the MTSL-labeled analog discussed before, a bimodal distance distribution was obtained also for SLIM **3•**-labeled YopO V599-**3•**/N624-**3•**. Notably, summing up the distance distributions of the orthogonally Cu^{2+}/SLIM-labeled YopO constructs resulted in a bimodal distribution as well. Albeit the bimodality is less pronounced in the summed distribution, the width and intensities of the individual modes are comparable to the SLIM/SLIM-labeled counterpart. The shift to slightly longer distances for SLIM/SLIM-labeled YopO can be rationalized by the presence of two flexible labels with longer linkers instead of just one label, which results in longer achievable interspin distances if both labels are facing in opposite directions. Hence, the substitution of a flexible spin label with the conformationally restricted dHis-Cu^{2+}(NTA) spin label in an orthogonal labeling can unravel the contribution of the individual spin labels to the distance distribution of two flexible labels. This is helpful especially if multiple structural models are available and if the distance distributions obtained for two flexible labels show ambiguous results.

4. Conclusion and Outlook

In the first part of this thesis, best-practice guidelines were set for spin labeling, sample preparation, and EPR characterization using the nitroxide spin label MTSL. Based on the example of YopO, four mutants were expressed, purified, and spin-labeled with MTSL. The labeling routine included excess label removal via SEC followed by a thorough sample characterization via cw-EPR, UV-vis, and ESI(+)-MS. For all constructs, excellent labeling efficiencies of 90%-100% were achieved. As a testimony of the careful sample preparation and handling, the PELDOR data and the resulting distance distributions were well reproducible across all seven laboratories participating in the ring test and over a range of measurement conditions and data analysis routines. Based on these results and discussions among the participants, community-approved guidelines were set, which cover sample preparation, PELDOR data acquisition, and data analysis and deposition. In addition, the guidelines include guidance in the interpretation of distance distributions which were categorized in five different cases depending on their shape and width. This benchmark study provides a valuable contribution to the field of structural biology and its significance is reflected by the number of citations (121 citations by March 2024, according to Google Scholar) following the publication of the work in October 2021 in the *Journal of the American Chemical Society*. The community-approved guidelines will improve the reliability and reproducibility of PDS-derived distance restraints and aim to make PDS methods more accessible to the wider community of structural biology. In combination with the advent of tools for protein structure prediction such as AlphaFold2, distance restraints from PDS-EPR provide a suitable and fast way for structural model verification with coarse-grained resolution.

In the second part of this thesis, a labeling routine for proteins using trityl spin labels was designed. On the example of YopO, it could be demonstrated that the previously employed methanethiosulfonate-conjugated trityl labels such as MTS-TSL **1•** have severe disadvantages concerning site-selectivity, excess label removal, and redox stability compared to the maleimide-conjugated Mal-TSL **2•** and their use is therefore discouraged. Taking the critical aggregation concentration of trityls above 60 µM into account, a labeling scheme was established that operates at low trityl concentrations and involves two SEC steps. It yields high labeling efficiencies and allows efficient removal of free excess label. In addition, a simple method for the fast and reliable determination of the labeling efficiency was introduced using UV-vis spectroscopy. The herein developed spin labeling protocol for proteins with maleimide-derivatized trityl spin labels complies with the aforementioned community guidelines and solves the previously encountered difficulties originating from unspecific labeling and aggregation of proteins. While the PDS data quality of the Mal-TSL **2•**-labeled YopO constructs exceeded the previous literature reports in terms of SNR and modulation depth, and was almost on par with trityl model compounds, it also revealed that the flexibility of the ester-linked maleimide bioconjugation group hampers the acquisition of high-resolution distance restraints. To address this issue, the new spin label SLIM **3•** with a reduced linker length was introduced and was shown to perform equally well in protein SDSL using the previously established labeling protocol. A benchmark test of YopO Y588C/N624C labeled with SLIM **3•**, Mal-TSL **2•**, and MTSL highlighted the enhanced sensitivity of trityls and showed that the shorter linker of SLIM **3•** improves the resolution of the distance distribution, which closely resembles the distribution obtained with the “gold standard” nitroxide MTSL. To further demonstrate the reduced flexibility of SLIM **3•** compared to Mal-TSL **2•**, RIDME experiments on labeled myoglobin were performed and analyzed using PDSFit. Here, the width of the distance distribution obtained for SLIM **3•**-labeled myoglobin was 60% lower than for the Mal-TSL **2•**-labeled analog, thereby emphasizing the resolution improvement due to the shorter

linker. Notably and similar to the distance distributions of YopO, a two-component system was necessary to satisfactorily fit the experimental data. Here, further investigation is needed to exclude model bias and/or structural perturbation of the protein. Exploiting the enhanced sensitivity of SLIM **3•**, DQC measurements on doubly SLIM **3•**-labeled YopO at 90 nM protein concentration and vtRIDME experiments on orthogonally Cu^{2+}/SLIM **3•**-labeled GB1 at 10 nM were performed, thereby setting new benchmarks for low-concentration PDS-EPR using a commercial Q-band EPR setup. This superior sensitivity of SLIM-type trityls make them an excellent spin label choice if the availability of the POI is limited or sub-micromolar concentrations are required to study, e.g., high binding affinities. The enhanced redox stability of SLIM **3•** compared to Finland-type trityl spin labels resulting from the electron-donating methylene linker and the stabilization of the trityl cation was demonstrated by CV experiments and by monitoring the EPR intensity in various reductive media. Exploiting these improved redox properties, *in-cell* experiments with SLIM **3•**-labeled YopO were conducted within *Xenopus laevis* oocytes and in HeLa cells. While high-quality DQC data were obtained within oocytes and a change in the distance distribution was observed and assigned to a conformational change of the α-helix, the quality of the DQC data obtained within HeLa cells was significantly lower and the time trace did not allow further interpretation due to a lack of modulation depth and oscillations. Using fluorescence microscopy, a strong aggregation tendency of YopO within the cytosol was observed under the chosen electroporation conditions, and further optimization is needed to reduce the amount of aggregated protein. To prove the general applicability of SLIM **3•** for PDS experiments in human cell systems, transition to an easier model system such as GB1 may help to reduce the aggregation tendency and refine the EP procedure. In the same context, a purification protocol for full-length YopO in complex with its specific chaperone SycO was established using a pET-Duet-1 expression system. Through complexation with SycO, the solubility of full-length YopO was significantly improved and protein yields high enough for SDSL with MTSL and SLIM **3•** were obtained. Subsequent *in vitro* PDS studies revealed that the binding of SycO does not affect the conformation of the α-helical backbone of YopO. Since the electroporation procedure was not yet optimized, no further endeavors were undertaken to transfect spin-labeled full-length YopO into HeLa cells. To simplify the trityl spin labeling and work-up procedure, the highly hydrophilic Ox-SLIM **4•** trityl, a chimera of the Ox063 trityl and the SLIM **3•** spin label, was introduced. However, SDSL with Ox-SLIM **4•** at increased concentrations in smaller reaction volumes comparable to the MTSL labeling procedure led to a significant amount of free label in the protein sample. In addition, although the tendency of unspecific binding to proteins was greatly reduced by the eight hydroxyethyl groups of Ox-SLIM **4•**, the spin label is prone to dimerization which led to a sharp initial decay in the DQC trace. Using the previously established trityl labeling protocol operating at low concentrations facilitated the removal of excess label and sufficiently suppressed the dimer formation of **4•**. Exploiting the enhanced phase memory time of bioconjugated Ox-SLIM **4•** compared to SLIM **3•**, the previously set concentration limit for trityl-trityl DQC with **3•** could be further reduced to just 45 nM at a prolonged time trace length of 4.5 µs. Owing the strong aggregation of SLIM **3•**-labeled YopO in the EP experiments, a spin label change to the more hydrophilic Ox-SLIM **4•** spin label can potentially facilitate the EP procedure of HeLa cells and enable the acquisition of high-quality *in-cell* PDS data. However, as the synthesis of Ox-SLIM **4•** is intricate and its accessibility therefore limited, these experiments could not be conducted over the course of this thesis.

For the labeling positions on the α-helical backbone of YopO's GDI domain, bi- or multimodal distance distributions were encountered throughout the first two sections of this thesis. Initially attributed to two conformations of the α-helix, the varying peak intensities and shifts of the relative populations in the distance distributions for different labels raised doubt on this theory.

Therefore, in the third part of this thesis, the solution structure of the YopO GDI α-helix backbone was assessed using the conformationally restricted dHis-Cu^{2+}(NTA) spin label. Site-selectivity assessment of Cu^{2+}(NTA) via cw-EPR and RIDME revealed unspecific binding to single histidine residues of YopO in the absence of a dHis-site, but a high selectivity if a dHis-site is available. These findings emphasize the general applicability of the dHis-Cu^{2+}(NTA) spin label, even for proteins with a high histidine abundance such as YopO. Although orientation selection is present for Cu^{2+} at Q-band frequencies using commonly applied rectangular pulses, it could be efficiently suppressed by acquiring RIDME and PELDOR time traces at three magnetic field positions. An in-depth analysis of the data using three methods unambiguously showed that the α-helical backbone of YopO's GDI domain adopts only a single, straight conformation in frozen solution. Using two orthogonally labeled dHis-cysteine YopO chimera mutants, the presence of preferred spin label conformers could be revealed, thereby confirming that the previously observed bimodal distributions stem from label rather than from protein conformations. Therefore, it was shown that the dHis-Cu^{2+}(NTA) spin label allows distinguishing between two closely related structural models, as well as differentiating between protein and spin label conformers. These results foster the use of the dHis-Cu^{2+}(NTA) label for other systems where ambiguities arise from flexible spin labels or small-scale conformational changes need to be solved.

5. Materials and Methods

5.1 Materials

The following section gives an overview of the utilized materials and methodologies with specific relevance to the experimental procedures.

5.1.1 Chemicals

Table 35: Utilized chemicals.

Compound	Manufacturer
1-Step™ TMB-Blotting substrate solution	Thermo Scientific
20% Sodium dodecyl sulfate (SDS)	Fisher Scientific
3-(*N*-morpholino)propanesulfonic acid (MOPS)	Carl Roth GmbH + Co. KG
30% acrylamide mix (37.5 : 1)	Carl Roth GmbH + Co. KG
5-aminolevulinic acid hydrochloride	Biosynth
Acetic Acid	Merck KGaA
Acetonitrile	Merck KGaA
Adenosine-5'-triphosphate disodium salt (ATP)	Carl Roth GmbH + Co. KG
Agar	Carl Roth GmbH + Co. KG
Agarose	Thermo Scientific
Alexa Fluor™ 488 C_5 Maleimide	Thermo Scientific
Amersham™ Hybond® P Western blotting membrane, PVDF	Merck KGaA
Ammonium persulfate (APS)	Carl Roth GmbH + Co. KG
Ampicillin	Carl Roth GmbH + Co. KG
Bromphenol blue	Carl Roth GmbH + Co. KG
BugBuster® 10x Protein Extraction Reagent	Merck KGaA
Chloramphenicol	Carl Roth GmbH + Co. KG
Coomassie Brilliant Blue R250	Carl Roth GmbH + Co. KG
Copper(II) sulfate	Carl Roth GmbH + Co. KG
Deuterium oxide	Deutero GmbH
di-Sodium hydrogen phosphate	Carl Roth GmbH + Co. KG
Dithiothreitol (DTT)	Carl Roth GmbH + Co. KG
dNTP Mix (10 mM each)	Thermo Scientific
Electrolytic Buffer E2	Invitrogen
Ethidium bromide	AppliChem GmbH
Ethylene glycol-d_6	Deutero GmbH
Ethylenediaminetetraacetic acid (EDTA)	Carl Roth GmbH + Co. KG
Formic Acid	Merck KGaA
Gibco™ DMEM, high glucose	Thermo Scientific
Gibco™ Fetal Bovine Serum (FBS)	Thermo Scientific
Gibco™ PBS pH 7.4	Thermo Scientific
Gibco™ Trypsin-EDTA (0.25%)	Thermo Scientific
Glutathione Sepharose™ 4B	Cytiva
Glycerol	Carl Roth GmbH + Co. KG
Glycerol-d_8	Merck KGaA
Glycin	Carl Roth GmbH + Co. KG
Goat anti-mouse IgG (H+L) secondary antibody, HRP (#31432)	Thermo Scientific
HisPur™ Ni-NTA resin	Thermo Scientific
Human platelet actin	Cytoskeleton Inc.
Hydrochloric acid (12M)	Merck KGaA
Isopropyl β-D-1-thiogalactopyranoside (IPTG)	Carbolution Chemicals GmbH
L(+)-arabinose	Carl Roth GmbH + Co. KG
Latrunculin B	Merck KGaA
Magnesium chloride hexahydrate	Carl Roth GmbH + Co. KG

Compound	Manufacturer
Magnesium sulphate	Carl Roth GmbH + Co. KG
Manganese(II) chloride monohydrate	Carl Roth GmbH + Co. KG
Methanol	Merck KGaA
Milkpowder (low fat)	Carl Roth GmbH + Co. KG
Mouse anti-GST-tag monoclonal antibody (MA4-004)	Thermo Scientific
N-2-Hydroxyethylpiperazine-*N'*-2-ethane sulphonic acid (HEPES)	Carl Roth GmbH + Co. KG
Nitrilotriacetic acid (NTA)	Merck KGaA
N-Tris(hydroxymethyl)methyl-2-aminoethanesulphonic acid (TES)	Carl Roth GmbH + Co. KG
Potassium chloride	Carl Roth GmbH + Co. KG
Potassium dihydrogen phosphate	Carl Roth GmbH + Co. KG
Pro-Q™ Diamond Phosphoprotein gel stain	Thermo Scientific
Rabbit muscle acetone powder	Pel-Freez Biologicals
Resuspension Buffer R	Invitrogen
Silicon Oil	Merck KGaA
Sodium acetate trihydrate	Carl Roth GmbH + Co. KG
Sodium azide	Carl Roth GmbH + Co. KG
Sodium chloride	Carl Roth GmbH + Co. KG
Sodium dihydrogen phosphate dihydrate	Carl Roth GmbH + Co. KG
Sodium hydrogen carbonate	Carl Roth GmbH + Co. KG
Sodium hydroxide	Carl Roth GmbH + Co. KG
Sodium hydroxide	Carl Roth GmbH + Co. KG
Tetramethylethylendiamine (TEMED)	Carl Roth GmbH + Co. KG
Tris(2-carboxyethyl)phosphine hydrochloride (TCEP)	Iris Biotech GmbH
Tris(hydroxymethyl)aminomethane (Tris)	Carl Roth GmbH + Co. KG
Tris(hydroxymethyl)aminomethane hydrochloride (Tris-HCl)	Carl Roth GmbH + Co. KG
Triton™ X-100	Carl Roth GmbH + Co. KG
Trypton/Pepton	Carl Roth GmbH + Co. KG
Tween® 20	Carl Roth GmbH + Co. KG
Xenopus laevis oocytes	EcoCyte Bioscience
Yeast extract	Carl Roth GmbH + Co. KG
β-Mercaptoethanol	Carl Roth GmbH + Co. KG

5.1.2 Devices, Kits, and Columns

Table 36: Utilized devices.

Device	Tradename	Manufacturer
10 µL capillaries	Disposable Capillaries	Hirschmann Laborgeräte
150 W TWT-amplifier	Model 187Ka	Applied Systems Engineering Inc.
Cell counter	Countess™ 3	Invitrogen
Centrifugal filter	Vivaspin® 20, 10 kDa MWCO PES	Cytiva
Centrifugal filter	Vivaspin® 20, 5 kDa MWCO PES	Cytiva
Centrifugal filter	Vivaspin® 6, 10 kDa MWCO PES	Cytiva
Centrifugal filter	Vivaspin® 6, 5 kDa MWCO PES	Cytiva
Centrifugal filter	Amicon® Ultra 0.5 10 kDa MWCO	Millipore
EPR Q-band tube 3 mm o.d.	3 mm Thin Wall Quartz EPR tube	Wilmad LabGlass
EPR spectrometer	EMXnano	Bruker Corporation
EPR spectrometer	EMXmicro	Bruker Corporation
EPR spectrometer	ELEXSYS E580	Bruker Corporation
EPR X-band tube 4 mm o.d.	4 mm Thin Wall Quartz EPR tube	Wilmad LabGlass
Helium flow cryostat	ER 4112HV	Bruker Corporation
Helium flow cryostat	CF935	Oxford Instruments
Bottle-top filter	Durapore® 0.22 µm PVDF membrane	Merck Millipore

Device	Tradename	Manufacturer
Microinjector	Nanoject II™	Drummond Scientific Company
Protein chromatography system	Äkta avant	Cytiva
Quartz glass cuvettes	ROTILABO® Quartz glass 0.7 mL (+plugs)	Carl Roth GmbH + Co. KG
Quartz glass cuvettes	Semi-Micro Cell 114F-QS 10x4 mm	Hellma GmbH & Co. KG
Resonator	ER 4122SHQ	Bruker Corporation
Resonator	ER 4119HS	Bruker Corporation
Resonator	ER 4122SHQE	Bruker Corporation
Resonator	ER 5106QT-2	Bruker Corporation
Sealing foil	Parafilm® M	Bemis Company, Inc.
Sonicator	Sonoplus SH 70 G	Bandelin GmbH & Co. KG
Spectropolarimeter	Jasco J-810	JASCO Corporation
Temperature controller	Mercury iTC503	Oxford Instruments
Thermocycler	Mastercycler® nexus	Eppendorf AG
Transfection System	Neon™ Transfection System	Invitrogen
UV-vis spectrophotometer	Cary100 UV-Vis	Agilent Technologies
UV-vis spectrophotometer	NanoDrop™ 2000	Thermo Scientific
Water purification system	Milli-Q® Direct	Merck Millipore

Table 37: Utilized kits.

Kit	Manufacturer
GeneJET Gel Extraction and DNA Cleanup MicroKit	Thermo Scientific
GeneJET Plasmid Miniprep Kit	Thermo Scientific

Table 38: Utilized chromatography columns.

Column	Manufacturer
Capto™ HiRes Q 10/100	Cytiva
ENrich™ Q 10x100	Biorad
PD-10 desalting column	Cytiva
HiPrep™ 26/10 Desalting	Cytiva
Superdex® 75 10/300 GL	Cytiva
HiLoad® 16/600 Superdex® 200 pg	Cytiva

5.1.3 Buffers, Enzymes, and Gel-Electrophoresis

All self-prepared media were autoclaved before use. All buffers for protein purification and sample preparation were filtered through a bottle-top filter (0.22 µm PVDF membrane).

Table 39: Utilized buffer solutions.

Buffer	Composition
TAE buffer	40 mM Tris, 0.1% acetic acid, 1 mM EDTA
SDS-PAGE buffer	25 mM Tris, 192 mM glycine, 0.1% SDS, pH 8.3
Coomassie Stain	45% Methanol, 10% acetic acid, 2.5 g/L Coomassie R250
LB medium	10 g/L Trypton/Pepton, 5 g/L yeast extract, 10 g/L NaCl, pH 7
Agar plate	10 g/L Trypton/Pepton, 5 g/L yeast extract, 10 g/L NaCl, 15 g/L agar, pH 7
6x agarose LD	10 mM Tris-HCl, 60 mM EDTA, 60% glycerol, bromphenol blue (1 tip), pH 7.6
YopO Basic buffer	50 mM Tris, 150 mM NaCl, 3 mM DTT, pH 8.0

Buffer	Composition
YopO Cleavage buffer	50 mM Tris, 150 mM NaCl, 1 mM EDTA, 1 mM DTT, 150 µg PreScission protease, pH 8.0
YopO IExA buffer	50 mM Tris, pH 8.0
YopO IExB buffer	50 mM Tris, 1 M NaCl, pH 8.0
YopO GF buffer	50 mM Tris, 50 mM NaCl, pH 8.0
YopO Phosphorylation buffer	50 mM Tris, 10 mM $MgCl_2$, 1 mM ATP, 2 mM $MnCl_2$, pH 8.0
YopO PDS buffer	100 mM TES, 100 mM NaCl, pH 7.4 (in D_2O)
YopO-Actin PDS buffer	4 mM TES, 0.4 mM ATP, 0.2 mM $CaCl_2$, 2 mM NaN_3, pH 7.5 (in D_2O)
SDS Fixing solution	45% methanol, 10% acetic acid
SDS Destaining solution	20% acetonitrile, 50 mM NaOAc, pH 4.0
Phosphate buffer	20 mM PO_i, 50 mM NaCl, pH 6.8
Myoglobin Basic buffer	50 mM Tris, 50 mM NaCl, pH 8.0
Myoglobin IExA buffer	50 mM Tris, pH 8.5
Myoglobin IExB buffer	50 mM Tris, 1 M NaCl, pH 8.5
Myoglobin GF buffer	50 mM Tris, 150 mM NaCl, pH 8.0
Myoglobin PDS buffer	100 mM TES, 100 mM NaCl, pH 7.4 (in D_2O)
YopO•(SycO) Basic buffer	50 mM Tris, 150 mM NaCl, 3 mM DTT, 5% glycerol, pH 8.0
YopO•(SycO) Cleavage buffer	50 mM Tris, 150 mM NaCl, 1 mM EDTA, 1 mM DTT, 150 µg PreScission protease, 5% glycerol, pH 8.0
YopO•(SycO) IExA buffer	50 mM NaCl, 5% glycerol, pH 8.0
YopO•(SycO) IExB buffer	50 mM NaCl, 1 M NaCl, 5% glycerol, pH 8.0
YopO•(SycO) PDS buffer	100 mM TES, 100 mM NaCl, pH 7.4 (in D_2O)
PBS buffer	137 mM NaCl, 2.7 mM KCl, 10 mM Na_2HPO_4, 1.8 mM KH_2PO_4, pH 7.4
MBS buffer	5 mM HEPES, 88 mM NaCl, 1 mM KCl, 1 mM $MgSO_4$, 2.5 mM $NaHCO_3$, 0.7 mM $CaCl_2$, pH 7.8
GB1 PDS buffer	150 mM NaCl, 42 mM Na_2HPO_4, 7.6 mM KH_2PO_4, pH 7.4 (in D_2O)
BugBuster® Buffer (1x)	50 mM Tris, 150 mM NaCl, 10% glycerol, 0.5% Triton™ X-100, 10% BugBuster® 10x Protein Extraction Reagent, pH 7.4
Lysis buffer	50 mM Tris, 150 mM NaCl, 10% glycerol, 0.5% Triton™ X-100, pH 7.4
Transfer buffer	25 mM Tris, 192 mM Glycin, 0.05% SDS, pH 8.4
TBST	50 mM Tris, 150 mM NaCl, 0.1% Tween® 20, pH 7.5
Blocking solution	5% (w/v) milkpowder (low fat) in TBST 1x
MOPS buffer	100 mM MOPS, 100 mM NaCl, pH 7.0
dHis buffer	50 mM PO_i, 150 mM NaCl, pH 7.4
8x SDS LD	125 mM Tris-HCl, 20% glycerol, 10% β-mercaptoethanol, 4% SDS (20%) bromphenol blue (1 tip), pH 6.8

Table 40: Utilized enzymes and premixed buffer solutions.

Enzyme / Enzyme buffer	Concentration	Manufacturer
10x buffer *PasI*	-	Thermo Scientific
10x T4 DNA ligase buffer	-	Thermo Scientific
DpnI 10x Tango buffer	-	Thermo Scientific
DpnI restriction enzyme	10 U/µL	Thermo Scientific
Fast alkaline phosphatase	1 U/µL	Thermo Scientific
FastDigest buffer (10x)	-	Thermo Scientific
FastDigest *EcoRI*	-	Thermo Scientific
FastDigest *NdeI*	-	Thermo Scientific
FastDigest *SalI*	-	Thermo Scientific
FastDigest *XhoI*	-	Thermo Scientific
PasI restriction enzyme	10 U/µL	Thermo Scientific

Enzyme / Enzyme buffer	Concentration	Manufacturer
Pfu 10x Buffer	-	Carl Roth GmbH + Co. KG
Pfu-Polymerase	5 U/µL	Carl Roth GmbH + Co. KG
Pierce™ universal nuclease	250 U/µL	Thermo Scientific
PreScission protease	1.5 mg/mL	homemade
T4 DNA ligase	5 U/µL	Thermo Scientific
TEV protease	1 mg/mL	homemade

5.1.3.1 Agarose Gel Electrophoresis

25 mL TAE buffer containing 1% w/v agarose was molten and mixed with 25 µl ethidium bromide (1:1000). The molten solution was poured into a previously prepared gel form with sample pockets and rested until it solidified. The gel was transferred to the gel chamber and the reservoir was filled with TAE buffer. Pockets were filled with PCR sample solutions (5 µL sample + 1 µL 6x agarose LD) and 2.5 µL of gene ruler in a separate well served as a standard (Figure 109). The electrophoresis program was executed (100 V, 300 mA, 30 min) and subsequently, DNA-intercalated ethidium bromide was visualized in a photo box using UV light.

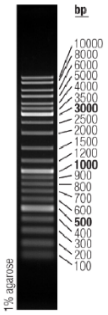

Figure 109: GeneRuler DNA Ladder Mix (Thermo Scientific) for agarose gel electrophoresis (Picture taken form the manufacturer's manual).

5.1.3.2 SDS-PAGE

The formulation for SDS gels with a varying content of acryl amide is given in Table 41.

Table 41: Formulation for 10%, 12%, and 15% SDS-PAGE running gels and 5% stacking gels.

Gel	Composition	
10% running gel (5 mL)	1.9 mL	ddH_2O
	1.7 mL	30% acrylamide mix (37.5 : 1)
	1.3 mL	1.5 M Tris pH 8.8
	50 µL	10% SDS
	50 µL	10%APS
	2 µL	TEMED
12% running gel (5 mL)	1.6 mL	ddH_2O
	2.0 mL	30% acrylamide mix (37.5 : 1)
	1.3 mL	1.5 M Tris pH 8.8
	50 µL	10% SDS
	50 µL	10% APS
	2 µL	TEMED
15% running gel (5 mL)	1.1 mL	ddH_2O
	2.5 mL	30% acrylamide mix (37.5 : 1)
	1.3 mL	1.5 M Tris pH 8.8
	50 µL	10% SDS
	50 µL	10% APS
	2 µL	TEMED

Gel	Composition	
5% stacking gel (2 mL)	1.36 mL	ddH_2O
	0.34 mL	30% acrylamide mix (37.5 : 1)
	0.26 mL	1.5 M Tris pH 8.8
	20 µL	10% SDS
	20 µL	10% APS
	2 µL	TEMED

Running gels were mixed and polymerized between two glass plates and then topped with the stacking gel and a comb to create sample pockets. Gels were placed in the electroporation chamber and the reservoir was filled with SDS-PAGE buffer. 4 µL of 8x SDS LD were added to 28 µL of protein sample and subsequently heated at 95 °C for 5 min. Gel pockets were loaded either with samples (10 µL for 15 well gels, 15 µL for 10 well gels) or the SDS-PAGE standard (Figure 110). The SDS-PAGE program was executed (175 V, 300 mA, 50 min) and subsequently, gels were first stained for 10 min in Coomassie Stain solution before destaining for 10 min in boiling water. Gels were imaged in a photo box using UV light and a visible light long-pass emission filter.

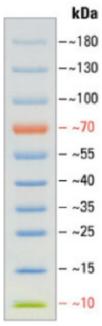

Figure 110: PageRuler Prestained Protein Ladder (Thermo Scientific) for SDS-PAGE (Picture taken form the manufacturer's manual).

5.1.4 Vectors and Protein Constructs

The protein constructs expressed and purified throughout this thesis are summarized in Table 42.

Table 42: Protein constructs used in this work. These constructs served as the template for any follow up mutations.

Protein	Vector	Mutation	ε_{280} (L mol^{-1} cm^{-1})	Mw (kDa)
$YopO_{89-729}$	pGEX-6p-1	C219A	43,390	71.2
$YopO_{1-729}$	pGEX-6p-1	C219A	56,380	81.7
$YopO_{1-729}$•$(SycO)_2$	pET-Duet-1	C219A (YopO)	98,570	116.6
Myoglobin	pBADHisTEV	Q8C	39,100	17.3

The purified GB1 protein was provided by *Dr. Katrin Ackermann* (University of St Andrews) and has a molecular weight of ~6.2 kDa and an extinction coefficient ε_{280} of 9,970 L mol^{-1} cm^{-1}.

5.1.5 Spin Labels

Table 43: Utilized spin labels and radicals.

Spin label	Target residue	Abbreviation	Manufacturer
(2,2,5,5-tetramethylpyrroline-1-oxyl-3-methyl)methanethiosulfonate (MTSL)	cysteine	R1[a]	Toronto Research Chemicals
Finland trityl	-	-	homemade
MTS-TSL	cysteine	**1•**	homemade
Mal-TSL	cysteine	**2•**	homemade
SLIM	cysteine	**3•**	homemade
Ox-SLIM	cysteine	**4•**	homemade
Copper(II)-nitrilotriacetic acid [Cu^{2+}(NTA)]	double histidine	dHis-Cu^{2+}(NTA)[b]	-

[a] The R1 abbreviation is only used for MTSL conjugated to a cysteine residue.
[b] Abbreviation for Cu^{2+}(NTA) coordinated to a dHis-site.

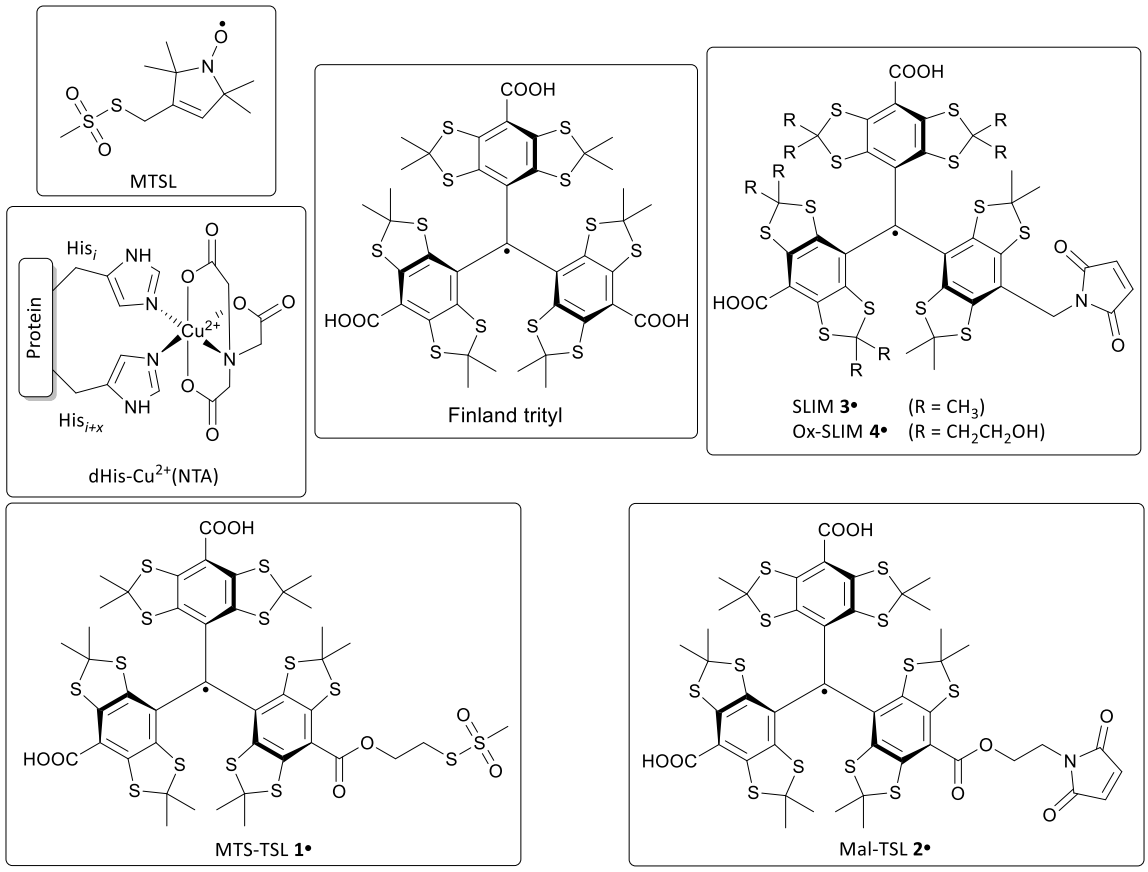

Figure 111: Spin labels used for protein SDSL in the context of this work.

Spin label stock solution were prepared by dissolving the respective spin label (except for Cu^{2+}(NTA), see section 5.2.2.3) in DMSO to a final concentration of 100 mM for MTSL and up to 10 mM for any trityl spin label. The final stock solution concentrations were verified by quantitative EPR spin-count experiments on an EMXnano spectrometer in triplicates and set as the mean value of the three independent measurements.

5.1.6 Computer Software and Plug-ins

Table 44: Utilized computer software and Plug-ins throughout this work.

Software / Plug-in	Publisher
Geneious 6.1.8	Dotmatics
MATLAB R2018b	MathWorks
MATLAB R2021b	MathWorks
EasySpin[108]	*Open Access*
OriginPro 8G	OriginLab
DeerAnalysis2019[122]	*Open Access*
DeerAnalysis2022[122]	*Open Access*
SnrCalculator[424]	*Open Access*
mtsslWizard[355]	*Open Access*
PyMOL™ 2.0.7	Schrödinger
MMM[368]	*Open Access*
PDSFit[384]	*Open Access*

5.2 Methods

This section provides an overview of the experimental procedures used throughout this work.

5.2.1 Mutagenesis, Cloning, and Protein Purification

5.2.1.1 *QuickChange* Mutagenesis and Transformation

Site-specific mutations were introduced using the *QuickChange* mutagenesis protocol.[425] Here, primers consist of a non-overlapping region and an overlapping region encoding for the changed amino acids. Primer sequences and the distinct melting temperatures of the forward (*fwd*) and reverse (*rev*) primers are given below (Table 45).

Table 45: Sequences and annealing temperatures for the primer pairs used in this thesis. Tm_{non} and Tm_o denote the annealing temperatures of the non-overlapping and overlapping regions of the primer with the template vector. If the annealing temperatures between the *fwd* and *rev* primers differed, the averaged melting temperatures were used. Primers were commercially obtained from Microsynth AG.

Mutation	Sequence	Tm_{non} (°C)	Tm_o (°C)
YopO			
S585C *fwd*	5′-CACAGCAAGGGCAGCCCGTGTCCTGTGAAACCT-3′	51.5	47.1
S585C *rev*	5′-GGAGAGTATTCAATTGCTGCGACAAGGTGCACTTAGC-3′	50.5	47.1
Y588C *fwd*	5′-CAAGGGCAGCCCGTGTCCTCTGAAACCTGTAGCTTCC-3′	57.6	48.0
Y588C *rev*	5′-GAATAGATAGTTGCGCTTTCGCACTCTCCTGCTGACACTGGAG-3′	58.0	48.0
V599C *fwd*	5′-GCTTCCTGAATCGATTAGCTGAGGCTAAGTGCACCTTG-3′	53.0	45.9
V599C *rev*	5′-GGAGAGTATTCAATTGCTGCGACAAGGTGCACTTAGCC-3′	53.0	45.9
Q603C *fwd*	5′-CGATTAGCTGAGGCTAAGGTCACCTTGTCGTGTCAATTG-3′	54.8	44.6
Q603C *rev*	5′-CTGCTGCTGCTGGAGAGTATTCAATTGACACGACAAGG-3′	54.4	44.6
N624C *fwd*	5′-GAGAGTGCGAAAGCGCAACTATCTATTCTGATTTGTCGTTCA-3′	54.8	48.5
N624C *rev*	5′-GAGCAACATCAGCCCAAGAACCTGAACGACAAATCAGAATA-3′	54.4	48.5
Y588H/N592H *fwd*	5′-CCACAGCTTCCTGCATCGATTAGCTGAGGCTAAGGTCACCTTG-3′	59.5	49.5
Y588H/N592H *rev*	5′-GATGCAGGAAGCTGTGGGTTTCAGAGGACACGGGCTGCC-3′	60.4	49.5
A595H/V599H *fwd*	5′-GTGTCCTCTGAAACCTACAGCTTCCTGAATCGATTACATGAGGCTAAGCACAC-3′	63.0	53.0
A595H/V599H *rev*	5′-CTGCTGGAGAGTATTCAATTGCTGCGACAAGGTGTGCTTAGCCTCATGTAATC-3′	63.0	53.0
S620H/N624H *fwd*	5′-CAGCAGGAGAGTGCGAAAGCGCAACTACATATTCTGATTCATCGTTC-3′	60.8	49.9
S620H/N624H *rev*	5′-GACGAGCAACATCAGCCCAAGAACCTGAACGATGAATCAGAATATGTAG-3′	61.1	49.9
E87K/F88T *fwd*	5′-GTCACCTTGTCGCAGCAATTGAATACTCTCCAGTGTCAGCAGG-3′	57.1	44.6
E87K/F88T *rev*	5′-GGGATATCAGACCTTAGCTCCTGCGAAGTGGTTTTTTGCG-3′	57.1	44.6
EcoRI-YopO *fwd*	5′-CTGAAGAATTCGATGTCCCCTATACTAGGTTATTGGAAAATTAAGGGC-3′	-	-
SalI-YopO *rev*	5′-ATAAAAGTCGACTCATCACATCCATTCCCGCTCCAACCGGTT-3′	-	-

Mutation	Sequence	Tm_{non} (°C)	Tm_o (°C)
SycO			
C30A *fwd*	5'-GACTGGCCGAACTGATCCTGAATGATCGCGTAGTCATC-3'	55.7	43.2
C30A *rev*	5'-CAGTTCGGCCAGTCCATACTCATCCTGTGACAGTTTGTC-3'	56.0	43.2
C75A *fwd*	5'-CTTCTTTGCCTACTCGATCAATGCGCTCAACAAAGATGG-3'	53.5	43.4
C75A *rev*	5'-CGAGTAGGCAAAGAAGAGCTGAGAAGCAGTCGAACG-3'	53.8	43.4
C87A *fwd*	5'-GGTCCGGCTTTTGCGTGGAGTGAAGAACTGGGC-3'	53.2	43.2
C87A *rev*	5'-GCAAAAGCCGGACCATCTTTGTTGAGCGCATTGATCG-3'	53.5	43.2

To verify primer annealing and plasmid amplification by PCR, an additional sample without polymerase served as a negative control (Table 46). PCR samples were mixed and loaded into a thermocycler and the *QuickChange* PCR program was run (Table 47).

Table 46: PCR sample preparation.

	Sample (µL)	Control (µL)
Template Vector	0.5	0.5
Pfu 10x Buffer	5	5
dNTP Mix (10 mM each)	1	1
Primer (*fwd*)	0.5	0.5
Primer (*rev*)	0.5	0.5
Pfu-Polymerase	0.5	-
ddH_2O	42	42.5

Table 47: *QuickChange* PCR thermocycler setup.

Repeats	Temperature (°C)	Time (s)	Step
1 cycle	95	300	Initial denaturing
3 cycles	95	60	Denaturing
	Tm_{non}-5	60	Annealing
	72	900	Extension
15 cycles	95	60	Denaturing
	Tm_o-5	60	Annealing
	72	900	Extension
2 cycles	95	60	Denaturing
	43	60	Annealing
	72	900	Extension
1 cycle	4	∞	Storage

After the PCR, the success of the vector amplification was checked via agarose gel electrophoresis using 5 µL of the crude PCR products. Unmutated template DNA was removed upon the addition of 5 µL 10x Tango buffer and 0.5 µL *DpnI* restriction enzyme to the remaining 45 µL of PCR sample and incubation for 2 h at 37 °C. Subsequently, samples were purified according to the GeneJET Gel Extraction and DNA Cleanup MicroKit manual, and the DNA concentration was quantified using the NanoDrop™ 2000 nucleic acid application. 50 µL of competent *E. coli* DH5α cells (homemade) were thawed for 20 min on ice before the addition of 100 ng plasmid DNA. After an additional 20 min incubation period, cell permeabilization and transformation of plasmid DNA was achieved via a heat shock (42 °C, 45 s) in a water bath and subsequently, cells were allowed to recover for 5 min on ice. After the addition of 1 mL LB medium, cells were grown for 1 h (37 °C, 180 rpm) before harvesting (14,000 rcf, 2 min), and resuspension in 100 µL LB medium. Resuspended cells were spread on an agar plate containing 0.3 mM ampicillin as a selection marker and plates were incubated overnight upside down (37 °C). After 18 h, up to four colonies were picked for overnight

cultures (10 mL LB medium, 0.3 mM ampicillin, 1 colony) and the samples were incubated for at least 18 h (37 °C, 180 rpm) before harvesting (4,000 rcf, 20 min), and subsequent plasmid purification following the user manual of the GeneJET Plasmid Miniprep Kit. After quantification with a NanoDrop™ 2000 using the nucleic acid application, purified plasmid DNA was sent for sequencing (Microsynth AG, plasmid DNA concentration ≥ 60 ng/µL). Sequencing results were evaluated using the Geneious software.

5.2.1.2 Cloning of $YopO_{1\text{-}729}$ into the pGEX-6p-1 Vector

PasI restriction cleavage was set up according to Table 48 using a synthetic gene encoding for the amino acids 1-88 of the YopO-wt (encoded on a pEX-A-128 vector, purchased from Eurofins Scientific) as the insert and the pGEX-6p-1 plasmid encoding for $YopO_{89\text{-}729}$ as the target vector.

Table 48: *PasI* restriction enzyme digest.

	Insert (µL)	**Vector (µL)**
Insert DNA (AA 1-89)	34 (2,500 ng)	-
Vector DNA ($YopO_{89\text{-}729}$)	-	12 (2,500 ng)
10x buffer *PasI*	5	5
PasI restriction enzyme	2.5	2.5
ddH_2O	0.5	0.5

After mixing, the *PasI* cleavage was incubated for 4 h at 55 °C before heating the reaction mixture to 80 °C for 20 min to inactivate the *PasI* restriction enzyme and prevent unspecific cleavage, as the *PasI* enzyme exhibits a star activity (see Thermo Scientific manual). Subsequently, 6 µL of FastDigest buffer (10x) and 4 µL of FastDigest *EcoRI* restriction enzyme was added to both, the insert and the vector sample, and incubated for 30 min at 37 °C before quenching the reaction upon heating to 80 °C for 5 min. Only to the vector sample, 1 µL of Fast alkaline phosphatase was added and the sample was incubated for 1 h at 37 °C before reaction clean up following the protocol for PCR purification of the GeneJet Gel Extraction and DNA Cleanup MicroKit. The complete insert sample was loaded onto an agarose gel (1%) and after agarose gel electrophoresis, the faint lower band corresponding to the gene fragment encoding for the first 88 amino acids of YopO was cut out and cleaned up using the GeneJet Gel Extraction and DNA Cleanup MicroKit. The ligation reaction of the insert with the vector at a molar ratio of 3:1 was set up according to Table 49.

Table 49: Insert-vector ligation setup.

	Reaction (µL)
Insert DNA (AA 1-89)	5 (20 ng)
Vector DNA ($YopO_{89\text{-}729}$)	4 (160 ng)
10x T4 DNA ligase buffer	2
T4 DNA ligase	0.2
ddH_2O	9

The ligation reaction was incubated for 16 h at 16 °C and subsequently, the crude ligation mixture was transformed into competent *E. coli* DH5α cells and subsequently purified and sequenced as described in section 5.2.1.1.

5.2.1.3 Cloning of $YopO_{1-729}$•$(SycO)_2$ into the pET-Duet-1 Vector

The GST-$YopO_{1-729}$ gene encoded on the pGEX-6p-1 vector (see section 5.2.1.2) was amplified via PCR using primers containing an *EcoRI* (*fwd*, 5'-start) and *SalI* (*rev*, 3'-end) restriction site according to Table 50+51.

Table 50: GST-$YopO_{1-729}$ PCR amplification setup.

	Sample (µL)	Control (µL)
Template Vector	0.5	0.5
Pfu 10x Buffer	5	5
dNTP Mix (10 mM each)	1	1
Primer (*fwd*)	0.5	0.5
Primer (*rev*)	0.5	0.5
Pfu-Polymerase	0.5	-
ddH_2O	42	42.5

Table 51: Thermocycler setup for $YopO_{1-729}$-wt gene amplification via PCR.

Repeats	Temperature (°C)	Time (s)	Step
1 cycle	95	300	Initial denaturing
	95	30	Denaturing
30 cycles	62.7	30	Annealing
	72	100	Extension
1 cycle	72	300	Final Extension
1 cycle	4	∞	Storage

Following gene amplification, the crude PCR product was purified using the GeneJet Gel Extraction and DNA Cleanup MicroKit. Subsequently, the GST-$YopO_{1-729}$ insert and the empty pET-Duet-1 vector (purchased from Novagen) were digested with *EcoRI* and *SalI* according to Table 52.

Table 52: *EcoRI* and *SalI* restriction enzyme digest.

	Insert (µL)	Vector (µL)
Insert DNA (GST-$YopO_{1-729}$)	40 (3,200 ng)	-
Vector DNA (pET-Duet-1)	-	5 (1,600 ng)
FastDigest buffer (10x)	10	10
EcoRI restriction enzyme	2.5	2.5
SalI restriction enzyme	2.5	2.5
ddH_2O	45	80

The restriction enzyme reactions proceeded for 3 h at 37 °C before the addition of 1 µL Fast alkaline phosphatase to the vector sample and an additional 1 h incubation period at 37 °C. Subsequently, both samples were cleaned up using the GeneJet Gel Extraction and DNA Cleanup MicroKit and the insert was ligated into the opened first multiple cloning site (MCS) of the pET-Duet-1 vector (molar ratio of insert to vector: 2:1) according to Table 53.

Table 53: Insert-vector ligation setup for GST-YopO$_{1-729}$ in the pET-Duet-1 vector.

	Reaction (µL)
Insert DNA (GST-YopO$_{1-729}$)	3.2 (275 ng)
Vector DNA (pET-Duet-1)	14 (84 ng)
10x T4 DNA ligase buffer	2
T4 DNA ligase	0.2

The ligation reaction was incubated for 16 h at 16 °C and subsequently, the crude ligation mixture was transformed into competent *E. coli* DH5α cells and subsequently purified and sequenced as described in section 5.2.1.1.

A synthetic gene encoding for SycO (vector: pEX-A-128) containing the restriction sites for *NdeI* (5'-start) and *XhoI* (3'-end) was purchased from Eurofins and cloned into the second MCS of the pET-Duet-1 vector containing the GST-YopO$_{1-729}$ gene in the first MCS. Therefore, both vectors were digested using the *NdeI* and *XhoI* restriction enzymes according to Table 54.

Table 54: *NdeI* and *XhoI* restriction enzyme digest.

	Insert (µL)	**Vector (µL)**
Insert DNA (SycO)	14 (4,000 ng)	-
Vector DNA (pET-Duet-1)	-	8.5 (2,000 ng)
FastDigest buffer (10x)	10	10
NdeI restriction enzyme	2.5	2.5
XhoI restriction enzyme	2.5	2.5
ddH_2O	71	76.5

The restriction digest was incubated for 3 h at 37 °C before the addition of 1 µL of Fast alkaline phosphatase to the vector sample and an additional incubation period of 1 h at 37 °C. Subsequently, the vector DNA was cleaned up following the protocol for PCR purification of the GeneJet Gel Extraction and DNA Cleanup MicroKit. The complete insert sample was loaded onto an agarose gel (1%) and after agarose gel electrophoresis, the faint lower band at ~500 bp corresponding to the SycO gene was cut out and cleaned up using the GeneJet Gel Extraction and DNA Cleanup MicroKit. The ligation of the SycO-insert into the opened MCS2 of the pET-Duet-1 vector (molar ratio of insert to vector: 2:1) was set up according to Table 55.

Table 55: Insert-vector ligation setup for SycO in the pET-Duet-1 vector.

	Reaction (µL)
Insert DNA (SycO)	7.55 (26 ng)
Vector DNA (pET-Duet-1)	10.25 (205 ng)
10x T4 DNA ligase buffer	2
T4 DNA ligase	0.2

The ligation reaction was incubated for 16 h at 16 °C and subsequently, the crude ligation mixture was transformed into competent *E. coli* DH5α cells and subsequently purified and sequenced as described in section 5.2.1.1.

5.2.1.4 Expression and Purification of Truncated YopO$_{89-729}$

Truncated YopO$_{89-729}$ constructs were expressed in *E. coli* Rosetta DE3 cells (homemade). 50 µL of competent expression cells were thawed for 20 min on ice before an additional incubation period of 20 min with 100 ng plasmid DNA. Cells were then heat-shocked (42 °C, 45 sec) and recovered

for 5 min on ice before the addition of 1 mL LB medium and incubation for 1 h (37 °C, 180 rpm). 100 µL of the cell suspension were plated on an agar plate containing 0.3 mM ampicillin and 0.1 mM chloramphenicol for selection purposes. The next day, a single colony was picked to prepare an overnight culture (100 mL LB medium, 0.3 mM ampicillin, 0.1 mM chloramphenicol, 1 colony) and cells were grown for ~18 h (37 °C, 180 rpm). Typically, 3 liters of main culture (1 L LB medium, 0.3 mM ampicillin, 0.1 mM chloramphenicol, 15 mL overnight culture) were set up and incubated (37 °C, 180 rpm) until an optical density at 600 nm (OD_{600}) of ~0.8 – 1.0 was reached. Protein expression was induced upon the addition of 0.1 mM IPTG and cultures were shifted to 16 °C and grown for 16 h before being harvested the next day (4,000 rcf, 4 °C, 20 min). Cell pellets were either used immediately or frozen at -80 °C for long-term storage.
Cell pellets were resuspended in five times v/w YopO Basic buffer and lysed via sonication (3 cycles, 2:30 min, 70% amplitude, 1s pulse : 1s pause). Insoluble cell debris was removed via centrifugation (48,500 rcf, 4 °C, 20 min) and the supernatant was collected and incubated with 3 mL Glutathion Sepharose™ 4B beads (equilibrated with YopO Basic buffer) for 1 h at room temperature and slight agitation. Subsequently, the bead suspension was passed over a benchtop gravity column and the collected flow-through was passed over the settled beads to maximize the protein yield. Beads were washed with 50 mL of YopO Basic buffer before being resuspended in 20 mL YopO Cleavage buffer and incubated overnight at 4 °C under slight agitation. The following day, the bead-suspension was loaded again onto a gravity column and the protein-containing eluate was diluted with 130 mL YopO IExA buffer containing 2.5 mM DTT. Subsequently, anion exchange chromatography was performed on an ÄKTA avant system using either an ENrich™ Q 10x100 or Capto™ HiRes Q 10/100 column, and the loaded protein was eluted using a linear gradient of YopO IExB buffer. The protein content was checked via SDS-PAGE and $YopO_{89-729}$ containing fractions were pooled and concentrated below 3 mL using a Vivaspin® 20, 10 kDa MWCO before adding DTT to a final concentration of 3 mM. The protein was loaded onto a HiLoad® 16/600 Superdex® 200 pg equilibrated with YopO GF buffer and a gel filtration was performed. The protein purity was checked via SDS-PAGE and the pure protein-containing fractions were pooled and concentrated using a Vivaspin® 20, 10 kDa MWCO. At a final protein concentration of ~100 µM (assessed using the NanoDrop™ 2000 A280 program and the extinction coefficient given in Table 42), the protein was split into 200 µL aliquots, flash-frozen in liquid nitrogen, and stored at -80 °C if not used immediately.

5.2.1.5 BugBuster® Expression Assay and Western Blot for GST-$YopO_{fl}$

Main cultures (2x 300 mL) of *E. coli* Rosetta DE3 cells containing the GST-$YopO_{fl}$ gene were prepared according to section 5.2.1.4. Protein expression was induced upon the addition of 0.2 mM IPTG and one baffled flask was shifted to 16 °C and the second one to 25 °C (both 180 rpm). At indicated time points, 1.5 mL were taken from the respective culture and processed as follows:

1. 1.5 mL of the culture was spun down (16,000 rcf, 4 °C, 10 min).
2. The supernatant was decanted and pipetted away and the obtained pellet was flash-frozen twice in liquid nitrogen.
3. The pellet was resuspended in 300 µL BugBuster® Buffer (1x) before adding 651 µL Lysis buffer containing 1 µL Pierce™ universal nuclease. The solution was incubated for 20 min at room temperature and slight agitation.
4. The sample was centrifuged (16,000 rcf, 4 °C, 20 min) and the resulting supernatant corresponded to the soluble protein fraction.
5. The remaining pellet was resuspended in 60 µL Urea and incubated for 5 min before the addition of 240 µL Lysis buffer. This sample is referred to as the pellet sample.

The respective samples were loaded onto a 10% SDS gel and SDS-PAGE was performed according to section 5.1.3.2.
For Western blotting, a PVDF membrane was moistened with methanol, rinsed with MilliQ water, and equilibrated together with the previously ran SDS gel in separate containers with Transfer buffer for 15 min. The equilibrated gel was placed on top of the PVDF membrane facing the cathode and the stack was sandwiched between two blotting papers soaked in Transfer buffer on each side before blotting the proteins onto the membrane (~1.5 mA/cm^2, max. 25 V, 1.5 h). The membrane was blocked with Blocking solution (10 mL, 1 h, gently shaking) and washed thrice with TBST (10 mL and 10 min each). Subsequently, the PVDF membrane was incubated (4 °C, o/n, gently shaking) with the primary mouse anti-GST antibody (5 mL, 1:1,000 working dilution in TBST) to detect GST-tagged proteins. After incubation, the membrane was washed thrice with TBST (10 mL and 10 min each) and incubated (1 h, room temperature, gently shaking) with the horseradish peroxidase (HRP) conjugated secondary goat anti-mouse IgG antibody (5 mL, 1:5,000 working dilution in TBST). In the last step, the membrane was rinsed thrice with TBST (10 mL for 10 min each) before visualization of GST-fused proteins on the blot using 10 mL 1-Step™ TMB-Blotting Substrate Solution (30 min incubation). Blue bands corresponding to GST and GST-tagged proteins appeared on the PVDF membrane and a photograph of the membrane was taken using a smartphone.

5.2.1.6 Expression and Purification of Full-Length $YopO_{1-729}$•$(SycO)_2$

Full-length $YopO_{1-729}$ constructs in complex with SycO ($YopO_{1-729}$•(SycO)) were expressed in *E.coli* Rosetta DE3 cells (homemade). 50 µL of competent expression cells were thawed for 20 min on ice before an additional incubation period of 20 min with 100 ng plasmid DNA. Cells were then heat-shocked (42 °C, 45 sec) and recovered for 5 min on ice before the addition of 1 mL LB medium and incubation for 1 h (37 °C, 180 rpm). 100 µL of the cell suspension were plated on an agar plate containing 0.3 mM ampicillin and 0.1 mM chloramphenicol for selection purposes. The next day, a single colony was picked to prepare an overnight culture (100 mL LB medium, 0.3 mM ampicillin, 0.1 mM chloramphenicol, 1 colony) and cells were grown for ~18 h (37 °C, 160 rpm). Typically, 3 liters of main culture (1 L LB medium, 0.3 mM ampicillin, 0.1 mM chloramphenicol, 15 mL overnight culture) were set up and incubated (37 °C, 160 rpm) until an OD_{600} of ~0.8 –1.0 was reached. Protein expression was induced upon the addition of 0.125 mM IPTG and cultures were shifted to 16 °C and grown for 16 h before being harvested the next day (4,000 rcf, 4 °C, 20 min). Cell pellets were either used immediately of frozen at -80 °C for long-term storage.
Cell pellets were resuspended into four times v/w YopO•(SycO) Basic buffer supplemented with 0.1 µL Pierce™ universal nuclease per 10 mL buffer and lysed via sonication (3 cycles, 2:30 min, 70% amplitude, 1s pulse : 1s pause). Insoluble cell debris was removed via centrifugation (30,000 rcf, 4 °C, 25 min) and the supernatant was collected and incubated with 4 mL Glutathione Sepharose™ 4B beads (equilibrated with YopO•(SycO) Basic buffer) for 1 h at 4 °C and slight agitation. The bead suspension was passed over a benchtop gravity column and the collected flow-through was passed over the settled beads once more to maximize the protein yield. Beads were washed with 30 mL YopO•(SycO) Basic buffer before being resuspended in 15 mL YopO•(SycO) Cleavage buffer and incubated for 5:30 h at 4 °C whilst slightly agitating the sample. Subsequently, the bead-suspension was loaded again onto a gravity column and the settled beads were washed with 15 mL YopO•(SycO) IExA buffer. Both elutions were combined and diluted with an additional 70 mL YopO•(SycO) IExA buffer containing 3 mM DTT. Anion exchange chromatography was performed on an ÄKTA avant system using a CaptoQ™ HiRes Q 10/100 column and the protein was eluted using a linear gradient of YopO•(SycO) IExB buffer. The protein purity was checked via SDS-PAGE and fractions containing full-length $YopO_{1-729}$ and SycO were pooled and concentrated

using a VivaSpin® 20, 10 kDa MWCO. At a final protein concentration of ~100 µM (assessed using the NanoDrop™ 2000 A280 program and the extinction coefficient for the $YopO_{1-729}$•$(SycO)_2$ complex given in Table 42), the protein was split into 200 µL aliquots, flash-frozen in liquid nitrogen, and stored at -80 °C if not used immediately.

5.2.1.7 Expression and Purification of Myoglobin

Myoglobin was expressed in *E. coli* BL21 cells (homemade) and purified according to previously established procedures.[342]

From a pipette tip of a previously prepared glycerol stock an overnight culture (50 mL LB medium, 0.15 mM ampicillin, 5 µL *E. coli* glycerol stock) was prepared and cells were grown for ~18 h (37 °C, 180 rpm). Typically, 3 liters of main culture (1 L LB medium, 0.15 mM ampicillin, 10 mL overnight culture) were set up and incubated (37 °C, 180 rpm) until an OD_{600} of ~0.5 – 0.8 was reached. Protein expression was induced upon the addition of 13 mM L(+)-arabinose and 2.4 mM 5-aminolevulinic acid to increase the heme-loading of myoglobin. Cultures were further incubated for 4 h (37 °C, 180 rpm) before the cells were harvested (4,000 rcf, 4 °C, 20 min) and either used immediately or frozen at -80 °C for long-term storage.

Cell pellets were resuspended in ten times v/w Myoglobin Basic buffer supplemented with 0.1 µL Pierce™ universal nuclease per 10 mL buffer and lysed via sonication (3 cycles, 2:30 min, 70% amplitude, 1s pulse : 1s pause). Insoluble cell debris was removed via centrifugation (48,500 rcf, 4 °C, 20 min) and the deeply red supernatant was incubated with 3 mL HisPur™ Ni-NTA resin (equilibrated with Myoglobin Basic buffer) for 1 h at room temperature and slight agitation. The suspension was passed over a benchtop gravity column and the deeply red resin was washed with 50 mL Myoglobin Basic buffer. Then, the resin was resuspended in 15 mL Myoglobin Basic buffer and 5 mL of TEV protease (1 mg/mL in 20 mM Tris, 500 mM NaCl, pH 7.5) were added. The His_6-tag cleavage suspension was incubated for 3 h at room temperature and then shifted to 4 °C for an additional 16 h incubation overnight, all whilst slightly agitating the sample. The following day, the suspension was loaded onto a gravity column and the elution was passed an additional time over the Ni-NTA resin to remove any remaining His_6-tagged protein impurities. The resin was washed twice with 10 mL Myoglobin IExA buffer and all elution fractions were combined to perform an anion exchange on an Äkta avant system using an ENrich™ Q 10x100 column against a linear gradient of Myoglobin IExB buffer. The protein content was checked via SDS-PAGE and the Myoglobin-containing flow-through was pooled and concentrated below 500 µL using a VivaSpin® 20, 5 kDa MWCO before adding DTT to a final concentration of 3 mM. The protein was loaded onto a Superdex® 75 10/300 GL equilibrated with Myoglobin GF buffer and a gel filtration was performed. The protein purity was checked via SDS-PAGE and the pure protein-containing fractions were pooled and concentrated using a VivaSpin® 20, 5 kDa MWCO. The protein-concentration was determined using the UV-vis application of the NanoDrop™ 2000 and the extinction coefficient given in Table 42) and if the absorption ratio between 409 nm and 280 nm was approximately 3:1, a sufficient heme-loading was assumed. The protein was flash-frozen in liquid nitrogen and stored at -80 °C if not used immediately.

5.2.2 Site-Directed Labeling of Proteins

5.2.2.1 MTSL Spin Labeling

All MTSL labeling procedures were conducted in the protein buffers of the last chromatographic purification step of the utilized proteins. Before the labeling reaction, up to 55 nmol of protein were incubated in a total volume of 2 mL with 3 mM DTT for 1 h at room temperature. Subsequently, the reducing agent was removed by passing the incubation solution over a PD-10 desalting column. Immediately after the elution, a 20-fold molar excess MTSL per cysteine from a

100 mM stock solution dissolved in DMSO was added to the 3.5 mL protein-containing PD-10 eluate and the labeling reaction was incubated for 2 h at room temperature before being shifted to 4 °C overnight for an addition 16 h incubation period.
The next day, the incubation solution was loaded either onto HiPrep™ 26/10 desalting column or split in two fractions and ran over a PD-10 desalting column to remove any excess and unbound spin label. The protein-containing fractions were pooled and concentrated to approximately 100 µM with a Vivaspin® 6 centrifugal filter with an appropriate molecular weight cutoff for the respective protein at hand.

Only Myoglobin: To the concentrated sample (below 2 mL), a 20-fold molar excess of $K_3[Fe(CN)_6]$ was added and incubated for 2 h at room temperature to convert MbO_2 to the MetMb form. The oxidizing agent was subsequently removed using a PD-10 desalting column.

Samples for pulsed dipolar EPR experiments were rebuffered to their respective deuterated PDS buffers. The buffer was exchanged by the addition of 2 mL deuterated PDS buffer per 200 µL of sample and subsequent concentration using a Vivaspin® 6 centrifugal filter with an appropriate molecular weight cutoff. The dilution/concentration cycle was repeated trice and samples were concentrated in the final run to approximately 100 µM. In the last step, any precipitates were removed by centrifugation in a microcentrifugal tube at 18,000 rcf and the supernatant was carefully collected. If not used immediately, samples were aliquoted to 100 µL, flash-frozen in liquid nitrogen, and stored at -80 °C.

5.2.2.2 Trityl Spin Labeling

All trityl labeling procedures were conducted in phosphate buffer (pH 6.8). Before the labeling reaction, 20 nmol of protein were incubated in a total volume of 2.5 mL with a five-fold molar excess of TCEP for 2 h at 4 °C. Subsequently, the reducing agent was removed by passing the incubation solution over a PD-10 desalting column and the labeling reaction was set up immediately afterwards.
The respective trityl spin label (dissolved in DMSO) was prediluted in 2.5 mL phosphate buffer and added to the collected 3.5 mL protein solution. The employed molar ratios for the utilized trityl spin label and proteins are given in Table 56.

Table 56: Molar ratios of the trityl spin labels and proteins utilized in the spin labeling reactions.

Protein	MTS-TSL 1•	Mal-TSL 2•	SLIM 3•	Ox-SLIM 4•
$YopO_{89-729}$	5 eq. / Cys	5 eq. / Cys	5 eq. / Cys	5 eq. / Cys
$YopO_{1-729}$•$(SycO)_2$	-	-	5 eq. / Cys	-
Myoglobin	-	5 eq. / Cys	5 eq. / Cys	-
GB1	-	-	3.5 eq. / Cys	-

After the spin label addition, the solution was gently homogenized by slowly pipetting up and down and subsequently shifted into the dark (fridge) and incubated for 16 h at 4 °C.
The following day, the incubation solution was split into at least three fractions (up to five fractions for best separation of the free label) and passed over a PD-10 desalting column to remove the spin label excess. The protein-containing fractions were pooled and concentrated to approximately 2 mL using a Vivaspin® 6 centrifugal filter with an appropriate molecular weight cutoff.

Only Myoglobin: To the concentrated sample (below 2 mL), a 20-fold molar excess of $K_3[Fe(CN)_6]$ was added and incubated for 2 h at room temperature to convert MbO_2 to the MetMb form.

The concentrated sample was loaded onto a HiPrep™ 26/10 desalting column to achieve complete free label separation and enhanced sample purity. The first elution peak showing an absorbance at 280 nm was pooled and concentrated before recording a UV-vis spectrum for the quantification of labeling efficiency (see section 3.2.2.1).

Samples for pulsed dipolar EPR experiments were rebuffered to their respective deuterated PDS buffers. The buffer was exchanged by the addition of 2 mL deuterated PDS buffer per 200 µL of sample and subsequent concentration using a Vivaspin® 6 centrifugal filter with an appropriate molecular weight cutoff. The dilution/concentration cycle was repeated trice and samples were concentrated in the final step to approximately 100 µM. In the last step, any precipitates were removed by centrifugation in a microcentrifugal tube at 18,000 rcf and the supernatant was carefully collected. If not used immediately, samples were aliquoted to 100 µL, flash-frozen in liquid nitrogen, and stored at -80 °C.

5.2.2.3 dHis-Cu^{2+}(NTA) Spin Labeling

Nitrilotriacetic acid (NTA) was dissolved in MilliQ water to a final concentration of 100 mM and pH-adjusted to pH 12 with 5 M NaOH. Copper(II) sulfate was dissolved in MilliQ water to a final concentration of 4 mM and pH-adjusted to pH 2 with 12 M HCl. The 4 mM copper(II) sulfate stock solution was further diluted to a copper(II) concentration of 3 mM with MOPS buffer, and then mixed in a 1:1 molar ratio with the NTA stock solution and pH-adjusted to pH 7.4 (HCl and/or NaOH) to yield the final Cu^{2+}(NTA) stock solution. The solution was aliquoted and stored at -20 °C until used.

The respective YopO construct was rebuffered thrice in deuterated dHis buffer using a VivaSpin® 6, 10 kDa MWCO PES to a protein concentration above 200 µM. Subsequently, one or two molar equivalents of the previously prepared Cu^{2+}(NTA) stock per YopO were added and the sample was diluted with dHis buffer to a final YopO concentration of 200 µM. The mixture was carefully mixed and incubated for 30 min at 4 °C.

5.2.2.4 Alexa Fluor™ 488 C_5 Maleimide Labeling

All Alexa Fluor™ 488 labeling reactions were conducted in phosphate buffer (pH 6.8). In a total of 500 µL phosphate buffer (pH 6.8), 25 nmol of protein (single-cysteine constructs only), a ten-fold molar excess of TCEP, and a five-fold molar excess of Alexa Fluor™ 488 C_5 Maleimide (5 mM stock solution in DMSO) were mixed. The reaction tube (Eppendorf tube) was wrapped in tinfoil and the solution was incubated for 18 h at 4 °C.
The following day, the incubation solution was passed over a PD-10 desalting column (equilibrated with PBS buffer, wrapped in tinfoil) and the protein-containing elution was concentrated down to ~200 µL using a Vivaspin® 6, 10 kDa MWCO. If the VivaSpin® flow-through was colorized by the remaining free fluorescence label, 3 mL PBS buffer were added to the concentrated protein, the solution was concentrated again, and the procedure was repeated until no coloration of the flow-through was observed by visual inspection. The labeling efficiency was quantified according to section 3.2.2.1 using the extinction coefficients for Alexa Fluor™ 488 given in section 3.2.7.3.

5.2.4 YopO Phosphorylation Assay

The phosphorylation assay setup was adapted from *Lee* et al.[328] YopO-wt or labeled YopO (2 µM) was incubated in the presence of G-actin (6 µM, extracted from rabbit muscle acetone powder according to *Spudich* et al.)[426] in YopO Phosphorylation buffer for 1.5 h at 37 °C. For each tested mutant, an additional sample without G-actin served as a negative control. After the incubation

period, the phosphorylation reaction was quenched upon the addition of 8x SDS LD and subsequent heating for 5 min at 95 °C.
Samples were loaded on a 10% SDS gel and after electrophoresis, the gel was placed in a Petri dish and soaked twice with 100 mL SDS Fixing solution for 30 min each before washing trice with MilliQ water (10 min, 100 mL each). Subsequently, the gel was stained with 100 mL Pro-Q™ Diamond Phosphoprotein gel stain in the dark for 90 min. Excess staining solution was removed using SDS Destaining solution (3 times, 30 min, 100 mL each) before a final wash in MilliQ water (2 times, 5 min, 100 mL each). The phosphorylated proteins were detected using a UV-table equipped with a 590 nm long-pass emission filter. Afterwards, the total protein was visualized by Coomassie staining of the same gel.

5.2.5 UV-vis Spectroscopy

Cary100 UV-Vis: Before each measurement, quartz glass cuvettes were thoroughly cleaned using Milli-Q® water and acetone, and the remaining solvent was evaporated under a dry nitrogen gas stream. The cuvette positions were aligned with the light path and a spectrum of the respective pure buffer solution was used as a baseline. Cuvettes were filled with 700 µL of sample solution and spectra were recorded from 600 nm to 200 nm at a scan rate of 0.3 s nm^{-1}.

NanoDrop™ 2000: Before measurements, the light path was cleaned using ethanol and wiped with an optical tissue. A sample volume of 3 µL was added onto the measurement pedestal and UV-vis spectra were recorded using the A280 application (YopO), UV-vis application (myoglobin or trityl-labeling quantifications), or nucleic acid application (DNA).

5.2.6 Mass Spectrometry

5.2.6.1 ESI(+)-MS

Throughout this work, protein samples have been subjected to ESI(+) mass spectrometry analysis at different mass spectrometry facilities and collaboration partners, each with different demands in sample preparation and used equipment. Below are descriptions of the preparation procedures and mass spectrometers used at the individual facilities.

Mass spectrometry service facility Marburg: A fraction of the purified (and labeled) protein before deuteration was diluted in MilliQ water to a final protein concentration of approximately 20 µM in a total volume of 20 µL. The sample was flash-frozen in liquid nitrogen and sent to the mass spectrometry service facility of the Philipps University Marburg via overnight express on dry ice. ESI(+)-spectra were then recorded and deconvoluted by the service facility team using a Waters Synapt G2-Si spectrometer.

CECAD Proteomics facility Cologne: 50 µL of the purified (and labeled) protein before deuteration with a concentration of approximately 20 µM was desalted by buffer exchange with a mixture of 0.1% formic acid and 20% acetonitrile in MilliQ water using a 10 kDa MWCO Amicon centrifugal concentrator (three times, 500 µL each). Subsequently, the sample was flash-frozen in liquid nitrogen and sent to the CECAD Proteomics facility at the University of Cologne via overnight express on dry ice. ESI(+)-spectra were then recorded and deconvoluted by the service facility team using an LTQ Orbitrap Discovery spectrometer.

BRSC mass spectrometry and proteomics facility St Andrews: A fraction of the purified (and labeled) GB1 protein before deuteration was diluted in 1% formic acid to a final protein

concentration of 1 µM. ESI(+)-spectra were then recorded and deconvoluted by *Dr. Katrin Ackermann* using a Waters Xevo G2 TOF mass spectrometer.

5.2.6.2 MALDI(+)-MS

MALDI(+)-MS samples were recorded at the mass spectrometry facility of the Chemical Institutes of the University of Bonn.

20 µL of the purified (and labeled) protein before deuteration with a concentration of approximately 20 µM were mixed with 2,5-Dihydroxyacetophenone (2,5-DHAP) matrix solution (in ethanol with diammonium hydrogen citrate) and the resulting suspension transferred onto a stainless steel MALDI target plate. The droplets were evaporated to dryness at room temperature before the measurements. MALDI(+)-spectra were measured by the facility team using a Bruker Daltonics ultrafleXtreme TOF/TOF spectrometer.

5.2.7 Circular Dichroism Spectroscopy

All CD spectra were recorded on a Jasco J-810 spectropolarimeter equipped with a computer-controlled Peltier element at 20 °C provided by the group of *Prof. Arne Luetzen*. Spectra were recorded using Semi-Micro Cell cuvettes (1 cm pathlength) at a protein concentration of 0.75 µM in dHis buffer. All spectra were baseline-corrected by subtraction of a previously measured buffer sample under the same conditions.

Thermal melts were recorded immediately after a CD scan using the same sample and cuvettes. The temperature was reduced to 4 °C and after thermal equilibration (~15 min), the temperature was gradually increased (2 °C per minute) up to 95 °C. Throughout the heating process, the ellipticity change at 220 nm was monitored (each 0.5 °C step). The baseline was corrected by a measurement of pure dHis buffer without protein under the same conditions.

5.2.8 *In-Cell* Sample Preparation

5.2.8.1 *Xenopus Laevis* Microinjections

The microinjection procedure of YopO Y588-**3•**/N624-**3•** into stage IV *Xenopus laevis* oocytes was adapted and adjusted from previous protocols.[164,427]

All oocytes were visually inspected for signs of apoptosis or cell defects before transfection experiments and only intact and healthy oocytes were used. Up to 30 oocytes were aligned with the dark animal hemisphere upwards on a Parafilm™-covered home-build acrylic glass plate with milled 1.5 mm x 1.5 mm grooves and covered in MBS buffer to prevent dehydration (Figure 112a). The injection needle was pulled over a Bunsen burner using glass capillaries with an outer diameter of 0.3 mm (supplement of the microinjector). If the needle was considered thin enough, it was filled with light silicon oil, mounted onto the microinjector, and filled with a concentrated solution of YopO Y588-**3•**/N624-**3•** (~400 µM, in YopO GF buffer) (Figure 112b). Each oocyte was carefully penetrated with the injection needle at the animal hemisphere under a microscope and 59.8 nL of the labeled protein solution was injected (Figure 112c). If leakage from the oocyte was observed or other mechanically applied damage was noticed, the respective oocyte was carefully discarded using a pipette. After complete injection to all oocytes, the oocytes were washed off the acrylic glass plate with MBS buffer into a Petri dish and more MBS buffer was added to wash away any potential protein sticking to the oocyte surface. After a last visual inspection of the oocytes (Figure 112d), up to 20 oocytes were transferred into a Q-band tube filled with MBS buffer (Figure 112e). Subsequently, the excess buffer on the oocytes was removed (Figure 112f) and the oocytes were incubated up to 2 h to allow homogenous distribution of the protein within the cells.

Subsequently, the Q-band tube was flash-frozen in liquid nitrogen and stored in a Dewar if measurements were not conducted immediately afterwards.

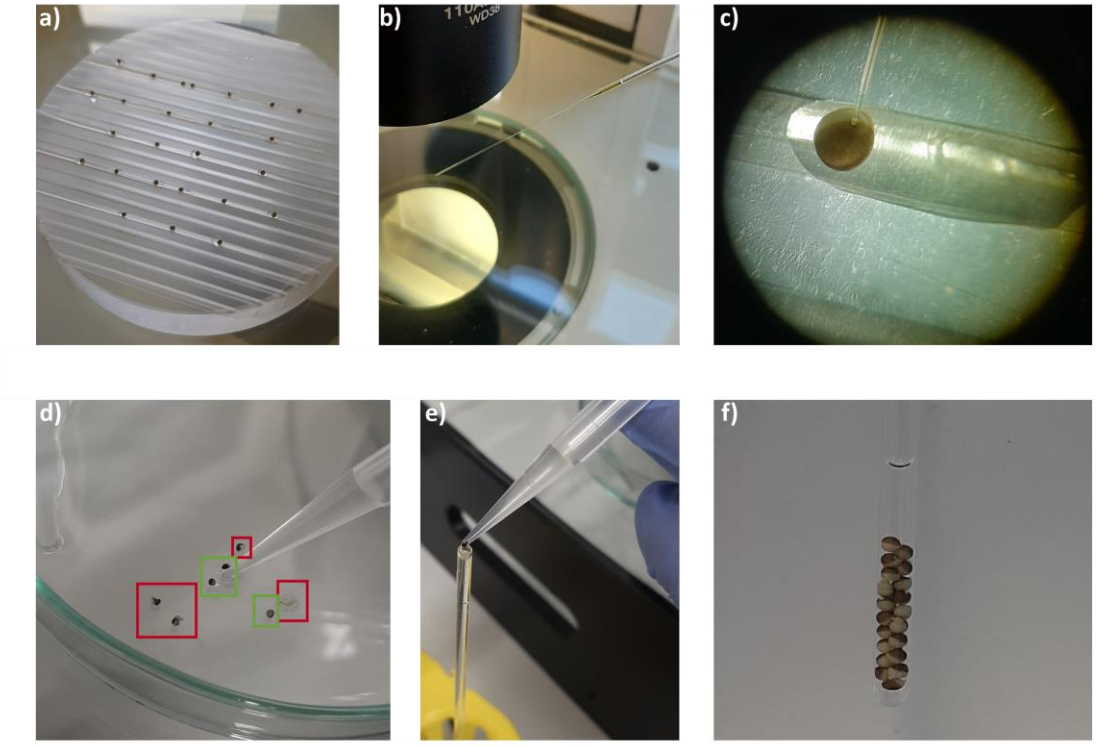

Figure 112: Key steps of the *Xenopus laevis* oocyte injection and sample preparation. **a)** *Xenopus* laevis oocytes aligned on the Parafilm™-covered acrylic glass plate. **b)** Mounted injection needle filled with YopO Y588-**3•**/N624-**3•**. **c)** Penetration and injection process of an oocyte viewed through the lens of the microscope. Picture taken with a smartphone through the lens. **d)** Washing and visual inspection of the oocytes on a Petri dish. Oocytes in red squares were damaged and sorted out while oocytes in green squares were suited for further processing. **e)** Oocyte transfer into a Q-band tube filled with MBS buffer using a pipette. Oocytes were just gently placed on the buffer surface and sank independently to the bottom of the tube. **f)** Final EPR sample after 2 h incubation before flash-freezing in liquid nitrogen.

The bulk spin concentration $c_{spin\ bulk}$ limit was estimated according to

$$c_{spin\ bulk} = \frac{N_{oocytes} \cdot c_{spin} \cdot 60\ nL}{V_{Q-band\ tube}} = \frac{20 \cdot 800\ \mu M \cdot 60\ \mu L}{70\ \mu L} = 13.7\ \mu M \qquad \text{(eq. 26)}$$

with $N_{oocytes}$ being the number of oocytes in the EPR tube, c_{spin} the initial spin concentration in the injection needle, and $V_{Q\text{-band tube}}$ the internal volume of the EPR tube. However, the final spin concentration is assumed to be smaller owing reduction of the spin label within cells. Taking the reduction of SLIM **3•** in oocyte lysate into account (~20% after 2 h), the estimated spin concentration within the bulk is approximately 11 µM.

5.2.8.2 HeLa Cell Electroporation

The electroporation workflow was adapted from *Kucher* et al.[387] HeLa cells (purchased from ATCC) were grown at 37 °C in a CO_2 incubator (5%) by *Philipp Schult* of the *Paeschke* group (University Clinics Bonn) in DMEM medium supplemented with 10% FBS on a culture dish (15 cm diameter) until it was fully covered. Typically, two culture dishes were used for the preparation of

one PDS-EPR sample and one culture dish was used for the transfection and seeding of A_{488}-labeled YopO. From three plates, approximately $1.25*10^7$ cells were obtained.
Cell-covered culture dishes were washed with 15 mL of pre-warmed Gibco™ PBS buffer before trypsinization and detachment of the adherend cells from the plate with 4 mL Gibco™ Trypsin-EDTA (0.25%) medium (10 min, 37 °C, CO_2 incubator). Trypsin was deactivated upon the addition of 21 mL DMEM medium, the plate was rinsed multiple times to enhance the number of harvested cells, and the combined 25 mL were transferred into a Falcon tube and centrifuged (500 rcf, 5 min). If multiple plates were used, the resuspended cells were pooled at this point and centrifuged together. The supernatant was removed and the cell pellet was resuspended in 25 mL pre-warmed Gibco™ PBS buffer, counted, and checked for viability. A volume containing a total number of $9.5*10^6$ cells (SLIM **3•**-labeled YopO) or $3.0*10^6$ cells (A_{488}-labeled YopO), respectively, was transferred in a new Falcon tube and centrifuged to pellet the cells (500 rcf, 5 min). Cell pellets were resuspended in Resuspension Buffer R to a final cell concentration of $3.2*10^7$ cells/mL and 40 µL of labeled protein resuspended in Resuspension Buffer R was added to give a final protein concentration of 20 µM in the cell slurry. 100 µL of the cell suspension was loaded into a 100 µL Neon™ pipette tip whilst carefully avoiding bubble formation at the electrode-solution-interface and positioned into the electroporation chamber of the Neon™ Transfection System filled with 3 mL Electrolytic Buffer E2. After the electroporation (1,000 V, 35 ms, 2 pulses) was performed, the pipette containing the electroporated cells was immediately eluted into a previously prepared Falcon tube containing 10 mL Gibco™ PBS buffer and gently homogenized. This procedure was repeated until the whole cell suspension was transfected. After two electroporations, the Neon™ pipette tip was exchanged for a new one. After the electroporation was completed, cells were spun down (500 rcf, 5 min) and the cell pellets were resuspended in 2 mL Gibco™ Trypsin-EDTA (0.25%) medium and incubated for 5 min at 37 °C to remove any aggregates or loosely bound YopO on the outer cell membrane. Trypsin was deactivated upon adding 8 mL DMEM medium and a total of ~$4*10^4$ cells were seeded onto a glass cover slip inside a 24-well cell culture plate which was incubated for 16 h at 37 °C inside a CO_2 incubator before fluorescence imaging. The remaining cells transfected with SLIM **3•**-labeled YopO were plated out on a 15 cm culture dish (filled up to 15 mL medium in total) and recovered for 3.5 h at 37 °C in a CO_2 incubator. Cells were visually inspected under a light microscope before removal of the medium and subsequent wash with 25 mL Gibco™ PBS buffer. The buffer was removed and cells were detached from the plate upon the addition of 4 mL Gibco™ Trypsin-EDTA (0.25%) medium (5 min, 37 °C). Trypsin was deactivated upon the addition of 21 mL DMEM medium and the cell suspension was centrifuged (500 rcf, 5 min). The supernatant was discarded and the cell pellet was resuspended in 10 mL deuterated PBS buffer and incubated for 10 min (37 °C) before another centrifugation step (500 rcf, 5 min). Again, the supernatant was discarded and in a final step, the pellet was resuspended in 200 µL deuterated PBS buffer containing 20% (v/v) glycerol-d_8 and transferred into a Q-band tube which was placed in a Falcon tube and centrifuged to collect the cells at the bottom of the tube (700 rcf, 5 min). The tube containing the electroporated cells was slowly frozen in liquid nitrogen and placed in a Dewar for long-term storage.

5.2.9 cw EPR Spectroscopy

5.2.9.1 Instrumentation

All cw-EPR spectra were recorded at X-band frequencies (~9.4 GHz) using either a Bruker EMXnano or Bruker EMXmicro EPR spectrometer. For measurements at room temperature, the EMXmicro spectrometer was equipped with an ER 4122SHQ resonator. For experiments at 100 K, the resonator was switched to an ER 4119HS resonator in conjunction with an ER 4141VT temperature control system and cooled using a continuous flow of cold nitrogen gas. Experiments below 100 K

were carried out using an ER 4122SHQE resonator, an ER 4112HV continuous flow helium cryostat, and a Mercury iTC503 temperature controller (Oxford Instruments).

5.2.9.2 cw-EPR Sample Preparation

Room temperature cw-EPR: Aqueous samples were filled into disposable 10 µL capillaries and sealed with super glue on both ends. After the glue had dried, capillaries were placed into an X-band quartz glass tube (4 mm outer diameter).

Low-temperature cw-EPR: Samples in Q-band tubes prepared for PDS-EPR studies (see section 5.2.10.2) were used for X-band cw-EPR measurements at cryogenic temperatures.

5.2.9.3 cw-EPR Spectra Simulation

cw-EPR spectra were simulated using the EasySpin toolbox for MATLAB. Room temperature spectra of the free spin labels were simulated using the "garlic"-routine implemented in EasySpin. Spectra of bioconjugated Mal-TSL **2•** were simulated using the "chili"-routine implemented in EasySpin. Spectra of bioconjugated SLIM **3•** were simulated using the "pepper"-routine implemented in EasySpin. Low-temperature cw-EPR spectra of free and bioconjugated Cu^{2+}(NTA) were simulated using the "pepper"-routine implemented in EasySpin. Explicit simulation parameters for the respective systems are given in the results and discussion section.

5.2.9.4 cw-EPR Stability Measurements

Xenopus laevis oocyte lysate: *Xenopus laevis* oocyte lysate was prepared according to the protocol published by *Karthikeyan* et al.[227] Oocytes were washed with MBS buffer and mechanically destroyed, and insoluble cell debris and lipids were removed by centrifugation (11,000 rcf, 15 min). The lipid layer from the top was carefully removed using a pipette tip; the crude cytoplasm was extracted using a pipette and immediately aliquoted (20 µL) and flash-frozen in liquid nitrogen. Approximately 70 µL cell lysate was obtained from 100 oocytes.

HeLa cell lysate: HeLa S3 cells (ATCC® CCL-2.2) provided by the group of *Prof. Ulrich Kubitscheck* were suspended in PBS buffer (600 µL per 10^8 cells), frozen in an ethanol/$CO_{2(s)}$ cooling bath for 5 min, and subsequently thawed in a water bath (37 °C). This cycle was repeated three times before thoroughly mixing the solution using a vortex mixer. Insoluble cell debris was removed by centrifugation (14,000 rcf, 5 min, 4 °C) and the supernatant was collected, aliquoted to 20 µL, and immediately flash-frozen in liquid nitrogen.

cw-EPR sample preparation and measurements: Samples were transferred into a 10 µL disposable capillary, sealed with superglue, and transferred into a Q-band quartz glass EPR tube (3 mm outer diameter). Tubes were immediately inserted into the EMXmicro EPR spectrometer (warmed up for at least 1 h before the experiment) and tuned properly. Subsequently, a cw-EPR spectrum was recorded every 15 min for up to 21 h. The dead time between sample preparation and the first scan was kept below 6 min. A home-written bash script[375] by *Florian Haege* was used to monitor the frequency and microwave power throughout the experiment and the signal intensities representative for the spin concentration were obtained as the double-integral of the spectrum for each timepoint.

5.2.10 Pulsed EPR Spectroscopy

5.2.10.1 Instrumentation

All pulsed EPR experiments were conducted at Q-band frequencies (~34 GHz) using a Bruker ELEXSYS E580 EPR spectrometer equipped with an ER5106QT-2 resonator and a 150 W TWT-

amplifier. The temperature was adjusted using a CF935 continuous-flow helium cryostat and an iTC503 temperature controller. All data was acquired using quadrature detection.

5.2.10.2 Pulsed EPR Sample Preparation

YopO: An aliquot of spin labeled and deuterated YopO was thawed, diluted 1:1 with ethylene glycol-d_6, and mixed gently. 80 µL of the resulting solution was transferred into a Q-band quartz glass tube (3 mm outer diameter) and flash-frozen in liquid nitrogen.

YopO + Actin: 1 mg of human platelet actin was dissolved in 100 µL D_2O (final concentration: 240 µM), aliquoted into 20 µL samples, flash-frozen in liquid nitrogen and stored at -80 °C. An aliquot of spin-labeled and deuterated YopO was thawed and 50 µL of labeled YopO were incubated for 2 h on ice with two equivalents of human platelet actin and a 10-fold molar excess of latrunculin B (625 µM in DMSO, added to prevent actin polymerization) in deuterated YopO-Actin PDS buffer. Subsequently, the incubation solution was diluted 1:1 with ethylene glycol-d_6, mixed gently, transferred into a Q-band quartz glass tube (3 mm outer diameter), and flash-frozen in liquid nitrogen.

Myoglobin: To a solution of spin-labeled and deuterated Mb, a 200-fold excess of NaN_3 was added. The solution was then diluted with Myoglobin PDS buffer and glycerol-d_8 to a final spin concentration of 40 µM and 20% v/v glycerol content. After gentle mixing, 80 µL of the resulting solution was transferred into a Q-band quartz glass tube (3 mm outer diameter) and flash-frozen in liquid nitrogen.

GB1: An aliquot of SLIM 3•-labeled GB1 was thawed and samples with a final volume of 65 µL in GB1 PDS buffer were prepared with varying concentrations of GB1 and Cu^{2+}(NTA) (Table 57) containing 50% v/v ethylene glycol-d_6. Samples were thoroughly mixed and incubated for 10 min on ice before transferring into a Q-band EPR tube (3 mm outer diameter) and flash freezing in liquid nitrogen.

Table 57: GB1 I6-**3•** and Cu^{2+}(NTA) concentrations in the RIDME samples.

GB1 I6-3• [nM]	Cu^{2+}(NTA)[a] [nM]
500	2250
100	2000
50	2000
25	2000
10	2000

[a] 100 µM stock solution of Cu^{2+}(NTA) in GB1 PDS buffer.

YopO + Cu^{2+}(NTA): After the incubation period (30 min at 4 °C), the labeled YopO was diluted 1:1 with ethylene glycol-d_6 to a final protein concentration of 100 µM, mixed gently, transferred into a Q-band quartz glass tube (3 mm outer diameter), and flash-frozen in liquid nitrogen.

5.2.10.3 Electron Spin Relaxation Measurements

Inversion Recovery: The spin-lattice relaxation time T_1 was assessed via inversion recovery experiments using the pulse-sequence depicted in Figure 11a (Section 1.2.2.2). Typical setup parameters for the different spin systems are given in Table 58.

Table 58: Typical pulse-sequence parameters for inversion recovery experiments on the spin systems used in this thesis.

Parameter	MTSL	Trityl	Cu^{2+}(NTA)
$\pi/2$	12 ns	12 ns	12 ns
π	24 ns	24 ns	24 ns
$\pi_{Inversion}$	24 ns	24 ns	24 ns
τ_1	300 ns	200 ns	300 ns
T	400 ns	400 ns	400 ns
T increment	100 µs	1 ms	4 µs
SRT	50 ms (50 K)	500 ms (50 K, 70 K) 1 s (10 K, 30 K)	2 ms (25 K) 4 ms (20 K)
SPP	1	1	5

2pESEEM: The phase memory time T_M was assessed via two-pulse electron spin echo envelope modulation experiments using the pulse sequence depicted in Figure 12a (section 1.2.2.2). Typical setup parameters for the different spin systems are given in Table 59.

Table 59: Typical pulse-sequence parameters for 2pESEEM experiments on the spin systems used in this thesis.

Parameter	MTSL	Trityl	Cu^{2+}(NTA)
$\pi/2$	12 ns	12 ns	12
π	24 ns	24 ns	24
τ_1	200 ns	200 ns	200 ns
τ_1 increment	8 ns	8 ns	4 ns (25 K) 8 ns (20 K)
SRT	6 ms (50 K)	15 ms (50 K) 7 ms (70 K)	500 µs (25 K) 1 ms (20 K)
SPP	10	1-10	10

5.2.10.4 PELDOR Experiments

All PELDOR experiments were performed using the four-pulse PELDOR sequence $\pi/2\ (\nu_A) - \tau_1 - \pi(\nu_A) - (\tau_1 + t) - \pi(\nu_B) - (\tau_2 - t) - \pi(\nu_A) - echo$ depicted in Figure 14 (section 1.2.2.4). Specific setup details for the different spin systems are given below and in Table 60.

MTSL: PELDOR measurements on MTSL-labeled proteins were conducted at 50 K. The pump pulse $(\pi)_B$ was applied at the magnetic field position with the maximum signal intensity of the field-swept EPR spectrum while the detection pulses were offset -100 MHz with respect to the pump frequency. The length of the pump pulse $(\pi)_B$ was determined by a transient nutation experiment and was set to the length that led to the maximum inversion of the magnetization. Deuterium ESEEM was suppressed using an 8-step modulation averaging cycle with a time increment of 16 ns. A two-step phase cycle was applied to remove undesired echoes and receiver baseline offsets.

Trityls: PELDOR measurements on trityl-labeled proteins were conducted at 50 K. The pump pulse $(\pi)_B$ was set to the magnetic field position with the maximum signal intensity of the field-swept EPR spectrum while the detection pulses were offset -15 MHz with respect to the pump frequency. The length of the pump pulse $(\pi)_B$ was determined by a transient nutation experiment and was set to the length that led to the maximum inversion of the magnetization. Deuterium ESEEM was suppressed using an 8-step modulation averaging cycle with a time increment of 16 ns. A two-step phase cycle was applied to remove undesired echoes and receiver baseline offsets.

Cu^{2+}: PELDOR measurements on Cu^{2+}(NTA)-labeled proteins were conducted at 20 K. The detection pulses were applied with a frequency offset of -100 MHz with respect to the pump frequency. The length of the pump pulse $(\pi)_B$ was determined by a transient nutation experiment and was set to the length that led to the maximum inversion of the magnetization. Deuterium ESEEM was suppressed using a 16-step modulation averaging cycle with a time increment of 8 ns. A two-step phase cycle was applied to remove undesired echoes and receiver baseline offsets. Experiments were optimized at the maximum of the field-swept EPR spectrum (1165 mT) and the magnetic field was changed to record field-dependent traces.

Table 60: Typical pulse parameters for PELDOR experiments on the spin systems used throughout this thesis.

Parameter	MTSL	Trityl	Cu^{2+}
$(\pi/2)_A$	12-16 ns	32 ns	12 ns
$(\pi)_A$	24-32 ns	64 ns	24 ns
$(\pi)_B$	14-16 ns	60 ns	14 ns
τ_1	232-260 ns	260 ns	270 ns
SRT	1 ms	15 ms	1 ms
SPP	3-10	3	10

5.2.10.5 DQC Experiments

All DQC experiments on trityl-labeled proteins were performed using the six-pulse DQC sequence $\pi/2 - \tau_1 - \pi - \tau_1 - (\pi/2 - T - \pi - T - \pi/2) - \tau_2 - \pi - \tau_2 - echo$ depicted in Figure 16a.

DQC experiments were performed at 50 K or 70 K, and the pulse sequence was applied at the magnetic field position with the maximum amplitude of the field-swept EPR spectrum. The interpulse delays τ_1 and τ_2 were incremented and decremented, respectively, with the same time interval, and the integral of the DQC echo was recorded as a function of $\tau_1 - \tau_2$. The phase was adjusted using the Hahn echo sequence in such a way that the summed echo amplitudes from $(\pi/2)_{+x}/\pi_{+x}$ and $(\pi/2)_{-x}/\pi_{-x}$ pulses averaged out. The same procedure was undertaken for $(\pi/2)_{+y}/\pi_{+y}$ and $(\pi/2)_{-y}/\pi_{-y}$ pulses. Deuterium ESEEM was suppressed using an 8-step modulation averaging cycle with a time increment of 16 ns. A 64-step phase cycle was applied to remove undesired echoes and receiver baseline offsets. Typical parameters for the DQC sequence are given in Table 70.

Table 70: Typical parameters for DQC experiments.

Parameter	Value
$\pi/2$	12 ns
π	24 ns
τ_1	200 ns
τ_1 increment	4 ns
τ_2	4500 ns – 7500 ns
τ_2 decrement	4 ns
T	50 ns
SRT	15 ms (50 K) 7 ms (70 K)
SPP	3

5.2.10.6 SIFTER Experiments

All SIFTER experiments on trityl-labeled proteins were performed using the SIFTER sequence $(\pi/2)_x - \tau_1 - \pi - \tau_1 - (\pi/2)_y - \tau_2 - \pi - \tau_2 - echo$ depicted in Figure 16b.

SIFTER experiments were performed at 50 K and the pulse sequence was applied at the magnetic field position with the maximum amplitude of the field-swept EPR spectrum. The interpulse delays τ_1 and τ_2 were incremented and decremented, respectively, with the same time interval, and the integral of the SIFTER echo was recorded as a function of $\tau_1 - \tau_2$. The phase was adjusted using the Hahn echo sequence in such a way that the summed echo amplitudes from $(\pi/2)_{+x}/\pi_{+x}$ and $(\pi/2)_{-x}/\pi_{-x}$ pulses averaged out. The same procedure was undertaken for $(\pi/2)_{+y}/\pi_{+y}$ and $(\pi/2)_{-y}/\pi_{-y}$ pulses. Deuterium ESEEM was suppressed using an 8-step modulation averaging cycle with a time increment of 16 ns. A 16-step phase cycle was applied to remove undesired echoes and receiver baseline offsets. Typical parameters for the SIFTER sequence are given in Table 71.

Table 71: Typical parameters for SIFTER experiments.

Parameter	Value
$(\pi/2)_x$	12 ns
$(\pi/2)_y$	12 ns
π	24 ns
τ_1	300 ns
τ_1 increment	4 ns
τ_2	4500 ns
τ_2 decrement	4 ns
SRT	15 ms
SPP	3

5.2.10.7 RIDME Experiments

All RIDME experiments were performed using the five-pulse RIDME sequence $\pi/2 - \tau_1 - \pi - (\tau_1 + t) - \pi/2 - T_{mix} - \pi/2 - (\tau_2 - t) - \pi - \tau_2 - echo$ depicted in Figure 15. Specific setup details for the different spin systems are given below and in Table 72.

Cu^{2+}/Cu^{2+}: RIDME measurements on Cu^{2+}/Cu^{2+} labeled YopO were conducted at 25 K. Experiments were optimized at the maximum amplitude of the field-swept EPR spectrum and the pulse sequence was then applied at the indicated magnetic field positions to record the field-dependent time traces. Deuterium ESEEM was suppressed using a 16-step modulation averaging cycle with an increment of 8 ns. An 8-step phase cycle was applied to remove undesired echoes and receiver baseline offsets.

Cu^{2+}/SLIM: RIDME measurements on the orthogonal spin pair Cu^{2+}/SLIM were conducted at 40 K. The pulse sequence was applied at the magnetic field position of SLIM **3•** with the maximum amplitude of the field-swept EPR spectrum. Deuterium ESEEM was suppressed using a 16-step modulation averaging cycle with an increment of 8 ns. An 8-step phase cycle was applied to remove undesired echoes and receiver baseline offsets.

Table 72: Typical parameters for RIDME experiments on the spin systems used in this thesis.

Parameter	Cu^{2+}/Cu^{2+}	Cu^{2+}/SLIM
$\pi/2$	12 ns	10 ns
π	24 ns	20 ns
τ_1	300 ns	200 ns
τ_2	4000 ns	6000 ns
T_{mix}	30 µs	100 µs
t	48 ns	48 ns
SRT	500 µs	10 ms
SPP	1	1

5.2.10.8 Data Processing

DeerAnalysis

Time traces were loaded into DeerAnalysis2019 or DeerAnalysis2022 and phase correction was done by the program automatically upon data input. The zero-time was set to the maximum of the time trace and traces were truncated if an artifact at long dipolar evolution times was observed. The chosen background functions were applied (see details for each measurement) and the background start suggested by DeerAnalysis was used as an initial guess for further optimization of the background to obtain an artifact-free Pake pattern. Distance distributions were computed by Tikhonov regularization and the automatically selected regularization parameter α was set to or close to the corner of the L-curve if over- or undersmoothing of the distance distribution was observed. The uncertainty of the distance distribution was assessed via the validation tool implemented in DeerAnalysis. Here, the starting point of the background fitting was varied while the remaining parameters (background dimensionality, background density, and modulation depth) were kept at the respective default values. Only for the DQC and SIFTER time traces in section 3.2.3.2 experimental backgrounds obtained from the singly Mal-TSL **2•**-labeled YopO L113C construct were utilized (for more information see Results and Discussion section 3.2.3.2).

Trityl DQC: If the decay of a DQC time trace was below 15% of its initial amplitude, DeerAnalysis refused background correction. In these instances, the value x in the "if min(td_fit)<x" command of the "update_DA.m" file responsible for the background fitting in DeerAnalysis was altered to 0.01 or below to allow the application of a background function and subsequent validation.

DEERNet

RIDME or PELDOR traces were loaded into DeerAnalysis2022 and the implemented DEERNet-routine was run using the background model for either RIDME or PELDOR. If the algorithm refused data analysis, the time trace was truncated until it could be processed by DEERNet.

PDSFit

Field-dependent RIDME and PELDOR data of YopO-short and YopO-long were analyzed using PDSFit.[384] In brief, PDSFit uses a parametrized geometric model of the spin system and a parametrized model of the PDS background to fit the time traces (Figure 113).

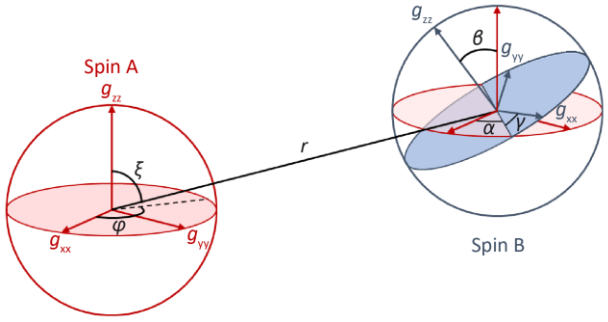

Figure 113: Geometric model of a two-spin system A and B used in PDSFit. Adapted from *Abdullin* et al.[384]

The two-spin system consists of spin A and B, in this case, both Cu^{2+} ions, and the reference coordinate system is set to coincide with the *g*-tensor principal axis of spin A. As the *g*-tensor of Cu^{2+} is axial,[280] the angles φ and γ do not influence the time trace and were set to zero. In this case, the geometric model consists of four parameters, namely *r*, ξ, α, and β which are approximated either by a Gaussian distribution (*r*) or von Mises distribution (ξ, α, and β). Therefore, each parameter is described by a distribution $P(x)$ with a mean value $\langle x \rangle$ and a width Δx (given as FWHM). A detailed summary of the approximations made by PDSFit and a workflow on the installation and execution of the program is given in the program's manual (https://github.com/dinarabdullin/PDSFit). The input parameters for the Cu^{2+} spin centers are given in Table 73.

Table 73: PDSFit input parameters for the equal Cu^{2+} spins A and B.

Parameter	Spin A / Spin B
g	(2.058, 2.058 ,2.276)
*g*Strain	(0.016, 0.016, 0.000)
A (MHz)	(26.0, 26.0, 513.0)
Abund	1.0
n	1
I	1.5
T1 (µs)	87
lwpp (MHz)	168
g_anisotropy_in_dipolar_coupling	1

The experimental parameters were extracted from the respective DSC data files. Background-optimization of RIDME and PELDOR time traces was done using a 3rd-order polynomial function $B(t) = 1 + c_1 t + c_2 t^2 + c_3 t^3$. PDS traces were fitted using Module 3 and Module 4 of PDSFit[384] and the resulting values for the parameters were extracted from the logfile. PDSFit was run on the Bonna cluster (University of Bonn).

6. Appendix

6.1 Supplementary Information Section 3.1

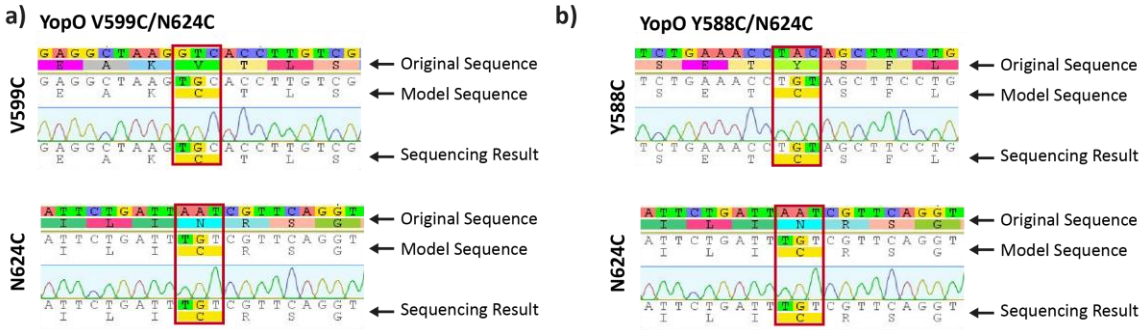

Figure A1: Sanger sequencing results for YopO V599C/N624C **(a)** and YopO Y588C/N624C **(b)**.

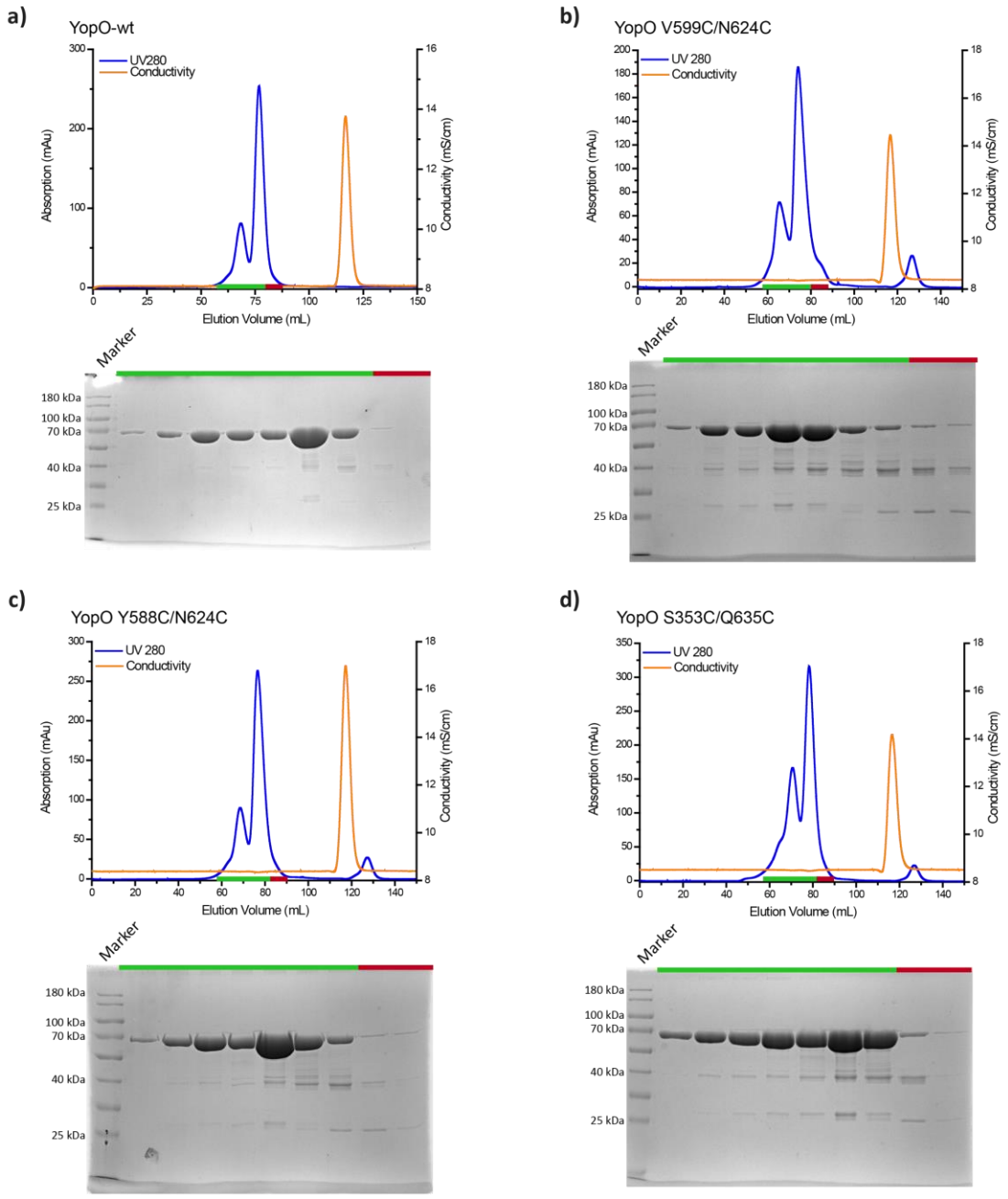

Figure A2: HiLoad® 16/600 Superdex® 200 pg gel filtration chromatogram (top) and Coomassie-stained 10% polyacrylamide gel (bottom) of YopO-wt **(a)**, YopO V599C/N624C **(b)**, YopO Y588C/N624C **(c)**, and YopO S353C/Q635C **(d)**. Only the fractions indicated by a green bar were further pooled and purified.

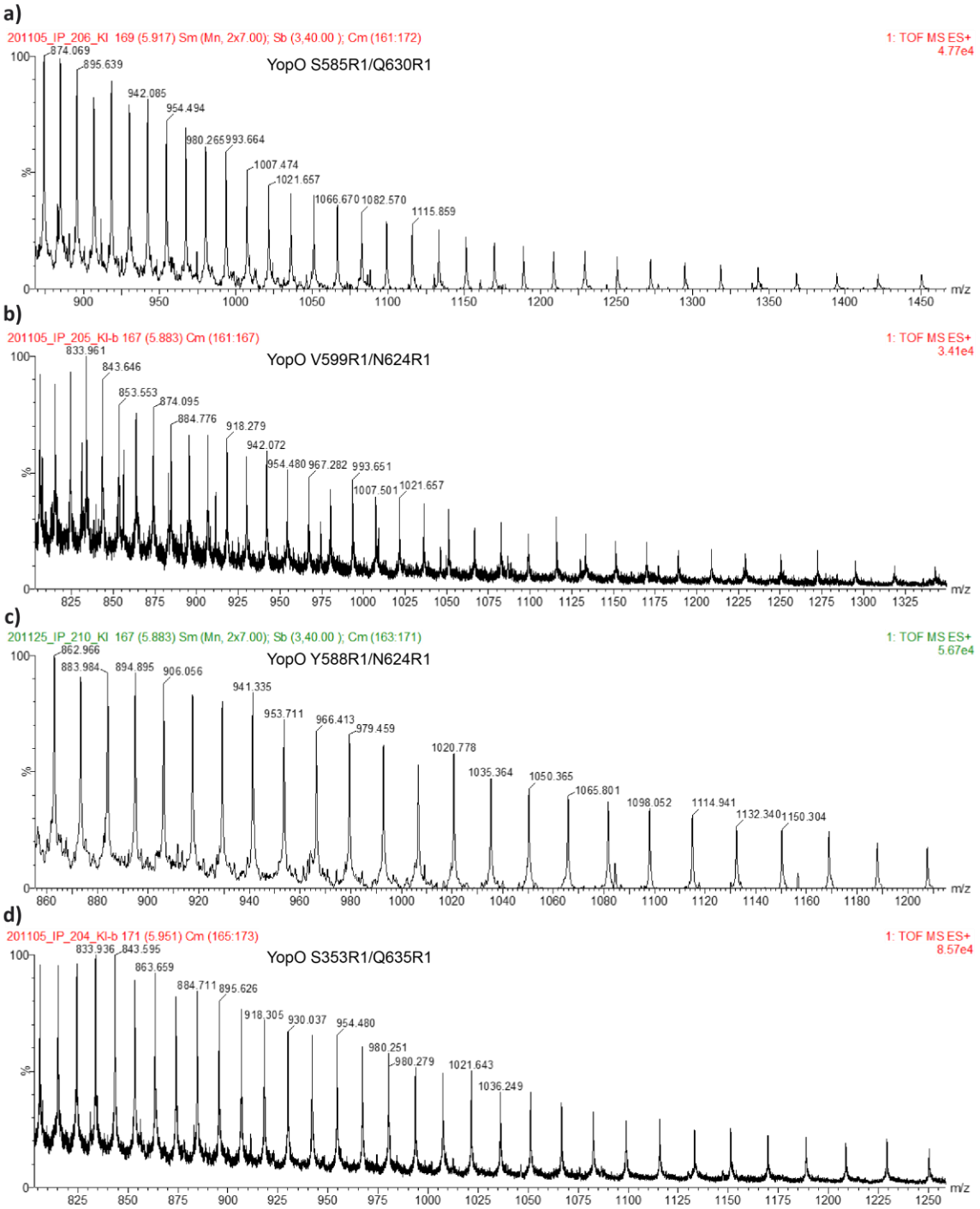

Figure A3: Raw ESI(+)-MS spectra of YopO S585R1/Q603R1 **(a)**, YopO V599r1/N624R1 **(b)**, YopO Y588R1/N624R1 **(c)**, and YopO S353R1/Q635R1 **(d)** recorded on a Synapt G2-Si spectrometer.

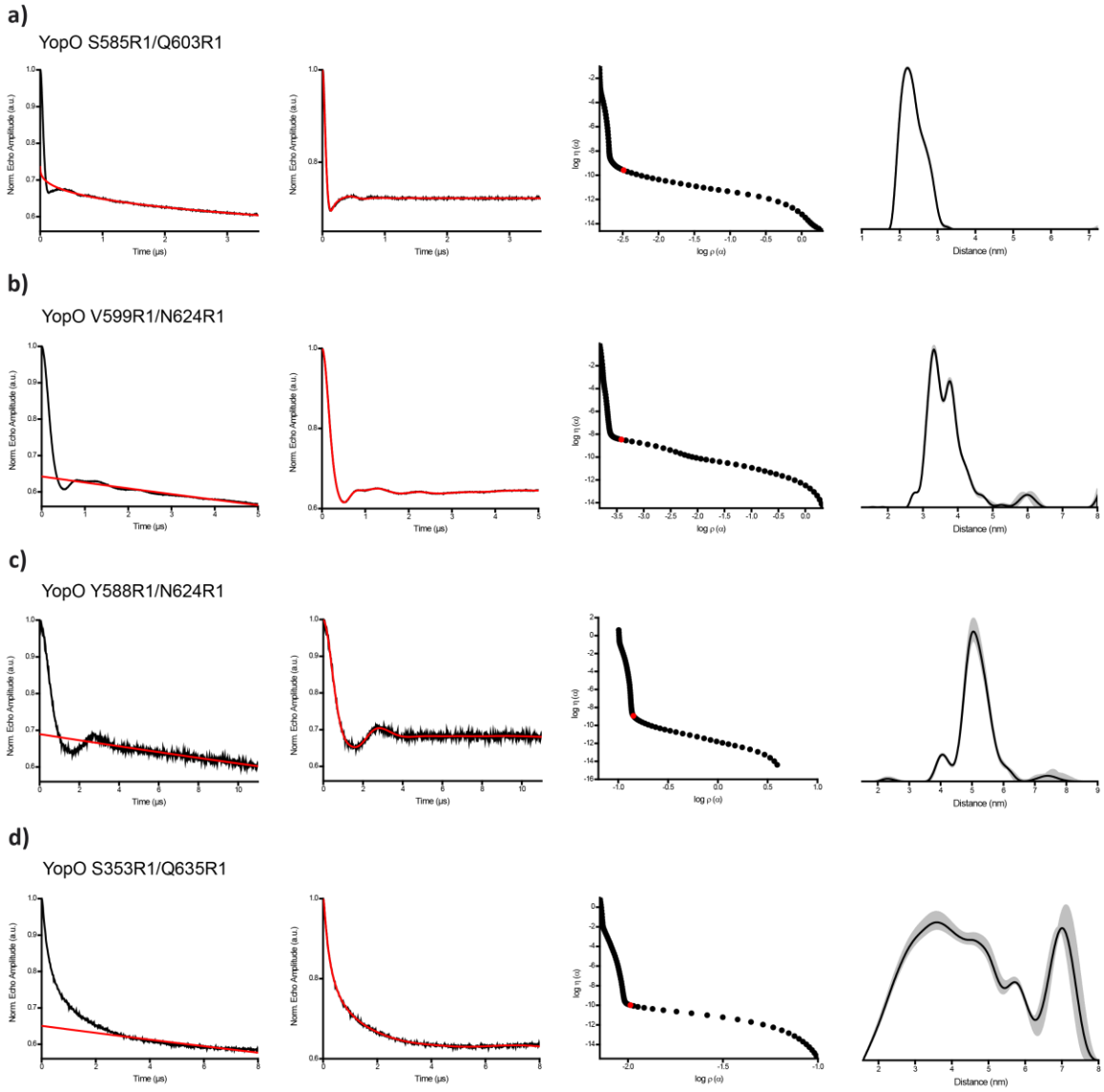

Figure A4: In-house DeerAnalysis results for the ring test constructs. From left to right: Original time trace (black) and background function (red); Background-corrected time trace (black) and fit (red); L-curve with the chosen regularization parameter (red); and resulting distance distribution (black) with the validation by DeerAnalysis shown as grey-shaded areas for YopO S585R1/Q603R1 **(a)**, YopO V599R1/N624R1 **(b)**, YopO Y588R1/N624R1 **(c)**, and YopO S353R1/Q635R1 **(d)**.

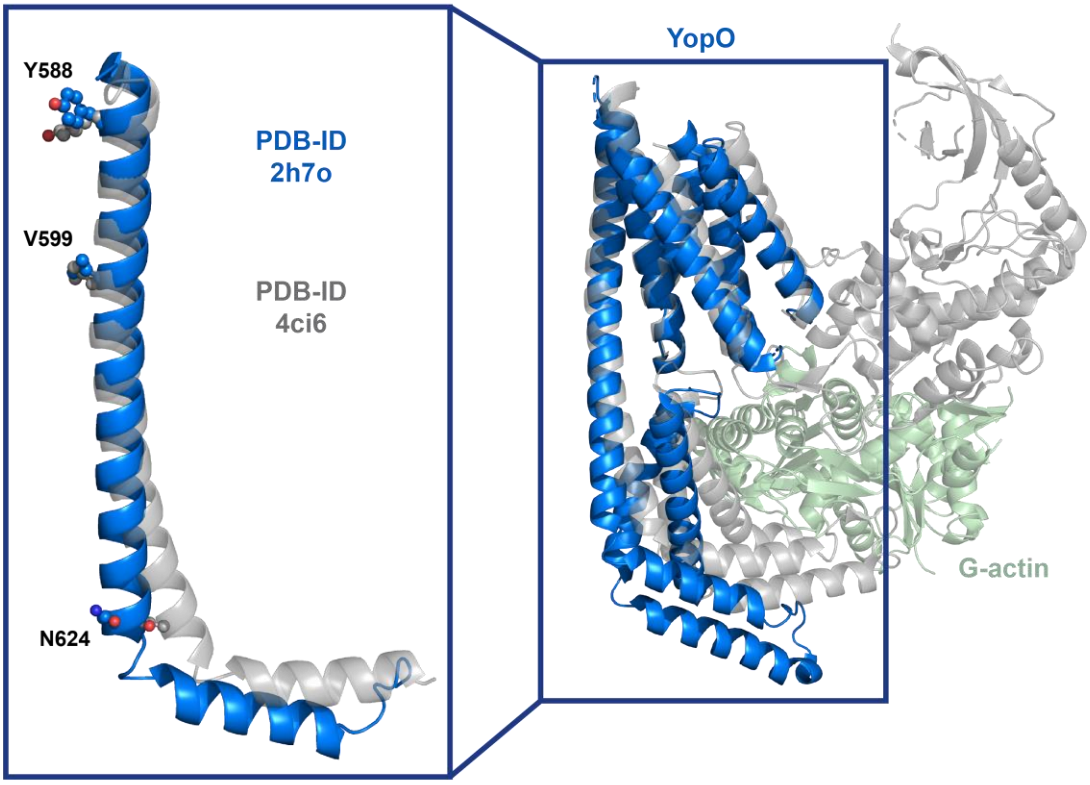

Figure A5: Overlay of the PDB-IDs 2h7o[326] (blue) and 4ci6[328] (grey, with G-actin shown in green). The inset (blue box) highlights the differences in the α-helical backbone shape and shows the MTSL-labeling sites for the constructs YopO V599C/N624C and YopO Y588C/N624C as ball and stick models.

6.2 Supplementary Information Section 3.2

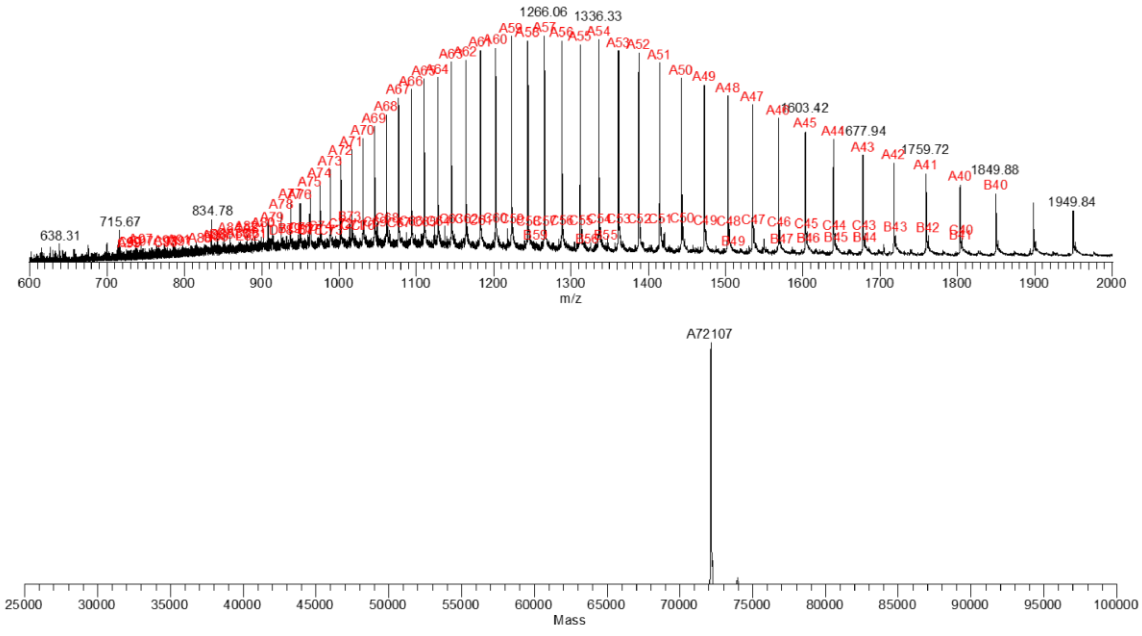

Figure A6: Raw (top) and deconvoluted (bottom) ESI(+)-MS spectra of YopO-wt incubated with Mal-TSL **2•** recorded on a Q-Exactive Plus Orbitrap spectrometer.

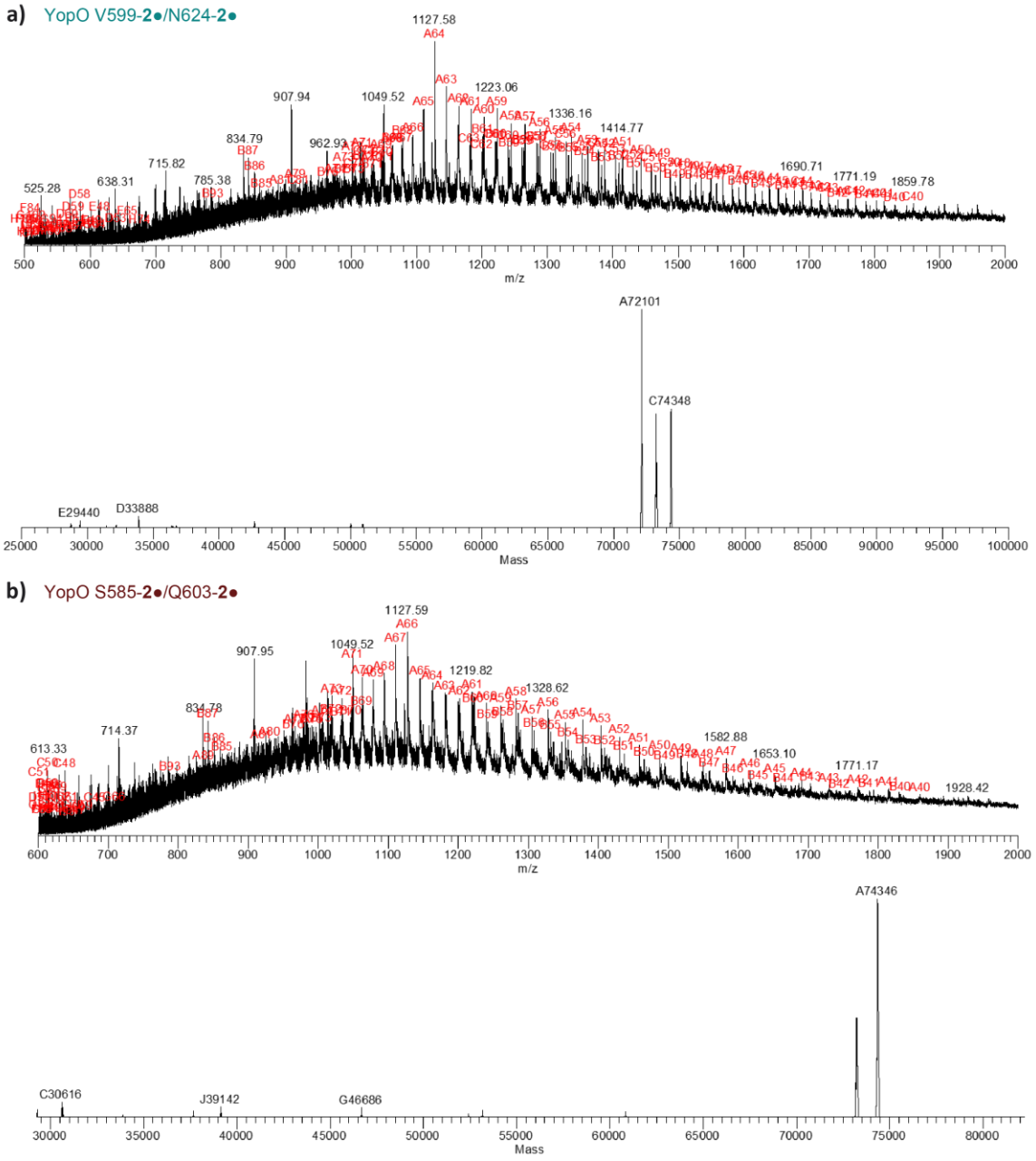

Figure A7: Raw (top) and deconvoluted (bottom) ESI(+)-MS spectra of YopO V599-**2•**/N624-**2• (a)** and YopO S585-**2•**/Q603-**2• (b)** recorded on a Q-Exactive Plus Orbitrap spectrometer.

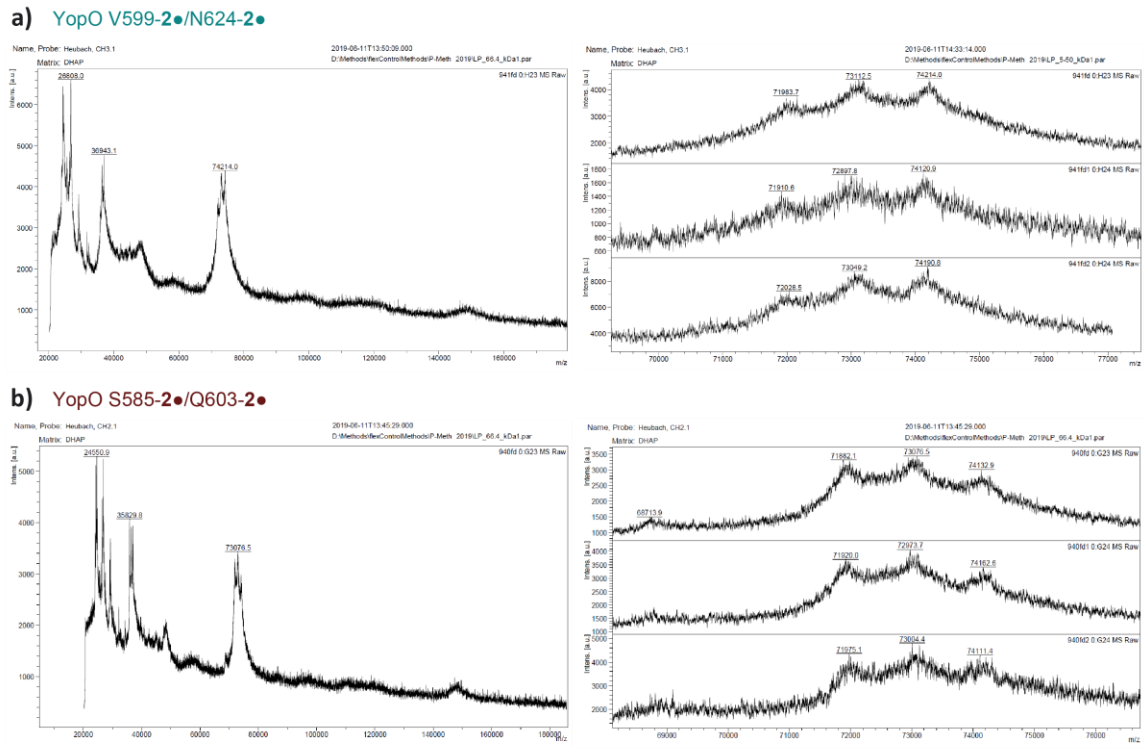

Figure A8: MALDI(+)-MS spectra of YopO V599-**2•**/N624-**2• (a)** and YopO S585-**2•**/Q603-**2• (b)** recorded on a Bruker Daltonics ultrafleXtreme TOF/TOF spectrometer. On the left: Whole range MS spectrum; on the right: Mass range excerpt of the mass peaks at ~73,000 m/z (three measurements).

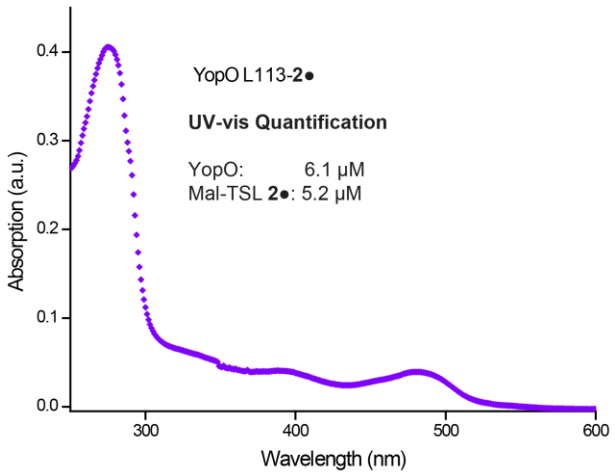

Figure A9: UV-vis spectrum and quantification according to section 3.2.2.1 of single-cysteine mutant YopO L113-**2•**. The spectrum was recorded using a Cary100 UV-vis spectrometer.

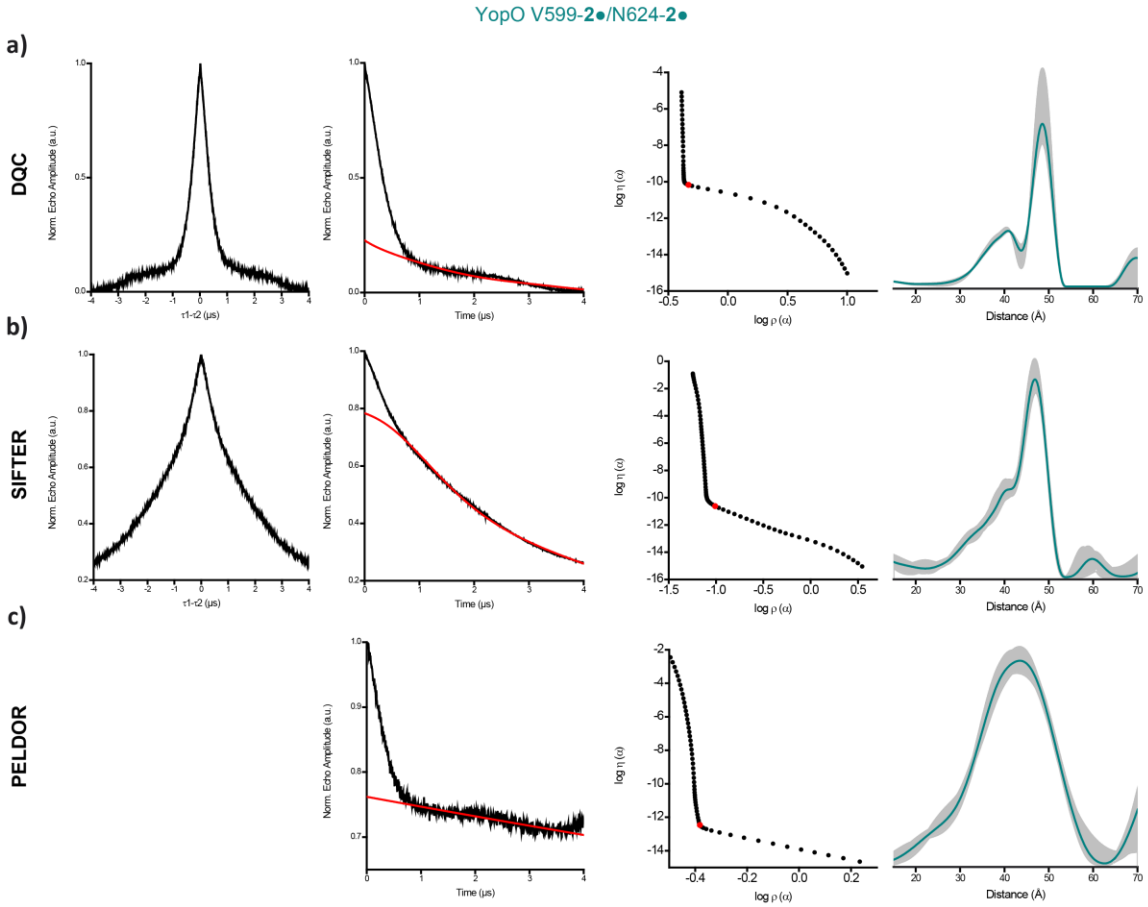

Figure A10: DeerAnalysis results for the DQC **(a)**, SIFTER **(b)**, and PELDOR **(c)** measurements of YopO V599-**2•**/N624-**2•**. From left to right: Unmirrored time traces (only DQC and SIFTER); mirrored (only DQC and SIFTER) time trace (black) and the background function (red); L-curve with the chosen regularization parameter (red); and resulting distance distribution (teal) with the validation by DeerAnalysis shown as grey-shaded areas.

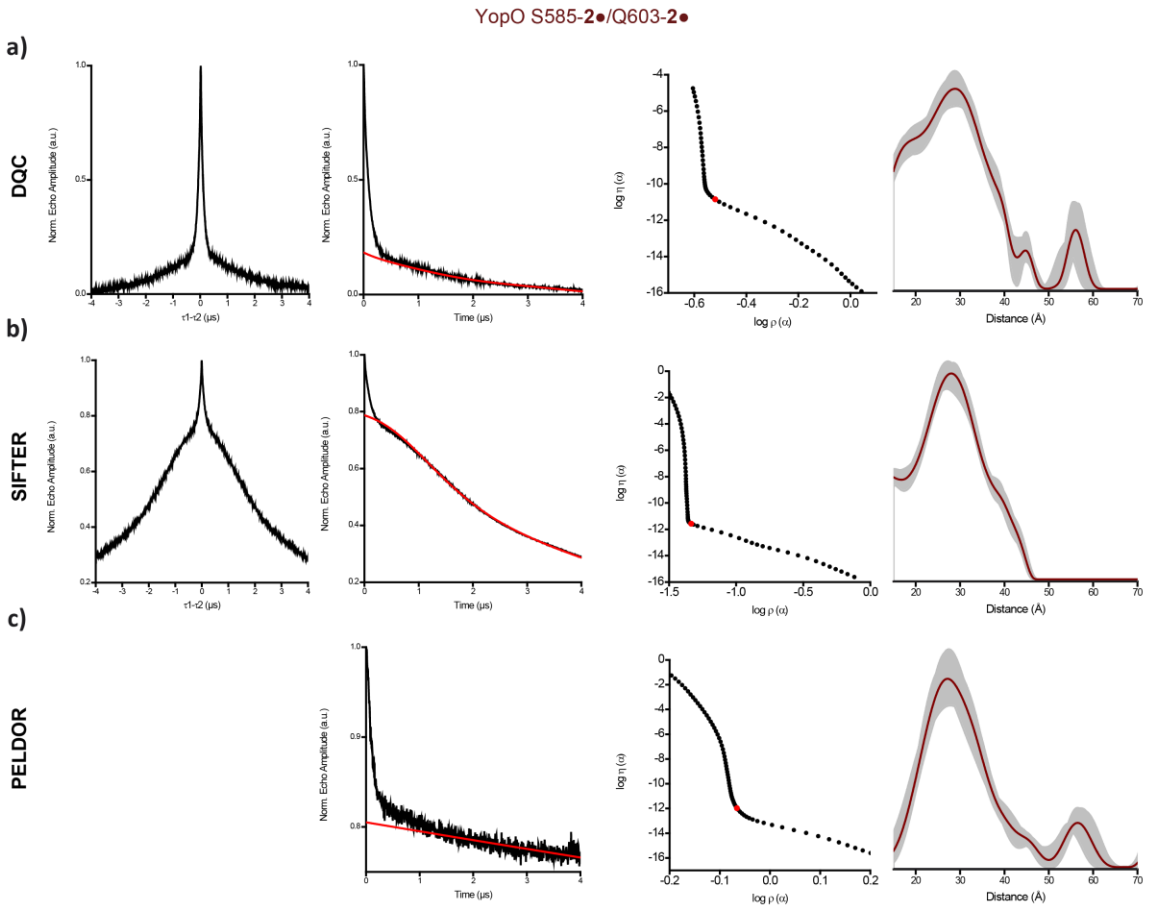

Figure A11: DeerAnalysis results for the DQC **(a)**, SIFTER **(b)**, and PELDOR **(c)** measurements of YopO S585-**2•**/Q603-**2•**. From left to right: Unmirrored time traces (only DQC and SIFTER); mirrored (only DQC and SIFTER) time trace (black) and the background function (red); L-curve with the chosen regularization parameter (red); and resulting distance distribution (brown) with the validation by DeerAnalysis shown as grey-shaded areas.

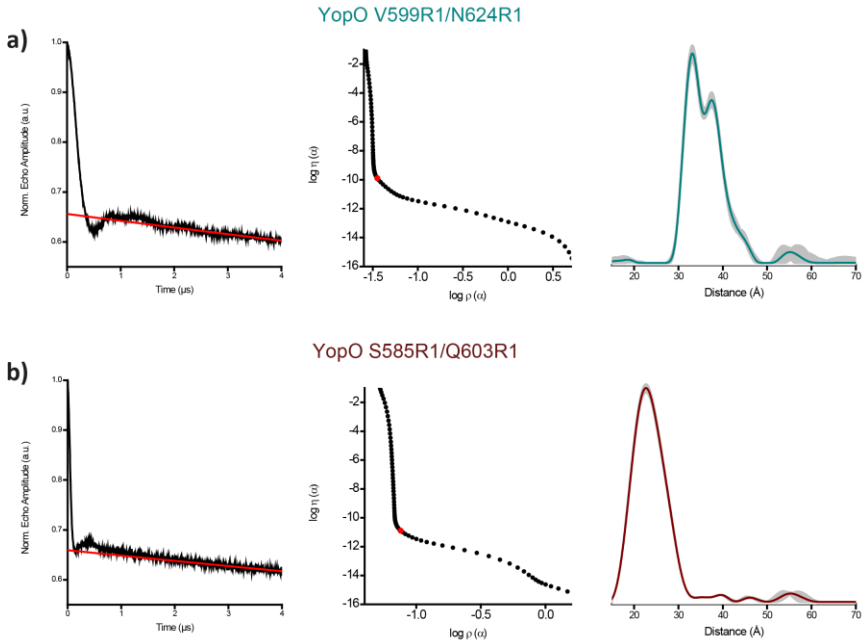

Figure A12: DeerAnalysis results for the PELDOR measurements of YopO S599R1/N624R1 **(a)** and YopO S585R1/Q603R1 **(b)**. From left to right: Time trace (black) and the background function (red, three-dimensional homogenous background); L-curve with the chosen regularization parameter (red); and resulting distance distribution (teal **(a)** / brown **(b)**) with the validation by DeerAnalysis shown as grey-shaded areas.

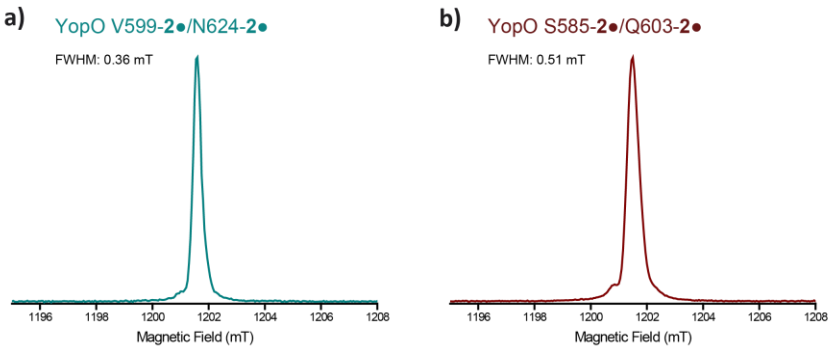

Figure A13: Q-band field-swept EPR spectra of YopO V599-**2•**/N624-**2• (a)** and YopO S585-**2•**/Q603-**2• (b)**.

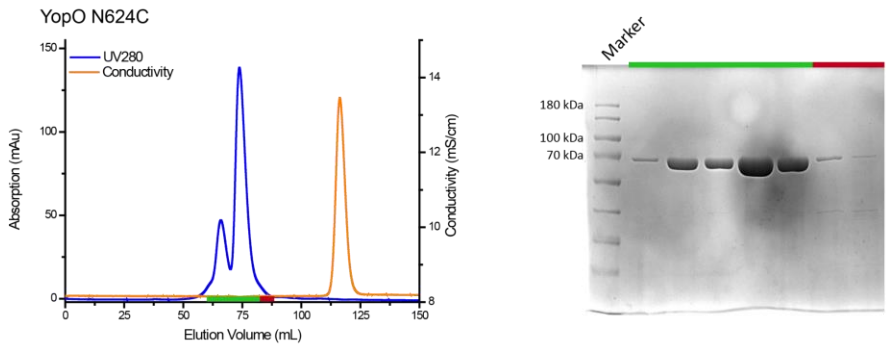

Figure A14: HiLoad® 16/600 Superdex® 200 pg gel filtration chromatogram (left) and Coomassie-stained 10% polyacrylamide gel (right) of YopO N624C. Only the fractions indicated by a green bar were further pooled and purified.

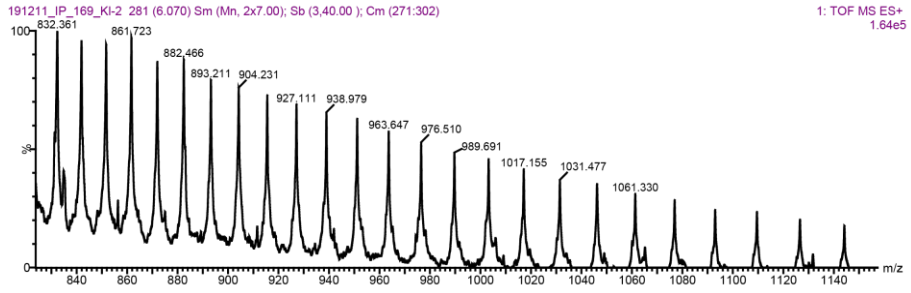

Figure A15: Raw high-resolution ESI(+)-MS spectrum of YopO N624-**3•** recorded on a Waters Synapt G2-SI spectrometer by the mass spectrometry facility in Marburg.

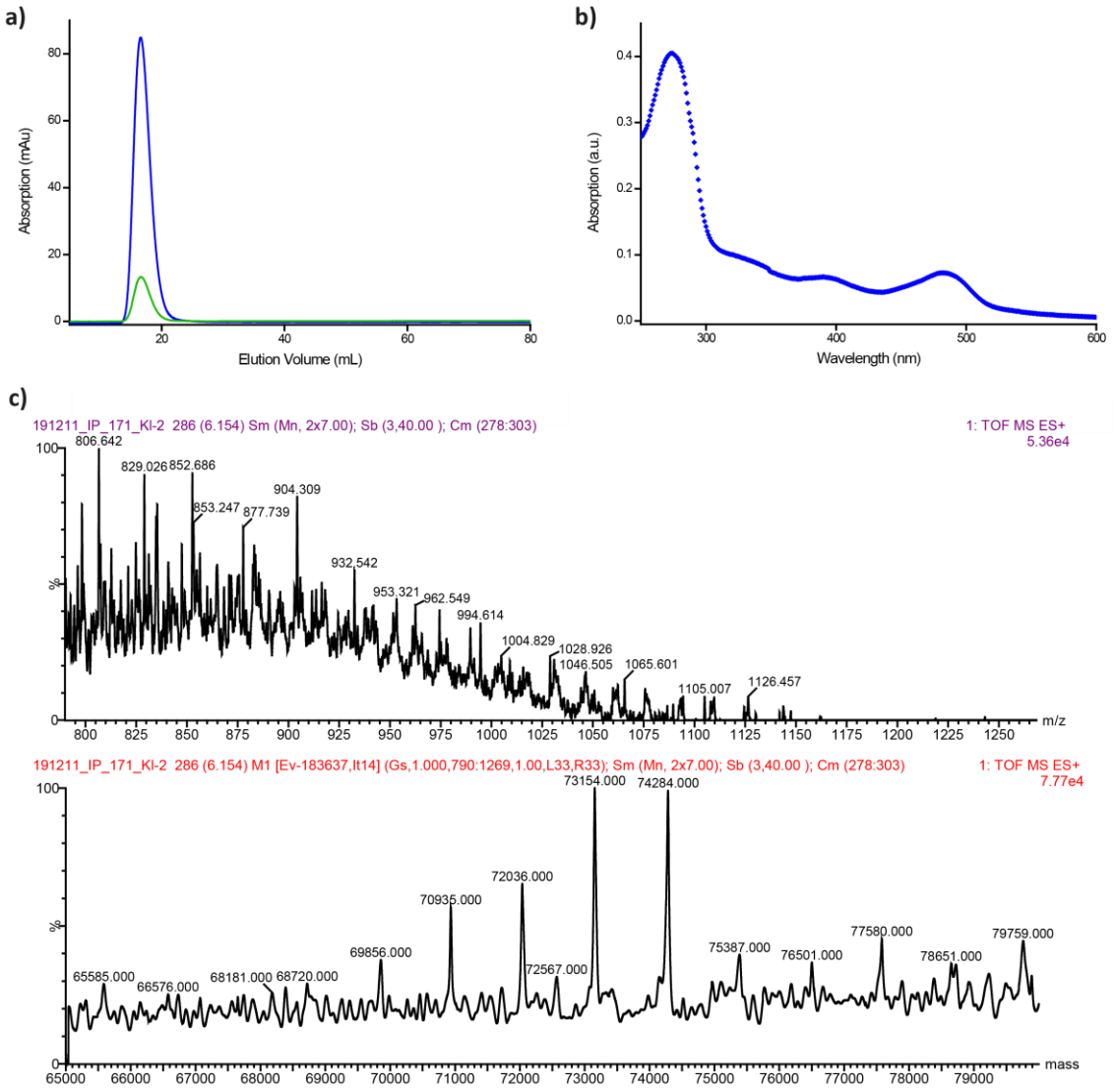

Figure A16: SEC chromatogram, UV-vis spectrum, and ESI(+)-MS spectrum of YopO Y588-**2•**/N624-**2•**. **a)** Chromatogram of the HiPrep™ 26/10 run with the absorption at 280 nm (blue) and 475 nm (green) of YopO Y588-**2•**/N624-**2•**. **b)** UV-vis spectrum of YopO Y588-**2•**/N624-**2•** after excess label removal recorded on a Cary100 UV-vis spectrometer. Quantification results: YopO = 4.5 µM; Mal-TSL **2•** = 9.6 µM; labeling efficiency: 106%. **c)** Raw (top) and deconvoluted (bottom) high-resolution ESI(+)-MS spectrum of YopO Y588-**2•**/N624-**2•** recorded on a Waters Synapt G2-SI spectrometer by the mass spectrometry facility in Marburg. Calculated mass: 74,283 Da; Found: 74,284 Da.

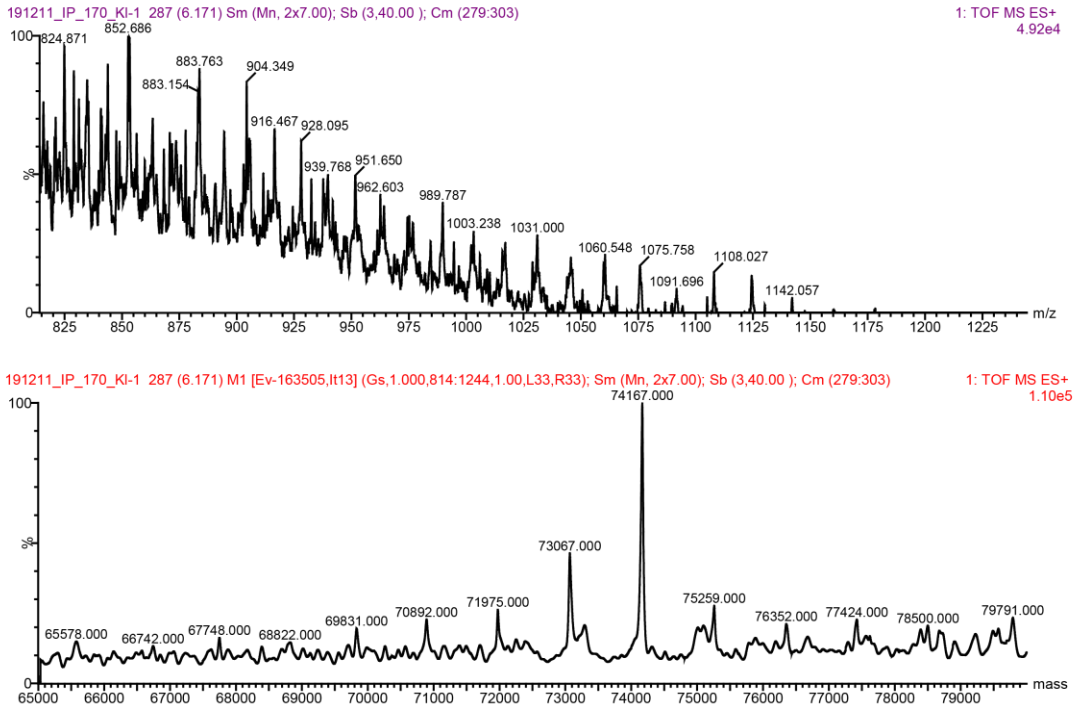

Figure A17: Raw (top) and deconvoluted (bottom) high-resolution ESI(+)-MS spectrum of YopO Y588-**3•**/N624-**3•** recorded on a Waters Synapt G2-SI spectrometer by the mass spectrometry facility in Marburg.

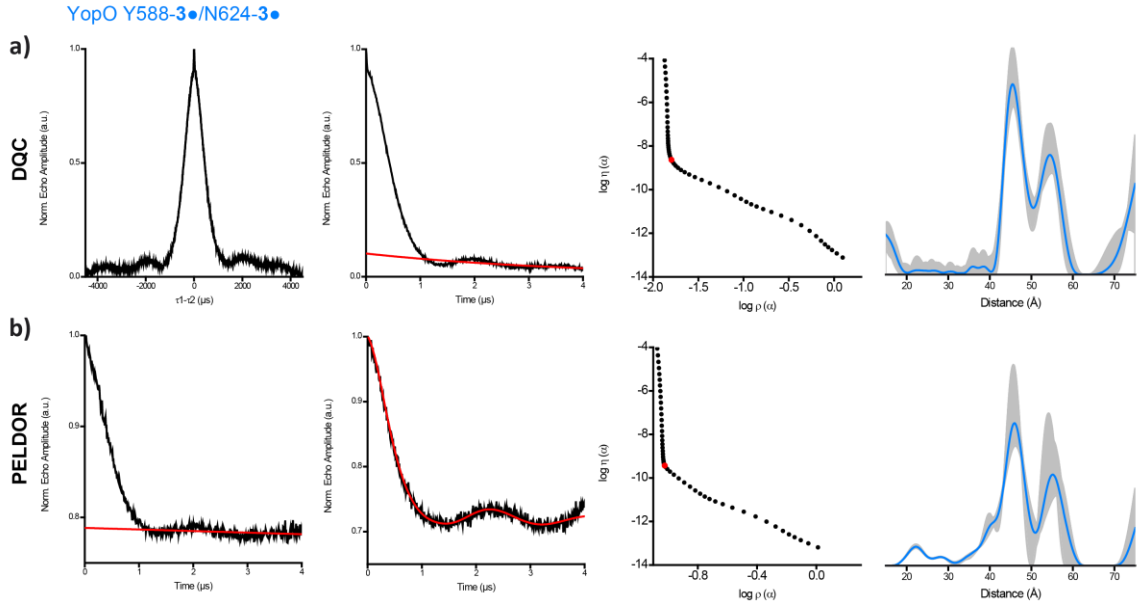

Figure A18: DeerAnalysis results for the DQC **(a)** and PELDOR **(b)** measurements of YopO Y588-**3•**/N624-**3•**. **a)** From left to right: Unmirrored DQC time trace; mirrored time trace (black) and the applied background function (red, three-dimensional homogenous background); L-curve with the chosen regularization parameter (red); and resulting distance distribution (blue) with the validation by DeerAnalysis shown as grey-shaded areas. **b)** From left to right: PELDOR time trace (black) and the applied background function (red, three-dimensional homogenous background); background corrected time trace (black) with the fit obtained by Tikhonov regularization (red); L-curve with the chosen regularization parameter (red); and resulting distance distribution (blue) with the validation by DeerAnalysis shown as grey-shaded areas.

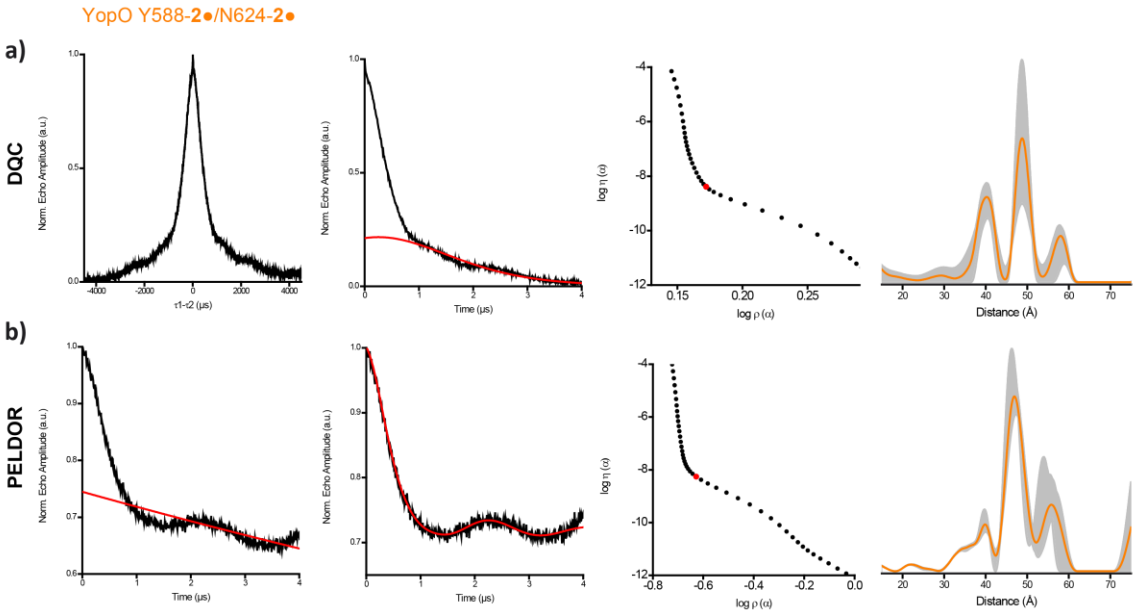

Figure A19: DeerAnalysis results for the DQC **(a)** and PELDOR **(b)** measurements of YopO Y588-**2•**/N624-**2•**. **a)** From left to right: Unmirrored DQC time trace; mirrored time trace (black) and the applied background function (red, 3rd-order polynomial function); L-curve with the chosen regularization parameter (red); and resulting distance distribution (orange) with the validation by DeerAnalysis shown as grey-shaded areas. **b)** From left to right: PELDOR time trace (black) and the applied background function (red, three-dimensional homogenous background); background corrected time trace (black) with the fit obtained by Tikhonov regularization (red); L-curve with the chosen regularization parameter (red); and resulting distance distribution (orange) with the validation by DeerAnalysis shown as grey-shaded areas.

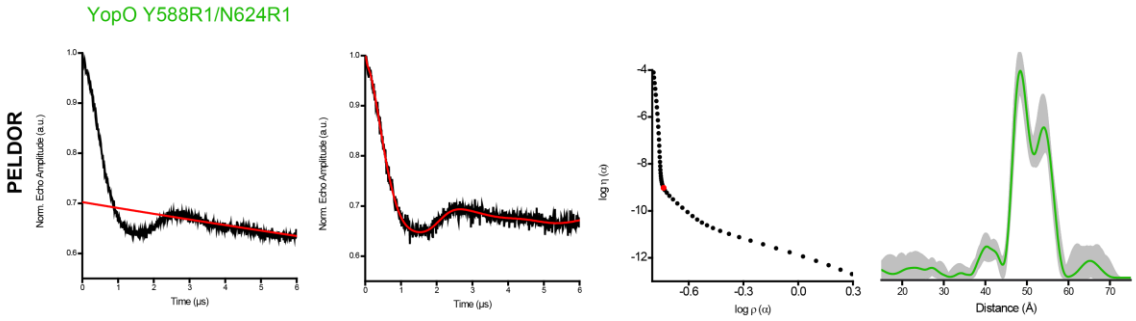

Figure A20: DeerAnalysis results for the PELDOR measurement of YopO Y588R1/N624R1. From left to right: PELDOR time trace (black) and the applied background function (red, three-dimensional homogenous background); background corrected time trace (black) with the fit obtained by Tikhonov regularization (red); L-curve with the chosen regularization parameter (red); and resulting distance distribution (green) with the validation by DeerAnalysis shown as grey-shaded areas.

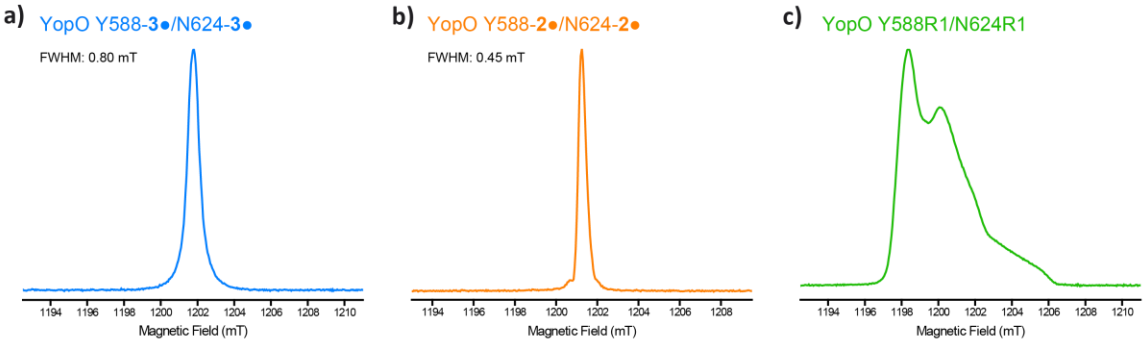

Figure A21: Q-band field-swept EPR spectra of YopO Y588-**3•**/N624-**3• (a),** YopO Y588-**2•**/N624-**2• (b)**, and YopO Y588R1/N624R1 **(c)**.

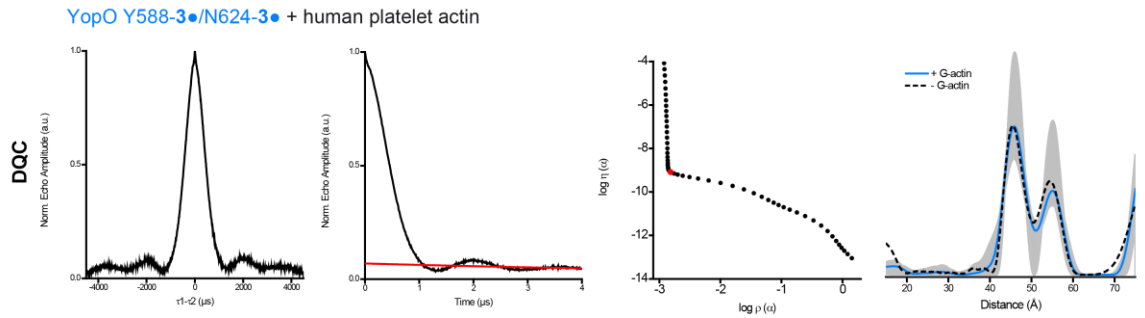

Figure A22: DeerAnalysis results for the DQC measurement of YopO Y588-**3•**/N624-**3•** incubated with human platelet actin. From left to right: Unmirrored DQC time trace; mirrored time trace (black) and the applied background function (red, three-dimensional homogenous background); L-curve with the chosen regularization parameter (red); and resulting distance distribution (blue) with the validation by DeerAnalysis shown as grey-shaded areas and the distance distribution of YopO Y588-**3•**/N624-**3•** in the absence of G-actin shown as black dashed lines.

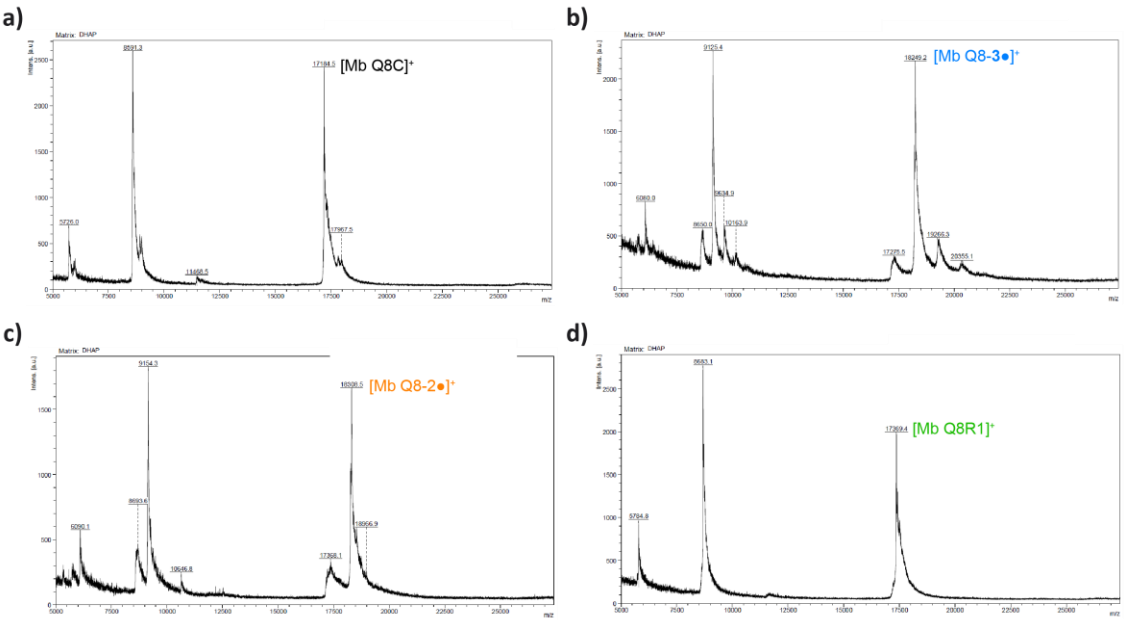

Figure A23: MALDI(+)-MS spectra of unlabeled Mb Q8C **(a)**, Mb Q8-**3• (b)**, Mb Q8-**2• (c)**, and Mb Q8R1 **(d)** recorded on a Bruker Daltonics ultrafleXtreme TOF/TOF spectrometer with the mass peaks corresponding to the respective entities highlighted by a colored tag.

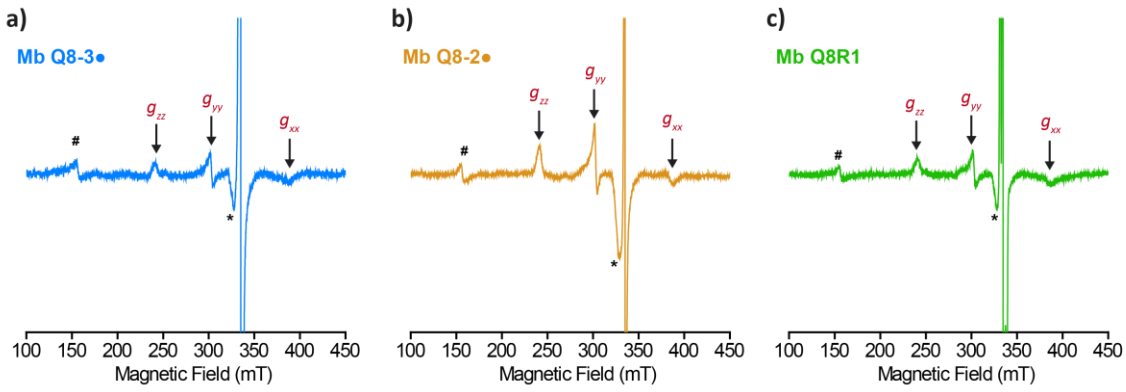

Figure A24: X-band cw-EPR spectra and spin-count results for Mb Q8-**3• (a)**, Mb Q8-**2• (b)**, and Mb Q8R1 **(c)**. Spectra were recorded on an EMXmicro spectrometer at 12 K. The field positions of g_{xx}, g_{yy}, and g_{zz} are indicated by black arrows. The signals marked with an asterisk stem from a resonator artifact, the signals marked by a hashtag correspond to free Fe^{3+}. Measurement settings: **(a)** 9.393 GHz microwave frequency, 1.763 mW microwave power, 100 kHz modulation frequency, 4.0 G modulation amplitude, 40.96 ms time constant, 10 pts/mT; **(b)** 9.389 GHz microwave frequency, 1.775 mW microwave power, 100 kHz modulation frequency, 4.0 G modulation amplitude, 40.96 ms time constant, 10 pts/mT; **(c)** 9.391 GHz microwave frequency, 1.766 mW microwave power, 100 kHz modulation frequency, 4.0 G modulation amplitude, 40.96 ms time constant, 10 pts/mT. Spectra were recorded by *Tobias Hett*.

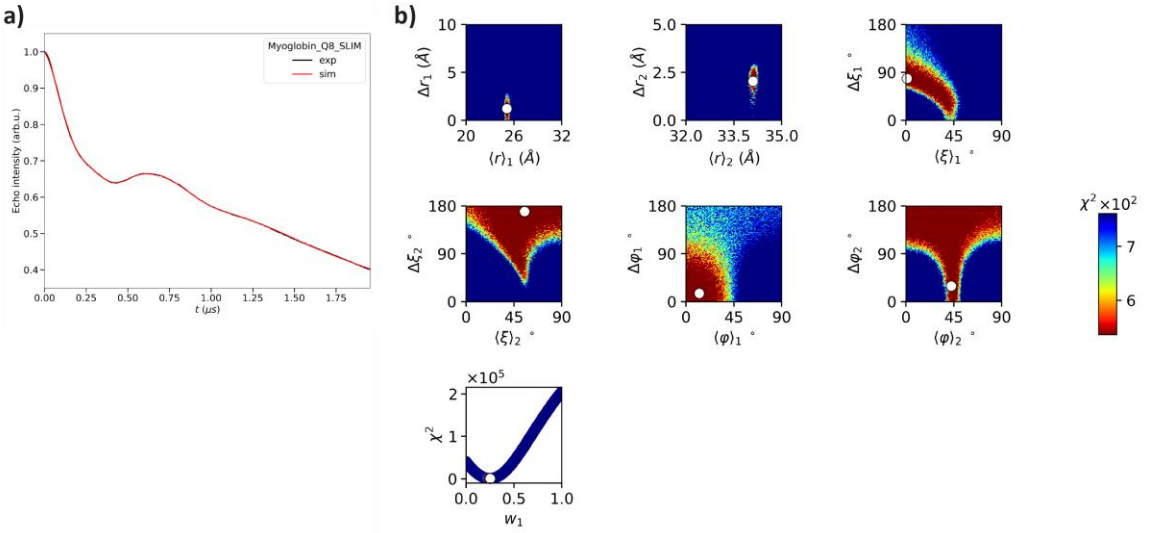

Figure A25: PDSFit results for Mb Q8-**3•**. **a)** Original six-pulse RIDME time trace (black) and simulation using the optimized parameters obtained by PDSFit (red). **b)** Two-dimensional error surfaces for the geometric parameters (Figure 113) used by PDSFit for a two-component system 1 and 2. Component 2 is discussed in the main text.

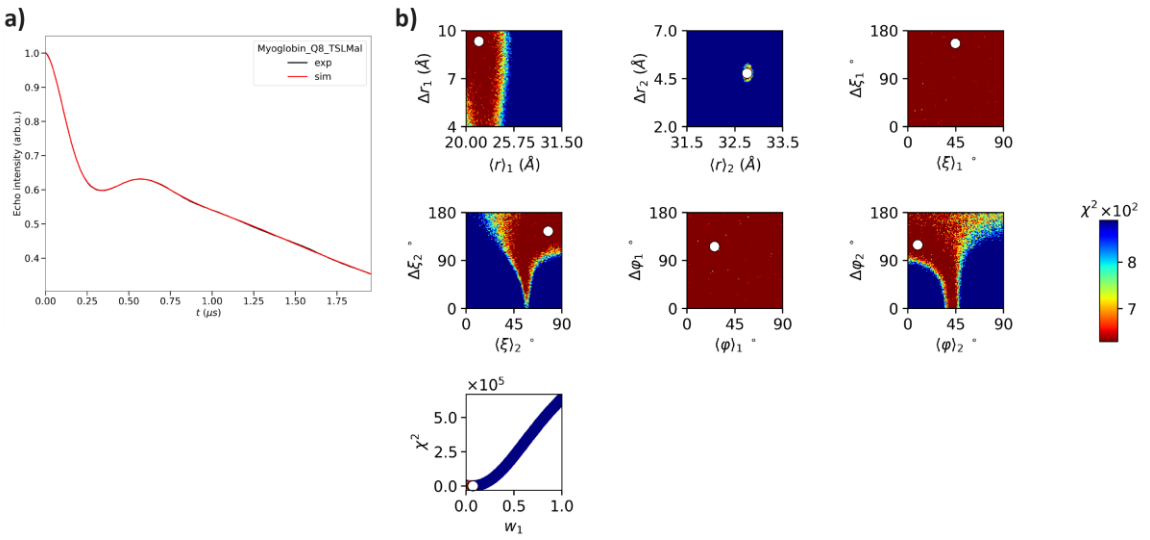

Figure A26: PDSFit results for Mb Q8-**2•**. **a)** Original six-pulse RIDME time trace (black) and simulation using the optimized parameters obtained by PDSFit (red). **b)** Two-dimensional error surfaces for the geometric parameters (Figure 113) used by PDSFit for a two-component system 1 and 2. Component 2 is discussed in the main text.

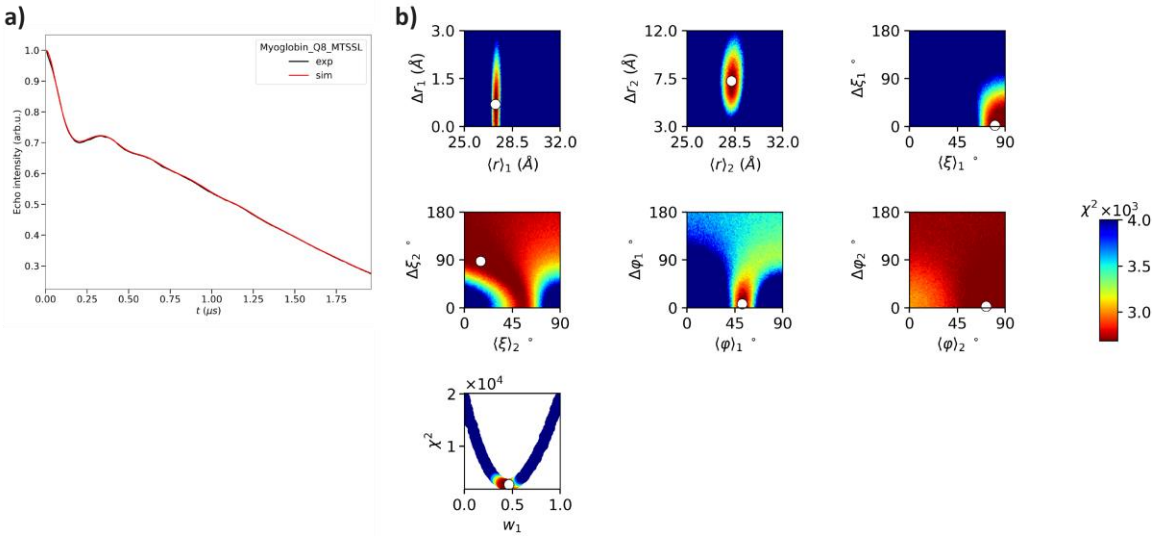

Figure A27: PDSFit results for Mb Q8R1. **a)** Original six-pulse RIDME time trace (black) and simulation using the optimized parameters obtained by PDSFit (red). **b)** Two-dimensional error surfaces for the geometric parameters (Figure 113) used by PDSFit for a two-component system 1 and 2. Component 1 is discussed in the main text.

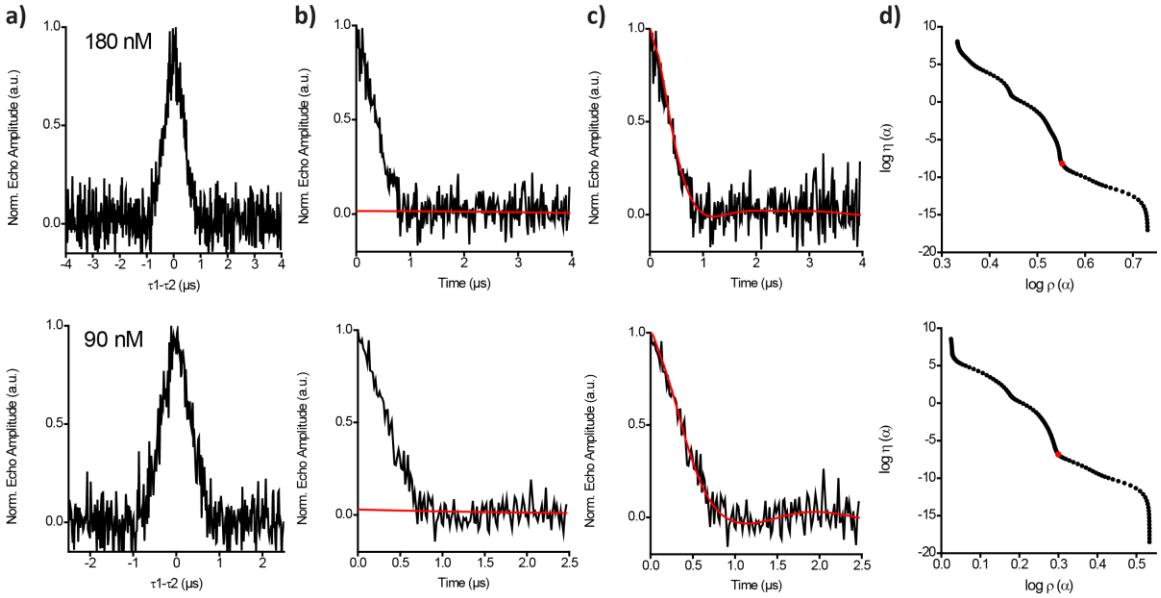

Figure A28: DeerAnalysis results for the DQC measurements of YopO Y588-**3•**/N624-**3•** at 180 nM (top) and 90 nM (bottom). From left to right: Unmirrored DQC time trace **(a)**; mirrored time trace (black) and the applied background function (red, three-dimensional homogenous background) **(b)**; background corrected time trace (black) with the fit obtained by Tikhonov regularization (red) **(c)**; and L-curve with the chosen regularization parameter (red) **(d)**.

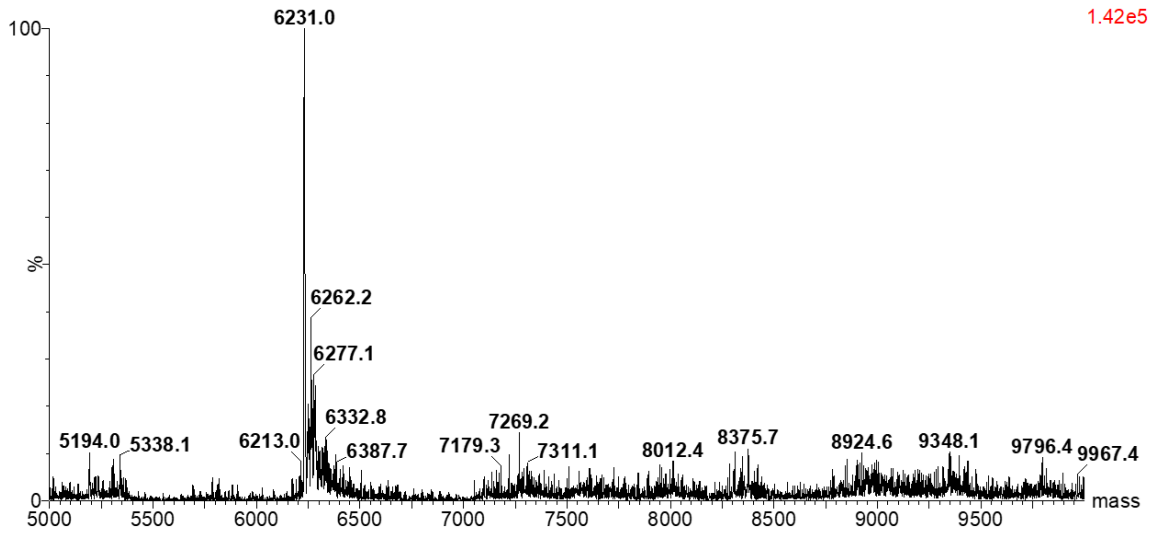

Figure A29: ESI(+)-MS spectrum of unlabeled GB1 I6C/K28H/Q32H recorded on a Waters Xevo G2 TOF mass spectrometer.

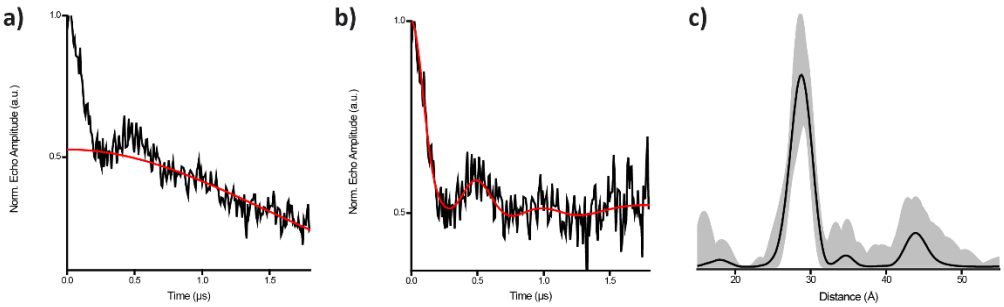

Figure A30: DeerAnalysis results for the vtRIDME time trace of GB1 I6-3•/28H+32H-Cu^{2+}(NTA) at 10 nM averaged over 60 h. From left to right: Raw vtRIDME time trace (black) and the applied background function (red) **(a)**; background corrected time trace (black) with the fit obtained by Tikhonov regularization (red) **(b)**; and the resulting distance distribution (black) with the uncertainty estimate shown as grey shaded area.

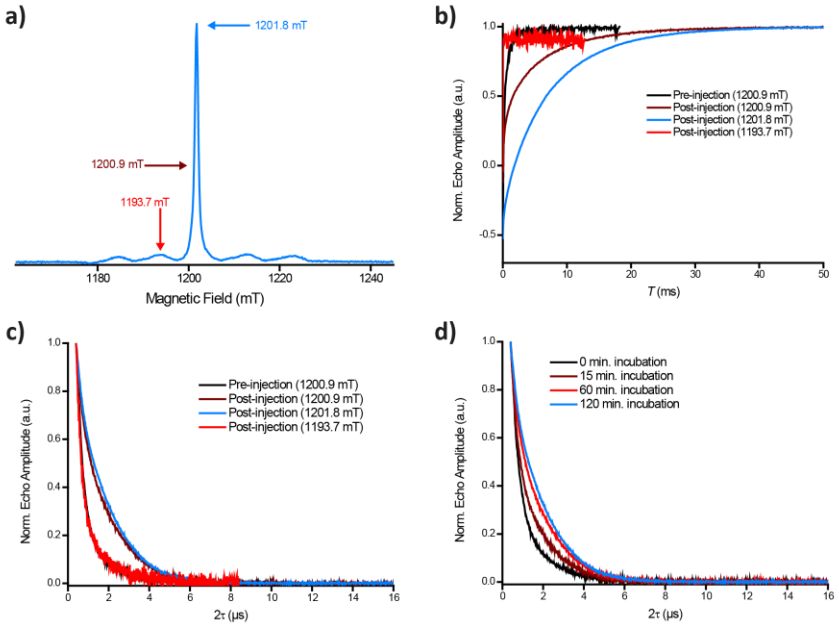

Figure A31: Echo-detected field swept EPR spectrum and relaxation measurements of YopO Y588-**3**•/N624-**3**• injected into *Xenopus laevis* oocytes. **a)** Field swept EPR spectrum of YopO Y588-**3**•/N624-**3**• injected into oocytes with the relevant field positions (SLIM **3**•: 1201.8mT; oocyte signal: 1200.9 mT; Mn^{2+} signal: 1193.7 mT) indicated by arrows. **b)** Inversion recovery traces at the field positions in **(a)** pre- and post-injection. **c)** 2pESEEM traces at the field positions in **(a)** pre- and post-injection. **d)** 2pESEEM traces recorded after different incubation periods of the oocytes after the microinjection procedure (field position: 1201.8 mT).

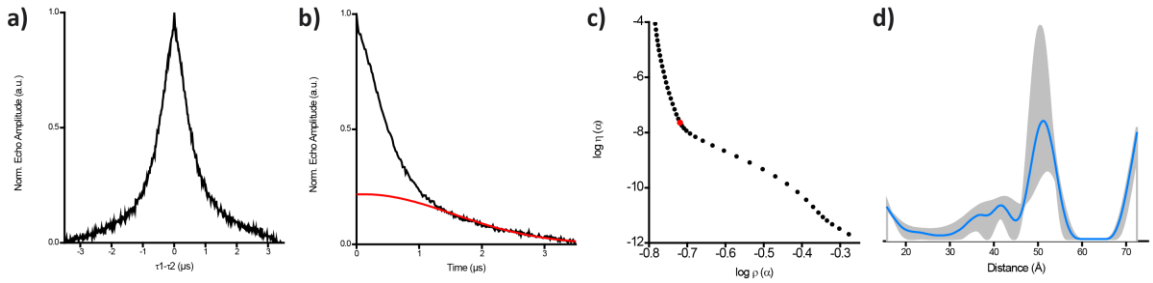

Figure A32: DeerAnalysis results for the DQC measurement of YopO Y588-**3•**/N624-**3•** in *Xenopus laevis* oocytes after an incubation period of 120 min. From left to right: Unmirrored DQC time trace **(a)**; mirrored time trace (black) and the applied background function (red, 3rd-order polynomial function) **(b)**; L-curve with the chosen regularization parameter (red) **(c)**; and resulting distance distribution (blue) with the validation by DeerAnalysis shown as grey-shaded areas **(d)**.

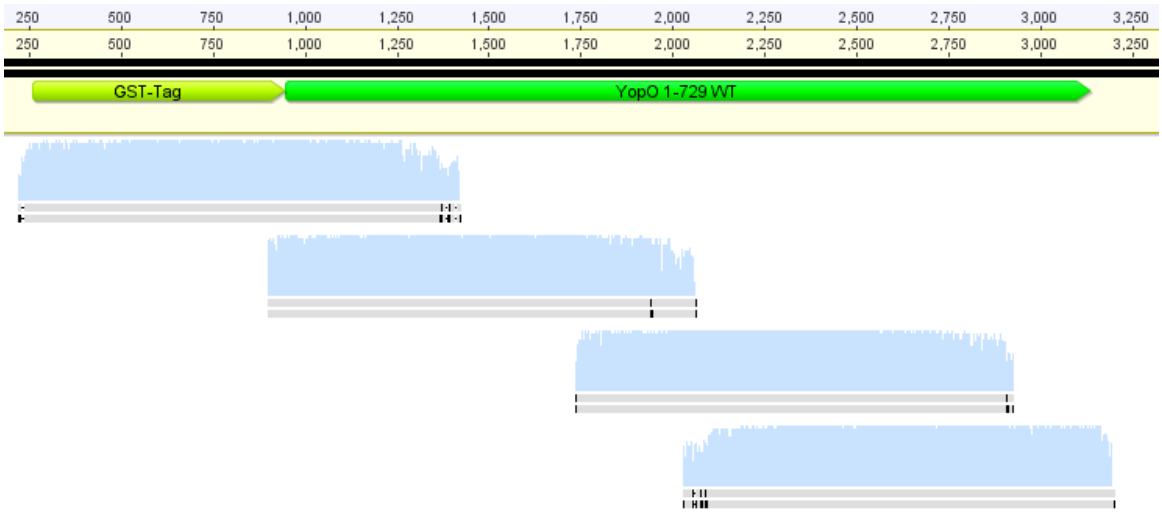

Figure A33: Sequencing results for the GST-YopO$_{1-729}$-wt construct (excerpt taken from Geneious). Modeled sequence of the GST-fused YopO$_{1-729}$-wt construct (top, GST in yellow and YopO$_{1-729}$ in green) and the aligned sequencing results of four individual primers chosen to cover the whole genome (bottom, blue). Deviations of the sequencing result from the model sequence are indicated as black bars. Here, black bars only appear in the low-confidence regions of the sequencing (start and end of the elongation) and are falsified by an additional sequencing result covering the same area in the high-confidence region.

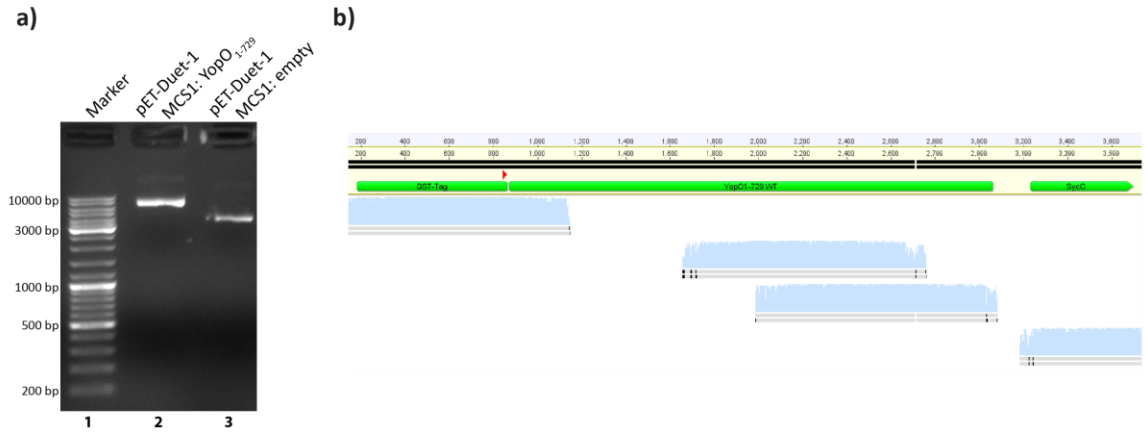

Figure A34: Cloning of GST-YopO$_{1-729}$ and SycO into the pET-Duet-1 vector. **a)** 1% agarose gel with GST-YopO$_{1-729}$ cloned into the first MCS of pET-Duet-1 (expected: ~8,300 bp, lane 2) and the empty pET-Duet-1 vector (5420 bp, lane 3) as a reference. **b)** Modeled sequence of the GST-YopO$_{1-729}$ and SycO (top) in the MCS1 and MCS2, respectively, and the aligned sequencing results of four individual primers chosen to cover the genome (bottom, blue). Deviations of the sequencing result from the model sequence are indicated as black bars. Here, black bars only appear in the low-confidence regions of the sequencing (start and end of the elongation).

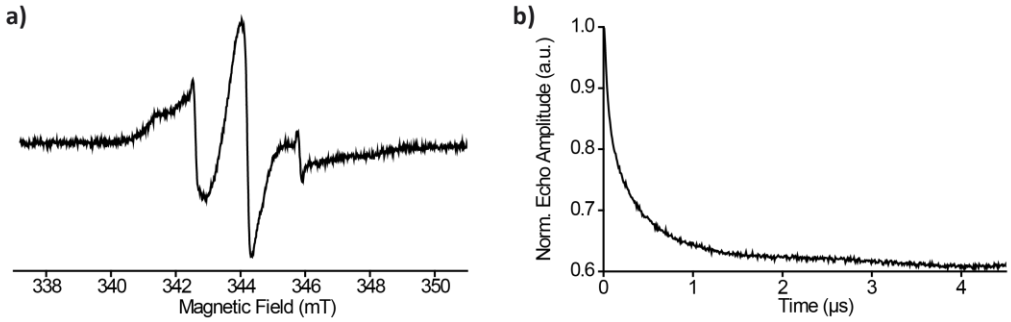

Figure A35: Room temperature X-band cw-EPR spectrum and PELDOR time trace of YopO$_{1-729}$(SycO)$_2$ labeled with MTSL. **a)** X-band cw-EPR spectrum of YopO$_{1-729}$(SycO)$_2$ (unknown concentration) labeled with MTSL (spin-count: 200 µM) recorded on a Bruker EMXnano spectrometer. Measurement settings: 9.6 GHz microwave frequency, 10 mW microwave power, 100 kHz modulation frequency, 1.0 G modulation amplitude, 20.48 ms time constant, 100 pts/mT. **b)** Normalized Q-band PELDOR time trace of the sample in **(a)** at a final spin concentration of 100 µM.

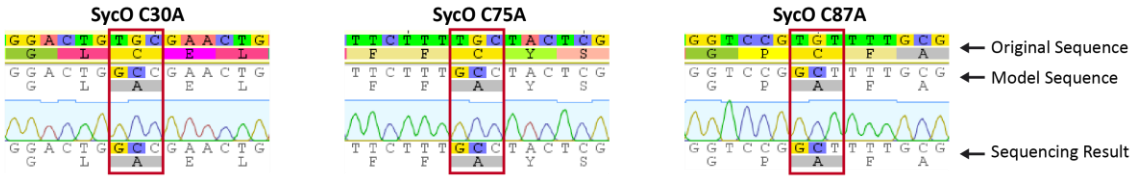

Figure A36: Sequencing results for the cysteine mutations to alanine in SycO with the exchanged amino acid shown in a red box. From left to right: SycO C30A, SycO C75A, and SycO C87A. Excerpt taken from Geneious.

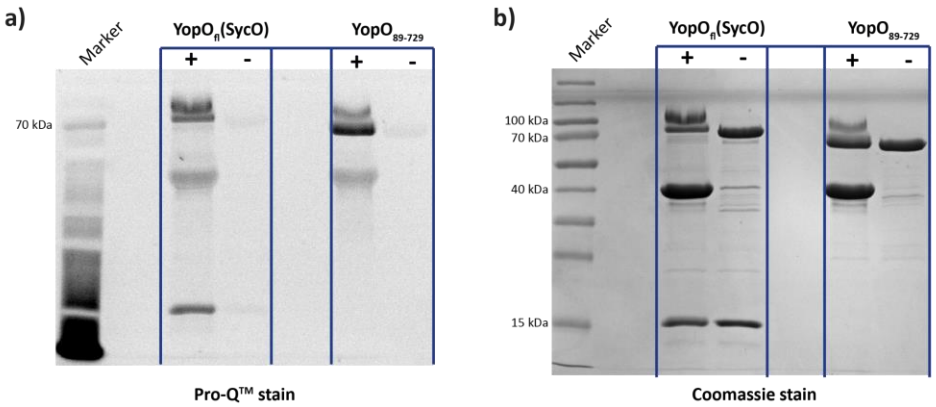

Figure A37: Activity assay of the YopO$_{fl}$(SycO) and soluble YopO$_{89-729}$ for comparison. **a)** 10% polyacrylamide gels and stained with Pro-Q™ to visualize phosphorylated proteins. **b)** SDS gel from **(a)** stained with Coomassie stain for visualization of total protein content. The lanes indicated with a (+)-sign contain G-actin while the lanes indicated with a (–)-sign are negative controls in the absence of G-actin. The YopO$_{fl}$(SycO) construct shows a similar kinase activity as the soluble YopO$_{89-729}$ reference sample.

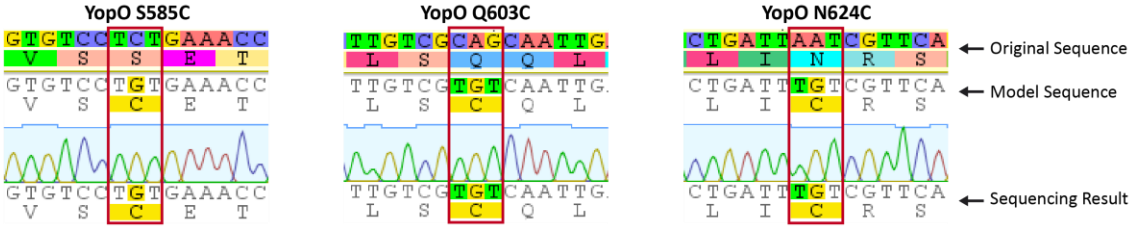

Figure A38: Sequencing results for the cysteine mutations in YopO$_{fl}$(SycO) with the exchanged amino acid shown in a red box. From left to right: YopO S585C, YopO Q603, and YopO N624C. Excerpt taken from Geneious.

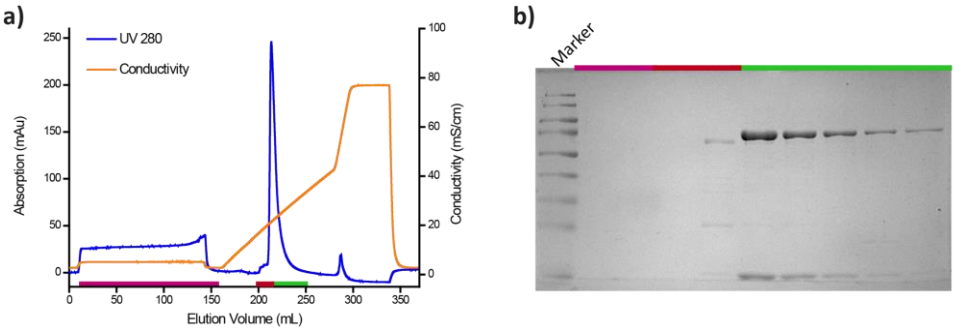

Figure A39: Purification of YopO$_{fl}$(SycO) S585C/Q603C. **a)** Chromatogram of the Capto™ HiRes Q 10/100 anion exchange run showing the absorption at 280 nm (blue) and conductivity (orange). The horizontal bars (purple, red, and green) correspond to the fractions taken for SDS-PAGE analysis. **b)** Coomassie-stained 10% SDS gel of the fractions shown in **(a)**. Only the green fractions marked with a green bar where pooled and concentrated. Final yield: 7.9 mg protein.

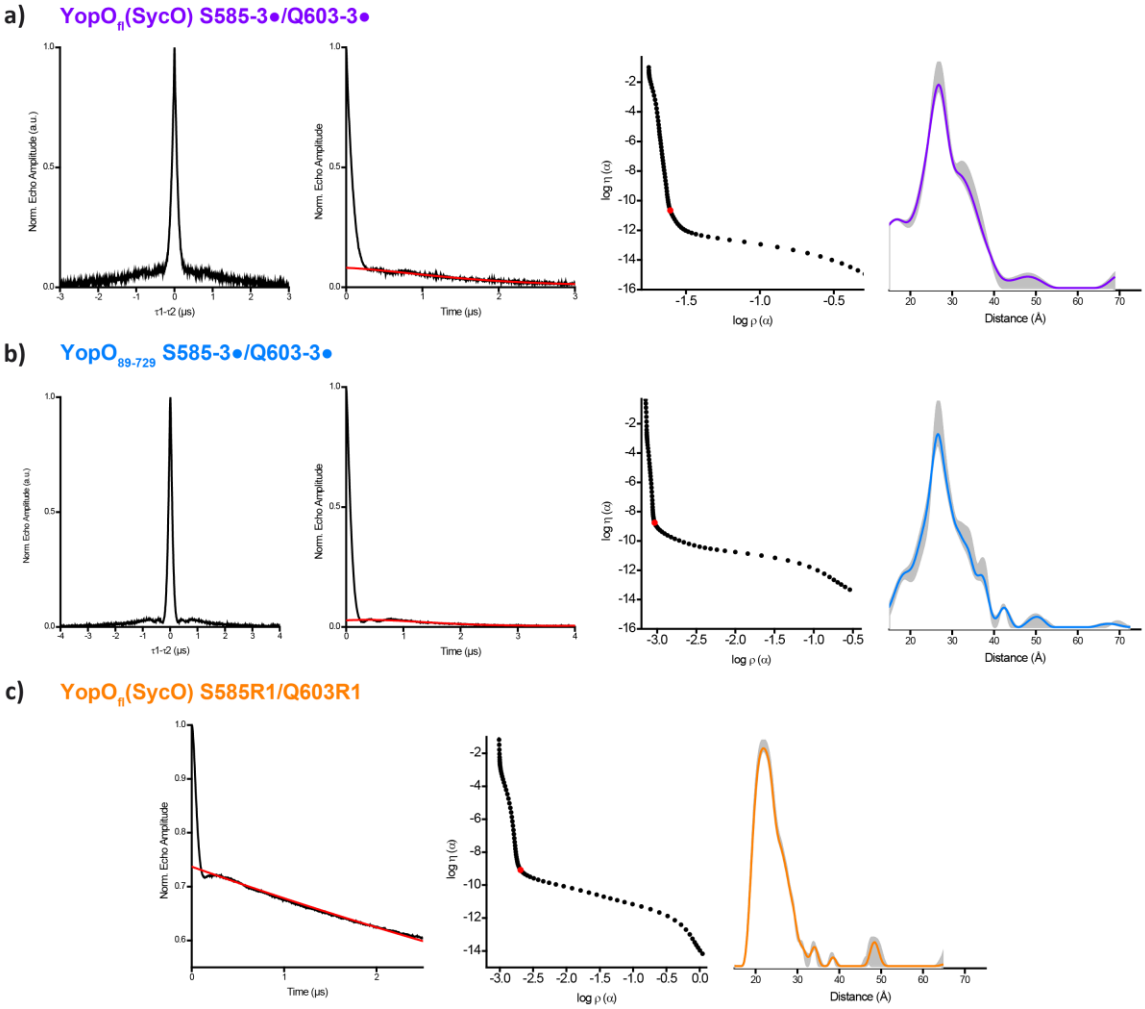

Figure A40: DeerAnalysis results for the *in vitro* DQC and PELDOR measurement of full-length and soluble YopO labeled with SLIM **3•** and MTSL. **a)** Data for YopO$_{fl}$(SycO) S585-**3•**/Q603-**3•**. From left to right: Unmirrored DQC time trace recorded at 70 K; mirrored time trace (black) and the applied background function (red, 3rd-order polynomial function); L-curve with the chosen regularization parameter (red); and resulting distance distribution (purple) with the validation by DeerAnalysis shown as grey-shaded areas. **b)** Data for YopO$_{89-729}$ S585-**3•**/Q603-**3•**. From left to right: Unmirrored DQC time trace recorded at 70 K; mirrored time trace (black) and the applied background function (red, 3rd-order polynomial function); L-curve with the chosen regularization parameter (red); and resulting distance distribution (blue) with the validation by DeerAnalysis shown as grey-shaded areas. **c)** Data for YopO$_{fl}$(SycO) S585R1/Q603R1. From left to right: PELDOR time trace (black) and the applied background function (red, three-dimensional homogenous background); L-curve with the chosen regularization parameter (red); and resulting distance distribution (orange) with the validation by DeerAnalysis shown as grey-shaded areas.

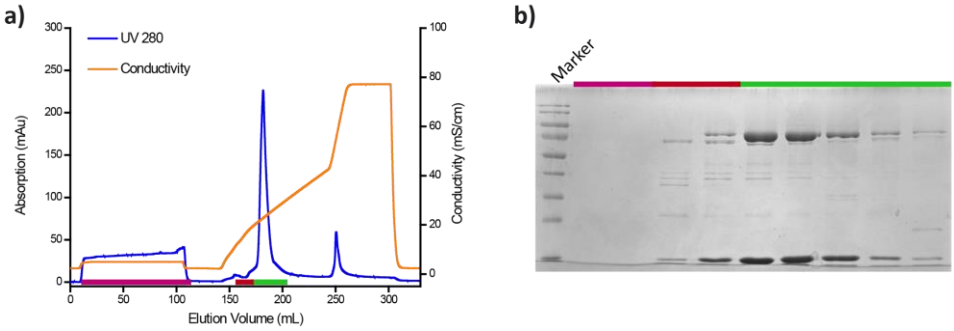

Figure A41: Purification of $YopO_{fl}$(SycO) N624C. **a)** Chromatogram of the Capto™ HiRes Q 10/100 anion exchange run showing the absorption at 280 nm (blue) and conductivity (orange). The horizontal bars (purple, red, and green) correspond to the fractions taken for SDS-PAGE analysis. **b)** Coomassie-stained 10% SDS gel of the fractions shown in **(a)**. Only the green fractions marked with a green bar where pooled and concentrated. Final yield: 7.7 mg protein.

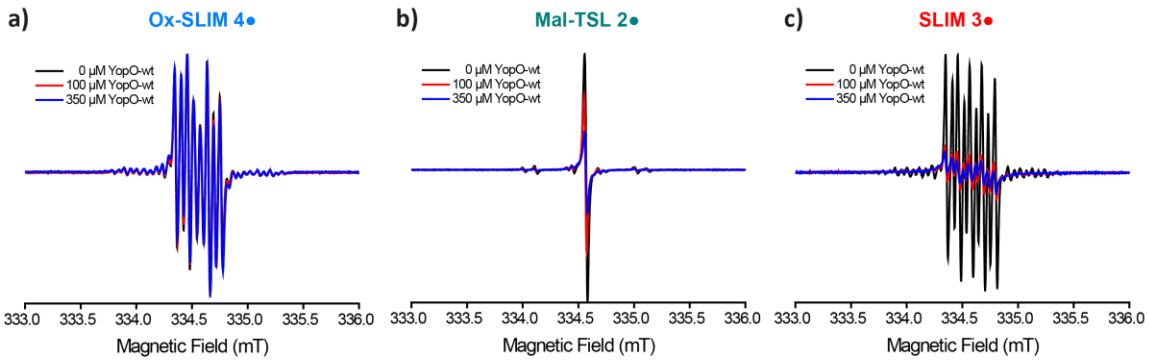

Figure A42: Room temperature X-band cw-EPR spectrum of 50 µM Ox-SLIM **4• (a)**, Mal-TSL **2• (b)**, and SLIM **3• (c)** incubated with no (black), 100 µM (red), and 350 µM (blue) of YopO-wt. Spectra were recorded on a Bruker EMXmicro spectrometer with 10 scans per sample. The double-integral values for each radical remained constant within a 10% deviation window. Measurement settings: 9.4 GHz microwave frequency, 0.550 mW microwave power, 100 kHz modulation frequency, 0.2 G modulation amplitude, 20.48 ms time constant, 500 pts/mT.

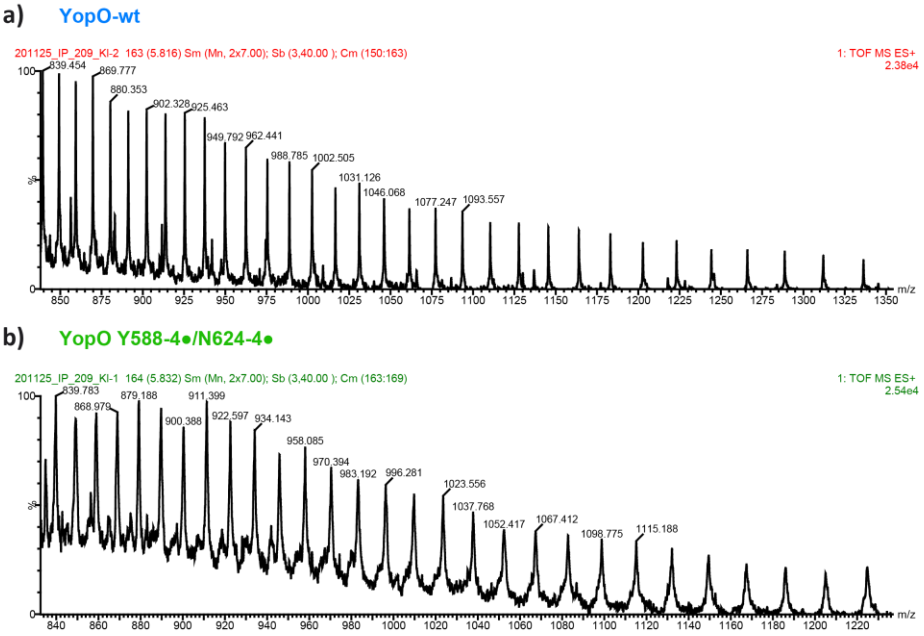

Figure A43: Raw high-resolution ESI(+)-MS spectra of YopO-wt incubated with Ox-SLIM **4•** **(a)** and YopO Y588-**4•**/N624-**4•** **(b)** recorded on a Waters Synapt G2-SI spectrometer by the mass spectrometry facility in Marburg.

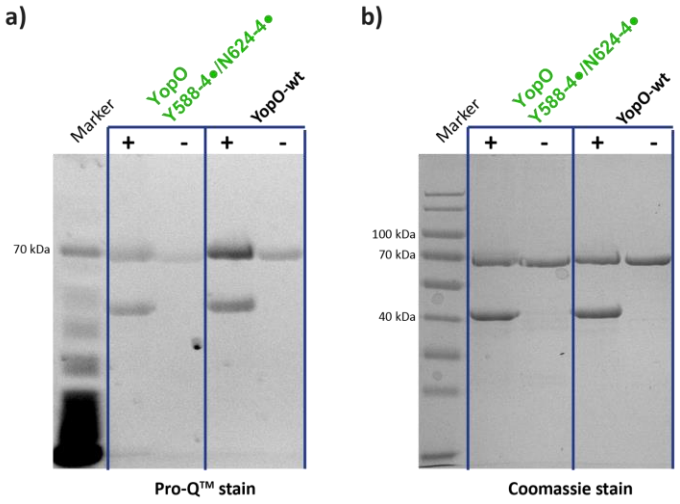

Figure A44: Activity assay of spin-labeled YopO Y588-**4•**/N624-**4•** and YopO-wt for comparison. **a)** 10% polyacrylamide gels and stained with Pro-Q™ to visualize phosphorylated proteins. **b)** SDS gel from **(a)** stained with Coomassie stain for visualization of total protein content. The lanes indicated with a (+)-sign contain G-actin while the lanes indicated with a (–)-sign are negative controls in the absence of G-actin. The spin-labeled YopO Y588-**4•**/N624-**4•** construct shows a slightly lowered kinase activity as the soluble YopO-wt reference sample.

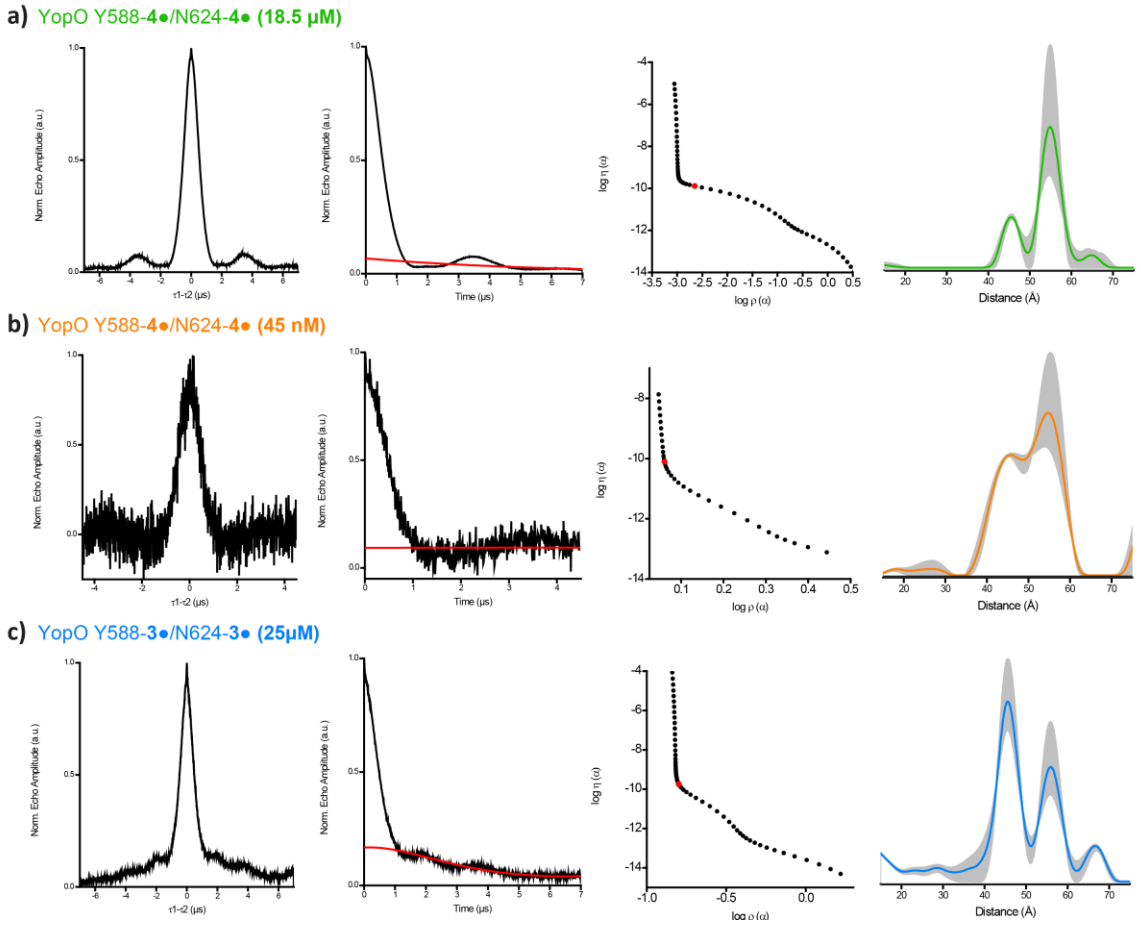

Figure A45: DeerAnalysis results for YopO Y588-**4•**/N624-**4•** at 18.5 µM **(a)**, 45 nM **(b)**, and YopO Y588-**3•**/N624-**3•** at 25 µM **(c)** protein concentration. From left to right: Unmirrored DQC time trace recorded at 50 K; mirrored time trace (black) and the applied background function (red, homogenous three-dimensional **(a+b)**, 3rd-order polynomial function **(c)**); L-curve with the chosen regularization parameter (red); and resulting distance distribution (colored) with the validation by DeerAnalysis shown as grey-shaded areas.

6.2 Supplementary Information Section 3.3

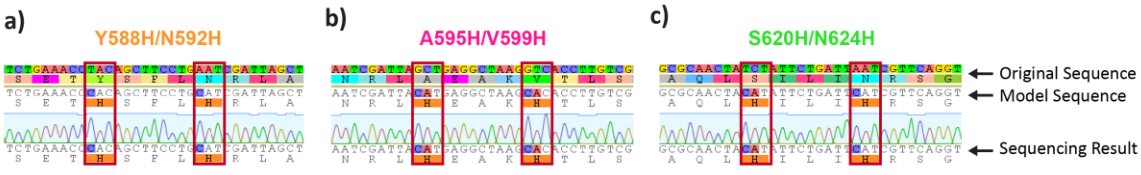

Figure A46: Sequencing results for the dHis mutations in YopO with the exchanged amino acid shown in a red box. **a)** YopO Y588H/N592H. **b)** YopO A595H/V599H. **c)** YopO S620H/N624H. Excerpt taken from Geneious.

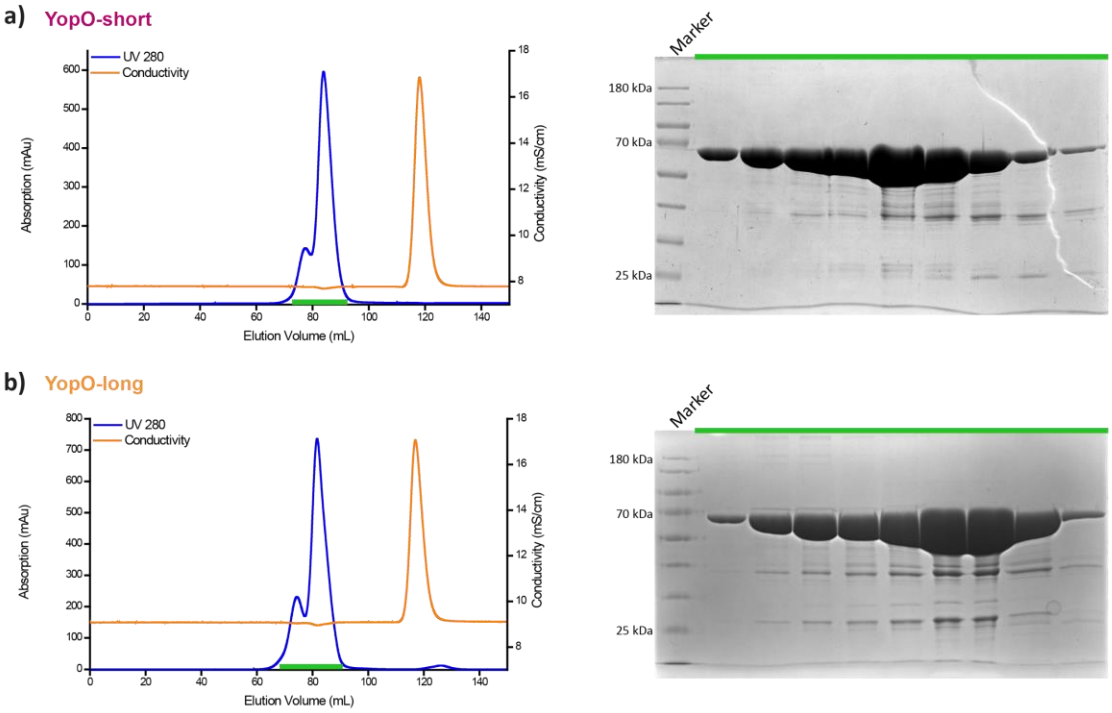

Figure A47: HiLoad® 16/600 Superdex® 200 pg gel filtration chromatogram (left) and Coomassie-stained 10% polyacrylamide gel (right) of YopO-short **(a)** and YopO-long **(b)**. The fractions indicated by a green bar were further pooled and purified.

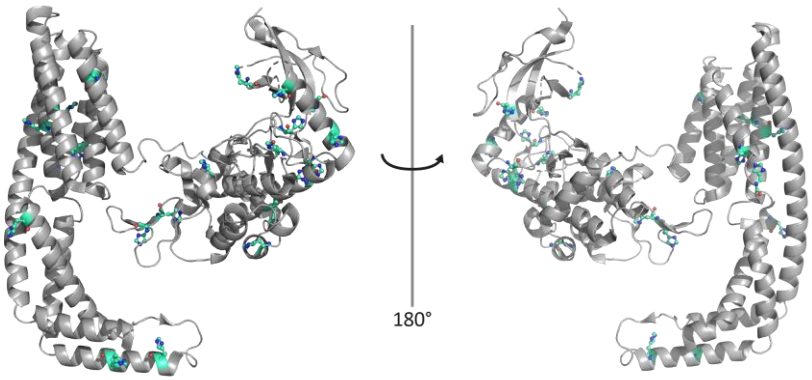

Figure A48: Structure of YopO (PDB-ID 4ci6, actin removed) with all native histidine residues shown as ball-and-stick model in cyan.

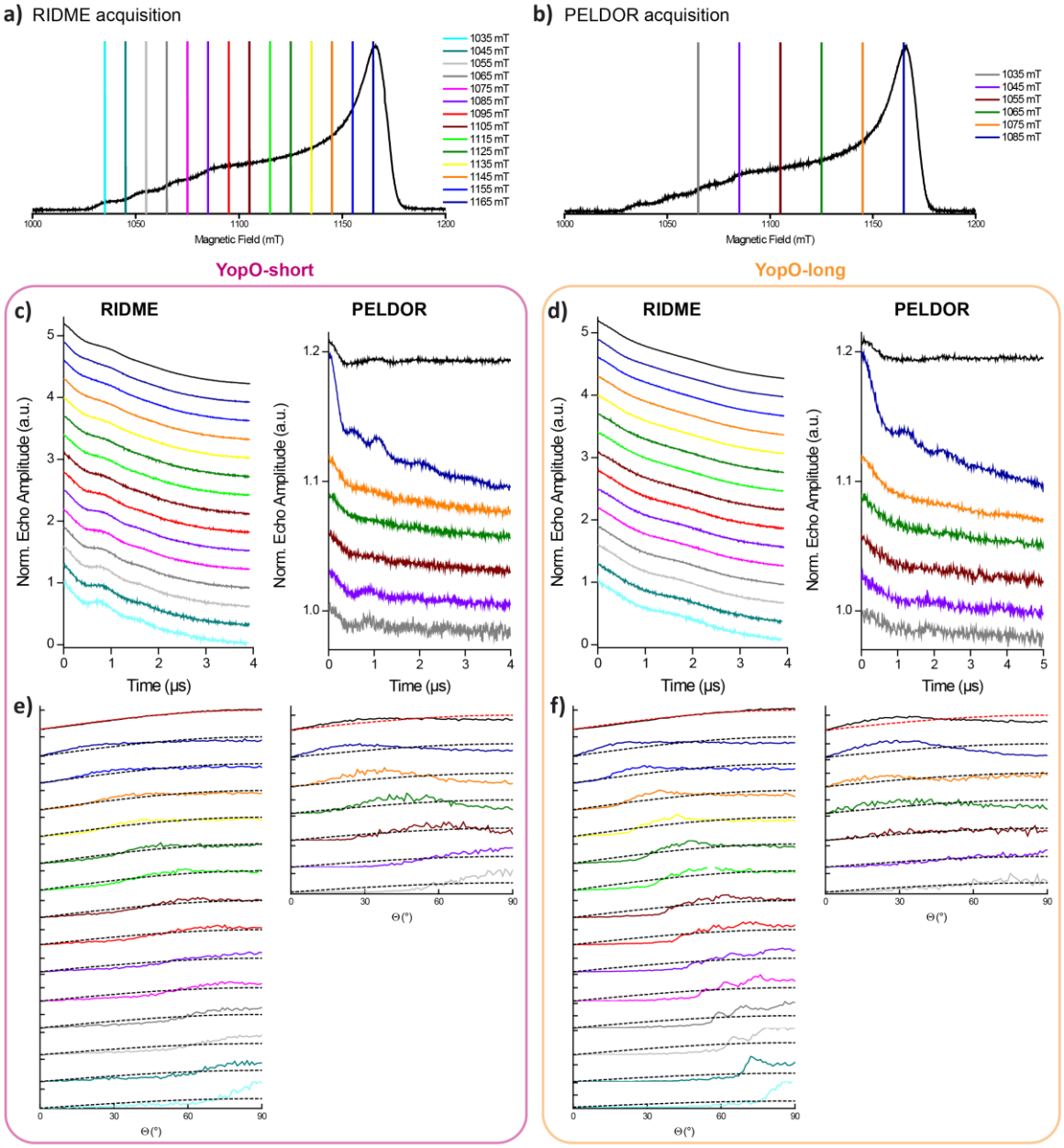

Figure A49: Data acquisition schemes, time traces, and dipolar angle *Θ* coverage of YopO-short and YopO-long for equally spaced magnetic fields. **a+b)** Representative Q-band field-swept EPR spectrum of YopO-short with the vertical, colored lines indicating the magnetic field positions for RIDME **(a)** and PELDOR **(b)** data acquisition. **c+d)** RIDME (left) and PELDOR (right) time traces of YopO-short **(c)** and YopO-long **(d)** acquired at 25 K (RIDME) and 20 K (PELDOR) at the field positions indicated in **(a)** and **(b)**, respectively. The summed, and in the case of PELDOR background corrected time traces, are shown in black. **e+f)** Coverage of the dipolar angle *Θ* obtained by PDSFit for the individual and summed RIDME (left) and PELDOR (right) time traces at the individual magnetic field positions of YopO-short **(c)** and YopO-long **(d)** using the same color code as **(c+d)**.

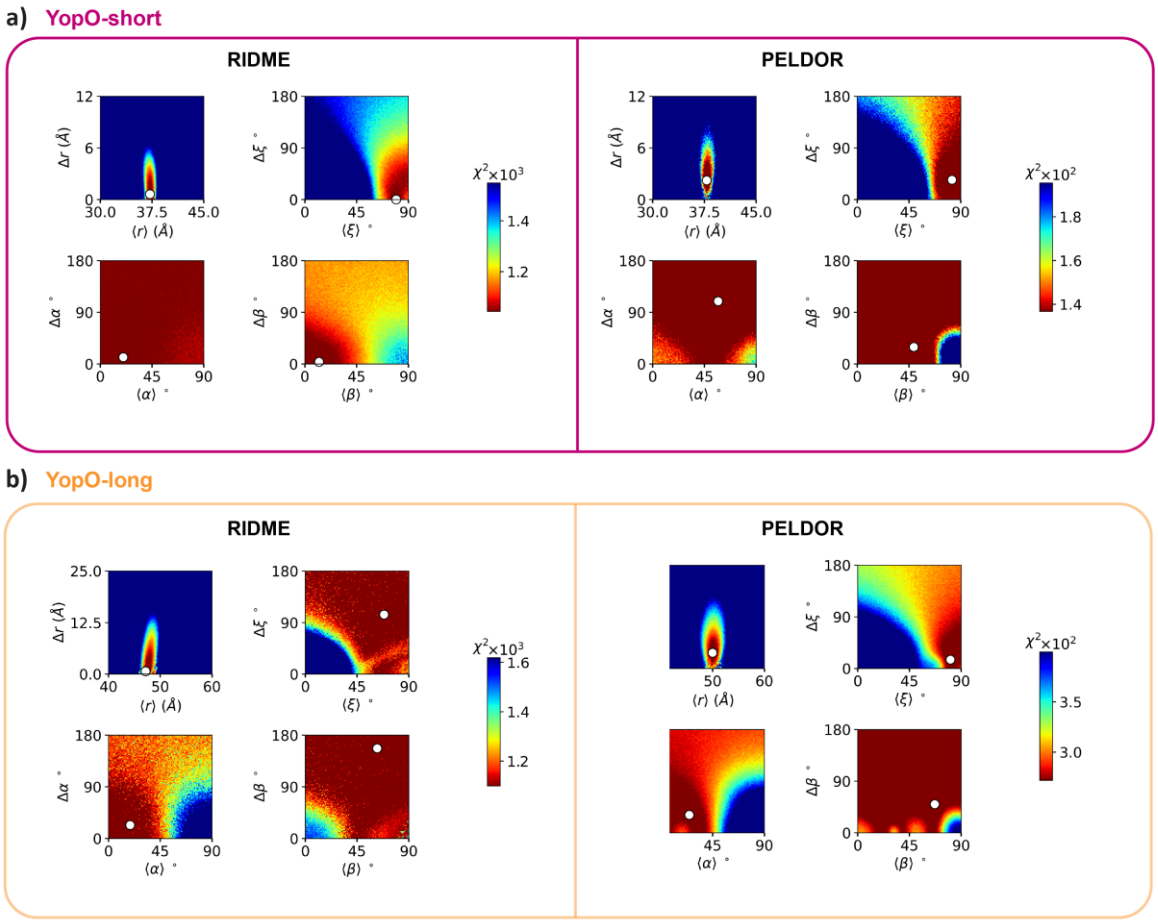

Figure A50: PDSFit results for YopO-short and YopO-long. **a)** Two-dimensional error plots of the four geometric parameters *r* (top left), *ξ* (top right), *α* (bottom left), and *β* (bottom right) fitted by PDSFit for RIDME (left) and PELDOR (right) on YopO-short. The best optimization paarameters are indicated by white dots. **b)** Same as **(a)** but for YopO-long.

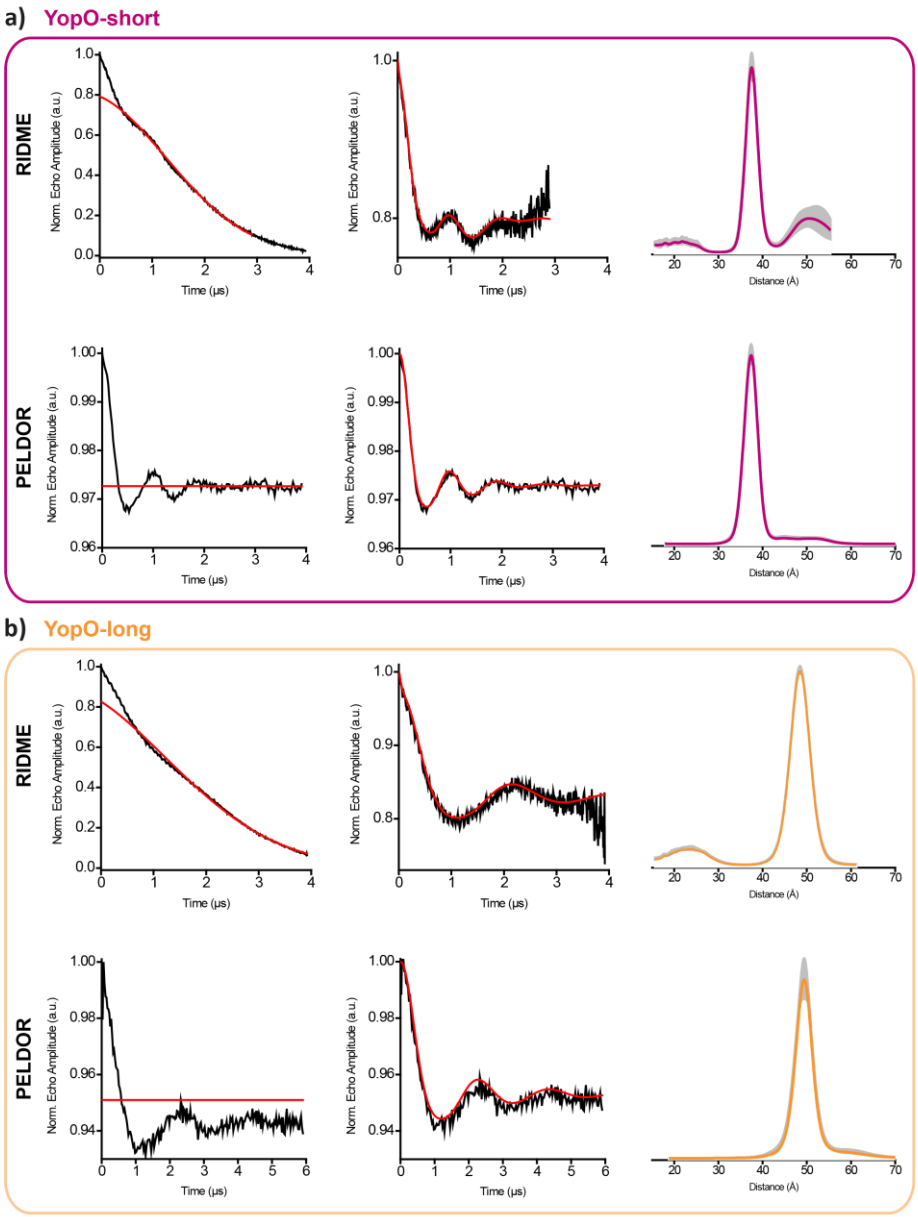

Figure A51: DEERNet results for YopO-short and YopO-long. **a)** DEENet results for RIDME (top row) and PELDOR (bottom row) on YopO-short. From left to right: Normalized time trace (black) and the chosen background function by DEERNet (red); background-corrected time trace (black) with the corresponding fit (red); and resulting distance distribution (colored) with the uncertainty estimates shown as grey-shaded areas. **b)** Same as **(a)** but for YopO-long.

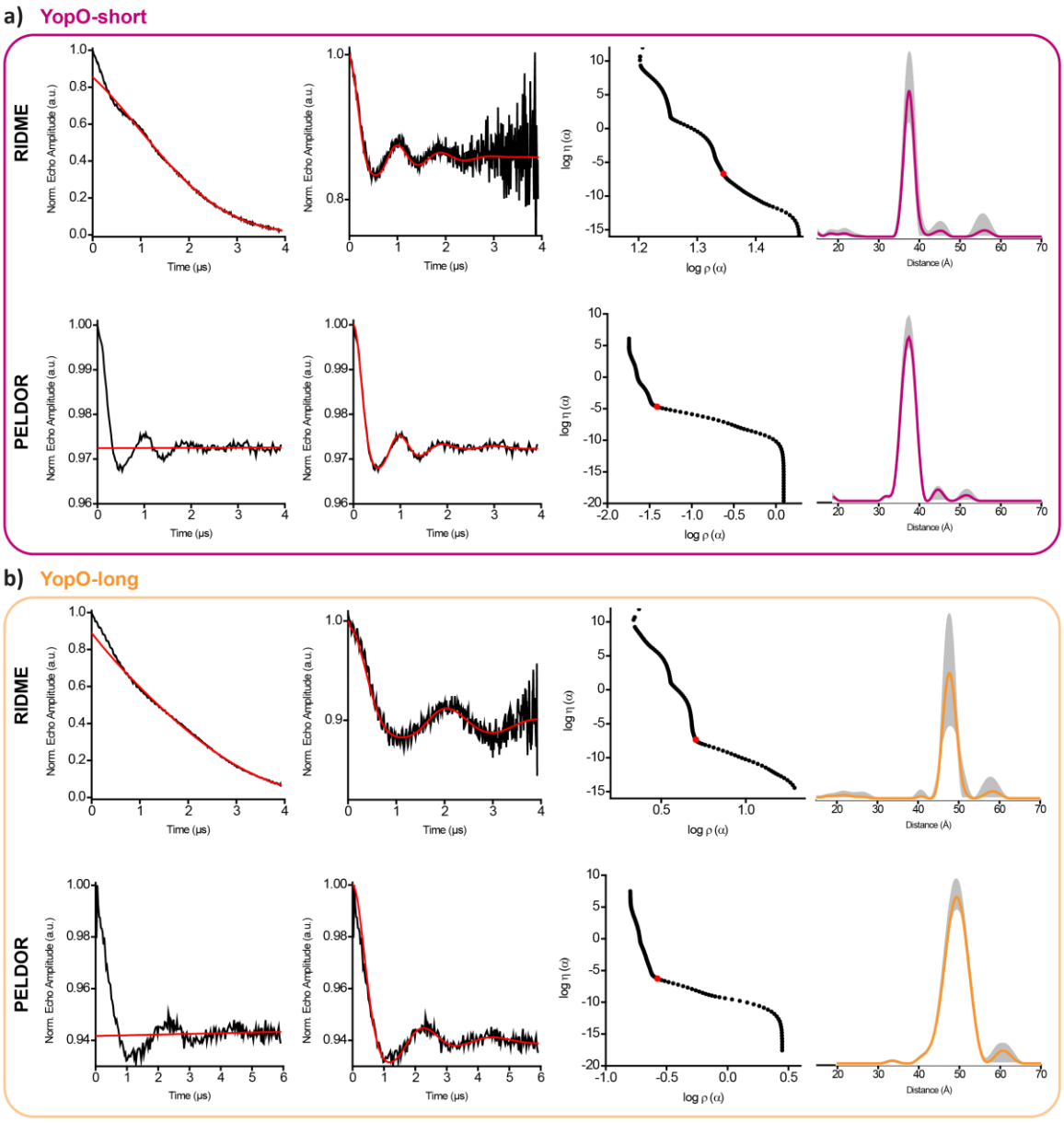

Figure A52: DeerAnalysis results for YopO-short and YopO-long. **a)** DeerAnalysis results for RIDME (top row) and PELDOR (bottom row) on YopO-short. From left to right: Normalized time trace (black) and the applied background function (red, RIDME: 3rd-order polynomial function, PELDOR: homogenous three-dimensional background); background-corrected time trace (black) with the corresponding fit (red); L-curve with the chosen regularization parameter (red); and resulting distance distribution (colored) with the validation by DeerAnalysis shown as grey-shaded areas. **b)** Same as **(a)** but for YopO-long.

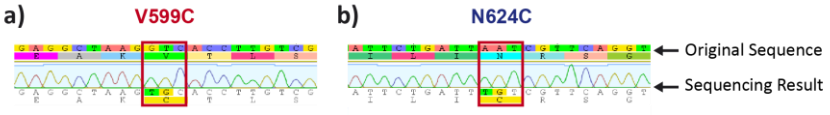

Figure A53: Sequencing results for the cysteine mutations in YopO with the exchanged amino acid shown in a red box. **a)** YopO V599C+S620H/N624H. **b)** YopO A595H/V599H+N624C. Excerpt taken from Geneious.

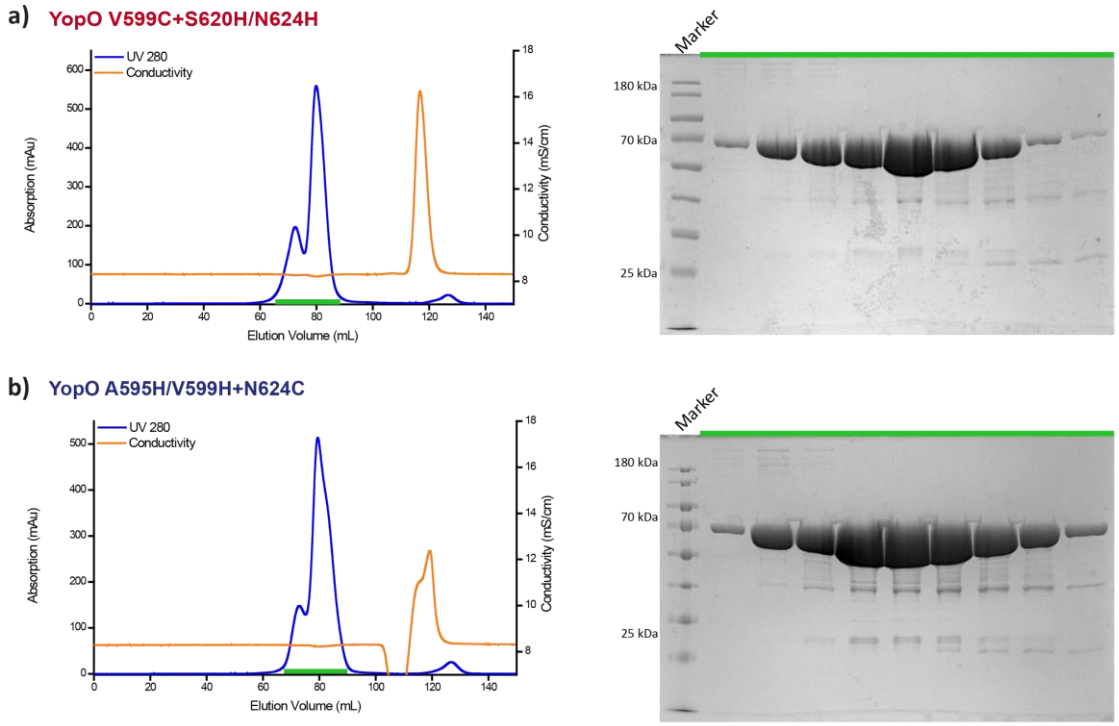

Figure A54: HiLoad® 16/600 Superdex® 200 pg gel filtration chromatogram (left) and Coomassie-stained 10% polyacrylamide gel (right) of YopO V599C+S620H/N624H **(a)** and YopO A595H/V599H+N624C **(b)**. The fractions indicated by a green bar were further pooled and purified.

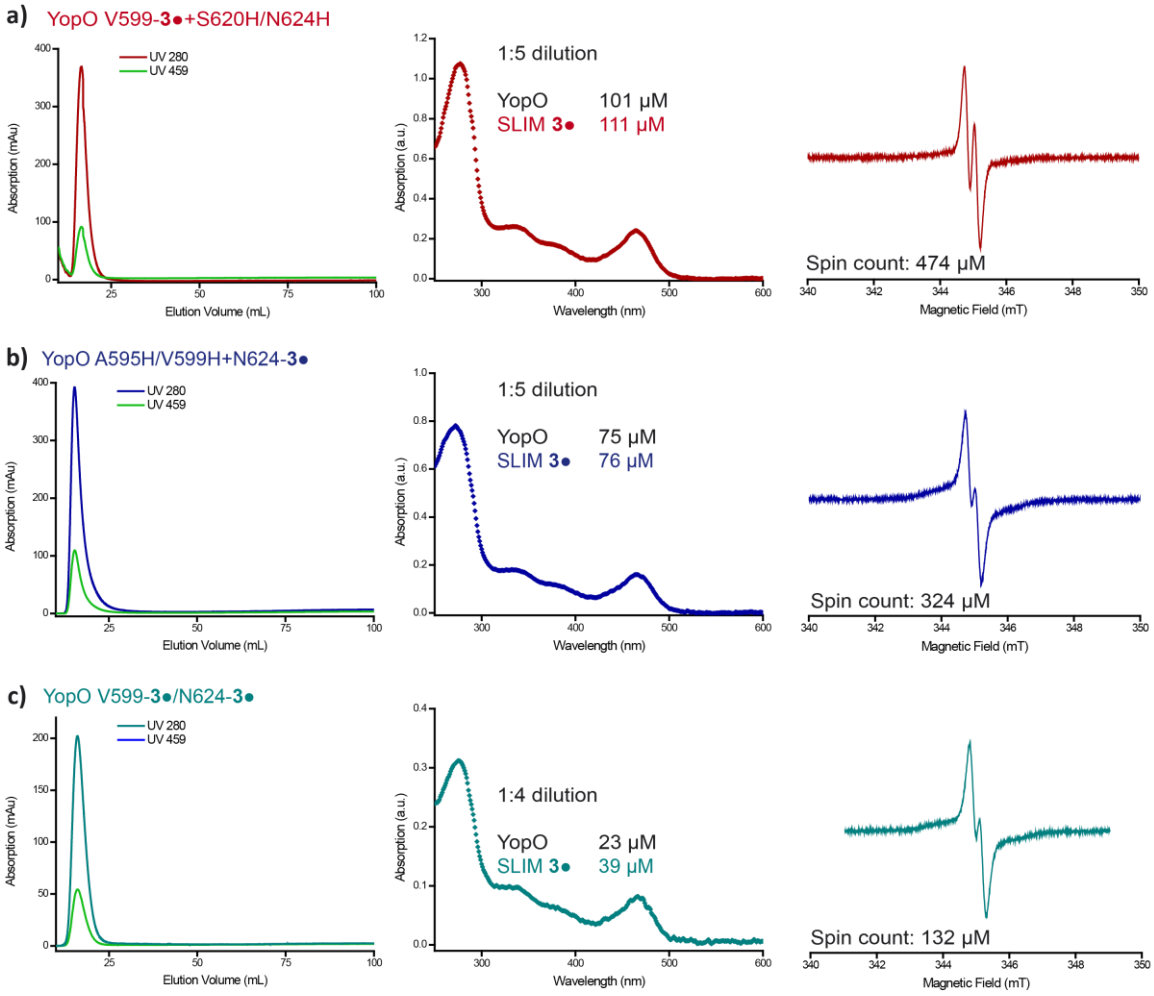

Figure A55: Spin labeling results for YopO V599-**3•**+S620H/N624H, YopO A595H/V599H+N624-**3•** and YopO V599-**3•**/N624-**3•**. **a)** Spin labeling result for YopO V599-**3•**+S620H/N624H. From left to right: Chromatogram of the HiPrep™ 26/10 runs after labeling with SLIM **3•**; UV-vis spectrum (1:5 dilution) and quantification of YopO V599-**3•**+S620H/N624H after excess label removal recorded on a NanoDrop™ 2000; room temperature X-band cw-EPR spectra of YopO V599-**3•**+S620H/N624H (505 µM) recorded on a Bruker EMXnano spectrometer. Measurement settings: 9.633 GHz microwave frequency, 1.0 mW microwave power, 100 kHz modulation frequency, 0.2 G modulation amplitude, 20.48 ms time constant, 500 pts/mT. **b+c)** Same as **(a)** but for YopO A595H/V599H+N624-**3• (b)** and YopO V599-**3•**/N624-**3• (c)**.

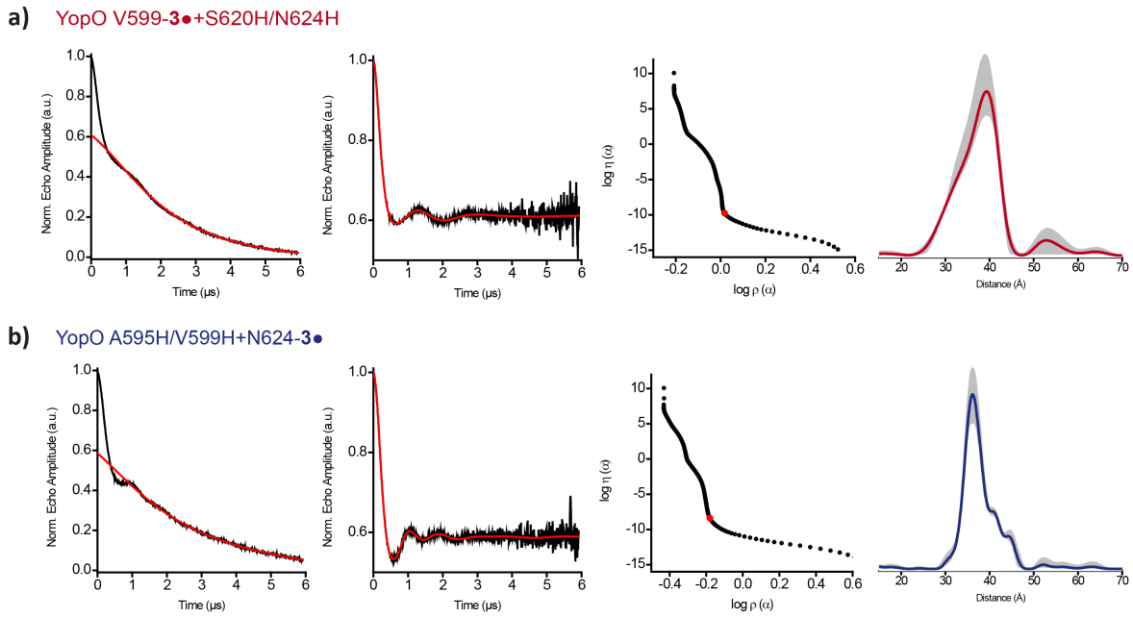

Figure A56: DeerAnalysis results for the RIDME measurements of YopO V599-**3•**+S620H/N624H **(a)** and YopO A595H/V599H+N624-**3•** **(b)**. From left to right: Normalized time trace (black) and the applied background function (red, 4th order polynomial function); background-corrected time trace (black) with the corresponding fit (red); L-curve with the chosen regularization parameter (red); and resulting distance distribution (colored) with the validation by DeerAnalysis shown as grey-shaded areas.

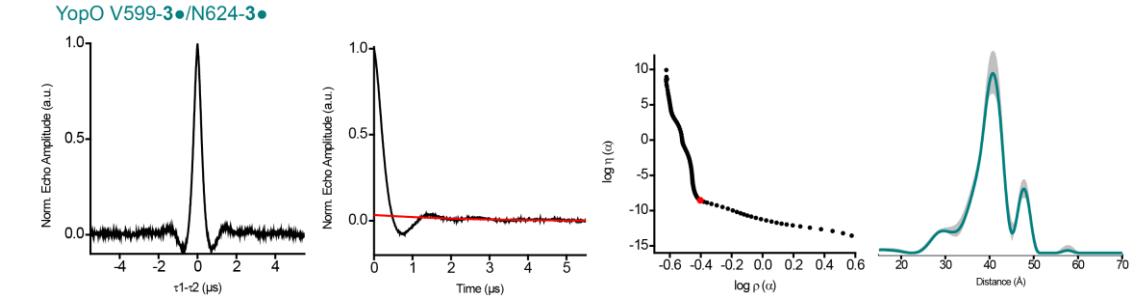

Figure A57: DeerAnalysis results for the DQC measurement at 70 K of YopO V599-**3•**/N624-**3•** (25 µM). From left to right: Unmirrored DQC time trace; mirrored time trace (black) and the applied background function (red, three-dimensional homogenous background); L-curve with the chosen regularization parameter (red); and resulting distance distribution (colored) with the validation by DeerAnalysis shown as grey-shaded area.

6.3 List of Abbreviations

2pESEEM	Two-pulse electron spin echo envelope modulation
AI	Artificial intelligence
BPTI	Bovine pancreatic trypsin inhibitor
CASP	Critical Assessment of Protein Structure Prediction
CD	Circular dichroism
CoA	Acetyl-coenzyme A
COSY	Correlation spectroscopy
Cryo-EM	Cryo-electron microscopy
ctRIDME	Constant time RIDME
CuAAC	Copper(I)-catalyzed azide-alkyne cycloaddition
cw	Continuous-wave
DAPI	4',6-diamidino-2-phenylindole
DEER	Double electron-electron resonance
DFT	Density functional theorems
DMSO	Dimethyl sulfoxide
DNA	Desoxyribonucleic acid
DOTA	Tetraxetan
DPA	Dipicolinic acid
DQC	Double quantum coherence
DTT	Dithiothreitol
EP	Electroporation
EPR	Electron paramagnetic resonance
ESEEM	Electron spin echo envelope modulation
ESI	Electronspray ionization
ESR	Electron spin resonance
FAK	Focal adhesion kinase
FAS	Fatty acid synthase
FDA	Food and Drug Administration
FFT	Fast-Fourier transformation
FID	Free induction decay
FRET	Förster resonance energy transfer
FT	Fourier transformation
fwd	forward
FWHM	Full width at half maximum
GDI	Guanidine nucleotide dissociation inhibitor
GFP	Green fluorescence protein
GSH	Glutathione
GST	Glutathione *S*-transferase
HE	Hahn echo
HIV-1	Human immunodeficiency virus type-1
hs	High-spin
HSA	Human serum albumin
IBP	Immunoglobulin-binding protein
IDA	Iminodiacetic acid
IEDDA	Inverse electron demand Dields-Alder
IgG	Immunoglobulin G
IPTG	Isopropyl β-D-1-thiogalactopyranoside
ITC	Isothermal calorimetry
ls	Low-spin
lwpp	Peak-to-peak line width
MAPK	Mitogen-activated protein kinase
MAS SSNMR	Magic-angle spinning solid-state NMR

Mb	Myoglobin
MCS	Multiple cloning site
MD	Molecular dynamics
metMb	Metmyoglobin
MHQ	Microsecond freeze-hyperquenching
MM	Molecular mechanics
MPLC	Medium-pressure liquid chromatography
MRI	Magnetic resonance imaging
MS	Mass spectrometry
MSD	Mean-square deviation
MTSL	Methanethiosulfonate spin label
MWCO	Molecular weight cut-off
NF-κB	Nuclear factor κB
NMR	Nuclear magnetic resonance
NOESY	Nuclear Overhauser enhancement spectroscopy
NPC	Nuclear pore complex
NQI	Nuclear quadrupole interaction
NQI	Nuclear quadrupole interaction
NTA	Nitrilotriacetic acid
OD_{600}	Optical density at 600 nm wavelength
p2p	Peak-to-peak
PCR	Polymerase chain reaction
PDB	Protein Data Bank
PDS-EPR	Pulsed dipolar electron paramagnetic resonance spectroscopy
PELDOR	Pulsed electron-electron double resonance
POI	Protein of interes
QM	Quantum mechanics
RE	Refocussed echo
rev	reverse
RF	Release factor
RFQ	Rapid freeze-quenching
RIDME	Relaxation induced dipolar modulation enhancement
rmsd	Root-mean-square deviation
RNA	Ribonucleic acid
RVE	Refocussed virtual echo
SAXS	Small-angle X-ray scattering
SDSL	Site-directed spin labeling
SDS-PAGE	Sodium dodecyl sulfate-polyacrylamide gel electrophoresis
SEC	Size-exclusion chromatography
SEC	Size-exclusion chromatography
SIFTER	Single frequency technique for refocusing dipolar couplings
smFRET	Single-molecule FRET
SNR	Signal-to-noise ratio
SPP	Shots per point
SRT	Shot repetition time
T3SS	Type-III secretion system
TAM	Tetrathiatriarylmethyl
tRNA	Transfer-RNA
TSL	Trityl spin label
UAA	Unnatural amino acid
vtRIDME	Variable time RIDME
XL-MS	Cross-linking mass spectrometry
YopO	*Yersinia* outer protein O
Yops	*Yersinia* outer proteins
YpkA	*Yersinia* protein kinase A
ZFS	Zero-field splitting

7. References

[1] L. H. Sullivan, *Lippincott's Magazine* **1896**, 403–409.

[2] R. D. Sleator, *Bioeng. Bugs* **2012**, *3*, 80–85.

[3] N. C. Barber, L. A. Stark, *CBE Life Sci. Educ.* **2014**, *13*, 21–24.

[4] F. U. Hartl, *Annu. Rev. Biochem.* **2017**, *86*, 21–26.

[5] O. J. Wouters, M. McKee, J. Luyten, *J. Am. Med. Assoc.* **2020**, *323*, 844–853.

[6] G. Kabue Kiriiri, P. M. Njogu, A. N. Mwangi, *Future J. Pharm. Sci.* **2020**, *6*, 27.

[7] C. Aplin, S. K. Milano, K. A. Zielinski, L. Pollack, R. A. Cerione, *J. Phys. Chem. B* **2022**, *126*, 6599–6607.

[8] B. D. Dorsey, R. B. Levin, S. L. Mcdaniel, J. P. Vacca, J. P. Guare, P. L. Darke, J. A. Zugay, E. A. Emini, W. A. Schleif, J. C. Quintero, J. H. Lin, I.-W. Chen, M. K. Holloway, P. M. D. Fitzgerald, M. G. Axel, D. Ostovic, P. S. Anderson, J. R. Huff, *J. Med. Chem.* **1994**, *37*, 3443–3451.

[9] N. A. Roberts, J. A. Martin, D. Kinchington, A. V. Broadhurst, J. C. Craig, I. B. Duncan, S. A. Galpin, B. K. Handa, J. Kay, A. Kröhn, R. W. Lambert, J. H. Merrett, J. S. Mills, K. E. B. Parkes, S. Redshaw, A. J. Ritchie, D. L. Taylor, G. J. Thomas, P. J. Machin, *Science* **1990**, *248*, 358–361.

[10] J. Erickson, D. J. Neidhart, J. VanDrie, D. J. Kempf, X. C. Wang, D. W. Norbeck, J. J. Plattner, J. W. Rittenhouse, M. Turon, N. Wideburg, W. E. Kohlbrenner, R. Simmer, R. Helfrich, D. A. Paul, M. Knigge, *Science* **1990**, *249*, 527–533.

[11] A. C. Anderson, *Chem. Biol.* **2003**, *10*, 787–797.

[12] C. L. Verlinde, W. G. Hol, *Structure* **1994**, *2*, 577–587.

[13] C. L. Ventola, *Pharm. Ther.* **2015**, *40*, 277–283.

[14] E. D. Brown, G. D. Wright, *Nature* **2016**, *529*, 336–343.

[15] "American Chemical Society International Historic Chemical Landmarks. Discovery and Development of Penicillin.," can be found under http://www.acs.org/content/acs/en/education/whatischemistry/landmarks/flemingpenicillin.html, **n.d.**

[16] A. Fleming, *Br. J. Exp. Pathol.* **1929**, *10*, 226–236.

[17] G. Nicola, R. Abagyan, *Curr. Protoc. Microbiol.* **2009**, *12*, 17.2.1-17.2.10.

[18] B. L. Staker, G. W. Buchko, P. J. Myler, *Curr. Opin. Microbiol.* **2015**, *27*, 133–138.

[19] H. M. Berman, J. Westbrook, Z. Feng, G. Gilliland, T. N. Bhat, H. Weissig, I. N. Shindyalov, P. E. Bourne, *Nucleic Acids Res.* **2000**, *28*, 235–242.

[20] S. E. Ealick, R. L. Walter, *Curr. Opin. Struct. Biol.* **1993**, *3*, 725–736.

[21] J. W. Pflugrath, *Curr. Opin. Struct. Biol.* **1992**, *2*, 811–815.

[22] J. Boyd, N. Soffe, I. Campbell, *Structure* **1994**, *2*, 253–255.

[23] R. F. Mould, *West. J. Med.* **1996**, *164*, 497–501.

[24] W. C. Röntgen, *Sitzung Physikal-Medicin Gesellschaft* **1895**, *137*, 132–141.

[25] M. Eckert, *Ann. Phys.* **2012**, *524*, A83–A85.

[26] M. von Laue, W. Friedrich, P. Knipping, *Eine Quantitative Prüfung Der Theorie Für Die Interferenz-Erscheinungen Bei Röntgenstrahlen*, Verl. D. Königl. Bayer. Akad. D. Wiss., München, **1912**.

[27] W. L. Bragg, *Proc. Cambr. Phil. Soc.* **1913**, *17*, 43–57.

[28] J. B. Sumner, *J. Biol. Chem.* **1926**, *69*, 435–441.

[29] J. C. Kendrew, G. Bodo, H. M. Dintzis, R. G. Parrish, H. Wyckoff, D. C. Phillips, *Nature* **1958**, *181*, 662–666.

[30] R. E. Franklin, R. G. Gosling, *Nature* **1953**, *171*, 740–741.

[31] J. D. Watson, F. H. C. Crick, *Nature* **1953**, *171*, 737–738.
[32] R. Wing, H. Drew, T. Takano, C. Broka, S. Tanaka, K. Itakura, R. E. Dickerson, *Nature* **1980**, *287*, 755–758.
[33] N. Jones, *Nature* **2014**, *505*, 602–603.
[34] H. Zheng, K. B. Handing, M. D. Zimmerman, I. G. Shabalin, S. C. Almo, W. Minor, *Expert Opin. Drug Discov.* **2015**, *10*, 975–989.
[35] C. S. Rapp, R. M. Pollack, *Proteins* **2005**, *60*, 103–109.
[36] E. M. Purcell, H. C. Torrey, R. V. Pound, *Phys. Rev.* **1946**, *69*, 37–38.
[37] F. Bloch, W. W. Hansen, M. Packard, *Phys. Rev.* **1946**, *69*, 127.
[38] M. Saunders, A. Wishnia, J. G. Kirkwood, *J. Am. Chem. Soc.* **1957**, *79*, 3289–3290.
[39] M. P. Williamson, T. F. Havel, K. Wüthrich, *J. Mol. Biol.* **1985**, *182*, 295–315.
[40] K. Wüthrich, *J. Biol. Chem.* **1990**, *265*, 22059–22062.
[41] D. Sakakibara, A. Sasaki, T. Ikeya, J. Hamatsu, T. Hanashima, M. Mishima, M. Yoshimasu, N. Hayashi, T. Mikawa, M. Wälchli, B. O. Smith, M. Shirakawa, P. Güntert, Y. Ito, *Nature* **2009**, *458*, 102–105.
[42] V. Tugarinov, R. Muhandiram, A. Ayed, L. E. Kay, *J. Am. Chem. Soc.* **2002**, *124*, 10025–10035.
[43] R. Puthenveetil, O. Vinogradova, *J. Biol. Chem.* **2019**, *294*, 15914–15931.
[44] P. Klukowski, R. Riek, P. Güntert, *Nat. Commun.* **2022**, *13*, 1–12.
[45] G. Comellas, C. M. Rienstra, *Annu. Rev. Biophys.* **2013**, *42*, 515–536.
[46] J. Frank, *Ultramicroscopy* **1975**, *1*, 159–162.
[47] J. Dubochet, M. Adrian, J.-J. Chang, J.-C. Homo, J. Lepault, A. W. McDowall, P. Schultz, *Q. Rev. Biophys.* **1988**, *21*, 129–228.
[48] R. Henderson, P. N. T. Unwin, *Nature* **1975**, *257*, 28–32.
[49] G. McMullan, A. R. Faruqi, R. Henderson, *Meth. Enzymol.* **2016**, *579*, 1–17.
[50] T. Nakane, A. Kotecha, A. Sente, G. McMullan, S. Masiulis, P. M. G. E. Brown, I. T. Grigoras, L. Malinauskaite, T. Malinauskas, J. Miehling, T. Uchański, L. Yu, D. Karia, E. V. Pechnikova, E. de Jong, J. Keizer, M. Bischoff, J. McCormack, P. Tiemeijer, S. W. Hardwick, D. Y. Chirgadze, G. Murshudov, A. R. Aricescu, S. H. W. Scheres, *Nature* **2020**, *587*, 152–156.
[51] B. Carragher, Y. Cheng, A. Frost, R. M. Glaeser, G. C. Lander, E. Nogales, H. W. Wang, *J. Microsc.* **2019**, *276*, 39–45.
[52] E. Nogales, S. H. W. Scheres, *Mol. Cell* **2015**, *58*, 677–689.
[53] M. Fischer, D. Rhinow, Z. Zhu, D. J. Mills, Z. K. Zhao, J. Vonck, M. Grininger, *Protein Sci.* **2015**, *24*, 987–995.
[54] Y. Cheng, *Curr. Opin. Struct. Biol.* **2018**, *52*, 58–63.
[55] D. Sirohi, Z. Chen, L. Sun, T. Klose, T. C. Pierson, M. G. Rossmann, R. J. Kuhn, *Science* **2016**, *352*, 467–470.
[56] D. Matzov, S. Aibara, A. Basu, E. Zimmerman, A. Bashan, M. N. F. Yap, A. Amunts, A. E. Yonath, *Nat. Commun.* **2017**, *8*, 1–7.
[57] K. Murata, M. Wolf, *Biochim. Biophys. Acta* **2018**, *1862*, 324–334.
[58] M. Serna, *Front. Mol. Biosci.* **2019**, *6*, 33.
[59] R. M. Glaeser, R. J. Hall, *Biophys. J.* **2011**, *100*, 2331–2337.
[60] T. Förster, *J. Biomed. Opt.* **2012**, *17*, 011002.
[61] J. Deal, D. J. Pleshinger, S. C. Johnson, S. J. Leavesley, T. C. Rich, *Cell. Signal.* **2020**, *75*, 109769.
[62] W. R. Algar, N. Hildebrandt, S. S. Vogel, I. L. Medintz, *Nat. Methods* **2019**, *16*, 815–829.
[63] B. Hochreiter, A. P. Garcia, J. A. Schmid, *Sensors* **2015**, *15*, 26281–26314.

[64] E. Lerner, T. Cordes, A. Ingargiola, Y. Alhadid, S. Y. Chung, X. Michalet, S. Weiss, *Science* **2018**, *359*, eaan1133.
[65] T. Ha, T. Enderle, D. F. Ogletree, D. S. Chemla, P. R. Selvin, S. Weiss, *Proc. Natl. Acad. Sci. U.S.A.* **1996**, *93*, 6264–6268.
[66] M. Isaksson, P. Hägglöf, P. Håkansson, T. Ny, L. B. Å. Johansson, *Phys. Chem. Chem. Phys.* **2007**, *9*, 3914–3922.
[67] J. Y. Yang, W. Y. Yang, *J. Am. Chem. Soc.* **2009**, *131*, 11644–11645.
[68] L. Ma, F. Yang, J. Zheng, *J. Mol. Struct.* **2014**, *1077*, 87.
[69] M. Beckers, F. Drechsler, T. Eilert, J. Nagy, J. Michaelis, *Faraday Discuss.* **2015**, *184*, 117–129.
[70] M. Karplus, J. A. McCammon, *Nat. Struct. Biol.* **2002**, *9*, 646–652.
[71] J. Pei, *Curr. Opin. Struct. Biol.* **2008**, *18*, 382–386.
[72] J. A. McCammon, B. R. Gelin, M. Karplus, *Nature* **1977**, *267*, 585–590.
[73] D. E. Shaw, P. Maragakis, K. Lindorff-Larsen, S. Piana, R. O. Dror, M. P. Eastwood, J. A. Bank, J. M. Jumper, J. K. Salmon, Y. Shan, W. Wriggers, *Science* **2010**, *330*, 341–346.
[74] J. R. Perilla, B. C. Goh, C. K. Cassidy, B. Liu, R. C. Bernardi, T. Rudack, H. Yu, Z. Wu, K. Schulten, *Curr. Opin. Struct. Biol.* **2015**, *31*, 64–74.
[75] A. D. Mackerell, *J. Comput. Chem.* **2004**, *25*, 1584–1604.
[76] S. A. Hollingsworth, R. O. Dror, *Neuron* **2018**, *99*, 1129–1143.
[77] P. Robustelli, S. Piana, D. E. Shaw, *Proc. Natl. Acad. Sci. U.S.A.* **2018**, *115*, E4758–E4766.
[78] V. Vennelakanti, A. Nazemi, R. Mehmood, A. H. Steeves, H. J. Kulik, *Curr. Opin. Struct. Biol.* **2022**, *72*, 9–17.
[79] T. J. Lane, D. Shukla, K. A. Beauchamp, V. S. Pande, *Curr. Opin. Struct. Biol.* **2013**, *23*, 58–65.
[80] C. B. Anfinsen, *Science* **1973**, *181*, 223–230.
[81] C. Levinthal, *J. Chim. Phys.* **1968**, *65*, 44–45.
[82] K. A. Dill, J. L. MacCallum, *Science* **2012**, *338*, 1042–1046.
[83] J. Jumper, R. Evans, A. Pritzel, T. Green, M. Figurnov, O. Ronneberger, K. Tunyasuvunakool, R. Bates, A. Žídek, A. Potapenko, A. Bridgland, C. Meyer, S. A. A. Kohl, A. J. Ballard, A. Cowie, B. Romera-Paredes, S. Nikolov, R. Jain, J. Adler, T. Back, S. Petersen, D. Reiman, E. Clancy, M. Zielinski, M. Steinegger, M. Pacholska, T. Berghammer, S. Bodenstein, D. Silver, O. Vinyals, A. W. Senior, K. Kavukcuoglu, P. Kohli, D. Hassabis, *Nature* **2021**, *596*, 583–589.
[84] M. Baek, F. DiMaio, I. Anishchenko, J. Dauparas, S. Ovchinnikov, G. R. Lee, J. Wang, Q. Cong, L. N. Kinch, R. Dustin Schaeffer, C. Millán, H. Park, C. Adams, C. R. Glassman, A. DeGiovanni, J. H. Pereira, A. V. Rodrigues, A. A. Van Dijk, A. C. Ebrecht, D. J. Opperman, T. Sagmeister, C. Buhlheller, T. Pavkov-Keller, M. K. Rathinaswamy, U. Dalwadi, C. K. Yip, J. E. Burke, K. Christopher Garcia, N. V. Grishin, P. D. Adams, R. J. Read, D. Baker, *Science* **2021**, *373*, 871–876.
[85] A. Perrakis, T. K. Sixma, *EMBO Rep.* **2021**, *22*, e54046.
[86] S. Subramaniam, G. J. Kleywegt, *Nat. Methods* **2022**, *19*, 20–23.
[87] M. Akdel, D. E. V. Pires, E. P. Pardo, J. Jänes, A. O. Zalevsky, B. Mészáros, P. Bryant, L. L. Good, R. A. Laskowski, G. Pozzati, A. Shenoy, W. Zhu, P. Kundrotas, V. R. Serra, C. H. M. Rodrigues, A. S. Dunham, D. Burke, N. Borkakoti, S. Velankar, A. Frost, J. Basquin, K. Lindorff-Larsen, A. Bateman, A. V. Kajava, A. Valencia, S. Ovchinnikov, J. Durairaj, D. B. Ascher, J. M. Thornton, N. E. Davey, A. Stein, A. Elofsson, T. I. Croll, P. Beltrao, *Nat. Struct. Mol. Biol.* **2022**, *29*, 1056–1067.
[88] A. B. Ward, A. Sali, I. A. Wilson, *Science* **2013**, *339*, 913–915.
[89] A. Sali, *J. Biol. Chem.* **2021**, *296*, 100743.

[90] M. P. Rout, A. Sali, *Cell* **2019**, *177*, 1384–1403.
[91] S. J. Kim, J. Fernandez-Martinez, I. Nudelman, Y. Shi, W. Zhang, B. Raveh, T. Herricks, B. D. Slaughter, J. A. Hogan, P. Upla, I. E. Chemmama, R. Pellarin, I. Echeverria, M. Shivaraju, A. S. Chaudhury, J. Wang, R. Williams, J. R. Unruh, C. H. Greenberg, E. Y. Jacobs, Z. Yu, M. J. De La Cruz, R. Mironska, D. L. Stokes, J. D. Aitchison, M. F. Jarrold, J. L. Gerton, S. J. Ludtke, C. W. Akey, B. T. Chait, A. Sali, M. P. Rout, *Nature* **2018**, *555*, 475–482.
[92] A. Loquet, N. G. Sgourakis, R. Gupta, K. Giller, D. Riedel, C. Goosmann, C. Griesinger, M. Kolbe, D. Baker, S. Becker, A. Lange, *Nature* **2012**, *486*, 276–279.
[93] E. K. Zavoisky, *J. Phys. USSR* **1945**, *9*, 211–216.
[94] K. Möbius, W. Lubitz, N. Cox, A. Savitsky, *Magnetochemistry* **2018**, *4*, 50.
[95] M. M. Roessler, E. Salvadori, *Chem. Soc. Rev.* **2018**, *47*, 2534–2553.
[96] O. Schiemann, G. Hagelueken, in *Bioanalytik* (Eds.: J. Kurreck, J.W. Engels, F. Lottspeich), Springer, Berlin, **2022**, pp. 527–552.
[97] A. van der Est, in *EPR Spectroscopy: Fundamentals and Methods* (Eds.: D. Goldfarb, S. Stoll), John Wiley & Sons, Chichester, **2018**, pp. 3–16.
[98] E. J. L. McInnes, D. Collison, in *EPR Spectroscopy: Fundamentals and Methods* (Eds.: D. Goldfarb, S. Stoll), John Wiley & Sons, Chichester, **2018**, pp. 63–79.
[99] G. Jeschke, "Einführung in die ESR-Spektroskopie," can be found under http://www.chemie.uni-konstanz.de/~agje, **2006**.
[100] A. Schweiger, G. Jeschke, *Principles of Pulse Electron Paramagnetic Resonance*, Oxford University Press, Oxford, **2001**.
[101] M. Brustolon, E. Giamello, *Electron Paramagnetic Resonance: A Practitioner's Toolkit*, John Wiley & Sons, Hoboken, **2008**.
[102] K. Möbius, A. Savitsky, *Appl. Magn. Reson.* **2023**, *54*, 207–287.
[103] D. Goldfarb, S. Stoll, *EPR Spectroscopy: Fundamentals and Methods*, John Wiley & Sons, Chichester, **2018**.
[104] G. Jeschke, in *EPR Spectroscopy: Fundamentals and Methods* (Eds.: D. Goldfarb, S. Stoll), John Wiley & Sons, Chichester, **2018**, pp. 401–421.
[105] S. S. Eaton, G. R. Eaton, in *EPR Spectroscopy: Fundamentals and Methods* (Eds.: D. Goldfarb, S. Stoll), John Wiley & Sons, Chichester, **2018**, pp. 175–190.
[106] J. A. Weil, J. R. Bolton, *Electron Paramagnetic Resonance*, John Wiley & Sons, Chichester, **2006**.
[107] W. Gerlach, O. Stern, *Z. Phys.* **1922**, *9*, 349–352.
[108] S. Stoll, A. Schweiger, *J. Magn. Reson.* **2006**, *178*, 42–55.
[109] E. L. Hahn, *Phys. Rev.* **1950**, *80*, 580.
[110] J. R. Biller, J. E. McPeak, S. S. Eaton, G. R. Eaton, *Appl. Magn. Reson.* **2018**, *49*, 1235–1251.
[111] M. Lindgren, G. R. Eaton, S. S. Eaton, B. H. Jonsson, P. Hammarström, M. Svensson, U. Carlsson, *J. Chem. Soc., Perkin Trans. 2* **1997**, *0*, 2549–2554.
[112] E. R. Canarie, S. M. Jahn, S. Stoll, *J. Phys. Chem. Lett.* **2020**, *11*, 3396–3400.
[113] R. Dastvan, B. E. Bode, M. P. R. Karuppiah, A. Marko, S. Lyubenova, H. Schwalbe, T. F. Prisner, *J. Phys. Chem. B* **2010**, *114*, 13507–13516.
[114] R. Ward, A. Bowman, E. Sozudogru, H. El-Mkami, T. Owen-Hughes, D. G. Norman, *J. Magn. Reson.* **2010**, *207*, 164–167.
[115] H. El Mkami, R. Ward, A. Bowman, T. Owen-Hughes, D. G. Norman, *J. Magn. Reson.* **2014**, *248*, 36–41.
[116] T. Schmidt, M. A. Wälti, J. L. Baber, E. J. Hustedt, G. M. Clore, *Angew. Chem. Int. Ed.* **2016**, *55*, 15905–15909.

[117] D. T. Edwards, T. Huber, S. Hussain, K. M. Stone, M. Kinnebrew, I. Kaminker, E. Matalon, M. S. Sherwin, D. Goldfarb, S. Han, *Structure* **2014**, *22*, 1677–1686.
[118] E. R. Georgieva, A. S. Roy, V. M. Grigoryants, P. P. Borbat, K. A. Earle, C. P. Scholes, J. H. Freed, *J. Magn. Reson.* **2012**, *216*, 69–77.
[119] O. Schiemann, T. F. Prisner, *Q. Rev. Biophys.* **2007**, *40*, 1–53.
[120] G. Jeschke, *Annu. Rev. Phys. Chem.* **2012**, *63*, 419–446.
[121] Y. W. Chiang, P. P. Borbat, J. H. Freed, *J. Magn. Reson.* **2005**, *172*, 279–295.
[122] G. Jeschke, V. Chechik, P. Ionita, A. Godt, H. Zimmermann, J. Banham, C. R. Timmel, D. Hilger, H. Jung, *Appl. Magn. Reson.* **2006**, *30*, 473–498.
[123] S. G. Worswick, J. A. Spencer, G. Jeschke, I. Kuprov, *Sci. Adv.* **2018**, *4*, eaat5218.
[124] L. F. Ibáñez, G. Jeschke, S. Stoll, *Magn. Reson.* **2020**, *1*, 209–224.
[125] D. Abdullin, G. Hagelueken, R. I. Hunter, G. M. Smith, O. Schiemann, *Mol. Phys.* **2015**, *113*, 544–560.
[126] T. H. Edwards, S. Stoll, *J. Magn. Reson.* **2016**, *270*, 87–97.
[127] E. Narr, A. Godt, G. Jeschke, *Angew. Chem. Int. Ed* **2002**, *41*, 3907–3910.
[128] M. Ji, S. Ruthstein, S. Saxena, *Acc. Chem. Res.* **2014**, *47*, 688–695.
[129] D. Abdullin, N. Florin, G. Hagelueken, O. Schiemann, D. Abdullin, N. Florin, G. Hagelueken, O. Schiemann, *Angew. Chem. Int. Ed.* **2015**, *54*, 1827–1831.
[130] A. D. Milov, A. B. Ponomarev, Y. D. Tsvetkov, *Chem. Phys. Lett.* **1984**, *110*, 67–72.
[131] A. D. Milov, K. M. Salikhov, M. D. Schirov, *Fiz. Tverd. Tela* **1981**, 975–982.
[132] M. Pannier, S. Veit, A. Godt, G. Jeschke, H. W. Spiess, *J. Magn. Reson.* **2011**, *213*, 316–325.
[133] R. E. Martin, M. Pannier, F. Diederich, V. Gramlich, M. Hubrich, H. W. Spiess, F. Diederich, Dipl.-C. R. E. Martin, H. W. Spiess, Dipl.-P. M. Pannier, M. Hubrich, *Angew. Chem. Int. Ed.* **1998**, *37*, 2833–2837.
[134] I. Ritsch, H. Hintz, G. Jeschke, A. Godt, M. Yulikov, *Phys. Chem. Chem. Phys.* **2019**, *21*, 9810–9830.
[135] L. V. Kulik, S. A. Dzuba, I. A. Grigoryev, Y. D. Tsvetkov, *Chem. Phys. Lett.* **2001**, *343*, 315–324.
[136] S. Milikisyants, F. Scarpelli, M. G. Finiguerra, M. Ubbink, M. Huber, *J. Magn. Reson.* **2009**, *201*, 48–56.
[137] D. Abdullin, M. Suchatzki, O. Schiemann, *Appl. Magn. Reson.* **2022**, *53*, 539–554.
[138] D. Abdullin, F. Duthie, A. Meyer, E. S. Müller, G. Hagelueken, O. Schiemann, *J. Phys. Chem. B* **2015**, *119*, 13539–13542.
[139] P. P. Borbat, J. H. Freed, *Chem. Phys. Lett.* **1999**, *313*, 145–154.
[140] S. Saxena, J. H. Freed, *J. Chem. Phys.* **1997**, *107*, 1317–1340.
[141] S. Saxena, J. H. Freed, *Chem. Phys. Lett.* **1996**, *251*, 102–110.
[142] P. Schöps, P. E. Spindler, A. Marko, T. F. Prisner, *J. Magn. Reson.* **2015**, *250*, 55–62.
[143] G. Jeschke, M. Pannier, A. Godt, H. W. Spiess, *Chem. Phys. Lett.* **2000**, *331*, 243–252.
[144] P. P. Borbat, J. H. Freed, in *EPR Spectroscopy: Fundamentals and Methods* (Eds.: D. Goldfarb, S. Stoll), John Wiley & Sons, Chichester, **2018**, pp. 425–459.
[145] A. Meyer, J. J. Jassoy, S. Spicher, A. Berndhäuser, O. Schiemann, *Phys. Chem. Chem. Phys.* **2018**, *20*, 13858–13869.
[146] D. Schulze-Makuch, L. N. Irwin, in *Life in the Universe. Advances in Astrobiology and Biogeophysics* (Eds.: D. Schulze-Makuch, L.N. Irwin), Springer, Berlin, Heidelberg, **2005**, pp. 77–100.
[147] P. Widder, J. Schuck, D. Summerer, M. Drescher, *Phys. Chem. Chem. Phys.* **2020**, *22*, 4875–4879.
[148] B. J. Gaffney, *Acc. Chem. Res.* **2014**, *47*, 3588–3595.

[149] D. E. Ash, R. S. Reczkowski, *J. Am. Chem. Soc.* **1992**, *114*, 10992–10994.
[150] W. R. Hagen, *J. Biol. Inorg. Chem.* **2018**, *23*, 623.
[151] M. Bennati, A. Weber, J. Antonic, D. L. Perlstein, J. Robblee, J. A. Stubbe, *J. Am. Chem. Soc.* **2003**, *125*, 14988–14989.
[152] B. A. Barry, G. T. Babcock, *Proc. Natl. Acad. Sci. U.S.A.* **1987**, *84*, 7099–7103.
[153] G. Jeschke, *Emerg. Top. Life Sci.* **2018**, *2*, 9–18.
[154] W. L. Hubbell, C. Altenbach, *Curr. Opin. Struct. Biol.* **1994**, *4*, 566–573.
[155] W. L. Hubbell, A. Gross, R. Langen, M. A. Lietzow, *Curr. Opin. Struct. Biol.* **1998**, *8*, 649–656.
[156] W. L. Hubbell, H. S. Mchaourab, C. Altenbach, M. A. Lietzow, *Structure* **1996**, *4*, 779–783.
[157] J. M. Crane, C. Mao, A. A. Lilly, V. F. Smith, Y. Suo, W. L. Hubbell, L. L. Randall, *J. Mol. Biol.* **2005**, *353*, 295–307.
[158] D. Klose, N. Voskoboynikova, I. Orban-Glass, C. Rickert, M. Engelhard, J. P. Klare, H. J. Steinhoff, *FEBS Lett.* **2014**, *588*, 3970–3976.
[159] G. E. Fanucci, D. S. Cafiso, *Curr. Opin. Struct. Biol.* **2006**, *16*, 644–653.
[160] S. A. Shelke, S. T. Sigurdsson, *Eur. J. Org. Chem.* **2012**, *2012*, 2291–2301.
[161] L. J. Brown, K. L. Sale, R. Hills, C. Rouviere, L. Song, X. Zhang, P. G. Fajer, *Proc. Natl. Acad. Sci. U.S.A.* **2002**, *99*, 12765–12770.
[162] P. P. Borbat, H. S. Mchaourab, J. H. Freed, *J. Am. Chem. Soc.* **2002**, *124*, 5304–5314.
[163] B. Joseph, A. Sikora, E. Bordignon, G. Jeschke, D. S. Cafiso, T. F. Prisner, *Angew. Chem. Int. Ed.* **2015**, *54*, 6196–6199.
[164] J. J. Jassoy, A. Berndhäuser, F. Duthie, S. P. Kühn, G. Hagelueken, O. Schiemann, *Angew. Chem. Int. Ed.* **2017**, *56*, 177–181.
[165] C. Altenbach, A. K. Kusnetzow, O. P. Ernst, K. P. Hofmann, W. L. Hubbell, J. Stein, W. L. H. Designed, *Proc. Natl. Acad. Sci. U.S.A.* **2008**, *105*, 7439–7444.
[166] T. Hett, T. Zbik, S. Mukherjee, H. Matsuoka, W. Bönigk, D. Klose, C. Rouillon, N. Brenner, S. Peuker, R. Klement, H. J. Steinhoff, H. Grubmüller, R. Seifert, O. Schiemann, U. B. Kaupp, *J. Am. Chem. Soc.* **2021**, *143*, 6981–6989.
[167] T. Schmidt, J. Jeon, W. M. Yau, C. D. Schwieters, R. Tycko, G. M. Clore, *Proc. Natl. Acad. Sci. U.S.A.* **2022**, *119*, e2122308119.
[168] S. Y. Park, P. P. Borbat, G. Gonzalez-Bonet, J. Bhatnagar, A. M. Pollard, J. H. Freed, A. M. Bilwes, B. R. Crane, *Nat. Struct. Mol. Biol.* **2006**, *13*, 400–407.
[169] L. J. Berliner, R. Jacques, *Spin Labeling: Theory and Applications*, Plenum Press, New York, **1989**.
[170] S. Ohnishi, H. M. McConnell, *J. Am. Chem. Soc.* **1965**, *87*, 2293–2293.
[171] T. J. Stone, T. Buckman, P. L. Nordio, H. M. McConnell, *Proc. Natl. Acad. Sci. U.S.A.* **1965**, *54*, 1010–1017.
[172] T. E. Wagner, C. J. Hsu, *Anal. Biochem.* **1970**, *36*, 1–5.
[173] M. D. Barratt, A. P. Davies, M. T. A. Evans, *Eur. J. Biochem.* **1971**, *24*, 280–283.
[174] M. Adackaparayil, J. H. Smith, *J. Org. Chem.* **1977**, *42*, 1655–1656.
[175] O. H. Hankovszky, K. Hideg, E. v. Goldammer, E. Matuszak, H. Kolkenbrock, H. Tschesche, H. R. Wenzel, *Biochim. Biophys. Acta* **1987**, *916*, 152–155.
[176] S. A. Shelke, S. T. Sigurdsson, in *Struct Bond* (Eds.: C.R. Timmel, J.R. Harmer), Springer, Berlin, Heidelberg, **2014**, pp. 121–162.
[177] C. Altenbach, T. Marti, H. G. Khorana, W. L. Hubbell, *Science* **1990**, *248*, 1088–1092.
[178] C. Altenbach, S. L. Flitsch, H. G. Khorana, W. L. Hubbell, *Biochemistry* **1989**, *28*, 7806–7812.
[179] J. P. Klare, H. J. Steinhoff, *Photosyn. Res.* **2009**, *102*, 377–390.
[180] J. P. Klare, *Biol. Chem.* **2013**, *394*, 1281–1300.

[181] O. Schiemann, N. Piton, J. Plackmeyer, B. E. Bode, T. F. Prisner, J. W. Engels, *Nat. Protoc.* **2007**, *2*, 904–923.
[182] M. F. Vicino, T. Hett, O. Schiemann, *Bio-protoc.* **2021**, *11*, e4004.
[183] M. Kerzhner, H. Matsuoka, C. Wuebben, M. Famulok, O. Schiemann, *Biochemistry* **2018**, *57*, 2923–2931.
[184] M. F. Peter, C. Gebhardt, R. Mächtel, G. G. M. Muñoz, J. Glaenzer, A. Narducci, G. H. Thomas, T. Cordes, G. Hagelueken, *Nat. Commun.* **2022**, *13*, 1–19.
[185] S. M. Marino, V. N. Gladyshev, *J. Biol. Chem.* **2012**, *287*, 4419–4425.
[186] R. A. Bednar, *Biochemistry* **1990**, *29*, 3684–3690.
[187] S. G. Tajc, B. S. Tolbert, R. Basavappa, B. L. Miller, *J. Am. Chem. Soc.* **2004**, *126*, 10508–10509.
[188] F. J. Chen, J. Gao, *Chem. Eur. J.* **2022**, *28*, e202201843.
[189] G. Wu, Y. Z. Fang, S. Yang, J. R. Lupton, N. D. Turner, *J. Nutr.* **2004**, *134*, 489–492.
[190] P. J. Roth, P. Theato, in *Thiol-X Chemistries in Polymer and Material Science* (Eds.: A. Lowe, C. Bowman), RSC Publishing, Cambridge, **2013**, pp. 77–90.
[191] N. S. Zefirov, N. V Zyk, E. K. Beloglazkina, A. G. Kutateladze, A. G. Kutateladze, *Sulfur Rep.* **1993**, *14*, 223–240.
[192] R. Igarashi, T. Sakai, H. Hara, T. Tenno, T. Tanaka, H. Tochio, M. Shirakawa, *J. Am. Chem. Soc.* **2010**, *132*, 8228–8229.
[193] M. Machida, M. I. Machida, Y. Kanaoka, *Chem. Pharm. Bull.* **1977**, *25*, 2739–2743.
[194] G. T. Hermanson, *Bioconjugate Techniques*, Elsevier Science, Amsterdam, **2013**.
[195] M. Davydova, G. D. Le Roi, P. Adumeau, B. M. Zeglis, *J. Vis. Ex.* **2019**, *2019*, 10.3791.
[196] J. M. J. M. Ravasco, H. Faustino, A. Trindade, P. M. P. Gois, *Chem. Eur. J.* **2019**, *25*, 43–59.
[197] E. Mileo, E. Etienne, M. Martinho, R. Lebrun, V. Roubaud, P. Tordo, B. Gontero, B. Guigliarelli, S. R. A. Marque, V. Belle, *Bioconjug. Chem.* **2013**, *24*, 1110–1117.
[198] C. Gmeiner, D. Klose, E. Mileo, V. Belle, S. R. A. Marque, G. Dorn, F. H. T. Allain, B. Guigliarelli, G. Jeschke, M. Yulikov, *J. Phys. Chem. Lett.* **2017**, *8*, 4852–4857.
[199] R. E. Bird, S. A. Lemmel, X. Yu, Q. A. Zhou, *Bioconjugate Chem.* **2021**, *32*, 2457–2479.
[200] C. J. Noren, S. J. Anthony-Cahill, M. C. Griffith, P. G. Schultz, *Science* **1989**, *244*, 182–188.
[201] K. Wals, H. Ovaa, *Front. Chem.* **2014**, *2*, 79913.
[202] T. S. Braun, P. Widder, U. Osswald, L. Groß, L. Williams, M. Schmidt, I. Helmle, D. Summerer, M. Drescher, *ChemBioChem* **2020**, *21*, 958–962.
[203] S. Kucher, S. Korneev, S. Tyagi, R. Apfelbaum, D. Grohmann, E. A. Lemke, J. P. Klare, H. J. Steinhoff, D. Klose, *J. Magn. Reson.* **2017**, *275*, 38–45.
[204] S. Kucher, S. Korneev, J. P. Klare, D. Klose, H. J. Steinhoff, *Phys. Chem. Chem. Phys.* **2020**, *22*, 13358–13362.
[205] P. Widder, F. Berner, D. Summerer, M. Drescher, *ACS Chem. Biol.* **2019**, *14*, 839–844.
[206] S. I. Presolski, V. P. Hong, M. G. Finn, *Curr. Prot. Chem. Biol.* **2011**, *3*, 153–162.
[207] M. R. Fleissner, E. M. Brustad, T. Kálai, C. Altenbach, D. Cascio, F. B. Peters, K. Hideg, P. G. Schultz, W. L. Hubbell, *Proc. Natl. Acad. Sci. U.S.A.* **2009**, *106*, 21637.
[208] A. Kugele, B. Silkenath, J. Langer, V. Wittmann, M. Drescher, *ChemBioChem* **2019**, *20*, 2479–2484.
[209] A. Rassat, P. Rey, *Bull. Soc. Chim. Fr.* **1967**, *3*, 815–818.
[210] S. R. Barbosa, E. M. Cilli, M. T. Lamy-Freund, A. M. L. Castrucci, C. R. Nakaie, *FEBS Lett* **1999**, *446*, 45–48.
[211] C. F. W. Becker, K. Lausecker, M. Balog, T. Kálai, K. Hideg, H. J. Steinhoff, M. Engelhard, *Magn. Reson. Chem.* **2005**, *43*, 34–39.
[212] S. Schreier, J. C. Bozelli, N. Marín, R. F. F. Vieira, C. R. Nakaie, *Biophys. Rev.* **2012**, *4*, 45–66.

[213] M. J. Schmidt, A. Fedoseev, D. Bücker, J. Borbas, C. Peter, M. Drescher, D. Summerer, *ACS Chem. Biol.* **2015**, *10*, 2764–2771.
[214] M. J. Schmidt, J. Borbas, M. Drescher, D. Summerer, *J. Am. Chem. Soc.* **2014**, *136*, 1238–1241.
[215] G. Bertram, S. Innes, O. Minella, J. P. Richardson, I. Stansfield, *Microbiology (N Y)* **2001**, *147*, 255–269.
[216] L. J. Berliner, H. M. McConnell, *Proc. Natl. Acad. Sci. U.S.A.* **1966**, *55*, 708–712.
[217] S. Ketter, A. Gopinath, O. Rogozhnikova, D. Trukhin, V. M. Tormyshev, E. G. Bagryanskaya, B. Joseph, *Chem. Eur. J.* **2021**, *27*, 2299–2304.
[218] L. Galazzo, G. Meier, M. Hadi Timachi, C. A. J. Hutter, M. A. Seeger, E. Bordignon, *Proc. Natl. Acad. Sci. U.S.A.* **2020**, *117*, 2441–2448.
[219] P. Roser, M. J. Schmidt, M. Drescher, D. Summerer, *Org. Biomol. Chem.* **2016**, *14*, 5468–5476.
[220] M. M. Haugland, E. A. Anderson, J. E. Lovett, *Electron Paramag. Reson.* **2017**, *25*, 1–34.
[221] A. Nilsen, R. Braslau, *J. Polym. Sci. Part A* **2006**, *44*, 697–717.
[222] M. Amar, S. Bar, M. A. Iron, H. Toledo, B. Tumanskii, L. J. W. Shimon, M. Botoshansky, N. Fridman, A. M. Szpilman, *Nat. Commun.* **2015**, *6*, 6070.
[223] L. J. Berliner, J. Grunwald, H. O. Hankovszky, K. Hideg, *Anal. Biochem.* **1982**, *119*, 450–455.
[224] C. Wuebben, S. Blume, D. Abdullin, D. Brajtenbach, F. Haege, S. Kath-Schorr, O. Schiemann, *Molecules* **2019**, *24*, 4482.
[225] T. Kálai, M. Balog, J. Jekˆ,, K. Hideg, *Synthesis (Stuttg)* **1999**, *6*, 973–980.
[226] V. Meyer, M. A. Swanson, L. J. Clouston, P. J. Boratyński, R. A. Stein, H. S. McHaourab, A. Rajca, S. S. Eaton, G. R. Eaton, *Biophys. J.* **2015**, *108*, 1213–1219.
[227] G. Karthikeyan, A. Bonucci, G. Casano, G. Gerbaud, S. Abel, V. Thomé, L. Kodjabachian, A. Magalon, B. Guigliarelli, V. Belle, O. Ouari, E. Mileo, *Angew. Chem. Int. Ed.* **2018**, *57*, 1366–1370.
[228] L. Columbus, T. Kálai, J. Jekö, K. Hideg, W. L. Hubbell, *Biochemistry* **2001**, *40*, 3828–3846.
[229] L. Galazzo, E. Bordignon, *Prog. Nucl. Magn. Reson. Spectrosc.* **2023**, *134–135*, 1–19.
[230] G. Jeschke, *Prog. Nucl. Magn. Reson. Spectrosc.* **2013**, *72*, 42–60.
[231] D. Abdullin, G. Hagelueken, O. Schiemann, *Phys. Chem. Chem. Phys.* **2016**, *18*, 10428–10437.
[232] M. R. Fleissner, M. D. Bridges, E. K. Brooks, D. Cascio, T. Kálai, K. Hideg, W. L. Hubbell, *Proc. Natl. Acad. Sci. U.S.A.* **2011**, *108*, 16241–16246.
[233] A. Bonucci, O. Ouari, B. Guigliarelli, V. Belle, E. Mileo, *ChemBioChem* **2020**, *21*, 451–460.
[234] M. J. Schmidt, A. Fedoseev, D. Bücker, J. Borbas, C. Peter, M. Drescher, D. Summerer, *ACS Chem. Biol.* **2015**, *10*, 2764–2771.
[235] J. T. Paletta, M. Pink, B. Foley, S. Rajca, A. Rajca, *Org. Lett.* **2012**, *14*, 5322–5325.
[236] I. A. Kirilyuk, Y. F. Polienko, O. A. Krumkacheva, R. K. Strizhakov, Y. V. Gatilov, I. A. Grigor'ev, E. G. Bagryanskaya, *J. Org. Chem.* **2012**, *77*, 8016–8027.
[237] M. M. Haugland, J. E. Lovett, E. A. Anderson, *Chem. Soc. Rev* **2018**, *47*, 668–680.
[238] R. Igarashi, T. Sakai, H. Hara, T. Tenno, T. Tanaka, H. Tochio, M. Shirakawa, *J. Am. Chem. Soc.* **2010**, *132*, 8228–8229.
[239] K. Singewald, M. J. Lawless, S. Saxena, *J. Magn. Reson.* **2019**, *299*, 21–27.
[240] M. J. Lawless, A. Shimshi, T. F. Cunningham, M. N. Kinde, P. Tang, S. Saxena, *ChemPhysChem* **2017**, *18*, 1653–1660.
[241] M. Drescher, *Top. Curr. Chem.* **2012**, *321*, 91–120.
[242] G. Jeschke, Y. Polyhach, *Phys. Chem. Chem. Phys.* **2007**, *9*, 1895–1910.

[243] G. Jeschke, A. Bender, H. Paulsen, H. Zimmermann, A. Godt, *J. Magn. Reson.* **2004**, *169*, 1–12.
[244] M. Gomberg, *J. Am. Chem. Soc.* **1900**, *22*, 757–771.
[245] J. Veciana, J. Carilla, C. Miravitlles, E. Molinsb, *J. Chem. Soc. Chem. Commun.* **1987**, 812–814.
[246] J. Guasch, X. Fontrodona, I. Ratera, C. Rovira, J. Veciana, *Acta Cryst. C* **2013**, *69*, 255–257.
[247] B. Kahr, J. E. Jackson, D. L. Ward, S.-H. Jang, J. F. Blount, *Acta Cryst. B* **1992**, *48*, 324–329.
[248] M. Elewa, N. Maltar-Strmečki, M. M. Said, H. A. El Shihawy, M. El-Sadek, J. Frank, S. Drescher, M. Drescher, K. Mäder, D. Hinderberger, P. Imming, *Phys. Chem. Chem. Phys.* **2017**, *19*, 6688–6697.
[249] T. J. Reddy, T. Iwama, H. J. Halpern, V. H. Rawal, *J. Org. Chem.* **2002**, *67*, 4635–4639.
[250] S. Andersson, F. Radner, A. Rydbeek, R. Servin, L. G. Wistrand, *Patent US-5530140-A*, **1994**.
[251] S. Andersson, F. Radner, A. Rydbeck, R. Servin, L. G. Wistrand, *Patent US-5728370-A*, **1998**.
[252] M. Jorgensen, F. Rise, S. Andersson, T. Almén, A. Aabye, L.-G. Wistrand, H. Wikström, K. Golman, R. Servin, P. Michelsen, *Patent PCT WO91/12024*, **1991**.
[253] N. C. Kunjir, G. W. Reginsson, O. Schiemann, S. T. Sigurdsson, *Phys. Chem. Chem. Phys.* **2013**, *15*, 19673–19685.
[254] M. K. Bowman, C. Mailer, H. J. Halpern, *J. Magn. Reson.* **2005**, *172*, 254–267.
[255] C. Decroos, Y. Li, G. Bertho, Y. Frapart, D. Mansuy, J. L. Boucher, *Chem. Res. Toxicol.* **2009**, *22*, 1342–1350.
[256] C. Decroos, Y. Li, A. Soltani, Y. Frapart, D. Mansuy, J. L. Boucher, *Arch. Biochem. Biophys.* **2010**, *502*, 74–80.
[257] G. W. Reginsson, N. C. Kunjir, S. T. Sigurdsson, O. Schiemann, *Chem. Eur. J.* **2012**, *18*, 13580–13584.
[258] I. Dhimitruka, M. Velayutham, A. A. Bobko, V. V. Khramtsov, F. A. Villamena, C. M. Hadad, J. L. Zweier, *Bioorg. Med. Chem. Lett.* **2007**, *17*, 6801–6805.
[259] W. Liu, J. Nie, X. Tan, H. Liu, N. Yu, G. Han, Y. Zhu, F. A. Villamena, Y. Song, J. L. Zweier, Y. Liu, *J. Org. Chem.* **2017**, *82*, 588–596.
[260] Y. Song, Y. Liu, C. Hemann, F. A. Villamena, J. L. Zweier, *J. Org. Chem.* **2013**, *78*, 1371–1376.
[261] B. Driesschaert, P. Levêque, B. Gallez, J. Marchand-Brynaert, *Tetrahedron Lett.* **2013**, *54*, 5924–5926.
[262] M. Poncelet, B. Driesschaert, O. Tseytlin, M. Tseytlin, T. D. Eubank, V. V. Khramtsov, *Bioorg. Med. Chem. Lett.* **2019**, *29*, 1756.
[263] Y. Song, Y. Liu, W. Liu, F. A. Villamena, J. L. Zweier, *RSC Adv* **2014**, *4*, 47649.
[264] N. Fleck, T. Hett, J. Brode, A. Meyer, S. Richert, O. Schiemann, *J. Org. Chem.* **2019**, *84*, 3293–3303.
[265] M. Poncelet, J. L. Huffman, V. V. Khramtsov, I. Dhimitruka, B. Driesschaert, *RSC Adv.* **2019**, *9*, 35073–35076.
[266] M. Thaning, *Patent PCT WO98/39277*, **1998**.
[267] D. Akhmetzyanov, P. Schöps, A. Marko, N. C. Kunjir, S. T. Sigurdsson, T. F. Prisner, *Phys. Chem. Chem. Phys.* **2015**, *17*, 24446–24451.
[268] J. H. Ardenkjær-Larsen, I. Laursen, I. Leunbach, G. Ehnholm, L. G. Wistrand, J. S. Petersson, K. Golman, *J. Magn. Reson.* **1998**, *133*, 1–12.
[269] A. J. Fielding, P. J. Carl, G. R. Eaton, S. S. Eaton, *Appl. Magn. Reson.* **2005**, *28*, 231–238.
[270] I. Dhimitruka, O. Grigorieva, J. L. Zweier, V. V. Khramtsov, *Bioorg. Med. Chem. Lett.* **2010**, *20*, 3946–3949.
[271] L. Yong, J. Harbridge, R. W. Quine, G. A. Rinard, S. S. Eaton, G. R. Eaton, C. Mailer, E. Barth, H. J. Halpern, *J. Magn. Reson.* **2001**, *152*, 156–161.

[272] A. J. Fielding, P. J. Carl, G. R. Eaton, S. S. Eaton, *Appl. Magn. Reson.* **2005**, *28*, 231–238.
[273] Z. Yang, Y. Liu, P. Borbat, J. L. Zweier, J. H. Freed, W. L. Hubbell, *J. Am. Chem. Soc.* **2012**, *134*, 9950–9952.
[274] Z. Yang, M. D. Bridges, C. J. López, O. Y. Rogozhnikova, D. V. Trukhin, E. K. Brooks, V. Tormyshev, H. J. Halpern, W. L. Hubbell, *J. Magn. Reson.* **2016**, *269*, 50–54.
[275] G. Y. Shevelev, O. A. Krumkacheva, A. A. Lomzov, A. A. Kuzhelev, O. Y. Rogozhnikova, D. V. Trukhin, T. I. Troitskaya, V. M. Tormyshev, M. V. Fedin, D. V. Pyshnyi, E. G. Bagryanskaya, *J. Am. Chem. Soc.* **2014**, *136*, 9874–9877.
[276] I. Marin-Montesinos, J. C. Paniagua, A. Peman, M. Vilaseca, F. Luis, S. Van Doorslaer, M. Pons, *Phys. Chem. Chem. Phys.* **2016**, *18*, 3151–3158.
[277] B. Joseph, V. M. Tormyshev, O. Yu. Rogozhnikova, D. Akhmetzyanov, E. G. Bagryanskaya, T. F. Prisner, *Angew. Chem. Int. Ed.* **2016**, *128*, 11538–11542.
[278] Y. Qu, Y. Li, X. Tan, W. Zhai, G. Han, J. Hou, G. Liu, Y. Song, Y. Liu, *Chem. Eur. J.* **2019**, *25*, 7888–7895.
[279] M. Poncelet, J. L. Huffman, V. V. Khramtsov, I. Dhimitruka, B. Driesschaert, *RSC Adv.* **2019**, *9*, 35073–35076.
[280] D. Abdullin, O. Schiemann, *Chempluschem* **2020**, *85*, 353–372.
[281] D. Goldfarb, *Phys. Chem. Chem. Phys.* **2014**, *16*, 9685–9699.
[282] A. M. Raitsimring, C. Gunanathan, A. Potapov, I. Efremenko, J. M. L. Martin, D. Milstein, D. Goldfarb, *J. Am. Chem. Soc.* **2007**, *129*, 14138–14139.
[283] A. Giannoulis, Y. Ben-Ishay, D. Goldfarb, *Meth. Enzymol.* **2021**, *651*, 235–290.
[284] A. Potapov, H. Yagi, T. Huber, S. Jergic, N. E. Dixon, G. Otting, D. Goldfarb, *J. Am. Chem. Soc.* **2010**, *132*, 9040–9048.
[285] M. Qi, A. Groß, G. Jeschke, A. Godt, M. Drescher, *J. Am. Chem. Soc.* **2014**, *136*, 15366–15378.
[286] Y. Yang, F. Yang, Y. J. Gong, J. L. Chen, D. Goldfarb, X. C. Su, *Angew. Chem. Int. Ed.* **2017**, *56*, 2914–2918.
[287] E. Matalon, T. Huber, G. Hagelueken, B. Graham, V. Frydman, A. Feintuch, G. Otting, D. Goldfarb, E. Matalon, A. Feintuch, D. Goldfarb, V. Frydman, T. Huber, G. Otting, B. Graham, G. Hagelueken, *Angew. Chem. Int. Ed.* **2013**, *52*, 11831–11834.
[288] A. Shah, A. Roux, M. Starck, J. A. Mosely, M. Stevens, D. G. Norman, R. I. Hunter, H. El Mkami, G. M. Smith, D. Parker, J. E. Lovett, *Inorg. Chem.* **2019**, *58*, 3015–3025.
[289] A. Martorana, G. Bellapadrona, A. Feintuch, E. Di Gregorio, S. Aime, D. Goldfarb, *J. Am. Chem. Soc.* **2014**, *136*, 13458–13465.
[290] E. H. Abdelkader, M. D. Lee, A. Feintuch, M. R. Cohen, J. D. Swarbrick, G. Otting, B. Graham, D. Goldfarb, *J. Phys. Chem. Lett.* **2015**, *6*, 5016–5021.
[291] E. Narr, A. Godt, G. Jeschke, *Angew. Chem. Int. Ed* **2002**, *41*, 3907–3910.
[292] B. E. Bode, J. Plackmeyer, T. F. Prisner, O. Schiemann, *J. Phys. Chem. A* **2008**, *112*, 5064–5073.
[293] Z. Yang, M. R. Kurpiewski, M. Ji, J. E. Townsend, P. Mehta, L. Jen-Jacobson, S. Saxena, *Proc. Natl. Acad. Sci. U.S.A.* **2012**, *109*, E993–E1000.
[294] A. M. Bowen, M. W. Jones, J. E. Lovett, T. G. Gaule, M. J. McPherson, J. R. Dilworth, C. R. Timmel, J. R. Harmer, *Phys. Chem. Chem. Phys.* **2016**, *18*, 5981–5994.
[295] Z. Yang, D. Kise, S. Saxena, *J. Phys. Chem. B* **2010**, *114*, 6165–6174.
[296] M. J. Lawless, S. Ghosh, T. F. Cunningham, A. Shimshi, S. Saxena, *Phys. Chem. Chem. Phys.* **2017**, *19*, 20959–20967.

[297] T. F. Cunningham, M. R. Putterman, A. Desai, W. Seth Horne, S. Saxena, T. F. Cunningham, M. R. Putterman, A. Desai, W. S. Horne, S. Saxena, *Angew. Chem. Int. Ed.* **2015**, *54*, 6330–6334.
[298] S. Ghosh, M. J. Lawless, G. S. Rule, S. Saxena, *J. Magn. Reson.* **2018**, *286*, 163–171.
[299] F. H. Arnold, B. L. Haymore, *Science* **1991**, *252*, 1796–1797.
[300] M. J. Lawless, J. R. Pettersson, G. S. Rule, F. Lanni, S. Saxena, *Biophys. J.* **2018**, *114*, 592.
[301] H. Sameach, S. Ghosh, L. Gevorkyan-Airapetov, S. Saxena, S. Ruthstein, *Angew. Chem. Int. Ed.* **2019**, *58*, 3053–3056.
[302] A. Gamble Jarvi, T. F. Cunningham, S. Saxena, *Phys. Chem. Chem. Phys.* **2019**, *21*, 10238–10243.
[303] J. L. Wort, K. Ackermann, A. Giannoulis, A. J. Stewart, D. G. Norman, B. E. Bode, *Angew. Chem. Int. Ed.* **2019**, *58*, 11681–11685.
[304] K. Singewald, J. A. Wilkinson, A. S. Saxena, *Bio Protoc.* **2021**, *11*, e4258.
[305] A. Gamble Jarvi, J. Casto, S. Saxena, *J. Magn. Reson.* **2020**, *320*, 106848.
[306] J. L. Wort, S. Arya, K. Ackermann, A. J. Stewart, B. E. Bode, *J. Phys. Chem. Lett.* **2021**, *12*, 2815–2819.
[307] X. Bogetti, Z. Hasanbasri, H. R. Hunter, S. Saxena, *Phys. Chem. Chem. Phys.* **2022**, *24*, 14727–14739.
[308] K. Singewald, X. Bogetti, K. Sinha, G. S. Rule, S. Saxena, *Angew. Chem. Int. Ed.* **2020**, *59*, 23040–23044.
[309] B. W. Wren, *Nat. Rev. Microbiol.* **2003**, *1*, 55–64.
[310] G. R. Cornelis, H. Wolf-Watz, *Mol. Microbiol.* **1997**, *23*, 861–867.
[311] G. V. Plano, K. Schesser, *Immunol. Res.* **2013**, *57*, 237–245.
[312] R. S. Dewoody, P. M. Merritt, M. M. Marketon, *Front. Cell. Infect. Microbiol.* **2013**, *3*, DOI: 10.3389/fcimb.2013.00004.
[313] S. C. Straley, G. V. Plano, E. Skrzypek, P. L. Haddix, K. A. Fields, *Mol. Microbiol.* **1993**, *8*, 1005–1010.
[314] K. Orth, *Curr. Opin. Microbiol.* **2002**, *5*, 38–43.
[315] G. I. Viboud, J. B. Bliska, *Annu. Rev. Microbiol.* **2005**, *59*, 69–89.
[316] K. Orth, Z. Xu, M. B. Mudgett, Z. Q. Bao, L. E. Palmer, J. B. Bliska, W. F. Mangel, B. Staskawicz, J. E. Dixon, *Science* **2000**, *290*, 1594–1597.
[317] S. Mukherjee, G. Keitany, Y. Li, Y. Wang, H. L. Ball, E. J. Goldsmith, K. Orth, *Science* **2006**, *312*, 1211–1214.
[318] C. N. Larock, B. T. Cookson, *Cell Host Microbe* **2012**, *12*, 799–805.
[319] C. Wei, Y. Wang, Z. Du, K. Guan, Y. Cao, H. Yang, P. Zhou, F. Wu, J. Chen, P. Wang, Z. Zheng, P. Zhang, Y. Zhang, S. Ma, R. Yang, H. Zhong, X. He, *Cell Death Dis.* **2016**, *7*, e2519–e2519.
[320] N. Hamid, A. Gustavsson, K. Andersson, K. McGee, C. Persson, C. E. Rudd, M. Fällman, *Microb. Pathog.* **1999**, *27*, 231–242.
[321] U. Von Pawel-Rammingen, M. V. Telepnev, G. Schmidt, K. Aktories, H. Wolf-Watz, R. Rosqvist, *Mol. Microbiol.* **2000**, *36*, 737–748.
[322] F. Shao, P. M. Merritt, Z. Bao, R. W. Innes, J. E. Dixon, *Cell* **2002**, *109*, 575–588.
[323] S. Håkansson, E. E. Galyov, R. Rosqvist, H. Wolf-Watz, *Mol. Microbiol.* **1996**, *20*, 593–603.
[324] E. E. Galyov, S. Håkansson, Å. Forsberg, H. Wolf-Watz, *Nature* **1993**, *361*, 730–732.
[325] S. J. Juris, A. E. Rudolph, D. Huddler, K. Orth, J. E. Dixon, *Proc. Natl. Acad. Sci. U.S.A.* **2000**, *97*, 9431–9436.
[326] G. Prehna, M. I. Ivanov, J. B. Bliska, C. E. Stebbins, *Cell* **2006**, *126*, 869–880.
[327] E. E. Galyov, S. Hakansson, H. Wolf-Watz, [E E Galyov, S. Hakansson, A. Forsberg, H. Wolf-Watz, *J. Bacteriol.* **1994**, *176*, 4543–4548.

[328] W. L. Lee, J. M. Grimes, R. C. Robinson, *Nat. Struct. Mol. Biol.* **2015**, *22*, 248–255.
[329] M. Aepfelbacher, *Rev. Physiol. Biochem. Pharmacol.* **2004**, *152*, 65–77.
[330] C. Trasak, G. Zenner, A. Vogel, G. Yüksekdag, R. Rost, I. Haase, M. Fischer, L. Israel, A. Imhof, S. Linder, M. Schleicher, M. Aepfelbacher, *J. Biol. Chem.* **2007**, *282*, 2268–2277.
[331] W. L. Lee, P. Singaravelu, S. Wee, B. Xue, K. C. Ang, J. Gunaratne, J. M. Grimes, K. Swaminathan, R. C. Robinson, *Sci. Rep.* **2017**, *7*, 1–12.
[332] M. F. Peter, A. T. Tuukkanen, C. A. Heubach, A. Selsam, F. G. Duthie, D. I. Svergun, O. Schiemann, G. Hagelueken, *Structure* **2019**, *27*, 1416-1426.e3.
[333] M. H. Ahmed, M. S. Ghatge, M. K. Safo, *Subcell Biochem.* **2020**, *94*, 345–382.
[334] G. B. Postnikova, E. A. Shekhovtsova, *Biochem. (Mosc.)* **2018**, *83*, 168–183.
[335] J. Koch, J. Lüdemann, R. Spies, M. Last, C. T. Amemiya, T. Burmester, *Mol. Biol. Evol.* **2016**, *33*, 3033–3041.
[336] H. Wajcman, L. Kiger, M. C. Marden, *C. R. Biol.* **2009**, *332*, 273–282.
[337] G. A. Ordway, D. J. Garry, *J. Exp. Biol.* **2004**, *207*, 3441–3446.
[338] M. Inai, Y. Miura, S. Honda, A. Masuda, T. Masuda, *J. Agric. Food Chem.* **2014**, *62*, 893–901.
[339] R. Maurus, C. M. Overall, R. Bogumil, Y. Luo, A. G. Mauk, M. Smith, G. D. Brayer, *Biochim. Biophys. Acta* **1997**, *1341*, 1–13.
[340] R. Maurus, R. Bogumil, N. T. Nguyen, A. G. Mauk, G. Brayer, *Biochem. J.* **1998**, *332*, 67–74.
[341] E. G. Panarelli, H. Van Der Meer, P. Gast, E. J. J. Groenen, *PLoS One* **2020**, *15*, e0232555.
[342] D. Abdullin, H. Matsuoka, M. Yulikov, N. Fleck, C. Klein, S. Spicher, G. Hagelueken, S. Grimme, A. Lützen, O. Schiemann, *Chem. Eur. J.* **2019**, *25*, 8820–8828.
[343] E. V. Sidorin, T. F. Solov'Eva, *Biochem. (Mosc.)* **2011**, *76*, 295–308.
[344] L. Björck, W. Kastern, G. Lindahl, K. Widebäck, *Mol. Immunol.* **1987**, *24*, 1113–1122.
[345] W. Choe, T. A. Durgannavar, S. J. Chung, *Materials* **2016**, *9*, DOI 10.3390/MA9120994.
[346] D. P. Nitsche-Schmitz, H. M. Johansson, I. Sastalla, S. Reissmann, I. M. Frick, G. S. Chhatwal, *J. Biol. Chem.* **2007**, *282*, 17530–17536.
[347] M. A. Vijayalakshmi, *Appl. Biochem. Biotechnol.* **1998**, *75*, 93–102.
[348] L. Chang, A. Perez, *J. Am. Chem. Soc.* **2022**, *144*, 14668–14677.
[349] T. Ikeya, T. Hanashima, S. Hosoya, M. Shimazaki, S. Ikeda, M. Mishima, P. Güntert, Y. Ito, *Sci. Rep.* **2016**, *6*, 1–11.
[350] J. R. Huth, C. A. Bewley, B. M. Jackson, A. G. Hinnebusch, G. M. Clore, A. M. Gronenborn, *Protein Sci.* **1997**, *6*, 2359–2364.
[351] J. Kuszewski, A. M. Gronenborn, G. M. Clore, *J. Am. Chem. Soc.* **1999**, *121*, 2337–2338.
[352] Y. Yang, F. Yang, Y. J. Gong, T. Bahrenberg, A. Feintuch, X. C. Su, D. Goldfarb, *J. Phys. Chem. Lett.* **2018**, *9*, 6119–6123.
[353] H. M. Berman, P. D. Adams, A. A. Bonvin, S. K. Burley, B. Carragher, W. Chiu, F. DiMaio, T. E. Ferrin, M. J. Gabanyi, T. D. Goddard, P. R. Griffin, J. Haas, C. A. Hanke, J. C. Hoch, G. Hummer, G. Kurisu, C. L. Lawson, A. Leitner, J. L. Markley, J. Meiler, G. T. Montelione, G. N. Phillips, T. Prisner, J. Rappsilber, D. C. Schriemer, T. Schwede, C. A. M. Seidel, T. S. Strutzenberg, D. I. Svergun, E. Tajkhorshid, J. Trewhella, B. Vallat, S. Velankar, G. W. Vuister, B. Webb, J. D. Westbrook, K. L. White, A. Sali, *Structure* **2019**, *27*, 1745–1759.
[354] O. Schiemann, C. A. Heubach, D. Abdullin, K. Ackermann, M. Azarkh, E. G. Bagryanskaya, M. Drescher, B. Endeward, J. H. Freed, L. Galazzo, D. Goldfarb, T. Hett, L. Esteban Hofer, L. Fábregas Ibáñez, E. J. Hustedt, S. Kucher, I. Kuprov, J. E. Lovett, A. Meyer, S. Ruthstein, S. Saxena, S. Stoll, C. R. Timmel, M. Di Valentin, H. S. McHaourab, T. F. Prisner, B. E. Bode, E. Bordignon, M. Bennati, G. Jeschke, *J. Am. Chem. Soc.* **2021**, *143*, 17875–17890.
[355] G. Hagelueken, D. Abdullin, O. Schiemann, *Meth. Enzymol.* **2015**, *563*, 595–622.

[356] L. Beerwerth, Analyse Der Dimerisierung Des Typ-III-Effektor Proteins YopO Aus Yersinia Mittels PELDOR Spektroskopie, Bachelor thesis, University of Bonn, **2018**.
[357] C. A. Heubach, Experiments on the Activation and the Trityl-Based Spin Labeling of the Yersinia T3SS Effector-Protein YopO/YpkA, **2018**.
[358] M. Sjodt, R. T. Clubb, *Bio Protoc.* **2017**, *7*, e2207.
[359] V. Venditti, N. L. Fawzi, *Methods Mol Biol.* **2018**, *1688*, 255.
[360] Y. Polyhach, E. Bordignon, R. Tschaggelar, S. Gandra, A. Godt, G. Jeschke, *Phys. Chem. Chem. Phys.* **2012**, *14*, 10762–10773.
[361] O. Schiemann, N. Piton, Y. Mu, G. Stock, J. W. Engels, T. F. Prisner, *J. Am. Chem. Soc.* **2004**, *126*, 5722–5729.
[362] G. Jeschke, *ChemPhysChem* **2002**, *3*, 927–932.
[363] J. Keeley, T. Choudhury, L. Galazzo, E. Bordignon, A. Feintuch, D. Goldfarb, H. Russell, M. J. Taylor, J. E. Lovett, A. Eggeling, L. Fábregas Ibáñez, K. Keller, M. Yulikov, G. Jeschke, I. Kuprov, *J. Magn. Reson.* **2022**, *338*, 107186.
[364] R. A. Stein, A. H. Beth, E. J. Hustedt, *Meth. Enzymol.* **2015**, *563*, 531–567.
[365] A. N. L. Batista, J. M. Batista, V. S. Bolzani, M. Furlan, E. W. Blanch, *Phys. Chem. Chem. Phys.* **2013**, *15*, 20147–20152.
[366] T. Arakawa, Y. Kita, S. N. Timasheff, *Biophys. Chem.* **2007**, *131*, 62–70.
[367] S. Bleicken, G. Jeschke, C. Stegmueller, R. Salvador-Gallego, A. J. García-Sáez, E. Bordignon, *Mol. Cell* **2014**, *56*, 496.
[368] G. Jeschke, *Prot. Sci.* **2021**, *30*, 125–135.
[369] S. Spicher, D. Abdullin, S. Grimme, O. Schiemann, *Phys. Chem. Chem. Phys.* **2020**, *22*, 24282–24290.
[370] J. Jacques Jassoy, C. A. Heubach, T. Hett, F. Bernhard, F. R. Haege, G. Hagelueken, O. Schiemann, *Molecules* **2019**, *24*, 2735.
[371] N. Fleck, C. A. Heubach, T. Hett, F. R. Haege, P. P. Bawol, H. Baltruschat, O. Schiemann, *Angew. Chem. Int. Ed.* **2020**, *59*, 9767–9772.
[372] N. Fleck, C. Heubach, T. Hett, S. Spicher, S. Grimme, O. Schiemann, *Chem. Eur. J.* **2021**, *27*, 5292–5297.
[373] K. Ackermann, C. A. Heubach, O. Schiemann, B. E. Bode, *J. Phys. Chem. Lett.* **2024**, *15*, 1455–1461.
[374] A. Giannoulis, Y. Yang, Y. J. Gong, X. Tan, A. Feintuch, R. Carmieli, T. Bahrenberg, Y. Liu, X. C. Su, D. Goldfarb, *Phys. Chem. Chem. Phys.* **2019**, *21*, 10217–10227.
[375] F. R. Haege, A Stability Study of Trityl and Nitroxide Spin Labels for In-Cell EPR Spectroscopy, **2019**.
[376] X. Tan, L. Chen, Y. Song, A. Rockenbauer, F. A. Villamena, J. L. Zweier, Y. Liu, *Chem. Res. Toxicol.* **2017**, *30*, 1664–1672.
[377] A. D. Milov, A. G. Maryasov, Y. D. Tsvetkov, *Appl. Magn. Reson.* **1998**, *15*, 107–143.
[378] G. Y. Shevelev, E. L. Gulyak, A. A. Lomzov, A. A. Kuzhelev, O. A. Krumkacheva, M. S. Kupryushkin, V. M. Tormyshev, M. V. Fedin, E. G. Bagryanskaya, D. V. Pyshnyi, *J. Phys. Chem. B* **2018**, *122*, 137–143.
[379] B. A. Springer, S. G. Sligar, *Proc. Natl. Acad. Sci. U.S.A.* **1987**, *84*, 8–9.
[380] S. A. Bylkas, L. A. Andersson, *J. Chem. Educ.* **1997**, *74*, 426.
[381] L. Tofani, A. Feis, R. E. Snoke, D. Berti, P. Baglioni, G. Smulevich, *Biophys. J.* **2004**, *87*, 1186–1195.
[382] H. G. T. Ly, T. N. Parac-Vogt, *ChemPhysChem* **2017**, *18*, 2451–2458.
[383] D. Abdullin, F. Duthie, A. Meyer, E. S. Müller, G. Hagelueken, O. Schiemann, *J. Phys. Chem. B* **2015**, *119*, 13539–13542.

[384] D. Abdullin, P. Rauh Corro, T. Hett, O. Schiemann, *Magn. Reson. Chem.* **2024**, *62*, 37–60.
[385] B. G. Wilhelm, S. Mandad, S. Truckenbrodt, K. Kroϔnert, C. Schäfer, B. Rammner, S. J. Koo, G. A. Claßen, M. Krauss, V. Haucke, H. Urlaub, S. O. Rizzoli, *Science* **2014**, *344*, 1023–1028.
[386] J. Kale, E. J. Osterlund, D. W. Andrews, *Cell Death Differ.* **2017**, *25*, 65–80.
[387] S. Kucher, C. Elsner, M. Safonova, S. Maffini, E. Bordignon, *J. Phys. Chem. Lett.* **2021**, *12*, 3679–3684.
[388] S. Arora, J. Gordon, M. Hook, *Front. Microbiol.* **2021**, *12:628798*, DOI 10.3389/FMICB.2021.628798.
[389] S. Shan, S. Luo, Z. Yang, J. Hong, Y. Su, F. Ding, L. Fu, C. Li, P. Chen, J. Ma, X. Shi, Q. Zhang, B. Berger, L. Zhang, J. Peng, *Proc. Natl. Acad. Sci. U.S.A.* **2022**, *119*, e2122954119.
[390] L. Fábregas Ibáñez, G. Jeschke, *Phys. Chem. Chem. Phys.* **2020**, *22*, 1855–1868.
[391] K. Ackermann, J. L. Wort, B. E. Bode, *J. Phys. Chem. B* **2021**, *125*, 5358–5364.
[392] K. Ackermann, J. L. Wort, B. E. Bode, *Chem. Commun.* **2022**, *58*, 8790–8793.
[393] G. Hagelueken, "Colab running mtsslWizard for bipedal labels," can be found under https://github.com/gha2012/mtsslWizard_colab/blob/main/mtsslWizard_colab.ipynb, **2023**.
[394] G. Hagelueken, "mtsslWizard for bipedal labels," can be found under https://github.com/gha2012/mtsslWizard_bipedal, **2023**.
[395] J. L. Wort, K. Ackermann, A. Giannoulis, B. E. Bode, *J. Magn. Reson.* **2023**, *352*, 107460.
[396] V. Vitali, K. Ackermann, G. Hagelueken, B. E. Bode, *Appl. Magn. Reson.* **2023**, 1–19.
[397] C. Decroos, V. Balland, J. L. Boucher, G. Bertho, Y. Xu-Li, D. Mansuy, *Chem. Res. Toxicol.* **2013**, *26*, 1561–1569.
[398] B. Driesschaert, A. A. Bobko, T. D. Eubank, A. Samouilov, V. V. Khramtsov, J. L. Zweier, *Bioorg. Med. Chem. Lett.* **2016**, *26*, 1742–1744.
[399] S. Okazaki, A. Mannan, K. Sawai, T. Masumizu, Y. Miura, K. Takeshita, *Free Radic. Res.* **2009**, *41*, 1069–1077.
[400] A. P. Jagtap, I. Krstic, N. C. Kunjir, R. Hänsel, T. F. Prisner, S. T. Sigurdsson, *Free Radic. Res.* **2015**, *49*, 78–85.
[401] C. Wuebben, Spin Labeling of and EPR Spectroscopic Studies on Functional Oligonucleotides, **2021**.
[402] I. Krstić, R. Hänsel, O. Romainczyk, J. W. Engels, V. Dötsch, T. F. Prisner, *Angew. Chem. Int. Ed.* **2011**, *50*, 5070–5074.
[403] F. Wojciechowski, A. Groß, I. T. Holder, L. Knörr, M. Drescher, J. S. Hartig, *Chem. Commun.* **2015**, *51*, 13850–13853.
[404] Y. Yang, B. Bin Pan, X. Tan, F. Yang, Y. Liu, X. C. Su, D. Goldfarb, *J. Phys. Chem. Lett.* **2020**, *11*, 1141–1147.
[405] H. X. Zhou, *FEBS Lett.* **2013**, *587*, 1053–1061.
[406] Y. Wang, M. Sarkar, A. E. Smith, A. S. Krois, G. J. Pielak, *J. Am. Chem. Soc.* **2012**, *134*, 16614–16618.
[407] J. R. Masters, *Nat. Rev. Cancer* **2002**, *2*, 315–319.
[408] M. Letzelter, I. Sorg, L. J. Mota, S. Meyer, J. Stalder, M. Feldman, M. Kuhn, I. Callebaut, G. R. Cornelis, *EMBO J.* **2006**, *25*, 3223–3233.
[409] C. Altenbach, K. J. Oh, R. J. Trabanino, K. Hideg, W. L. Hubbell, *Biochemistry* **2001**, *40*, 15471–15482.
[410] A. Alex, V. Piano, S. Polley, M. Stuiver, S. Voss, G. Ciossani, K. Overlack, B. Voss, S. Wohlgemuth, A. Petrovic, Y. Wu, P. Selenko, A. Musacchio, S. Maffini, *Elife* **2019**, *8*, e48287.
[411] Z. Hasanbasri, K. Singewald, T. D. Gluth, B. Driesschaert, S. Saxena, *J. Phys. Chem. B* **2021**, *125*, 5265–5274.

[412] V. M. Tormyshev, A. S. Chubarov, O. A. Krumkacheva, D. V. Trukhin, O. Y. Rogozhnikova, A. S. Spitsyna, A. A. Kuzhelev, V. V. Koval, M. V. Fedin, T. S. Godovikova, M. K. Bowman, E. G. Bagryanskaya, *Chem. Eur. J.* **2020**, *26*, 2705–2712.
[413] C. A. Heubach, Z. Hasanbasri, D. Abdullin, A. Reuter, B. Korzekwa, S. Saxena, O. Schiemann, *Chem. Eur. J.* **2023**, *29*, e202302541.
[414] S. Ghosh, S. Saxena, G. Jeschke, *Appl. Magn. Reson.* **2018**, *49*, 1281–1298.
[415] K. Singewald, J. A. Wilkinson, Z. Hasanbasri, S. Saxena, *Protein Sci.* **2022**, *31*, e4359.
[416] B. F. Korzekwa, Application of Metal Ion Spin Labels for EPR Distance Measurements Based on the Double-Histidine Motif, **2021**.
[417] N. J. Greenfield, *Nat. Protoc.* **2006**, *1*, 2527.
[418] D. M. Rogers, S. B. Jasim, N. T. Dyer, F. Auvray, M. Réfrégiers, J. D. Hirst, *Chem* **2019**, *5*, 2751–2774.
[419] D. M. Engelhard, A. Meyer, A. Berndhäuser, O. Schiemann, G. H. Clever, *Chem. Commun.* **2018**, *54*, 7455–7458.
[420] A. Gamble Jarvi, K. Ranguelova, S. Ghosh, R. T. Weber, S. Saxena, *J. Phys. Chem. B* **2018**, *122*, 10669–10677.
[421] A. Doll, G. Jeschke, *J. Magn. Reson.* **2014**, *246*, 18–26.
[422] D. Klose, S. P. B. Vemulapalli, M. Richman, S. Rudnick, V. Aisha, M. Abayev, M. Chemerovski, M. Shviro, D. Zitoun, K. Majer, N. Wili, G. Goobes, C. Griesinger, G. Jeschke, S. Rahimipour, *Phys. Chem. Chem. Phys.* **2022**, *24*, 6699–6715.
[423] V. Vitali, K. Ackermann, G. Hagelueken, B. E. Bode, *Appl. Magn. Reson.* **2023**, *55*, 187–205.
[424] D. Abdullin, P. Brehm, N. Fleck, S. Spicher, S. Grimme, O. Schiemann, *Chem. Eur. J.* **2019**, *25*, 14388–14398.
[425] H. Liu, J. H. Naismith, *BMC Biotechnol.* **2008**, *8*, 91.
[426] J. A. Spudich, S. Watt, *J. Biol. Chem.* **1971**, *246*, 4866–4871.
[427] M. Azarkh, V. Singh, O. Okle, I. T. Seemann, D. R. Dietrich, J. S. Hartig, M. Drescher, *Nat. Protoc.* **2013**, *8*, 131–147.